CONF-760601-P2
Distribution Category UC-34

PROCEEDINGS OF THE CONFERENCE ON NEUTRON SCATTERING

GATLINBURG, TENNESSEE, U.S.A, JUNE 6-10, 1976

R. M. Moon, Editor

VOLUME II

September 1, 1976

NOTICE
This report was prepared as an account of work sponsored by the United States Government. Neither the United States nor the United States Energy Research and Development Administration, nor any of their employees, nor any of their contractors, subcontractors, or their employees, makes any warranty, express or implied, or assumes any legal liability or responsibility for the accuracy, completeness or usefulness of any information, apparatus, product or process disclosed, or represents that its use would not infringe privately owned rights.

Sponsored by

OAK RIDGE NATIONAL LABORATORY
and the
U.S. ENERGY RESEARCH AND DEVELOPMENT ADMINISTRATION

MASTER

This document is
PUBLICLY RELEASABLE
Larry E. Williams
Authorizing Official
Date: 04/05/2007

DISTRIBUTION

DISCLAIMER

This report was prepared as an account of work sponsored by an agency of the United States Government. Neither the United States Government nor any agency Thereof, nor any of their employees, makes any warranty, express or implied, or assumes any legal liability or responsibility for the accuracy, completeness, or usefulness of any information, apparatus, product, or process disclosed, or represents that its use would not infringe privately owned rights. Reference herein to any specific commercial product, process, or service by trade name, trademark, manufacturer, or otherwise does not necessarily constitute or imply its endorsement, recommendation, or favoring by the United States Government or any agency thereof. The views and opinions of authors expressed herein do not necessarily state or reflect those of the United States Government or any agency thereof.

DISCLAIMER

Portions of this document may be illegible in electronic image products. Images are produced from the best available original document.

TABLE OF CONTENTS

VOLUME I

Preface iii

HISTORY

Physics With Early Neutrons, *C. G. Shull** 1

STRUCTURES

Structures of One Dimensional Compounds, *S. W. Peterson** *and A. H. Reis, Jr.* 17

Determination of Hydration and Hydrogen Atom Location in Proteins *B. P. Schoenborn**, *G. Darling, and J. Cain* 35

Secondary Extinction in Neutron Diffraction, *V. F. Sears* 36

Non-Planarity of Hydroxamic Acids. A Neutron Diffraction Study of Hydroxyurea, *W. E. Thiessen, H. A. Levy and B. D. Flaig* . . 40

Dodecatungstophosphoric Acid Hexahydrate, $(H_5O_2^+)_3(PW_{12}O_{40}^{3-})$. The True Structure of Keggin's "Pentahydrate" from Single-Crystal X-ray and Neutron Diffraction Data, *G. M. Brown, M. -R. Noe-Spirlet, W. R. Busing and H. A. Levy* 41

Crystal Structure of Tripotassium Hydroxylaminetrisulfonate Sesquihydrate, $K_3[SO_3ON(SO_3)_2]\cdot 3/2H_2O$, *G. M. Brown and O. A. W. Strydom* 43

Structural Studies of the $BaPb_{1-x}Bi_xO_3$ System, *D. E. Cox and A. W. Sleight* 45

High Pressure Neutron Diffraction Study of α-Si_3N_4, *J. D. Jorgensen, T. G. Worlton, S. R. Srinivasa and L. Cartz* 55

Neutron Diffraction Studies of Carbohydrates, *V. J. James, J. Ollis, J. D. Stevens and F. H. Moore* 62

Combined X-ray and Neutron Diffraction Studies of the Intermetallic System $(Cr_{1-x}Fe_x)_{1+\delta}Sb$, *E. Hellner, G. Heger, D. Mullen and W. Treutmann* 71

Crystal Structure of High-Temperature, Superionic Conductors: Silver Iodide, Cuprous Iodide and - Bromide, *W. Bührer* 77

Two-Dimensional Structure of Mono and Bilayer of Krypton Absorbed on Graphite, *P. Thorel, B. Croset, C. Marti, and J. P. Coulomb* 85

Clustering in $Cu^{65}_{0.435}Ni^{62}_{0.565}$ and its Temperature Dependence, *J. Vrijen, C. van Dijk and S. Radelaar* 92

Neutron Small Angle Scattering Studies on Aluminum Alloys, *D. Allen, J. E. Epperson, V. Gerold, G. Kostorz, S. Messoloras and R. J. Stewart* 102

Neutron Scattering From Specifically Deuterated Lipid Membranes, *G. Büldt, A. Seelig, J. Seelig and G. Zaccai* 109

LATTICE DYNAMICS

Investigations of Phonon Perturbations by Defects, *R. M. Nicklow** 117

Investigations on the Lattice Dynamics of the Carbides and Nitrides of Niobium and Titanium, *F. Gompf, L. Pintschovius, W. Reichardt and B. Scheerer* 129

Phonon Spectra of Chevrel-Phase Molybdenum Chalcogenide Superconductors, *S. K. Sinha, S. D. Bader, G. S. Knapp, G. E. Ostrowski and R. N. Shelton* 136

Phonon Dispersion and Mode Softening in $Pb_{.87}Sn_{.13}Te$, *W. J. Daughton, E. Gurmen and C. W. Tompson* 145

The Lattice Dynamics of the Deuterium Peroxide Crystal, *S. F. Trevino, M. K. Farr, P. A. Gigüere and J. L. Arnau* 152

Neutron Scattering from Interstitials in AgCl and AgBr at High Temperatures, *R. F. Wood and M. Mostoller* 160

Resonant Modes of Complex Defects in Solids, *M. Mostoller and R. F. Wood* 167

Lattice Dynamics of MnO, *V. Wagner, W. Reichardt and W. Kress* . . 175

Lattice Dynamics of α-Arsenic, *W. Reichardt and K. H. Rieder* . . 181

Lattice Dynamics of Neon at High Pressure, *J. Eckert, J. D. Axe and W. B. Daniels* 187

Low-Dimensional Features in Phonon Dispersion Surfaces, *B. Dorner* 194

Overlap Shell Model and Bond Charge Model in Lattice Dynamics of Cubic Crystals, *K. Kunc and H. Bilz* 195

Lattice Vibrations in $Rb_{1-c}K_c$ Alloys in the Coherent Potential Approximation, *M. Mostoller and T. Kaplan* 202

Phonon Dispersion in NiO, *R. A. Coy, C. W. Tompson and E. Gürmen* 210

Lattice Dynamics of GeS, *W. Kress, A. Frey, B. Dorner and W. Kaiser* 216

Temperature Dependence of the Phonon Density of States for Some A15 Compounds, *E. Schneider, P. Schweiss and W. Reichardt* . . 223

Effect of the Superconducting Transition on the Frequencies and Damping of Transverse Acoustic Phonons in Lead†, *V. I. Bobrovsky, B. N. Goshchitskii, A. V. Mirmelstein and Yu. N. Mikhailov* 230

Mode Gruneisen Parameters of KBr Determined by Inelastic Neutron Scattering, *M. K. Farr and S. F. Trevino* 237

Pressure Dependence of Phonon Frequencies in Potassium, *J. Meyer, G. Dolling, J. Kalus, C. Vettier and J. Paureau* 243

Generalized Susceptibilities and Electronically Driven Phonon Anomalies in Transition Metal Carbides, *M. Gupta and A. J. Freeman* 250

MOLECULAR DYNAMICS

Neutron Scattering by Molecules, Polymers, and Absorbed Species, *J. W. White** 261

Dynamics of Molecular Crystals, *G. Dolling** 263

Reorientations of Cyclic Ether Molecules in Clathrate Deuterates, *J. Vanderhaeghen, W. Wegener, S. Hautecler, E. Legrand and L. Van Gerven* 281

Ammonium Ion Dynamics in $(NH_4)_2SO_4$ and $[(NH_4)_xK_{1-x}]_2SO_4$, *P. P. Chandra, B. A. Dasannacharya, P. S. Goyal, P. K. Iyengar, K. R. Rao, C. L. Thaper and A. H. Venkatesh* 288

Quasi-Elastic Neutron Scattering Study of Single Crystal Ammonium Perchlorate, *N. J. Chesser and H. J. Prask* 295

Diffusive Motions of Molecules on Catalytic Surfaces, *R. Stockmeyer, H. J. Stortnik and H. M. Conrad* 303

Rotational Motion in Plastic-Crystalline Adamantane: Results from High Resolution Quasielastic Neutron Scattering, *R. E. Lechner* 310

Orientational Dynamics of Molecular Crystals, *H. de Raedt and K. H. Michel* 317

Quasi-Elastic Scattering From Dilute Polymer Solutions, *R. E. Ghosh and J. S. Higgins* 323

Tunnelsplitting and Rotational Potentials in Dimethylacetylene and Tetramethyllead by μeV-Neutron Spectroscopy, *A. Kollmar and B. Alefeld* 330

Potential-Function Calculations of Lattice Vibrations in Formic Acid and Comparison with Neutron-Scattering Spectrum, *C. V. Berney, D. H. Johnson, S. Yip and S. H. Chen* 337

Dynamical Properties of Small Fluid Particles, *S. W. Lovesey and P. Schofield* 343

Conformational Motions of Long Chain Molecules in Rubbers and Networks, *J. S. Higgins* 344

PHASE TRANSITIONS

Incommensurate Structural Phase Transformations, *J. D. Axe** . . . 353

Liquid Crystals and Neutron Scattering, *T. Riste** 379

Magnetic Critical Scattering: Static and Dynamic Scaling Theories, *J. M. Hastings** 393

Soft Phonon and Central Peak Scattering in a Molecular Crystal System: $C_6Cl_4O_2$ (Chloranil), *W. D. Ellenson and J. K. Kjems* . 394

Structural and Magnetic Transitions in $BaMnF_4$, *S. M. Shapiro, R. A. Cowley, D. E. Cox, M. Eibschütz and H. J. Guggenheim* . . 399

Incommensurate Lattice-Instability in K_2SeO_4, *M. Iizumi, J. D. Axe, G. Shirane and K. Shimaoka* 406

Critical Scattering From Structural Phase Transitions Associated With a Homogeneous Deformation of the Crystal, *R. A. Cowley* . 412

Order-Disorder in Iron-Cobalt Alloys, *M. F. Collins and J. A. Oyedele* 418

Magnetic Short Range Order in Gd, *H. R. Child* 425

Investigation of the Dynamical Structure Factor of $K_2Pt(CN)_4Br_{0.3} \cdot 3.2D_2O$ (KCP), *L. Pintschovius, B. Renker and R. Comès* 432

Hydrogen Bonding and Structural Phase Transitions in $(CH_3NH_3)_2MnCl_4$, *G. Heger and D. Mullen* 439

Spatial Distribution of the Para- and Ferroelectric Phases During the First-Order Phase Transition in DKDP, *C. M. E. Zeyen and H. Meister* 445

Observation of a Reorientation of the Holmium Moments in $HoAl_2$ With Polarized Neutron Diffraction, *B. Barbara, J. X. Boucherle, M. F. Rossignol and J. Schweizer* 452

Observation of a Spatial Cross-Over in Polymer Solutions by Small Angle Neutron Scattering, *B. Farnoux* 459

Neutron and Light Scattering by Polymer Diffusive Modes in Solution: A Comparison, *G. Jannink* 465

Small Angle Neutron Scattering by Polymer Solutions: Tricritical Effects, *M. Daoud* 466

Distribution of Transport Currents in Type-II Superconductors Investigated by Neutron Small Angle Scattering, *J. Schelten and D. M. Kroeger* 473

Small Angle, Double Silicon Crystal, Neutron Diffraction Studies of the Fluxoid Lattice in Superconducting Niobium, *F. Tasset, D. K. Christen, S. Spooner and H. A. Mook* 481

HYDROGEN IN METALS

Neutron Scattering Studies of the Diffusion of Hydrogen in Metals *J. M. Rowe** 491

Neutron Diffraction Studies of Transition Metal Hydride Complexes *T. F. Koetzle and R. Bau* 507

Deuterium-Site Occupancy in the α and β Phases of TiD_x, *H. A. Alperin, H. Flotow, J. J. Rush and J. J. Rhyne* 517

A Method for Determination of the Position of Hydrogen in a Metal *T. Matsumoto* 522

A Neutron Scattering Study of the Vibrational Modes of Hydrogen in the Superconducting Compound, Th_4H_{15}, *J. F. Miller, C. B. Satterthwaite, T. O. Brun, J. D. Jorgensen and K. Sköld* . . . 529

The Optical Phonon Spectra of PdH_x at 80 K for X = 0.29, 0.51, 0.63, 0.7., *J. D. Jorgensen, K. Sköld, A. Rahman, C. A. Pelizzari, H. E. Flotow, R. J. Miller, R. Standley and T. O. Brun* 535

Inelastic Neutron Scattering Lineshapes in $PdD_{.63}$, *C. J. Glinka, J. M. Rowe, J. J. Rush, A. Rahman, S. K. Sinha and H. E. Flotow* 536

Coherent Neutron Scattering Study of the Vibrations of Interstitial Deuterium in α-$VD_{0.7}$, *J. J. Rush, J. M. Rowe, C. J. Glinka, N. Vagelatos and H. E. Flotow* 543

Microscopic Calculation of the Phonon Dispersion in LiD, *R. Zeyher* 550

The Motions of Hydrogen in α-Palladium-Hydride, *W. Kley, W. Drexel, A. Murani, D. Tocchetti, I. Sosnowska and D. K. Ross* . 558

The Investigations of Hydrogen Diffusion in Nb With Interstitial Traps by Quasielastic Neutron Scattering, *D. Richter, K. W. Kehr and T. Springer* 568

VOLUME II

MAGNETIC MOMENT DISTRIBUTIONS

Magnetic Form Factor of 3d and 4d Paramagnetic Metals, *R. M. Moon*, W. C. Koehler, and J. W. Cable* 577

Theoretical Determinations of Magnetization Densities and Neutron Magnetic Form Factors in Metals, *A. J. Freeman* 592

Magnetisation Distribution in a Partially Disordered Au_4V Alloy, *P. J. Brown and K. R. A. Ziebeck* 616

Polarized-Neutron Studies of ^{242}PuP and $^{242}PuFe_2$, *G. H. Lander and J. F. Reddy* 623

The Structural and Magnetic Properties of MnAs Studied by Substituting Mn With Other Transition Metals, *A. F. Andresen, K. Selte and A. Kjekshus* 630

Magnetic Moment Distribution in Cu_2MnAl, *V. C. Rakhecha, R. Chakravarthy and N. S. Satya Murthy* 638

A Neutron Diffraction Study of Cobalt-Doped $YbFeO_3$, *S. K. Paranjpe and R. J. Begum* 643

Polarized Neutron Study of the Nitroxide Radical in the Di-(2,2,6,6-Tetramethyl-4-Piperidinyl-1-Oxyl) Suberate, *P. J. Brown, A. Capiomont, P. Chenavas, P. Radhakrishna and J. Schweizer* . 650

Small Angle Neutron Scattering Study of a Au-15 at.% Fe Alloy†, *A. P. Murani* 657

Small Angle Scattering of Neutrons and Magnetic Structure of Invar Alloys†, *A. Z. Men'shikov, S. K. Sidorov and V. A. Shestakov* 663

Temperature Dependence of Magnetic Moment Distribution Around Mn Impurities in Iron, *F. Mezei* 670

Asphericity of Spin Density in Disordered Ferromagnetic Alloys, *F. Menzinger and F. Sacchetti* 677

Magnetic Defect Scattering From γ-Mn Cu & γ-Mn Pd, *J. R. Davis and T. J. Hicks* 684

Reduced A-Site Moment in Fe_3O_4, *V. C. Rakhecha, R. Chakravarthy and N. S. Satya Murthy* 690

The Influence of Anisotropy on the d=2 and d=3 Magnetic Ordering in Layer-Type Antiferromagnets $K_2Mn_{1-x}Fe_xF_4$, Studied by Neutron Diffraction, *L. Bevaart, E. Frikkee and L. J. de Jongh* 697

Effect of a Bloch Wall as a Helical Magnetic Structure on the Passage of Neutrons, *O. Schärpf* 706

Measurement of Neutron Birefringence in Magnetic Structures, *O. Schärpf and H. Strothmann* 713

Magnetic Domain Structures Studied by Neutron Depolarization, *W. H. Kraan, M. Th. Rekveldt and J. J. Van Loef* 720

MAGNETIC EXCITAIONS

Magnetic Excitations in Itinerant Electron Systems, *J. F. Cooke** 723

Magnetic Excitations in Rare Earth Metals, *J. G. Houmann** *and H. Bjerrum Møller* 743

Neutron Scattering From Isolated Clusters of Magnetic Ions, *W. J. L. Buyers, E. C. Svensson and T. M. Holden* 771

Spin Wave Dispersion in $Li_{0.13}Fe_{2.87}O_4$, *V. C. Rakhecha, K. R. Rao and N. S. Satya Murthy* 778

Spin Waves in Ferrimagnetic $ErFe_2$, *J. J. Rhyne, N. C. Koon, J. B. Milstein and H. A. Alperin* 783

Spin Wave Dispersion in Tb-Y Alloys, *N. Wakabayashi and R. M. Nicklow* 789

Theoretical Calculation of the Exchange Integral for Europium, *J. F. Cooke and H. L. Davis* 793

Spectral Density Functions for Amorphous Solids, *D. G. Hall and J. S. Faulkner* 800

Polarization Dependence of Magnetic Neutron Scattering, *M. Blume* 807

The Dynamics of the One-Dimensional Ferromagnetic Chain System $CsNiF_3$, *M. Steiner* 811

Elementary Excitations in Some 3d Metal Alloys†, *K. Mikke and J. Jankowska* 818

The Generalized Susceptibility of $Mn_{.73}Ni_{.27}$, *B. Hennion, M. T. Hutchings, R. D. Lowde, M. W. Stringfellow and D. Tocchetti* . 825

Influence of the Order-Disorder Transition in Fe_3Al on the Low-Energy Spin Waves, *E. Frikkee and K. Mikke* 832

Magnon-Phonon-Hybridisation in $FeCl_2$, *K. R. A. Ziebeck and J. G. Houmann* 840

Static and Dynamic Response Functions for a Classical Paramagnet in an Applied Field, *S. W. Lovesey and J. M. Loveluck* 847

Investigation of Spin Dynamics of Dilute Magnetic Alloys by Diffuse Neutron Scattering, *M. Loewenhaupt, H. Scheuer and W. Schmatz* 856

A Study of Crystal-Field Split Levels of Pr^{3+} in PrF_3 by Inelastic Neutron Scattering, *N. Shamir, M. Melamud and H. Shaked* 864

Inelastic Neutron Scattering Measurements on $CeAl_3$ and $Ce_{.8}Th_{.2}$, *A. S. Edelstein, R. Majewski, S. K. Sinha, T. Brun, C. A. Pelizzari and H. R. Child* 873

Some Experiments on Neutron Inelastic Scattering at the Pulsed Reactor IBR-30, *K. Hennig, L. Kaun, B. Lippold and W. Matz* . . 878

LIQUIDS AND GASES

Structure of Liquids, *A. H. Narten** 889

Dynamics of Simple Fluids, *P. A. Egelstaff** 909

Neutron Scattering From Quantum Liquids, *R. A. Cowley** 935

Short Wavelength Collective Density Excitations in Monatomic Liquids, *S. W. Lovesey and J. W. E. Lewis* 954

Neutron Diffraction Studies of Tetrachloride Liquids and Liquid Mixtures, *J. H. Clarke, J. C. Dore and G. W. Stanton* 955

Observation of Enhanced Self Diffusion in High Density Gaseous Hydrogen by Incoherent Neutron Scattering, *T. A. Postol, S. H. Chen and K. Sköld* 962

Neutron Scattering From Dilute and Moderately Dense Gases, *J. W. Dufty, L. J. Groome, K. E. Gubbins and P. A. Egelstaff* 968

Neutron Diffraction Studies of Liquids at High Momentum Transfer, *J. H. Clarke, J. C. Dore and G. Walford* 975

Low Frequency Molecular Vibrations in 1-Bromopentane and 1,5-Dibromopentane by Neutron Inelastic Scattering, *Y. P. Sharma, H. R. Danner and H. Kim* 982

The Dynamics of Liquid ^{3}He, *H. R. Glyde and F. C. Khanna* 989

Neutron Scattering Study of Elementary Excitations in Liquid Helium-3, *K. Sköld, C. A. Pelizzari, R. Kleb and G. E. Ostrowski* 996

Excitation Spectrum of ^{3}He-^{4}He Mixtures, *P. A. Hilton, W. G. Stirling and R. Scherm* 1003

The Dynamic Structure Factor of Nonsuperfluid Liquid ^{4}He, *A. D. B. Woods, E. C. Svensson and P. Martel* 1010

Low-Momentum-Transfer Neutron Scattering From Liquid ^{4}He at T = 4.2 K and P = 2.5 MPa, *E. C. Svensson, W. G. Stirling, A. D. B. Woods and P. Martel* 1017

Neutron Diffraction Studies of Heavy Water, *J. H. Clarke, J. C. Dore and G. Walford* 1022

The Structure Factor of Liquid Aluminum by Neutron Diffraction, *O. J. Eder and B. Kunsch* 1028

NEUTRON OPTICS AND TECHNIQUES

Neutron Small-Angle Scattering: Experimental Techniques and Applications, *W. Schmatz** 1037

Neutron Interferometry, *S. A. Werner**, *R. Colella, A. W. Overhauser and C. F. Eagen* 1060

Recent Developments in Polarised Neutrons, *J. B. Hayter** 1074

The Perfect Crystal Neutron Interferometer: A Tool for Novel and Precise Measurement, *W. Bauspiess, U. Bonse and H. Rauch* . . . 1094

Polarized Neutrons and Polarized Nuclear Targets, *A. Abragam, G. L. Bacchella, H. Glättli, A. Malinovski, P. Mériel, J. Piesvaux, M. Pinot and P. Roubeau* 1103

Gamma Rays and/or Neutrons?, *W. B. Yelon* 1110

Use of Single Crystal Silicon as a Thermal Neutron Filter, *R. M. Brugger and W. Yelon* 1117

Iron-Germanium Multilayer Neutron Polarizing Monochromators, *J. W. Lynn, J. K. Kjems, L. Passell and A. M. Saxena* 1123

Applications of the Fly's Neutron Camera: Diffraction Tomography and Phase Transition Studies, *J. B. Davidson and A. L. Case* 1124

Neutron Diffraction Topography: Recent Results in the Investigation of Domains and Crystal Defects, *M. Schlenker and J. Baruchel* 1136

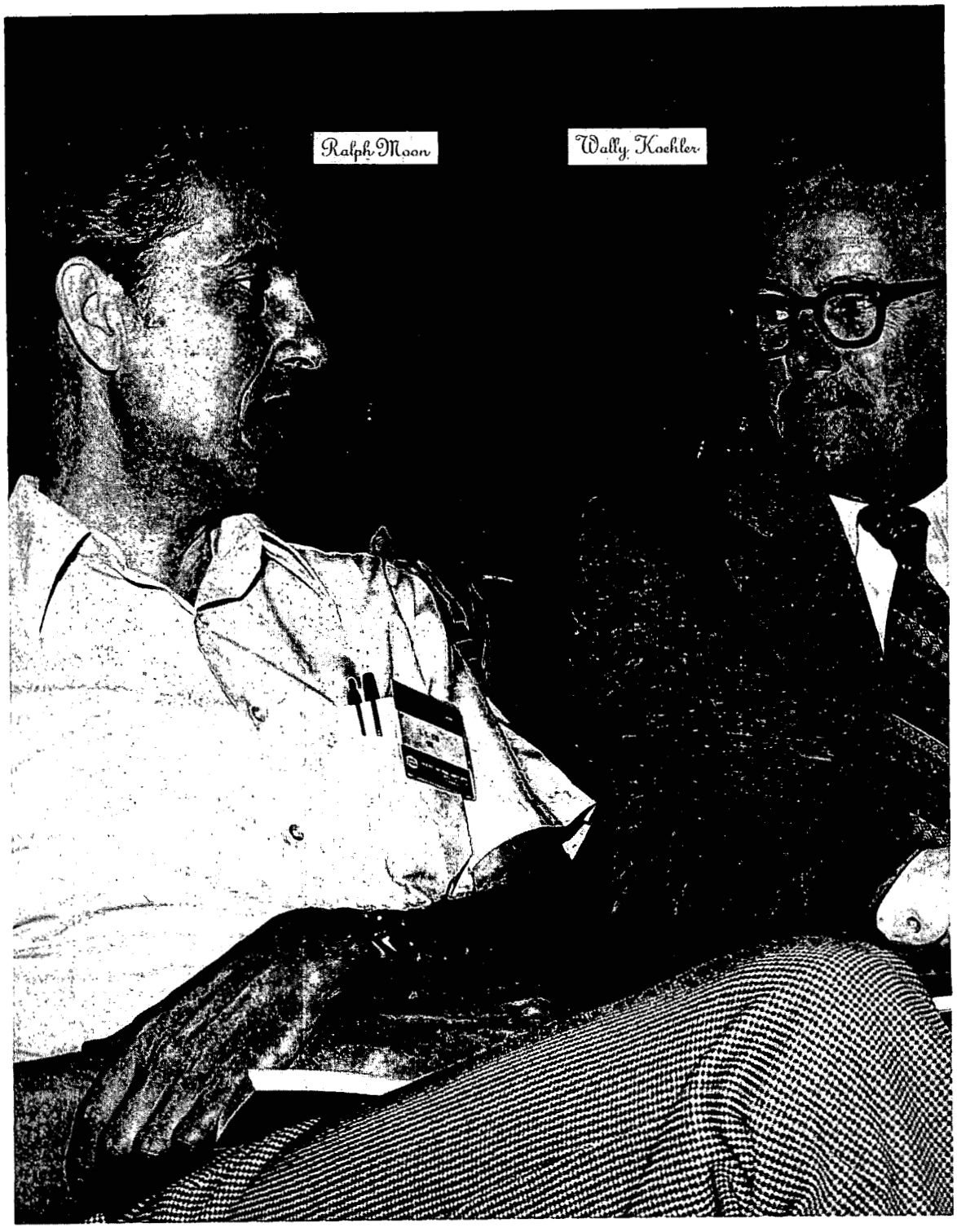
Progress in Neutron Monochromator Development at the Institut Laue-Langevin, *A. Freund* 1143

Neutron Properties of Curved Monochromators, *G. Albertini, A. Boeuf, S. Lagomarsino, S. Mazkedian, S. Melone and F. Rustichelli* 1151

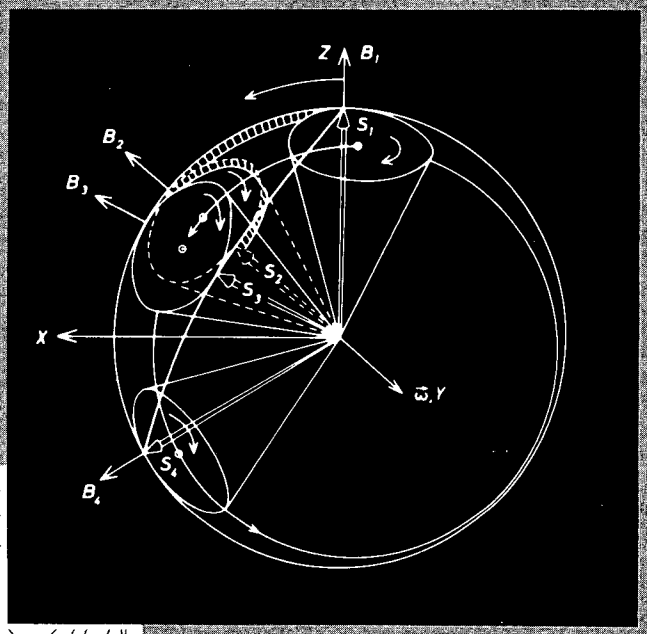
Survey of Detection Systems and Electronics for I.L.L. Experiments†, *J. Jacobé* 1159

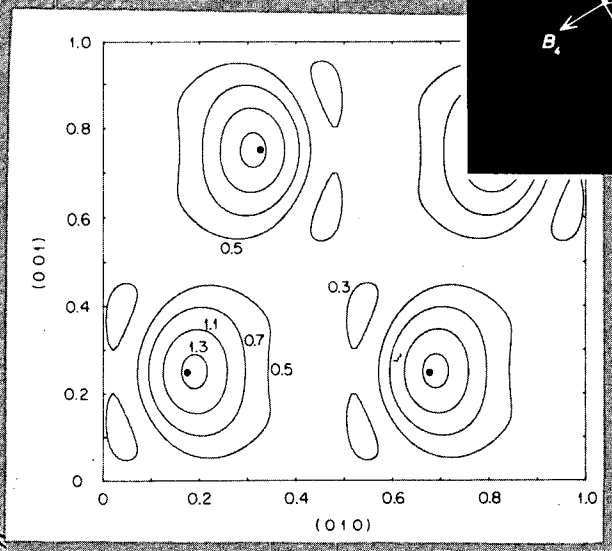
Author Index 1169

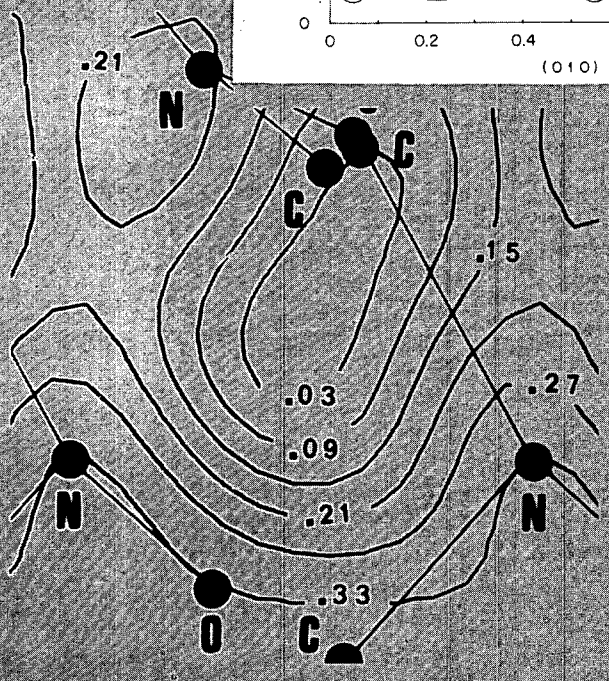
*Invited Speaker
†Paper not presented at conference


Ralph Moon
Wally Koehler

MAGNETIC MOMENT DISTRIBUTIONS







MAGNETIC FORM FACTOR OF 3d AND 4d PARAMAGNETIC METALS*

R. M. Moon, W. C. Koehler and J. W. Cable
Solid State Division, Oak Ridge National Laboratory
Oak Ridge, Tennessee 37830

ABSTRACT

A survey of published results on magnetic-form factors of Cr, V, Sc and Pd is presented, together with a preliminary report on new results for Ti, Y and Nb. The data clearly show the inadequacy of free atom or extreme tight-binding models in describing the outer electronic density in transition metals. In several cases there is good agreement with APW calculations, giving confidence in the accuracy of the APW wave functions. Experimental errors limiting the accuracy of polarized-beam measurements are discussed.

INTRODUCTION

One of the continuing goals of neutron diffraction research at many laboratories throughout the world has been the accurate measurement of magnetic form factors. In these measurements the Fourier transform of the magnetic moment density is observed. In contrast to the x-ray case, where the form factor is the Fourier transform of the total (core plus outer) electronic charge density, the magnetic form factor is determined almost entirely by the electrons outside of closed shells. It is this fact which gives a significance to the magnetic form factors which transcends the field of magnetism. These measurements supply the most sensitive experimental evidence on the spatial distribution of the outer electrons which are responsible for all the interesting chemical and physical properties of solids. Our concern is with the general wave function problem of electrons in solids and our measurements can serve as valuable tests for the accuracy of theoretical calculations which yield these wave functions.

*Research sponsored by the United States Energy Research and Development Administration under contract with Union Carbide Corporation.

Accurate magnetic form factor measurements began with the introduction of polarized-beam diffractometers[1] in the early 1960's. Most of the early work involved ferromagnetic samples where the relatively large electronic moments resulted in easily measured effects with the polarized beam technique. In recent years the addition of split-coil superconducting magnets to polarized-beam diffractometers and the availability of high flux reactors have made it possible to extend the form factor measurements to a number of paramagnetic metals. Since the calculation of paramagnetic energy bands is considerably easier than for ferromagnets this promises to be an area for fruitful interaction between theorists and experimentalists, as is already evident by the work of Freeman[2] and colleagues. In this paper we review the published work on 3d and 4d paramagnetic metals and present a preliminary report of our work on Ti, Y and Nb.

Before the first of the polarized-beam results were available, band theorists had given us a qualitative picture of the behavior of d electrons in the transition metals, as illustrated in Fig. 1 from the APW calculation on Fe by Wood.[3] For energies near the top of the band the 3d wave functions are very much like those calculated for the free atom, while for states near the bottom of the band the wave functions are significantly expanded relative to the free atom case. This behavior is not peculiar to Fe but is a general property of d electrons in metals. Since the induced spin in a paramagnet is associated with states at the Fermi level, it follows that we should expect to find, for metals near the right-hand end of the transition series, spin form factors which are similar to the free atom case. In moving to the left across the periodic table we should find spin form factors which fall off faster as a function of momentum transfer than their atomic

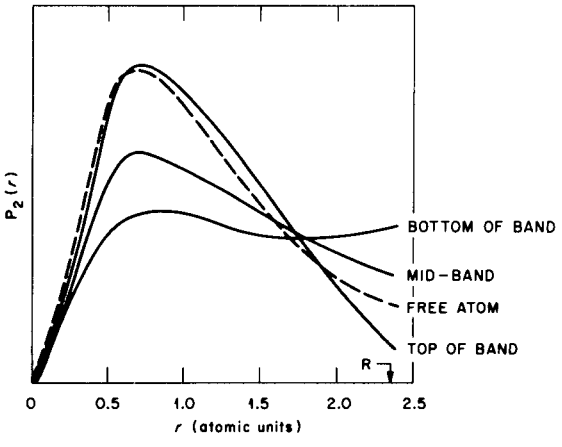


Fig. 1. Energy dependence of 3d radial wave functions in Fe. (See Ref. 3.)

counterparts, indicating expanded wave functions. The real situation is more complicated because of orbital contributions to the induced moment, but the general expectation should still be valid. Atomic models of the magnetic moment density should get progressively worse in approaching the left end of the transition series because of the expanded wave functions at the bottom of the d band.

It was somewhat surprising that this effect had not been seen with neutrons prior to our recent experiments. The first of the paramagnetic metal form factors to be observed was V by Shull and Ferrier,[4] who found good agreement with an atomic model based on a $3d^3 4s^2$ configuration. Similarly, the experimental form factor for Cr, both in the ordered state[5] and in the paramagnetic state,[6] is consistent with an atomic model based on a $3d^4 4s^2$ configuration. These results, at least in the case of Cr, are in agreement with band calculations.[7-8] The desire to see the 3d wave function expansion with neutrons was one of our strong motivations in undertaking measurements on Ti and Sc.

Another motivation was related to our earlier work on metallic Gd.[9] Except for the first two reflections the Gd results were in good agreement with Dirac-Fock calculations for the 4f electrons in the free atom. We attributed the extra scattering seen for the first two reflections to conduction electron polarization. Our results were in poor quantitative agreement with an APW calculation of the conduction spin density by Harmon and Freeman.[10] Because the presence of the large 4f moment complicated both the experimental and theoretical efforts to define the conduction electron spin density it was natural to turn to related systems in which the 4f contribution is not present. Gd has the hcp structure with 3 electrons in d and s states outside the 4f shell. The most logical candidate would be La except for the difficulty in obtaining single crystals. Both Y and Sc are also good choices and we have now carried out measurements on both of these materials. The Sc results[11] are in good agreement with APW calculations by Gupta and Freeman[12] and the wave function expansion is clearly evident in both experiment and theory.

EXPERIMENTAL

The small induced moments, typically several milli-Bohr magnetons, make the use of the polarized-beam technique[1] a necessity in measuring paramagnetic form factors. In this technique the ratio, R, of Bragg intensities is observed as the neutron spin is changed from parallel to anti-parallel to the applied field. In the limit of small magnetic scattering and a single-element sample this ratio is given by the equation

$$R-1 = \frac{4}{b}\left[\frac{\gamma e^2}{2mc^2}\langle M_z(\vec{\tau})\rangle + B\langle I_z\rangle + \hat{n}\cdot\vec{P}\,\frac{\gamma e^2}{2mc^2}\,\frac{m}{m_N}\,\frac{b'}{b}\,(Z-f(\vec{\tau})\cot\theta)\right] \quad (1)$$

where b is the coherent nuclear scattering amplitude, γ is the neutron moment in nuclear magnetons, $\langle M_z(\vec{\tau})\rangle$ is the Fourier transform of the electronic magnetization evaluated at the reciprocal lattice vector $\vec{\tau}$, B is the spin-dependent nuclear scattering amplitude, $\langle I_z\rangle$ is the nuclear polarization, m_N is the neutron mass, b' is the imaginary part of the nuclear amplitude, Z is the atomic number, $f(\vec{\tau})$ is the x-ray form factor, and θ is the Bragg angle. The unit vector $\hat{n}$ is in the direction $\vec{k} \times \vec{k}_o$ (the final and initial neutron wave vectors) and $\vec{P}$ is the neutron polarization. The second and third terms are usually quite small, which is fortunate since our goal is to measure $\langle M_z(\vec{\tau})\rangle$. Even if B is large, since the nuclear polarization varies inversely with temperature and the induced magnetization is nearly temperature independent, the importance of the nuclear term can be easily reduced by operating at a relatively high temperature. The third term is the neutron spin-neutron orbit contribution first predicted by Schwinger[13] and observed by Shull.[14] It can be readily calculated or experimentally separated since it is independent of both temperature and applied field and reverses sign in going from left- to right-handed scattering.

As in any diffraction experiment involving accurate intensity measurements, extinction and simultaneous Bragg reflections can result in serious errors. We have reduced these errors by working with small,

distorted samples and by making measurements at several wavelengths selected to avoid simultaneous reflections.

The small magnetic contribution to the Bragg intensity makes it necessary to achieve statistical uncertainties of 10^{-4} or better in R. At this level of statistical uncertainty there are new sources of error to consider which are usually insignificant for measurements on ferromagnets. Observations on a single peak may extend over a period of several days so that instrumental drifts in counting efficiency or mechanical stability can produce an error because of the sequential nature of the observations. This error can be reduced by using short counting times and reversing the neutron spin many times during the course of an experiment. Some experimenters[6] reverse the neutron spin many times per second but we have found that counting times in the 10-20 second range usually result in a drift correction which is quite small relative to the statistical uncertainty. If the drift correction is not small, it probably means that the crystal has shifted off the peak position and this can lead to an error which is not reduced by using faster counting cycles.

This peak positioning error is one of several undesirable magnetic field effects which have been discussed by Moon, Koehler and Shull.[15] These effects arise because as the neutrons enter the magnetic field at the sample position they are subject to a force proportional to the gradient of the field modulus, and the direction of this force is opposite for the two neutron spin states. This results in different velocity and position distributions for the two spin states at the sample location and affects the observed intensity ratio. Perhaps the most important of these effects is the change in velocity, or change in wavelength, resulting in a different Bragg angle (by about 10^{-4} deg.) for the two spin states. As shown in reference 15 the error in the flipping ratio is given by

$$\Delta R = - \frac{2|\mu_N|}{m_N v_o^2} \tan\theta \; H \frac{1}{S(\theta)} \frac{dS(\theta)}{d\theta} , \qquad (2)$$

where μ_N is the neutron moment, v_o is the neutron velocity, H is the central field and $S(\theta)$ defines the shape of the crystal rocking curve. It is

thus very important to position the crystal so that $dS/d\theta$ is as close to zero as possible. To illustrate the magnitude of this effect we show in Fig. 2 the calculated error in R as a function of wavelength for Gaussian peak shapes of various widths when the crystal is off the peak position by 0.02°. Recall that we want to reduce the total error to around 1×10^{-4}, so this effect can be quite serious. The task of setting and maintaining the crystal position to better than 0.02° over the course of an experiment is non-trivial, especially when the crystal is mounted in the center of a superconducting magnet. Sample support and control mechanisms are light weight to avoid excessive heat flow. Coolant levels vary slowly with time producing changing thermal gradients along the sample support. Our experience is that a shift of about 0.02° frequently occurs over a 24-hour period. The ideal crystal for these measurements has a broad, flat-topped rocking curve.

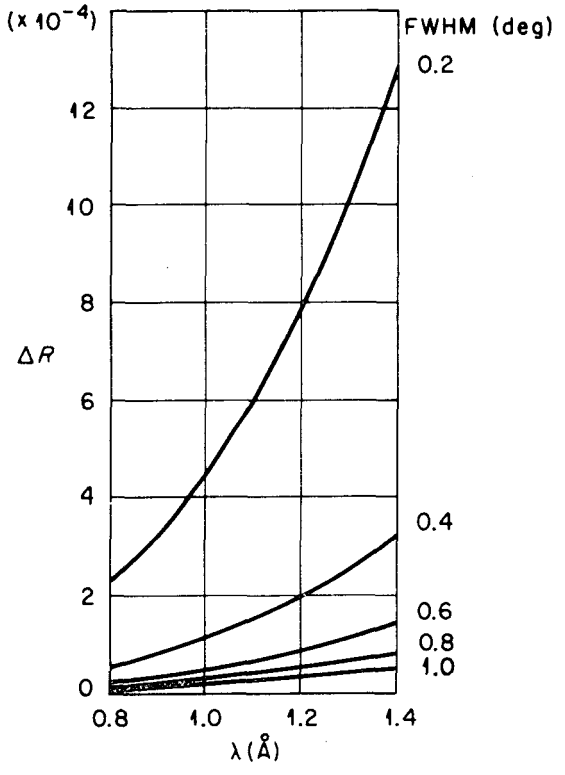


Fig. 2. Calculated error in flipping ratio for crystal misset off the peak position by 0.02° assuming Gaussian peak shapes of various widths. (H = 57.2 kOe, $\sin\theta/\lambda$ = 0.26 $(Å)^{-1}$)

We would like to point out another adverse field effect, one that was not discussed in reference 15. This effect is peculiar to superconducting magnets constructed for polarized beam work. When the first of the split-coil superconducting magnets was constructed at Brookhaven, it was found[16] that severe depolarization occurred for neutrons traveling in the median plane between the two coils through a zero-field region where the magnetic field was reversing direction. This was corrected by running the two coils with unequal currents, thus moving the zero-field region out

of the neutron beam. Subsequently, many magnets for polarized beam work have been designed with unequal turns in the two coils so that the coils can be operated with equal currents and still avoid zero-field regions along the neutron path. This cure for the depolarization problem has the undesirable side-effect that there is a vertical field gradient all along the neutron flight path. This produces a vertical separation of the two neutron spin states, as in the Stern-Gerlach experiment. The vertical angular deviation between two neutrons with opposite spins, each initially traveling on the same horizontal track with equal velocities, is given by

$$\delta(\uparrow) - \delta(\downarrow) = - \frac{2|\mu_N|}{m_N v_o^2} \int \frac{\partial H}{\partial z} \, d\rho \ , \qquad (3)$$

where the integration is along the neutron path, both into and out of the magnet. For our magnet operated at 60 kOe this angular deviation is about 6×10^{-4} deg., resulting in a vertical separation at the counter position of about 10^{-3} cm. Ordinarily this is not a problem because the counter diameter is large compared to the sample and the slits in front of the counter are wide enough to accept the entire reflected beam. However, if the crystal is slightly misaligned so that the reciprocal lattice vector is not exactly in the horizontal plane, the observed intensity can be sensitive to the vertical divergence with a resulting error in the flipping ratio. This can produce an apparent front-back effect, that is, different results when the crystal is rotated 180° about a vertical axis. If in one case the reflected beam is limited from above, it will be limited from below in the other case, and the error due to the vertical field gradient will be opposite in direction for the two cases.

We have demonstrated this effect by intentionally limiting the reflected beam from above, and then below, and observing the change in the flipping ratio, as illustrated in Fig. 3. At the top of this figure the upper half of the beam is cut off and the upper data point was observed. Because spin-up neutrons are bent down and spin-down neutrons are bent up, the mask absorbs more of the spin-down neutrons and the flipping ratio is more positive than it should be. When the lower half of the beam is cut

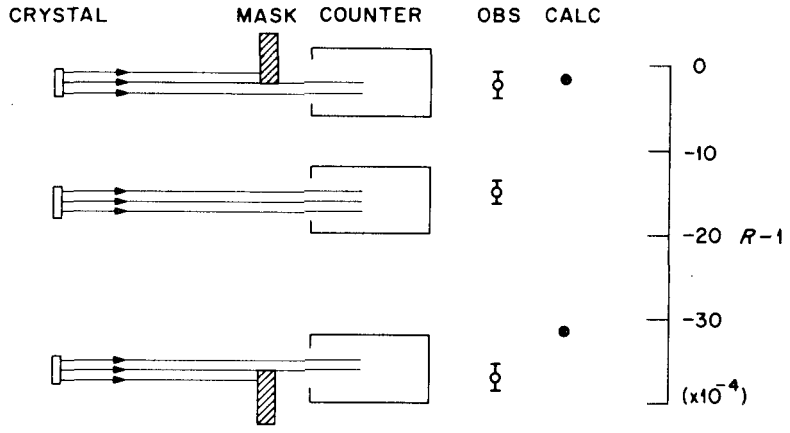


Fig. 3. Error produced by vertical component of field gradient in Ti(002) reflection.

off the lowest data point was observed, and the middle point, or true point, was observed with no limits on the reflected beam. The calculated points were obtained using Eq. (3) and the middle data point as a reference value. An auxiliary experiment in which the intensity was measured as a function of the mask position served to determine the sensitivity of the observed intensity to the neutron's vertical velocity component and was used in the calculation. The true data point is negative because the nuclear amplitude of Ti is negative.

We have seen that these field effects can produce very serious errors in polarized beam measurements. With a reasonable amount of experimental caution, reliable results can be obtained to accuracies in the flipping ratio of about 10^{-4}, but this seems to be approaching the limit that can be obtained with this technique. Further efforts to reduce the statistical errors must also be accompanied by very careful experimental control and knowledge of the field effects to avoid unreliable results.

Impurities in the sample, especially if they carry a local magnetic moment, can also lead to serious errors. Since an isolated magnetic impurity will make a contribution to the suceptibility which has a T^{-1} dependence, it is possible to reduce the influence of impurities by

operating at a relatively high temperature. We have collected most of our data at 100°K, a temperature chosen to reduce the effects of impurities and nuclear polarization yet still maintain a reasonable He lifetime in the cryostat. In addition we have used highly purified materials. The Sc crystals were cut from a sample loaned to us by F. H. Spedding and the Y crystals were grown from material purchased from the Ames Laboratory.

For the hexagonal crystals, the applied field of 57.2 kOe was in the basal plane, either along an $\vec{a}$ or $\vec{b}$ direction.

SURVEY OF RESULTS

From the measured flipping ratios, with small corrections for the nuclear polarization and neutron spin-neutron orbit contributions according to Eq. (1), we obtain a set of numbers giving the Fourier transform of the magnetization evaluated at reciprocal lattice positions. These are related to the generalized static susceptibility,[6,8]

$$\langle M_z(\vec{\tau})\rangle = \beta^{-1}\chi^{zz}(\vec{\tau},0)H \ , \tag{4}$$

where β is the Bohr magneton. The susceptibility may be written as the sum of several contributions,

$$\chi^{zz}(\vec{\tau},0) = -\chi_{dia}^{core}(\vec{\tau}) - \chi_{dia}^{Lan}(\vec{\tau}) + \chi_{sp}(\vec{\tau}) + \chi_{orb}(\vec{\tau}) \ , \tag{5}$$

where the first term is the diamagnetic contribution from the core electrons, the second is the Landau diamagnetism of the outer electrons, the third is the Pauli spin paramagnetism and the fourth is the Van Vleck orbital paramagnetism. For transition metals the largest contributions will be from the Pauli and Van Vleck terms. The Pauli spin paramagnetism arises from a shift of the spin-up and spin-down energies when a magnetic field is applied resulting in a repopulation of states at the Fermi level. The Van Vleck paramagnetism comes from an admixture of higher excited states into an unperturbed ground state by the applied field. Even though the unperturbed ground state has zero angular momentum the new ground state will have a non-zero angular momentum and a small orbital moment.

Only the core diamagnetic term is easy to calculate and we have chosen to correct the data for this contribution and present a magnetic form factor describing the total magnetization of the outer electrons. If χ is the atomic susceptibility measured in a standard bulk susceptibility experiment, then

$$\chi = \chi^{zz}(0,0) \ , \tag{6}$$

and we define the form factor for the outer electrons as

$$f(\vec{\tau}) = \frac{\langle M_z(\vec{\tau})\rangle + \beta^{-1}\chi_{dia}^{core}(0) f_{dia}(\vec{\tau})H}{\beta^{-1}[\chi + \chi_{dia}^{core}(0)]H} \tag{7}$$

where $f_{dia}(\vec{\tau})$ can be calculated following the equations given by Stassis,[17] and

$$\chi_{dia}^{core}(0) = \frac{e^2}{6mc^2} \sum \langle r_i^2 \rangle \ , \tag{8}$$

where the sum goes over the core electrons.

A summary of the experimental results on the 3d metals is shown in Fig. 4. Also shown are calculated curves based on an atomic model. In this model the Landau diamagnetism is ignored and the proportion of spin and orbital moments is obtained from other experiments. The spherical atomic form factors are taken from the work of Watson and Freeman[18,19] (the spin form factor is $\langle j_o \rangle$ and the orbital form factor is $\langle j_o \rangle + \langle j_2 \rangle$). There are several difficulties in constructing the atomic model:

(1) the proportion of spin and orbital moment is not well established in all cases,

(2) the distribution of spin moment between 4s and 3d states is not accurately known, although the 3d spin should be dominant in all cases,

(3) The shape of the atomic curve can be significantly altered by shifting electrons from 4s to 3d states.

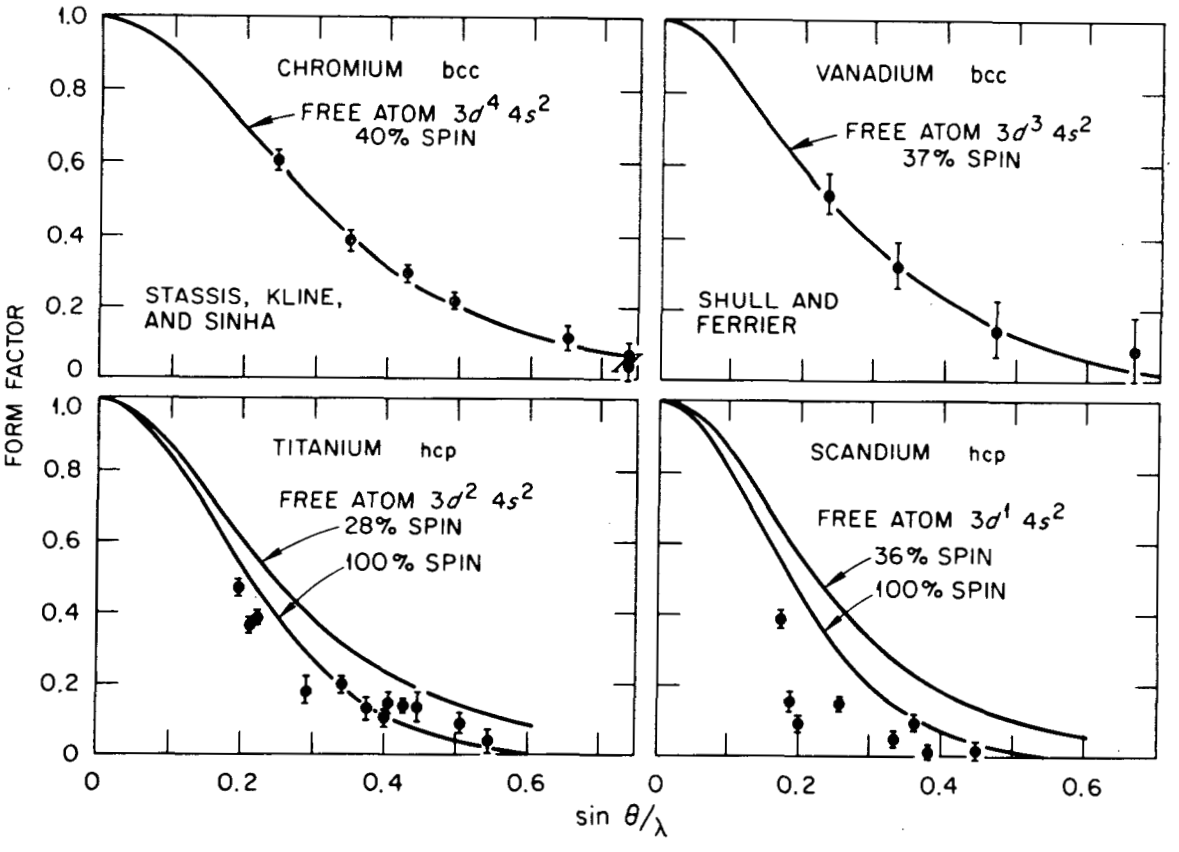


Fig. 4. Summary of paramagnetic form factors for 3d elements.

For Cr and V we have taken the atomic curve from the original publications by Stassis *et al.*[6] and Shull and Ferrier.[4] In these cases the assigned proportions of spin and orbital moment are in reasonable agreement with gyromagnetic ratio results.[20] For Ti and Sc we have retained the $3d^{n-2}4s^2$ configuration to have a consistent model for all four cases. In the case of Ti, Collings and Ho[21] have used low temperature specific heat data to calculate the spin susceptibility, and have attributed the difference between the measured susceptibility and the calculated spin susceptibility to an orbital contribution. This seems to ignore the possibility of exchange enhancement of the spin contribution, so we prefer to think of their result as an upper limit on the orbital contribution. We believe the true spin fraction lies somewhere between 28% (Collings and Ho) and 100% (strong exchange enhancement). A similar situation exists in the case of Sc. From specific heat measurements[22] and susceptibility

measurements[23] we conclude that the lower limit on the spin fraction of the total susceptibility is 36%. It would be highly desirable to have gyromagnetic ratio results to remove this ambiguity for Ti and Sc. However, we will see that for Sc, the agreement between our results and the calculated APW spin form factor by Gupta and Freeman,[12] strongly suggests that the orbital contribution is quite small.

We believe that Fig. 4 demonstrates the predicted wave function expansion relative to the free atom for states near the bottom of the 3d band. As expected, the effect is strongest in the case of Sc where the Fermi level is close to the bottom of the 3d band. Aside from the effect of expanded radial wavefunctions, the fact that the crystal structure changes from bcc for Cr and V to hcp for Ti and Sc undoubtedly has a strong influence on these results. It is clear that for elements near the beginning of the d transition bands the atomic model gives poor agreement with experimental magnetic form factors and solid state effects must be considered.

The task of calculating all the contributions to $\chi^{zz}(\vec{q},0)$ is formidable, and a relatively complete calculation has been made only in the case of Cr by Oh *et al.*[8] They found that the orbital form factor in the metal is spherically symmetric and very close to the free ion form factor. Unfortunately, as they point out, this result may be due to the fact that they were dealing with a nearly half-full band and should not be generalized to other cases. Their calculated spin form factor is slightly contracted in reciprocal space relative to the free ion result. By combining their calculated orbital susceptibility with the spin susceptibility scaled by an exchange enhancement factor of 2.53 they were able to obtain excellent agreement with the neutron results of Stassis *et al.*[6] However, the agreement at q = 0 with the bulk susceptibility was not satisfactory, indicating their calculation did not adequately treat the diamagnetic terms.

The calculation by Gupta and Freeman[2,12] on the spin form factor of Sc is in good agreement with our experimental results. This suggests that the orbital contribution is quite small, as expected for a nearly empty d band.[24] Confirmation of this suggestion by a gyromagnetic ratio

measurement and by theoretical calculation of the orbital contribution would be of value.

The available experimental data on the 4d series are shown in Fig. 5 together with some appropriate atomic calculations for comparison. Gyromagnetic ratio measurements have been reported for Pd and Nb,[20] but for Y the two calculated curves reflect the uncertainty resulting from specific heat and susceptibility measurements.

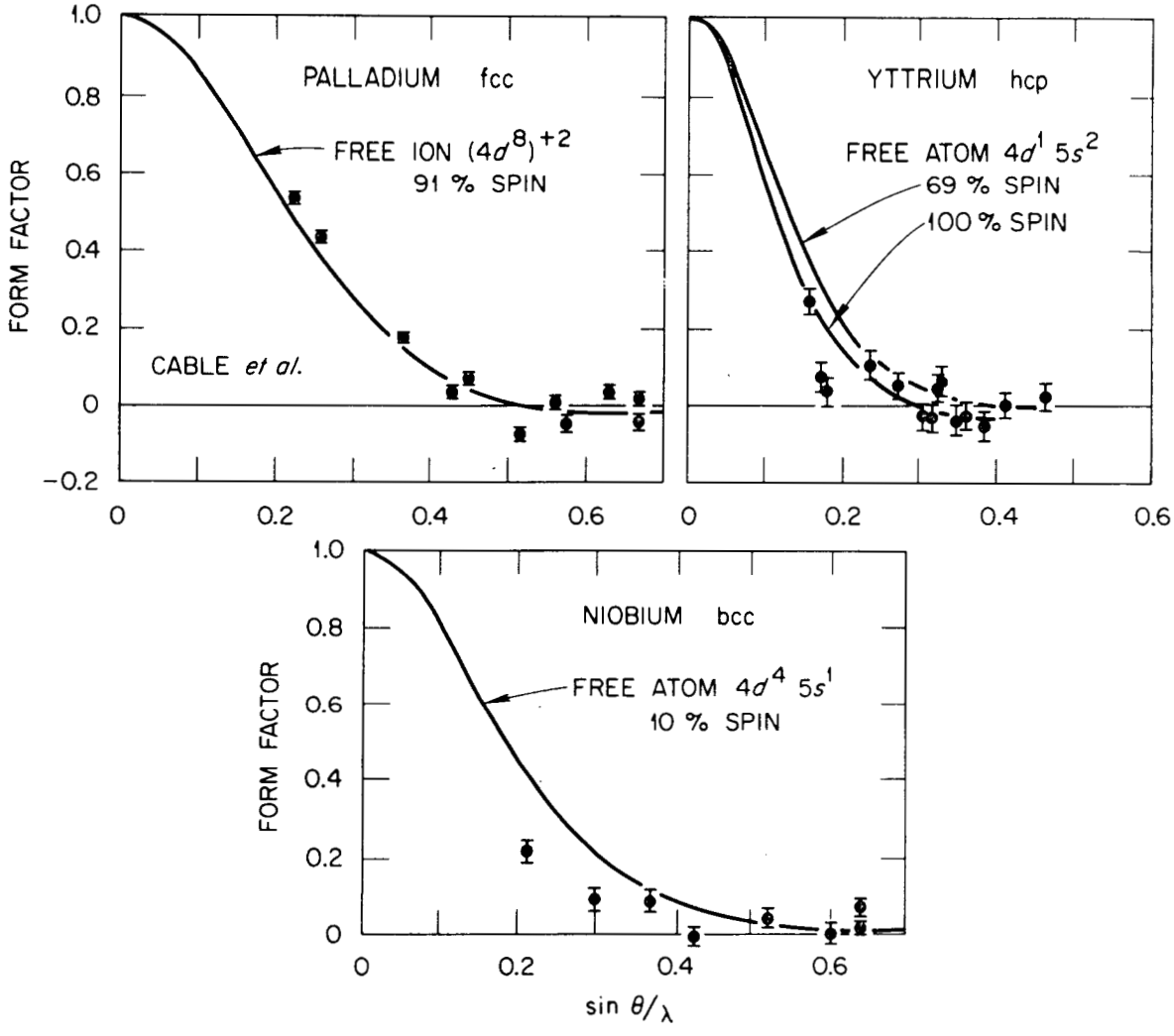


Fig. 5. Summary of paramagnetic form factors for 4d elements.

Note the behavior of the first four data points in the Y case and compare with Sc in Fig. 4. We believe this behavior may be characteristic of 3 electrons in d and s states in a hcp structure. Suggestions of this

behavior are found in the residual scattering amplitude of Gd[9] and Er,[26] but the large 4f contribution makes it very difficult to see the 5d and 6s electrons. Experiments on Lu are now in progress at the Ames Laboratory and it will be very interesting to see if the Sc and Y pattern is repeated in this case.

The only calculation performed to date on the 4d series is the APW work of Freeman, Harmon, and Watson-Yang[27] on Pd, which is in very good agreement with the experimental form factor by Cable *et al.*[28] Freeman and colleagues have theoretical work on Y in progress. For Y it may be sufficient to calculate only the spin contribution, but Nb is a case where the orbital contribution should be calculated also.

SUMMARY

The experimental results on paramagnetic form factors clearly show the inadequacy of atomic or extreme tight-binding models to describe the outer electron density in transition metals. In several cases APW calculations have resulted in good agreement with the experimental data, giving confidence in the wave functions obtained in the APW method. The calculation of the Van Vleck orbital contribution should be attempted in more metals. The adequate treatment of diamagnetism in the outer electrons remains as a challenge for the theorists. The combination of theory and experimental results on paramagnetic form factors promises to greatly expand our understanding of the transition metals, particularly their magnetic behavior.

REFERENCES

1. R. Nathans, C. G. Shull, G. Shirane, and A. Andresen, J. Phys. Chem. Solids 10, 138 (1959).
2. A. J. Freeman, Proc. of the Conf. on Neutron Scattering, Gatlinburg, 1976.
3. J. H. Wood, Phys. Rev. 117, 714 (1960).
4. C. G. Shull and R. P. Ferrier, Phys. Rev. Lett. 10, 295 (1963).
5. R. M. Moon, W. C. Koehler, and A. L. Trego, J. Appl. Phys. 37, 1036 (1966).

6. C. Stassis, G. R. Kline, and S. K. Sinha, Phys. Rev. B 11, 2171 (1975).
7. S. Asano and J. Yamashita, J. Phys. Soc. Japan 23, 714 (1967).
8. K. H. Oh, B. N. Harmon, S. H. Liu, and S. K. Sinha, to be published in Phys. Rev. B.
9. R. M. Moon, W. C. Koehler, J. W. Cable and H. R. Child, Phys. Rev. B 5, 997 (1972).
10. B. N. Harmon and A. J. Freeman, Phys. Rev. B 10, 1979 (1974).
11. W. C. Koehler and R. M. Moon, Phys. Rev. Lett. 36, 616 (1976).
12. Raju P. Gupta and A. J. Freeman, Phys. Rev. Lett. 36, 613 (1976).
13. J. Schwinger, Phys. Rev. 73, 407 (1948).
14. C. G. Shull, Phys. Rev. Lett. 10, 297 (1963).
15. R. M. Moon, W. C. Koehler and C. G. Shull, Nucl. Instrum. Methods 129, 515 (1975).
16. O. Steinsvoll, G. Shirane, R. Nathans, and M. Blume, Phys. Rev. 161, 499 (1967).
17. C. Stassis, Phys. Rev. Lett. 24, 1415 (1970).
18. R. E. Watson and A. J. Freeman, Acta Cryst. 14, 27 (1961).
19. A. J. Freeman and R. E. Watson, Acta Cryst. 14, 231 (1961).
20. R. Huguenin, G. P. Fells and D. N. Baldock, J. Phys. F 1, 281 (1971).
21. E. W. Collings and J. C. Ho, Phys. Rev. B 2, 235 (1970).
22. T. W. E. Tsang, K. A. Gschneidner, and F. A. Schmidt (to be published).
23. F. H. Spedding and J. J. Croat, J. Chem. Phys. 58, 5514 (1973).
24. C. M. Place and P. Rhodes, J. Appl. Phys. 39, 1282 (1968).
25. N. V. Volkenshtein, E. V. Galoshina and N. I. Shchegolikhina, Soviet Phys. JETP 29, 79 (1969).
26. C. Stassis, G. R. Kline, A. J. Freeman and J. P. Desclaux, Phys. Rev. B 13, 3916 (1976).
27. A. J. Freeman, B. N. Harmon and T. J. Watson-Yang, Phys. Rev. Lett. 34, 281 (1975).
28. J. W. Cable, E. O. Wollan, G. P. Felcher, T. O. Brun and S. P. Hornfeldt, Phys. Rev. Lett. 34, 278 (1975).

THEORETICAL DETERMINATIONS OF MAGNETIZATION DENSITIES AND NEUTRON MAGNETIC FORM FACTORS IN METALS*

A. J. Freeman
Physics Department
Northwestern University
Evanston, Illinois 60201

and

Argonne National Laboratory
Argonne, Illinois 60439

ABSTRACT

Whereas a variety of experimental methods yield information which has been related directly to the electronic band structure, there are few experiments which yield direct information about the nature of wavefunctions in metals. Perhaps the one outstanding exception is the determination of the neutron magnetic form factor which gives the Fourier transform of the magnetization density. In the past few years, accurate neutron experiments have shown the inadequacy of the commonly used free atom/ion Hartree-Fock form factors. This paper describes recent advances in high resolution energy band studies of APW wavefunctions, magnetization densities, and neutron form factors in metals. Illustrative results obtained in our Laboratory for several important transition and rare-earth metal systems are presented and compared with experiments carried out at ORNL, ANL, and Ames Laboratory. Unlike the case of the ferromagnetic metals, we find very good agreement with experiment for the paramagnetic metals studied to date.

---

*Supported by the National Science Foundation, the Air Force Office of Scientific Research and the Energy Research and Development Administration.

INTRODUCTION

Highly precise experiments, such as neutron magnetic scattering, which measure physical phenomena requiring solid state wavefunctions as opposed to eigenvalues for their description, are still relatively new; the strong interaction between solid state theory and experiment has only just recently begun. For these metals, comparisons of experimental results with free ion-atom form factors are no longer as useful as they were in the past. Band structure studies are now so well developed that meaningful detailed comparisons with experiment may now be undertaken in order to explain and predict wavefunction dependent phonomena. By contrast, since eigenvalues and energy bands are not as sensitive as wavefunctions to potential approximations they are less likely to provide as much detailed knowledge of electronic interactions in solids. Thus the study of phenomena requiring wavefunctions for their description may well be the key to assessing the limits of the single particle model and to understanding the role of many-body effects in metals.

This paper outlines several of the important considerations for an accurate single particle description of the spin density in metals. As we will see, the comparison of the energy band calculations with the experimental form factor results has provided insight into the conduction electron interactions and has revealed that some challenging information about the distribution and nature of the conduction electrons is contained in the neutron magnetic scattering data.

In this paper, we illustrate the present "state of the art" in obtaining accurate spin densities and neutron magnetic form factors by describing results obtained for several rare-earth (Gd and Er) and transition metals (Sc, Pd, and Pt). Because of space limitations, this paper is restricted to the work carried out in my group and represents a personal, rather than a broad-scope view.

THEORETICAL DETERMINATION OF APW WAVEFUNCTIONS AND SPIN DENSITIES

In order to obtain easily both the eigenvalues and normalized wavefunctions, we employed the APW method in which each augmented plane wave (APW) of the basis set is a plane wave in the interstitial region, and is expanded in the angular momentum representation inside the muffin-tin spheres, with the radial function obtained by integrating the Schrödinger equation. [For Pt metal, we used the relativistic APW (RAPW) method to obtain accurate solutions of the Dirac equation.] Thus each Bloch wavefunction is given as a linear combination of APW's

$$\Psi_{\vec{k},n}(\vec{r}) = \sum_i A_{i,n}(\vec{k})\Phi_{\vec{k}_i}(\vec{r}) \; ; \; \vec{k}_i = \vec{k} + \vec{K}_i \qquad (1)$$

with the $A_{i,n}(\vec{k})$ to be determined variationally from a solution of the Schrödinger or Dirac equations; $\Phi_{k_i}(\vec{r})$ is an APW

$$\Phi_{\vec{k}_i}(\vec{r}) = \frac{1}{\sqrt{V}} e^{i\vec{k}_i \cdot \vec{r}} \qquad \text{outside the sphere and} \qquad (2a)$$

$$\Phi_{\vec{k}_i}(\vec{r}) = e^{i\vec{k}_i \cdot \vec{r}_\nu} \sum_{\ell m} A_{\ell m} R_{\ell,E}(\rho) Y_{\ell,m}(\hat{\rho}) \qquad \text{for } |\hat{\rho}| = |\vec{r}-\vec{r}_\nu| < R_\nu \qquad (2b)$$

where V is the volume of the unit cell, R_ν is the radius of the νth sphere centered at $\vec{r}_\nu$, and the $A_{\ell m}$ are determined such that each APW is continuous at the sphere boundary. Although each APW is continuous across the sphere boundary, there remains a discontinuity in slope, which is manifest in the calculated wavefunction. This slope discontinuity in the wavefunction has been studied in detail and is not a problem in form factor calculations.[1]

The character of the wavefunctions on the Fermi surface is determined by obtaining the different ℓ contributions to the charge density for each wavefunction. If the charge density is expanded inside each muffin-tin sphere as

$$\rho(\vec{r}) = \sum_{L,M} C_L(r)\, Z_{L,M}(\hat{r}) \tag{3}$$

where $Z_{L,M}(\hat{r})$ are lattice harmonics, then the amount of different ℓ character in the wavefunction can be easily seen from the different ℓ contributions to $C_0(r)$. [Here ℓ refers to the wavefunction expansion in Eq. (2) and L refers to the charge density expansion in Eq. (3).] The ℓth contribution to $C_0(r)$ is simply given by

$$C_0^{\ell}(r) = \sum_{m} |A_{\ell m}|^2 R_{\ell}^2(r) \tag{4}$$

An estimate of the percentage of each ℓ character in the wavefunction (P_ℓ) may be obtained from the relation

$$P_\ell \approx 4\pi \int_0^{R_{ws}} r^2 C_0^{\ell}(r)\, dr \tag{5}$$

The spin density may be obtained by merely subtracting the charge density for spin down electrons from that for spin up electrons:

$$\rho(\vec{r}) = \sum_{\vec{k}}^{\text{occupied}} \{ |\psi_{\vec{k},\uparrow}(\vec{r})|^2 - |\psi_{\vec{k},\downarrow}(\vec{r})|^2 \} \ . \tag{6}$$

This expression is useful for ferromagnets such as Gd metal where the spin up and spin down wavefunctions for a particular $\vec{k}$ point may differ considerably. However, for a paramagnetic metal, the induced moment is exceedingly small and there is very little difference between the spin up and the corresponding spin down wavefunctions. (For Pd, for example, the band splitting is much less than 1 mRy, even for applied fields as large as 100 kGauss.) In this simpler case the spin density arises from spin up states at the Fermi level for which the corresponding spin down state is unoccupied. Equation (6) then reduces to

$$\rho(\vec{r}) = \frac{2V}{(2\pi)^3} \sum_n \int_{E=E_F} \frac{dA_n(\vec{k})}{|\nabla_k E_n(\vec{k})|} |\Phi_{\vec{k},n}(\vec{r})|^2 \tag{7}$$

where $dA_n(\vec{k})$ is the infinitesmal Fermi surface element for band n. The results given for the spin density are normalized by the density of states,

$$N(E_F) = \sum_n N_n(E_F) = \frac{2V}{(2\pi)^3} \sum_n \int_{E=E_F} \frac{dA_n(\vec{k})}{|\nabla_k E_n(\vec{k})|} \qquad (8)$$

In practice, the integral over the Fermi surface may be evaluated by dividing each sheet of surface into hundreds of small areas ΔA_{in}, evaluating the representative gradients (using the Hellman-Feynman theorem) and obtaining wavefunctions for each surface element.

The spin density is then obtained from

$$\rho(\vec{r}) = \sum_n \rho_n(\vec{r}) = \sum_n \frac{2V}{(2\pi)^3} \sum_i \frac{\Delta A_{n_i}(\vec{k})}{|\nabla_k E_n(\vec{k})_i|} |\Phi_{\vec{k}_i}(\vec{r})|^2 \qquad (9)$$

As an indication of the quality of results, the number of wavefunctions used in our calculations for Pd were 87, 368, and 181 for bands 4, 5 and 6, respectively. The $\rho(\vec{r})$ results were identical when about half this number of wavefunctions were used - implying the spin densities are well converged.

SELECTED RESULTS OF SPIN DENSITIES IN METALS

Ferromagnetic Gd Metal

For ferromagnetic Gd, Harmon and Freeman[2] obtained the conduction electron spin density from the spin up and spin down charge densities which were calculated from a sum of occupied wavefunctions. The spherically averaged densities are shown in Fig. 1. The increase in the charge density near the sphere radius is from the $\ell = 0$ and $\ell = 1$ character of the wavefunctions, while the large shoulder (at the maximum of the atomic 5d function) comes from the $\ell = 2$ character of the states. Subtraction of the two densities nearly removes the $\ell = 0$ character and gives a spin density of predominantly d character which is not of atomic nature. The density is very much expanded compared to an atomic

5d function.

The nonspherical contributions to the charge density are shown in Fig. 2. Here the charge density has been expanded inside the APW sphere according to Eq. (3). The C_{53}, C_{60}, and C_{66} densities did not give contributions as large inside the spheres and are therefore not shown. These figures indicate that the largest nonspherical contribution to both the total charge density and the spin density has $\ell = 3$ character. The $\ell = 3$ contributions to the density result from the mixed $\ell = 1$ and $\ell = 2$ character of the wavefunctions (not from $\ell = 2$ and $\ell = 3$ character as might be expected for a system with f electrons. All the wavefunctions were found to have less than 3% $\ell = 3$ character). The large $\ell = 3$ term and the significant $\ell = 4$ term cause the spin density around each atomic site to point toward the nearest neighbor site.

Contours of the spin density in the basal plane were found to be essentially the same as the experimentally derived density of Moon, et al.[3] but with considerably smaller magnitude. For example, the calculated density at the "c" site is -0.002 μ_B/A^3. The spin up density at this site is 0.043 μ_B/A^3 and the spin down density is 0.045 μ_B/A^3 implying that a major shift of charge is required to obtain the experimental value (-0.037 μ_B/A^3). The general agreement in shape is, however, a good indication that it is the spread out d-like conduction electrons which are contributing most to the neutron magnetic form factor results.

Paramagnetic Sc Metal

To better understand the neutron form factor studies in Gd and to avoid the complications inherent in the rare-earth metals with their dominant 4f contribution to the scattering, Gupta and Freeman[4] have studied paramagnetic scandium. As a "sister" metal, Sc has an electronic structure and physical properties which resemble closely those of the hcp rare-earth metals.

In neutron measurements from a paramagnetic metal, one usually applies a uniform magnetic field and studies the paramagnetic scattering amplitude of the induced moment. Since the induced moment is small, only the electrons at the Fermi surface will be involved - as can be

shown using linear response theory.[5,6] As shown by Stassis et al,[5] for a uniform external field H, the Fourier transform of the induced moment is given as

$$M(\vec{G}) = H \int_{F.S.} \frac{d\, s_k}{|\nabla_k E_k|} \langle \psi_k | e^{-i\vec{G}\cdot\vec{r}} | \psi_k \rangle, \tag{10}$$

where the integration is restricted to the Fermi surface. Eq. (10) may be rewritten as

$$M(\vec{G}) = H\, \rho(\vec{G}), \tag{11}$$

where $\rho(\vec{G})$ is the Fourier transform of

$$\rho(\vec{r}) = \int_{F.S.} \frac{d\, s_k}{|\nabla_k E_k|} \psi_k^*(\vec{r})\psi_k(\vec{r}) \tag{12}$$

Here $\rho(\vec{r})$ [Cf. Eq. (9)] is the spin density arising from the field induced uncompensated states, and the factor multiplying the charge density, $\psi_k^*(\vec{r})\psi_k(\vec{r})$, is a local density of states weighting function which takes account of the detailed structure of the eigenstates at the point[6] k. Thus the neutron form factor, i.e. the Fourier transform of the magnetization density, will be expected to provide highly useful information about the behavior of electrons at the Fermi surface. The spin density at E_F was found using some 325 points in the 1/24th Brillouin zone at which the wavefunctions were determined.

In Fig. 3 we show the ρ_{LM} for some values of LM arising in the lattice harmonics decomposition of $\rho(\vec{r})$. We see that the main contributions to the spin density arise from the L = 0 and M = 0 term (i.e., the spherical part) and the L = 3, M = 3 term arising from interference between the ℓ = 1 and ℓ = 2 terms of the wave function. The L = 2, M = 0, and the L = 4, M = 0 contributions are considerably smaller. To better understand the spherical charge density ρ_{oo}, we further decomposed it into its respective ℓ = 0, 1 or 2 character in order to determine its s, p, or d behavior. (Higher ℓ components, i.e., $\ell > 2$ were not included

since they were found to be rather small.) The induced spin density inside the spheres shown in Fig. 4, was found to be largely d-like except close to the sphere radius where it has considerable p character. This d spin density itself is quite extended spatially in contrast to the atomic 3d density expected for the free atom ion. Such a large expansion of the 3d density in Sc is in sharp contrast with the results obtained[6] for Pd metal--to be described shortly--and reflects the importance of solid state boundary conditions: wavefunctions near the bottom of the d band are only required to be even under reflection across the Wigner-Seitz boundary whereas the free atom wavefunction must approach zero at large distances.

Paramagnetic Pd Metal

Even before this recent work on Sc metal, Cable et al.[7] determined an accurate neutron magnetic form factor for paramagnetic Pd metal and showed that the magnetization was contracted by about 15% relative to the Hartree-Fock Pd^{2+} free ion density function (which is already contracted by about the same amount relative to the neutral free atom). Freeman, Harmon and Yang[2] obtained accurate APW solutions and, using Eqs. (7-9) with wavefunctions calculated separately for the fourth, fifth, and sixth bands at 87, 368, and 181 different points, respectively, on the Fermi surface obtained the results of the individual, spherically averaged, normalized-band spin densities, $\rho_j(r)$, shown in Fig. 5. Both the fourth and fifth bands have a localized distribution arising from the $\ell = 2$ (or d-like) electrons; by contrast, the sixth-band density is much more expanded indicating the large s- and p-like character of some of its wave functions. A surprising finding of these results is that the dominant fifth-band contribution yields a spin density which is even more localized than the Hartree-Fock spin densities obtained by Freeman and Watson[8] for the free Pd^{2+} ion (also shown in Fig. 5). This is all the more remarkable when one recalls that the solid-state potential is derived from a superposition of neutral free-atom densities taken from the Hartree-Fock-Slater calculation with an assumed $4d^{10}$ configuration in which the 4d radial density is much more expanded spatially than the $4d^8$ ionic configuration.

The explanation for these highly contracted densities comes from considering the way the d orbitals are affected when placed in the solid.[6] From an elementary viewpoint, the interaction among d orbitals on neighboring atomic sites can be thought of as producing bonding and antibonding states. The boundary condition for the lower energy bonding states requires that the wavefunction be an even function between sites, whereas the antibonding states are required to have a node at the Wigner-Seitz cell boundary. In the solid, of course, a continuous range of radial densities is obtained. This is illustrated in Fig. 6 in which we show the $\ell = 2$ or d-like radial probability density for energies near the bottom, middle and top of the d bands. The antibonding wavefunctions at the Fermi energy are at the top of the d bands and the boundary condition that they go through zero at the Wigner-Seitz cell boundary (rather than at ∞ as for atomic wavefunctions) causes them to be more contracted than the corresponding 4d wavefunctions in the free ion. It is thus clear why the free ion model fails, and that solid state effects are responsible for the highly contracted spin density observed in Pd.

Paramagnetic Pt Metal

Because Pt metal has a similar band structure and Fermi surface (but a smaller exchange enhancement) to that of its 'sister' metal, Pd, Yang, Freeman and Koelling[9] have undertaken a study of its magnetization density in order to assess the importance of relativistic effects on its wavefunctions at E_F which lies near the top of the d bands. Since this work is as yet unpublished, we give some details of their study here. The energy eigenvalues $E_n(\vec{k})$ were obtained using the relativistic-augmented-plane-wave (RAPW) method applied to a warped-muffin-tin (WMT) approximation to the crystal potential constructed from the standard overlapping atomic charge density model with a lattice constant $a = 7.3983$ a.u. using the full Slater exchange ($\alpha = 1$) approximation. The Pt atomic charge density used in the overlapping procedure was calculated using a Dirac-Slater code for an assumed $5d^{10}\ 6s^{0}$ configuration as this corresponds more closely to the almost full d-band structure of the metal.

RAPW energy eigenvalues were obtained on a cubic mesh of linear dimension ($\pi/6a$) within 1/48 of the Brillouin zone (B.Z.). These eigenvalues were then least-squares fit with a Fourier series that included 60 stars of primitive translation vectors. The quality of the fits to the first six bands is good; the rms error is about 2 mRy for the first five bands and twice this value for 6th band; the maximum differences between the RAPW and the fitted eigenvalues is about two times the rms errors quoted.

The density of states was calculated by subdividing the irreducible 1/48 of the B.Z. into 6144 tetrahedrons within which the dispersion relation was assumed to be linear. The density of states is then given by a sum on analytic expressions for each tetrahedron. The Fermi energy $E_F = 0.6215$ Ry is obtained from the satisfication of the requirement that the number of holes be equal to the number of electrons. The constructed Fermi surface is found to be in excellent agreement with the experimental results of other calculations.

The field induced spin density was found using Eqs. (7-9) but with the relativistic wave functions determined at 387 tetrahedra which intersect the Fermi surface. The results for the 4th, 5th and 6th band contributions is shown in Fig. 7. There are two very interesting features to note. First, the spherical part of the induced spin densities is very localized and almost entirely d-like. The spherical part of the spin density for band 6 of Pt is obviously different from that of Pd where the s-p character of the wave function is significant (cf. Fig. 5). Second, the spherical part of the spin density for Pt metal is slightly more expanded than that for the Pt^{+2} free ion calculated by the Dirac-Fock-Slater method whereas for Pd, the situation is reversed (but note that Pd^{+2} was calculated by the Hartree-Fock method). A comparison of the Pt and Pd 6th band densities is shown in Fig. 8.

NEUTRON MAGNETIC FORM FACTORS

In analyzing their results, Moon et al.[3] separated from the measured magnetic form factor a contribution representing the localized 4f electrons and obtained a form factor which is presumably characteristic of the polarized conduction electrons. The 4f density was found to be spherically symmetric with a radial dependence significantly expanded relative to the Freeman-Watson[10] non-relativistic Hartree-Fock (H-F) wavefunctions for the free trivalent ion. The conduction electron density was found to be long range and oscillatory, i.e., quite different from that expected for the atomic 5d and 6s orbitals.

Freeman and Desclaux,[11] using relativistic Dirac-Fock (D-F) solutions for the Gd^{3+} ion, obtained a 4f electron form factor in excellent agreement with the localized form factor found by Moon et al.[3] The expansion of the observed 4f radial density relative to the Hartree-Fock results was found to be an indirect relativistic effect: the relativistic contraction of the core electrons which results in a more effective screening of the nuclear charge. The magnetic form factor of Tb^{3+}, obtained by polarized neutron measurements[12] on a truly ionic material, $Tb(OH)_3$, (in which the magnetization arises only from the unpaired 4f electrons) was also found to be in excellent agreement with the calculated D-F form factor. The theoretical situation for the conduction electron contribution to the form factor is less clear. As mentioned above, an extensive spin-polarized augmented-plane-wave (APW) study of the band structure, conduction electron polarization, spin densities and neutron magnetic scattering in ferromagnetic Gd, was performed by Harmon and Freeman.[2] The calculated conduction electron spin density was found to be only in qualitative agreement with the experimental observations,[3] because of lack of agreement at the first of several inner reflections from which the spin density is derived. Harmon and Freeman discussed other possible contributions to the magnetization density and concluded that a non-spherical contribution, possibly arising from the 4f shell, was needed to explain the discrepancy.

The theoretical study of Sc metal by Gupta and Freeman[4] described above was undertaken in close collaboration with the experimental work of Koehler and Moon[13]. Thus it was hoped that a combined theoretical and experimental study would yield the distribution and nature of the conduction electrons of this important transition metal and (by analogy) the heavy rare-earth metals as well. As seen from Fig. 3, the theoretical APW magnetization density was found to be very expanded spatially and hence to be very different from that expected of a free atom/ion 3d density. The resultant form factor in Fig. 9 shows the interesting, but peculiar feature, of falling rapidly with $\frac{\sin\theta}{\lambda}$ then oscillating but yet remaining positive for the first ten reflections. This apparently large anisotropy is due to the asphericity in spin density and to interference, through the Fourier transform, between the inner and outer parts of the magnetization density. This predicted anomalous form factor is found to be in good agreement with the experiment of Koehler and Moon[13]. The orbital contribution to the form factor was not included becuase of the lack of knowledge about the gyromagnetic ratio for the metal. Exchange enhancement effects were also not included because as was found to be the case for chromium,[14] the general shape of the curve is expected not to be greatly affected by such effects.

Koehler and Moon[13] have also considered the nature of the experimental moment density shown in Fig. (10a). As stated by them, "we have represented the hexagonal close packed structure in terms of an orthorhombic structure with $a = a_H$, $b = 3a_H$, and $c = c_H$. The atomic positions in this cell are then $(0\ \frac{1}{3}\ \frac{3}{4})$, $(0\ \frac{2}{3}\ \frac{1}{4})$, $(\frac{1}{2}\ \frac{1}{6}\ \frac{1}{4})$ and $(\frac{1}{2}\ \frac{5}{6}\ \frac{3}{4})$. We do not have full three-dimensional data but we do effectively have a complete set of data in an $(0k\ell)$ zone from which we can calculate the projection of the point density on the orthohexagonal b-c plane and which we show in the Figure as a contour map. The numbers are multiples of $10^{-3}\ \mu_B/A^2$ and the dark circles represent the projections of the atomic sites. In the projection the moment density is a maximum near the atomic sites but it is rather large, $\sim 0.3 \times 10^{-3}\ \mu_B/A^2$, and positive at the interatomic positions in contrast to the diffuse density in Gd." They have also prepared a similar map constructed from the Gupta and

Freeman values. As seen from Fig. 10(b), the theoretical results give quite good agreement with the experimental contour map shown in Fig. 10(a). This good agreement gives added confidence to the theoretical results.

In order to better understand the Gd results, Stassis, Kline, Freeman and Desclaux[15] have recently reported results of a detailed experimental and theoretical study of the coherent paramagnetic scattering of neutrons in erbium, a heavy rare-earth metal whose open 4f shell, unlike that of Gd, possesses an orbital magnetic moment giving rise to a relatively large magnetic anisotropy. At room temperature, erbium is paramagnetic and the 4f shell in the metal is in the $^4I_{15/2}$ state. The 4f shell possesses both spin and orbital magnetic moments and the relatively large magnetic anisotropy can be easily observed in a neutron diffraction experiment. In their experiment they chose to study the spatial distribution of the field induced magnetization in paramagnetic erbium by measuring the angular distribution of the coherent paramagnetic scattering amplitude. The polarized neutron technique was used to perform the measurements, since this method gives highly precise results when the coherent paramagnetic scattering amplitude is small in comparison with the coherent nuclear scattering amplitude, a condition fulfilled in the present experiment. For the same reason the depolarization of the incident beam by the sample is small and its effect on the measurements can be easily assessed. The measurements were performed using high purity single crystals, whose properties have been extensively studied by both magnetization measurements[16] and neutron diffraction techniques[17] at the Ames Laboratory.

Stassis et. al.[15] found that the localized part of the form factor agrees well with that determined for the Er^{3+} ion from relativistic Dirac-Fock (D-F) calculations. The angular dependence of the conduction electron contribution to the coherent scattering amplitude, given in Fig. 11, was obtained by subtracting from the experimental values the 4f-contribution given by the D-F calculations. As was the case with Gd, the observed angular distribution is quite different from an atomic 5d or 6d atomic form factor; it exhibits an oscillatory character which shows the unusual, but interesting, feature of remaining positive for

all the significant reflections ($\sin\theta/\lambda < 0.3$) shown in Fig. 11. In the absence of energy band determinations of the conduction electron magnetization density for Er, a detailed comparison of the experimental data with theory is not possible at present. Neither the magnetization density of ferromagnetic or paramagnetic Gd metal yields an oscillatory form factor.

It is striking, however, that the APW calculation for paramagnetic Sc by Gupta and Freeman[4] gave a magnetic form factor with an angular dependence which is qualitatively similar to that obtained for Er, and in very good agreement with the measurements of Koehler and Moon[13] on Sc metal. Gupta and Freeman[4] attributed the unusual angular dependence to the asphericity of the spin density and more importantly to interference effects, through the Fourier transform, between the inner and outer parts of the radial density. The qualitative similarity between their observations for Sc and those for Er is consistent with the assumption that the small angle contribution to the magnetic scattering amplitude is due to the polarization of the conduction band, since it is well known that the conduction band structure of the heavy rare earth metals is similar to that of the hcp 3d transition metals.[18]

Let us now consider the magnetic field induced form factors of Pd and Pt metals. The result of Freeman et al.[6] for Pd is shown in Fig. 12. As expected from Fig. 5, the fourth- and fifth-band form factor contributions have the same angular dependence but differ markedly from the sixth band. As an estimate of the spherical part of the orbital contribution to the form factor we have calculated the matrix elements of the operator $(g_0 - \frac{1}{2} g_2)$ from the spin-density functions for each individual band and for total contributions defined as in Eq.(9). The total magnetic form factor is taken as

$$f_{tot} = g^{-1}[2f_{spin}+(g-2)f_{orb}]$$

in order to compare with the experimental form factor of Cable et al. and the free-ion Hartree-Fock calculations. The final result is not sensitive to the approximate treatment of the orbital form factor, since with $g = 2.20$ from gyromagnetic measurements the orbital contribution

to the form factor is only 10% of the total. We see from Fig. 12 that the agreement between the APW form factor and experiment is very good and is in much better agreement than that given by the Hartree-Fock Pd^{2+} calculations for which the experimental asphericity ($85\%t_{2g}$) has been assumed. The mean square deviation for f_{tot} compared with experiment is 0.023, whereas that for f^{HF} is 0.035; the experimental mean square error is 0.017. In addition to the overall agreement between the theoretical and experimental form factors, there is also very good agreement between the measured and calculated asymmetry parameters.[6] Exchange enhancement was found to have a small effect on the form factor and to mainly enhance the already dominant 5th band contribution.

The neutron form factor results for Pt follow the expectations elicited by the results shown in Figs. 7 and 8. The form factor for the total bare(unenhanced) spin density is given in Table I as f^{spin}_{total}. Here f^{spin}_{tot} is calculated only inside muffin-tin spheres; the anisotropy arising from the L=4 term in the spin density expansion has been included in these results. Since the induced magnetic form factor mainly consists of the orbital and spin form factors, Yang, Freeman and Koelling[9] first estimated the orbital contribution by considering the Einstein-de Haas measurement[19] of the gyromagnetic ratio g', which for Pt is 1.62 ± 0.08. This indicates the presence of approximately a 23.5% orbital contribution and 76.5 % spin contribution. Because of the very localized spin density in Pt, we use the free ion formula to evaluate the orbital contribution using the RAPW spherical part of spin density, $4\pi r^2 C_0(r)$, instead of the atomic spherical distribution, $4\pi r^2 R^2(r)$, to perform the average of $(g_0 - \frac{1}{2} g_2)$. As expected from the work on Pd, this approximation is not expected to introduce a significant error. In comparing the orbital form factor with the spin form factor, we see that the orbital form factor is higher for low $\sin\theta/\lambda$. The total unenhanced form factor was obtained from Eq.(13) where the g factor is obtained from g' using the Kittel-Van Vleck relation which is expected to be valid for Pt metal.

Experiments now in progress by Maglic, Brun, and Cable will provide the information necessary to check out the predictions of these results,

including the anisotropic contributions, and will provide a severe test of RAPW theory.

ACKNOWLEDGMENT

As discussed in the text, the work here was done in collaboration with a number of colleagues. I am grateful to each of them for close cooperation on the various parts described above.

REFERENCES

1. B. N. Harmon, D. D. Koelling and A. J. Freeman, J. Phys. C 6, 2294 (1973)
2. B. N. Harmon and A. J. Freeman, Phys. Rev. B 10, 1979 (1974)
3. R. M. Moon, W. C. Koehler, J. W. Cable and H. R. Child, J. Phys. 32, 296 (1971); R. M. Moon, W. C. Koehler, J. W. Cable and H. R. Child, J. Appl. Phys. 42, 1303 (1971); R. M. Moon and W. C. Koehler, Phys. Rev. Lett. 27, 407 (1971)
4. R. P. Gupta and A. J. Freeman, Phys. Rev. Lett. 36, 613 (1976)
5. C. Stassis, G. R. Kline and S. K. Sinha, Phys. Rev. B 11, 2171 (1975)
6. A. J. Freeman, B. N. Harmon and T. J. Watson-Yang, Phys. Rev. Lett. 34, 281 (1975)
7. J. W. Cable, E. O. Wollan, G. P. Felcher, T. O. Brun and S. P. Hornfeldt, Phys. Rev. Lett. 34, 278 (1975)
8. A. J. Freeman and R. E. Watson (unpublished)
9. T. J. Watson-Yang, A. J. Freeman and D. D. Koelling (to be published)
10. A. J. Freeman and R. E. Watson, Phys. Rev. 127, 2058 (1962)
11. A. J. Freeman and J. P. Desclaux, Int. J. Magnetism 3, 311 (1972)
12. G. H. Lander, T. O. Brun, J. P. Desclaux and A. J. Freeman, Phys. Rev. B 8, 3237 (1973)
13. W. C. Koehler and R. M. Moon, Phys. Rev. Lett. 36, 616 (1976)
14. See Ref. 5
15. C. Stassis, G. R. Klein, A. J. Greeman and J. P. Desclaux, Phys. Rev. B 13, 3916 (1976)
16. F. H. Spedding and W. J. Gray (unpublished)
17. M. Habenschuss et al., Phys. Rev. B 10, 1020 (1974)
18. A. J. Freeman in Magnetic Properties of Rare-Earth Metals, R. J. Elliott, Editor (Plenum Press, 1972) and references therein.
19. R. Hugvenin, G. P. Pells and D. N. Baldock, J. Phys. F 1, 281 (1971)

Table 1. Neutron magnetic form factor of Pt metal derived from the RAPW spin density[9], showing f_{tot}^{spin}, f_{tot}^{orb} and $f_{tot} = \frac{2}{g} f_{tot}^{spin} + \frac{g-2}{g} f_{tot}^{orb}$

hkℓ	f_{tot}^{spin}	f_{tot}^{orb}	$\frac{2}{g} f_{tot}^{spin} + \frac{g-2}{g} f_{tot}^{orb}$
000	1.0	1.0	1.0
111	0.43944	0.61946	0.48166
200	0.26808	0.52881	0.32923
220	0.07579	0.28437	0.12471
311	-0.03528	0.18200	0.01568
222	0.05280	0.15759	0.07738
400	-0.15458	0.09112	-0.09694
331	0.01063	0.06255	0.02280
420	-0.05332	0.05558	-0.02777
422	0.00632	0.03618	0.01332
333	0.05489	0.02762	0.04849
511	-0.07912	0.02762	-0.05408
440	0.02188	0.01987	0.02140
531	0.01012	0.01763	0.01188
442	0.04735	0.01716	0.04026
600	-0.07621	0.01716	-0.05430
620	-0.02622	0.01624	-0.01626
533	0.04688	0.01625	0.03969
622	0.00620	0.01635	0.00858
444	0.05729	0.01700	0.04783

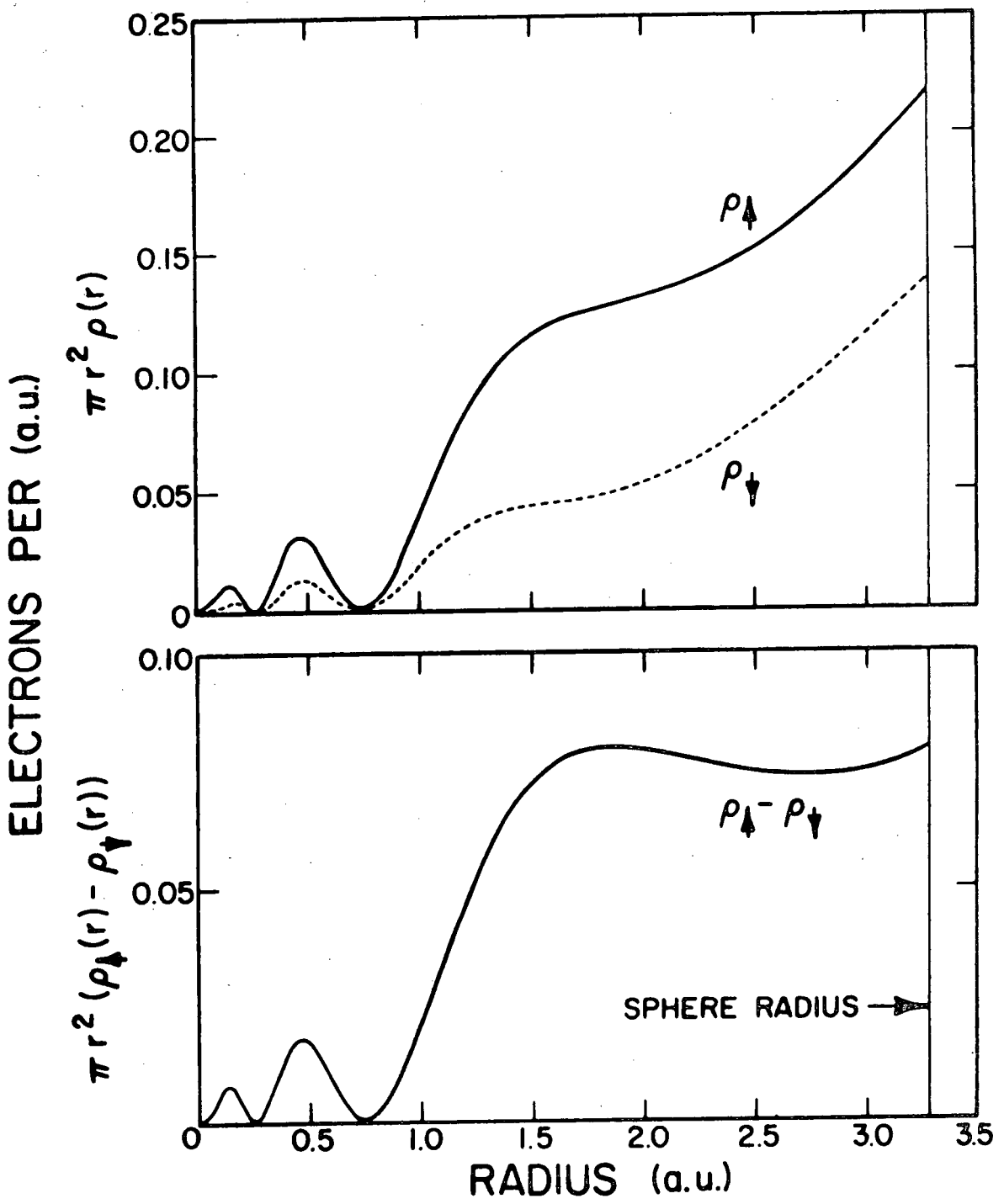
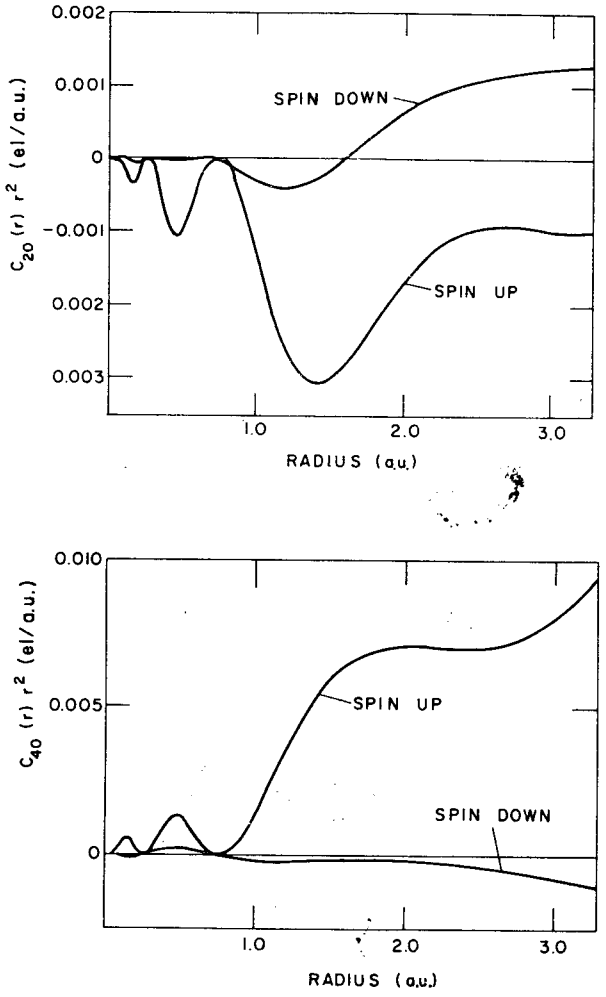


Fig. 1. The APW spherical charge and spin densities of ferromagnetic gadolinium metal[2].



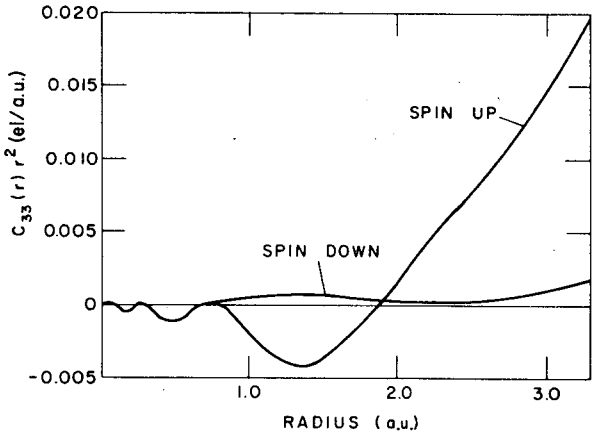


Fig. 2. The C_{20}, C_{33} and C_{40} non-spherical contributions to the APW charge density in ferromagnetic Gd metal[2].

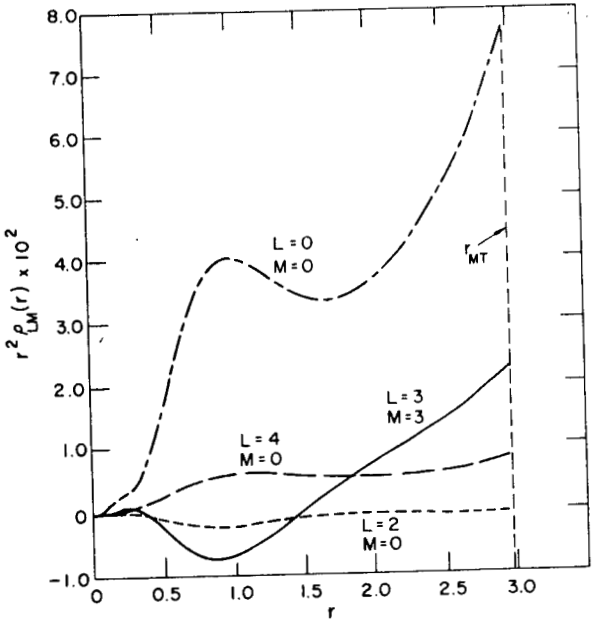


Fig. 3. Radial charge densities for some LM values arising in the lattice harmonics decomposition[4].

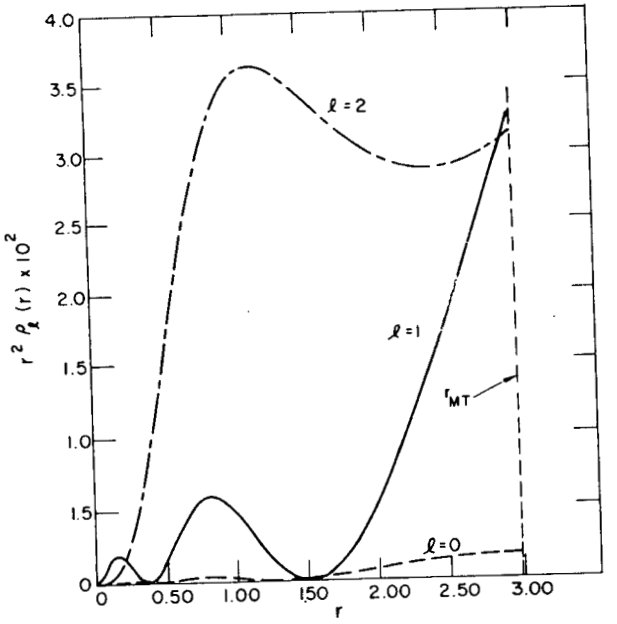


Fig. 4. Spherical harmonic contributions to the L = 0 charge density shown in Fig. 3.

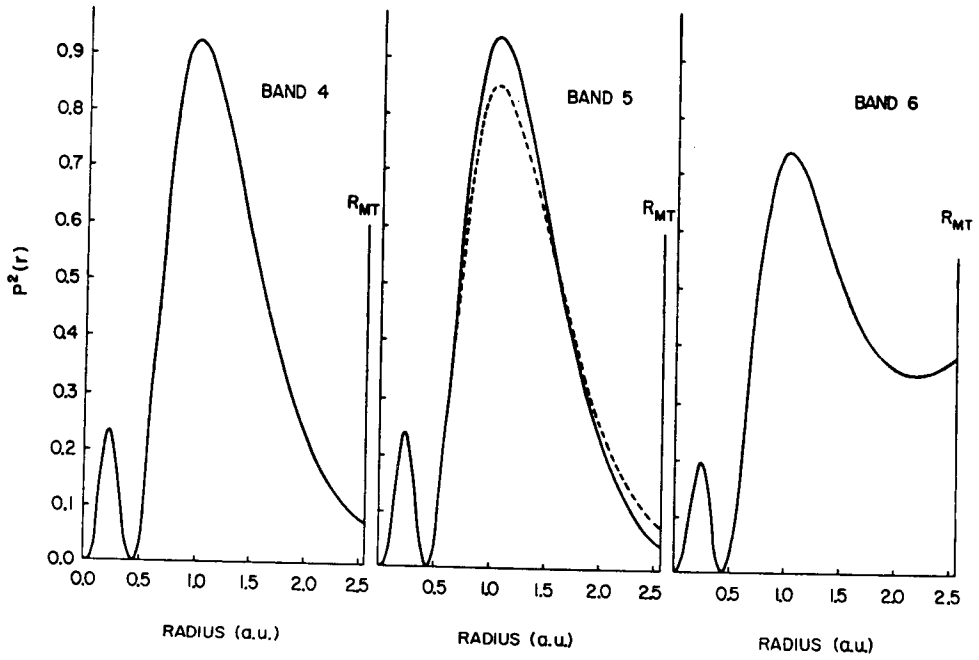


Fig. 5. The band 4,5, and 6 contributions to the induced spin density in Pd[6].

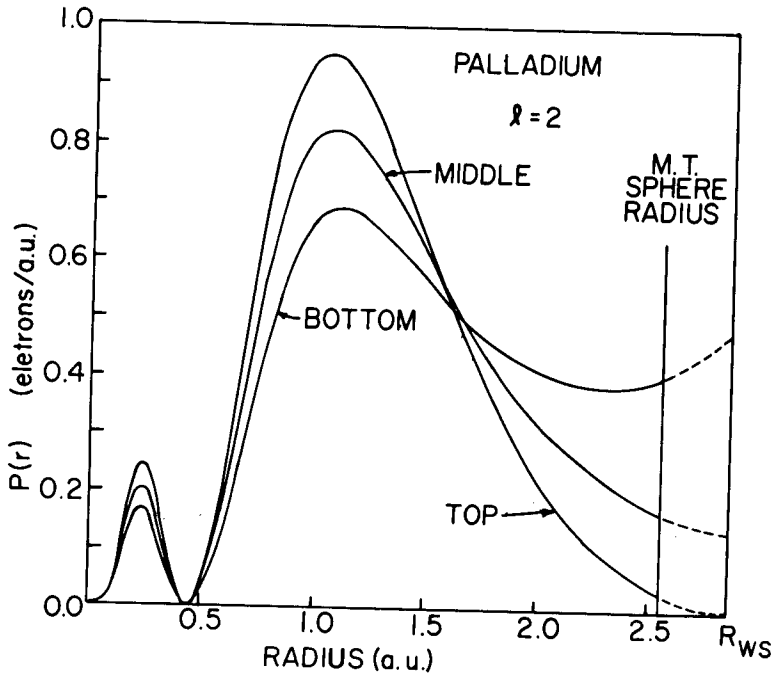


Fig. 6. Energy dependence of the $\ell = 2$ radial density in Pd metal[6].

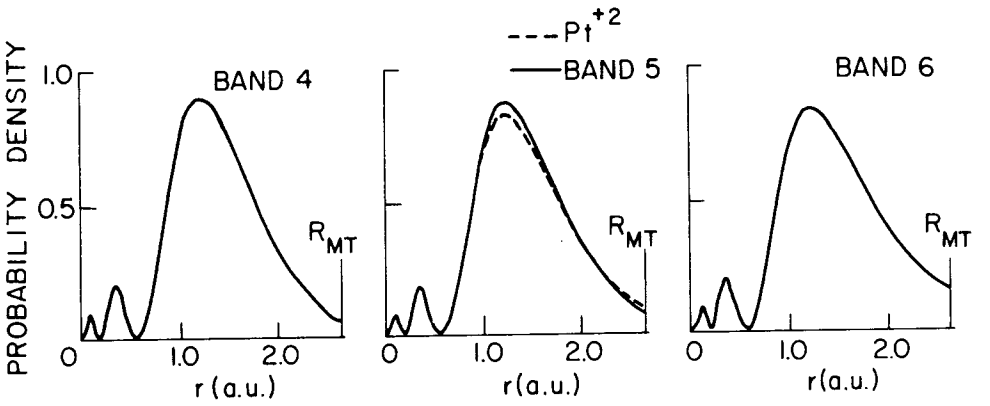


Fig. 7. Normalized radial spin densities for bands 4,5, and 6 and for comparison the 4d HFS radial density for the Pt^{2+} free ion (dashed curve)[9].

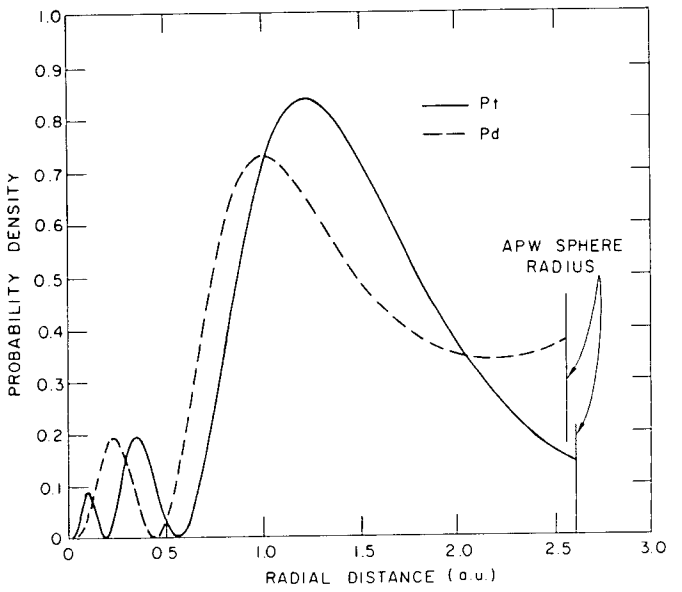


Fig. 8. Comparison of the APW Pd and Pt induced spin densities[9].

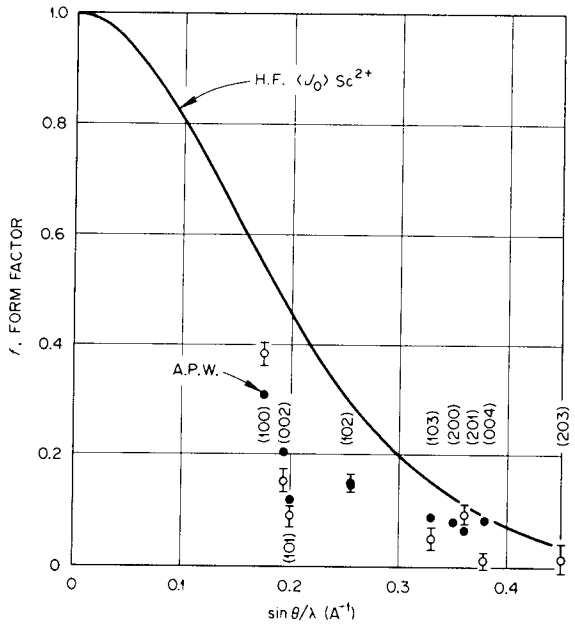


Fig. 9. The paramagnetic form factor of metallic scandium. Open circles are experimental points[13], closed circles are theoretical results[4], and solid line is a free-ion calculation.

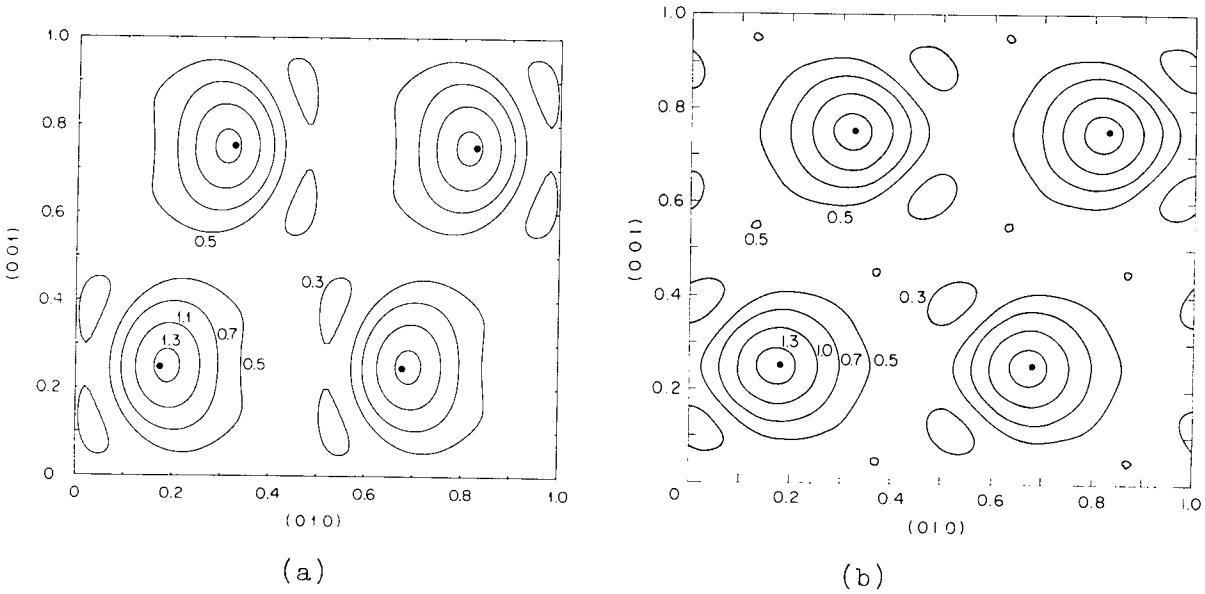


Fig. 10. Projected magnetic moment density in paramagnetic scandium at 100 K and 57.2 kOe. The contours are in units of 10^{-3} μ_B/A^2 with errors in the range 0.03 to 0.08. Atomic sites are indicated by solid circles. a) Experimental results[13]; b) theoretical results[4].

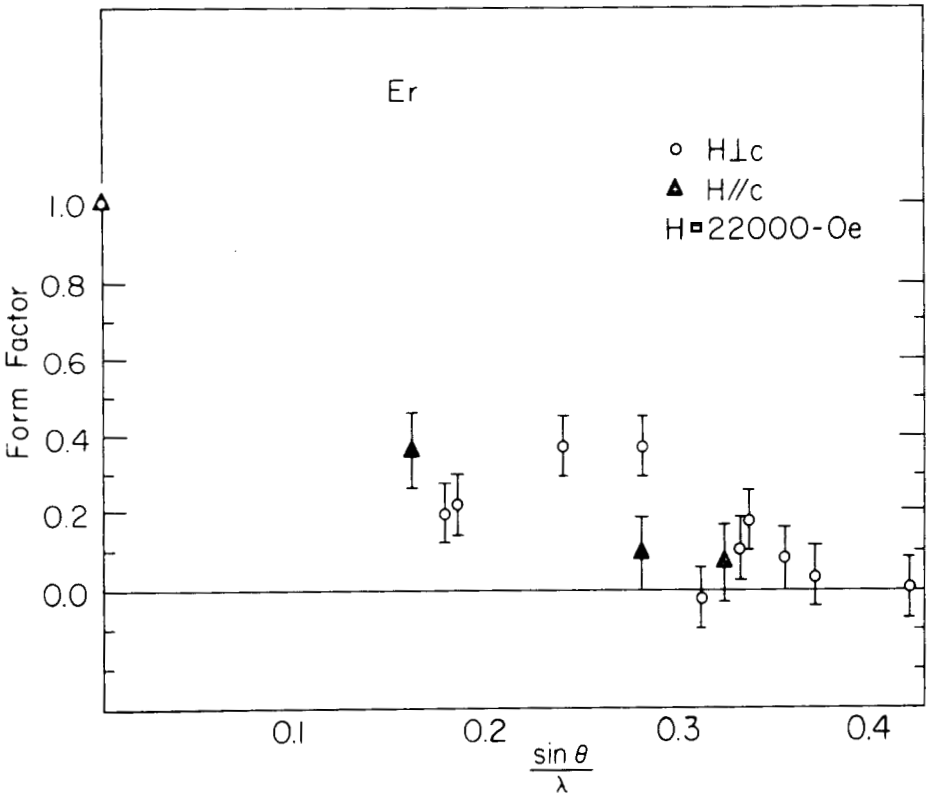


Fig. 11. Angular dependence of the conduction-electron contribution to the coherent paramagnetic scattering amplitude of erbium.

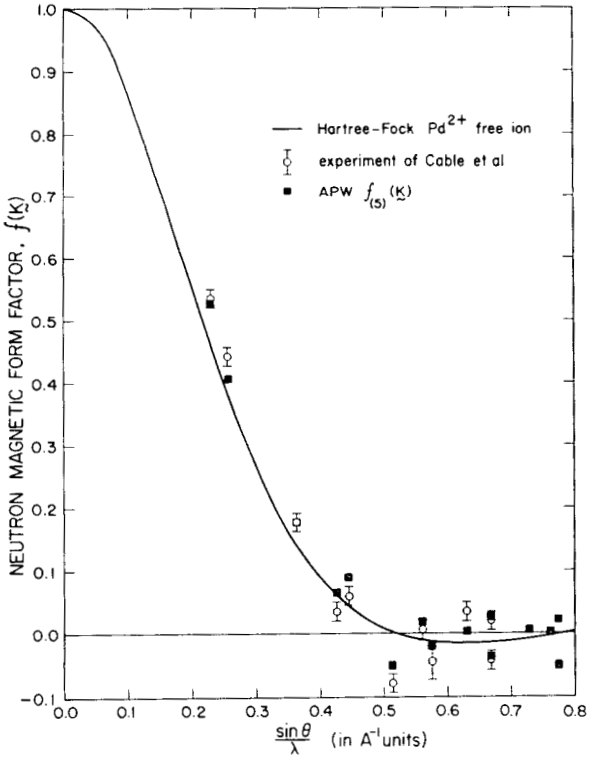


Fig. 12. Comparison between the experimental[7] form factor and the total band 5 form factor[6], the solid curve is the free ion Pd^{2+} Hartree-Fock form factor using the experimental asphericities.

MAGNETISATION DISTRIBUTION IN A PARTIALLY DISORDERED Au_4V ALLOY

P.J. Brown and K.R.A. Ziebeck
Institut Laue-Langevin, BP 156 Centre de Tri, 38042 Grenoble Cedex, France.

ABSTRACT

The magnetisation density distribution in a partially-ordered single crystal of Au_4V has been determined using polarised neutron diffraction. The results show that the magnetisation is essentially localised on the vanadium sites of the ordered structure. If it is assumed that only the vanadium atoms on these sites carry a moment then the localised moment per vanadium atom is $0.58 \pm 01\mu B$. The magnetic form factor of this localised moment has been shown to be in good accord with that calculated by Freeman and Watson[1] for the Vanadium $3d^34s^2$ configuration. The magnetisation density distribution obtained by Fourier inversion shows some aspherical characteristics. A quantitative measure of the asphericity was obtained from a least squares fit between the measured magnetic structure factors and a model in which a localised vanadium atom carrying a moment is superposed on a uniform magnetisation density. The localised moment was allowed to have both spin and orbital contributions within the dipole approximation. The spin moment was allowed to assume an aspherical distribution consistent with its four-fold symmetry. The parameters of the model obtained from the refinement suggest that there is a small negative orbital moment of $-0.026\mu B$, a negative background polarisation of $-2 \times 10^{-4}\ \mu B\ \text{Å}^{-3}$ and indicate that the spin density is extended in the directions of the nearest neighbour vanadium sites.

INTRODUCTION

Gold vanadium alloys in the composition range 8-28 at.% V have been shown[2] to undergo an order-disorder transition at 565°C. The ordered alloy has a structure of the Ni_4Mo ($D1_a$) type. The lattice is tetragonal, space group I4/m with lattice parameters $a = 6.38$, $c = 3.98$ Å and the atomic positions occupied are :

2V in 2(a) 0,0,0 ; 8Au in 8(h) x,y,o

The ordered structure can be simply related to the disordered face-centred-cubic phase and the ordering process consists of a separation of the vanadium atoms from one another, so that in the completely ordered phase all the twelve near neighbours of any vanadium atom are gold atoms. The closest distance of approach of vanadium atoms in the ordered alloy is 3.98 Å corresponding to their separation along the c-axis.

Crevelling et al[3,4] were the first to report that the ordered phase of Au_4V is ferromagnetic with a Curie temperature of 59°K. They and subsequent investigators [5,6] have found that the magnetic properties of this alloy exhibit an unusual sensitivity the state of atomic order. Crevelling and Luo[4] have interpreted this behaviour and also the susceptibilities of dilute Au-V alloys in terms of a model in which d-electron localisation is inhibited by the presence of other vanadium atoms at distances of less than about 3.5 Å. They point out that the V-V distance in the ordered alloy (3.98 Å) is too great for direct exchange to be significant and suggest an exchange mechanism involving the conduction band.

We have undertaken a polarised neutron diffraction study of Au_4V both in the hope of obtaining further evidence for the models which have been proposed to account for the magnetic moments of vanadium atoms and to determine the detailed magnetisation density associated with these moments. Up to the present time the only measurement of the magnetic form factor of vanadium is that of Shull and Ferrier[7] on paramagnetic vanadium. It is of some interest to compare this form factor with one for vanadium atoms which have a spontaneous magnetic moment.

EXPERIMENTAL

Measurements were made at a wavelength of 0.98 Å of the polarisation ratios of all reflections hkl out to $\sin\theta/\lambda = 0.6$ Å^{-1} with l = 0, 1, 2. Higher l values could not be obtained because the detector is limited to a tilt of 35° out of the horizontal plane. Owing to the large magneto-crystalline anisotropy the sample could not be saturated in any direction other than c with the field available. In addition to the polarisation ratios, measurements were made of the integrated intensities of 18 inde-

pendent hk0 reflections in order to determine the positional parameters of the gold sites and the degree of order in the sample. In order to check for the presence of extinction the polarisation ratios of a few strong reflections were remeasured with a neutron wavelength of 0.81 Å, no significant differences were found between these and those measured at 0.98 Å. It was concluded that extinction was not significant because of the low scattering cross-section of our sample.

Measurements of magnetisation versus field at 4.2°K in our alloy were kindly made for us by Dr. J.G. Booth, University of Salford, on a polycristalline sample from the same ingot as the single crystal. From these measurements the saturation magnetisation was determined as $0.568 \pm .016 \mu B$/cell and the anisotropy constant K_1 as 7.3×10^6 erg cm^{-3}.

ANALYSIS OF THE RESULTS

The integrated intensities obtained in the measurements were corrected for the Lorentz effect and for absorption. The nuclear structure factors for these reflections were then obtained by subtracting the magnetic contribution which was calculated from the measured flipping ratios. A least squares refinement of the x and y parameters of the gold sites together with the occupancy of the gold and vanadium sites was then carried out using these structure factors. The gold positional parameters were found to $x = 0.2019 \pm 0005$, $y = 0.3989 \pm 0005$ and the occupancy as 0.518V + 0.482Au on the vanadium sites and 0.869Au + 0.131V on the gold sites.

The ratios of the magnetic to nuclear structure factors were calculated from the observed polarisation ratios making appropriate corrections for depolarisation flipping efficiency and the inclination of the scattering vector to the polarisation direction. The nuclear structure factors were calculated using the parameters obtained from the refinement described above and hence the set of magnetic structure factors shown in table 1 was obtained. Each magnetic structure factor is the mean of several measurements of each of several equivalent reflections. The standard deviations shown are either those given by counting statistics or those

deduced from the deviations of individual results from the mean, whichever is the greater.

A Fourier projection calculated using the hk0 magnetic structure factors showed a large accumulation of magnetisation density located around the vanadium sites at 000 and 1/2 1/2 1/2 with very little density elsewhere. In particular there is no evidence for any significant magnetisation localised on the gold sites even though these contain 12% of vanadium atoms. In the light of this result the magnetic structure factors were calculated for a model in which a moment of 0.284μB (equal to the measured magnetisation per formula unit) was located at each of the vanadium sites 000 and 1/2 1/2 1/2 and had a magnetic form factor corresponding to the vanadium $3d^3 4s^2$ configuration as calculated by Freeman and Watson[1]. These calculated structure factors (column 4 of Table 1) are in good agreement with those observed, there being only a few reflections for which the differences are significantly greater than the standard deviations of the observations. At this stage a Fourier synthesis was calculated using as coefficients the differences between the observed structure factors and those of the model. The resulting maps again showed no significant accumulation of density at the gold sites, but suggested that there is some degree of asphericity in the magnetisation distribution around the vanadium site. On the basis of this result it was decided to attempt to refine a more sophisticated model in which the spin density could be aspherical. Additionally, the high magneto-crystalline anisotropy of the alloy suggests that spin orbit coupling must be important and for this reason the model was extended to allow for orbital magnetic scattering within the dipole approximation (Marshall and Lovesey). No attempt was made to constrain the sum of spin and orbital moments to the measured magnetisation, so the model also allows a uniform background polarisation. The point symmetry of the vanadium site is 4/m and for this symmetry the five d functions split into three singly degenerate and one doubly degenerate combination.

The cartesian forms of these are :

$$\text{Singly degenerate} : (3z^2-r^2)/r^2 \quad ; \quad (x^2-y^2)/r^2 \; ; \quad 2xy/r^2$$

Doubly degenerate : zx/r^2 ; zy/r^2

In the final model therefore there are five variable parameters ; m_s and m_l the spin and orbital moments and the coefficients a_{zx}, $a_{(x^2-y^2)}$, a_{xy} of the symmetrised d-functions. The fourth coefficient, that of the $(3z^2-r^2)/r^2$ function, being obtained from the other three by normalisation. A least squares refinement of these five parameters was carried out using the form factors (jo) corresponding to the $3d^3 4s^2$ configuration and (j2) and (j4) for the $3d^3$ configuration of vanadium[1]. The results obtained are

$$m_s = 0.314 \pm .005 \quad ; \quad m_l = -0.014 \pm .005 \mu B$$

the percentages of the spin moment in each of the symmetrised d-functions are : $(3z^2-r^2)$ = 25% ; zx = zy = 21% ; s^2-y^2 = 18% ; xy = 16%. In the refinement only those reflections for which the observed structure factor is greater than twice the standard deviation were included and the observations were weighted according to their standard deviations. The structure factors calculated from this model as refined are shown in column 5 of table 1.

The sum of the spin and orbital localised moments given by the refinement is 0.300μB compared with the local magnetisation per vanadium site of 0.284μB, which suggests that there is a small negative delocalised density amounting on average to -2×10^{-4} μB A^{-3}. If it is assumed that only vanadium atoms on the vanadium sites carry a moment, then each vanadium atom has a spin moment of $0.60 \pm .01\mu B$ and an orbital moment of $-0.03 \pm .01\mu B$. If as suggested later only vanadium atoms with no vanadium neighbours carry a moment then these values are 2.5 and - 0.13μB.

DISCUSSION

It is probable that the ordered moment in Au_4V arises from the formation of virtual d-states at the vanadium sites. This is consistent with estimations of the magnetic carrier ratio $^{qs}/_{qc}$ and susceptibility measurements which indicate a high but narrow density of d-states at the

Fermi surface. It is clear from our results that the observed form factor for the ordered moment in Au_4V does not differ significantly from that observed for pure vanadium metal. The results indicate that the magnetisation distribution is associated with the vanadium sites and arises predominantly from electron spin moment. The small negative orbital contribution is approximately an order of magnitude less than than estimated from susceptibility measurements.

It is not clear from existing bulk magnetisation results to what extent the number of nearest neighbour vanadium atoms is significant in inhibiting the formation of a local moment. However it is known that the covalent mixing of d-orbitals associated with nearest neighbour vanadium atoms drastically reduces the density of d-states and therefore the local moment. Our observation that there is no observable moment on the Au sites in our crystal suggests that just one near vanadium neighbour is sufficient to destroy its local moment. We calculate that if two nearest neighbours were required, the Au sites should have a moment approximately 10% of that on the V sites.

The large distance between the atoms with ordered moments implies that they couple ferromagnetically by spin interaction through the full d-band of the Au matrix. The observation of a polarisation of the background electron density supports this assertion.

REFERENCES

1. A.J. Freeman and R.E. Watson, Acta Cryst. 14, 231 (1961).
2. E. Stolz and K. Schubert, Z. Metallk. 53, 433 (1962).
3. L. Creveling, H.L. Luo and G.S. Knapp, Phys. Rev. Lett. 18, 851 (1967).
4. L. Creveling and H.L. Luo, Phys. Rev. 176 (2), 614, (1968).
5. G.Y. Chin, V.H. Wernick, R.C. Sherwood and D.R. Mendorf, Solid State Commun. 6, 153 (1968).
6. J.R. Asik, R.V. Gambino and T.R. McGuire, J. Phys. Chem. Solids 33, 391 (1972).
7. C.G. Shull and R.P. Ferrier, Phys. Rev. Lett. 10 (7), 295 (1963).
8. P.J. Brown and J.B. Forsyth, Proc. Phys. Soc. 92, 125 (1967).
9. W. Marshall and S.W. Lovesey, Theory of Thermal Neutron Scattering, p. 152, OUP, Oxford, 1971.

Table I

Observed and Calculated Magnetic Structure Factors

h	k	l	Obs.	Std Devn.	Calc. Model 1	Calc. Model 2	h	k	l	Obs.	Std Devn.	Calc. Model 1	Calc. Model 2
2	0	0	0.4014	0.0004	0.3932	0.3941	3	2	1	0.1527	0.0089	0.1634	0.1661
4	0	0	0.1439	0.0092	0.1586	0.1548	5	2	1	0.0357	0.0139	0.0582	0.0581
6	0	0	0.0612	0.0203	0.0432	0.0388	7	2	1	-0.0128	0.0501	0.0113	0.0101
1	1	0	0.4776	0.0035	0.4697	0.4726	2	3	1	0.1581	0.0098	0.1634	0.1658
3	1	0	0.2437	0.0138	0.2431	0.2406	4	3	1	0.0765	0.0082	0.0753	0.0756
5	1	0	0.0862	0.0124	0.0833	0.0788	6	3	1	0.0253	0.0148	0.0196	0.0186
7	1	0	-0.0047	0.0451	0.0170	0.0131	1	4	1	0.1089	0.0082	0.1250	0.1261
2	2	0	0.2700	0.0088	0.2832	0.2815	3	4	1	0.0497	0.0226	0.0753	0.0754
4	2	0	0.1190	0.0083	0.1221	0.1179	5	4	1	-0.0841	0.0374	0.0259	0.0249
6	2	0	0.0323	0.0046	0.0330	0.0288	2	5	1	0.0435	0.0228	0.0582	0.0575
1	3	0	0.2305	0.0090	0.2431	0.2406	4	5	1	-0.0242	0.0294	0.0259	0.0248
3	3	0	0.1116	0.0127	0.1387	0.1346	1	6	1	-0.0153	0.0509	0.0340	0.0325
5	3	0	0.0687	0.0374	0.0493	0.0449	3	6	1	0.0065	0.0082	0.0196	0.0182
2	4	0	0.1288	0.0052	0.1221	0.1179	2	7	1	-0.0409	0.0840	0.0113	0.0095
4	4	0	0.0331	0.0063	0.0566	0.0522	2	0	2	0.1740	0.0419	0.1786	0.1880
6	4	0	0.0629	0.0213	0.0147	0.0110	4	0	2	0.0732	0.0256	0.0818	0.0866
1	5	0	0.0857	0.0232	0.0833	0.0788	6	0	2	0.0416	0.0334	0.0215	0.0230
3	5	0	0.0129	0.0248	0.0493	0.0449	1	1	2	0.1705	0.0686	0.2056	0.2161
5	5	0	0.0157	0.0052	0.0170	0.0131	3	1	2	0.1239	0.0172	0.1200	0.1269
2	6	0	0.0613	0.0328	0.0330	0.0288	5	1	2	0.0623	0.0169	0.0424	0.0454
1	7	0	0.0397	0.0159	0.0170	0.0131	2	2	2	0.1827	0.0296	0.1361	0.1437
3	7	0	-0.1136	0.0699	0.0093	0.0057	4	2	2	0.0802	0.0266	0.0633	0.0675
1	0	1	0.4484	0.0153	0.4082	0.4163	6	2	2	0.0307	0.0208	0.0167	0.0182
3	0	1	0.2323	0.0103	0.2164	0.2204	1	3	2	0.1502	0.0152	0.1200	0.1263
5	0	1	0.0810	0.0058	0.0753	0.0754	3	3	2	0.0619	0.0202	0.0720	0.0765
7	0	1	0.0045	0.0660	0.0152	0.0139	5	3	2	-0.0254	0.0256	0.0247	0.0267
2	1	1	0.2865	0.0042	0.2929	0.2989	2	4	2	0.0816	0.0136	0.0633	0.0669
4	1	1	0.1585	0.0085	0.1250	0.1266	4	4	2	0.0371	0.0247	0.0283	0.0304
6	1	1	-0.0263	0.0614	0.0340	0.0332	1	5	2	0.0214	0.0624	0.0424	0.0444
1	2	1	0.2838	0.0130	0.2929	0.2987	3	5	2	0.0002	0.0263	0.0247	0.0262

POLARIZED-NEUTRON STUDIES OF ^{242}PuP and ^{242}PuFe$_2$*

G. H. Lander and J. F. Reddy
Materials Science Division
Argonne National Laboratory
Argonne, Illinois 60439

ABSTRACT

The magnetic cross section from ferromagnetic PuP and $PuFe_2$ has been measured at 5 K with polarized neutrons in applied fields of up to 60 kOe. For both systems the angular dependence of the cross section is very small, indicating that the electronic configuration is Pu^{3+} with $J = 5/2$. The unusual form factor arises as a consequence of the partial cancellation of the spin and orbital moments in Pu^{3+}. The saturation magnetization values are smaller than the moments deduced from the neutron experiments, suggesting the presence of a large conduction-electron polarization, which is antiparallel to the $5f$ moment. The importance of magnetically induced preferred orientation and neutron depolarization in these anisotropic systems is discussed.

INTRODUCTION

The most difficult problem in studying actinide systems is in characterizing their electronic structure. In most cases, even the ionization state is not well established. For the last several years actinide compounds have been studied at Argonne National Laboratory with a variety of experimental techniques; magnetization, nuclear-gamma-ray resonance, resistivity, de Haas van Alphen, NMR, low-temperature x-ray and neutron diffraction. Recently we have reported investigations on uranium and neptunium compounds with the NaCl and Laves phase (C-15) crystal structures.[1,2] In extending neutron experiments to plutonium compounds, the main difficulty is that the most abundant isotope ^{239}Pu has a high fission cross section for thermal neutrons. The most suitable isotope[3] is ^{242}Pu, which, although a weak neutron emitter, has a negligible absorption and fission cross section and may be obtained with less than 0.1% contamination of ^{239}Pu. In

*Work supported by the U.S. Energy Research and Development Administration.

the present experiment we have measured the magnetic scattering from two plutonium ferromagnets, PuP (T_C = 125 K) and $PuFe_2$ ($T_C \approx$ 600 K).

EXPERIMENTAL

The samples of PuP and $PuFe_2$, 1.53 and 1.97 g, respectively, were prepared as described by Lam et al.[4] and Aldred et al.[2] The room temperature lattice parameters are 5.652 Å and 7.190 Å for ^{242}PuP and $^{242}PuFe_2$, respectively. The stoichiometry of both compounds was checked by measuring the intensities from unpolarized neutron patterns. PuP has the NaCℓ structure, $PuFe_2$ the Laves phase structure. Crystallographic refinements using scattering lengths of $b_{242(Pu)} = 0.81$, $b_P = 0.51$, and $b_{Fe} = 0.951$ ($\times 10^{-12}$) cm showed the samples were well ordered (crystallographic residuals of $\approx$ 0.02). A small amount (<1%) of an impurity phase Pu_3P_4 was present in the PuP sample. No other phases were observed in the $PuFe_2$ sample.

To measure the magnetic cross section, the samples were placed in a superconducting magnet assembly (H_{max} = 60 kOe) at the CP-5 Research Reactor and the spin-dependent neutron cross section measured as a function of applied magnetic field at 5 K. In both compounds the cross section was essentially independent of the external magnetic field. Because of the large orbital magnetic moment on the Pu^{3+} ion, these materials have large magnetocrystalline anisotropies and the application of a magnetic field leads to substantial preferred orientation.[2] Fig. 1 illustrates the situation for PuP. The reorientation of the domains and particles has three important consequences; (a) it allows the easy axis of magnetization to be determined and this is <100> for both PuP and $PuFe_2$, (b) it greatly enhances the Bragg intensities of certain reflections (whereas others are reduced in intensity) and thus leads to an increase in the experimental accuracy, and (c) it reduces the extent of neutron beam depolarization through the sample. Although both the incident beam polarization P_i and the flipping efficiency e are high (>0.992), the neutron beam is depolarized by domains that have magnetic components perpendicular to the quantization axis of the neutron spin. In a completely saturated ferromagnetic powder the depolarization will be small, but in these anisotropic systems

we are unable to achieve saturation with 60 kOe. To measure the depolarization of the transmitted neutron beam, the flipping ratio from a small CoFe analyzer crystal placed directly behind the specimen was measured. If the polarization of the beam emerging from a specimen of thickness t (= 0.635 cm) is P and the depolarization in the specimen is uniform, then the polarization of the beam after travelling a distance d may be written[5] $P' = P_i e - \beta d$, where $\beta = (1/t) \ln (P_i/P')$. The depolarization is defined as 1 - D, where $D = \int \exp(-\beta d)\, dV$ integrated over the whole crystal. The depolarization as a function of the applied field is shown for $PuFe_2$ and $NpFe_2$ in Fig. 2. The depolarization for PuP was less than 0.01 at all fields. As expected from a simple argument involving domain walls,[6] D decreases logarithmically with increasing field.

RESULTS AND DISCUSSION

The neutron experiments determine the quantity $\mu f(\vec{\kappa})$, where μ is the magnetic moment, $f(\vec{\kappa})$ is the magnetic form factor, and $\vec{\kappa}$ is the scattering vector, $|\vec{\kappa}| = 4\pi \sin\theta/\lambda$. The results are shown in Figs. 3 and 4. The first and most important, point is that the reduction in the values of $\mu f(\vec{\kappa})$ with increasing κ is anomously small. The magnetic form factor from uranium ions,[7] for example, falls by a factor of four between $\sin\theta/\lambda = 0$ and 0.4 Å^{-1}. The unusual Pu form factor occurs because of the partial cancellation of the spin and orbital angular momenta in the f^5 configurations. In the Russell-Saunder's Hunds rule ground state for f^5: $^6H_{5/2}$, S = 5/2, L = 5, J = 5/2, and g = 2/7. The spin density is antiparallel to the orbital current density. Since the orbital density is more contracted in real space than the spin density, the subtraction of these two leads to regions of negative density with respect to the total magnetization. The Fourier transform of such a quantity, which is related to the magnetic form factor, has a maximum at $\kappa > 0$. Such a form factor has been observed[8] in samarium ($4f^5$). As a first approximation, we may write[7]

$$\mu f(\vec{\kappa}) = \mu(\langle j_o \rangle + c_2 \langle j_2 \rangle + ...) \qquad (1)$$

where the $\langle j_i \rangle$ are integrals related to the spatial extent of the 5f electrons and are functions of κ only, and the c_i coefficients are determined

by the electronic state of the ion. Since $\langle j_o \rangle = 1$ at $\kappa = 0$ and then decreases, whereas $\langle j_2 \rangle = 0$ at $\kappa = 0$ and slowly increases, to obtain a value of the form factor with a maximum at $\kappa > 0$ the c_2 coefficient must be large. For d electrons no free-ion configuration has a large c_2 coefficient. In f electron systems[9] the dipole approximation gives values of c_2 of 1.50, 1.75, 2.33, and 6.00 for f^2, f^3, f^4 and f^5 configurations. There is, therefore, a large difference between the form factor of f^4 and f^5 states. This situation implies that neutron experiments can give unique information about the electronic structure of Sm($4f^5$) and Pu($5f^5$) ions.

The broken lines in Figs. 3 and 4 are best fits to free-ion $5f^5(^6H_{5/2})$ form factors with $c_2 = 5.42$ and relativistic Dirac-Fock $\langle j_i \rangle$ radial integrals.[10] Although the error bars are rather large for the $PuFe_2$ experiment on account of the iron moment of 1.45 μ_B, the experimental points for both compounds clearly have a less distinct maximum than that predicted for the $^6H_{5/2}$ state (broken lines). In the case of PuP a detailed analysis leads to the experimental parameters

$$\mu = 0.77 \pm 0.07\ \mu_B \text{ and } c_2 = 3.8 \pm 0.7. \qquad (2)$$

In calculating the theoretical cross section from Pu^{3+} ions, we have used the tensor-operator method.[11] The first important modification of the $^6H_{5/2}$ state is to consider the effect of the spin-orbit coupling parameter[12] $\xi = 2260\ cm^{-1}$, which mixes states of different S and L components into the ground state J = 5/2 manifold. The resulting intermediate coupling wave function gives $\mu = 0.962\ \mu_B$, $c_2 = 3.80$. The effect of the intermediate coupling is then to reduce the theoretical value of c_2 so that good agreement with experiment is obtained. More complete calculations, which are now in progress, must also take account the crystal-field interaction and the possible effects of mixed J configurations.

The important conclusions are as follows: (a) The plutonium ion in both PuP and $PuFe_2$ is in a tripositive state, i.e., an f^5 configuration. (b) The neutron magnetic form factor cannot be understood on the basis of the Russell-Saunder's Hunds rule $^6H_{5/2}$ state, but requires (as expected)

intermediate coupling wave functions. (c) A substantial negative conduction-electron polarization exists. In PuP magnetization experiments[4] give 0.42 μ_B, and the discrepancy of -0.35 μ_B between the neutron and magnetization values for the moments is similar to that found in uranium and neptunium ferromagnets.[1,2]

ACKNOWLEDGMENTS

We are grateful to R. L. Hitterman for experimental assistance and to D. J. Lam and A. T. Aldred for a number of useful discussions.

REFERENCES

1. A. T. Aldred, B. D. Dunlap, A. R. Harvey, D. J. Lam, G. H. Lander, and M. H. Mueller, Phys. Rev. B 9, 3766 (1974).
2. A. T. Aldred, B. D. Dunlap, D. J. Lam, G. H. Lander, M. H. Mueller, and I. Nowik, Phys. Rev. B 11, 530 (1975).
3. G. H. Lander and M. H. Mueller, Acta Cryst. B 27, 2284 (1971).
4. D. J. Lam, F. Y. Fradin, and O. L. Kruger, Phys. Rev. 187, 606 (1969).
5. P. J. Brown and J. B. Forsyth, Brit. J. Appl. Physics, 15, 1529 (1964).
6. M. Burgy, D. J. Hughes, J. R. Wallace, R. B. Heller, and W. E. Wolf Phys. Rev. 80, 953 (1950).
7. A. J. Freeman, J. P. Desclaux, G. H. Lander, and J. Faber, Jr., Phys. Rev. B 13, 1168 (1976); ibid B 13, 1177 (1976).
8. W. C. Koehler and R. M. Moon, Phys. Rev. Letters 29, 1468 (1972).
9. G. H. Lander and T. O. Brun, J. Chem. Phys. 53, 1387 (1970).
10. We are grateful to A. J. Freeman for supplying us with the relativistic $\langle j_i \rangle$ integrals for plutonium.
11. W. Marshall and S. W. Lovesey, "Theory of Thermal Neutron Scattering," (Oxford U. P., London, 1971) Ch. 6, p. 127.
12. J. G. Conway and K. Rajnak, J. Chem. Phys. 44, 348 (1966).

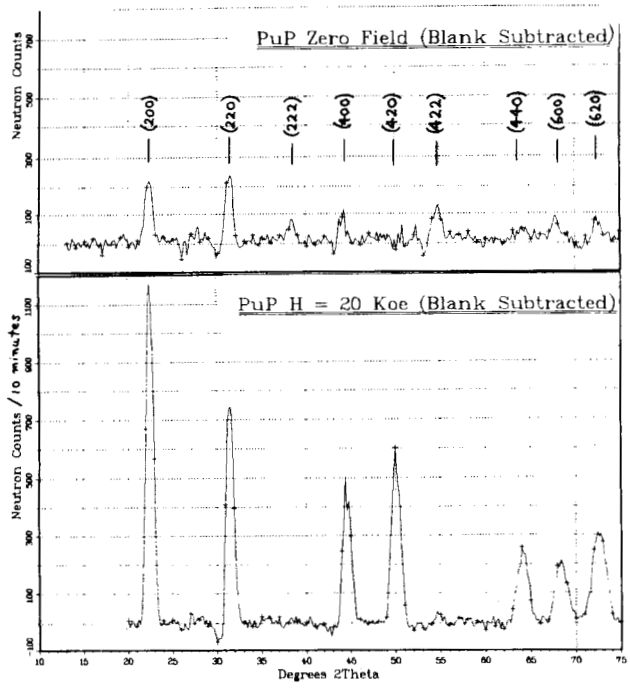


Fig. 1. Neutron patterns from ^{242}PuP taken before (top) and after (below) the application of a 20 kOe field.

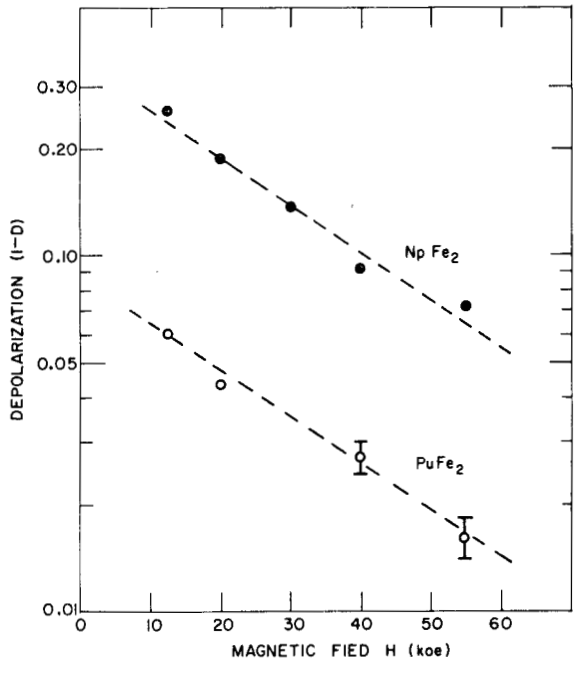


Fig. 2. Neutron depolarization as a function of applied magnetic field for polycrystalline samples of $NpFe_2$ and $PuFe_2$.

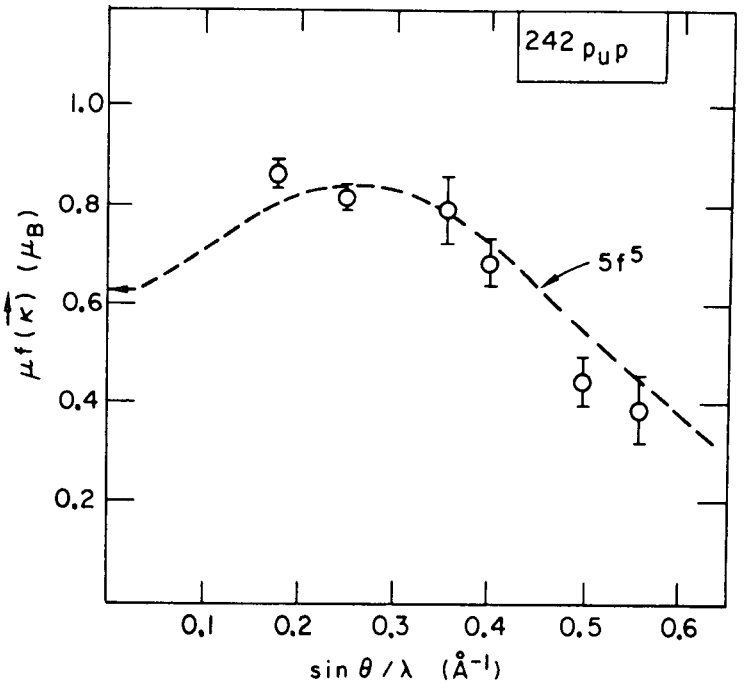


Fig. 3. Results for PuP. The broken line is a best fit to the data with a $5f^5$:$^6H_{5/2}$ free ion configuration. The saturation magnetization of PuP (Ref. 4) is 0.42.

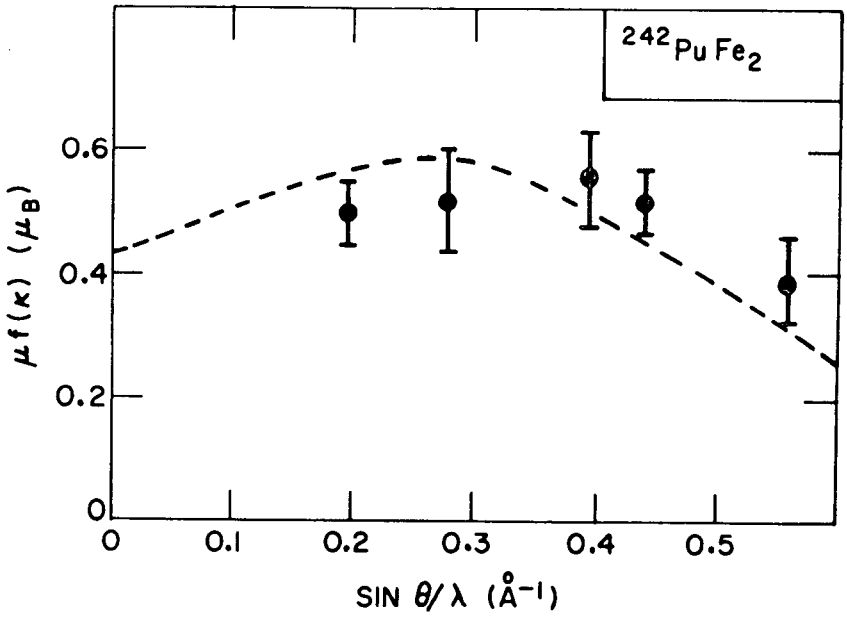


Fig. 4. Results for $PuFe_2$. The broken line is appropriate for a $5f^5$: $^6H_{5/2}$ configuration.

THE STRUCTURAL AND MAGNETIC PROPERTIES OF MnAs STUDIED BY SUBSTITUTING Mn WITH OTHER TRANSITION METALS

A.F. Andresen
Institutt for Atomenergi, Kjeller, Norway

K. Selte and A. Kjekshus
Chemistry Department, University of Oslo, Oslo 3, Norway

ABSTRACT

On cooling from high temperature MnAs transforms at 387 K from the NiAs-type to the MnP-type structure. However, on further cooling to 306 K it again reverts back to the NiAs-type structure and becomes ferromagnetic. It has been shown that by applying a pressure it is in fact possible to retain the MnP-type structure down to the lowest temperatures. We have found this to be the case also when a small amount of Mn is substituted by another transition element (V, Cr, Fe, Co). All the ternary phases thus prepared develop a helical magnetic structure which is different from that observed in other MnP-type compounds. The propagation vector lies along the othorhombic a-axis instead of c-axis, and the double helix runs through a different set of atoms. By extrapolating to zero substitution it is possible to derive a Néel-temperature of $T_N = 210 \pm 1$ K for a hypothetical helimagnetic mode of MnAs.

INTRODUCTION

MnAs has been found to exhibit several interesting phenomena both with respect to its crystallographic and magnetic properties. Fig. 1 summarizes certain aspects of its behaviour as a function of temperature. As indicated in the central portion of the diagram the crystal structure at atmospheric pressure is of the NiAs-type both at high and low temperature, separated by an intermediate region of MnP-type structure. At low temperature the compound is ferromagnetic with a Curie point of 317 K, at which temperature there is a first order transition to a paramagnetic MnP-type phase. This transformation has associated with it a thermal hysteresis, a latent heat, a discontinuous change in electrical resistivity and a discontinuous change in density.

It has been shown by Menyuk et al.[1] that by applying a pressure it is possible to stabilize the MnP-type structure to lower temperatures. Their phase diagram is shown on the right hand side of Fig. 1. We have found that by substituting a small amount of Mn with another transition metal (V, Cr, Fe, Co) it is also possible to stabilize the MnP-type structure and to make it the stable structure down to liquid helium temperature. Such a substitution leads to a contraction of the lattice, and is thus equivalent to the application of a pressure except for a change in the number of electrons. The phase diagrams obtained for these ternary systems are shown in the left hand side of Fig. 1.

Whereas pure MnAs becomes ferromagnetic at low temperature, the MnP-type phases containing a small amount of other transition metals develop a spiral magnetic structure at low temperature. This is, however, of another type than that found in other MnP-type compounds (MnP, FeP, CrAs, FeAs). A description of this structure will be given in the following detailed discussion of the ternary systems.

THE SYSTEM $Mn_{1-t}Fe_tAs$

In this system there is only a limited solid solubility[2]. This can be ascribed to the different electronic states of the constituents. In MnAs having the NiAs-type structure the Mn atoms are in a high spin state, whereas in FeAs with the MnP-type structure the Fe atoms are in a low spin state.

There are three types of magnetic structure appearing (Fig. 2). For t close to one we obtain the normal double spiral structure propagating along the c-axis, c-type (Fig. 2, A). However, for $0.03 < t < 0.12$ we observe another double spiral structure with the propagation vector along the a-axis, a-type (Fig. 2, C). This structure also differs from the c-type spiral structure by displaying a phase difference between the spirals through atoms 1 and 3 (correspondingly 2 and 4) instead of between atoms 1 and 2 (correspondingly 3 and 4). The Néel point is 210 ± 1 K at $t = 0.05$ and 206 ± 1 K at $t = 0.10$. The moment is $1.6 \pm 0.1\ \mu_B$.

In an intermediate region $0.65 < t < \sim 0.90$ we observe an antiferro-

magnetic structure (Fig. 2, B) with two interpenetrating, mutually perpendicular spin systems. This can also be considered a spiral magnetic structure propagating along the a-axis, with a period which is commensurate with the unit cell length, namely 2 a. Since the moment is very low, $0.71 \pm 0.04\ \mu_B$ at 5 K, this solution is somewhat uncertain. The Néel point at t = 0.85 is 54 ± 1 K.

THE SYSTEMS $V_{1-t}Mn_tAs$ AND $Mn_{1-t}Co_tAs$

The phase diagrams for these two systems are shown in Fig. 3. Whereas there is a large miscibility gap in the system $Mn_{1-t}Co_tAs$[3] there is a complete mutual solubility of VAs and MnAs[4]. No magnetic ordering has been found in either VAs or CoAs down to liquid helium temperature, and the addition of a small amount of MnAs does not produce any cooperative magnetic phenomena. However, close to MnAs an a-type spiral structure appears in both systems. The Néel temperature decreases rather rapidly with increasing amount of either V or Co. At 5 % V the Néel temperature is 206 K, at 10 % V 200 K and at 30 % V 142 K. With the addition of Co the decrease is even more rapid. At 5 % Co 196 K, at 10 % Co 174 K and at 15 % Co 152 K. In particular in the system $V_{1-t}Mn_tAs$ the spiral structure can be followed over a large range of compositions, $\sim 0.60 < t \leq 0.95$. The spiral period increases with increasing amount of V and the highest value observed is 11.8·a at 30 % V.

THE SYSTEM $Cr_{1-t}Mn_tAs$

This system has previously been studied by Kazame and Watanabe[5] who found the c-type helical structure to exist up to t = 0.6. For $0.7 < t < 0.95$ they deduced an antiferromagnetic structure. This conclusion was mainly based on the presence of a magnetic peak which they indexed as the (001) reflection. We have found this peak to be the $(001)^{\bullet}$ peak due to an a-type spiral structure, and have also observed the $(000)^{\pm}$ reflection which occurs at a very low angle. Thus, in this system there is a transition between the c-type and the a-type spiral structure as the composition is changed, and in between there is a ferromagnetic region.

It is interesting to note that on cooling a single phase sample of

composition $Cr_{0.05}Mn_{0.95}As$ below 250 K a separation in two phases is observed. One is an NiAs-type phase with a composition close to MnAs. The other retains the MnP-type structure and has a composition close to $Cr_{0.10}Mn_{0.90}As$. This phase separation is reversible with a hysteresis of about 30°. The phase border is therefore close to t = 0.90 at 250 K and the ionic movement is large even at this low temperature. The Néel temperature at t = 0.90 is 210 K.

CONCLUSIONS

In all these ternary systems having MnAs as one constituent and crystallizing with the MnP-type structure, we observe a new type of spiral structure with the propagation vector along the a-axis. This is undoubtedly connected with the particular ratio between the interatomic distances found in the vicinity of MnAs. The tendency for spiral formation in MnP-type compounds can be ascribed to the zig-zag chains of metal atoms formed by the orthorhombic deformation of the NiAs-type structure. This leads to 4 nearest neighbour metal-metal contacts instead of 2 as in the NiAs-type structure. The formation of an a-axis spiral when the compositions are close to MnAs can probably be ascribed to the relatively short metal-metal distances along the a-axis for these compositions. In ferro-magnetic MnAs where the interactions along the a-axis (hexagonal c-axis) dominate, the moments are also perpendicular to this axis.

In several respects phases with the a-type spiral structure show characteristic features different from those with the c-type spiral structure. Thus the a-type spiral is stable over a larger range of composition than the c-type spiral. In the system $V_{1-t}Mn_tAs$, for instance, the a type spiral is stable up to a substitution level of 40 % V, whereas the c-type spiral usually disappear at a substitution level of only 5 - 10 %.

The Néel temperature decreases with increasing amount of substitution and more rapidly for phases with the c-type spiral structure than for phases with the a-type spiral structure. The rate of decrease depends on the type of atom being substituted. Thus, substitution with Cr and Fe leads to none or only a slight decrease, whereas substitution with V

and Co leads to a more rapid decrease. Extrapolating to zero substitution leads for all systems to a hypothetical Néel temperature of 210 ± 1 K for pure MnAs. This is close to the Néel temperature obtained from the high pressure data of Menyuk et al.[1] by extrapolating to a pressure of 1 atm. (Fig. 1).

REFERENCES

1. N. Menyuk, J.A. Kafalas, K. Dwight, and J.B. Goodenough, Phys. Rev. 177, 942 (1969).
2. K. Selte, A. Kjekshus, and A.F. Andresen, Acta Chem. Scand. A28, 61 (1974).
3. K. Selte, A. Kjekshus, G. Valde, and A.F. Andresen. Submitted for publication in Acta Chem. Scand.
4. K. Selte, A. Kjekshus, G. Valde and A.F. Andresen, Acta Chem. Scand. A30, 8 (1976).
5. N. Kazæme and H. Watanabe, J. Phys. Soc. Japan 30, 1319 (1971).

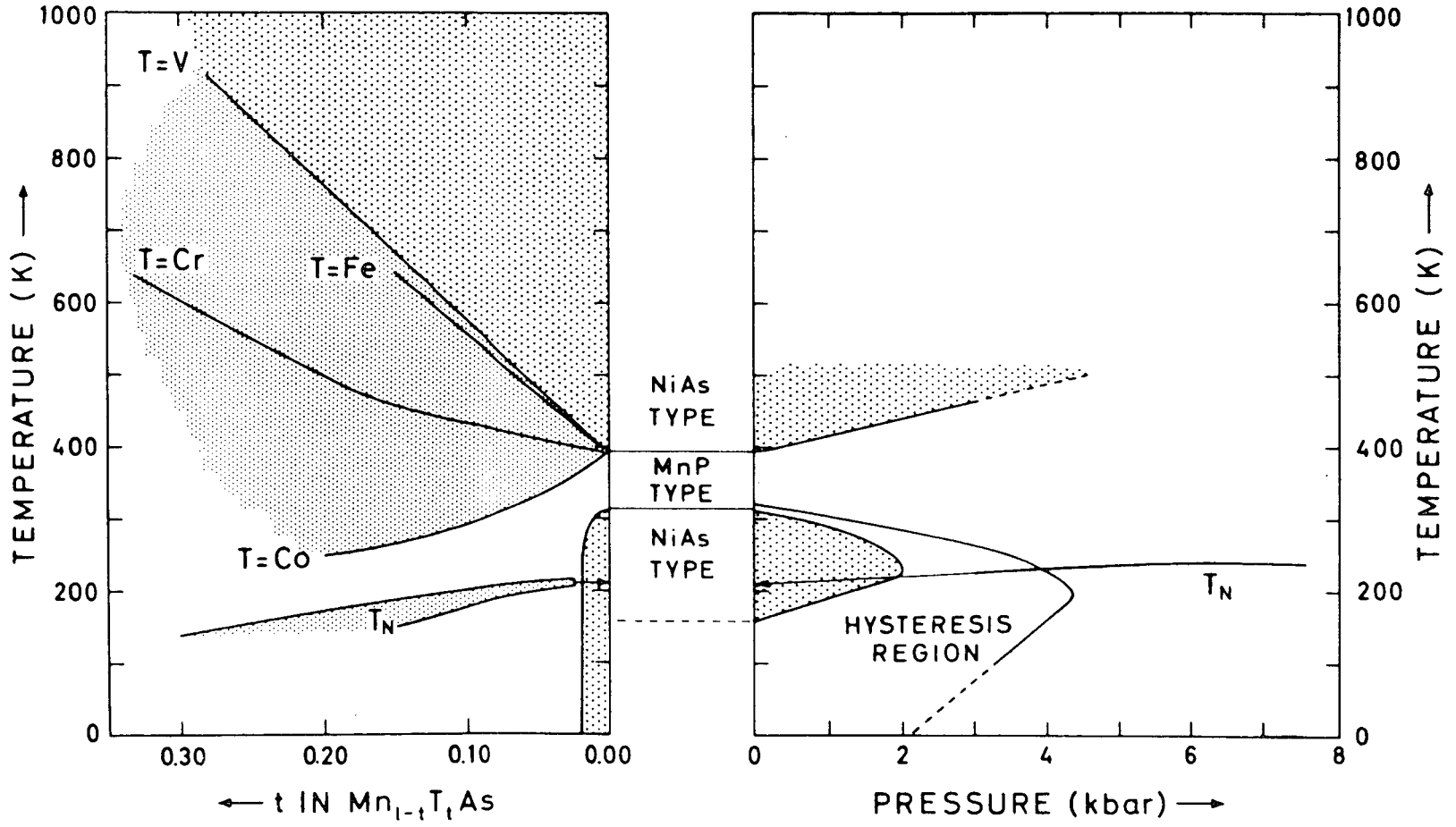


Fig. 1. Phase relationships in MnAs and $Mn_{1-t}T_tAs$ (T = V, Cr, Fe, Co). Right hand side according to Menyuk et al.[1]

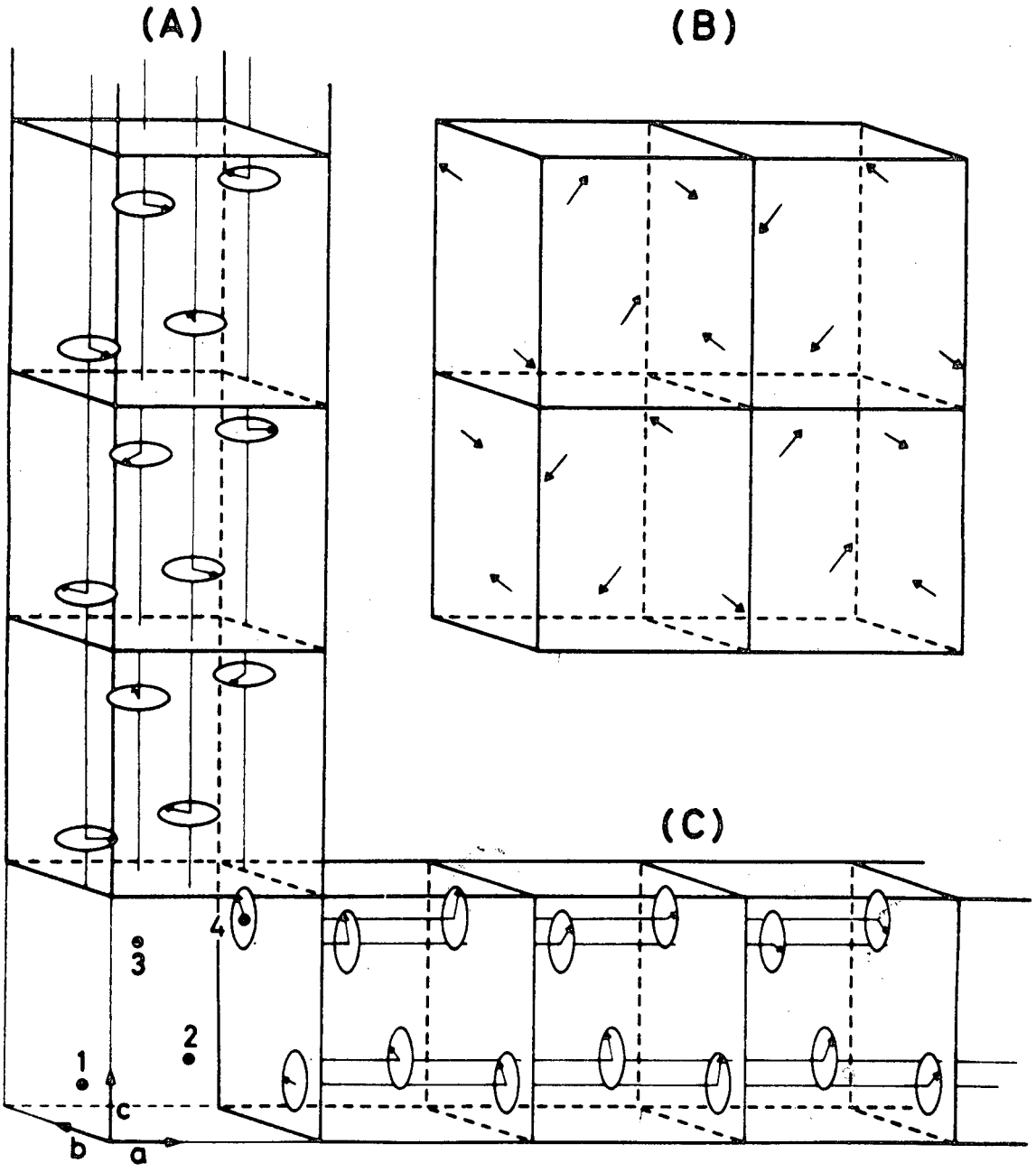


Fig. 2. Magnetic structures appearing in the $Mn_{1-t}Fe_tAs$ system. (A) is c-type spiral structure. (C) is a-type spiral structure

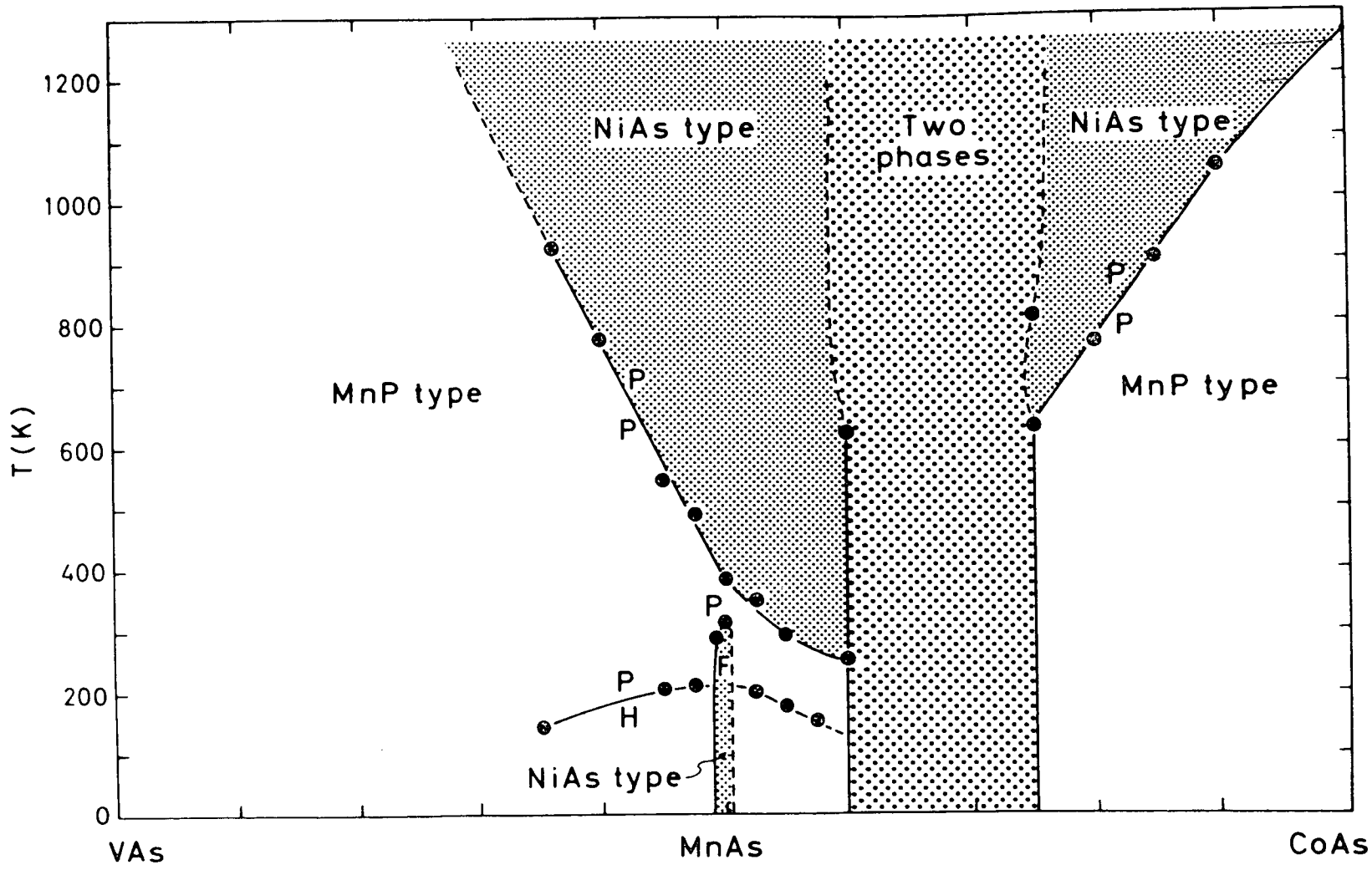


Fig. 3. Phase diagrams for the systems $V_{1-t}Mn_tAs$ and $Mn_{1-t}Co_tAs$

MAGNETIC MOMENT DISTRIBUTION IN Cu_2MnAl

V.C. Rakhecha, R. Chakravarthy and N.S. Satya Murthy
Solid State Physics Section, Nuclear Physics Division
Bhabha Atomic Research Centre, Bombay 400 085, India

ABSTRACT

The Heusler alloy $Cu_2Mn_{0.863}Al_{1.057}$ with an $L2_1$ structure has been studied by the polarised neutron technique. Magnetic structure amplitudes of 47 reflections up $\sin\theta/\lambda = 0.87$ A^{0-1} in $\langle 110\rangle$, $\langle 100\rangle$ and $\langle 112\rangle$ zones have been measured. The nuclear structure amplitudes were least-squares refined from the polarisation ratios, the M/N values (M = magnetic structure amplitude, N = nuclear structure amplitude for the unit cell), as well as from the unpolarised neutron Bragg intensity measurements. The experimental results can be well explained in terms of a localised moment of 2.76 μ_B for the nominal Mn-sites and Mn^{2+} free ion form factor. The asymmetry of the moment distribution is small. The Cu-sites may also have a small moment of $< -0.05\,\mu_B$. The moment distribution in this Heusler alloy therefore seems to be very much like that found in another Heusler alloy Pd_2MnSn.

INTRODUCTION

In this paper we present more extensive polarised neutron measurements on the Heusler alloy Cu_2MnAl than any reported previously[1,2]. Polarisation ratios were measured for 47 independent reflections in three different zones $\langle 001\rangle$, $\langle 110\rangle$ and $\langle 112\rangle$. Integrated Bragg intensity measurements with unpolarised neutrons were also made on the same crystal to determine the nuclear scattering parameters. The composition of the sample* is known to be $Cu_2Mn_{0.863}Al_{1.057}$ and its saturation magnetisation

* The crystals used in the measurements were cut from a bigger crystal supplied by Siltronix, France.

value at 300°K is 2.89 μ_B per formula unit*.

UNPOLARISED NEUTRON MEASUREMENTS

The Heusler $L2_1$ structure[3] consists of four interpenetrating f.c.c. sublattices A, B, C and D. In ordered Cu_2MnAl the A and C sites are occupied by Cu and the B and D sites respectively by Mn and Al and the structure is centrosymmetric. The non-zero structure amplitudes belong to three groups of reflections[3] (h, k, l all even or all odd) which for nuclear scattering are shown to be

$$\begin{aligned} &h\ k\ l \text{ all odd} && N = 4\,(b_{Mn} - b_{Al}) \\ &(h+k+l)/2 = 2n+1 && N = 4\,(2b_{Cu} - b_{Mn} - b_{Al}) \\ &(h+k+l)/2 = 2n && N = 4\,(2b_{Cu} + b_{Mn} + b_{Al}) \end{aligned}$$

Unpolarised neutron measurements were made ($\lambda = 1.24$ Å) for 11 high angle reflections ((511) and beyond) in $\langle 110 \rangle$ zone using the same crystal which was used in polarised neutron measurements. Refinement of the site-scattering amplitudes was carried out with the constrint

$$\begin{aligned} &2\langle b_{Cu}\rangle + \langle b_{Mn}\rangle + \langle b_{Al}\rangle = \\ &2\text{x}0.76 - 0.863\text{x}0.37 + 1.057\text{x}0.35 \simeq 1.57 \end{aligned} \qquad (1)$$

and for different values of extinction parameter g[4]. The fit did not converge satisfactorily however with extinction also as a free parameter**. However extinction made only a slight difference in the values of different scattering amplitudes. Following values were finally obtained

---

* This value was further confirmed by measurements kindly made by Dr. M.J. Patni and Prof. C.M. Srivastava, I.I.T. Bombay.

** Some 180° equivalents had somewhat different intensities which could not be understood. This may partly be the reason for this behaviour.

$$\langle b_{Cu} \rangle = 0.75 \times 10^{-12} \text{ cm}$$
$$\langle b_{Mn} \rangle = (-0.28 \pm 0.01) \times 10^{-12} \text{ cm}$$
$$\langle b_{Al} \rangle = (0.36 \pm 0.01) \times 10^{-12} \text{ cm} \qquad (2)$$

These values indicate that Cu- and Al- sites are almost fully occupied by the respective ions and the excess Al goes to the Mn-sites.

POLARISED NEUTRON MEASUREMENTS

Three samples employed in the measurements (λ = 0.92 Å, Polarisation P = 0.93, flipping f = 0.99) in different zones were parallelopiped in shape, about 1 mm thick and 10 mm long. A saturating magnetising field of 8 Koe was used in the measurements. Polarisation ratios for most reflections were measured for at least two equivalents in the same zone. Also most reflections (particularly at low angles) common to different zones were measured separately to detect any multiple Bragg effects. Only slight variations were observed for some reflections ((220), (311), (400)) which indicate that these effects are small compared to other uncertainties in the experiment (long term fluctuations of flipping, lack of depolarisation measurements for the sample).

ANALYSIS AND RESULTS

The M/N-values were derived with the inclusion of varying amounts of extinction in the analysis of polarisation ratios which was seen to affect most the (111) and (200) reflections and to a lesser extent (220). The M/N-values of the three groups of reflections mentioned above indicated directly that the respective magnetic structure amplitudes scaled closely to the Mn^{2+} free ion form factor. In view of the non-perfect atomic composition of the sample it was thought best to analyse directly the polarisation ratios and the M/N-values (obtained with varying amounts of extinction correction) in terms of nuclear scattering parameters, magnetic moments at different sites and model form factors (spherically

averaged form factors derived from the experimental M-values themselves, or Mn^{2+} form factor for the Mn-site). The extinction parameter g refined from the polarisation ratios was found to range around 50 depending on the form factor and the weighting scheme used. The M/N-values obtained subsequently were refined for nuclear scattering parameters and magnetic moments at Mn- and Cu-sites, (Al-site moment assumed zero). Following values were obtained (with g = 10)

$$\begin{aligned} \langle b_{Cu} \rangle &= 0.76 \times 10^{-12} \text{ cm} \\ \langle b_{Mn} \rangle &= (-0.29 \pm 0.01) \times 10^{-12} \text{ cm} \\ \langle b_{Al} \rangle &= (0.34 \pm 0.01) \times 10^{-12} \text{ cm} \\ \langle \mu_{Mn} \rangle &= 2.76 \pm 0.05 \ \mu_B \\ \langle \mu_{Cu} \rangle &= -0.02 \pm 0.03 \ \mu_B \end{aligned} \qquad (3)$$

The nuclear scattering amplitudes obtained here compare well with those obtained in the unpolarised neutron case (Eq. (2)). The magnetic structure amplitudes calculated with the above moment values and with the Mn^{2+} free ion form factor[5] for the Mn-sites lie on the continuous curve in Fig. 1. The experimental M values, shown in the same figure (dots), are seen to lie closely on the calculated curve. This leads to the conclusion that the magnetic moment is well localised and almost completely resides on the Mn-sites with an Mn^{2+} free ion like distribution. Similar results were obtained by Ishikawa et al[6] for another Heusler alloy Pd_2MnSn. Comparing the value of Mn-site moment with the magnetisation value of $2.89 \mu_B$ it appears that the balance may be ascribed to the conduction electron polarisation. The moment on the individual Mn atoms (at 300°K) turns out to be $3.2 \mu_B$ which agrees well with that obtained by Takata[2].

REFERENCES

1. J.B. Forsyth, Acta Cryst. Suppl. 16, A126 (1963).
2. H. Takata, J. Phys. Soc. Japan 20, 1743 (1965).
3. Peter J. Webster, Contemp. Phys. 10, 571 (1969).

4. W.H. Zachariasen, Acta Cryst. 23, 558 (1967).

5. R.E. Watson and A.J. Freeman, Acta Cryst. 14, 27 (1961).

6. Y. Ishikawa, K. Tajima and P. Radhakrishna, Annual Report of Institut Max Von Laue. Paul Langevin, p.111, 1974.

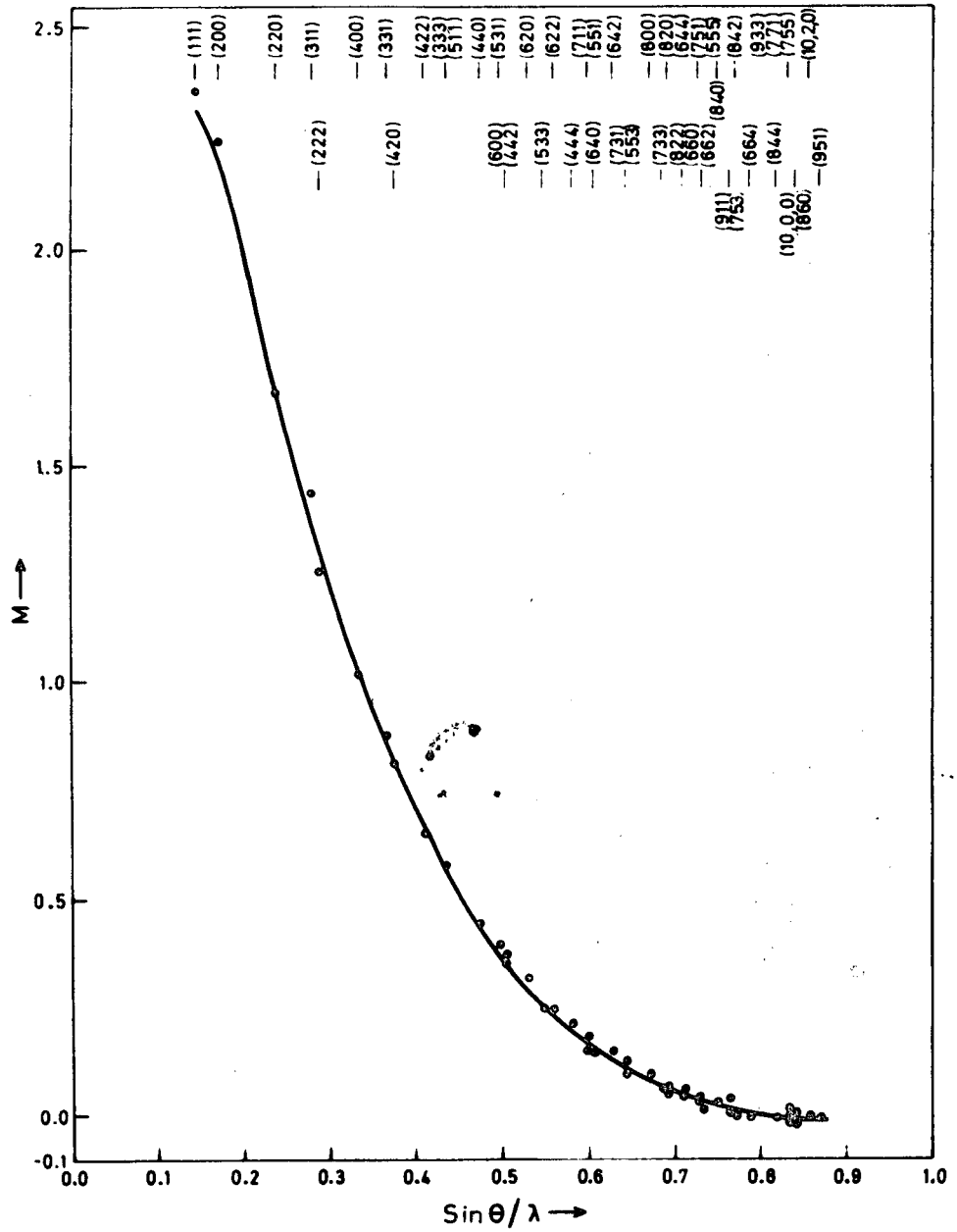


Fig. 1. Magnetic Structure Amplitudes in $Cu_2Mn_{0.863}Al_{1.057}$

A NEUTRON DIFFRACTION STUDY OF COBALT-DOPED $YbFeO_3$

S. K. Paranjpe and R. J. Begum
Solid State Physics Section, Nuclear Physics Division,
Bhabha Atomic Research Centre, Trombay,
Bombay 400 085, India.

ABSTRACT

$YbFeO_3$ belongs to the family of orthoferrites which show weak ferromagnetic properties because of canted antiferromagnetic ordering. We report here our measurements of nuclear and magnetic structure factors on a single crystal sample of $YbFeO_3$ doped with 9% cobalt. Intensities of 75 purely nuclear reflections, mostly from $/\underline{\ }001/\underline{\ }$ zone have been used to determine the atomic coordinates by the least squares refinement technique. 36 magnetic reflections have been measured in $/\underline{\ }100/\underline{\ }$ and $/\underline{\ }010/\underline{\ }$ zones upto $\sin\theta/\lambda = 0.67\ A^{-1}$. At room temperature only the Fe moments are ordered and hence an analysis of the experimental data has straightway given the form factor of Fe^{3+} ions in octahedral environment. This has been compared with other experimental and calculated Fe^{3+} form factors. Substitution of Fe by a small amount of Co does not have any appreciable effect on the atomic coordinates, but the magnetic properties are drastically altered.

INTRODUCTION

Like many other rare earth orthoferrites, $YbFeO_3$ crystallizes with an orthorhombic distortion of the perovskite structure. Its a and b axes correspond approximately to the face diagonals of the cubic unit cell of the ideal perovskite while the c axis is twice that of the cubic cell. In a perovskite ABO_3, as shown in Fig. 1, the A ions have 12 equidistant oxygen neighbours while the B ions have an octahedral coordination of oxygen ions. In an orthoferrite, the A ions and the oxygen

ions are displaced from their ideal cubic positions and consequently the oxygen polyhedra around A ions get quite distorted. But the displacement of oxygen ions around B ions still leaves the polyhedra an almost regular octahedron. Rare earth iron orthoferrites contain Fe^{3+} ions in these octahedral sites only and thus offer opportunities of studying Fe^{3+} form factor in octahedral environment.

Pure $YbFeO_3$ exhibit two first order magnetic transitions[1,2] corresponding to the independent ordering of the Fe and Yb moments. The Fe moments are coupled by strong antiferromagnetic interactions, but are slightly canted with respect to each other to give rise to a small spontaneous moment perpendicular to the antiferromagnetic axis. Hence $YbFeO_3$ has weak ferromagnetic properties. At temperatures below about 8°K, the direction of the spontaneous magnetisation is along the a axis, but changes to the c axis when the temperature is increased and the ordering of rare earth moments disappear. A single crystal specimen of $YbFe_{0.91}Co_{0.09}O_3$ has been used in the present experiment. Such dopings may change the atomic coordinates as well as the magnetic properties. Our results show that in this particular case the unit cell dimensions and the atomic coordinates remain practically unchanged after doping, but a drastic change takes place in the magnetic properties. The Co doping has resulted in a reorientation of the spontaneous moment from the c to the a axis, presumably due to changes in the magneto-crystalline anisotropy.

EXPERIMENT AND RESULTS

The single crystal sample of Co-doped $YbFeO_3$ used in the present study was kindly supplied by Dr. K.G. Srivastava. The exact percentage of Co doping was confirmed by X-ray fluorescence spectroscopy. Unpolarised neutrons of wavelength 1.24 Å have been used to measure reflections from $\lfloor\bar{0}01\bar{\rfloor}$, $\lfloor\bar{1}10\bar{\rfloor}$, $\lfloor\bar{0}10\bar{\rfloor}$ and $\lfloor\bar{1}00\bar{\rfloor}$ zones at room temperature only. Reflections occur at exactly the same positions as calculated on the basis of the unit cell dimensions of pure $YbFeO_3$:[3]

$$a = 5.233 \text{ Å}$$

$$b = 5.557 \text{ Å}$$

$$c = 7.570 \text{ Å}$$

The magnetic and the chemical unit cells are identical in dimensions and as a result many reflections have mixed nuclear and magnetic intensities. Hence an accurate estimation of nuclear intensities is essential to deduce the magnetic contributions. 75 independent and purely nuclear reflections have been measured, mostly in $\lfloor\bar{0}01\bar{\rfloor}$ and $\lfloor\bar{1}10\bar{\rfloor}$ zones. Only those reflections for which h+k is odd and l is odd simultaneously can have magnetic contributions. The nuclear reflections were corrected for absorption and possible extinction, both of which were found to be negligible. A least-squares refinement of these reflections was carried out to determine the atomic co-ordinates. Initial values were taken from Marezio et al.[3]

$YbFeO_3$ belongs to the space group D_{2h}^{16}. The unit cell contains 4 distorted perovskite units with the following atom positions :

Fe at 4(b) $0\ \frac{1}{2}\ 0,\ 0\ \frac{1}{2}\ \frac{1}{2},\ \frac{1}{2}\ 0\ 0,\ \frac{1}{2}\ 0\ \frac{1}{2}$

Yb at 4(c) $\pm$ (x y 1/4, $\frac{1}{2}$+x $\frac{1}{2}$-y 3/4)

Oxygen I at 4(c) $\pm$ (x y 1/4, $\frac{1}{2}$+x $\frac{1}{2}$-y 3/4)

Oxygen II at 8(d) $\pm$ (x y z, $\frac{1}{2}$-x $\frac{1}{2}$+y $\frac{1}{2}$-z,

$\bar{x}\ \bar{y}\ \frac{1}{2}$+z, $\frac{1}{2}$+x $\frac{1}{2}$-y $\bar{z}$)

The final parameters as obtained by the least-squares refinement are given below :

		Initial	Final
Debye-Waller Factor		0.0	0.400 $\pm$ 0.056
Yb	x	0.98064	0.9794 $\pm$ 0.0008
	y	0.07076	0.0708 $\pm$ 0.0007
Oxygen I	x	0.1169	0.1168 $\pm$ 0.0023
	y	0.4537	0.4505 $\pm$ 0.0014
Oxygen II	x	0.6886	0.6890 $\pm$ 0.0016
	y	0.3077	0.3075 $\pm$ 0.0020
	z	0.0599	0.0601 $\pm$ 0.0013
R		33.9%	8.4%

The (0kl) reflections with both k and l odd separately have no nuclear contributions. Hence all such reflections measured in $/\bar{1}00\bar{/}$ zone can be analysed easily to yield the moment direction. From the beginning it was clear that the ordering cannot be of G_x type as reported for pure $YbFeO_3$ [1,2], since in that case q^2 values should be same for all reflections in $/\bar{1}00\bar{/}$ zone and the intensities of (011)

and (013) would be same when corrected for form factor effects. However, the observed intensity of (013) was very much weaker. Besides the intensities of (011) and (101) reflections were also found to be nearly equal which is not possible in the case of G_x ordering. A trial analysis of reflections in $/\bar{1}00/\bar{}$ zone showed that the ordering is of G_z type. Out of 18 reflections, only 12 reflections have been used to determine the form factor. q^2 values are very small for 4 reflections and the remaining two are too weak to be measured accurately. Division by very small q^2 results in large errors. Unfortunately most of the reflections in $/\bar{0}10/\bar{}$ have also very small q^2 values and the form factors extracted from only 5 of them are reliable. The experimental form factor values are shown in Fig. 2 alongwith other experimental and theoretical Fe^{3+} form factor values. Results of $/\bar{1}00/\bar{}$ zone are given in Table 1.

Table 1. Evaluation of the Form Factors for Fe^{3+} from $/\bar{1}00/\bar{}$ Zone Reflections of $YbFe_{0.91}Co_{0.09}O_3$.

hkl	$\sin\theta/\lambda$	I_{obs}	I_{corr}*	f
011	0.112	342.00	10.75	0.903
013	0.218	19.25	1.18	0.583
031	0.278	50.06	3.91	0.452
033	0.335	19.81	1.86	0.376
035	0.427	5.18	0.61	0.274
051	0.455	10.00	1.25	0.250
053	0.492	3.15	0.42	0.157
037	0.533	1.7	0.24	0.216
055	0.558	2.0	0.29	0.149
071	0.633	1.35	0.20	0.101
057	0.645	0.65	0.099	0.100
073	0.660	1.20	0.182	0.099

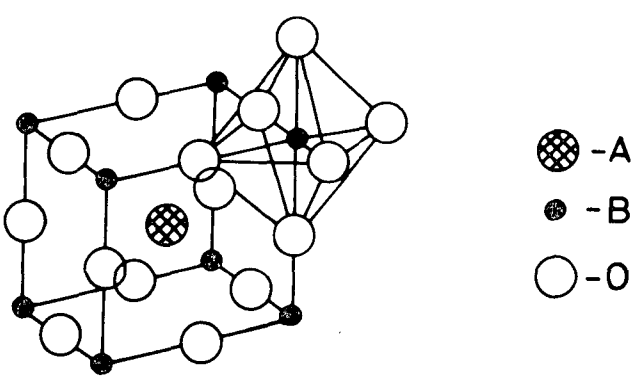
*I_{corr} are the observed intensities after correction for Lorentz and temperature factors.

CONCLUSION

It has been established that the spin reorientation phenomenon in orthoferrites is controlled by magnetic anisotropy considerations. The weak magnetic interaction between iron and rare earth ions can cause a polarisation of the latter. At high temperatures the polarisation is negligible and so is the associated anisotropy. When the temperature is lowered, both the polarisation and the anisotropy increase and the iron spins can suffer a reorientation. So it is not unexpected that the substitution of Fe even by a small amount of cobalt which is highly anisotropic can effect a spin reorientation.

REFERENCES

1. D. Treves, J. Appl. Phys. 36, 1033 (1965).
2. J. Mareschal, J. Sivardiere, J. Phys. 30, 967 (1969).
3. M. Marenzio, J. P. Remeika and P. D. Dernier, Acta Cryst. B26, 2008 (1970).



ABO_3

Fig. 1. Unit cell of perovskite structure.

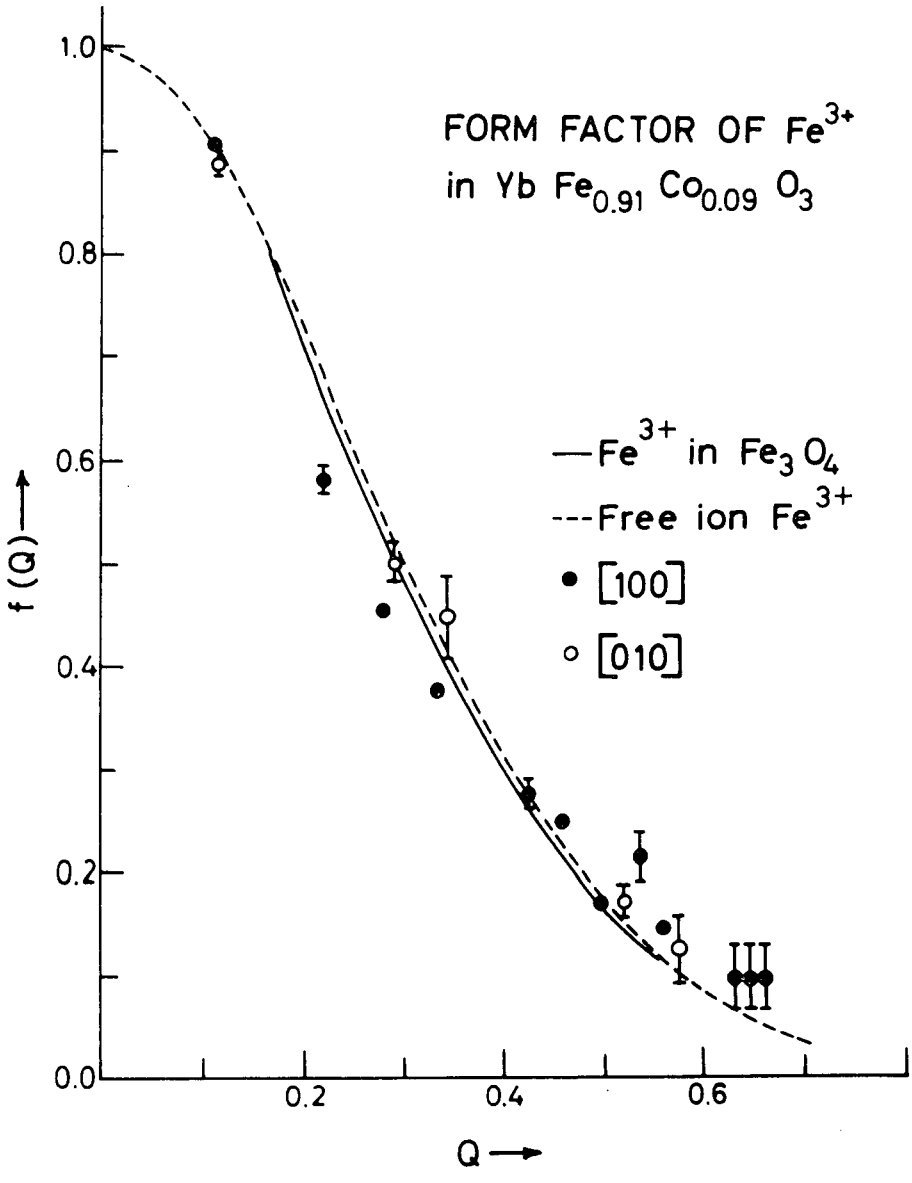


Fig. 2. Experimental and observed form factors for Fe^{3+} ions.

POLARIZED NEUTRON STUDY OF THE NITROXIDE RADICAL IN THE DI-(2,2,6,6-TETRAMETHYL-4-PIPERIDINYL-1-OXYL) SUBERATE

P.J. Brown*, A. Capiomont+, P. Chenavas*, P. Radhakrishna* and J. Schweizer*,x

*Institut Laue-Langevin, 156X, 38042 Grenoble Cedex, France
+Laboratoire de Spectrométrie Physique, 53X, 38041 Grenoble, France
xDRF Centre d'Etudes Nucléaires, 85X, 38041 Grenoble, France

ABSTRACT

Di-(2,2,6,6-tetramethyl-4-piperidinyl-1-oxyl) suberate $C_{26}H_{46}N_2O_6$ is the first known nitroxide free radical which orders ferromagnetically at low temperature. Its Curie temperature is 0.38°K. It crystallizes in the monoclinic system $P2_1/C$ with two molecules in a cell, each at a centre of symmetry. A polarized neutron study has been carried out at 1.5°K in the paramagnetic phase, with the moments aligned vertically and parallel to the $[\bar{4}3\bar{3}]$ direction of the crystal by a magnetic field. The magnetic amplitudes of the reflections of the horizontal plane have been measured by comparison with the nuclear amplitudes, allowing a Fourier projection of the spin density, projection along an axis perpendicular to the π plane of the NO orbitals of one of the two molecules of the cell. The spin density is equally distributed between N and O.

INTRODUCTION

Much interest has been paid recently to the experimental studies of the chemical bond. Coupled X-ray and neutron experiments have allowed the valence electron charge density in several molcules to be located. On the other hand, whereas magnetic scattering of neutrons, which is sensitive to spin density, has been widely used to locate 3d or 4f electron magnetism, only a few studies have been made of the spin density associated with unpaired p electrons (1). Such studies can however yield very useful information about the nature of the chemical bond in many cases, such as that of nitroxyl free radicals, where there remain unanswered questions.

NITROXYL RADICALS

Nitroxyl radical compounds are those which contain the $>N-O$ group with one unpaired electron. In a majority of cases the unpaired spin is concentrated on an antibonding p_π orbital built mainly from 2p atomic orbitals on the nitrogen and oxygen atoms. There have been many studies, theoretical and experimental, to find the distribution of spin on the NO group, but the different results do not agree. Some investigators[2,3] give a spin density mostly concentrated on the nitrogen atom whereas others[4,5] suggest that it is located mainly on oxygen.

These compounds present a wide variety of magnetic behaviour[6,7] which can generally be associated with a negative coupling between neighbouring radicals : pair coupling, chain ordering and three-dimensional antiferromagnetic ordering have been described. A few of the compounds show positive interaction. A knowledge of the spin distribution between N and O may be of some help in understanding the exchange mechanism which occurs in these compounds. We have therefore undertaken a polarized neutron study to determine this distribution and have selected for that study the di-(2,2,6,6-tetramethyl-4-piperidinyl-1-oxyl) suberate, a biradical molecule, $C_{26}H_{46}N_2O_6$ which has a centrosymmetric crystal structure and is the first known organic ferromagnet.

CRYSTAL STRUCTURE AND MAGNETIC PROPERTIES OF SUBERATE

The crystal structure of this compound has been determined by Capiomont[8] with X-rays at room temperature. The molecule crystallizes in the monoclinic system, space group $P2_1/c$ with cell dimensions : a = 6.106 Å, b = 21.39 Å, c = 13.34 Å and $\beta = 125.15°$. Two molecules, which are situated at the centers of symmetry are contained in the cell. The projection of the structure of the biradical along the b direction is represented in figure 1. The two rings of the molecule have a chair conformation. Each of them has a symmetry plane containing the N - O atoms. The length of this N - O bond is 1.28 Å similar to those found in other nitroxyl radicals. The configuration of the bonds around the N atom is pyramidal and the NO direction makes an angle of 18° with the plane of CNC atoms.

The magnetic properties of suberate have been investigated by Veyret[7]. Between 1.2°K and 300°K the compound is paramagnetic ; its susceptibility follows a Curie-Weiss law with a Curie constant corresponding to the independent spins s = 1/2 per molecule and a paramagnetic Curie temperature θ_p = +0.7°K indicating positive interactions. Below 0.38°K it orders ferromagnetically and between 0.38°K and 1.2°K the susceptibility indicates short range magnetic order.

EXPERIMENTAL

The crystal used in the experiment was grown from a saturated ethanol solution whose temperature was kept at 40°C. The crystals grew as needles, their long axis parallel to $\vec{a}$ and were all twinned on (110). In the crystal selected the twins were separated with a razor blade and the crystal used had dimensions 4 x 2 x 1 mm.

Previous experiments had shown that, on cooling, this compound undergoes very anisotropic contractions which may result in destruction of the crystal. To minimize damage to the crystal, it was wrapped in thin aluminium foil before being glued to the sample holder and cooled to liquid helium temperature very slowly.

The crystal was oriented with an axis $[4\bar{3}3]$ vertical. This axis is nearly parallel to the CC direction of the $\begin{matrix} C \\ C \end{matrix}\!\!>$ N - O group of one of the two molecules of the cell. Collecting magnetic structure factors in the horizontal plane enables thus a spin density projection on the π plane of the N - O bonds of that molecule.

Measurements of flipping ratios were made at 1.5°K with a 16.5 kOe field. At this temperature the crystal is still paramagnetic but the moment polarized by the field is 1.63 μ_B/molecule. The neutron beam at λ=0.84 Å was polarized either by an CoFe monochromator or by a Cu_2MnAl one which provides a higher flux. All reflections for which (-4h+3k-3l=0) with $\frac{\sin\theta}{\lambda} < 0.4$ Å^{-1} but three, were measured. The three missing reflections were too weak to be observed. The measured R values were only slightly different from unity (a few per cent) because of the large number of non magnetic atoms in the cell (80 atoms for 1.63 μ_B).

At 4.2°K and without any field, integrated intensities were also

recorded with non polarized neutrons to provide a good knowledge of the nuclear intensities.

RESULTS

In polarized neutron experiments the nuclear structure factor F_N is usually calculated from the crystal structure of the compound. For this case the crystal structure is too imprecise to provide valuable F_N values and this for two reasons : firstly, the structure has been determined at room temperature and thermal parameters do not correspond to the situation at 1.5°K, and secondly, the structure has been determined with X-rays which yield very uncertain position parameters for hydrogen atoms (more than half of the atoms). To overcome this difficulty we used nuclear structure factors deduced from integrated intensities at 4.2°K with the signs calculated from the room temperature X-ray crystal structure[9].

With the magnetic structure factors thus obtained a spin density projection has been performed along the $[\bar{4}3\bar{3}]$ direction (figure 2). On this map magnetic densities have been integrated over squares of edge $2\delta = 0.4$ Å which corresponds to the resolution determined by a maximum value of $\frac{\sin\theta}{\lambda} = 0.4$ Å^{-1}. This map clearly shows that spin density is located on the N - O radicals. On the molecule whose π plane is perpendicular to the projection direction, one can see that the density is maximum in bands perpendicular to the N - O bond, with a minimum between N and O. This corresponds as expected to an antibonding wave function built from atomic 2p orbitals of nitrogen and oxygen, perpendicular to the N-O direction. In spite of the overlap between densities of different nitroxyl radicals it is clear that magnetic density is not unbalanced between nitrogen and oxygen. This result contradicts ab initio calculations on simple H_2NO nitroxyl radicals which favor either oxygen[4] or nitrogen[2] location. It agrees however with parametric calculations made on the compound TMPO[10] which lead to $\rho_O \simeq \rho_N$.

REFERENCES

1. D.E. Cox, E.J. Samuelsen and K.H. Beckurts, J. Phys. 32C1, 582 (1971).
2. A.W. Salotto and L. Burnelle, J. Chem. Phys. 53, 333 (1970).
3. Yu.S. Karimov, M.K. Makova and E.G. Rozantsev, Theor. Eksper. Khim. 5, 701 (1969).
4. Y. Ellinger, Thèse, Université de Grenoble, p.116 (1973).
5. J. Douady, Y. Ellinger, A. Rassat, R. Subra and G. Berthier, Mol. Phys. 17, 217 (1969).
6. A. Blaise, H. Lemaire, J. Pilon and C. Veyret, C.R. Acad. Sc. 274, 157 (1972).
7. C. Veyret, Thèse, Université de Grenoble, p.III.41 (1975).
8. A. Capiomont, Acta Cryst B28, 2298 (1972).
9. A low temperature neutron refinement of the structure is presently undertaken.
10. H. Hayat and B.L. Silver, J. Phys. Chem. 77, 72 (1973).

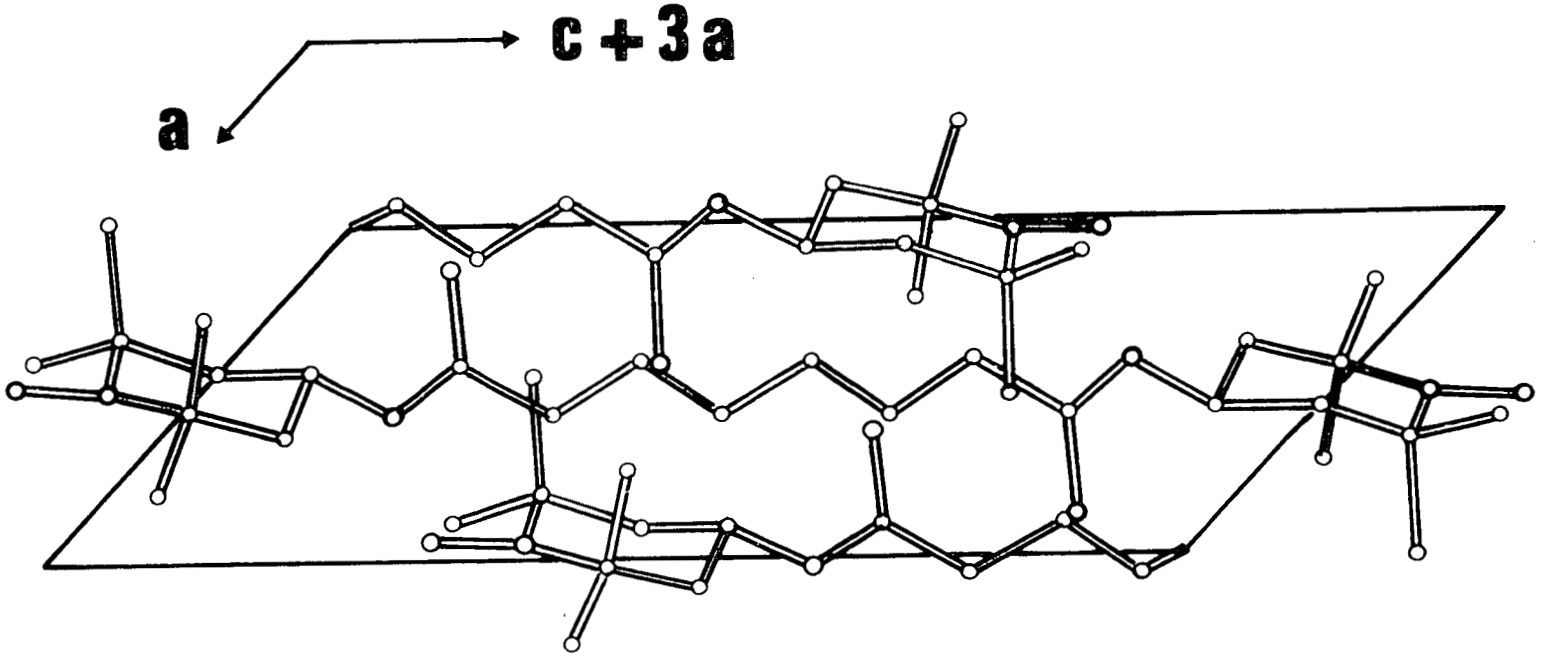


Fig. 1 Projection of the suberate crystal structure on the (a,c) plane.

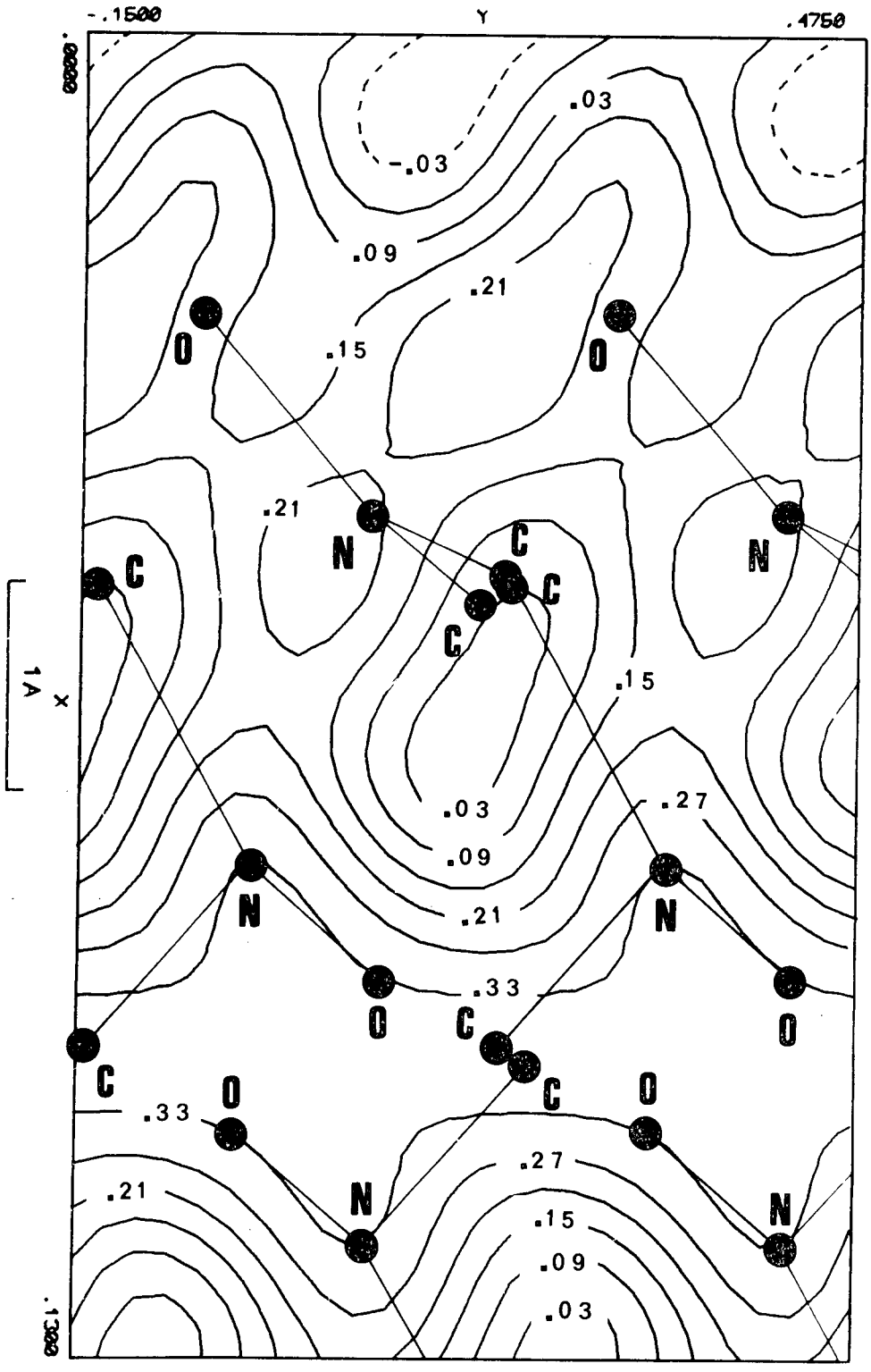


Fig. 2 Projection of the spin density on the π plane of one of the two molecules of the cell. The difference between equal density lines is 0.06 $\mu_B/\text{Å}^2$.

SMALL ANGLE NEUTRON SCATTERING STUDY OF A Au-15 at.% Fe ALLOY

A.P. Murani
Institut Max von Laue-Paul Langevin, 156X-38042 Grenoble Cedex, France

ABSTRACT

Small angle neutron scattering measurements on a Au-Fe alloy containing 15 at.% Fe are reported. These reveal a continuum of q-dependent freezing temperatures, or sharp discontinuities in the scattered intensity as a function of temperature, similar to those observed earlier in alloys containing 10 and 13 at.% Fe. The results are interpreted as showing an evolution of the spin system into magnetic clusters whose relaxation times influence the magnetic properties of the alloy.

The critical concentration for ferromagnetism in Au-Fe alloys is close to 16 at.% Fe[1]. Alloys with lower Fe concentration show a varying range of magnetic properties but have one unifying common feature in that they show a single sharp cusp in their low-field magnetic susceptibility[2] which is often recognized as a characteristic property of spin-glasses in general.

Recent theoretical interest in spin-glasses has been directed towards seeking an explanation of the sharp cusp in the susceptibility in terms of a magnetic phase transition[3]. There remain, nevertheless, some unexplained features such as the broad maximum in the specific heat instead of the sharp anomaly predicted theoretically[4].

Alternative ideas on spin-glasses derive from the observation of superparamagnetic moments in the Curie-Weiss susceptibility close to but above the temperature of the sharp cusp[5]. It is argued that even in random substitutional solid solution alloys there are wide, statistical fluctuations in concentration over microscopic dimensions and that spins within these more concentrated regions become correlated, without particular directional order, at temperatures T such that kT is of the order of or less than their mutual interaction energy H_{int}. Such regions of

correlated spins evolve in size with decreasing temperature as more distant spins also become correlated, resulting in an increase of the total anisotropy energy E_a of the magnetic clusters which will be related in some way to their size.

The relaxation time τ of the magnetic clusters may be assumed to follow approximately the Néel formula for superparamagnetic particles[6], namely

$$\tau = \tau_0 \exp (E_a/kT) \qquad (1)$$

where τ_0 is some intrinsic relaxation time of the spins, E_a the anisotropy energy and kT the thermal energy. Hence in analogy with superparamagnetic particles, a magnetic cluster will appear frozen when its relaxation time τ becomes long compared with the "measurement time" of a given probe. Such ideas have been discussed previously in relation to the magnetic properties of a Au-15 at.% Fe alloy[7] and in a semi-qualitative theory of spin-glasses by Smith[8]. The Néel theory has also been used in an analysis of the low temperature magnetic properties of Au-Fe alloys by Tholence and Tournier[9].

Small angle neutron scattering measurements reported here on a Au-15 at.% Fe alloy supplement those made earlier on two alloys containing 10 and 13 at.% Fe[10]. The measurements were made using neutrons of wavelength 7.3 Å ($\Delta\lambda/\lambda \sim 8$ %, fwhm) in the q-range 5×10^{-3} to 30×10^{-3} Å^{-1} obtained by using a flight path of 10 m between the sample and the multi-detector grid of 64x64 (1 sq. cm) elements.

The alloy was prepared using the normal metallurgical techniques of arc melting followed by homogenising anneal, and water quenching, after which it was forged into a plate 0.5 mm thick. A final anneal at 900°C for one day followed by water quenching was given to the sample just prior to transferring it into the cryostat for the measurements. The small angle scattering from the alloy at room temperature was very much smaller than that observed at low temperatures and closely similar to that from the other two lower concentration alloys, providing adequate confirmation

for the good solid solution character of the alloys.

Results in Fig. 1 show the scattered intensity as a function of temperature for a range of q values. The results are very similar to those obtained earlier for alloys containing 10 and 13 at.% Fe, and show a series of discontinuities in the intensity at temperatures T_F which vary with q. There are, however, some small differences such as, for this alloy, the temperatures T_F of the discontinuities are lower for a given q and also that the scattering cross-section is larger than for the other two alloys.

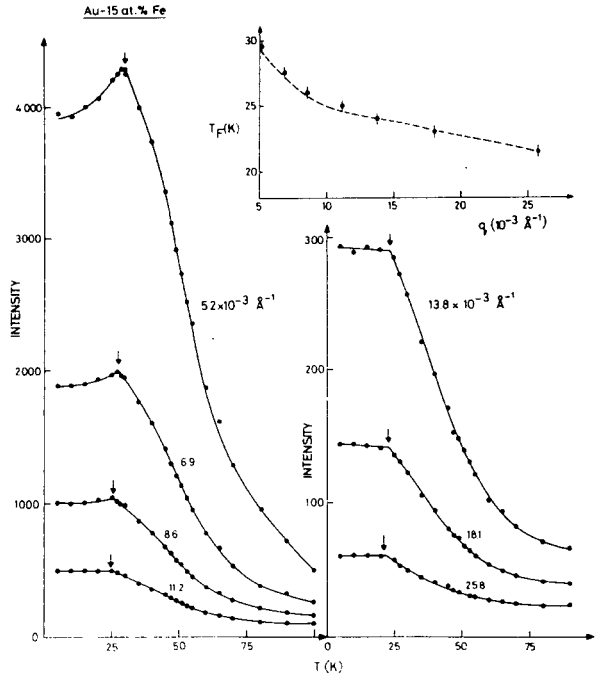


Fig. 1 Scattered intensity as a function of temperature for a series of q values. The arrows mark the freezing temperatures T_F which are shown as a function of q in the inset.

The discontinuities in the forward scattering observed here appear to be similar to the critical scattering peaks in normal ferromagnetic systems. However, the plots of the inverse intensity vs q^2, Fig. 2, show that the scattering is in fact different from normal ferromagnetic critical scattering given by the Ornstein-Zernike correlation function[11] which may be expressed as

$$I = I_0 / r_1^2 (\kappa_1^2 + q^2) \qquad (2)$$

where I_0 is a constant, r_1 the strength at the interaction and κ_1 the inverse correlation range. We note that there is considerable curvature in the plots and an extrapolation to zero inverse intensity gives positive intercepts on the q^2 axis, except at low temperatures when the

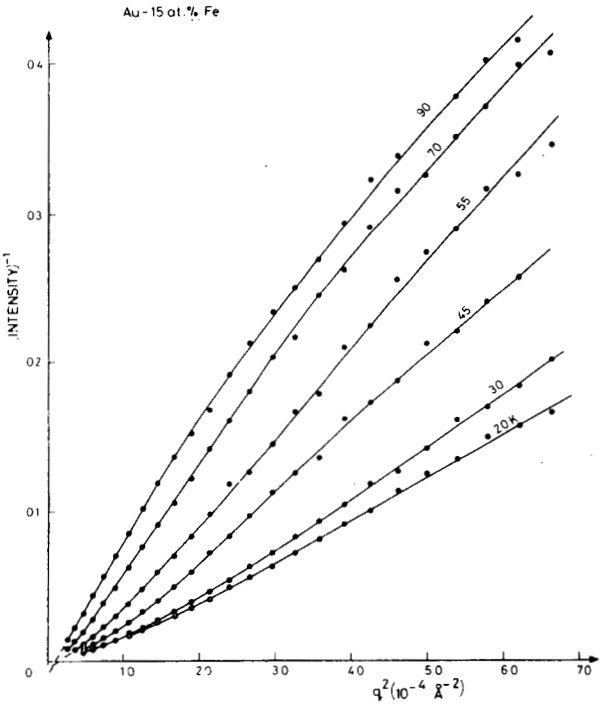


Fig. 2 Inverse intensity against q^2 for a series of temperatures for the Au-15 at.% Fe alloy.

intercepts are closer to zero. Similar behaviour is also obtained for the 10 and the 13 at.% Fe alloys and would appear to be a characteristic property of these alloys. The positive intercept suggests that the total form factor of the clusters has a maximum at finite q values. This helps to account for the fact that for q values to the right of the peak, where these measurements are made, the scattering is larger (for the lowest q values) and much more strongly temperature dependent than expected at q = 0 from the static susceptibility of the alloys.

From Néel formula (1) it follows that for a constant value of τ at the freezing temperature T_F we must have

$$E_a/kT_F = \text{constant} \qquad (3)$$

The relationship between E_a and the cluster size will, in general, be rather complex. If, however, we assume E_a to be directly proportional to the cluster size R and the latter proportional to 1/q, since the form factors are strongly peaked in the forward direction, we have

$$T_F \alpha R \alpha \frac{1}{q}$$

In Fig. 3 we show the inverse temperature $1/T_F$ against q which includes also the results for the 10 and 13 at.% Fe alloys. Not surprisingly, one finds that such a simple relationship does not hold.

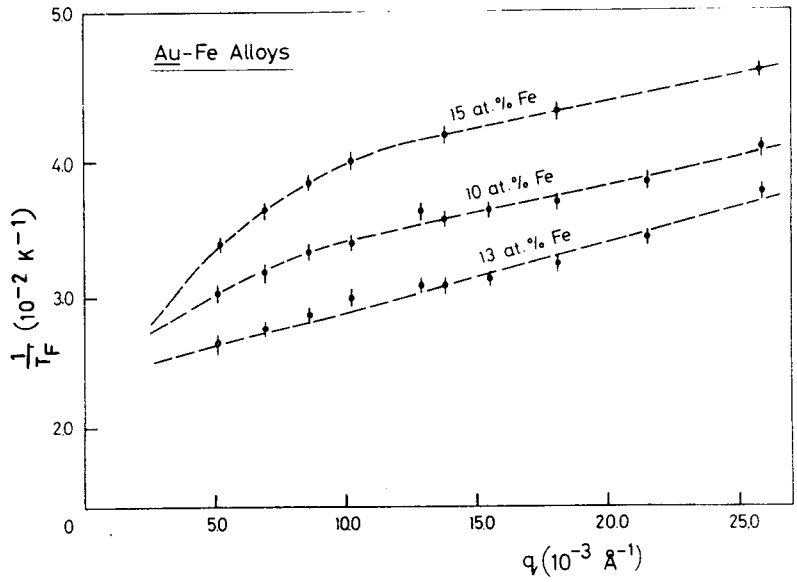


Fig. 3 Plot of $\frac{1}{T}$ against q for Au-Fe alloys containing 10, 13 and 15 at.% Fe.

It is interesting to note the variation in the values of T_F, for a fixed value of q, among the three alloys which suggests that the anisotropy energy E_a of the clusters is related in some complex way to the directional correlations among the spins which become progressively more

ferromagnetic with increasing Fe concentration.

In conclusion, the present results show a continuum of freezing temperatures corresponding to a distribution of magnetic clusters into which the spin system evolves with decreasing temperature. The results supplement the observation of a single sharp cusp in the magnetic susceptibility, a macroscopic quantity, whose response is dominated by the largest clusters. It is evident that the relaxation times of the spins play an important role in the magnetic properties of the alloys, where the sharpness of the freezing anomalies are due to the exponential variation of the relaxation times with inverse temperature and the fact that the anisotropy energy E_a is also strongly temperature dependent.

REFERENCES

1. A.P. Murani, S. Roth, P. Radhakrishna, B.D. Rainford, B.R. Coles, K. Ibel, G. Göltz and F. Mezei, J. Phys. F : Metal Phys. 6, 425 (1976).
2. V. Cannella and J.A. Mydosh, Phys. Rev. B6, 4220 (1972).
3. K. Adkins and N. Rivier, J. Physique 35, C4-237 (1974).
   S.F. Edwards and P.W. Anderson, J. Phys. F : Metal Phys. 5, 965 (1975).
   K.H. Fischer, Phys. Rev. Lett. 34, 1438 (1975).
   D. Sherrington and B.W. Southern, J. Phys. F : Metal Phys. 5, 249 (1975).
4. L.E. Wenger and P.H. Keesom, Phys. Rev. B11, 3497 (1975).
5. V. Cannella in Amorphous Magnetism, edited by H.O. Hooper and A.M. de Graff (Phnum N.Y. 1973) pp. 195-206.
6. L. Néel, C.R. Acad. Sci., Paris 228, 664 (1949).
7. A.P. Murani, J. Phys. F : Metal Phys. 4, 757 (1974).
8. D.A. Smith, J. Phys. F : Metal Phys. 5, 2148 (1975).
9. J.L. Tholence and R. Tournier, J. Physique 35, C4-229 (1974).
10. A.P. Murani, to be published.
11. L. Van Hove, Phys. Rev. 95, 1374 (1954).

SMALL ANGLE SCATTERING OF NEUTRONS AND MAGNETIC STRUCTURE OF INVAR ALLOYS

A.Z.Men'shikov, S.K.Sidorov, V.A.Shestakov
Institute for Metal Physics, Sverdlovsk, USSR

ABSTRACT

Neutron scattering cross sections were measured in the wide temperature range (80-1000°K) at different directions of a magnetic field with respect to the scattering vector. The treatment of the experimental data has been done on the basis of the theory developed for neutrons scattering by ferromagnetic alloys with magnetic inhomogeneities. It has shown that the magnetic structure of invar alloys in the ground state is characterized by the occurence of static magnetization fluctuations of size about 10-12 A. Centres of fluctuations caused by antiferromagnetic iron pair interactions are iron atoms surrounded only by atoms of the same sort in the nearest coordination sphere (Z=12). The concentration of these fluctuations is about 0.5% in invar alloy and increases with increasing of iron content.

The magnetic structure and magnetic ground state of FCC iron-nickel alloys are very peculiar in connection with the invar problem. It has been established that $\bar{\mu}(c)$ increases linearly up to 50 at.% Fe and decreases rapidly in the concentration interval of 50-75 at.% Fe (Fig.1). Such a $\bar{\mu}(c)$-behaviour can be explained on the basis of the suggestion of a noncollinear and inhomogeneous magnetic structure due to the existence of mixed exchange interaction ($J_{Ni-Ni} > 0$, $J_{Ni-Fe} > 0$, $J_{Fe-Fe} < 0$) established experimentally in these alloys by Hatherly et al[1]. One could therefore hope that magnetic small angle scattering of neutrons would make it possible to observe the effect due to the inhomogeneity of magnetic structure of iron-nickel alloys.

THEORY

For the description of incoherent scattering of neutrons by binary alloys with the occurence of magnetic inhomogeneities we used the general thermodynamical theory of critical scattering developed by Krivoglaz[2]. According to this theory the differential cross section of unpolarized neutrons in an arbitrary magnetic field is written down as

$$\frac{d\sigma}{d\Omega} = C\ V\ f_n^2\ kT\left[\frac{1+e_z^2}{\chi_\perp+\alpha K^2} + \frac{1-e_z^2}{\chi_{\parallel}+\alpha K^2}\right] \qquad (1)$$

here $\chi_\perp$ and $\chi_{\parallel}$ are the transversal and longitudional components of the magnetic susceptibility tensor:

$$\chi_\perp/\chi_o = (k_\perp r_1)^{-2},\quad \chi_{\parallel}/\chi_o = (k_{\parallel} r_1)^{-2} \qquad (2)$$

where r_1 and k are the phenomenological parameters dependent on temperature. It is adopted that k^{-1} characterizes the spin correlation radius.

In contrast to pure ferromagnets there are peculiarities in alloys due to the deviations of magnetization $\overline{\delta M^2}$, concentration $\overline{\delta c^2}$. Supposing spherical magnetic inhomogeneities one can prove for K=0 that

$$\frac{d\sigma}{d\Omega} = CVf_n^2 kT2\chi_\perp + NCf_n^2(1-e_z^2)c(1-c)\left(\frac{d\bar{\mu}}{dc}\right)^2 \qquad (3)$$

In the collinear ferromagnet case $\chi_\perp=0$ and the formula (3) turns into the well-know Marshall's [3] formula.

To compare the experimental data with the theoretical ones, we[4,5,6] obtained the expression for $\bar{\mu}(c)$ as follows

$$\bar{\mu}(c,\ T) = \bar{\mu}_z^{(1)}(1-c) + \bar{\mu}_z^{(2)}c \qquad (4)$$

where 1 - Ni, 2 - Fe, c - concentration of iron atoms,

$$\mu_z^{(1)} = g\mu_B S_1 a_1 \sigma_1 \quad , \quad \mu_z^{(2)} = g\mu_B S_2 a_2 \sigma_2 \tag{5}$$

$$a_1 = \left[1 - \lambda_1 \lambda_2 Z^2 \frac{c}{1-c}(1-p'_{22})p'_{22}\right] \quad , \quad a_2 = (1 - \lambda_2 Z p'_{22}) \tag{6}$$

λ_1, λ_2 are certain dimensionless coefficients, Z - the number of nearest sites. Here $p'_{22} = \frac{1}{Z}\sum_{x}^{z} P_z(n,c)n$ is the effective probability of replacing the site closest to the atom 2 by critical number (X-1,2,...Z) of the same sorts in which cancellation of the Z-projection of the magnetic moment of atom 2 takes place. For disordered iron-nickel alloys X=12. $P_z(n,c)$ is the binomial distribution. Reduced magnetization σ_1 and σ_2 can be expressed in terms of the Brillouin function $\sigma_1 = B_1(E_1/kT)$, $\sigma_2 = B_2(E_2/kT)$, E_1, E_2 are the interaction energies of the atom magnetic moments of sort 1 or 2 with the superimposed effective molecular fields.

$$E_1 = -2ZS_1^2 J_{11}\left[a_1\sigma_1(1-c) + a_2\sigma_2 c J_{12}S_2/J_{11}S_1\right] \tag{7}$$

$$E_2 = -2ZS_1S_2J_{11}\left[a_1\sigma_1(1-c)J_{12}/J_{11} + a_2\sigma_2 c J_{22}S_2/J_{11}S_1\right] \tag{8}$$

where J_{11}, J_{12}, J_{22} are parameters of pair exchange interaction.

EXPERIMENT AND DISCUSSION

The small-angle scattering of neutrons (2θ =1-5°, λ =1,13 Å) was measured in the temperature region 80-1100°K. The universal cryostat was placed in a circle electromagnet producing the field of ~10 KOe. Corrections were introduced for the thermal, multiple and inelastic scattering of neutrons.

The experimental angular dependences $(d\sigma/d\Omega)_{\parallel}$ are

shown in Fig.2. We see that for alloys in the region of sharp variation of the average magnetic moment (Fig.1) a significant increase of the small-angle scattering intensity is observed and the effect increases with the increasing of the iron content. The analogous angular dependences exist for $(d\sigma/d\Omega)_0$ and $(d\sigma/d\Omega)_\perp$ at different temperatures. But there are some peculiarities which are displayed clearly on experimental difference curves $(d\sigma/d\Omega)_{0-\parallel}$ and $(d\sigma/d\Omega)_{0-\perp}$(Fig.3). The angular dependences of these cross-sections are shown on Fig.4. The typical rising in small angles and the appearance of the wide maximum on the temperature dependence $(d\sigma/d\Omega)_{0-\perp}$ is due to the scattering effect of neutrons by spin waves.

As it follows from Eqs.2,3 the experimental data of the temperature dependences of forward cross section $(d\sigma/d\Omega)_\parallel$ $(d\sigma/d\Omega)_0$ permit to calculate tne $\chi_\perp$ and $\chi_\parallel$ values and nence transversal and longitudional spin correlations $\kappa_\perp^{-1}$ and $\kappa_\parallel^{-1}$ which are shown in Fig.5 for some alloys. It is found that for invar alloy 65Fe κ^{-1} is dependent on temperature rather weakly and what is more this value decreases at the Curie point (T_c). The extrapolation on T=0°K gives the value of $k_\perp^{-1}$ about 9-10 Å at K=0,1 and about 11-12 Å at K=0.

The physical matter of the transversal spin correlation $k_\perp^{-1}$ in the ground state of investigated invar alloys, should be considered. First this correlation is static one in contrast to the dynamical correlation at the Curie point. Secondly the nature of $k_\perp^{-1}$ consists in the antiferromagnetic interaction between iron atoms which in a certain statistical fluctuation disorients magnetic moments relative to the direction of spontaneous magnetization and hence generates local spin fluctuation.

The centres of such fluctuations in our opinion[7] are iron atoms surrounded in the nearest sphere only by iron atoms. The concentration of these statistic fluctuations equal 0.5% in invar alloy and sharply rises with the in-

creasing of iron content. In fact this conclusion has been made on the basis of the above mentioned phenomenological calculation of $\bar{\mu}(c)$ for Fe-Ni-alloys. These fluctuations with X=12 do not contribute to the $\bar{\mu}$ and what is more they extend their influence on the subsequent coordination spheres as $\lambda_2 > 1$ (exactly 2,9). As it follows from the experiments the value of k_1^{-1}=11-12 Å corresponds to the propagation of the spin density deviation through 3-4 coordination spheres in invar alloy.

Cross section scattering dependences on concentration and temperature due to the magnetic moment Z-projection variation are shown in Figs.6,7. In these cases the theoretical values $d\bar{\mu}/dc$ are calculated using Eqs.4-8 and experimental results from Figs.3,4. As one can see quite good quantitative agreement between the theoretical and experimental data is observed. As for the temperature dependences the agreement has qualitative character.

REFERENCES

1. M.Hatherly, K.Hirakawa, R.D.Lowde, J.F.Mallet, M.W.Stringfellow and B.Torrie, Proc.Phys.Soc. 84, 55, (1964).
2. M.A.Krivoglaz. Dokl. Acad. Nauk SSSR, 118, 51, (1958).
3. W.L.Marshall. J.Phys. (Proc.Phys.Soc.), C1,1,88, (1968).
4. S.K.Sidorov and A.V.Doroshenko, Fiz. Met. Metallovedenie, 19, 786, (1965).
5. A.Z.Men'shikov, S.K.Sidorov, V.E.Archipov, Sov.Phys. - JETP, 61, 311, (1971).
6. V.E.Arkchipov, A.Z.Men'shikov, S.K.Sidorov, Sov.Phys. - JETP, 61, 1501, (1971).
7. A.Z.Men'shikov, V.A.Shestakov, S.K.Sidorov, Sov.Phys. - JETP, 70, 163, (1976).

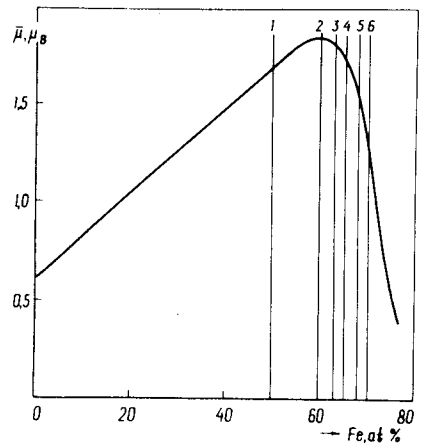


Fig.1. The concentration dependence of $\bar{\mu}$ of Fe-Ni alloys. (Investigated alloys are marked).

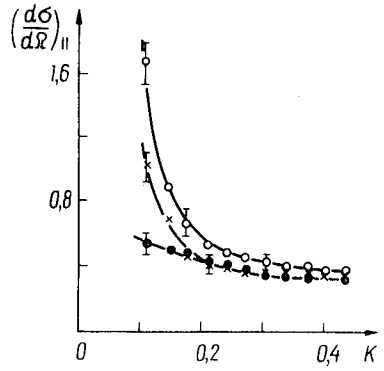


Fig.2. The angular dependence of cross section (in b/sr-at in all in the Figs.): ● - 50, × - 60, o - 65 Fe.

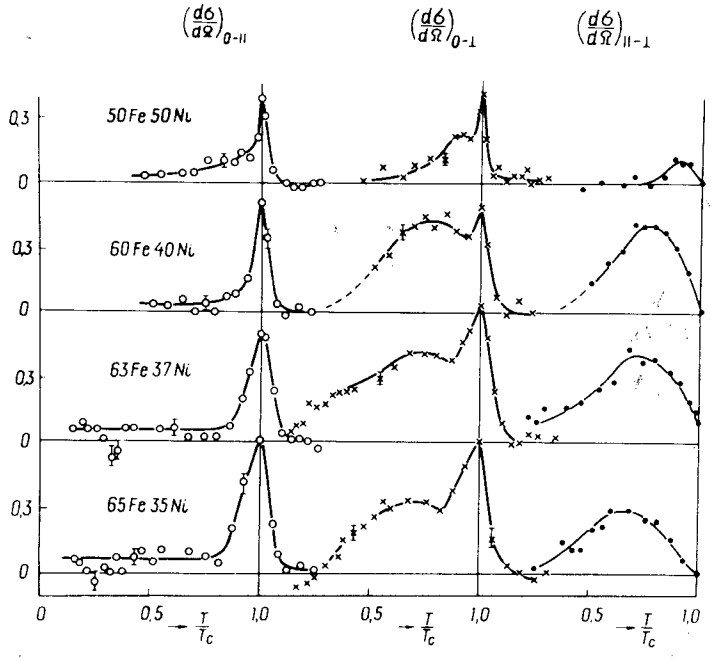


Fig.3. The temperature dependence of experimental difference cross section for K=0,1.

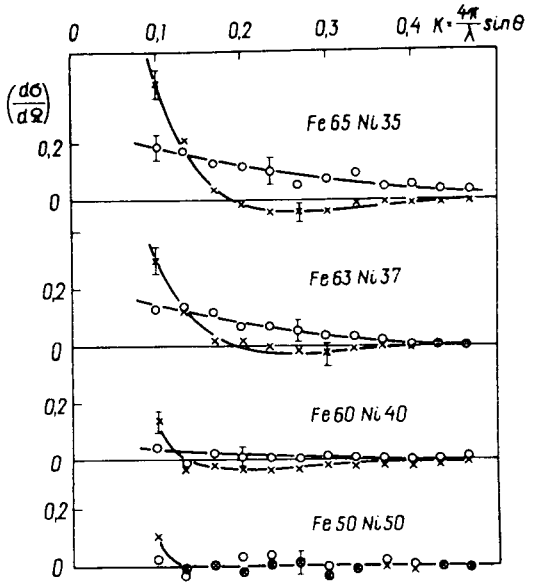


Fig.4. The angular dependence of experimental difference cross sections at 80K
o- $(d\sigma/d\Omega)_{o-\parallel}$, x- $(d\sigma/d\Omega)_{o-\perp}$

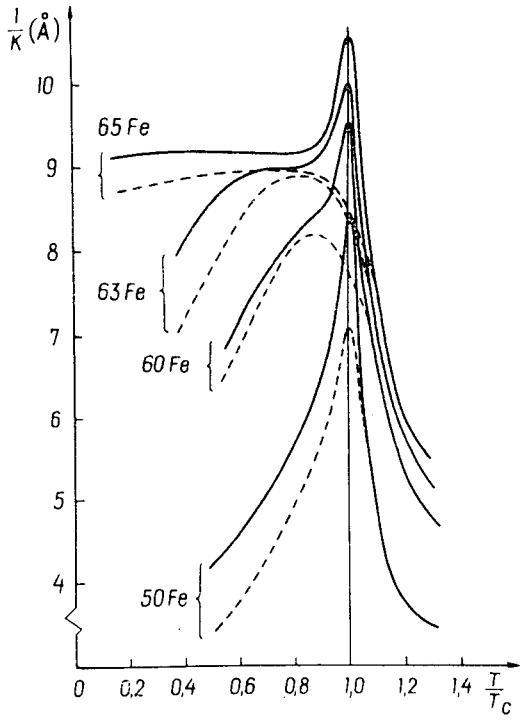


Fig.5. The temperature dependence of $1/k_{\parallel}$ (solid, and $1/k_{\perp}$ (dashed).

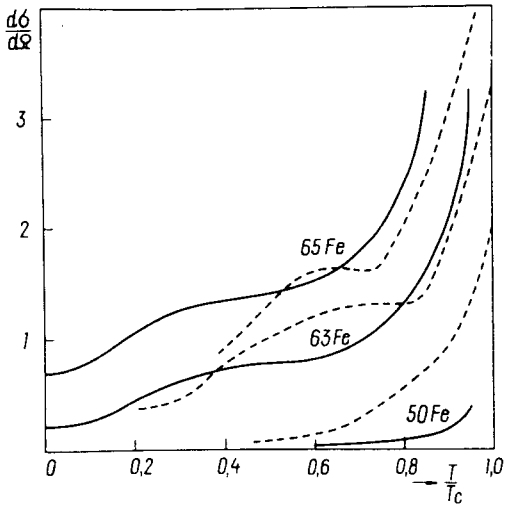


Fig.6. The temperature dependence of the cross section due to only $(d\bar{\mu}/dc)$ (solid - theory, dashed - experiment).

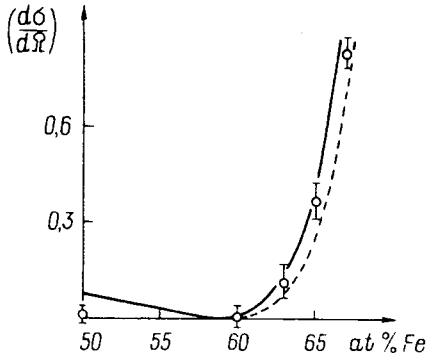


Fig.7. The concentration dependence of the cross section due to only $(d\bar{\mu}/dc)$ - experiment, lines - theory: solid - without correlation, dashed - with one.

TEMPERATURE DEPENDENCE OF MAGNETIC MOMENT DISTRIBUTION AROUND Mn IMPURITIES IN IRON

F. Mezei
Institut Laue-Langevin, 156X Centre de Tri, 38042 Grenoble Cedex, France.

ABSTRACT

The magnetic moment distribution around Mn impurities in Fe (0.80 % Mn) and Fe(2.8 % Mn) alloys has been studied using diffuse scattering of polarized 4.90 Å wavelength neutrons in the momentum and temperature range of 0.2 - 2.4 $Å^{-1}$ and 4.2 - 700 K°, respectively. Statistical spin flip modulation time-of-flight technique has been utilized, with the help of a pulsed D.C. Larmor precession coil spin flipper in order to separate elastic and inelastic contributions within the neutron polarization dependent scattering which proved to be indispensable at elevated temperatures. The present measurements show that the Mn moment changes by 0.80 ± 0.10 μ_B between 0 and 700 K° in a considerably slower fashion than suggested by previous workers. The moment perturbation in neighbouring Fe atom shells, on the other hand, is found to be dramatically temperature dependent, adding up to a 1.5 μ_B decrease between 0 and 700 K°. The Mn moment at 0 K° was found to be 0.64 ±0.15 μ_B.

INTRODUCTION

Ever since the discovery of the anomalous temperature dependence of the hyperfine field at Mn nuclei in Fe by Koi[1] et al. in 1964 and the proposition of a simple, molecular field model for explaining it by Jaccarino et al.[2], the magnetic behaviour of Mn impurities in Fe attracted considerable interest and created a lasting confusion[3]. The central point in this controversy is the magnitude, and, especially, the temperature dependence of the magnetic moment on the Mn atom. To explain the hyperfine field anomaly, a substantial and strongly temperature dependent moment had to be assumed, while earlier neutron scattering measurements by Collins and Low[4] indicated no moment with an error[5] of ± 0.5 μ_B at room temperature. Thus the lack of more precise neutron data played an important role in the Fe(Mn) story by leaving room for speculations about as big as 1-2 μ_B 0 K° moment on the Mn with a very rapid

decrease with temperature.

It was only recently that additional neutron data became available on this problem[6,7]. Unfortunately these suffered too from relatively poor statistical accuracy (± 0.3 μ_B) and, in addition, they are not free from probable systematic errors. In one of these studies[6] the neutron wavelength used was below cutoff, so it was susceptible to distortions by multiple magnetic Bragg scattering. On the other hand, both experiments were done without energy analysis of scattered neutrons, and thus the data are not free from contamination by strongly temperature-dependent magnetovibrational scattering.

The aim of the present study is therefore to produce more accurate and, possibly, more error-free data, especially on the crucial temperature dependence of the Mn moment, μ_{Mn}, in iron. Indeed, a ± 0.07 μ_B error has been achieved in comparing μ_{Mn} values at different temperatures, while due to the much more difficult problem of absolute calibration of the cross sections, μ_{Mn} itself could only be determined with an error of ± 0.15 μ_B. The extension of the investigated κ range to 2.32 Å^{-1} was proved to be very instrumental in obtaining these data.

EXPERIMENTAL

Two Fe(Mn) samples were investigated which were kindly provided by G.G. Low who has used them in his original work[4]. They were re-analysed by wet chemistry and the Mn concentrations were found to be 0.80 and 2.81 at.%, respectively. The data presented here are those obtained on the more concentrated sample. The 0.8 % Mn sample showed similar quantitative behaviour but with a much poorer statistical significance.

The D7 diffuse scattering machine at the Laue-Langevin Institut has been used. The 4.83 Å incoming neutron beam was polarised and monochromated by a Heusler single crystal. 32 independent detectors were used simultaneously to detect scattered neutrons. To eliminate neutron polarization-dependent inelastic scattering contributions, the statistical spin-flip-modulation technique[8] was used with the help of a DC coil spin flipper[9]. Only a single channel (the elastic one) of the spin modulated

time-of-flight (TOF) spectra has been monitored[8]. The TOF resolution was 8 %, which was poor enough to get almost all of the elastic intensity into the monitored channel. The overall efficiency of the system was 88±0.5 %, the losseses being due to incomplete polarization, and, mostly, to the tails of the incoming TOF spectrum not being contained completely in the elastic TOF channel.

A magnetic field of 12 kOe was applied to the 0.6x1.8x5.0 cm sample, which was found to be magnetically saturated. The sample temperature was controlled with an accuracy of 0.5 K° in the cryostat for the low temperature work and to ± 5° in the furnace.

The normalization of the data to obtain absolute cross sections and to calibrate the detectors to each other was made with the help of a standard Va sample.

In this experiment the elastic scattering on the sample was altogether less than 10 %, so no multiple scattering corrections were made. On the other hand, absorption and the temperature dependent inelastic scattering, both acting as sheer losses for the elastic intensities were corrected for. The spin dependence of the sample transmission (due to phonon and Mn impurity scattering contributions) was estimated to be about 2 % and it was taken into account, independently of the temperature, however. It was estimated that the comparison to the V sample together with all these corrections should fix the absolute scale for measured cross-sections with an accuracy of 5-10 %. This could be controlled by comparing the room temperature neutron data extrapolated to zero momentum with the saturation magnetization data[10] (only available from room temperature) giving $d\mu/dc = -2.11\ \mu_B$. This comparison suggested that the neutron cross-sections are scaled 10-20 % too high. Therefore, still within the limits of the estimated error, a 10 % lower calibration factor has been adopted and thus the neutron data became consistent with the magnetization measurements, within errors of statistical origin, and the final error of the scale should be about ± 5 %.

RESULTS

In view of the relatively low Mn concentration, the difference elastic cross-section for both incoming spin directions has been attributed to the effect of isolated impurities and described for the polycrystalline sample as :

$$\left(\frac{d\sigma}{d\Omega}\right)_{\uparrow} - \left(\frac{d\sigma}{d\Omega}\right)_{\downarrow} = 1.078\ e^{-2W}\ c(1-c)(b_{Mn}-b_{Fe})F(\kappa)\ x$$
$$x\ \left[(\mu_{Mn} - \mu_{Fe}) + \sum_i Z_i\ \Delta\mu_i\ \frac{\sin\kappa R_i}{\kappa R_i}\right]\ 10^{-12}\ \frac{cm}{\mu_B} \qquad (1)$$

where e^{-2W} is the Debye-Waller factor, $b_{Mn} - b_{Fe} = -1.34 \times 10^{-12}$ cm is the difference of nuclear scattering amplitudes, c is the Mn concentration, $F(\kappa)$ the magnetic form factor for iron, $\mu_{Fe} = 2.22\ \mu_B$, the Fe moment and $\Delta\mu_i$, Z_i and R_i are the difference between the moment and μ_{Fe}, the number and the distance from the Mn atom, respectively, for the i'th Fe atom neighbours of a Mn atom.

Two of the corrected spectra are shown in Fig. 1. The sample error bars represent 2σ statistical errors only. These experimental curves were fitted by equation (1) in order to determine μ_{Mn} and the $\Delta\mu_i$'s as functions of the temperature. ($\mu_{Fe}(T/T_c)$ was taken to be that of pure iron[3]). As far as μ_{Mn} is concerned, this fit is fairly unique, since in the κ range of 2.0 - 2.3 $\mathring{A}^{-1}$ the cross-section hardly depends on the choice of $\Delta\mu_i$'s. On the other hand, the determination of $\Delta\mu_i$'s is not so unique, in view of their large number. In doing this the following procedure has been adopted.

Since R_1 and R_2 are hardly different, $\Delta\mu_1$ and $\Delta\mu_2$ cannot be distinguished, and the only pertinent quantity is $M_1 = Z_1\ \Delta\mu_1 + Z_2\ \Delta\mu_2$. First a fit has been tried assuming that all the other $\Delta\mu_i$'s vanish. This was found to be possible within errors for all temperatures as illustrated by the dashed lines in Fig. 1. However, while the fits were completely satisfactory at higher temperatures, a systematic deviation was found for 305 K°, and, less pronouncedly, for 5 and 100 K°. To improve the fits at these two lower temperatures, any or several out of $\Delta\mu_4, \Delta\mu_5 \ldots \Delta\mu_{10}$ could be considered. The most natural choice was to invoke as above, a

single parameter $M_2 = Z_4\Delta\mu_4 + Z_5\Delta\mu_5 + \ldots + Z_{10}\Delta\mu_{10}$. The corresponding R_i's range from 4.75 to 7.45 Å. The result of such a fit for 305 K° is represented by the dotted line in Fig. 1. For higher temperatures M_2 was found to be zero with an error of $\pm$ 0.3 μ_B. The results are summarized in Table 1.

Table 1

T(K°)	$\mu_{Mn} - \mu_{Fe}(\mu_B)$	$M_1(\mu_B)$	$M_2(\mu_B)$
5-100	- 1.58 ± 0.05	- 0.55 ± 0.15	0.3 ± 0.2
305	- 1.75 ± 0.05	- 0.75 ± 0.15	0.55± 0.3
428	- 1.94 ± 0.05	- 1.05 ± 0.10	
568	- 2.03 ± 0.07	- 1.45 ± 0.15	
684	- 2.03 ± 0.08	- 1.90 ± 0.20	

CONCLUSIONS

The magnetic moment of Mn impurities determined from Table 1 and taking into account the temperature dependence of μ_{Fe}, are shown in Fig.2. The error bars show statistical errors only which are relevant to the comparison of μ_{Mn}'s at different temperatures. Calibration adds 0.1 μ_B error, not shown in the figure. The decrease of μ_{Mn}, especially between 5 K° and 305 K° was found to be much slower and more regular than suggested by earlier reports both on neutron and hyperfine field studies. On the other hand, there is an important change of the magnetization on the 14 Fe atoms in the 1st and 2nd neighbouring shells, also shown in Fig. 2 as the average moment of these atoms $\overline{\mu_1}$. The dashed line represents μ_{Fe} with no near Mn neighbours. These $\overline{\mu_1}$'s tend to be lower at low temperatures than suggested by Cable and Child[7].

The appearance of the positive magnetization disturbance (described by M_2) at low temperatures, as mentioned above, is still not a completely necessary consequence of these data. It could merely indicate some ordering effects or the occurrence of a real rather long range (about 6 Å on the whole) magnetization increase around the Mn impurities, which

would amount to 0.005 to 0.01 μ_B per Fe atom involved. This is not completely unreasonable, since the conduction electron polarization is about - 0.2 μ_B per Fe atom.

In summary, with the present set of improved neutron data, a meaningful comparison can be made, for the first time, between magnetisation and hyperfine field behaviour of Mn impurities and their neighbours in Fe. Not surprisingly, all of the proposed hyperfine field schemes[3], involving merely assumptions on the magnetisation behaviour, turn out to be in more or less flagrant, but in all cases significant contradiction to the findings of the present experiment. It also remains to be seen what type of theory could explain the T dependence of the Mn and neighbouring Fe moments.

ACKNOWLEDGEMENTS

The author is indebted to Dr. W. Just for his kind help in using his diffuse scattering instrument, to Dr. G.G.Low for the loan of his samples and to Drs. I.Campbell and I.Vincze for valuable discussions.

REFERENCES

1. Y.Koi, A. Tsujimura, and T. Hihara, J. Phys. Soc. Jap. 19,1493 (1964).
2. V. Jaccarino, L.R. Walker, and G.K. Wertheim, Phys. Rev. Lett. 13, 752 (1964).
3. I. Vincze and I.A. Campbell, J. Phys. F: Metal Phys. 3, 647 (1973); P.J.Schurer, K. W. Maring, F. Van der Woude, and G.A. Sawatzky, Int. J. Magnetism 4, 291 and 297 (1973) and references therein.
4. M. F. Collins and G.G. Low, Proc. Phys. Soc. London 86, 535 (1965).
5. I.A.Campbell, Proc. Phys. Soc. London 89, 71 (1966).
6. Y. Nakai and N. Kunitomi, J. Phys. Soc. Jap. 39, 1257 (1975).
7. H. R. Child and J.W. Cable, Phys.Rev. B 13, 227 (1976).
8. F. Mezei and P. Pelloniosz, Nucl. Inst. and Meth. 99, 613 (1972).
9. F. Mezei, Z. Phys. 255, 146 (1972).
10. A. Arrott and J. E. Noakes, Iron and its Dilute Solid Solutions, Eds. C.W. Spencer and F.E. Werner (Interscience, New York, 1963) p. 81.

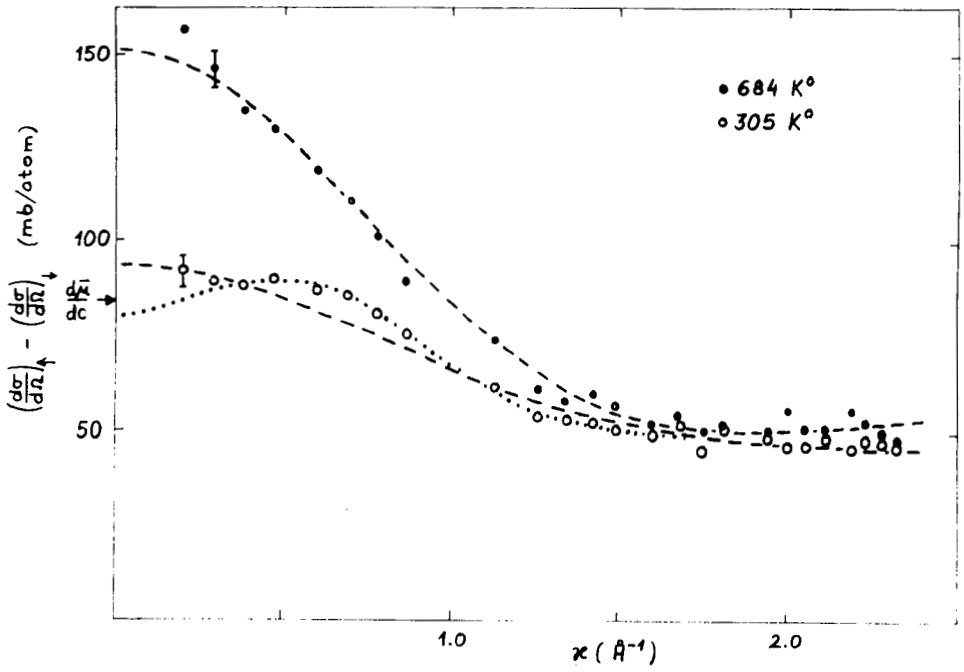


Fig. 1. Measured and fitted difference cross-sections for Fe(2.8 % Mn) at two temperatures.

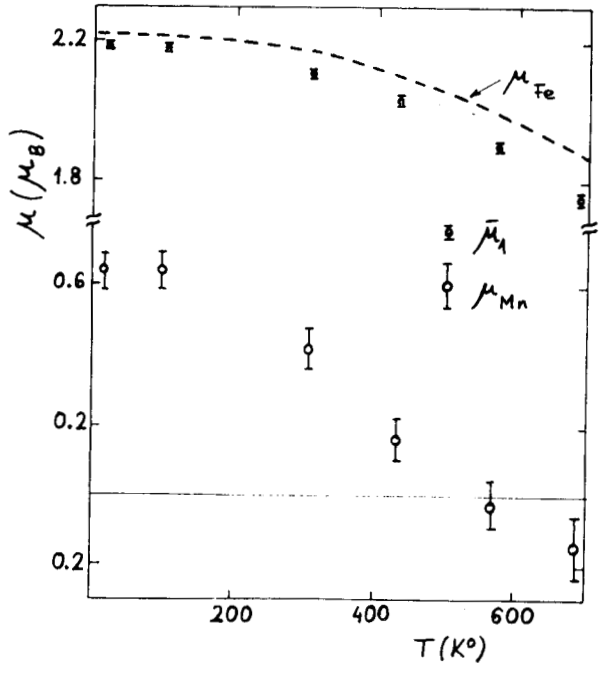


Fig. 2. Temperature dependence of the magnetic moments on Mn atoms (μ_{Mn}) and nearest neighbour Fe atoms ($\bar{\mu}_1$) as compared to that of pure iron (μ_{Fe}).

ASPHERICITY OF SPIN DENSITY IN DISORDERED FERROMAGNETIC ALLOYS.*

F.Menzinger
Istituto Fisico, Università, L'Aquila, Italy
and F.Sacchetti
Consiglio Nazionale delle Ricerche, c/o C.S.N.Casaccia,
C.P.2400, Rome, Italy

ABSTRACT

Asphericity of the spin distribution can be deduced from the neutron experimental data with a minimum of ad hoc assumptions and, at the same time, is a direct result of the of the calculated density of states, which can be obtained with CPA. We present here new results on Cu-Ni alloys as obtained by neutron diffraction and we show that these results together with those for other systems previously investigated are in good agreement with CPA calculations[1,2].

INTRODUCTION

In the present decade several studies of ferromagnetic disordered alloys have been completed by means of the coherent scattering of polarized neutrons. Attention has been given to similarities and differences with respect to pure elements. In fact in 3d-metals[3-8] it has always been found that the spin density is contracted with respect to the

*Work supported by Gruppo Nazionale di Struttura della Materia

charge density of the free ion. This behaviour is the evidence of the differences between the wave functions of free ions and those of the solid.

In all of the original experimental work, the analysis of the measured form factor has been done by means of a comparison with the free-ion form factors and good agreement between these experimental and theoretical form factors was obtained if a constant negative polarization of the non-d electrons was assumed. This assumption has been criticized in the case of pure Ni by Hodges et al.[9], particularly in view of the s-d exchange coupling and Fermi-surface magneto-optical experiments. In pure Fe also the wave functions calculated by Duff and Das[10] do not contain this constant negative polarization. Then this assumption has not direct experimental evidence and is in contrast with theory.

Although the situation with regards to the radial dependence of the spin density appears to be somewhat unsettled, it must be noted that the models adopted for the form factor analysis are of a phenomenological character and their use is mainly justified in order to obtain such data which are the least sensitive to the choice of the model. One such datum is the amount of the asperical magnetic moment. In fact this quantity, which is usually found to be non zero in 3d-metals, is obtained in the fitting procedure to the experimental form factor directly from the coefficient of the aspherical form factor $\langle j_4 \rangle$, which is slowly varying with the electron configuration as shown in the atomic case by Watson and Freeman[11]. Moreover the aspheri-

city can be directly calculated from the theoretical density of states of the electronic bands. Several calculations of the density of states in ferromagnetic elements[10,12] are now available. In the case of the ferromagnetic alloys, the density of states with orbital degeneracy have been obtained by means of the Coherent Potential Approximation (CPA) for several systems such as Co-Ni[1], Fe-Ni[6], Fe-Cr[7], Cu-Ni[2].

ANALYSIS OF EXPERIMENTS AND DISCUSSION.

In the present work we analyse the polarized neutron experiments on fcc ferromagnetic transition binary alloys with the purpose of comparing experimental and theoretical aspherical magnetic moments. Relevant experiments are those on Co-Ni[8], Co-Fe[14], Fe-Ni[6,13,15], Cu-Ni[16,17]. In order to get a coherent view of the situation we re-analyse these alloys with the following phenomenological model.

The experimental magnetic structure factors are fitted with the expression:

$$F_M(hkl) = \mu_1 \langle j_o \rangle + \mu_a A_{hkl} \langle j_4 \rangle + \mu_T [(g-2)/g] f_{orb} \qquad (1)$$

where $\langle j_o \rangle$, $\langle j_4 \rangle$, A_{hkl}, g, f_{orb} are standard symbols, F_M is the magnetic structure factor in units of Bohr magnetons per atom, μ_1 is aparameter of the fit which in the case of a magnetic moment of purely 3d origin would be the 3d-spin part of the magnetic moment μ_T, while μ_a (which is also a parameter of the fit) is the aspherical magnetic moment which originates from the splitting of the d-band in a cubic

crystalline field. It can be noted that $\mu_a = \frac{3}{2}\mu_e - \mu_t$, where μ_e and μ_t are the magnetic moments of the e_g and t_{2g} subbands in the case that the non-d contribution to the magnetic moment are of prevalent s-character. It must be emphasized that the main purpose in using the fit (1) is to extract from the data μ_a which can be compared with theory. Instead the spherical part, which is sensitive to the choice of the form factor, gives the parameter μ_1 that has not a definite physical meaning as such. The results are shown in Fig. 1 for Cu-Ni[2,16,17] and for Co-Ni[8]. Our experiment on Cu-Ni, to be described more completely elsewhere[17], was done at 123°K on two compositions: 14 and 45 at.%Cu. It can be seen that the agreement with CPA (upper curve) is good.

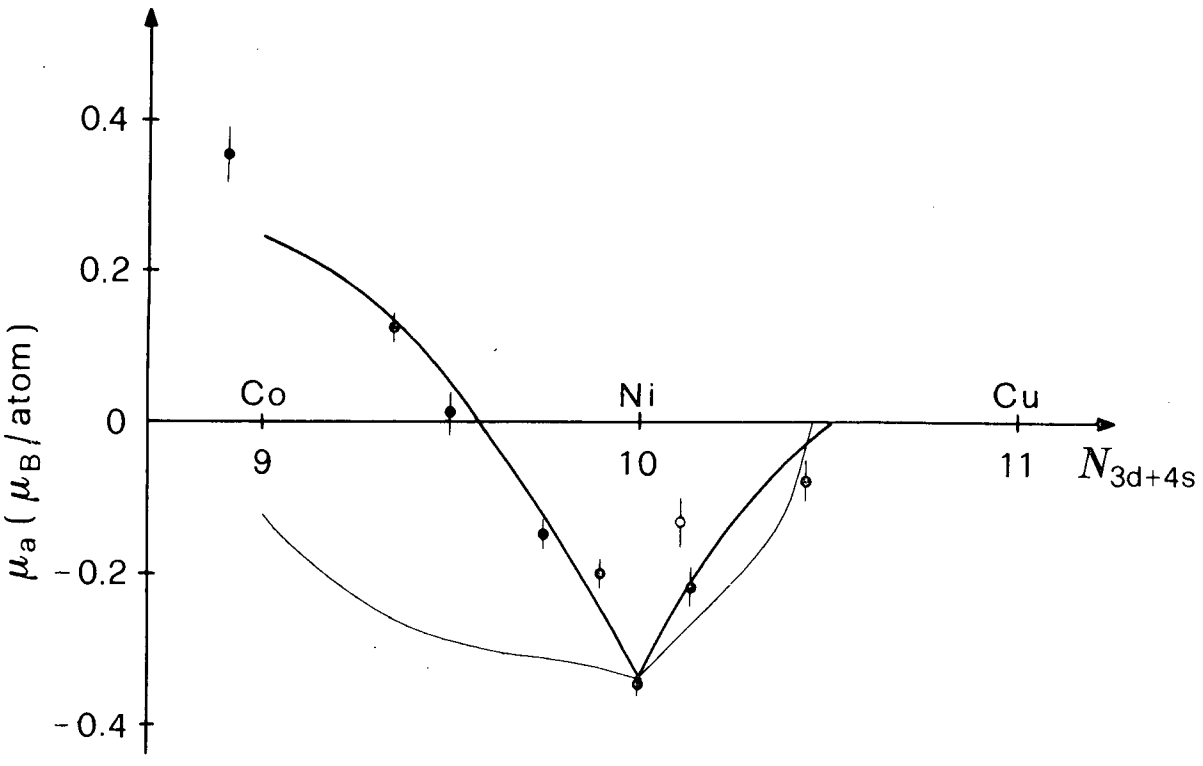


Fig.1. Aspherical moment as a function of number of outer electrons for Co-Ni and Cu-Ni. Also shown is Fe-Co[14] and pure Ni[5]. Upper curve is by CPA, lower one by rigid band.

The results for fcc Fe-Ni, shown in Fig. 2 are also in good agreement with CPA.

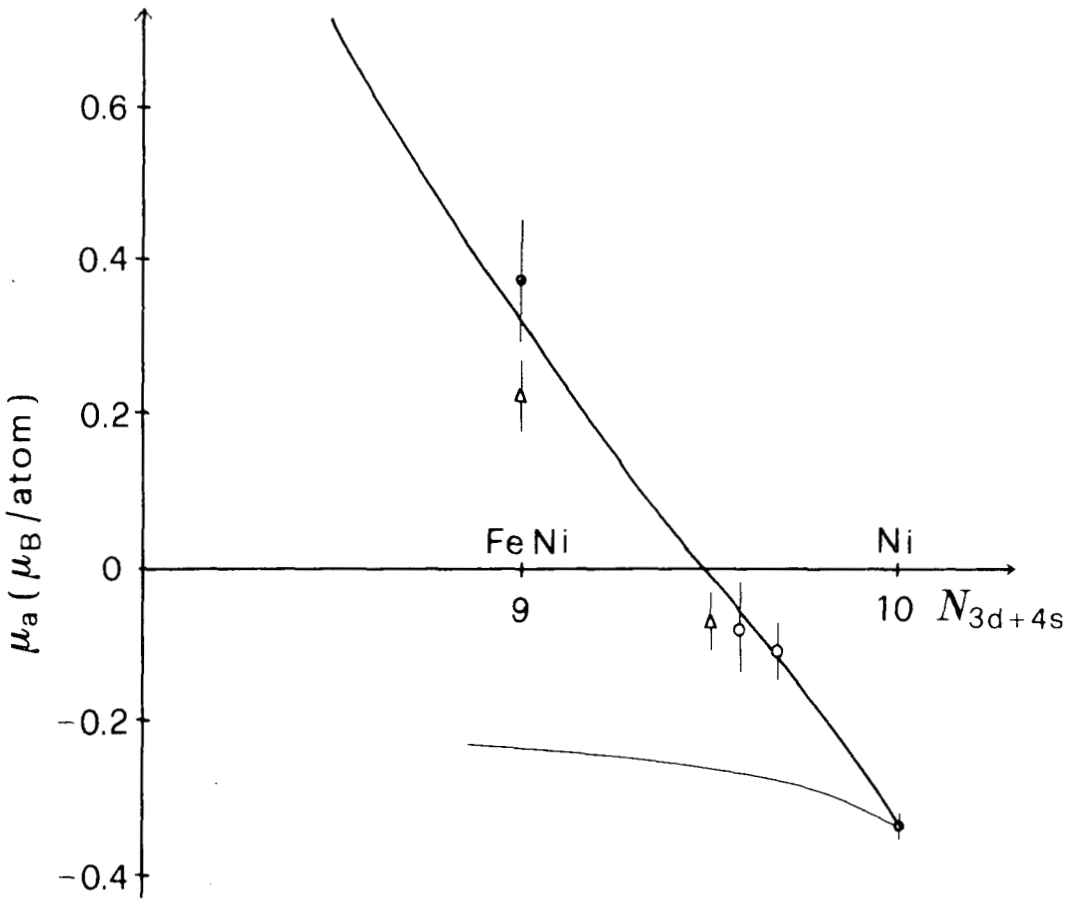


Fig. 2. Aspherical moment for Fe-Ni: experiments of Refs. 13-15. Upper curve: CPA, lower one: rigid band model.

One may question whether these results could be affected by a different influence of temperature and magnetic field on the various alloys, since the Curie temperature is largely varying with composition. This variation was only partially compensated by the choice of lower temperatures in the case of the Cu-Ni experiment with respect to those on Ni, Co-Ni and Fe-Ni. Though the influence of temperature was investigated on some Co-Ni alloys, and it was found that the asphericity does not vary appreciably[18], however one may

note that, approaching the Curie temperature with increasing Cu concentration (T_c= 148°K for the 45 at%Cu alloy), the distribution of electrons in the subbands may change with temperature and magnetic field appreciably. We may estimate this effect. From the CPA calculations[2], we know that the largest contribution to the density of states at the Fermi level is from t_{2g} electrons in these alloys, then we may assume that the susceptibility is mostly of t_{2g} character. From this and knowing that for Ni-45 at.%Cu the susceptibility is $1.4 \times 10^{-6} \mu_B$/Oe, we may crudely estimate that the aspherical moment at zero magnetic field should be $-0.023 \mu_B$ as compared to the measured value of $-0.033 \mu_B$ obtained with a magnetic field of 7 KOe, i.e. a value closer to the CPA curve.

Finally we note that the results of the asphericity determinations in these alloys allow to discriminate clearly against theories, of static electronic properties of alloys, more primitive than CPA, such as the rigid band model. In fact the aspherical magnetic moments can be calculated for these alloys in the rigid band model starting from the pure Ni bands and filling it with the electrons in such a way as to keep the total spin magnetic moment equal to the experimental values. In this way we obtain the lower curves shown in Figs. 1, 2. It can be seen that they do not agree with the experiments.

REFERENCES

1. F.Leoni and F.Sacchetti, Nuovo Cim. 21B, 97 (1974).
2. F.Sacchetti, Nuovo Cim., in press (1976).
3. C.G.Shull and Y.Yamada, Journ.Phys.Soc.Japan,17,BIII,1 (1962).
4. R.M.Moon,Phys.Rev.136, A195 (1964).
5. H.A.Mook, Phys.Rev. 148, 495 (1966).
6. F.Menzinger, F.Sacchetti and F.Leoni, Nuovo Cim. 20B,1 (1974).
7. G.Frollani, F.Menzinger and F.Sacchetti,Phys.Rev.B, 11, 2030 (1975).
8. B.Antonini, F.Menzinger, A.Paoletti and F.Sacchetti, Intern.J.Magnetism 1, 183 (1971).
9. L.Hodges, H.Ehrenreich and N.D.Lang, Phys.Rev.152, 505 (1966), and private communication.
10. K.J.Duff and I.P.Das, Phys.Rev. B 3, 192, 2294 (1971).
11. R.E.Watson and A.J.Freeman, Acta Cryst. 14, 27 (1961).
12. J.Callaway and C.S.Wang, Phys.Rev. B 7,1096 (1973).
13. L.Dobrzynsky, Intern.J.Magnetism 6, 291 (1974).
14. F.Menzinger and A.Paoletti, Nuovo Cim. 10B, 565 (1972).
15. J.W.Cable and E.O.Wollan, Phys.Rev. B 7, 2005 (1973).
16. Y.Ito and J.Akimitsu, J.Phys.Soc.Japan 35, 1000 (1973).
17. F.Sacchetti, P.De Gasperis and F.Menzinger, submitted to Phys.Stat.Solidi.(1976).
18. G.Kàdàr and F.Menzinger, Solid State Comm. 12, 909 (1973).

MAGNETIC DEFECT SCATTERING FROM γ-Mn Cu & γ-Mn Pd

J.R. Davis and T.J. Hicks*
Physics Department, Monash University
Clayton 3168, Australia

ABSTRACT

The antiferromagnetic defect scattering from a 10 at.% Mn Cu alloy and a 10 at.% Mn Pd alloy has been separated out using polarization analysis. The magnetic defect in Mn Cu is largely on first neighbours but for Mn Pd the greatest disturbance is on second neighbours. There appears to be no moment at the impurity site in both cases. In fitting our polycrystalline results with a cubic defect we have calculated $\frac{d\mu}{dc} = -4.3 \pm 0.6\ \mu_B$ at.$^{-1}$ for Mn Cu and $+3.1 \pm 0.3\ \mu_B$ at.$^{-1}$ for Mn Pd from the intensity expected at the (001) position. This compares well with $\frac{d\mu}{dc}$ obtained from the variation of magnetic Bragg scattering with composition for both alloy systems.

The nature and extent of defects in ferromagnetic metals has been extensively studied[1]. In this case a definitive separation of the magnetic diffuse scattering from the nuclear effects was achieved by manipulating the direction of magnetization using an externally applied magnetic field. This is not nearly so effective with paramagnetic and antiferromagnetic materials.

We have had some success in separating out diffuse magnetic scattering from paramagnetic materials using polarization analysis[2]. We now present the first separation of defect scattering from antiferromagnetic materials using polarization analysis. In this paper we restrict our attention to the magnetic scattering although we also have the nuclear data.

For this study we have chosen the antiferromagnet γ-Mn with

---

* On study leave during 1976 at I.L.L. B.P. 156X, 38042 Grenoble, France

additions of 10 at.% Cu and 10 at.% Pd. The impurities were selected because whilst addition of Cu to γ-Mn decreases the sublattice moment[3], addition of Pd increases it[4]. The magnetic structure of γ-Mn is shown in figure 1. After melting together the spectroscopically pure components the specimens cut from the ingots were annealed in a vacuum at 1100°C for 48 hrs and quenched in water to retain the γ phase. The alloys were single phase and face centred tetragonal ($c/a \lesssim 1$) and contained 9.2 ± 0.1 at.% Cu and 10.2 ± 0.1 at.% Pd by analysis. The neutron measurements were carried out on the LONGPOL instrument[6] at Lucas Heights.

The polycrystalline magnetic diffuse scattering is shown in figure 2 for the two alloys. These results have been corrected for nuclear spin scattering from the manganese[7], isotopic scattering from the Cu and multiple scattering. Of these connections the multiple scattering connection was by for the largest, being 12 mb sr^{-1} at $^{-1}$ for Mn Cu and 17 mb sr^{-1} at $^{-1}$ for Mn Pd. The effects of atomic clustering and short range order have also been taken out of the results.

The problem we face in interpreting this data is that the specimens are multi-domain and polycrystalline. We therefore adopt the simplifying assumption that the defect has cubic symmetry to facilitate some analysis. In this we are guided by the low values of cross-section in the region $K = 0.5$ to 0.7 $\mathring{A}^{-1}$ where the cross-section must be fairly isotropically close to zero. If the defect is cubic then the appropriate expression for the cross-section also assuming superposing defects is [8]:

$$\frac{d\sigma}{d\Omega} = {}^{2}/_{3}\left(\frac{e^2\gamma}{2mc^2}\right)^2 c(1-c)\, f^2(\underset{\sim}{K})\, M^2(\underset{\sim}{K}) \qquad (1)$$

where c is concentration, $f(\underset{\sim}{K})$ atomic form factor, $M(\underset{\sim}{K})$ Fourier transform of the defect and the factor 2/3 comes from the averaging over domains in a multidomain sample containing defects with cubic symmetry. We write:

$$M(\underset{\sim}{K}) = \mu_i - \mu_{Mn} + G(\underset{\sim}{K} - \underset{\sim}{t}) \qquad (2)$$

in which we have separated the moment disturbance at the impurity site $(\mu_i - \mu_{Mn})$ from the rest of the disturbance

$$G(K-t) = \sum_{\underset{\sim}{R}} g'(\underset{\sim}{R}) \exp(i\underset{\sim}{K}.\underset{\sim}{R}) \qquad (3)$$

where the $g'(R)$ are the moment disturbances at sites $\underset{\sim}{R}$ with respect to the direction of the moment at the site replaced by the impurity. Then

$$g'(\underset{\sim}{R}) = g(\underset{\sim}{R}) \exp(-i\,\underset{\sim}{t}.\underset{\sim}{R}) \qquad (4)$$

in which the $g(\underset{\sim}{R})$ are the moment disturbances with respect to the moments being disturbed. $\underset{\sim}{t}$ is the vector of the antiferromagnetic periodicity. For this structure $\underset{\sim}{t} = \underset{\sim}{K}_{001}$. One consequence of this model of independent superposing defects is that $\frac{d\bar{\mu}}{dc} = \mu_i - \mu_{Mn} + G(0)$ (5)

and thus the cross-section at (001) is proportional to $\left(\frac{d\bar{\mu}}{dc}\right)^2$.

To fit our results with the above model we averaged (1) over all directions including the $g'(\underset{\sim}{R})$ as parameters such that $g'(\underset{\sim}{R})$ is the same for all $\underset{\sim}{R}$ in the same shell of neighbours (thus imposing cubic symmetry on the defect). The resulting expression was least squares fitted to the measured cross-sections but with the restriction $\mu_i = 0$. (Both Pd and Cu have zero moment in Fe[1]). The resulting $g'(\underset{\sim}{R})$ are shown in table 1.

Table 1. Magnetic Defect Parameters

Alloy	$\mu_i-\mu_{Mn}$	$g'(R_1)$	$g'(R_2)$	$g'(R_3)$	$\frac{d\bar{\mu}}{dc}$ (001)	$\frac{d\bar{\mu}}{dc}$ (Bragg)
Mn Cu	-2.4 $\pm 0.1\mu_B$	0.38 $\pm 0.05\mu_B$	-0.1 $\pm 0.06\mu_B$	0.03 $\pm 0.1\mu_B$	-4.3 $\pm 0.6\mu_B$ at $^{-1}$	-4.2 $\pm 0.3\mu_B$ at $^{-1}$
Mn Pd	-2.9 $\pm 0.1\mu_B$	-0.22 $\pm 0.05\mu_B$	0.86 $\pm 0.05\mu_B$	-0.02 $\pm 0.1\mu_B$	3.1 $\pm 0.3\mu_B$ at $^{-1}$	3.2 $\pm 0.1\mu_B$ at $^{-1}$

Because of the restricted range of K and the limited number of points no more than three g'(R) could be fitted. Beyond this number there were severe unphysical oscillations in all parameters. As the number of g'(R)

was increased from one just to three however the parameters remained relatively constant. In table 1, $\frac{d\bar{\mu}}{dc}$ (001) is calculated from G(0) by equation (5), and compares well with $\frac{d\bar{\mu}}{dc}$ (Bragg) obtained from magnetic Bragg intensities from a range of alloys [3,4]. It is interesting to note at this point that because the moment direction is (001) there will be no magnetic diffuse scattering at the (001) position even though $\frac{d\bar{\mu}}{dc}$ is large for both alloys.

The main features to emerge from these measurements are that

(a) The decrease in sublattice moment with addition of copper occurs both at the impurity site and at first neighbours.

(b) The increase in sublattice moment with addition of palladium occurs mainly on second neighbours. About 5 μ_B is added at second neighbours to a palladuim impurity.

(c) The assumption of cubic symmetry in the analysis is self consistent with the defect around a palladuim impurity because most of the defect occurs at the impurity site and at the ferromagnetically coupled and therefore cubically symmetric second neighbours. The validity of the cubic assumption is less clear for the Mn Cu alloy because the moment change is at first the neighbours which have mixed moment directions and therefore tetragonal symmetry.

REFERENCES

1. M.F. Collins and G.G. Low, Proc. Phys. Soc. 86, 535 (1965).
2. N. Ahmed, S.J. Campbell and T.J. Hicks, International Conference on Magnetism, Moscow 1973, Proceedings 4, 91 (1974).
   N. Ahmed and T.J. Hicks, Solid State Commun. 15, 415 (1974)
   N. Ahmed and T.J. Hicks, J. Phys. F., 4, 124 (1974)
   N. Ahmed and T.J. Hicks, J. Phys. F., 5, 2168 (1975)
3. G. Bacon, I. Dunmur, J.H. Smith and R. Street, Proc. Roy. Soc. 241 A, 223 (1957).
4. T.J. Hicks, A.R. Pepper and J.H. Smith, J. Phys. C. 1, 1683 (1968).
5. D. Jeneghetti and S.S. Sidhu, Phys. Rev. 105, 130 (1957).
6. S.J. Campbell, N. Ahmed, T.J. Hicks, R. Ebdon and D.A. Wheeler,

J. Phys. E, 7, 195 (1974).

N. Ahmed, S.J. Campbell, and T.J. Hicks, J. Phys. E, 7, 199 (1974)

7. J.R. Davis and T.J. Hicks, J. Phys. C.9, L177 (1976).
8. W. Marshall and S.W. Lovesey, Theory of Thermal Neutron Scattering, p 527, Oxford (1971).

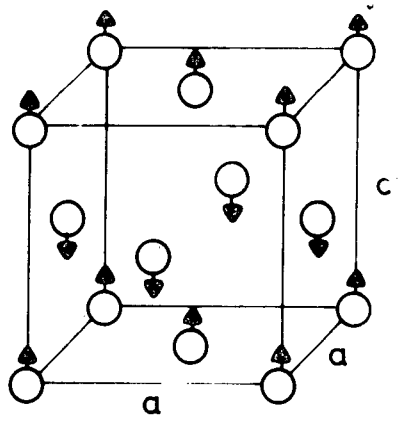


Fig. 1. Magnetic structure of γ-Mn.

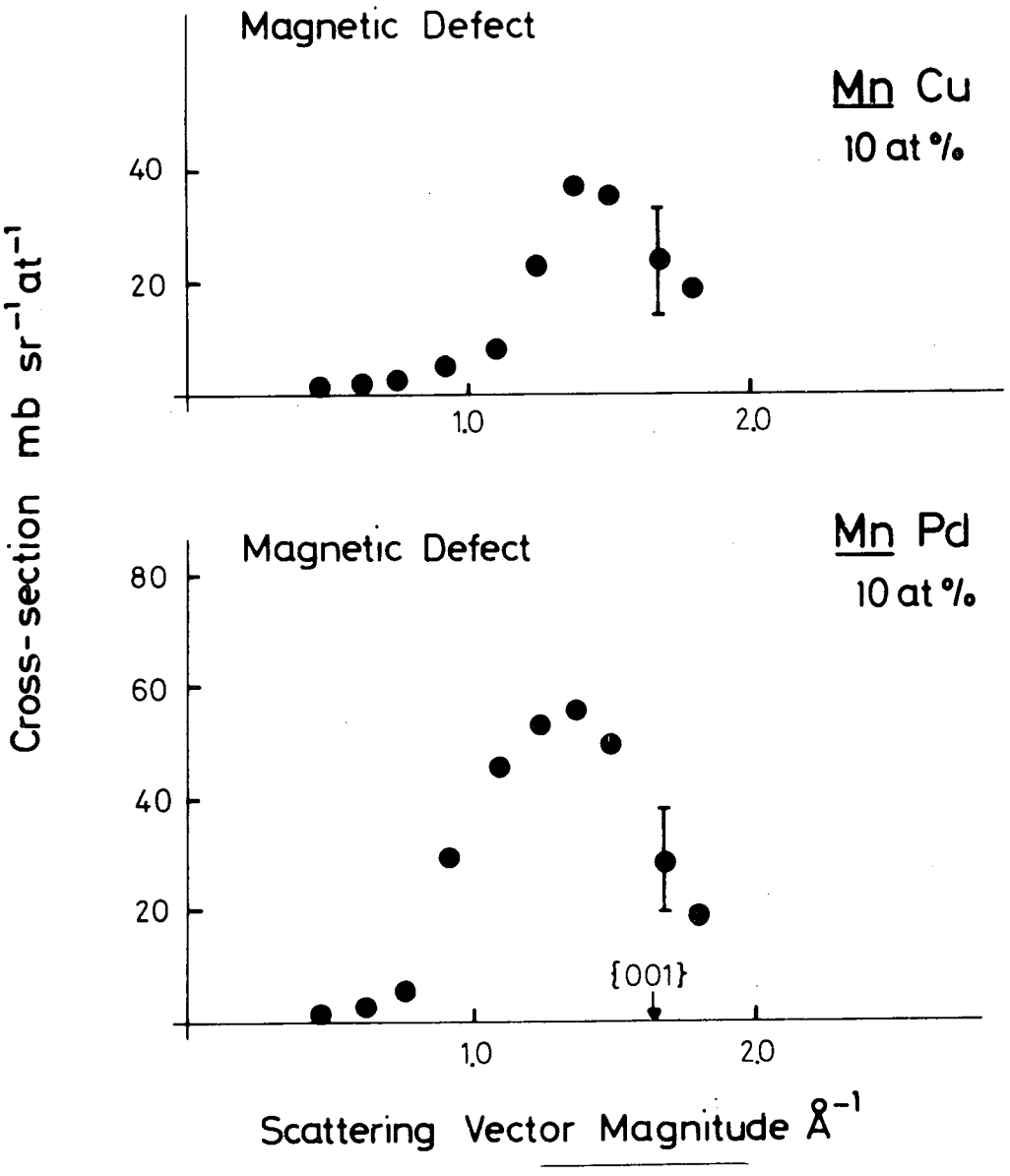


Fig. 2. Magnetic diffuse scattering from Mn Cu and Mn Pd.

REDUCED A-SITE MOMENT IN Fe_3O_4

V.C. Rakhecha, R. Chakravarthy and N.S. Satya Murthy
Solid State Physics Section, Nuclear Physics Division
Bhabha Atomic Research Centre, Bombay 400 085, India

ABSTRACT

A polarised neutron study of magnetite (Fe_3O_4) has been made for 49 reflections in <110> zone and the magnetic structure amplitudes have been deduced. It is seen in conjunction with the measured saturation magnetisation for the specimen that the A-site moment has an apparently lower value of $\sim 3.8 \mu_B$ for the Fe^{3+} ions (at 300°K). The magnetic form factors for the A-site reflections are found to be close to that for the Fe^{3+} free ion though (220) is lower. The magnetic structure amplitudes can not generally be explained on the basis of ionic model for the cation sites thus pointing to the complex magnetic moment distribution in the crystal resulting from covalent interactions.

EXPERIMENTAL

Polarised neutron measurements on natural magnetite (Fe_3O_4) had been reported earlier[1]. A subsequent analysis of that data showed that there existed significant extinction and possible multiple Bragg effects which could not be properly accounted for. Fresh measurements ($\lambda = 0.92$ Å) on 49 reflections in <110> zone have now been made on a relatively thinner crystal (1.2 mm x 0.8 mm x 12 mm) obtained from the same parent crystal. In the present crystal many four-fold reflections had quite different path lengths which facilitated satisfactory extinction correction to the data. Correction for incomplete incident neutron polarisation (P=0.93) and flipping efficiency (f = 0.99) and sample depolarisation were applied alongwith extinction and a set of values of $\gamma (= M/N)$ for different Bragg reflections were obtained (M = magnetic structure amplitude, N = nuclear structure amplitude).

DEPOLARISATION, EXTINCTION AND MULTIPLE BRAGG SCATTERING

The value of the sample depolarisation coefficient was determined experimentally from measurements on flat Fe_3O_4 samples placed alternately before and after a $Co_{92}Fe_8$(200) crystal analyser in the sample position. A check was made for the effect of multiple Bragg scattering for (220) and (440) reflections by turning the crystal about the scattering vector. For (220) the polarisation ratio was observed at eight orientations of the crystal in a range of 25° and the values were found to vary between 0.058 and 0.070 (value in normal experiment 0.061). Five measurements for (440) gave the same value as in the normal experiment.

Unpolarised neutron integrated Bragg intensity measurements were made for seven independent u-parameter sensitive reflections in ⟨112⟩ zone (λ = 1.24 A) in order to estimate the u-parameter and the extinction parameter g in Zachariasen's theory[2]. The A, B and oxygen site scattering amplitudes were assumed to be 0.951, 0.938 and 0.575 respectively. The lower nuclear scattering amplitude of 0.938 for the B sites was taken on the basis of Ti impurities estimated from x-ray fluorescence measurements and assumed to go to B sites.* The values determined were: u = 0.2551 ± 0.0011 and g = 75 ± 20.

The extinction parameter g was independently arrived at from polarisation ratios for (444) reflections which showed about 2% change for the equivalents with effective path lengths differing nearly by a factor

---

* A qualitative optical spectrographical analysis of the sample showed that the sample contained predominantly Ti and to a lesser extent V, Cr, Mn, Zn, and Al. Other impurities were less than 20 ppm. X-ray fluorescence measurements gave a semi-quantitative estimate of Ti impurities of about one atomic percent of Fe.

of two. The value obtained from the analysis* was g = 50. The assumption of common temperature factors for different ions, as well as for the nuclear and magnetic scattering was made and this results in exact cancellation of the same in the ratio of M and N. $\lambda/2$ correction was also incorporated in the calculations but was seen to be rather unimportant due to the lower polarisation of the incident beam.

RESULTS

The analysed γ-values are tabulated in Table 1. The error estimates have been made on the basis of statistical errors in the values of polarisation ratios (usually better than 1%), 1% error in polarisation and flipping (arising principally from long term fluctuations of r.f. current and frequency). For some weak high angle reflections the errors are much larger. Also for some reflections with M and N both small and comparable it is not absolutely unambiguous to choose between the two roots of γ. The values given in the table represent with fair certainty the correct choice, i.e. the choice close to the model values for M**. The choice of M for (220) however was especially ascertained

---

* The method followed is essentially the same as that in Ref. 3. In the presence of depolarisation and extinction the expression for the polarisation ratio (R) was taken as

$$R = (f_1 (1+\gamma^2) + f_2 (2\gamma))/(f_1' (1+\gamma^2) + f_2' (2\gamma))$$

where $f_1 = Y_+ (1+PD) + Y_- (1-PD)$ and $f_2 = Y_+ (1+PD) - Y_- (1-PD)$

and f_1' and f_2' are obtained by replacing P by P(1-2f) in the expression for f_1 and f_2. Y_+ and Y_- are the extinction factors for the two states of neutron spin corresponding respectively to the coherent structure amplitudes (N+M) and (N-M). D is the polarisation transmission. The two roots of γ in the above equation were obtained by iteration initiated with model M values. Identical γ-values were sought for equivalent reflections with different path lengths.

** Those corresponding to A and B site moments obtained in the subsequent analysis and the corresponding form factors deduced for the A and B sites.

to be correct from the unpolarised neutron measurements described above. (i.e. by removing the nuclear contribution).

The A-site-only reflections with h+k = 4n+2, k+l = 4n+2, h+l = 4n (and cyclic) have the simplest structure factors. Both the nuclear and magnetic structure amplitudes for them depend only on A sites and only weakly on oxygen due to the departure of the u-parameter from the ideal value of 0.25 and due to the existence of moment density in general positions in the crystal. These reflections therefore provide the A site moment in the ionic model, with the least ambiguity. In Fig. 1, the form factors of the A-site reflections derived with an assumed moment of 3.82 μ_B are shown. Except (220) which is lower, all points fall closely on the Fe^{3+} free ion form factor curve (dotted). The magnetic moment density at A and B sites was integrated out, using the M-values, over circular areas of varying radii in the (110) projection*. The A- and B-site moments were also calculated with reference to the moment density at the oxygen sites (in (110) projection) averaged over rectangular cells of up to $\sim$0.5 x 0.5 A^2 area[5]. The B-sites with 2 or 4 atoms in projection** showed some differences thus indicating a non-zero moment distribution about oxygen site and possible overlap effects in the projection.

The maximum moment values per atom obtained for the A and B-sites with the corresponding radii (R_A) are

---

* The required value of M_{000} for forward magnetic scattering was obtained from the measured saturation magnetization for a specimen from the same parent crystal. The saturation magnetisation at room temperature was determined to be 3.47 μ_B per Fe_3O_4 formular unit, the value being about 9% lower than the reported values. The measurements were kindly made by Dr. M.J. Patni and Prof. C.M. Srivastava, I.I.T. Bombay. A Mossbauer pattern of the sample was also obtained. The internal fields at the A and B sites and the isomer shift values compared closely with those reported in the literature.

** There are 2 A sites, 2 or 4 B sites and 4 oxygens in (110) projection. The bracketed numbers in the text after the appropriate site indicate numbers in the projection.

A-site (2)	R_A = 1.2 Å	Moment = 3.82 μ_B
B-site (2)	R_A = 1.0 Å	Moment = 3.47 μ_B
B-site (4)	R_A = 1.4 Å	Moment = 3.96 μ_B

The spherically averaged form factors for the A and B sites are also derived[6] and that for the A site is shown in fig. 1. It is seen that this is quite close to the Fe^{3+} free ion curve. These facts point out that the magnetic moment density associated with the A sites (inside a 1.2 Å radius) is almost Fe^{3+} free ion like. However the associated

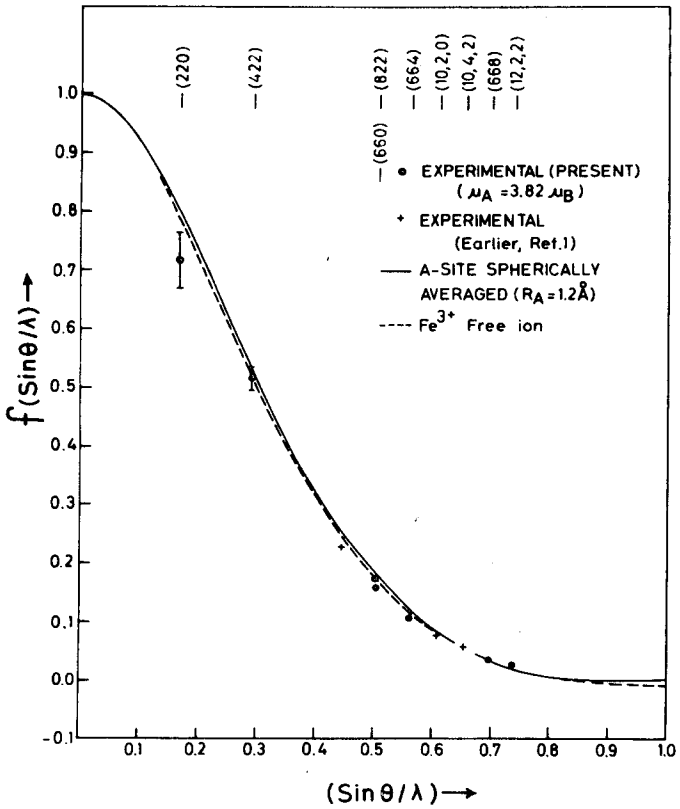


Fig. 1. A- Site Form Factors in Magnetite.

moment shows a considerable reduction ($\sim 9\%$), even after considering the $\sim 9\%$ lower saturation magnetisation for the sample. The lower value of (220) form factor may possibly be ascribed to a change of sign of moment density for $R_A \gtrsim 1.2$ Å. The above conclusions are not likely to be affected by the presence of impurities which all tend to reduce the A site nuclear scattering amplitude; thus the estimate of M values from the γ-values for A site reflections can only be an overestimate and not the reverse.

A similar conclusion for the B sites may also be drawn but here the structure factors are more complex and the oxygen sites play an important role both with respect to nuclear and magnetic structure amplitudes. The analysis is accordingly much less unambiguous. However it is clear from the spin density projection map, that despite the size of the estimated errors on M-values, there are regions of significant moment density outside the A and B site and around the oxygen sites. Attempts to reconcile the polarisation ratios, as well as the observed M/N values in various least-squares refinements with moments on A and B sites alone and including the crystal field modification of the magnetic 3d-electron wave functions gave only a qualitative agreement. Inclusion of an oxygen moment improved the situation to some extent. The magnetic moment density distribution in Fe_3O_4 is therefore concluded to be complex, resulting from covalent interactions between the cations and the oxygen ligands. The reduced A-site moment is apparently a consequence of this[7].

REFERENCES

1. R. Srinivasan, V.C. Rakhecha, S.K. Paranjpe, R.J. Begum, L. Madhav Rao and N.S. Satya Murthy, Proceedings of the International Conference on Magnetism (Moscow), IV, p.246, 1973.
2. W.H. Zachariasen, Acta Cryst. 23, 558 (1967).
3. G.H. Lander, T.O. Brun and O. Vogt, Phys. Rev. B7, 1988 (1973).
4. W.C. Hamilton, Phys. Rev. 110, 1050 (1959).
5. R.M. Moon, Int. J. Magnetism 1, 219 (1971).
6. P.J. Brown and C. Wilkinson, Acta Cryst. 18, 398 (1965).
7. J. Hubbard and W. Marshall, Proc. Phys. Soc. 86, 561 (1965).

Table 1. Experimental M/N Values for Magnetite

h k l	$\sin\theta/\lambda$	$\gamma = M/N$	$\Delta\gamma/\gamma$	N	M	h k l	$\sin\theta/\lambda$	$\gamma = M/N$	$\Delta\gamma/\gamma$	N	M
1 1 1	0.1033	4.405	0.03	3.025	13.326	7 5 5	0.5933	0.359	0.05	-2.914	-1.046
2 2 0	0.1687	-0.767	0.08	-7.686	5.895	7 7 1	0.5933	-0.393	0.06	1.636	-0.643
3 1 1	0.1978	0.117	0.03	-12.581	-1.477	9 3 3	0.5933	0.401	0.05	-3.076	-1.234
2 2 2	0.2066	-3.443	0.03	-3.274	11.274	7 7 3	0.6168	0.008	0.50	7.940	0.064
4 0 0	0.2385	0.620	0.06	25.643	15.899	6 6 6	0.6197	-0.339	0.05	-2.355	0.799
3 3 1	0.2599	11.652	0.04	-0.634	-7.386	10 2 2	0.6197	-0.475	0.05	-2.344	1.113
4 2 2	0.2921	-0.564	0.04	7.530	-4.246	7 7 5	0.6613	0.006	0.40	-10.371	-0.061
3 3 3	0.3098	0.100	0.04	10.200	1.025	11 1 1	0.6613	0.007	0.20	-10.210	-0.069
5 1 1	0.3098	0.066	0.05	14.973	0.994	8 8 0	0.6746	0.006	0.20	39.787	0.227
4 4 0	0.3373	0.071	0.03	40.703	2.874	9 5 5	0.6825	0.102	0.04	7.617	0.778
3 3 5	0.3910	0.044	0.06	-12.612	-0.557	8 6 6	0.6954	-0.029	0.20	-8.282	0.237
6 2 2	0.3955	-1.823	0.04	-2.963	5.401	11 3 3	0.7030	0.002	2.50	7.971	0.017
4 4 4	0.4131	0.279	0.03	25.333	7.078	8 8 4	0.7156	0.027	0.05	24.425	0.669
5 5 1	0.4258	0.645	0.07	5.376	3.466	12 0 0	0.7156	0.035	0.04	24.404	0.864
7 1 1	0.4258	7.053	0.05	-0.624	-4.398	7 7 7	0.7230	-0.102	0.10	-3.919	0.401
5 5 3	0.4580	0.037	0.05	-14.922	-0.552	12 2 2	0.7352	-0.036	0.19	7.536	-0.268
8 0 0	0.4770	0.033	0.05	40.391	1.325	9 9 1	0.7613	-0.002	3.00	7.526	-0.016
7 3 3	0.4881	-2.241	0.04	-1.707	3.825	9 9 3	0.7798	-0.002	1.00	-17.063	0.029
6 6 0	0.5060	-0.154	0.03	-8.306	1.281	11 5 5	0.7798	-0.002	1.50	-12.412	0.024
8 2 2	0.5060	-0.179	0.03	-7.684	1.377	13 1 1	0.7798	0.007	0.25	17.222	0.119
5 5 5	0.5164	0.026	0.09	17.293	0.448	12 4 4	0.7911	0.010	0.10	24.115	0.241
6 6 2	0.5198	-0.608	0.05	-2.656	1.612	9 9 5	0.8154	0.004	0.32	19.416	0.080
9 1 1	0.5433	0.363	0.04	5.366	1.948	13 3 3	0.8154	0.006	0.25	-15.042	-0.096
6 6 4	0.5594	-0.135	0.03	6.916	-0.936	8 8 8	0.8263	-0.001	1.80	39.204	-0.035
8 4 4	0.5843	0.018	0.05	40.089	0.742						

THE INFLUENCE OF ANISOTROPY ON THE d=2 AND d=3 MAGNETIC ORDERING IN LAYER-TYPE ANTIFERROMAGNETS $K_2Mn_{1-x}Fe_xF_4$, STUDIED BY NEUTRON DIFFRACTION

L. Bevaart, E. Frikkee
Reactor Centrum Nederland,
Petten (N.H.), The Netherlands

L.J. de Jongh
Kamerlingh Onnes Laboratory
Leiden, The Netherlands

ABSTRACT

The transitions to 3-dimensional long-range order (d=3 LRO) in the layered antiferromagnets K_2MnF_4 and Rb_2FeF_4 (T_c = 42.2 K and 56.3 K, resp.) are attributed to the combined effect of spin anisotropy and weak interlayer interactions. The spin anisotropy in K_2MnF_4 is axial, while it is planar in Rb_2FeF_4. Doping K_2MnF_4 with increasing amounts of Fe^{2+} will initially decrease the (overall) axial anisotropy to some minimum value, and thereafter increase the planar anisotropy. The results of neutron-scattering experiments on $K_2Mn_{1-x}Fe_xF_4$ single crystals with x = 0.023, 0.028, 0.061 and 0.12 are reported. For x = 0.061 and x = 0.12 the anisotropy is planar. The minimum of the overall anisotropy is found in between x = 0.023 and x = 0.028. This minimum is correlated with a minimum in T_c and a maximum in the apparent value of β. For x = 0.023 and x = 0.028 a spin reorientation takes place at $T_R < T_c$. In the temperature range $T_R < T < T_c$ d=2 and d=3 LRO coexist, while for $T < T_R$ complete d=3 LRO is gradually established.

INTRODUCTION

Since it became clear that the spin systems in the layered compounds A_2MF_4 (A = K,Rb; M = Mn,Fe,Co,Ni) are close approximations to theoretical two-dimensional (d=2) model systems, many experimental investigations have been performed on these compounds[1-10]. An almost ideal example for the d=2 Heisenberg model is K_2MnF_4; the principal deviation from this model is a small axial anisotropy (≈0.5%) due to magnetic dipolar interactions, which results in a term $-DS_z^2$ ($D_{Mn} > 0$) in the Hamiltonian. Hence the system becomes d=2 Ising-like and a transition to antiferromagnetic long-range order (LRO) is observed at T_c = 42.14 K.[6]

Although LRO in three dimensions appears for $T < T_c$, the d=2 Ising character is confirmed by the observed value for the critical exponent $\beta = 0.15 \pm 0.01$ ($\beta = 0.125$ for the d=2 Ising model). The observation for $T > T_c$ of critical neutron scattering along lines in reciprocal space, and the absence of any increase in the critical scattering close to the magnetic reciprocal lattice points corresponding to the d=3 antiferromagnetic order, are additional indications for purely d=2 spin-spin correlations. From these results it has been concluded[4] that at T_c a transition to d=2 LRO is induced by axial anisotropy, and that the ordering in the third dimension is a secondary effect, brought about by small interplanar interactions in combination with the establishment of LRO within the planes.

Neutron scattering experiments on Rb_2FeF_4 ($T_c = 56.3$ K)[4] have shown that the spin alignment in the ordered phase is along the crystallographic [110] and [$\bar{1}$10] directions, in contrast to the preferred [001] direction in K_2MnF_4 (cf. fig. 1). For the Fe^{2+} ions the dipolar anisotropy is very weak in comparison with the single-ion anisotropy, which favours the $S_z = 0$ state ($D_{Fe} < 0$). It may therefore be expected that substitution of Mn^{2+} by increasing amounts of Fe^{2+} will lead to a change in sign of the "average" anisotropy parameter. From susceptibility measurements[11] on mixed compounds $K_2Mn_{1-x}Fe_xF_4$ one may conclude that this change in sign occurs in the range $0.02 < x < 0.06$.

In order to investigate the influence of small anisotropic perturbations on the magnetic ordering, elastic neutron scattering experiments were carried out on four single crystals containing 2.3, 2.8, 6.1 and 12 at.% Fe. Although the experiments were performed both above and below T_c, in the present paper the emphasis will be on the ordered phase, i.e. the influence of the Fe concentration upon the value of T_c, on the d=2 and d=3 magnetic order, and on the value of the critical exponent β.

EXPERIMENT

The experiments were performed on a triple-axis spectrometer (operated in double-axis mode) at the HFR Reactor in Petten. An incident beam with a wave length $\lambda = 1.475$ Å was obtained by means of a Zn (0002) monochromator. A 20' collimator was used in front of the monochromator, while 30' horizontal and vertical collimators were mounted between sample and detector. The samples were prepared by Breed[12] by growing from the melt with an excess of the Fe compound, and were shaped as flat platelets with the largest surface perpendicular to the c-axis. Their weights varied from 38 mg for $x = 0.061$ to 125 mg for $x = 0.12$. The crystals were glued onto an aluminium backing, oriented with the $[\bar{1}10]$ direction vertical and mounted in a variable-temperature, ^{4}He-flow cryostat.

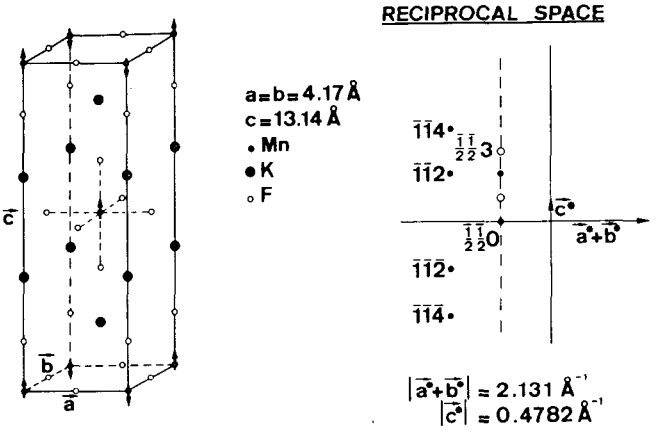


Fig. 1. Chemical unit cell and reciprocal lattice plane $(\bar{1}10)$ of K_2MnF_4. The indicated spin structure corresponds to domain type 1 and magnetic superlattice reflections ○ in reciprocal space. The magnetic reflections ● are due to domain type 2 where the spin at position $(\frac{1}{2},\frac{1}{2},\frac{1}{2})$ is reversed.

The experimental procedure may be explained by means of fig. 1, which shows the crystal structure and $(\bar{1}10)$ reciprocal lattice plane for K_2MnF_4. For this magnetic structure and tetragonal crystal symmetry there is no net interaction between spins in adjacent planes, which allows the formation of two domain types with a different stacking sequence of planes. Domains 1 with parallel spins at positions (0,0,0)

and $(\frac{1}{2},\frac{1}{2},\frac{1}{2})$ give rise to superlattice reflections $(\bar{\frac{1}{2}},\bar{\frac{1}{2}},1)$, $(\bar{\frac{1}{2}},\bar{\frac{1}{2}},3)$, etc., whereas the reflections $(\bar{\frac{1}{2}},\bar{\frac{1}{2}},0)$, $(\bar{\frac{1}{2}},\bar{\frac{1}{2}},2)$ are due to domains 2 where the spins in the plane $z = \frac{1}{2}$ are reversed. The line $(\bar{\frac{1}{2}},\bar{\frac{1}{2}},\zeta)$ in reciprocal space corresponds to d=2 LRO in the ab-plane.

For each sample the intensities of the four magnetic reflections indicated in fig. 1 have been measured between T_c and 4.4 K. These results were used to determine the relative population of domains 1 and 2, as well as the spin direction. In addition, extensive measurements were made on the d=2 spin-spin correlations by scanning both along and across the ridge $(\bar{\frac{1}{2}},\bar{\frac{1}{2}},\zeta)$ between 4.4 K and 60 K. Scans across the ridge for fixed values of ζ (usually ζ = 0.36, 0.72 and 2.7) were used to determine which of the spin components are correlated. In this way a fairly complete picture of the d=2 correlations was obtained as a function of temperature.

RESULTS

As regards the results for $T \geq T_c$, the present mixed compounds show a similar behaviour of the d=2 correlations as the pure A_2MF_4 compounds[6,9,11]. The ridge $(\bar{\frac{1}{2}},\bar{\frac{1}{2}},\zeta)$ becomes observable at $T/T_c \approx 1.4$, and its width decreases with T until it reaches a minimum value at T_c which is only slightly larger than the instrumental resolution function.

In all samples d=3 LRO starts to develop at a well-defined T_c. For each sample the intensities of the four reflections satisfy the relation $I(T)/I(0) = B^2(1-T/T_c)^{2\beta}$ in a large temperature range. However, for x = 0.023 and 0.028 clear deviations from this relation are observed at a temperature T_R (see figs. 2 and 3). From the change in the relative intensities of magnetic reflections corresponding to the same domain type (see, for example, the $(\bar{\frac{1}{2}},\bar{\frac{1}{2}},1)$ and $(\bar{\frac{1}{2}},\bar{\frac{1}{2}},3)$ reflections in fig. 2) it may be concluded that a spin reorientation occurs for $T < T_R$. A summary of the spin ordering characteristics for the d=3 LRO, derived from the intensities of the Bragg reflections, is given in table 1.

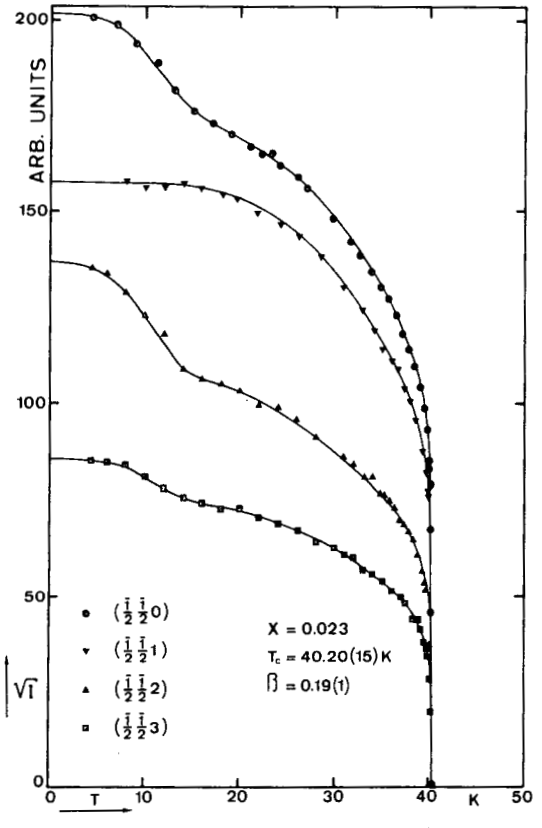


Fig. 2. Variation of the intensities of magnetic reflections with temperature for x = 0.023.

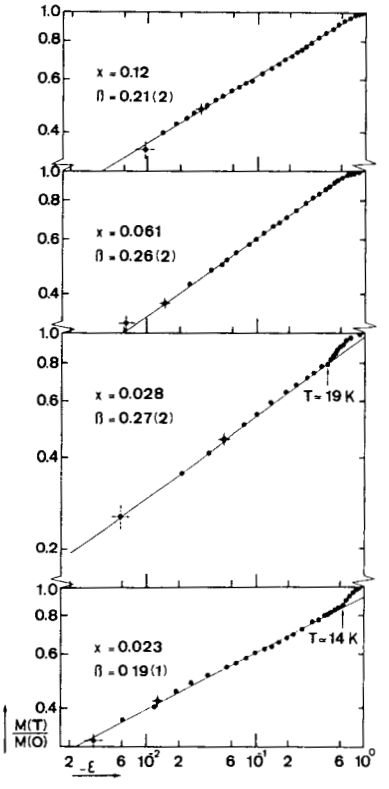


Fig. 3. Variation of d=3 LRO as a function of $-\varepsilon = (1-T/T_c)$ for different Fe concentrations x. Data points refer to the magnetic reflection $(\frac{1}{2},\frac{1}{2},0)$.

Table 1. Ordering characteristics for d=3 LRO in $K_2Mn_{1-x}Fe_xF_4$. Uncertainties are given in brackets in units of the last decimal place. For tilted structures ϕ indicates the angle between the spins and the [001] direction.

x	T_c(K)	T_R(K)	β	spin direction	domains 1 - 2 (%)
0[6]	42.14		0.15(1)	[001]	
0.023	40.20(15)	14(2)	0.19(1)	$T > T_R$: [001]	53-47
				$T = 4.4K$: $\phi = 35(5)^\circ$	
0.028	36.91(5)	19(2)	0.27(2)	$T > T_R$: [110], [$\bar{1}$10]	54-46
				$T = 4.4K$: $\phi = 59(5)^\circ$	
0.061	42.30(5)		0.26(2)	[110], [$\bar{1}$10]	48-52
0.12	44.0 (1)		0.21(2)	[110], [$\bar{1}$10]	52-48 (24K) 49-51 (4.4K)

A systematic investigation of the ridge $(\frac{1}{2},\frac{1}{2},\zeta)$ for $T < T_c$ shows that the decrease of the intensity in the ridge below T_c is proportional to the increase of the intensity in the magnetic Bragg reflections. However, for the samples with $x = 0.023$ and $x = 0.028$ the ridge intensity remains constant after the initial decrease just below T_c, until it tends to zero below T_R (cf. fig. 4). This persistence of d=2 correlations, with a correlation length >400 Å, has not been reported previously for the pure compounds, nor did we observe it in the samples with $x = 0.061$ and $x = 0.12$. It may be seen from fig. 4 that in between T_c and T_R a considerable part of the spin system does not participate in the d=3 LRO. A comparison of the intensities for $\zeta = 0.36$ and 2.70 indicates that the spin correlations contributing to the ridge intensity are $\langle S_x S_x \rangle$ and $\langle S_y S_y \rangle$, both for the $x = 0.023$ and $x = 0.028$ crystal.

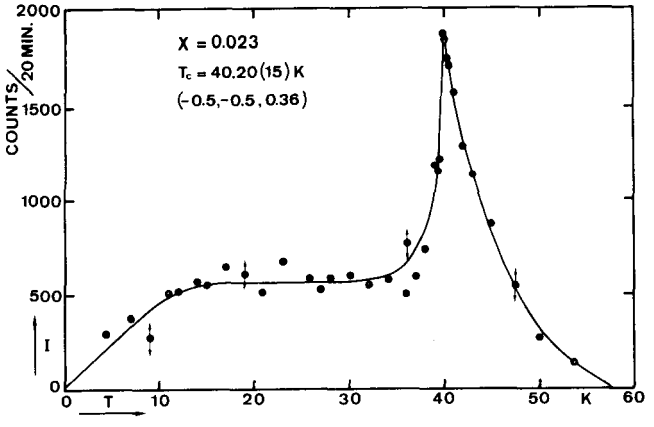


Fig. 4. Intensity observed at a fixed point on the magnetic ridge $(\frac{1}{2},\frac{1}{2},\zeta)$. Similar results are obtained for the $x = 0.028$ sample.

DISCUSSION

In view of the unexpected behaviour of the samples with $x = 0.023$ and 0.028 a distinction should be made between the temperature ranges $T < T_R$ and $T_R < T < T_c$ in the discussion of the d=3 LRO. For $T_R < T < T_c$ the spins stay aligned along crystallographic symmetry directions, and it is obvious (cf. table 1, column 5) that the sign of the average anisotropy changes in between $x = 0.023$ and $x = 0.028$. In accord with theoretical arguments, e.g. based upon Green-function techniques[13], Monte-Carlo calculations[14], and high-temperature series analyses[15,16], the value of T_c decreases when the axial anisotropy is decreased, and reaches a minimum value in the above concentration range. The apparent value of β shows a maximum in the same range.

In the interval $T < T_R$, where all spins gradually become involved in the d=3 LRO, the preferred orientation is in the symmetry planes (110) and $(\bar{1}10)$. The angle ϕ between the spins and the c-direction at 4.4 K has been determined by fitting the data with a model involving 4 non-equivalent domains with collinear spins, aligned ferromagnetically in the (110) and $(\bar{1}10)$ planes. For $\phi = 0^o$ and 90° this model becomes equivalent to the magnetic structures of K_2MnF_4 and Rb_2FeF_4, respectively. Comparison of the magnetic structures at 4.4 K shows a gradual change of ϕ for Fe concentrations $0 < x < 0.061$.

The experimental results shown in figs. 2 and 4 suggest a direct relation between the gradual decrease of d=2 LRO below T_R and the reorientation of the spins involved in d=3 LRO. Let us first consider the range $T_R < T < T_c$ where d=2 and d=3 LRO coexist. For the $x = 0.023$ sample different spin components participate in the two ordering patterns. The largest part of the spin system is involved in d=3 LRO and is oriented along [001]. On the other hand, the ridge intensity may be explained by d=2 long-range correlations between spins oriented along [110] and $[\bar{1}10]$. In the x=0.028 crystal the situation is less clear because the same spin components are involved in both d=2 and d=3 LRO.

For an explanation of the experimental results, two effects seem to be most significant:

1. the competition between the dipolar anisotropy, which increases with decreasing T, and the temperature-independent single-ion anisotropy of the Fe^{2+} ions,
2. spatial variations of the local, effective anisotropy as a result of the statistical distribution of the Fe ions. These fluctuations will be particularly important if the average anisotropy is small.

The coexistence of d=2 and d=3 LRO between T_c and T_R is probably a result of the local fluctuations in the anisotropy. In the samples with $x = 0.023$ and 0.028 the absolute value of the average anisotropy will be smallest*, and hence the establishment of LRO and the preferred spin direction will

* The reduction in the apparent "average" anisotropy is also evidenced by a reduction of the spin-flop field.[11]

be affected by local variations in the anisotropy. This could lead to a "mismatching" of ordering patterns and may explain why in different parts of the same crystal d=2 and d=3 LRO are coexisting. Below T_R full d=3 LRO is gradually established, probably because the magnetic dipolar anisotropy becomes larger than the local crystal-field anisotropy, forcing the spins in the remaining d=2 regions into a d=3 LRO pattern. The stable spin configuration at $T \approx 0$ will depend on the ratio between the two competing anisotropic terms in the Hamiltonian.

For the samples with $x = 0.061$ and 0.12 no spin reorientation is observed, which indicates that the crystal-field anisotropy is too large to be compensated by the dipolar anisotropy. In both crystals the magnetic structure is the same as in Rb_2FeF_4[4]. It has been emphasized[4] that in this structure two of the four possible domains, i.e. domains 1 with spins along $[\bar{1}10]$ and domains 2 with spins along $[110]$, are not populated, a fact that is probably related to a small deformation of the crystal structure. This deformation, which reduces the crystal symmetry from tetragonal to orthorhombic, has been observed with optical methods[3]. An attempt to observe the change in crystal symmetry by neutron diffraction was made by scanning the strong $(\bar{1}\bar{1}2)$ nuclear reflection along the $[110]$ direction for the $x = 0.028$ crystal at temperatures above and below T_c. However, the splitting of the $(\bar{1}\bar{1}2)$ reflection below T_c, which should show up if the interplanar distance $d_{\bar{1}\bar{1}2}$ is different in $[110]$ and $[\bar{1}10]$ domains, could not be detected. Hence we conclude that the change in the unit cell dimension along $[110]$ is smaller than 3×10^{-3} Å.

A full report including the susceptibility measurements will appear elsewhere[11]. The authors are indebted to J.V. Lebesque for the loan of the single crystals and to H.H.A. Plas for his technical assistance during the experiments.

REFERENCES

1. D.J. Breed, Physica 37, 35 (1967).
2. D.J. Breed, K. Gilijamse, and A.R. Miedema, Physica 45, 205 (1969).
3. G.K. Wertheim, H.J. Guggenheim, H.J. Levinstein, D.N.E. Buchanan, and

R.C. Sherwood, Phys. Rev. 173, 614 (1968).

4. R.J. Birgeneau, H.J. Guggenheim, and G. Shirane, Phys. Rev. B1, 2211 (1970).
5. R.J. Birgeneau, J. Skalyo Jr., and G. Shirane, Phys. Rev. B3, 1736 (1971).
6. R.J. Birgeneau, H.J. Guggenheim, and G. Shirane, Phys. Rev. B8, 304 (1973).
7. E.J. Samuelsen, J. Phys. Chem. Solids 35, 785 (1974).
8. H. Ikeda and K. Hirakawa, Sol. State Comm. 14, 529 (1974).
9. H. Ikeda, J. Phys. Soc. Japan 37, 660 (1974).
10. L.J. de Jongh and A.R. Miedema, Adv. Phys. 23, 1 (1974).
11. L. Bevaart, J.V. Lebesque, E. Frikkee, and L.J. de Jongh, to be published.
12. D.J. Breed, thesis, Amsterdam (1969).
13. M.E. Lines, Phys. Rev. 164, 736 (1967).
14. K. Binder and D.P. Landau, Phys. Rev. B13, 1140 (1976).
15. N.W. Dalton and D.W. Wood, Proc. Phys. Soc. 90, 459 (1967).
16. T. Ishikawa and T. Oguchi, J. Phys. Soc. Japan 31, 1021 (1971).

EFFECT OF A BLOCH WALL AS A HELICAL MAGNETIC STRUCTURE ON THE PASSAGE OF NEUTRONS

O.Schärpf
Institut A für Physik, Technische Universität
33 ~~Braunschweig~~, Mendelssohnstr.1, FR Germany
Brunswick

ABSTRACT

Observed refraction by 90° Bloch walls[2] and spin echo measurements[4] give experimental evidence for the possibility of a continuum description of interaction of neutrons with magnetization. This allows to apply a solution of the Schrödinger equation for a helical structure[7] to interpret the small angle scattering results of neutrons by Bloch walls. The precessing spin polarization[1] in the wall is represented and its mode of formation is given. The behavior of the wave field in the wall and its contribution to reflection and transmission is shown. This makes clear why simple Born approximation in the form of the Fourier transformation cannot give a good description of the observations[9] and shows possibilities how this can be replaced also in more complicated cases.

INTRODUCTION

Using one type of Bloch wall of well defined orientation we investigate experimentally and theoretically the behavior of neutrons traversing helical magnetic structures with a pitch of about 200 nm. With small grazing angles of incidence the precessing spin polarization[1] in the wall mainly determines the measured small angle scattering.

We use a continuum description of interaction of the neutrons with the B-field in the interior of the crystal. That this is possible we learn from the measured refraction behavior of the neutrons by the walls[2] and from our spin echo measurements[3,4] with polarized polychromatic long wave length neutrons. We obtained this spin echo after the neutrons had traversed through a magnetically saturated Nickel sheet. This sheet gives a displace-

ment of the echo that corresponds to a homogeneous field of the saturation induction on a distance of the foil thickness. In the setup of the neutron spin echo this distance is equivalent to a weak homogeneous guide field of the length of the echo displacement. If the interaction of the neutrons in the interior of the ferromagnetic sheet would have been other than precession about the saturation direction, no echo of the polychromatic neutrons would have been possible.

Bloch walls are boundaries between two ferromagnetically saturated domains of different magnetization direction. They can be described as a region with the orientation of the electron spin moments changing continuously through it from one domain to the next. The wall structure represents a balance between magnetocrystalline anisotropy and the exchange interaction. This associates an effective thickness with the domain boundary different for different wall orientations and magnetization directions in the adjacent domains. Therefore we ought to use only one sort of Bloch walls if we want to test the behavior of neutrons in such structures. If one applies a field, the directions of the adjacent magnetization directions can quantitatively be changed and thereby also the wall thickness is altered. There is a well known and elaborated theory of this behavior of the Bloch wall. The method to obtain regularly arranged Bloch walls[5] (and also 180° Bloch walls[6]) is described elsewhere.

SCHRÖDINGER EQUATION FOR THE BLOCH WALL AS A HELICAL STRUCTURE

We assume the Bloch wall as a piece of a helix. Fig.1 gives a sketch of the magnetization in the investigated wall. The Schrödinger equation for a neutron in this magnetic structure is

$$-\frac{\hbar^2}{2m}\Delta\begin{pmatrix}\psi_1\\ \psi_2\end{pmatrix} + \mu\left[B_x \sin 2ky \begin{pmatrix}\psi_2\\ \psi_1\end{pmatrix} + iB_y \begin{pmatrix}-\psi_2\\ \psi_1\end{pmatrix} + B_x \cos 2ky \begin{pmatrix}\psi_1\\ -\psi_2\end{pmatrix} = E\begin{pmatrix}\psi_1\\ \psi_2\end{pmatrix}\right] \quad (1)$$

where $2mE/\hbar^2 = k_x^2 + k_o^2 + k_z^2$; $b_{x,y} = 2m\mu B_{x,y}/\hbar^2$;

μ = magnetic moment of the neutron.

The general solution of this Schrödinger equation is[7]

$$\begin{pmatrix}\psi_1\\ \psi_2\end{pmatrix} = e^{i(k_x x+k_z z)} \sum_{n=1}^{4} \alpha_n e^{-i\lambda_n y}\left[e^{-iky}\begin{pmatrix}1\\ i\end{pmatrix} + \Lambda_n e^{iky}\begin{pmatrix}1\\ -i\end{pmatrix}\right] \qquad (2)$$

with λ_n as solution of the equation

$$0 = \lambda^4 - \lambda^2(2k^2+2k_o^2) - \lambda 4kb_y + k_o^4 - b_y^2 - b_x^2 + k^4 - 2k^2k_o^2 \qquad (3)$$

and $$\Lambda_n = (k_o^2 + b_y - (\lambda_n - k)^2)/b_x \qquad n = 1,2,3,4. \qquad (4)$$

This solution is generally applicable for many types of wall by suitable selection of B_x, B_y. For $B_y=0$ one has 180° walls. For $B_x=B_y$ one has 90° walls etc. This solution has four arbitrary constants α_n. To determine the α_n one has to apply the continuity conditions for the wave function and their derivatives at the two sides of the Bloch wall. This results in eight equations which determine eight coefficients viz. the four α_n of the waves in the wall and the two reflected and the two transmitted components.

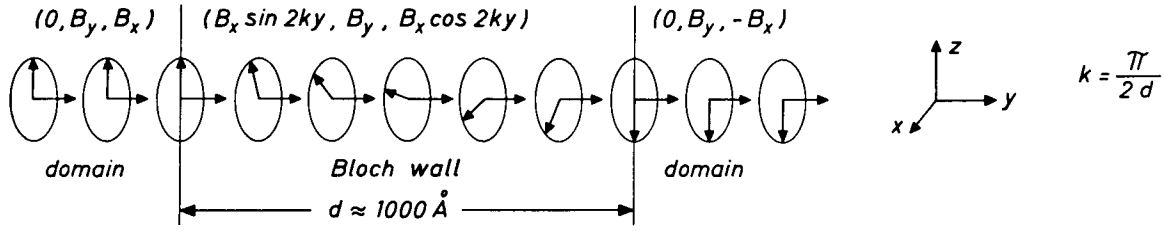


Fig.1. Transition of magnetization direction from one domain to the other in a 90° Bloch wall. Suitable selection of B_x, B_y also allows other types of wall to be considered

PROPERTIES OF THE SOLUTION

To understand the behavior of the neutrons in traversing this structure one has to take into account their relation to the varying magnetic field. The spin direction of the neutrons with small grazing angles of incidence experiences a slowly varying direction of induction B with an angular velocity $\vec{\omega}$. As this angular velocity $\vec{\omega}$ is near the Larmor precession frequency $\vec{\omega}_L$, one has to look for a

description of the resulting precession of the neutron spin in this case. Fig.2 gives a description of this resulting behavior in the case of a 180° wall, if the boundary conditions (i.e. refraction or reflection) are neglected. One obtains a spin precession with the vector angular velocity $\vec{W} = \vec{\omega} + \vec{\omega}_L$. The precession cone has a cone angle of $\theta = \arcsin(\omega/W)$. Simultaneously with the precession the cone is unrolled upon a plane parallel to the wall.[8] The arrow of the spin describes the line $S_1S_2S_3S_4$ in fig.2, a sort of cycloid along a meridian on the surface of a sphere. With this picture in mind one has an easy method to consider the resulting precession with ω near Larmor frequency - also in more complicated cases.

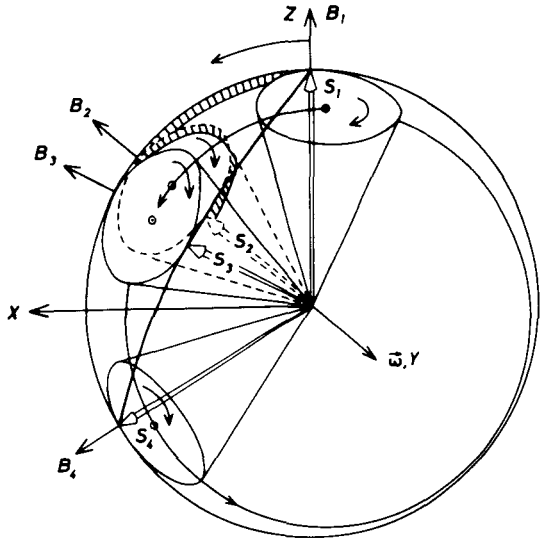


Fig.2.Precessing spin polarization in a rotating magnetic induction B(t).The precessing spin polarization results from a simultaneous rotation about the y-axis with $\vec{\omega}$ and a precession about an axis $\vec{W} = \vec{\omega} + \vec{\omega}_L$ with |W|. These are coupled by the precession cone angle $\theta = \arcsin(\omega/W)$ giving an unrolling of the cone on the x-z-plane.

Fig.3 shows the stereographic projection of the precessing spin polarization of the neutron traversing the helical wall. This is calculated for different grazing angles θ for a 180° wall with thickness d= 2074 Å and for a neutron wavelength λ=2.3 Å, B_s=19700 Oerstedt. Here the calculations are made with regard to the boundary conditions. The points give the local spin direction of the neutron in 1/10 steps of the wall thickness. The behavior is here (for larger θ) the same as described above in the simple time dependent case without respect to boundary conditions. This is clear because in this case the reflected intensity is small and the amplitudes of the waves with wave vector going backwards in the wall are small. The behavior of the amplitudes of the transmitted neutron wave by this same wall is given in fig.4 together with small sketches

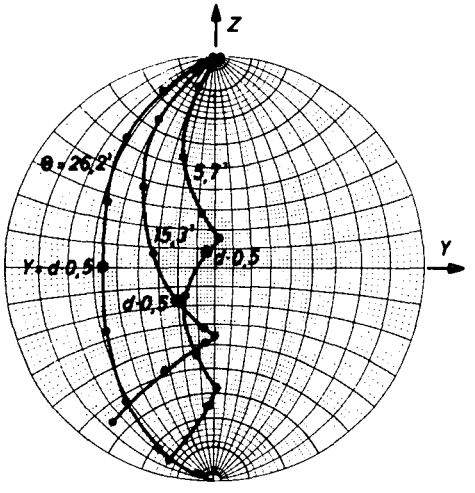


Fig.3.Stereographic projection of the spin polarization for different grazing angles Θ and incident spin up (=line begins at the north pole).The end of the line is the spin polarization at the rear of the wall.

of the spin polarization. From this the distribution of the transmitted part of the wave into a spin up and a spin down part is clear. E.g. at Θ = 26.2' (=minutes of arc) the neutron spin is reversed at the rear of the wall. Therefore one obtains only a component which is transmitted with spin flip. At larger angles Θ this reversal can only be partly. Thus for larger Θ the component without spin flip will become larger. With smaller Θ the experienced angular frequency ω is smaller, the cone angle of fig.2 is smaller and thus the unrolling of the cone will be doubled or threefold etc. The minima of the amplitude without spin-flip are obtained if the unrolling ends with the spin arrow in antiparallel direction i.e. at the south pole. This is only possible if $2W/\omega$ is a whole number. The maxima result analogously.One easily can understand that this behavior is strongly dependent on the wall thickness. For d = 0, if one has the simple case of refraction, all neutrons are transmitted without spin flip. Fig.5 shows the intensity of transmitted neutrons for different wall thicknesses.

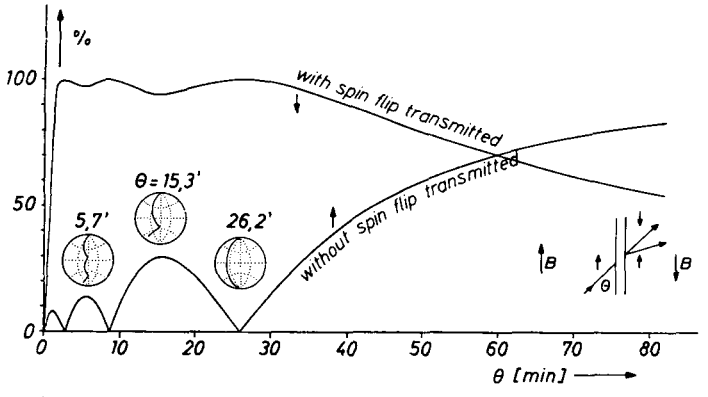


Fig.4.Amplitudes of the transmitted neutron wave as a function of Θ. For some angles of Θ a small sketch of the precessing spin polarization in the wall is given. Incident spin up, 180° wall, d=2074 Å, λ =2.3Å, iron.

Fig.6 shows the behavior of neutrons with incident spin down in a wall with wall width d = 2631 Å. Here one would expect total reflection at an angle Θ_c = 13.5'. At angles greater than this angle

Θ_c the behavior is analogous to that described above. But at angles smaller Θ_c the behavior is changed. Here the neutron spin simply is forced to rotate in the wall in the same way as the magnetization. Then the neutron spin at the rear side of the wall is simply inverted. Only at very small angles of incidence the behavior is further changed, as one obtains a reflected part only without spin flip. This also very easily can be understood if one has in mind the process of refraction. Then a neutron with spin flip would have negative energy, i.e. it could not propagate in this medium. In this manner the neutron is forced to follow the magnetization direction.

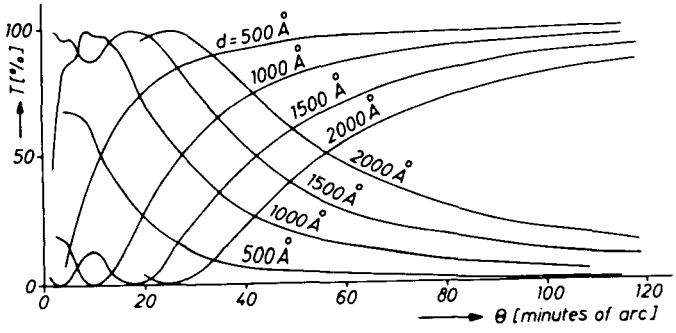


Fig.5. Transmitted intensities for different wall widths d; incident spin up, λ =2.3 Å, 180° wall.

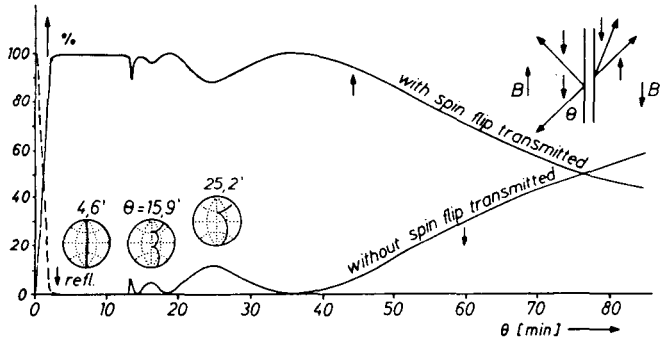


Fig.6. Intensities of the transmitted and reflected neutron wave as a function of Θ for incident spin down. λ =2.3 Å, d=2631 Å, 180° wall.

Fig.7 shows the reflection behavior for a wall with d=2074 Å, neutron wavelength λ =2.3 Å, 180°-wall, for incident spin up. For some angles Θ the resulting density of the neutron wave field in different depths in the wall is given. The density of the wave field with Θ=1' at y=0, i.e. at the entrance side of the neutrons in the wall, is high. This is because the reflection here is high and the incident and reflected amplitudes together can fulfill the continuity conditions with this wave field. At Θ=2' the reflected intensity is zero and the density of the wave field at y=0 is 1, i.e. equal to the incident density. At Θ=3' it is a little higher than one giving small reflected intensity. From this one can understand the oscillating behavior of the reflection. The distribution of this intensity to spin up and down is given by the spin direction at y=0 and y=d, the latter for the transmitted

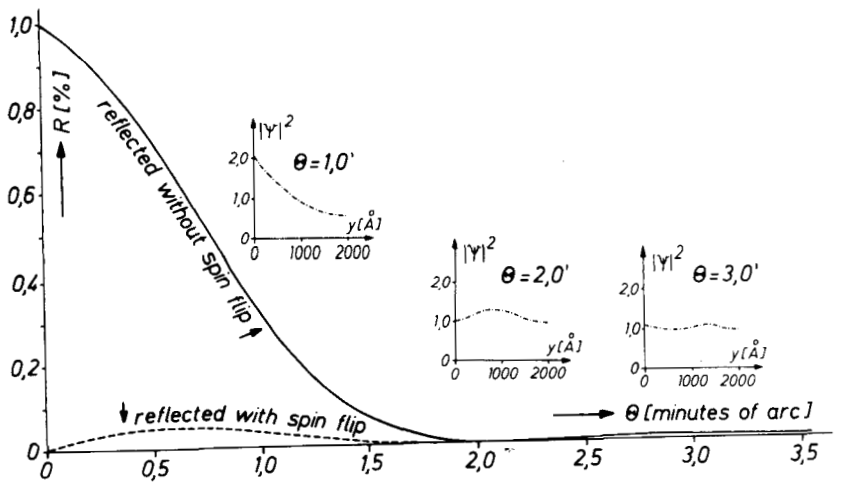


Fig.7. Reflection behavior for incident spin up. For some angles of incidence the resulting density of the neutron wave field in different depths in the wall is given. λ =2.3 Å, d=2074 Å.

wave. The density at the rear side of the wall (y=d) immediately gives the density of the transmitted part of the beam.

It is clear that the Born approximation in the simple form of the Fourier transformation cannot give this behavior of the spin. The precessing spin polarization described above, in connection with the refraction behavior described in[2] renders possible the interpretation of neutron scattering by magnetic structures as Bloch walls. It gives totally other results than Born approximation. This urges upon the supposition that in more difficult cases e.g. small angle scattering by dislocations[10] also other results ought to be expected. It is indispensable to extend these observations to those structures.

REFERENCES

1. J. B. Hayter, Neutron Diffraction Conference, RCN-234, Petten 1975, p.141.
2. O. Schärpf and H. Strothmann, this issue.
3. F. Mezei, Z.Phys. 255, 146 (1972).
4. O. Schärpf and H. Warnecke, JMMM, 2, 113 (1976).
5. M. L. Néel, J. Phys. Radium, 5, 241 and 265 (1944).
   G. Dedié, J. Niemeyer, Ch. Schwink, Phys.stat.sol.(b),43,163(1971).
6. V. Ungemach and Ch. Schwink, JMMM, 2, 167 (1976).
7. O. Schärpf and R. Seifert, Neutron Diff. Conf.,Petten 1975,p.90.
8. Ch. Schwink and O. Schärpf, Z.Phys. B21, 305 (1975).
9. O. Schärpf, Physica 80B, 289 (1975).
10. W. Vorbrugg und O. Schärpf, Phil.Mag. 32, 629 (1975).

MEASUREMENT OF NEUTRON BIREFRINGENCE IN MAGNETIC STRUCTURES

O. Schärpf
Institut A für Physik, Technische Universität
Mendelssohnstr. 1, D33 ~~Braunschweig~~ Braunschweig
H. Strothmann
Physikalisch-Technische Bundesanstalt
Bundesallee 100, D33 Braunschweig
Federal Republic of Germany

ABSTRACT

Regularly arranged Bloch walls separating domains in which the angles between magnetization directions are 90° or (with an applied field) 56.2°, allow the refraction to be measured in the case where only a magnetization component is reversed at the boundary. The results of very precise angle measurements are described by a simple continuum model of refraction, from a solution of the Schrödinger equation. This shows that the fundamental dependence of magnetic scattering on the magnetization component normal to the scattering vector, given by Halpern and Johnson, in this case does not give the correct description.

INTRODUCTION

The use of the Born approximation in the simple Fourier transformation expression for analyzing neutron scattering by magnetic structures of 100 nm and more, in some cases gives incorrect results[1]. One of the main reasons is that this method does not take the refraction into account which occurs in these structures. Looking for the law of refraction, one generally only finds a law for the case where, in the boundary, the full magnetization is reversed: i.e. for the case of a 180° wall. S. De Benedetti[2] gives a short survey of the magnetic interaction between neutrons and electrons, first treated by Halpern and Johnson[3]. The main result of this treatment by the Born approximation is that only the component of the magnetization perpendicular to the scattering vector is effective. De Benedetti applies this to the refractive index (p.182). He states that the refractive index is affected only by the component of the atomic magnetic moments in the direction

of the wave vector of the neutrons, since to compute the refractive index one requires the forward scattering amplitude. However, he only applies this to a case which seems to be the 180° geometry. If one interprets his sentence as only that component is effective for refraction which is changed in the refracting boundary, for the neutron wavelength of 0.23 nm one obtains the deflections given in fig. 6, for different angles of magnetization directions 2ϑ in neighbouring domains. The scattering vector in the refracting case is normal to the boundary. The angle the magnetization direction makes with the normal to the boundary is ϑ. The deflection would then be given by

$$\alpha_{\pm} = \arcsin \frac{\sqrt{k_y^2 \pm 2k_B^2 \sin\vartheta}}{\sqrt{k^2 \pm k_B^2}} - \theta \qquad (1)$$

where $k = 2\pi/\lambda$, θ = grazing angle of incidence, $k_y = k \sin\theta$, $k_B^2 = 2m\mu B/\hbar^2$, B = saturation induction, μ = magnetic moment of neutron. This dependence of magnetic scattering on the magnetization component normal to the scattering vector is a result all neutron physicists believe to be very fundamental. Nevertheless it is only a consequence of the Fourier transformation resulting from the Born approximation. Since in our case an exact solution is also possible, one does not need an approximation.

EXPERIMENTAL SETUP

Regularly arranged parallel <110>-90° Bloch walls in iron single crystals, separating magnetic domains with magnetization directions of 90° to each other[4], are used to investigate the refraction of neutrons at boundaries between two such regions (fig. 1a). By use of an applied field the angle between the directions of magnetization of neighbouring domains can be varied further between 90° and 0°. We used the setup in fig. 1a with high resolution (5 seconds of arc = 5"), using two silicon single crystals in parallel positions[5] to investigate the dependence of the refraction on the direction of incidence. The angle of deflection α can easily be determined in this arrangement by adjusting the analyzer

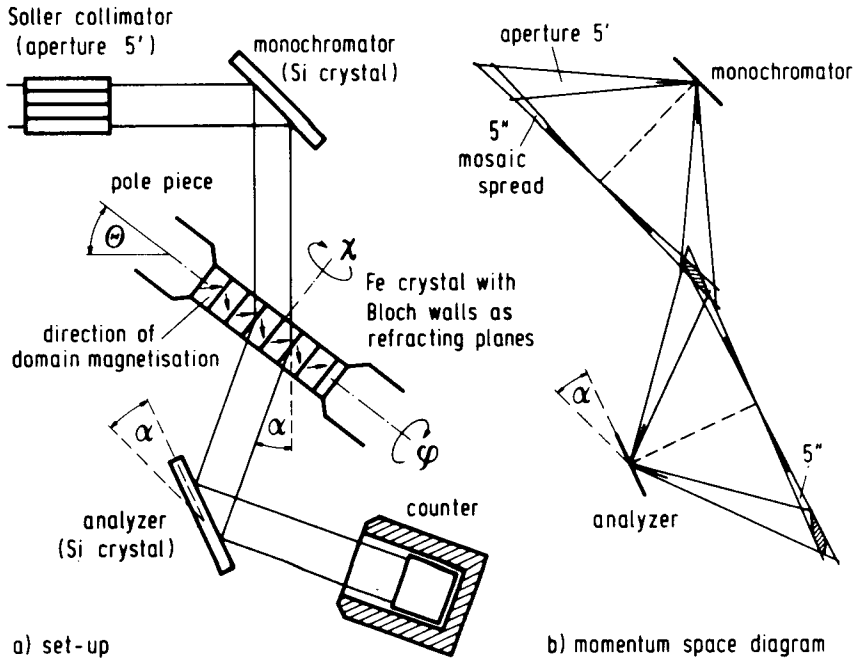


Fig. 1a) Experimental setup giving the different angles for adjustment of the walls and the principle of the measurement.
1b) Momentum-space diagram, showing the resolution of the method.

crystal in such a manner, that the refracted and thus deflected beam fulfills the Bragg condition for the analyzer. So one obtains very exact measurements of the angle of deflection, when the deflection takes place in the horizontal plane only. To avoid deflections not in this plane, one has to set the refraction plane in a perpendicular position. Since this plane consists of zigzag pieces[6] of the investigated wall, one has to incline the crystal by an angle χ (fig. 1a). This can be done with the setup in fig. 2.

Fig. 1b shows the momentum-space diagram of the setup. One would expect a spread of the deflected beam because the two momentum-space elements of the monochromator and analyzer intersect one another at an angle of deflection α. Since this angle is very small (less than 1 minute of arc) this beam spread is less than one second of arc. An additional much greater beam spread comes from the distribution of wall directions[6], as nearly 100 walls were used at low fields and nearly 1000 walls at high fields.

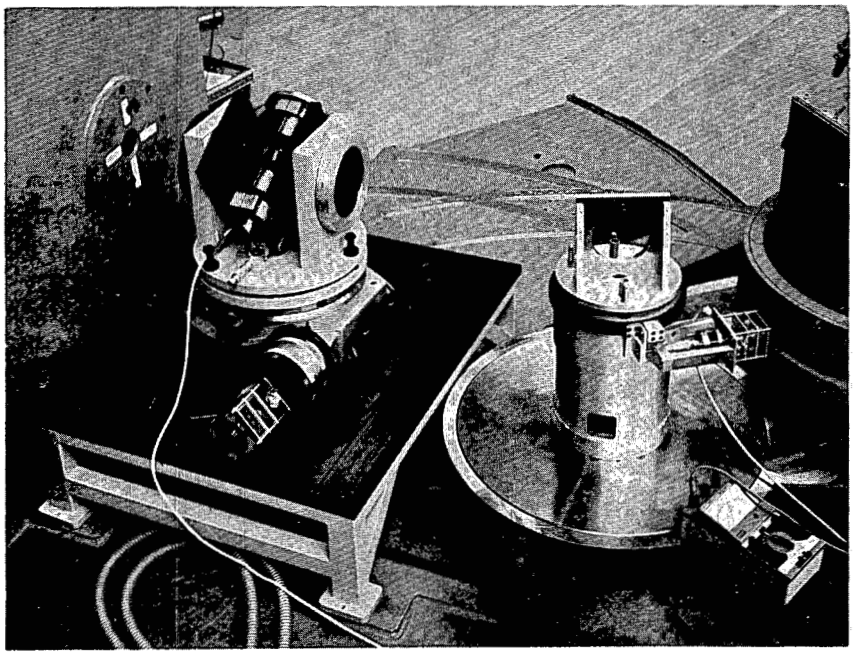


Fig. 2. Setup for the magnet with the Fe-crystal holder allowing adjustment of Θ, ϕ, χ. On the right is the analyzer crystal holder, with automatic control gear for variation of α.

METHOD OF MEASUREMENT

First the position of the zero grazing angle of incidence has to be determined. To make the procedure of finding this position clear, we shall give the directions and angles in stereographic projection (fig. 3). $\vec{n}_1$ and $\vec{n}_2$ are the directions of the normals of the zigzag pieces. Using an X-ray goniometer[7] we found the exact position of the rotation about the crystal axis ϕ. The angle $\chi = 27^{\circ}$ (fig. 1a) is known from elsewhere[6]; it is the inclination of the crystal axis allowing the normal $\vec{n}_1$ to be obtained by suitable rotation ϕ in the horizontal direction perpendicular to the direction of the neutrons. Changing Θ and representing the counting rate as a function of Θ, one obtains a curve as given in fig. 4. The Θ position with maximum intensity is the desired zero position of Θ. In this case no neutrons hit the walls and therefore none are deflected out of the direct beam, thus giving maximum intensity. The sharpness of the curve in fig. 4 also gives an indication of the distribution of the wall directions. This defines a range of grazing angles of incidence

and hence the observed spread of the deflected beam (also quantitatively correct).

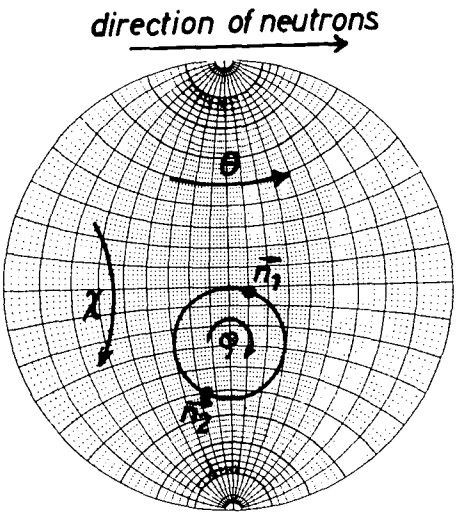


Fig. 3. Stereographic projection of the normals of the zigzag pieces of the walls, together with the angles of adjustment.

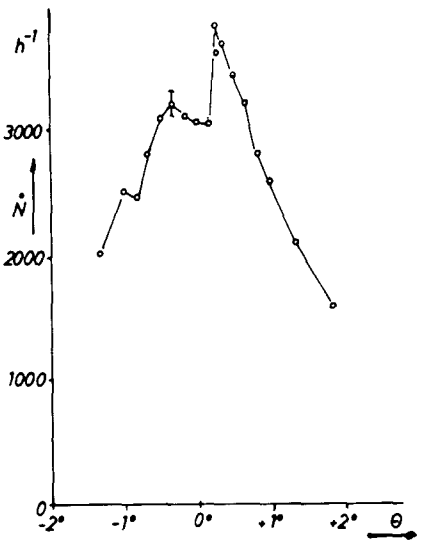


Fig.4. Intensity of direct beam as a function of the grazing angle θ, to determine the position of zero grazing angle.

RESULTS AND DISCUSSION

Fig. 5 shows the deflected beams observed for different angles of incidence. These deflected beams are clearly separated from the direct beam. We took measurements at two field strengths 6 A/cm and 200 A/cm (measured as a tangential field at the surface with a Hall probe). In the first case the magnetization directions make an angle of 90° with each other. In the second case this angle is 56.2°. One should observe a large difference in the measured angles of deflection if the normal component is the effective component (fig. 6). Instead, the angles remain the same at different fields for the same angle of incidence, and for both fields are clearly larger than would be expected if the component of the magnetization only were reversed in the boundary. They correspond very well to the full alteration of the magnetization in the wall, i.e. a 180° wall. Since it is well known that the walls used are

90° walls, the reason for this behavior must be found.

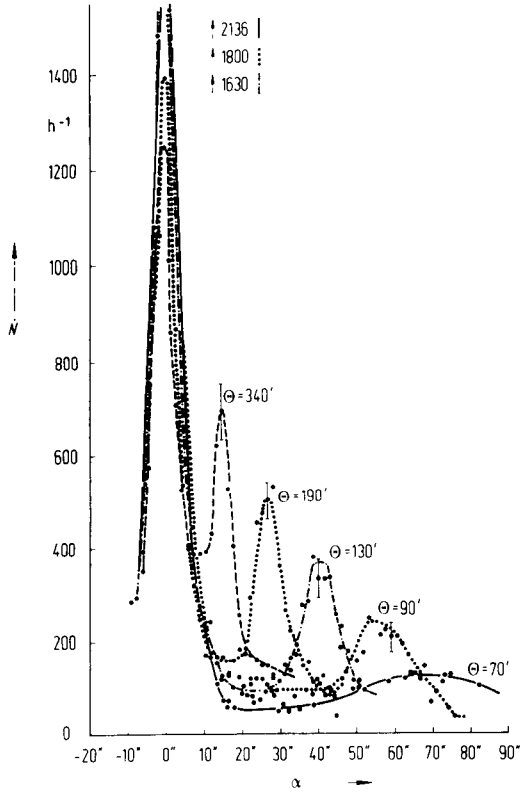


Fig.5. Count rate as a function of the angle α of the analyzer for different Θ, with 6 A/cm applied field, λ ◘ 0.23 nm.

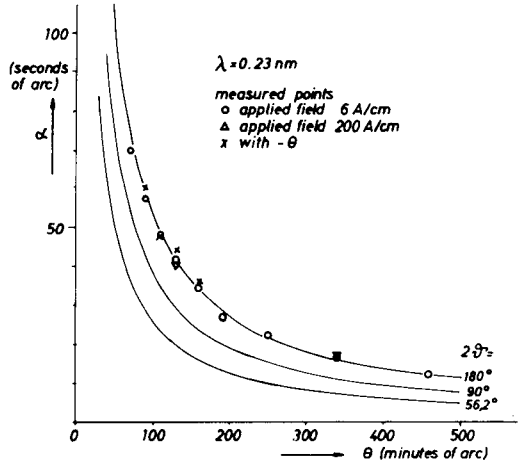


Fig. 6. Angle of deflection α of the auxiliary maximum in fig. 5 as a function of grazing angle Θ for our measurements, together with curves calculated using eq.(1).

The observed behavior corresponds fully to the simple solution of the Schrödinger equation of the problem, with a continuum description of the interaction of the neutron with the induction field B. The geometry of the problem is shown in fig.7. The Schrödinger equation for a neutron in this magnetic structure is

$$-\Delta \begin{pmatrix}\psi_1\\ \psi_2\end{pmatrix} + k^2_{B_x}\begin{pmatrix}\psi_2\\ \psi_1\end{pmatrix} + ik^2_{B_y}\begin{pmatrix}-\psi_2\\ \psi_1\end{pmatrix} \pm k^2_{B_z}\begin{pmatrix}\psi_1\\ -\psi_2\end{pmatrix} = k^2\begin{pmatrix}\psi_1\\ \psi_2\end{pmatrix} \qquad (2)$$

where $k^2_{B_h} = 2 m\mu B_h/\hbar^2$, $h \square x, y, z$; $k^2 \square k_x^2 + k_y^2 + k_z^2$; $k_y \square k \sin\Theta$

This equation has the solution

$$\begin{pmatrix}\psi_1\\ \psi_2\end{pmatrix} = e^{i(k_x x + k_z z)} \sum_{\nu=1}^{4} \begin{pmatrix}A_\nu\\ B_\nu\end{pmatrix} e^{ik_\nu y} \qquad (3)$$

with a different set of $\begin{pmatrix}A_\nu\\ B_\nu\end{pmatrix}$, $\nu = 1, 2, 3, 4$ for $y < 0$ and $y > 0$.

k_ν are the solution of the characteristic equation

$$k_\nu^4 + 2k_y^2 k_\nu^2 + k_y^4 - k_{B_x}^4 - k_{B_y}^4 - k_{B_z}^4 = 0 \qquad (4)$$

giving $k_\nu = \pm\sqrt{k_y^2 \pm k_B^2}$, $\nu = 1, 2, 3, 4$, (5)

i.e. only the wave vector component k_y is changed and then B is fully effective (B $\square$ 1.97 Tesla), not just the component B_z. Expressing this result by a law of refraction immediately gives eq.(1) with $\sin\vartheta = 1$.

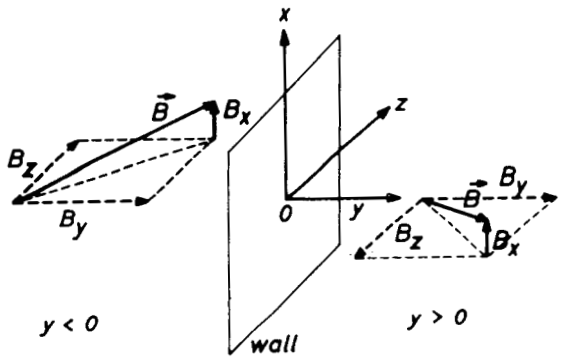


Fig. 7. Geometry of the components of the magnetic induction B at both sides of the wall for eq.(2).

This solution also allows the reflected and refracted intensities to be determined. The measured deviations from these intensities at smaller angles of incidence are appreciable. The deviation is caused by the helical structure of the walls and allows the wall thickness[6, 4] to be estimated.

The authors wish to thank Ing. (grad.) G. Borghold for his help. The experiments were performed at the FMRB, Braunschweig.

REFERENCES

1. O. Schärpf, Physica 80B, 289 (1975)
2. S. De Benedetti, Nuclear Interactions, p.179, Wiley, NY, 1964
3. O. Halpern and M.H. Johnson, Phys. Rev. 55, 898 (1939)
4. O. Schärpf, this issue
5. S.S. Shil'stein, V.A. Semenkov, M. Kalanov, JETP 63, 2214 (1972)
6. O. Schärpf, K. Brandt, JMM-Intermag Conference June 1976
7. U. Keyser, O. Schärpf, Ch. Schwink ,JMMM-Intermag Conf. June 1976

MAGNETIC DOMAIN STRUCTURES STUDIED BY NEUTRON DEPOLARIZATION

W. H. Kraan, M. Th. Rekveldt and J. J. Van Loef
Interuniversitair Reactor Instituut
Delft, The Netherlands

ABSTRACT

According to the neutron depolarization method developed at our institute a polarized monochromatic neutron beam is transmitted in a direction perpendicularly through a flat ferromagnetic sample (x direction). The polarization direction of the incoming beam may be adjusted by a polarization rotator in front of the sample in either one of the x, y or z directions. After transmission through the sample the polarization of the beam can be analyzed in the x, y or z direction. In this manner a (3x3) depolarization matrix can be determined from which the diagonal elements give the depolarization factors D_{xx}, D_{yy} and D_{zz}. These depolarization factors have been obtained at a neutron wave length of 1.6Å and at several values of λ in the range between 4.0 and 6.0Å. These factors are directly related to the product $B_s^2\delta$, where B_s is the saturation magnetization within the domains of the sample and δ is the mean size of the magnetic domains. Hence by measuring this quantity in various directions knowledge is obtained about the shape and character of the domains[1].

The method has previously been applied to study iron, nickel and $CrBr_3$ near T_c, to nickel at room temperature under various degrees of stress and to a number of ferrites. At this conference the first results will be reported of a study of magnetic domains in a 20 micron thick nickel layer electroplated onto a copper sheet as a backing. More details will be published elsewhere[2]. The electroplating of nickel has been carried out using conventional techniques and the thickness of the layer was measured with a microscope. Before the depolarization experiments were performed, a magnetic field of 2400A/cm was applied on the sample in a direction perpendicular to the plane of the layer. The depolarization experiments were carried out without the presence of an external field unless stated otherwise. At the sample position of the neutron polarimeter no magnetic fields are present.

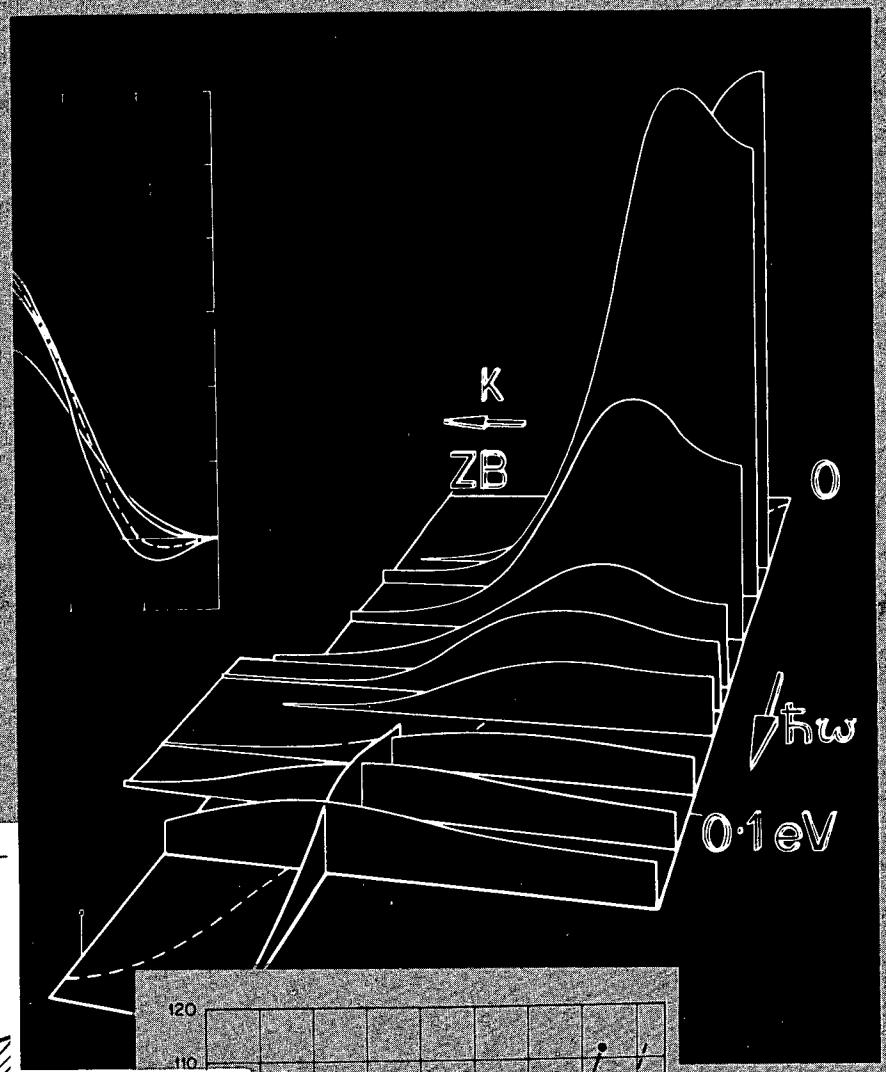
According to the results no depolarization has been observed when the polarization direction of the neutrons impinging on the sample is perpendicular to the layer. The depolarization factors in the other two directions D_{yy} and D_{zz} on the other hand indicate nearly full depolarization. This suggests that the nickel layer consists of needle shaped domains with magnetization directions perpendicular to the plane of the layer, and separated by 180° walls. The depolarization factors D_{yy} and D_{zz} nearly follow a cosine dependence on the neutron wave length, which can be obtained by assuming that

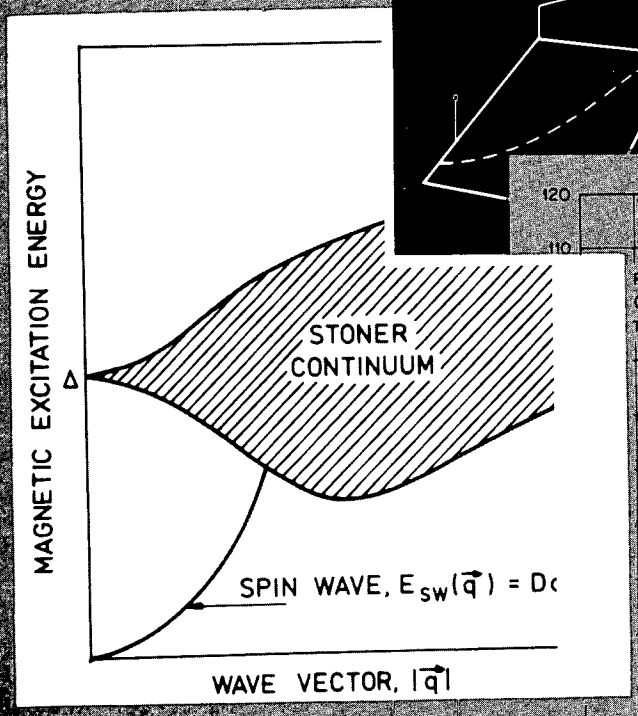
the effective size of the 180° domains is 15 micron. Apparently closure domains are responsible for the difference with the actual thickness of the nickel layer. Subsequently with 4Å neutrons the depolarization factors have been measured as a function of the canting angle of the sample around the y-axis. From the change of D_{yy} and D_{zz} with the canting angle it is possible to determine the mean domain size along the plane of the layer, for which 1 to 2 micron is found. In addition the domain structure has been studied as a function of an external magnetic field applied parallel to the layer. From the results it appears that the magnetization of the layer mainly arises from domain wall motion in a way such that the surface closure domains grow at the expense of the bulk domains as the magnetic field increases. At a field strength of 600A/cm the bulk domains have disappeared. As a general conclusion, the neutron depolarization method applying a full polarization analysis turns out to be a powerful method in obtaining detailed information on magnetic domain structures in ferromagnetic bulk material.

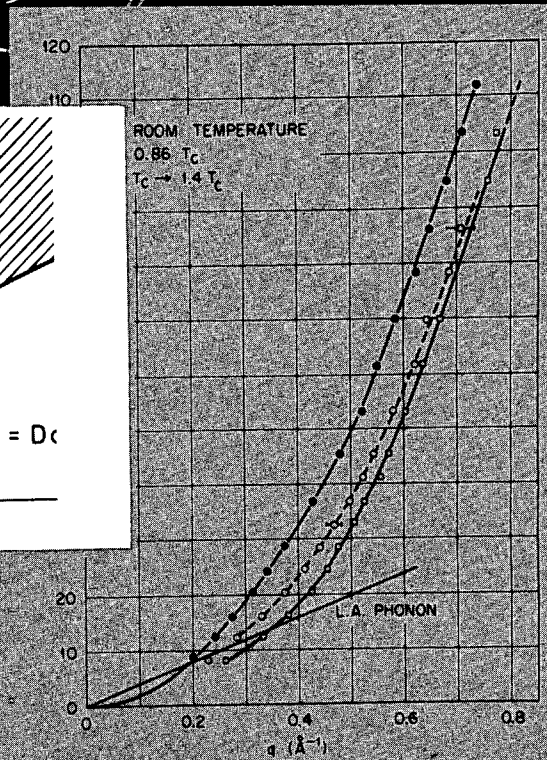
---

1. M. Th. Rekveldt, Thesis, University of Technology, Delft (1972) and subsequent papers.
2. W. H. Kraan and M. Th. Rekveldt, ICM 1976. IUPAP-International Conference on Magnetism, Amsterdam (to be published in Physica).

MAGNETIC EXCITATIONS







MAGNETIC EXCITATIONS IN ITINERANT ELECTRON SYSTEMS*

J.F. Cooke+
Solid State Division, Oak Ridge National Laboratory
Oak Ridge, Tennessee 37830

ABSTRACT

Inelastic neutron scattering experiments have, during the past few years, yielded a substantial amount of fundamental information about magnetic excitations in the 3-d transition metals nickel and iron. Of particular importance is the experimental observation of the disappearance of spin-waves into a "Stoner continuum" and the observation that excitations exist well above the Curie temperature. The low temperature spin-wave behavior has been found to be in excellent agreement with quantitative predictions based on the itinerant model of magnetism. Higher temperature results appear to be inconsistent with the traditional concept of a temperature dependent spin-splitting of the electronic energy bands.

The applicability of the itinerant electron model of magnetism to the 3-d transition metal series has been a point of controversy for a number of decades.[1] Experimental information about the static properties of these systems seems to indicate that the electrons which are responsible for the magnetic properties are itinerant in character, occupying relatively narrow energy bands. This evidence is, however, not conclusive.[1,2,3]

---

*Work sponsored in part by the U.S. Energy Research and Development Administration under contract with Union Carbide Corporation.

+Presently a visiting scientist at Physics Dept., Research Establishment Risø, DK-4000 Roskilde, Denmark.

In order to obtain a more detailed test of the itinerant model we must consider the dynamics of these systems. The natural starting point for such an investigation is the frequency and wave-vector dependent susceptibility, $\chi(\vec{q},\omega)$. This quantity is defined as the linear response of a system to the application of a small magnetic field and contains all of the relevant information about the dynamics of a magnet. Well defined peaks in the imaginary part of the susceptibility, $\mathrm{Im}\chi(\vec{q},\omega)$, are associated with the magnetic excitations of the system. These excitations are usually called spin-waves or magnons. Since the inelastic neutron scattering cross section is proportional to $\mathrm{Im}\chi(\vec{q},\omega)^4$ it is clear that neutron experiments can provide a considerable amount of detailed information about magnetic excitations. This type of experimental information coupled with theoretical calculations of the susceptibility can provide a rather sensitive test of the theory on a fundamental level.

This kind of test is not easy to carry out for the 3-d metals. As will be shown later on a theoretical calculation of $\chi(\vec{q},\omega)$, and thus the spin-wave energy, ultimately requires a "realistic" calculation of the electronic energy bands and wave functions as well as sums of functions of these quantities over the first Brillouin zone. Thus, from a theoretical point of view one is faced not only with determining an explicit expression for $\chi(\vec{q},\omega)$ for a many electron system but also with a large scale computer calculation in order to obtain numerical results. There are also experimental difficulties, which arise because the spin wave energies in the 3-d metals extend to energies well above 100 meV.

As the result of the relatively recent availability of high-flux reactors and large core high speed computers a considerable amount of progress has been made during the past few years in investigating the validity of the itinerant

model for describing the magnetic properties of the 3-d transition metal series. The purpose of this paper is to give a general review of these recent developments. This review will be concerned with the transition metal ferromagnets nickel and iron, which have been the most extensively studied to date. It will be shown that the itinerant model provides an excellent quantitative, as well as qualitative, model for describing the observed low temperature spin-wave behavior and that the traditional higher temperature extrapolation of the low temperature theory is inconsistent with the neutron measurements.

The paper is divided into five main sections. The first section presents an elementary development of concepts which are important in the itinerant electron model and it is shown how these relatively simple concepts lead to the prediction of the disappearance of spin-waves. In section two a review of recent spin-wave measurements in nickel and iron will be given. A brief review of recent theoretical calculations of $\chi(\vec{q},\omega)$, and the theory on which they are based, together with a comparison with experiment is given in section three. A general discussion of the finite temperature results is given in section four and section five contains a summary of results and conclusions.

BASIC CONCEPTS

The itinerant model of magnetism is based on the concept that the electrons occupy energy bands and are therefore free to move throughout the crystal. In order to describe systems with some sort of long range magnetic order (ferromagnetic, anti-ferromagnetic, etc.), it is necessary to include in the energy band description correlation effects between electrons with opposite spin. One way of seeing this is to consider the

magnetic moment distribution. In an itinerant magnet we expect this to be a continuous periodic function of distance which peaks up around lattice positions. In order to obtain a moment distribution which does not fluctuate randomly with time the motion of opposite spin electrons must clearly be correlated. As a result of these correlation effects the electronic energies and wave functions must be spin dependent.

For example, if we consider a single band ferromagnet the simplest approximation of the itinerant theory yields the following expression for the electronic energy[5]

$$E(\vec{k},\sigma) = \varepsilon(\vec{k}) - \tfrac{1}{2}(n_{\sigma}-n_{-\sigma})I \qquad (1)$$

where n_{σ} is the number of electrons with spin σ, and $\vec{k}$ is the wave-vector. The function $\varepsilon(\vec{k})$ is the energy the electrons would have if the system was non-magnetic ($n_{\sigma} = n_{-\sigma}$). The parameter I is a measure of the interaction energy between electrons of opposite spin. The energy difference between electrons of opposite spin at the same $\vec{k}$ is

$$\Delta = E(\vec{k}\uparrow) - E(\vec{k}\downarrow) = (n_{\downarrow}-n_{\uparrow})I \qquad (2)$$

and it is independent of $\vec{k}$. Therefore, in this approximation the energy bands of opposite spin have the same $\vec{k}$ dependence and are rigidly separated from one another by the spin-splitting constant Δ.

We are now in a position to describe the types of magnetic excitations which are possible in an itinerant magnet. The simplest type is a single-particle electronic transition from an occupied state of a given spin σ and wave-vector $\vec{k}$ to an unoccupied state of opposite spin ($-\sigma$) and wave-vector

$\vec{k}+\vec{q}$. This type of excitation creates an electron-hole pair and is called a Stoner excitation.

It is convenient to group Stoner excitations by keeping $\vec{q}$ fixed and allowing $\vec{k}$ to range over all possible values. We then obtain an excitation energy spectrum of the form

$$E_{ST}(\vec{q}) = \varepsilon(\vec{k}+\vec{q}) - \varepsilon(\vec{k}) + \Delta \ , \ \vec{k} \text{ arbitrary} \qquad (3)$$

The important thing to notice about Stoner excitations is that they do not exist for all energies. This is shown schematically in fig. 1.

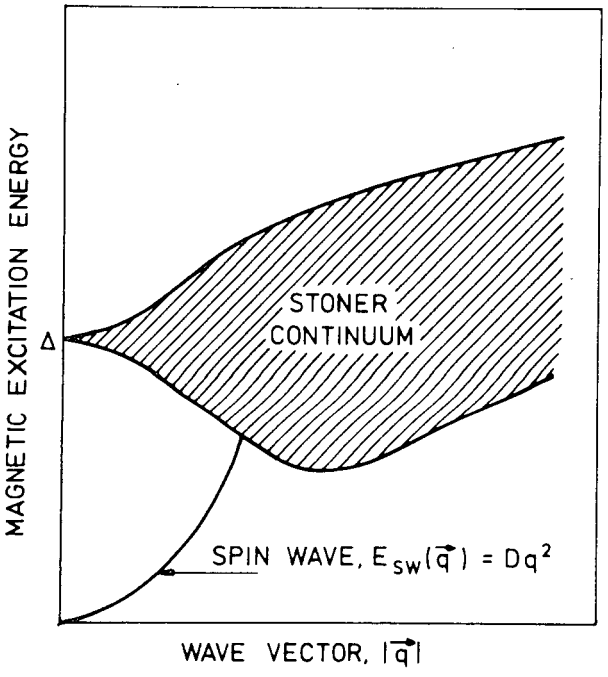


Fig. 1. Magnetic excitation spectra for a single band itinerant electron ferromagnet.

At $\vec{q} = 0$, $E_{ST}(\vec{q}) = \Delta$. For fixed $\vec{q} \neq 0$ we see from Eq. (3) that as $\vec{k}$ is varied E_{ST} ranges from some minimum to some maximum value which depends on the details of the band structure.

The spin-wave in this model consists of a bound state between an electron of a given spin and a hole of opposite spin. It is straightforward to show that for low $\vec{q}$ the spin-wave energy is given by

$$E_{sw}(\vec{q}) \simeq D\, q^2 \qquad (4)$$

where D depends on derivations of $\varepsilon(\vec{k})$. This dispersion curve is also shown schematically in fig. 1. If the band structure is such that the spin-wave energy remains entirely below the Stoner continuum, then the spin-wave will be a well defined magnetic excitation out to the Brillouin zone boundary. On the other hand if the Stoner continuum lies at a low enough energy then there is the possibility that the spin-wave dispersion curve will run into the continuum. When this happens the spin-wave, which is a bound electron-hole pair, will be degenerate in energy with a Stoner excitation, which is a single-particle electron-hole excitation, and we know from general arguments that the spin-wave will decay.

This process would show up as a rather dramatic effect in a neutron scattering experiment. In the region outside the Stoner continuum the neutron cross section can be written in terms of a simple delta function singularity[6]

$$\left(\frac{d^2\sigma}{d\Omega d\omega}\right)_{sw} \sim \delta(\omega - E_{sw}(\vec{q})) \qquad (5)$$

where $d\Omega$ is the differential solid angle into which the scattering takes place. The "width" of this peak is proportional to the inverse lifetime, τ^{-1}, of the spin-wave which, of course, is zero outside the Stoner continuum. Inside the continuum τ^{-1} is not zero and the delta function singularity will broaden with a corresponding drop in the peak height. Thus as the spin-wave enters the Stoner continuum the spin-wave peak could actually disappear. This effect is in sharp contrast to what one would expect from purely localized electron systems where spin-waves are well defined for all $\vec{q}$.

EXPERIMENTAL RESULTS

During the past few years a number of inelastic neutron scattering experiments have been carried out on the 3-d transition ferromagnets nickel and iron. Because of the relative high spin-wave energies which occur in these materials large single crystals as well as a high-flux reactor are required in order to insure reasonable statistics. The nickel experiments were performed on a large single crystal of ^{60}Ni. Unfortunately, large single crystals of pure iron cannot be grown because of a bcc to fcc phase transition which occurs at 1180° K. By alloying Fe with a small amount (> 4% at. %) of Si the bcc phase can be stabilized and large crystals can be grown. Neutron experiments have thus far been carried out on large single crystals of a number of alloys, as well as on a small single crystal of "pure" iron.

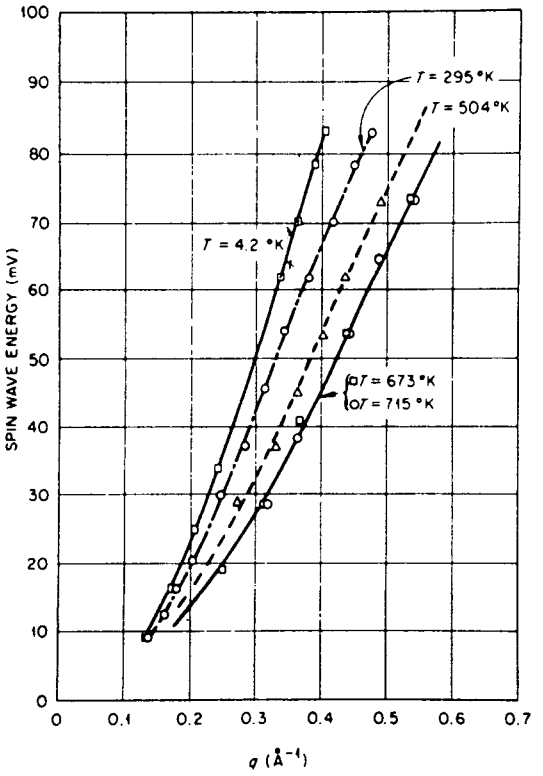


Fig. 2. Spin-wave dispersion in nickel as a function of temperature.

The spin-wave dispersion curves obtained for Ni by Mook et al.[7] and Fe(12 at. % Si) by Lynn[8] are shown in figures 2 and 3 respectively for various temperatures. The curves at each temperature for both Ni and Fe were found to be isotropic and could be fit reasonably well, but not exactly, by a quadratic dispersion curve of the form given in (4). For temperatures outside the critical region the

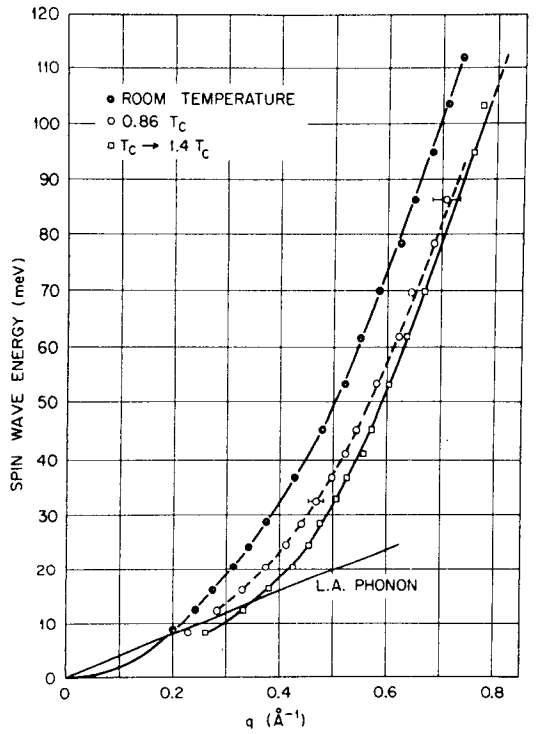


Fig. 3. Fe (12 at. % Si) spin-wave spectra as a function of temperature.

dispersion curves are well defined down to zero energy, and because of the Goldstone theorem there is no energy gap. As $T \to T_c$ the dispersion curves at low $\vec{q}$ become over-critically damped as one expects from hydrodynamic theory.[9,10]

The dispersion curves renormalize with temperature as one would expect from spin-wave-spin-wave interactions. One interesting aspect of these dispersion curves is that well defined spin-waves exist well above the Curie temperature in both Ni and Fe. In addition, it was found that $E_{sw}(\vec{q})$ did not change with temperature for $T > T_c$. The widths of the spin-wave peaks were smaller than the instrumental resolution for $T < T_c$. As $T \to T_c$ intrinsic widths could be detected and were found to increase rather sharply for $T \simeq T_c$. For $T > T_c$ the widths remained constant with T in Fe while a small increase with T was detected in Ni. These widths are, however, still small compared to $E_{sw}(\vec{q})$, and indeed well defined for $T > T_c$. The experimental results extend only up to temperatures where the (rather expensive) samples begin to evaporate and thus it is not clear at present how high in temperature well defined spin-waves actually exist in Ni and Fe.

The reason the curves in figures 2 and 3 do not extend out to the Brillouin zone boundary is shown in figures 4[7,11]

and 5[8]. The curves in these figures represent the integrated area under the spin-wave peaks plotted as a function of $\vec{q}$ for various temperatures. These results clearly demonstrate that spin-waves exist only over a limited range of $\vec{q}$. The rather sharp drop in the intensity shown in these figures signals the disappearance of spin-waves as predicted by the itinerant model.

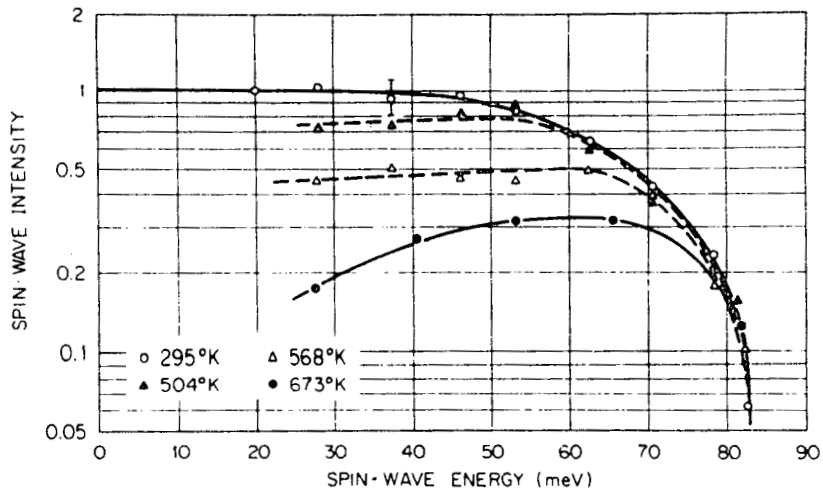


Fig. 4. Spin-wave intensity versus energy for the (111) direction in nickel at different temperatures.

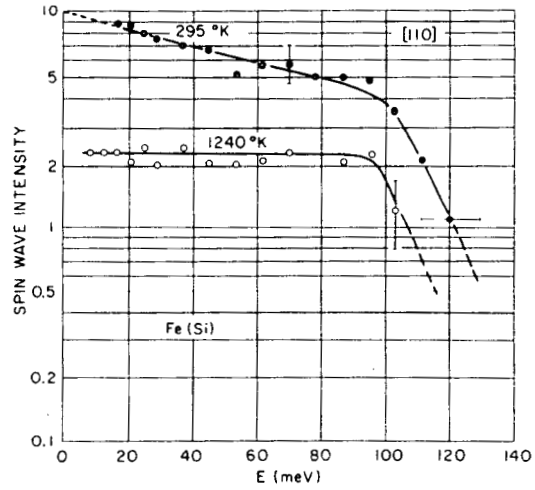


Fig. 5. Spin-wave intensity versus energy at room temperature and 1.28 T_c for the (110) direction of Fe(12 at. % Si).

This effect was found to be more or less isotropic in iron[8] but anisotropic in nickel.[11] Figures 4 and 5 illustrate probably the most surprising result obtained from the neutron measurements, which is that the energy at which the spin-waves disappear, the so-called cut-off energy, is essentially independent of temperature. As we shall see later on this result is inconsistent with the

assumption that the electronic spin-splitting energy is temperature dependent. It does appear, however, that the low temperature experimental results are in good overall qualitative agreement with predictions of the itinerant model. The important question is, however, how good a quantitative model is it. In order to answer this question we must have a closer look at the detailed formalism.

GENERAL THEORY

As mentioned earlier the frequency and wave-vector dependent susceptibility is a tensor. For cubic systems, like Ni and Fe, this tensor is diagonal and the neutron scattering cross section can be written in terms of a longitudinal and a transverse part. Since we are interested in calculating the spin-wave scattering cross section, $(d^2\sigma/d\Omega d\omega)_{sw}$, then only the transverse part, $\chi_T(\vec{q},\omega)$ need be considered. We have explicitly[4]

$$\left(\frac{d^2\sigma}{d\Omega d\omega}\right)_{sw} = \text{const.} \times \text{Im}\ \chi_T(\vec{q},\omega) \tag{6}$$

where

$$\chi_T(\vec{q},\omega) = \frac{1}{2\pi}\int_{-\infty}^{\infty} e^{-i\omega t} < s^-_q(t)\ s^+_{-q}(0) > dt$$

$$S^{\pm} = S^x \pm iS^y \tag{7}$$

The operators appearing in Eqs. (6) and (7) are the space Fourier transforms of the spin operators for the (full) electronic system. From Eq. (7) it follows that a calculation of $\chi_T(\vec{q},\omega)$ involves the calculation of the time Fourier transform of the correlation function $<S^-_q(t)S^+_{-q}(0)>$ for a many electron system.

It is a simple matter to calculate $\chi_T(\vec{q},\omega)$ if the electrons do not interact, in which case one generates the so-called non-interacting susceptibility, $\chi_0(\vec{q},\omega)$[6]. In an important paper published in 1963 Izuyama, Kim, and Kubo[6] derived an approximate expression for χ_T for a ferromagnet based on a model Hamiltonian previously proposed by Hubbard.[2] This Hamiltonian is in turn based on the assumption that opposite spin electrons interact only if they sit on the same lattice site. Within the random phase approximation, Izuyama et.al. found that

$$\chi(\vec{q},\omega) = \frac{\chi_o(\vec{q},\omega)}{1-I\chi_o(\vec{q},\omega)} \tag{8}$$

where I is the interaction energy discussed previously (see Eq. (1)). Thus, the effect of including electron-electron interactions is to enhance the non-interaction susceptibility by the factor $1/(1-I\chi_o(\vec{q},\omega))$. Then, from (8) and (6)

$$\left(\frac{d^2\sigma}{d\Omega d\omega}\right)_{sw} \sim \frac{\chi_o''(\vec{q},\omega)}{\left(1-I\chi_o'(\vec{q},\omega)\right)^2+\left(I\chi_o''(\vec{q},\omega)\right)^2} \tag{9}$$

where

$$\chi_o(\vec{q},\omega) = \lim_{\eta\to 0} \frac{1}{N}\sum_{\vec{k}} \frac{f_{\vec{k}+\vec{q}}-f_{\vec{k}}}{\hbar\omega-\varepsilon(\vec{k}+\vec{q})+\varepsilon(\vec{k})-\Delta-i\eta} \tag{10}$$
$$= \chi_o'(\vec{q},\omega)+i\chi_o''(\vec{q},\omega)$$

The quantity f is the Fermi occupation number and N represents the number of lattice sites. From Eqs. (10) and (3) we see that $\chi_o''(\vec{q},\omega)$ is just the density of states for Stoner excitations. Thus for $(\vec{q},\omega)$ outside the Stoner continuum $\chi_o''(\vec{q},\omega) = 0$, and the right hand side of Eq. (9) reduces to the delta function form given in Eq. (5), where the spin-wave energy

is defined by

$$I\chi_o'(\vec{q},E_{sw}(\vec{q})) = 1 \qquad (11)$$

Inside the Stoner continuum the spin-wave peak will broaden with a width which depends on $\chi_o''(\vec{q},\omega)$. These results provide a mathematical basis for the purely qualitative arguments regarding the disappearance of spin-waves given earlier in the paper.

A numerical investigation of the result given in Eq. (9) using a single parabolic band has been carried out by Thompson[11,12] for nickel. By choosing parameters appropriately it was shown that the dispersion curve as well as the disappearance of spin-waves along the (100) direction could be described reasonably well. The calculation also predicted that the wave-vector at which the spin-waves disappeared was independent of direction, which is inconsistent with experiment.[11] This undoubtedly is due to the oversimplification of the complicated Ni band structure. In order to include "realistic" energy bands in the calculation the single band expression given in (9) must be generalized to the multi-band case.

In a paper published in 1970 Lowde and Windsor[13] proposed and numerically investigated such a generalization. Their expression for χ_T was identical to that given in (8) but with $\chi_o(\vec{q},\omega)$ calculated for a multi-band system. By using "realistic" energy bands they found that a good fit to the spin-wave dispersion energy could be obtained only if the parameter I was replaced by a $\vec{q}$ dependent function, $I(\vec{q})$. However, with $I(\vec{q})$ chosen in this manner it was found that the spin-waves disappeared at much too low an energy.

The enhanced susceptibility expression given in Eq. (8)

is not, however, the most general form which can be obtained from a random phase approximation (RPA) of the many electron problem. In a recent paper the author[14] derived general equations for the relevant Green's function and energy bands which are required to calculate $\chi_T(\vec{q},\omega)$ within a generalized RPA. This theory was restricted to the case of a ferromagnet and, because of the use of the RPA, to low temperatures.

The equations which were obtained involved matrix elements of a screened coulomb potential calculated with respect to the electronic wave functions, and thus these matrix elements are functions of electronic energy band indices and wave-vectors. If this band and wave-vector dependence is ignored the equations can easily be solved to yield the enhanced susceptibility expression given in Eq. (8), where I is screened coulomb matrix element.

It was argued that this constant matrix element approximation is not appropriate for the 3-d transition metal series and a method was proposed for including, in a self-consistent but approximate way, the band and wave-vector dependence of these matrix elements. This approximation leads to two important results. First, in contrast to the constant matrix element approximation, it generates an expression for the spin dependent part of electronic energy, which is both wave-vector and band dependent. The other result is that $\chi_T(\vec{q},\omega)$ is no longer given by the enhanced susceptibility expression given in Eq. (8), but has the general form

$$\chi_T(\vec{q},\omega) \sim \sum_{\mu\nu} \left(I-\Gamma(\vec{q},\omega)\right)^{-1}_{\mu\nu} \qquad (12)$$

The complex matrix Γ is given in terms of Brillouin zone sums of a function of the electronic energies and wave functions, and I is the unit matrix. The sum in Eq. (12) is over a complete set of symmetry indices. As mentioned earlier this re-

sult reduces to the enhanced susceptibility form if the band and wave-vector dependence of the (screened) coulomb matrix elements is ignored.

Although the general form for χ_T given in Eq. (12) is different from the enhanced susceptibility expression it can be shown that it leads to the same qualitative predictions regarding the disappearance of spin-waves. The main quantitative differences are that the spin-wave energy is now determined by a more complicated condition than that given in Eq. (11), and that the width of the spin-wave peak is not related to the full density of Stoner excitations, but to a certain symmetry projected density of Stoner excitations. In addition, as the result of the inclusion of hybridization and multi-band effects this symmetry projected density of Stoner excitations is found to be non-zero for (all) energies up to a maximum energy which is related to the full band width. Thus the relatively simple picture given in figure 1 is not exactly correct. It can still be a useful concept, however, provided we reinterpret the region label "Stoner continuum" to mean the region when the appropriate symmetry projected density of Stoner excitation is large enough to damp out the spin-waves.

An extensive series of calculations of $\chi_T(\vec{q},\omega)$ based on the general expression given in (12) have been carried out by Cooke, Davis, and Lynn. These calculations were based on "realistic" energy bands for Ni and Fe. That is, energy bands which give the correct Fermi surface, magnetic moment, correct symmetry character of the moment, etc. An important feature of this theory is that χ_T depends only on the electronic energy bands and wave functions and once these have been obtained χ_T is uniquely determined. The explicit information needed to carry out the Brillouin zone sums was generated by the Slater-Koster[17] and Hodges, Ehrenreich, and Lang[18] inter-

polation schemes for Fe and Ni respectively. The zone sums were carried out using both the Gilat-Raubenheimer[19] and the tetrahedron linear integration schemes.[20]

Representative numerical results for the transverse neutron scattering intensity are given in fig. 6 for nickel. These results are for various values of $\vec{q}$ along (100) and were obtained recently using the tetrahedron linear integration procedure.[21] They are essentially identical to those published previously by Cooke and Davis,[15] but are plotted here on a relative intensity scale to show the variation of the shape of the spin-wave peaks with $\vec{q}$. These results show two important features. First there exist well defined spin-wave peaks out to the zone boundary along (100). Second, there are two peaks for $.25 \lesssim |\vec{q}| \lesssim .34$. A plot of these peak positions is shown in fig. 7. This clearly shows an "optical" magnetic excitation interacting with the acoustic spin-wave branch which extends out to the zone boundary. These features were not observed in earlier experiments, but have been found in recent neutron experiments.[22] The experimentally observed "optical" branch is in excellent agreement with the theoretical predictions. The spin-wave curve was observed to bend over as shown in fig. 7 and then to remain relatively flat out to the zone boundary. This, however, does not represent a serious dis-

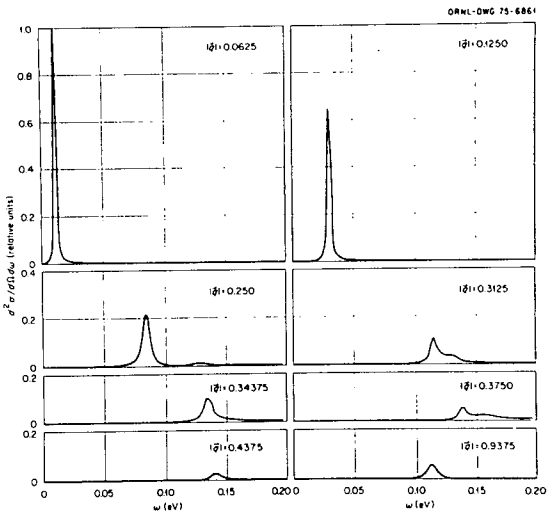


Fig. 6. Neutron scattering intensity ($\sim \mathrm{Im}\chi_T(\vec{q},\omega)$) as a function of energy for various values of $|\vec{q}|$ (in units of $2\pi/a$) along (100) for nickel.

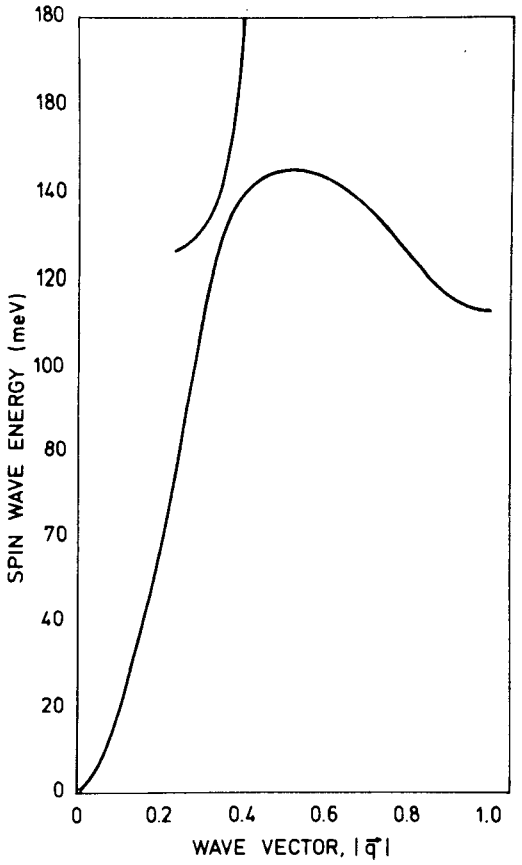


Fig. 7. Theoretical results for the low temperature spin-wave dispersion as a function of $|\vec{q}|$ (in units of $2\pi/a$) along (100) for nickel.

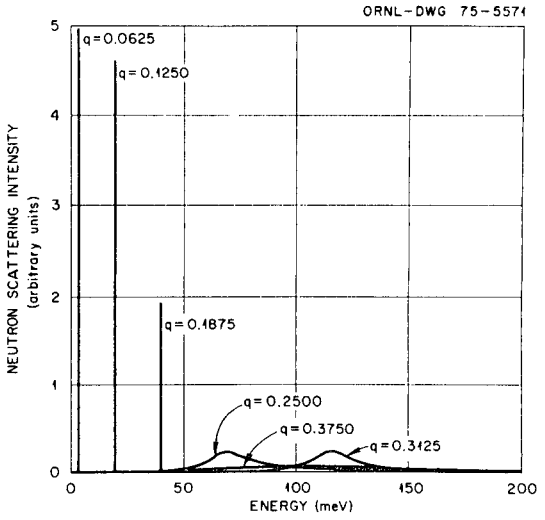


Fig. 8. Neutron scattering intensity ($\sim \mathrm{Im}\chi_T(\vec{q},\omega)$ versus energy as a function of $|\vec{q}|$ (in units of $2\pi/a$) for iron.

crepany with theory because, as pointed out by Cooke and Davis, a relatively small change in the ferromagnetic band structure was found to generate a dispersion curve with this feature.[15] The theoretical calculations predicted that the spin-waves disappear in the other symmetry directions as discussed previously[15] at approximately the correct energies.

Numerical result for the scattering intensity obtained for Fe are shown in fig. 8.[16,21] These results show the disappearance of spin-waves in the (100) direction. They were found to be essentially isotropic in $\vec{q}$ and indicate that the spin-waves should disappear at approximately the same energy as that found from experiment. No "optical" branch was found in these calculations. The dispersion curve obtained from the

peak position is also in excellent agreement with experiment.[16]

FINITE TEMPERATURE THEORY

The theoretical results presented in the previous section are restricted to low temperature because of the use of the random phase approximation. In particular, the RPA theory neglects spin-wave-spin-wave interactions which are responsible for the temperature renormalization of the spin-wave energy shown in figures 2 and 3. In order to investigate this and other finite temperature behavior it is necessary to go beyond RPA.

This, of course, is not an easy task and the traditional approach of extending the theory to higher temperature is simply to extrapolate the low temperature results. Several suggestions have been made which, in terms of the relatively simple theory outlined in the first section, amount to replacing the spin-splitting parameter, Δ, defined in Eq. (2) by a temperature dependent function which goes to zero as $T \rightarrow T_c$.[13] Thus we have the self-consistent picture of the energy bands for opposite spin electrons collapsing into a single set of bands at T_c thereby giving rise to the paramagnetic state. It appears from the experimental results given in figures 6 and 8 that this extrapolation is not correct. The reason is that if Δ becomes temperature dependent then we would expect (see figure 1) that the Stoner continuum would shift with temperature. This in turn implies that the spin-wave cut-off energy would also be temperature dependent, in contradiction with experiment.

There have been several recent attempts at extending the theory beyond RPA.[23,24,25] The approaches which have been suggested thus far are based either directly on many body

perturbative techniques[23,24] or on quasi-spin models coupled with the coherent potential approximation.[25] The quasi-spin formalism differs from the direct perturbation theory in that it involves a reformulation of the problem in terms of "localized" interacting spins. These theories have been shown to yield results which are in qualitative agreement with some finite temperature measurements but they do not, as yet, provide a complete answer to the questions raised by the finite temperature neutron experiments. The development of a realistic formalism for treating the finite temperature properties of itinerant systems must therefore await future study.

CONCLUSIONS

It is evident from the material presented in this paper that a considerable amount of progress has been made in the study of magnetic excitations in itinerant electron systems. Inelastic neutron scattering experiments have now mapped out the complete spin-wave dispersion curves along the principle symmetry directions at various temperatures in ferromagnetic Ni and Fe. These experiments have not only determined the detailed shape and temperature renormalization of these curves, but have established that these excitations exist only over a limited range of wave-vectors and at temperature well above the curve temperature.

The low temperature experimental results have been shown to be in excellent quantitative agreement with theoretical calculations based on the itinerant electron model of magnetism provided "realistic" energy bands are used and the band and wave-vector dependence of the electron-electron interaction matrix element is taken into account. It should be stressed here that the ferromagnetic energy bands used in these calculations were generated from paramagnetic bands

published in the literature using the self-consistent procedure dictated by the theory. No attempt has been made to determine a set of bands which would give a good fit to the data.

The experimental observation that the spin-wave cut-off energy is independent of temperature was shown to be inconsistent with the assumption that the spin-splitting between energy bands of opposite spin is temperature dependent. The development of a good quantitative model for describing this effect as well as the temperature dependent behavior of the dispersion curves still remains a formidable challenge.

ACKNOWLEDGEMENT

The author wishes to thank DAEC, Risø for its hospitality and Dr. P.-A. Lindgård for reading and commenting on the manuscript.

REFERENCES

1. C. Herring, Magnetism, Vol. 4, edited by G. T. Rado and H. Suhl (London, Academic Press) (1966).
2. J. Hubbard, Proc. Roy. Soc. A 276, 238 (1963).
3. S. Doniach, J. Appl. Phys. 39, 751 (1968).
4. W. Marshall and S. W. Losesey, Thermal Neutron Scattering (Oxford, U.P., London) (1971).
5. E. D. Thompson, Adv. Phys. 14, 213 (1965).
6. T. Izuyama, D. Kim, and R. Kubo, J. Phys. Soc. Japan 18, 1025 (1963).
7. H. A. Mook, J. W. Lynn, and R. M. Nicklow, Phys. Rev. Letters 30, 556 (1973).
8. J. W. Lynn, Phys. Rev. B11, 2624 (1975). Also see H. A. Mook and R. M. Nicklow, Phys. Rev. B1, 336 (1973).

9. M. F. Collins, V. J. Minkiewicz, R. Nathans, L. Passell, and G. Shirane, Phys. Rev. 179, 417 (1969).
10. S. Boronkay and M. F. Collins, Int. J. Magn. 4 205 (1973).
11. The spin-wave disappearance was first observed in Ni by H. A. Mook, R. M. Nicklow, E. D. Thompson, and M. K. Wilkinson, J. Appl. Phys. 40, 1450 (1969).
12. E. D. Thompson, Phys. Rev. Letters, 19, 635 (1967).
13. R. D. Lowde and C. G. Windsor, Adv. in Phys. 19 813 (1970).
14. J. F. Cooke, Phys. Rev. B7, 1108 (1973).
15. J. F. Cooke and H. L. Davis, AIP Conf. Proc. 10, 1218 (1973).
16. J. F. Cooke, J. W. Lynn, and H. L. Davis, AIP Conf. Proc. 24, 329 (1975).
17. J. C. Slater and G. F. Koster, Phys. Rev. 94, 1498 (1954).
18. L. Hodges, H. Ehrenreich, and N. D. Lang, Phys. Rev. 152, 505 (1966).
19. G. Gilat and L. J. Raubenheimer, Phys. Rev. 144, 390 (1966).
20. G. Lehmann and M. Taut, Phys. Stat. Sol. 54, 469 (1972).
21. J. F. Cooke and H. L. Davis, to be published.
22. H. A. Mook, private communication.
23. J. B. Sokoloff, Phys. Rev. Letters 31, 1417 (1973).
24. D. M. Edwards, Phys. Lett. 33A, 183 (1970).
25. S. H. Liu, to be published in Phys. Review.

MAGNETIC EXCITATIONS IN RARE EARTH METALS

J. G. Houmann and H. Bjerrum Møller
Research Establishment Risø
DK-4000 Roskilde, Denmark

ABSTRACT

This paper reviews the information which has been obtained on the magnetic interactions in the rare earth metals from experimental investigations, by inelastic neutron scattering, of the dispersion relation for the magnetic excitations in these metals. Most of the experimental observations can be described in terms of an isotropic Heisenberg interaction and single-ion crystal field anisotropy. However recent experiments indicate the existence of more complicated terms in the interaction between the ions. The question of magnetic ordering of Pr and the mechanisms through which it may occur are also discussed.

INTRODUCTION

The magnetic properties of the rare earth metals are due to the incompletely filled 4f shell, which is shielded by the outer closed 5s and 5p shells. The spin S, orbital angular moment L, and total angular moment J are determined by the intra-ionic interactions and may be calculated from Hund's rules. Thus we first maximize the total spin S and then the angular moment L, subject to maximum spin. The spin-orbit coupling now couples the spin S and the angular moment L parallel for more than half filled shells and antiparallel for less than half filled shells. The resulting total angular moment $J = L + S$ or $J = L - S$, is the constant of motion. The component of the magnetic moment parallel to J is $g\mu_B J$, and the component of the spin parallel to J is $(g-1)J$ where g is the Landé factor, $g = \frac{3}{2} + \frac{S(S+1)-L(L+1)}{2J(J+1)}$. These quantities are

listed in Table 1 for all of the rare earth ions.

Table 1. Basic Properties of Free Ions. g is Landés Factor

Ion	No. of 4f electr.	S	L	J	g	gJ	(g-1)J
La^{+3}	0	0	0	0	0	0	0
Ce^{+3}	1	1/2	3	5/2	6/7	2.14	-0.36
Pr^{+3}	2	1	5	4	4/5	3.20	-0.80
Nd^{+3}	3	3/2	6	9/2	8/11	3.27	-1.23
Pm^{+3}	4	2	6	4	3/5	2.40	-1.60
Sm^{+3}	5	5/2	5	5/2	2/7	0.72	-1.78
Eu^{+2}	7	7/2	0	7/2	2	7.0	3.5
Gd^{+3}	7	7/2	0	7/2	2	7.0	3.5
Tb^{+3}	8	3	3	6	3/2	9.0	3.0
Dy^{+3}	9	5/2	5	15/2	8/6	10.0	2.5
Ho^{+3}	10	2	6	8	5/4	10.0	2.0
Er^{+3}	11	3/2	6	15/2	6/5	9.0	1.5
Tm^{+3}	12	1	5	6	7/6	7.0	1.0
Yb^{+2}	14	0	0	0	0	0	0
Lu^{+3}	14	0	0	0	0	0	0

Because the extension of the 4f shell is small relative to the inter-ionic distance in the metal, the overlap between 4f wave functions on neighboring ions is negligible, and there is no significant direct exchange. There is however an indirect exchange interaction between the ions, arising because the 4f electrons on an ion polarise the conduction electron gas, which in turn interacts with the 4f electrons on the neighboring ions. An indirect exchange interaction between the magnetic ions via the conduction electrons is therefore established. The interaction between the localized 4f electrons and the conduction electrons has the Heisenberg form

$$H_{sf} = - \sum_{i\ell} j_{sf}(\vec{r}-\vec{R}_\ell)\ \vec{S}_\ell \cdot \vec{s}_i \qquad (1)$$

where $\vec{s}_i$ is the spin of the conduction electron at position $\vec{r}$ and $\vec{S}_\ell$ represents the spin operator of the localized moment

of the rare earth ion at position $\vec{R}_\ell$. The indirect exchange interaction between magnetic ions at positions $\vec{R}_\ell$ and $\vec{R}_{\ell'}$, which involve two such s-f interactions can under certain assumptions also be written in the Heisenberg form[1]

$$H_{ex} = - \sum_{\ell\ell'} J(\vec{R}_\ell - \vec{R}_{\ell'}) \, \vec{J}_\ell \cdot \vec{J}_{\ell'} \qquad (2)$$

The Fourier transform

$$J(\vec{q}) = \sum_\ell J(\vec{R}_\ell) \, e^{i\vec{q}\cdot\vec{R}_\ell} \qquad (3)$$

of the exchange parameter $J(\vec{R}_\ell)$ is related to the susceptibility of the conduction electrons $\chi(\vec{q})$ and the Fourier transform $j(\vec{q})$ of the sf exchange parameter through the expression[1]

$$J(\vec{q}) = \frac{4(g-1)^2}{N} \, |j(\vec{q})|^2 \chi(\vec{q}) \qquad (4)$$

Here the factor $(g-1)^2$ enters because the exchange interaction is expressed in terms of the total angular momentum operator J.

The susceptibility of the conduction electron gas may in principle be calculated from the electronic structure in a simplified model.[1]

$$\chi(\vec{q}) = \frac{1}{N} \sum_{\vec{k}jj'} \frac{f_{j,\vec{k}} - f_{j',\vec{k}+\vec{q}}}{\varepsilon_{j',\vec{k}+\vec{q}} - \varepsilon_{j,\vec{k}}} \qquad (5)$$

where $f_{j,\vec{k}}$ is the Fermi occupation function and $\varepsilon_{j,\vec{k}}$ is the energy of the conduction electron. Calculations of $J(\vec{q})$ from the band structure using expressions (4) and (5) have been carried out for several rare earth metals.[2] If "nesting"[1] of parts of the Fermi surface occurs, this can give rise to maxima in $\chi(\vec{q})$ and therefore in $J(\vec{q})$ for the wave vector $\vec{q} = \vec{Q}$

connecting the two parts of the Fermi surface. Such a maximum in $J(\vec{q})$ at $\vec{q} = \vec{Q}$ can be shown[1] to favor a periodic magnetic structure with a wave vector $\vec{Q}$. This structure may well be incommensurate with the lattice, since it is determined from the electronic structure.

The charges on the neighboring rare earth ions produce an electric field which acts on the 4f charge distribution of a given atom. This crystal field must have the symmetry of the lattice and for an hcp structure takes the form

$$H_{cF} = \sum_{\ell} \{B_{20}O_{20,\ell} + \ldots\ldots B_{66}O_{66,\ell}\} \qquad (6)$$

expressed in terms of the Stevens operators[4]

$$\begin{aligned} O_{20} &= 3J_{\zeta}^{2} - J(J+1) \\ O_{66} &= \frac{1}{2}\left[(J^{+})^{6} + (J^{-})^{6}\right] \end{aligned} \qquad (7)$$

ζ is the c-direction of the hcp structure.

The crystal field parameters $B_{\ell m}$ are often written in the form[3]

$$B_{\ell m} = A_{\ell m} \langle r^{\ell} \rangle \alpha_{\ell} \qquad (8)$$

where $\langle r^{\ell} \rangle$ is averaged over the 4f wave functions, α_{ℓ} is the Stevens factor, containing the dependence of the crystal field parameters on the quantum numbers J, L and S of the rare earth ion, and $A_{\ell m}$ are the crystal field potentials from the ions on the surrounding lattice sites, corrected for the effects of screening by the outer shell electrons.

The competition between the crystal field anisotropy, which tends to align the magnetic moments in certain crystallographic directions, and the exchange interaction, which may

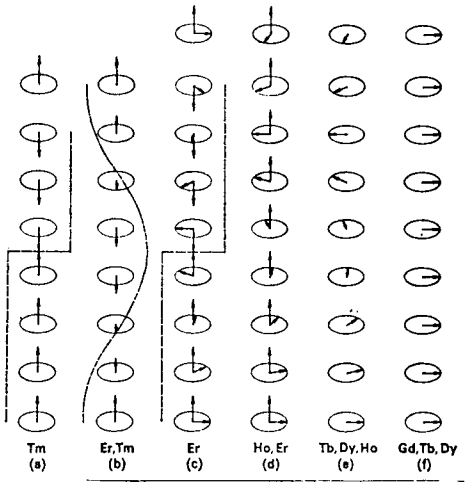


Fig. 1. Schematic representations of the magnetic structures of heavy rare earth metals. The moments are supposed to be parallel in a given hexagonal layer; (after ref. 3).

favor periodic structures, incommensurable with the lattice periodicity, gives rise to the complicated and unusual magnetic structures of the rare earth metals, some of which are shown in Fig. 1.

In this paper, we shall review the information on the exchange interaction and crystal field anisotropy that has been obtained through inelastic neutron scattering studies of the magnetic excitations in the rare earth metals. In particular it will be shown that an interpretation of some of the experimental results requires the inclusion of other types of interaction than those discussed in this introduction (magnetoelastic effects, two-ion anisotropy). Interactions among the excitations[5,6,7] or with other types of excitations (phonons[8,9], conduction electrons[5,10]), will not be discussed in this paper.

MAGNETIC EXCITATIONS

The type of excitations and the way in which an expression for the excitation energies is obtained from the Hamiltonian

$$H = H_{ex} + H_{CF} \qquad (9)$$

depend on the relative magnitude of the exchange interaction and the crystal field.

In the heavy rare earth metals the exchange is large compared to the crystal field. The magnetic excitations are

therefore spin waves, i.e., collective propagating excitations of the ions from the $\langle J_z \rangle = J$ ground state. The crystal field constitutes an anisotropy field acting upon the total angular momentum operator J, to create preferred directions of magnetization.

The spin wave dispersion relation is usually obtained by introducing creation and annihilation operators instead of the J-operators in (9), using the Holstein Primakoff transformation.[11] A diagonalization of the Hamiltonian yields the expression for the spin wave dispersion relation which may be written in the general form[12]

$$\varepsilon^2(\vec{q}) = [A(\vec{q}) + B(\vec{q})][A(\vec{q}) - B(\vec{q})] \tag{10}$$

For the specific case of spin waves propagating in the c-direction of a basal plane ferromagnet (e.g. Tb)[13]

$$\begin{aligned} A(\vec{q}) + B(\vec{q}) &= J[J(0) - J(\vec{q})] + \frac{2}{3} J_1 B_{20} + 6 J_5 B_{66} \\ A(\vec{q}) - B(\vec{q}) &= J[J(0) - J(\vec{q})] + 36 J_5 B_{66} \end{aligned} \tag{11}$$

where we have used the abbreviation

$$J_n = (J-\tfrac{1}{2})(J-1)\ldots(J-\tfrac{n}{2}) \tag{12}$$

for the n-term product of factors involving J.

If we rewrite (11) as follows

$$\begin{aligned} A_{\vec{q}} &= A(\vec{q}) - A(0) = J[J(0) - J(\vec{q})] \\ B_{\vec{q}} &= B(\vec{q}) - B(0) = 0 \\ A(0) &= \tfrac{1}{3} J_1 B_{20} + 21 J_5 B_{66} \\ B(0) &= \tfrac{1}{3} J_1 B_{20} - 15 J_5 B_{66} \end{aligned} \tag{13}$$

we see that the single ion terms in the Hamiltonian give constant terms in the dispersion relation, whereas the two-ion terms (here isotropic exchange) give rise to q-dependent terms. For isotropic exchange the only q-dependent term that enters is $J(\vec{q})$ which can therefore be determined from a measurement of the dispersion relation $\varepsilon(\vec{q})$, provided the anisotropy constants are known.

For other structures the expressions for the dispersion relation are more complicated.[14] For periodic structures of wave vector $\vec{Q}$ the quantities $J(\vec{Q}+\vec{q})$ and $J(\vec{Q}-\vec{q})$ enter into the expressions for the dispersion relations in addition to $J(\vec{q})$, but it is still in principle possible to determine $J(\vec{q})$.

As an example, Fig. 2 shows the measured spin wave dispersion relation in Tb in the ferromagnetic regime.[14,15] Tb has, like most of the heavy rare earth metals, the hcp structure, which contains two atoms per unit cell. This gives rise to two branches of the dispersion relation, an acoustic and an optical. The c-direction of the hcp structure has a particularly high symmetry, since the two sublattices form alternate equally separated planes normal to the c-axis. The double zone representation[16] with only one branch of the dispersion relation can therefore be used for this direction, as shown in the figure. Notable features are the energy gap for q = 0 resulting from the single ion anisotropy, and the strong dispersion due to the exchange coupling. The

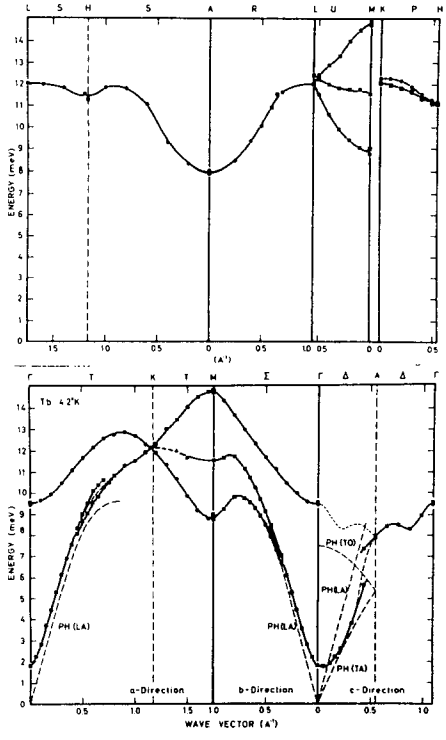


Fig. 2. Magnon dispersion relations for Tb along symmetry lines in the zone at 4.2 K. Certain phonon branches and the effects of magnon-phonon interactions are also shown; (after ref. 14).

measurements also show the effects of a strong magnon-phonon interaction, for which the measurements were corrected before further interpretation. The small splitting between the acoustic and optical branches along the line KH, is absent in the simple model, but requires some kind of anisotropic two-ion coupling.

In the light rare earth metals the crystal fields are somewhat stronger as a result of the greater extension of the 4f electrons. Further the exchange energy is weaker than in the heavy rare earth metals, since it depends on $(g-1)^2 J(J+1)$, which as seen in Table 1 is considerably smaller for the light rare earth ions. As a result of those two effects the exchange interaction and crystal field anisotropy are comparable in the light rare earth metals, and the crystal field causes a splitting of the 2J+1 levels of a given J, which is of the same order as the dispersion of the levels due to exchange.

In a simple model consisting of only two levels, both singlets, with splitting Δ, a simple molecular field calculation gives the following result for the inverse susceptibility along the z direction[17]

$$\frac{1}{\chi} = \frac{\Delta}{2(g\mu_B\alpha)^2} - \frac{J(0)}{(g\mu_B)^2} \qquad (14)$$

α is the matrix element of J_z, that couples the two states. There exists therefore a critical ratio of exchange to crystal field, below which no ordering occurs. This critical ratio is determined from[17]

$$\frac{1}{\chi} = 0 \quad \text{or} \quad \frac{2J(0)\alpha^2}{\Delta} = 1 \qquad (15)$$

The elementary excitations of such an induced moment system, below the critical ratio, are excitations of ions from the ground state to the excited state. In the absence

of exchange these excitations are single ion excitations. Exchange couples the ions together and give rise to collective propagating excitations, which need not carry a magnetic moment.

The dispersion relation for the excitations in our simple model is[17]

$$\varepsilon(\vec{q}) = \Delta \sqrt{1 - \frac{2\alpha^2 J(\vec{q})}{\Delta}} \qquad (16)$$

Also in this case $J(\vec{q})$ can therefore be determined from a measurement of $\varepsilon(\vec{q})$ provided the level scheme is known.

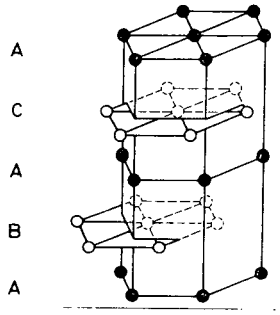


Fig. 3. The double hexagonal close-packed (dhcp) crystal structure of Pr.

Pr is the only light rare earth element in which excitations have so far been studied. Pr has a double hexagonal closed packed structure (Fig. 3) in which there are two types of ionic sites placed in an environment of respectively hexagonal and cubic symmetry. When dealing with crystal field excitations, the two systems can be considered independent of each other, and only the excitations propagating on the hexagonal sites will be discussed here. The crystal field level scheme for these sites consists of a $|m_J\rangle = |0\rangle$ singlet ground state and $|m_J\rangle = |\pm 1\rangle$ doublet as the first excited state. Higher lying states can be ignored in the low temperature limit, since they are not excited from the ground state by neutron scattering. The equation for the dispersion relation (Eq. 16) still holds but the excitations are of course now doubly degenerate and both acoustic and optical modes occur because of the hcp symmetry of the type of sites considered. For the c-direction the double zone representation can be used and one doubly degenerate mode is expected. Fig. 4 shows the dispersion relation for the excitations propagating on the hexagonal sites at 6.4 K.[18] Gen-

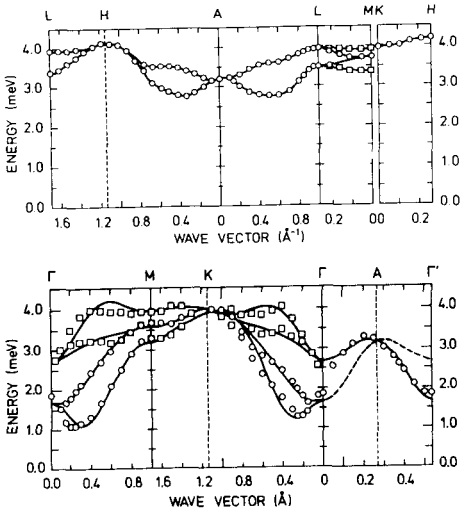


Fig. 4. Dispersion relations for magnetic excitations propagating on the hexagonal sites in Pr at 6.4 K (after ref. 18). The full lines on the lower part of the figure represent a fit to the data; (after ref. 7).

erally two optical and two acoustic modes are observed, as a result of a splitting of the otherwise degenerate $|\pm 1\rangle$ state by the anisotropic exchange field.[19] This will be discussed in more detail in the section about Indirect Exchange Interaction. In the absence of exchange the excitation energy should equal the crystal field splitting Δ (= 3.2 meV, see the section about Soft Modes and Central Peaks in Pr) independent of q. The effect of the exchange is to create a dispersion of the excitation energies around Δ.

CRYSTAL FIELD ANISOTROPY

As explained in the section about Magnetic Excitations, the crystal field anisotropy influences the dispersion relation and creates for example, an energy gap for q = 0 in the spin wave spectrum for a ferromagnet. However, the dominant contribution to the energy of the spin waves in the rare earth metals comes from the exchange interaction, the anisotropic component of which may give a contribution for q = 0. Further, terms of magnetoelastic nature also contribute to the energy gap, as will be shown later. The isolated effects of the single ion crystal field are therefore best studied in systems that do not order and in which the exchange interactions are negligible. Dilute alloys of heavy rare earth metal ($\sim$ 1%) in Y, Sc and Lu are examples of such systems. They are non-magnetic, the crystalline structures are hcp, the lattice

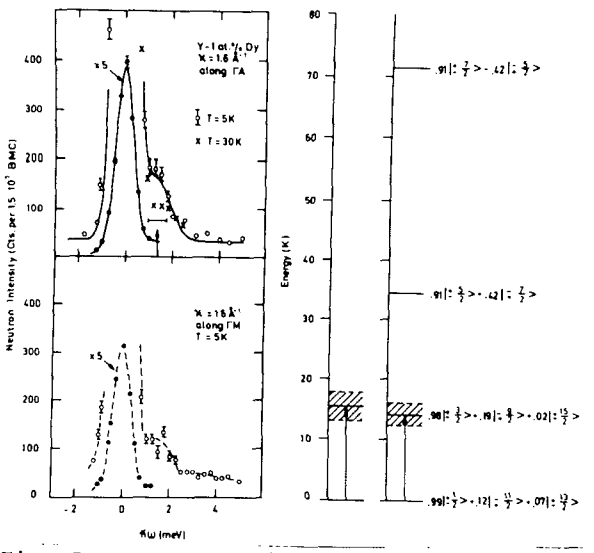


Fig. 5. a. Inelastic neutron spectra for Y-1.1 at.% Dy at 5 K. Resolution and uncertainties are indicated. The full line is a least squares fit to the spectrum.
b. Transition energy with uncertainties obtained from Fig. 5a.
c. Crystal field levels and wave functions obtained from magnetization measurements; (after ref. 20).

constants and the electronic structures are similar to those of the heavy rare earth metals. They can therefore be regarded as a non magnetic matrix, providing a pure crystalline electric field on the site of the magnetic rare earth ions.

The crystal field transition measured in Y-1% Dy[20] and shown in Fig. 5(b) is in good agreement with the level diagram in Fig. 5(c), deduced from measurements of the magnetic susceptibility.[21] In the fitting to the susceptibility data the weak exchange between the magnetic ions was taken into account in the molecular field approximation.

Table 2 shows the values for the crystal field anisotropy parameters $B_{\ell m}$ that were found.[20] Since the Stevens factors α_ℓ contain all the dependence of the crystal field parameters $B_{\ell m}$ on the quantum numbers of the probing ion and $\langle r^\ell \rangle$ does not vary greatly among the heavy rare earth metals, $B_{\ell m}/\alpha_\ell$ should be a measure of the crystal field potentials of the host lattice. This is indeed seen to be the

Table 2. Crystal field parameters in K divided by Stevens factors for 4 alloy systems

host-solute	B_{20}/α_2	B_{40}/α_4	B_{60}/α_6	c/a for host
Sc-Er	-29±3	8.2^{-2}_{+5}	18.1±2	1.592
Lu-Er	-55.7±7	9.6±2	16.1±2	1.584
Y-Er	-111±13	13.5±6	12.0±3	1.573
Y-Dy	-115±12	7.5±3.5	13.1±3	1.573

case. $B_{\ell m}/\alpha_\ell$ does not depend on the probing ion (solute), but does depend on the host, which provides the crystal field. The increasing values of B_{20}/α_2 obtained for Sc, Lu and Y are in agreement with the fact that B_{20} depends on the deviation of the c/a-ratio from the value for the ideal hcp structure (1.633). This deviation also increases, in going from Sc through Lu to Y.

In the case of Y-Dy it was necessary to correct the susceptibility data for ordering effects to obtain agreement with the neutron data. Previously reported results[21], which were not corrected for this effect showed an apparent dependence of the crystal field potential on the probing ion.

In the simple model considered so far, where the only source of anisotropy is the single ion crystal field, it should be possible to cancel the hexagonal anisotropy B_{66} by an applied magnetic field in the hard direction of magnitude

$$H_c = \frac{36}{g\mu_B} J_5 B_{66} \qquad (17)$$

At that field, the spin wave energy gap at q = 0 in a ferromagnet should therefore vanish, and a measurement of the critical field H_c should allow a determination of the hexagonal anisotropy B_{66}.

Measurements of the magnon energy gap versus applied magnetic field have been performed on Tb[22] and Dy[23], and the results for Tb are shown in Fig. 6a. Since the spin wave energy does not go to zero at the critical field - only kinks in the curves are observed - there must be contributions to the anisotropy, that cannot be cancelled by an applied field. These contributions have their origin in the interaction between the magnetic moments and the lattice strain, the magneto-elastic coupling. In the ordered phase it is energetically favorable for the solid to distort in such a way as to

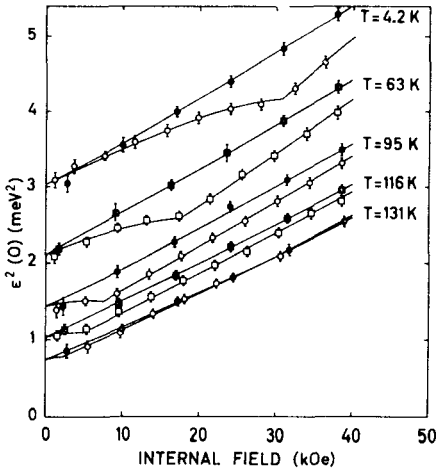


Fig. 6a. Dependence of the square of the magnon energy gap on applied internal magnetic field in Tb. Open symbols represent results for the field in the hard direction and closed the easy direction. The full lines are least-squares fits of the energy gap expression, given in the text, to the experimental results.

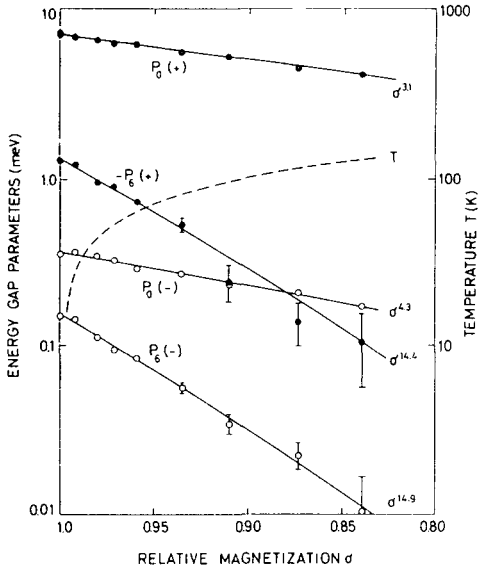


Fig. 6b. Anisotropy parameters P(ℓ) in Tb as a function of magnetization, deduced from the results of Fig. 6a and similar measurements at different temperatures; (after ref. 22).

minimize the Coulomb interaction between neighboring aspherical 4f-charge distributions. This magnetostriction modifies the crystal field, and this contribution to the crystal field is called the magneto-elastic anisotropy. Since the strain follows a slow rotation of the magnetic moments, the magneto-elastic anisotropy does not create any preferred direction. However in the uniform q = 0 mode, where all spins move together with a non vanishing frequency, the lattice cannot respond to the rapid precession of the moment, because the uniform phonon modes have zero frequency. The lattice therefore remains frozen,[24] and there will be a restoring force on the magnetic moments from the magnetoelastic anisotropy,

and consequently a contribution to the q = 0 energy gap, that cannot be cancelled by an applied magnetic field.

The experimental results shown in Fig. 6a have been analyzed in terms of the quantities[22]

$$\begin{aligned} P_0(+) &= \tfrac{2}{3}J_1B_{20} + C_\gamma(2C^2 + A^2) \\ P_6(+) &= 6J_5B_{66} + 3C_\gamma AC + \Delta M \\ P_0(-) &= 0 + 4C_\gamma(C^2 + A^2) \\ P_6(-) &= 36J_5B_{66} + 10C_\gamma AC \end{aligned} \tag{18}$$

where the terms A(0)+B(0) and A(0)-B(0) have been divided into terms that are independent of rotation of the moments in the basal plane, $P_o(+)$ and $P_o(-)$, and terms $P_6(+)$ and $P_6(-)$ that depend on the angle ϕ between the magnetic moment and the hard direction. Here $c_\gamma = 2(c_{11}-c_{12})$ is an elastic constant and C and A are the first order and second order magnetostriction coefficients.[24]

In terms of these parameters the expression for the spin wave energy for field H in the hard direction is[22]

$$\begin{aligned} \varepsilon_\phi^2 = {} & [P_0(+) + P_6(+)\cos 6\phi + g\mu_B H\cos\phi] \\ & [P_0(-) - P_6(-)\cos 6\phi + g\mu_B H\cos\phi] \end{aligned} \tag{19}$$

where the relation between the angle ϕ of orientation of the moments relative to the hard direction and the applied magnetic field is[22]

$$g\mu_B H = g\mu_B H_c \frac{\sin 6\phi}{6\sin\phi} \text{ for } H < H_c \tag{20}$$

It should be pointed out that other terms than those included in (18) may be significant. These may be of higher

order or resulting from possible two ion anisotropy (see later). The analysis is therefore only carried out in terms of the P's, and the results for Tb[22] are shown in Fig. 6b, as a function of the relative magnetization. A comparison[22] of the results on Fig. 6b with the measured macroscopic values for the crystal field parameters[25] and the magnetostriction coefficients[26] indicates in fact, that there must be other large contributions to the energy gap than those included in (18). In particular it seems that the dominant contribution to the basal plane anisotropy results from other sources.

INDIRECT EXCHANGE INTERACTION

The magnon dispersion relations have been measured in a number of the heavy rare earth metals[5,6,14,15,16,27,28,29] and the Fourier transformed exchange parameters have been deduced from these measurements as described in the section about Magnetic Excitations.

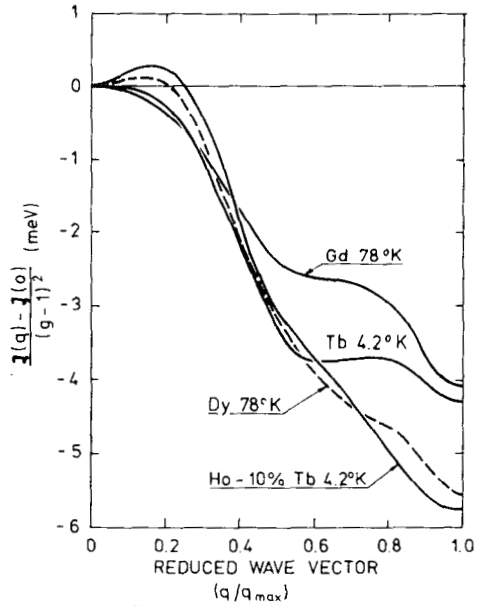


Fig. 7. The exchange function $[J(q)-J(0)]/(g-1)^2$ in the c-direction for a number of ferromagnetic heavy rare earths; (after ref. 14).

The exchange function $[J(\vec{q})-J(0)]/(g-1)^2$ for a number of ferromagnetic heavy rare earth metals[14] is compared in Fig. 7. This function should, according to (4), be identical for all of the heavy rare earth metals if the conduction electron band structure and the 4f wave functions were identical, and if the effective coupling between the ions were entirely of the isotropic Heisenberg form (2). There are in fact notable differences in the q-dependences for the different

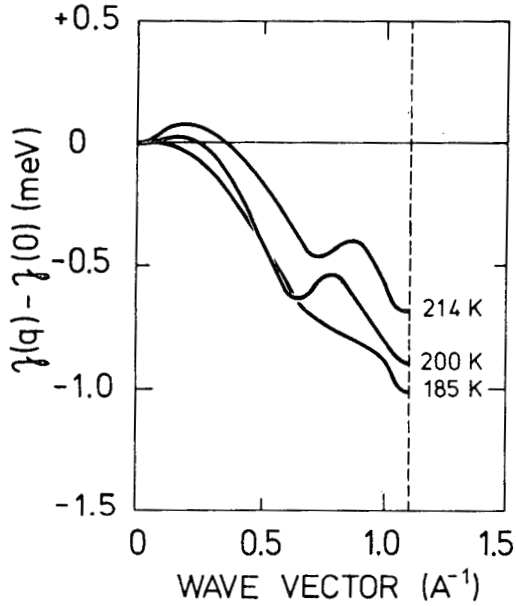


Fig. 8a. The exchange function $\mathcal{J}(q)-\mathcal{J}(0)$ in the c-direction of Tb-10% Ho as a function of temperature in the helical and ferromagnetic (110 K) phases.

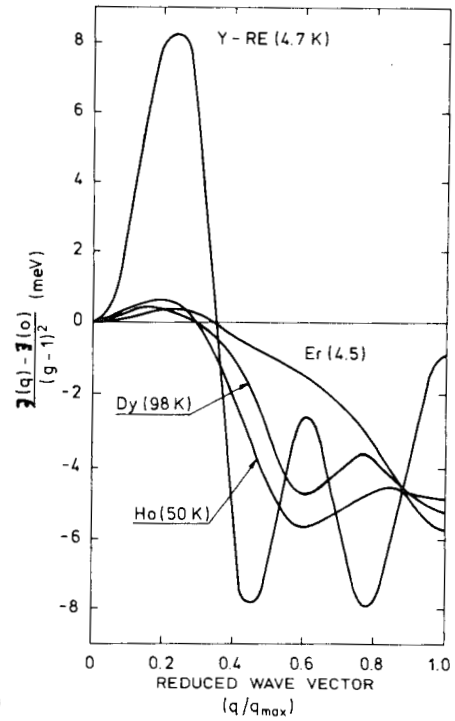


Fig. 8b. The exchange function $[\mathcal{J}(q)-\mathcal{J}(0)]/(g-1)^2$ in the c-direction for a number of heavy rare earth in the helical and cone (Er) phases; (after refs. 14, 32, 33).

metals, probably due to the differences in the band structure and hence $\chi(\vec{q})$. The average magnitude of the function also appears to increase with L, which may be an indication that there is some coupling between the orbital angular moments on the ions.[30]

Fig. 8a and 8b show $[J(\vec{q})-J(0)]/(g-1)^2$ for a number of heavy rare earths,[6,31,32,33] with periodic structures. The measurements on Y, which is non-magnetic, were performed on alloys of 10% Tb in Y and 10% Ho in Y. Both of these alloys have an exchange interaction that is larger than the crystal field and they both show spiral ordering with a turn angle of 50°. Well-defined spin waves were observed in both cases. In a mean lattice approximation, in which each atomic

site is assumed to be occupied by an average atom one obtains the usual expression for the spin wave energies, but with the exchange parameter $J(\vec{q})$ replaced by $cJ(\vec{q})$, where c is the concentration of rare earths in Y, whereas the crystal field terms are unchanged. If this model is used to interpret the measured dispersion relations in the two alloys, the same result is obtained for $[J(\vec{q})-J(0)]/(g-1)^2$ in both cases,[33] showing that it is the $J(\vec{q})$ related to the conduction electron susceptibility $\chi(\vec{q})$ of Y, that is measured, in accordance with the general picture given in the introduction.

In the helical phases $J(\vec{q})$ has a maximum at the $\vec{Q}$ which characterizes the periodic structure. As discussed in the introduction, this peak is associated with details of the band structure which result in a maximum in $\chi(\vec{q})$. The magnitude of the peak correlates qualitatively with the stability of the periodic structures. The very large peak in $J(\vec{q})$ for Y-RE appears to be consistent with the fact that when the pure metals are diluted with Y the tendency toward helical magnetic ordering increases rapidly with increasing Y concentration. In Ho-10% Tb and Dy the peak is sufficiently pronounced that a residuum survives the transition to the ferromagnetic phase, and its relatively large size in the helical phase of Ho is consistent with the observation that this metal retains a periodic structure down to the lowest temperature, in zero field. In contrast, Gd and Tb have no maximum at non-zero q in the ferromagnetic phase, although Tb-10% Ho, which presumably behaves similarly to pure Tb, in the helical phase has a pronounced peak which shifts and decreases in size as the temperature is lowered. At the Curie temperature, the peak in $J(\vec{q})$ has been reduced to the point where it is not sufficient to maintain the periodic structure against the magnetoelastic forces, which increase with

decreasing temperature and ultimately drive the structure ferromagnetic. The change in the band structure at the transition then eliminates the peak in $J(\vec{q})$ in the ferromagnetic phase. On the other hand, in Dy and Ho-10% Tb in which T_c is so low that the effect of the magnetization on the band structure is essentially fully developed, it is the rapid variation of the magnetoelastic and anisotropy forces with magnetization which determines the transition temperature. $J(\vec{q})$ still changes abruptly at T_c, but not sufficiently to eliminate the maximum entirely.

In all of the experiments discussed so far, with the exception of Er, only one q-dependent quantity, the dispersion relation $\varepsilon(\vec{q})$, was measured, and therefore only one q-dependent function, the isotropic exchange parameter $J(\vec{q})$, was determined. To investigate two-ion anisotropy it is necessary to measure one more q-dependent quantity.

For Er in the conical magnetic structure the dispersion relations in the positive and negative c-direction are different as shown in Fig. 9.[32] It can be shown that both the single-ion and two-ion anisotropy terms that may enter into the determination of the dispersion relation, cancel out in the expression for the difference between the spin wave energies for the positive and negative q-direction[32]

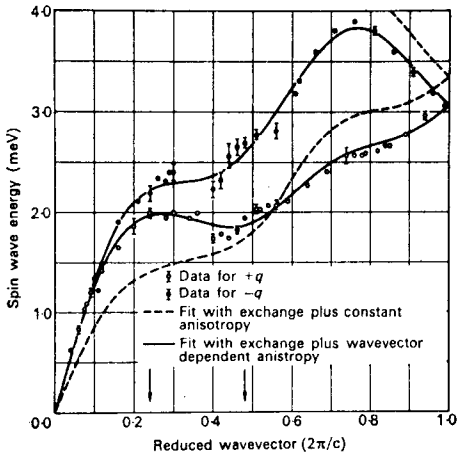


Fig. 9. Magnon energies in the c-direction of the cone phase of Er. The dashed and full lines are the results of different fits (described in the text) to the data; (after ref. 32).

$$\Delta(q) \equiv \varepsilon(-\vec{q}) - \varepsilon(\vec{q}) = J[J(\vec{Q}-\vec{q}) - J(\vec{Q}+\vec{q})] \qquad (21)$$

so that this difference gives $J(q)-J(0)$ shown in Fig. 8b rather

directly. However, to obtain a satisfactory fit to the dispersion relation $\varepsilon(\vec{q})$ at low temperatures, it is necessary[34] to introduce wave vector dependent anisotropy of the same magnitude as the isotropic exchange, in addition to the single ion anisotropy.

There is one more piece of experimental evidence that the Hamiltonian (9) containing isotropic exchange and single ion anisotropy, including magnetoelastic contributions is not adequate. Measurements of the field dependence of the spin wave energies for arbitrary q in a ferromagnet provide information on one more q-dependent quantity $B_{\vec{q}}$, in addition to $A_{\vec{q}}$ (see Eq. 13). With a magnetic field H in the direction of easy magnetization, the expression for the dispersion relations are[35]

$$\varepsilon_H^2(\vec{q}) = [A(\vec{q}) + B(\vec{q}) + g\mu_B H][A(\vec{q}) - B(\vec{q}) + g\mu_B H] \quad (22)$$

from which it is seen that the initial slope $\alpha(\vec{q})$ in a plot of $\varepsilon_H^2(\vec{q})$ versus H is given by[35]

$$\alpha(\vec{q}) \equiv \frac{1}{g\mu_B} \frac{d\varepsilon_H^2(\vec{q})}{dH}\bigg|_{H=0} = 2A(\vec{q}) \quad (23)$$

(22) and (23) gives[35]

$$A_{\vec{q}} \pm B_{\vec{q}} = \tfrac{1}{2}\alpha(\vec{q}) \pm \tfrac{1}{2}\sqrt{\alpha^2(\vec{q}) - 4\varepsilon_0^2(\vec{q})} - [A(0) \pm B(0)] \quad (24)$$

where A(0) and B(0) were determined in the section about Crystal Field Anisotropy. $A_{\vec{q}} + B_{\vec{q}}$ and $A_{\vec{q}} - B_{\vec{q}}$ can therefore be determined from measurements of $\varepsilon_o(\vec{q})$ and $\alpha(\vec{q})$. The results for Tb at 4.2 K are shown in Fig. 10, for fields in both hard and easy directions. When the magnetic moment points in the hard direction $B_{\vec{q}} \simeq 0$, but if the field is in the easy direction, $B_{\vec{q}}$ is definitely different from zero, being

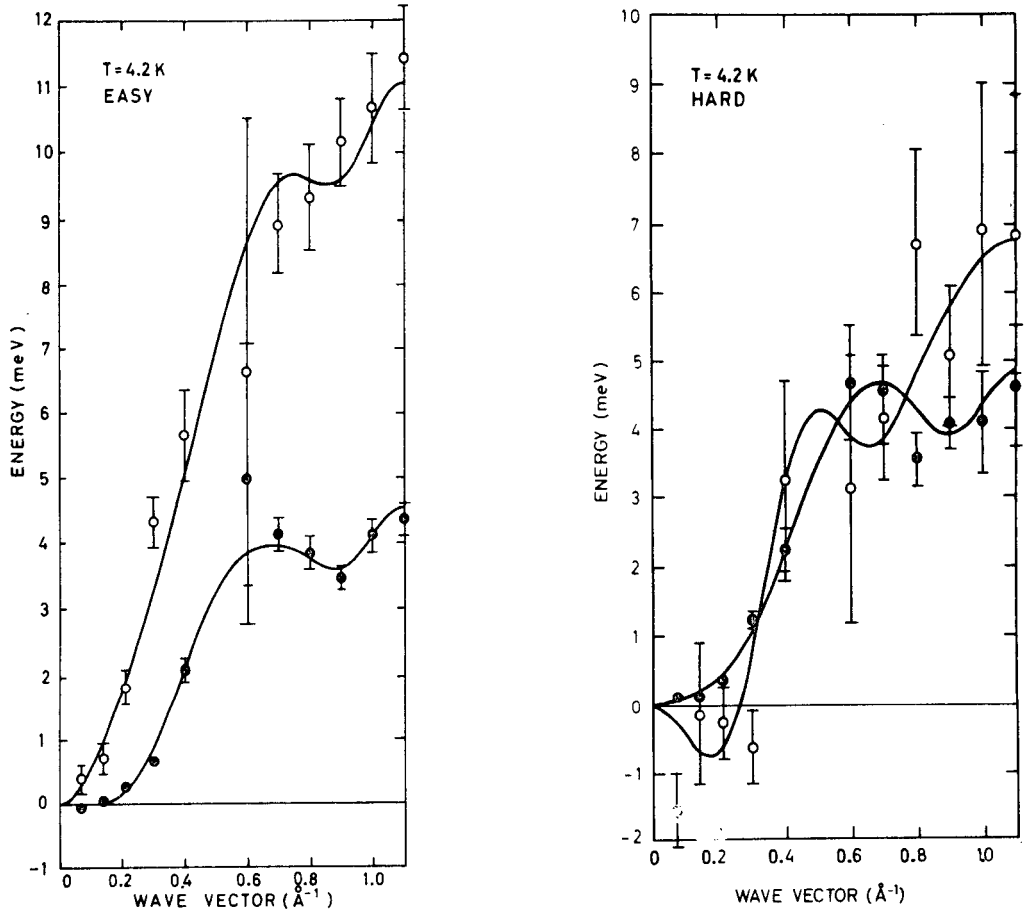


Fig. 10. $\vec{q}$ dependence of the two components $A_{\vec{q}}+B_{\vec{q}}$ and $A_{\vec{q}}-B_{\vec{q}}$ of the magnon energies in the c-direction of Tb at 4.2 K (open and closed symbols, respectively). The effective q-dependent anisotropy is given by half the difference between the two energy components $B_{\vec{q}}$, which is deduced to be of an appreciable magnitude when the magnetization is along an easy axis, (a), whereas $B_{\vec{q}}$ is quite small in the hard axis configuration, (b); (after ref. 35).

about $\frac{1}{2}A_{\vec{q}}$ at low temperature. There is therefore, in the model used so far, a strong q-dependent two-ion anisotropy of magnitude about 1/3 of the isotropic part of the exchange interaction. This two-ion anisotropy decreases with increasing temperature and vanishes completely at about 150 K, above which temperature the exchange is effectively isotropic.

It has, however, recently been pointed out[36] that the crystal field anisotropy has not been treated correctly in the theories that lead to the previously quoted expressions

for the spin wave energies. The Holstein Primakoff transformation[11], commonly used, assumes a level diagram with pure J_z-states and equidistant splittings, and ignores the effect of the crystal field in mixing the pure states and changing the level splittings. A new consistent transformation using the matching of matrix element method leads to q-dependent single-ion contributions.[36] Whether this explains the apparent large two-ion anisotropy in the heavy rare earth metals is still a matter of discussion.[37]

In the light rare earth metal Pr, a splitting of the otherwise degenerate $|\pm 1\rangle$ state is observed, as pointed out in the section about Magnetic Excitations. If the Hamiltonian is written in the form[19]

$$H = V_c - \sum_{\nu,i>i'} J^{\nu\nu}_{ii'}(\vec{R}_i-\vec{R}_{i'})J^{\nu}_i \cdot J^{\nu}_{i'} - \sum_{\nu,j>j'} J^{\nu\nu}_{jj'}(\vec{R}_j-\vec{R}_{j'}) J^{\nu}_j \cdot J^{\nu}_{j'} - \sum_{\nu,ij} J^{\nu\nu}_{ij}(\vec{R}_i-\vec{R}_j)J^{\nu}_i \cdot J^{\nu}_j \qquad (25)$$

in which anisotropy of the exchange interaction is included by allowing different values for J^{xx}, J^{yy}, and J^{zz} (ν represents the cartesian coordinates and the indices i and j refer to sites on the two sublattices, respectively), the following expression for the excitation energies is obtained[19]

$$\varepsilon^2(\vec{q})_{\pm,\nu=x,y} = \Delta^2 - \alpha^2\Delta[J^{\nu\nu}(\vec{q}) \pm |J'^{\nu\nu}(\vec{q})|] \qquad (26)$$

where Δ is the crystal field splitting between $|0\rangle$ and $|\pm 1\rangle$, α is the matrix element of J^+ or J^- between these states and $J(\vec{q})$ and $J'(\vec{q})$ are the Fourier transforms of J_{ii} and J_{ij} respectively. The four branches of the dispersion relation correspond to acoustic and optical modes (+ and - respective-

ly) each with J^x and J^y excitations. The four branches (Fig. 4) of the excitons propagating in the basal plane are seen generally to be clearly resolved. For the excitations propagating along the c-axis, symmetry eliminates the splitting between the J^x and J^y modes, and the use of the double-zone representation further reduces the number of branches to one. From these dispersion relations, it is obvious that the exchange interaction is strongly anisotropic. The Holstein Primakoff transformation was not used in deriving the expression for the excitation energies, and therefore the theory[36] for explaining the apparent large anisotropy of Tb and Er as originating from single ion anisotropy, cannot explain the observed two-ion anisotropy in Pr.

SOFT MODES AND CENTRAL PEAKS IN Pr

In the section about Magnetic Excitations it was shown that in a singlet ground-state system there exists a critical ratio of exchange to crystal field, below which no magnetic ordering occurs. For a number of years there has been a controversy about the existence of ordering in Pr. Neutron diffraction on single crystals has failed to show any evidence for ordering above 0.4 K.[38] However, a longitudinal wave magnetic structure has been observed in monocrystalline samples of dilute Pr-Nd alloys.[38] The wave vector which characterizes this structure corresponds very closely to the wave vector of the lowest energy mode in the excitation spectrum between Γ and M,[18] and the inelastic neutron scattering measurements further identify the mode as corresponding to a longitudinal fluctuation of the ionic moment. This mode may therefore be consider as an incipient soft mode in Pr. It does indeed have the most rapid temperature variation at higher temperatures as shown in Fig. 11,[18] but below about

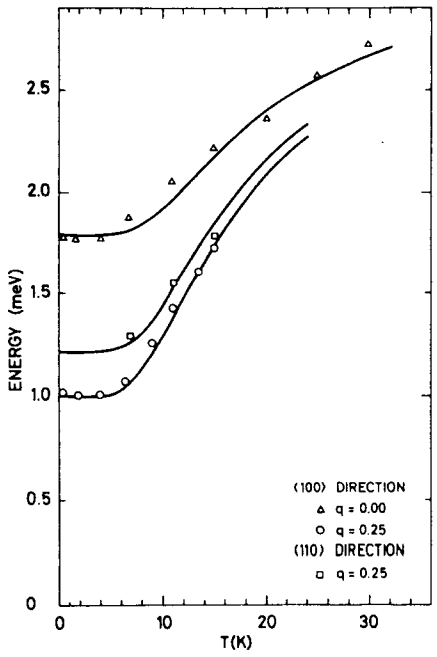


Fig. 11. Temperature dependence of selected magnetic excitations in Pr. The full lines are calculated in the RPA-approximation, as described in the text; (after ref. 18).

7 K neither it nor any other excitation decreases appreciably in energy as the temperature is further reduced to 0.4 K. This is easily understood in the Random-Phase Approximation, which introduces a temperature renormalization R(T) of the second term in Eq. (26) which is just the difference in Boltzmann population factors between the ground state and excited state

$$R(T) = n_o - n_1 = (1-e^{-\Delta/kT})/(1+2e^{-\Delta/kT}) \qquad (27)$$

The temperature dependence of the excitations predicted by this theory[18] is plotted in Fig. 11 for a Δ of 3.2 meV and values of the exchange which give agreement with the low-temperature limit of the energies. The exchange interaction determined in this way is approximately 90% of that, which would be required to drive the energy of the soft mode to zero.

It therefore appears that although there is considerable softening of the lowest energy mode, the exchange is not strong enough to drive it to zero. Ordering may however also occur as a result of the divergence of the longitudinal static susceptibility, corresponding to excitations within degenerate excited states carrying a magnetic moment.[39] Even though the population of such an excited state is vanishingly small the integrated intensity[39]

$$S_o^{zz}(\vec{q}) = \frac{\langle \delta J^2_{zd} \rangle_T / (1-2J(\vec{q})\chi_{CF}(0,T)}{1-2J(\vec{q})\chi(0,T)} \qquad (28)$$

of the central mode which it gives rise to diverges at T_C for $\vec{q} = \vec{Q}$, the characteristic wave vector of the structure. Here $\langle \delta J_{zd} \rangle_T$ is the diagonal spin fluctuation, $\chi_{CF}(0,T)$ is the crystal field or inelastic part for $\omega = 0$ of the susceptibility and $\chi(0,T)$ is total static longitudinal susceptibility. The transition temperature T_c is given by the equation[39]

$$\chi(0,T_c) = \frac{1}{2J(\vec{Q})} \qquad (29)$$

The transition may therefore also be driven by a catastrophic growth of the intensity of an elastic mode of the system.

A search for elastic scattering around the dispersion relation minima has therefore been carried out as a function of temperature.[40] Quasi-elastic magnetic scattering was observed around the q-vector, corresponding to the wave vector of the magnetic order in dilute Pr-Nd alloys. The peaks are very weak and have a linewidth about five times that of the nuclear Bragg peaks. The peak intensity decreases almost linearly with increasing temperature and is unobservable above about 15 K. It therefore seems that although central peaks are observed in Pr, there is no evidence for magnetic order resulting from a divergence of the static susceptibility.

However, the exchange is very close to the critical value for antiferromagnetic ordering and recent heat capacity measurements[41] suggest that at lower temperatures, a nuclear ordering[42] occurs which may be accompanied by electronic ordering.

CONCLUSION

The experimental information on the dispersion relations in the rare earth metals, which has been reviewed in this paper, has led to a substantial improvement in our understanding of the magnetic interactions in these metals. Most of the experimental data can be interpreted with a simple model containing an isotropic Heisenberg exchange interaction and single-ion anisotropy, with rather large magnetoelastic contributions to the latter. The magnitude of the maxima in $J(\vec{q})$ correlate qualitatively with the stability of periodic structures in the different metals, and the occurrence of the peaks can in turn be related to the band structure. The single-ion anisotropy is composed of crystal-field and magnetoelastic contributions, which may be studied through the field dependence of the magnon energy gap. The crystal fields in dilute alloys depend only on the host material, as would be anticipated from a model in which they arise from the charges in neighboring sites, screened by the conduction electrons.

There is, however, in the experimental observations, evidence of more complicated interactions between the magnetic moments. The fact that $[J(\vec{q})-J(0)]/(g-1)^2$ is different for the different heavy rare earth metals, being larger for the metals of large L, indicates the existence of a coupling between the orbital angular moments on the ions. The small splitting of the acoustic and optical branches along KH in Tb requires an anisotropic two-ion coupling. Other contributions to the magnetic coupling, perhaps also of two-ion origin, seems necessary to account for the measurements of the energy gap as a function of applied magnetic field in Tb. The interpretation of the dispersion relations for Er in the conical phase require q-dependent anisotropy, which is also

found in Tb from measurements of the field dependence of the spin wave energies. Finally a large two-ion anisotropy is found in Pr. A proper transformation which includes the effect of the crystal field on the level diagram, which is ignored in the Holstein Primakoff transformation, has been shown to introduce q-dependent anisotropy from single-ion terms in the Hamiltonian, so that it may not be necessary to introduce two-ion anisotropy to explain the Er and Tb data. In addition to introducing q-dependent anisotropy this new transformation also has the effect of changing the measured $J(\vec{q})$ values. For Er this effect increases the $J(\vec{q})$ in Fig. 8b relative to $J(\vec{q})$ for Gd, which is not influenced, and therefore leads to the surprising conclusion that the orbital coupling dominates over the spin coupling. In view of this it would be of great interest to try to make a theoretical prediction of the relative magnitude of the isotropic and anisotropic part of the coupling between orbital moments.

The experiments carried out to elucidate the possible ordering of the light rare earth metal Pr and the mechanisms through which it may occur, show that although there is an incipient soft mode, its energy does not go completely to zero, nor does the static susceptibility corresponding to the q-vector of this mode diverge.

ACKNOWLEDGEMENTS

We are grateful to A. R. Mackintosh for a critical reading of the manuscript and to J. F. Cooke for valuable discussions.

REFERENCES

I. A general reference to the subject treated in this paper is: Magnetic Properties of Rare Earth Metals, edited by R. J. Elliott, Plenum Press 1972, and the references given therein.

1. A review is given by A. J. Freeman in Magnetic Properties of Rare Earth Metals, chapter 6 (see ref. I).
2. See ref. 1 and P.-A. Lindgård, B. N. Harmon and A. J. Freeman, Phys. Rev. Letters, 35, 383 (1975).
3. A review is given by R. J. Elliott in Magnetic Properties of Rare Earth Metals, chapter 1 (see ref. I).
4. K. W. H. Stevens, Proc. Phys. Soc. A65, 209 (1952).
5. M. Nielsen, H. Bjerrum Møller and A. R. Mackintosh, J. Appl. Phys. 41 1174 (1970).
6. R. M. Nicklow, J. Appl. Phys. 42, 1672 (1971); R. M. Nicklow, N. Wakabayashi, M. K. Wilkinson and R. E. Reed, Phys. Rev. Letters 26, 140 (1971).
7. P. Bak, Phys. Rev. Letters 34, 1230 (1975) and Phys. Rev. B 12, 5203 (1975).
8. J. Jensen and J. G. Houmann, Phys. Rev. B12, 320 (1975).
9. J. G. Houmann, J. Jensen, B. D. Rainford, A. R. Mackintosh, O. D. McMasters and K. A. Geschneidner, Jr., to be published.
10. H. Bjerrum Møller, to be published.
11. T. D. Holstein and H. Primakoff, Phys. Rev. 58, 1098 (1940).
12. P.-A. Lindgård and O. Danielsen, Phys. Rev. B11, 351 (1975).
13. K. Niira, Phys. Rev. 117, 129 (1960).
14. A review is given by A. R. Mackintosh and H. Bjerrum Møller in Magnetic Properties of Rare Earth Metals, chapter 5 (see ref. I).
15. H. Bjerrum Møller, J. G. Houmann and A. R. Mackintosh, J. Appl. Phys. 39, 807 (1968).
16. H. Bjerrum Møller and J. G. Houmann, Phys. Rev. Letters 16, 737 (1966).
17. Y.-L. Wang and B. R. Cooper, Phys. Rev. 172, 539 (1968). ibid. 185, 696 (1969); references given therein.
18. J. G. Houmann, M. Chapellier, A. R. Mackintosh, P. Bak, O. D. McMasters and K. A. Gschneidner, Jr., Phys. Rev. Letters 34, 587 (1975); B. D. Rainford and J. G. Houmann, Phys. Rev. Letters 26, 1254 (1971).
19. P.-A. Lindgård and J. G. Houmann, in Rare Earths and Actinides, (Institute of Physics, London, 1971).
20. O. Rathmann and P. Touborg, Phys. Rev. B (to be published); references given therein.
21. J. Høg and P. Touborg, Phys. Rev. B9, 2920 (1974); J. Høg and P. Touborg, Phys. Rev. B (to be published).
22. J. G. Houmann, J. Jensen and P. Touborg, Phys. Rev. B12, 332 (1975); references given therein.
23. R. M. Nicklow and W. C. Koehler, Solid State Div. Ann. Progr. Rep., ORNL-5028, p. 84 (Dec. 31, 1974) (unpublished).

24. E. A. Turov and V. G. Sharov, Sov. Phys. -Solid State 7, 166 (1965); B. R. Cooper, Phys. Rev. 169, 281 (1968); P.-A. Lindgård, J. de Physique 32, C1-238 (1971).
25. J. J. Rhyne and A. E. Clark, J. Appl. Phys. 38, 1379 (1967); J. L. Feron, G. Huy and R. Pauthenet, CNRS Report No. 180, p. 19, (Paris 1970), (unpublished).
26. J. J. Rhyne and S. Legvold, Phys. Rev. 138, A507 (1965).
27. W. C. Koehler, H. R. Child, R. M. Nicklow, H. G. Smith, R. M. Moon and J. W. Cable, Phys. Rev. Letters 24, 16 (1970).
28. H. Bjerrum Møller, in Neutron Inelastic Scattering, Vol. II, p. 3, (IAEA, Vienna 1968).
29. H. Bjerrum Møller, M. Nielsen and A. R. Mackintosh, in Les Eléments des Terres Rares, Vol. II, p. 277, (CNRS, Paris 1970).
30. T. A. Kaplan and D. H. Lyons, Phys. Rev. 129, 2072 (1963).
31. H. Bjerrum Møller, J. G. Houmann and A. R. Mackintosh, Phys. Rev. Lett. 19, 312 (1967).
32. R. M. Nicklow, N. Wakabayashi, M. K. Wilkinson and R. E. Reed, Phys. Rev. Letters 27, 334 (1971).
33. N. Wakabayashi and R. M. Nicklow, Phys. Rev. B10, 2049 (1974).
34. J. Jensen, J. Phys. F4, 1065 (1974).
35. J. Jensen, J. G. Houmann and H. Bjerrum Møller, Phys. Rev. B12, 303 (1975).
36. P.-A. Lindgård, Phys. Rev. Lett. 36, 385 (1976); P.-A. Lindgård and A. Kowalska, J. Phys. C: Solid State Phys. (to be published); P.-A. Lindgård and J. F. Cooke (to be published).
37. J. Jensen (to be published).
38. B. Lebech, K. A. McEwen and P.-A. Lindgård, J. Phys. C: Solid State Phys. 8, 1684 (1975).
39. W. J. L. Buyers, AIP Conference Proceedings 24, p. 27 (1974); references given therein.
40. B. Lebech, W. J. L. Buyers, J. G. Houmann, A. R. Mackintosh, O. D. McMasters and K. A. Gschneidner, Jr. (to be published).
41. P. E. Lindelof, I. E. Miller and G. R. Pickett in Proceedings of the 14th International Conference on Low Temperature Physics, Vol. III, p. 204, (Finland 1975) (North-Holland Publishing Company).
42. T. Murao, J. Phys. Soc. Japan 39, 1629 (1975).

NEUTRON SCATTERING FROM ISOLATED CLUSTERS OF MAGNETIC IONS

W.J.L. Buyers, E.C. Svensson and T.M. Holden
Chalk River Nuclear Laboratories
Atomic Energy of Canada Limited
Chalk River, Ontario, Canada, K0J 1J0

ABSTRACT

The application of neutron-scattering techniques to the determination of the exchange interactions J between magnetic ions in small isolated clusters is demonstrated in measurements on $KMn_{0.1}Zn_{0.9}F_3$. The observed transition frequencies for isolated pairs and triplets give exchange constants, e.g. $J = 0.100 \pm 0.004$ THz for the lowest pair transition, that compare favorably in accuracy with the best available results from electron paramagnetic resonance.

Information about the exchange interactions J between magnetic ions in small isolated clusters is most commonly obtained by electron paramagnetic resonance (EPR). In this method[1], J is usually determined from the temperature dependence of the signal intensity, and the accuracy is normally limited to about 10% and is often only 20-50%. Neutron inelastic scattering offers a more direct method of studying the exchange interactions since the energies of the transitions can be directly determined and this leads to rather accurate values for J. In contrast to EPR or optical techniques, direct information about the wave functions of the states can also be obtained from the wave-vector dependence of the intensities.

In this paper we demonstrate the use of neutron-scattering techniques for determining the exchange interactions between magnetic ions in small isolated clusters. The measurements were carried out on a single crystal of $KMn_{0.1}Zn_{0.9}F_3$ in which the concentration $c = 0.1$ of magnetic ions was well below the critical concentration $c_o = 0.31$ for the existence of long-range magnetic order. The magnetic ions lie on a simple cubic lattice and interact essentially[2] with nearest-neighbor antiferromagnetic exchange as described by the Hamiltonian

$$H_{12} = 2J\vec{S}_1 \cdot \vec{S}_2 \ . \qquad (1)$$

The energy-level schemes for pairs and triplets of Mn^{2+} ions (spin 5/2) are shown in Fig. 1. The levels are labelled with the values of the total spin S. For the triplet, the levels are separated into bands according to the values of $\vec{S}_{13} = \vec{S}_1 + \vec{S}_3$. All transitions with $\Delta S = \pm 1$ within bands or $\Delta S = 0, \pm 1$ between adjacent bands are allowed. At $T = 0$ only transitions at a frequency $\nu = 2J$ for the pair and at $\nu = 5J$ and $\nu = 7J$ for the triplet will be observable.

The excitation frequencies are independent of the wave-vector transfer $\vec{Q}$, but the intensities can vary markedly. For example, the integrated intensity $I(\vec{Q})$ of the neutron scattering by the $\nu = 2J$ transition of

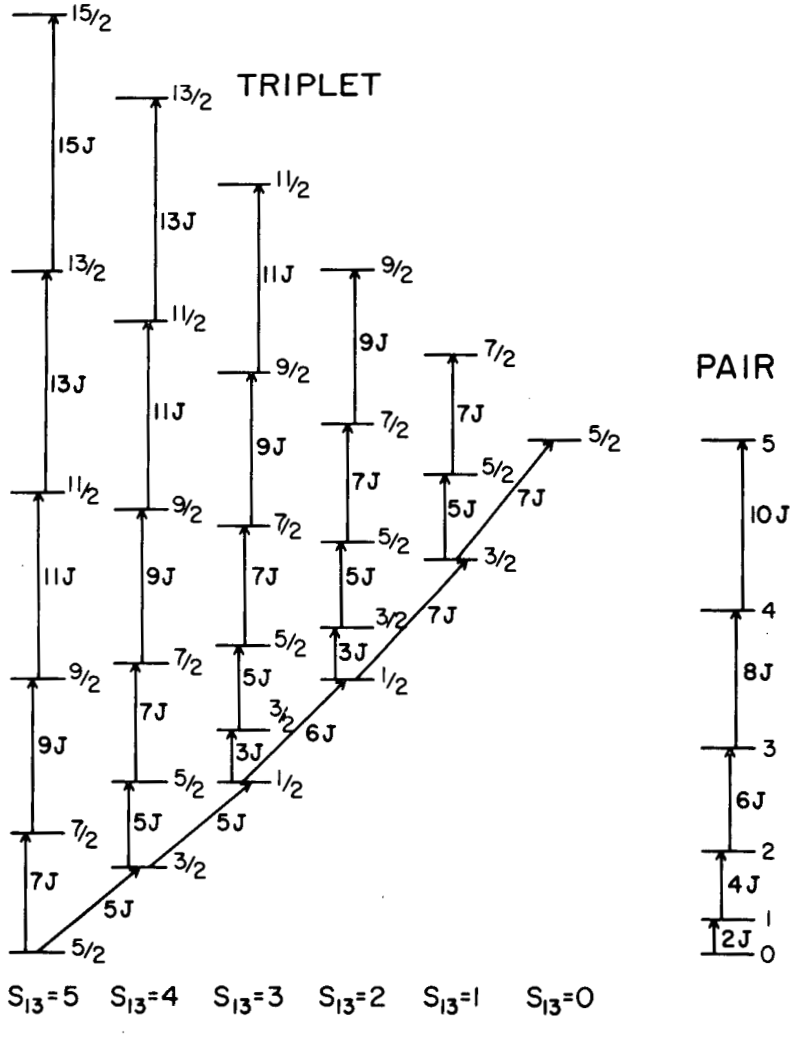


Fig. 1. Energy levels of isolated pairs and triplets of Mn^{2+} ions.

randomly oriented pairs is given by

$$I(\vec{Q}) \propto f^2(\vec{Q}) \; [\sin^2(aQ_x/2) + \sin^2(aQ_y/2) + \sin^2(aQ_z/2)] \qquad (2)$$

where $f(\vec{Q})$ is the magnetic form factor and a is the lattice constant.

The present study was also undertaken partly to obtain information on the limitations of the spin-wave[3] and the Ising[4] approaches which are commonly applied[5] to substitutionally disordered antiferromagnets at relatively large concentrations c of magnetic ions. For small c, Ising theory gives $\nu = 2JS$ for the isolated pair which depends on S and for Mn^{2+} is 2.5 times greater than the exact result $\nu = 2J$.

The measurements were carried out using a triple-axis crystal spectrometer operated in the constant-$\vec{Q}$ mode. Silicon (111) planes and pyrolytic graphite (002) planes were used for the monochromator and analyser respectively. The scattered-neutron energy E' was held constant at either 1.450 or 1.608 THz. Quartz and pyrolytic-graphite filters were placed in the incident and scattered beams respectively. The specimen of nominal composition $KMn_{0.1}Zn_{0.9}F_3$ was oriented with a $(1\bar{1}0)$ axis vertical. Measurements were carried out at several values of $\vec{Q}$ at 4.3 K and also at 2, 20, 50, 100 and 300 K at $\vec{Q} = 2\pi a^{-1}$ (0.55,0.55,0.55). The lattice constant, a, of the specimen was 4.0703 Å at 4.3 K.

The spectra observed at 2 and 20 K at (0.55,0.55,0.55) are shown in Fig. 2. The three inelastic peaks observed at 2 K correspond to the 2J transition of an isolated pair and the 5J and 7J transitions of an isolated triplet (see Fig. 1). The difference curve at the bottom of Fig. 2 most clearly shows the main changes on heating to 20 K, namely the substantial decrease in the intensity of the 2J pair peak and the appearance of two additional peaks which correspond to the 4J and 6J excited-state transitions of an isolated pair. The 2J peak is clearly visible up to 100 K and there is still a very weak peak at this position at 300 K.

The $\vec{Q}$ dependence of the 2J pair peak has been studied in detail at 4.3 K using higher resolution (E' = 1.450 THz) than employed for the measurements of Fig. 2. Distributions obtained at three $\vec{Q}$ values are

shown in Fig. 3. The frequency is essentially constant but the intensity of the peak is strongly $\vec{Q}$ dependent as shown in the lower part of Fig. 3. The intensity variation predicted by Eq. (2) is in excellent agreement with experiment. The intensity variations of the higher frequency peaks are also qualitatively as expected from the exact theory.

The frequencies and effective exchange constants for the observed transitions are listed in Table 1. The values of J for $KMn_{0.1}Zn_{0.9}F_3$ are considerably larger than the value[2] $J = 0.079 \pm 0.001$ THz for $KMnF_3$. This is largely attributable to the smaller lattice constant - 3.25%

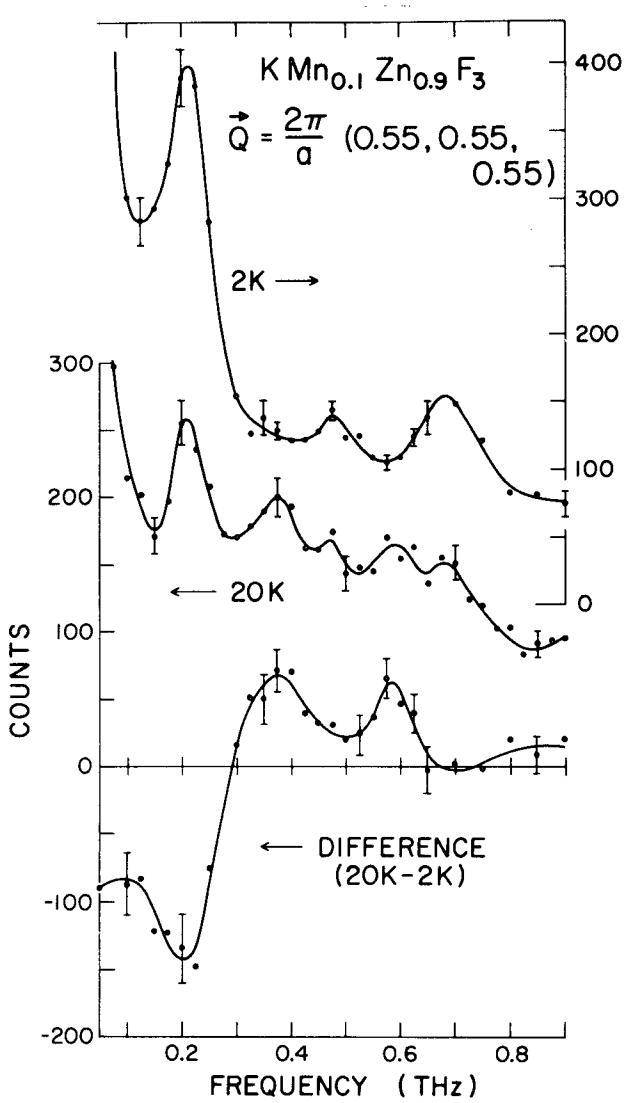


Fig. 2. Scattered-neutron distributions for $E' = 1.608$ THz and $\vec{Q} = 2\pi a^{-1}$ (0.55,0.55,0.55) in $KMn_{0.1}Zn_{0.9}F_3$ at 2 K and 20 K and their difference.

smaller for $KZnF_3$ than for $KMnF_3$. Krebs[6] has made a particularly accurate EPR determination of the exchange constant for Mn^{2+} pairs in $KMn_{0.01}Zn_{0.99}F_3$ since he was able to normalize his intensities to a normally-forbidden single-ion line. He obtained $J = 0.103 \pm 0.006$ THz, in excellent agreement with our value for the 2J transition.

The values of J obtained from the different transitions agree within the estimated errors. The values for the triplet tend to be slightly lower than for the 2J pair transition and this is consistent with the larger "local" lattice constant caused by the higher manganese concentration in a triplet. The excited-state pair transitions also give slightly lower values than the 2J transition as expected because of lower exchange striction[1] for excited states.

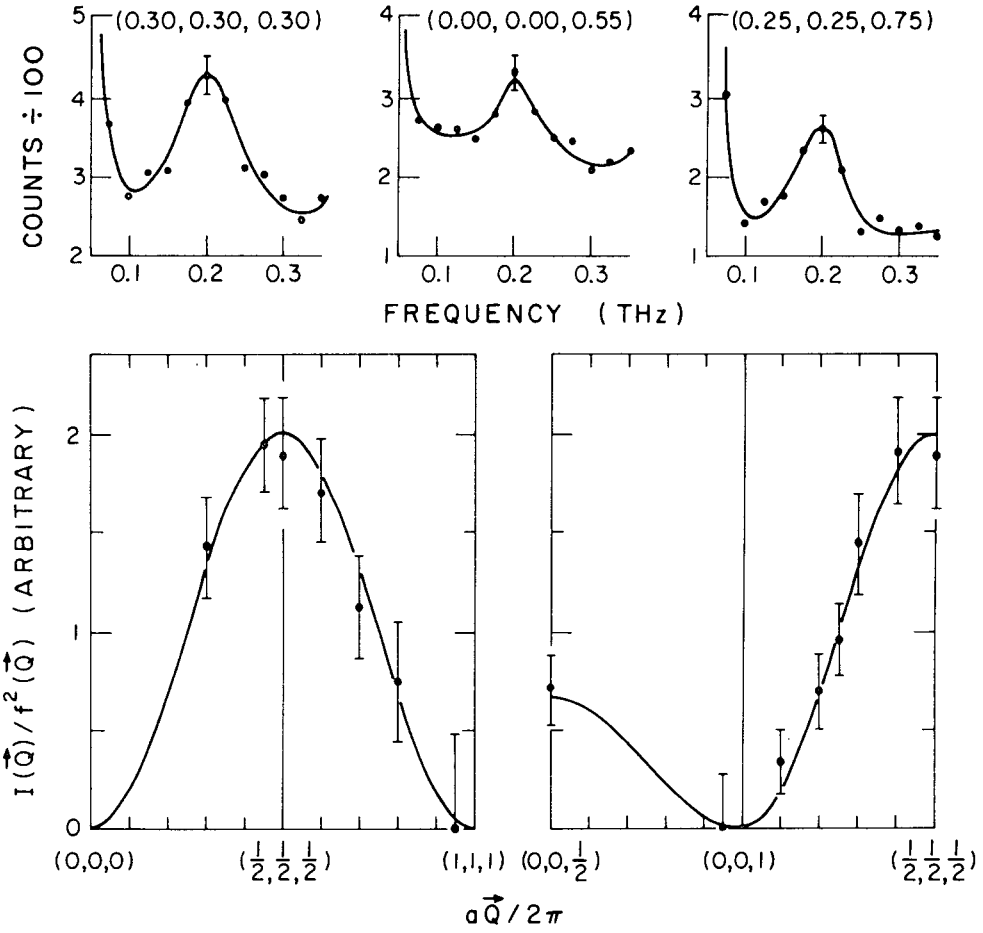


Fig. 3. Neutron scattering by the 2J pair transition at 4.3 K with $E' = 1.450$ THz: (Upper part) Distributions labelled with the values of $a\vec{Q}/2\pi$. (Lower part) Experimental intensities and the predictions (curve) of Eq. (2).

Table 1. Frequencies ν and exchange constants J for pair and triplet transitions (see Fig. 1).

Identification	ν(THz) Theory	ν(THz) Experiment	J(THz)
Pair $S = 0 \rightarrow S = 1$	2J	0.200 ± 0.008	0.100 ± 0.004
Triplet ($S_{13} = 5$, $S = 5/2$) $\rightarrow$ ($S_{13} = 4$, $S = 3/2$)	5J	0.478 ± 0.010	0.096 ± 0.002
Triplet ($S_{13} = 5$, $S = 5/2$) $\rightarrow$ ($S_{13} = 5$, $S = 7/2$)	7J	0.683 ± 0.014	0.098 ± 0.002
Pair $S = 1 \rightarrow S = 2$	4J	0.375 ± 0.015	0.094 ± 0.004
Pair $S = 2 \rightarrow S = 3$	6J	0.585 ± 0.015	0.098 ± 0.003

The results are very well described by the exact theory for isolated pairs and triplets and show that at $c = 0.1$ there is no vestige of spin-wave-like behavior or of the spin-dependent Ising resonances often used[3-5] as a guide to understanding the excitations in systems with higher concentrations of magnetic ions ($c \gtrsim c_o$). In contrast, Alben and Thorpe[3] have suggested that spin-wave theory based on the Néel state is applicable for $c < c_o$. Their numerical calculations for a computer-generated model of a square lattice gave rise to a peak at 5J in the density of states for Mn^{2+} ions which they associated with the 5J triplet transition. Our measurements and calculations show however that the dominant triplet peak is the 7J peak rather than the 5J peak. Since Alben and Thorpe do not obtain a 7J peak, we feel that one should treat with caution their suggestion that spin-wave theory is applicable in the region $c < c_o$.

We have shown that neutron-scattering techniques can be successfully applied to determine the exchange interactions between magnetic ions in small isolated clusters, and, for $KMn_{0.1}Zn_{0.9}F_3$, have determined J with somewhat better accuracy than can normally be obtained in EPR measurements. Considerably greater accuracy could be achieved with the neutron technique if desired. We have also, for the lowest pair transition, determined the structure factor which confirms the expected localized

character of the wave functions and the antiferromagnetic alignment of the spins.

The authors would like to acknowledge numerous stimulating discussions with M. Harvey and the invaluable technical assistance of H. Nieman, D. Tennant and M. Potter.

REFERENCES

1. See, e.g., J. Owen and E.A. Harris, in Electron Paramagnetic Resonance (edited by S. Geschwind) Ch. 6, Plenum Press, New York, 1972.
2. S.J. Pickart, M.F. Collins and C.G. Windsor, J. Appl. Phys. 37, 1054 (1966).
3. R. Alben and M.F. Thorpe, AIP Conf. Proc. 29 (in press).
4. See W.J.L. Buyers, D.E. Pepper and R.J. Elliott, J. Phys. C 6, 1933 (1973) and references therein.
5. See O.W. Dietrich, G. Meyer, R.A. Cowley and G. Shirane, Phys. Rev. Lett. 35, 1735 (1975) and E.C. Svensson, W.J.L. Buyers and T.M. Holden, AIP Conf. Proc. 29 (in press) and references therein.
6. J.J. Krebs, J. Appl. Phys. 40, 1137 (1969).

SPIN WAVE DISPERSION IN $Li_{0.13}Fe_{2.87}O_4$

V.C. Rakhecha, K.R. Rao and N.S. Satya Murthy
Solid State Physics Section, Nuclear Physics Division
Bhabha Atomic Research Centre, Trombay, Bombay 400085
India

ABSTRACT

The acoustic spin wave dispersion branch in a synthetic ferrite crystal, $Li_{0.13}Fe_{2.87}O_4$, has been measured in the $\langle 001 \rangle$ direction upto 0.55 of the Brillouin zone boundary. The effective intersublattice exchange constant J_{AB}, between the A and B sublattices has been evaluated to be -30.1 ± 0.75°K on the basis of the Heisenberg model with spin-only values for the moments and assuming zero intra-sublattice exchange. The assumption of small or zero B-B exchange is justified from the results of an earlier paramagnetic scattering study of the completely normal $ZnFe_2O_4$ in this laboratory. Comparison of the present measurements with those in Fe_3O_4 and $Li_{0.5}Fe_{2.5}O_4$ shows that the effect of substitutional replacement in Fe_3O_4 of Fe ions on B-sites by Li^+ ions is to increase the spin wave energy.

INTRODUCTION

The cation distribution in the ferrite $Li_{0.13}Fe_{2.87}O_4$ is

$$Fe^{3+}\left[Li^{+}_{0.13}\ Fe^{2+}_{0.74}\ Fe^{3+}_{1.13}\right] O^{2-}_4$$

Its composition is intermediate to that of Fe_3O_4 and $Li_{0.5}Fe_{2.5}O_4$ which respectively have the cation distributions

$$Fe^{3+}\left[Fe^{3+}\ Fe^{2+}\right] O^{2-}_4 \qquad \text{and} \qquad Fe^{3+}\left[Fe^{3+}_{1.5}\ Li^{+}_{0.5}\right] O^{2-}_4$$

The A-sites in all these ferrites are occupied by Fe^{3+} ions. The Li^+ ions go substitutionally to the B-sites and thus affect the cation distribution there. In particular the introduction of Li^+ ions on the

B-sites increases the proportion of Fe^{3+} ions at the expense of Fe^{2+} ions; for $Li_{0.5}Fe_{2.5}O_4$ only the Fe^{3+} ions are present. Spin wave measurements have been reported previously for Fe_3O_4 [1,2] and $Li_{0.5}Fe_{2.5}O_4$ [3] and interpreted [1,3,4] to deduce the inter-and intra-sublattice exchange constants in these ferrites. Measurements on $Li_{0.13}Fe_{2.87}O_4$ were thought to be interesting due to its intermediate composition. It is expected that the observed relative changes in spin wave dispersion and in the exchange constants should bear relation to the cation distribution on the B-sites.

EXPERIMENTAL

The crystal* used in the present measurements was cylindrical in shape with both the height and diameter approximately 28mm. All the measurements were made with the $\langle 110 \rangle$ axis vertical and about the Brillouin zone centred on the (004) reciprocal lattice vector on a triple axis unpolarised neutron spectrometer. The constant E and constant $\vec{Q}$ methods were employed and neutron groups were measured for the wave vector $\vec{q}$ of the spin waves along the $\langle 001 \rangle$ direction. During a scan the incident energy was kept fixed. The crystal was aligned and rigidly placed between the pole pieces of an electromagnet which provided a vertical field of $\sim$2 Koe at the sample. Most of the measurements were made without the field but some were done both with and without the field to qualitatively distinguish spin wave scattering from the phonon scattering. A reduction in scattering with the field on as compared to without the field was taken to indicate spin wave scattering. The largest reduced wave vector of spin waves (acoustic branch) measured was $qa/2\pi = 0.55$ (a = cell parameter = 8.33 Å).

---

*The crystal was kindly loaned by Dr. Frank. J. Bruni, Research Materials Program, Oak Ridge National Laboratory, USA.

RESULTS AND DISCUSSION

The experimental points on the dispersion curve are shown in fig. 1. The continuous curve in the figure is obtained by fitting a thoretical expression as explained below. The spin wave dispersion relations have been worked out for Fe_3O_4 by several workers[5,6] on the basis of the Heisenberg model. There are six spin wave branches including the acoustic branch. Situation in $Li_{0.13}Fe_{2.87}O_4$ is complicated by the simultaneous presence of Li^+, Fe^{3+} and Fe^{2+} ions on the B-sites. We have interpreted the present measurements by using an average spin value $S_B = 2.1525$ for the B-sites and then adopting the spin wave theory for Fe_3O_4 [5]. The effective exchange integral J_{AB} at room temperature, between the A and B sublattices, has been evaluated by fitting the following expression for the spin wave energy ($\hbar\omega$) to the experimental points (with $\vec{q}$ along $\langle 001 \rangle$)

$$\hbar\omega = 12\, J_{AB} \Big| (S_A - 2S_B)/2 - 1/3\,(J_{BB}S_B - J_{AA}S_A)\gamma/J_{AB} + \Big\{ \Big[(S_A + 2S_B)/2 - 1/3\,(J_{BB}S_B + J_{AA}S_A)\gamma/J_{AB} \Big]^2 - 2/9\, S_A S_B \beta^2 \Big\}^{\frac{1}{2}} \Big|$$

where $\gamma = 1 - \cos(qa/4)$ and $\beta = 2\cos(qa/4) + \cos(3qa/4)$

The value of J_{AB} is found* to be $-30.1 \pm 0.75\,^{\circ}K$ with J_{AA} and J_{BB} assumed zero. An attempt to extract J_{AA} and J_{BB} was not successful pointing to the need for measuring the acoustic branch right up to the zone boundary

*No resolution correction has been included at present in the treatment of data. This may be important however as suggested by systematically higher energies in low q region. A zero energy gap at q=0 was assumed apriori in the analysis.

and in the low q region and also the optical branches[4]. The spin wave energies in $Li_{0.13}Fe_{2.87}O_4$ are seen to be slightly higher than in Fe_3O_4 but lower than in $Li_{0.5}Fe_{2.5}O_4$ as expected also from the behaviour of Neel temperatures (953°K in $Li_{0.5}Fe_{2.5}O_4$ and 848°K in Fe_3O_4). The exchange constants in the three ferrites mentioned here are compared in Table 1.

Table 1. Exchange Constants in $Li_{0.13}Fe_{2.87}O_4$, Fe_3O_4 and $Li_{0.5}Fe_{2.5}O_4$

Substance	J_{AA}(°K)	J_{AB}(°K)	J_{BB}(°K)	Ref.
$Li_{0.13}Fe_{2.87}O_4$	assumed 0	-30.1±0.75	assumed 0	present
Fe_3O_4	-17.9±7.0	-28.1±0.45	3.59±0.8	(4)
Fe_3O_4	assumed 0	-27.84	assumed 2.78	(5)
$Li_{0.5}Fe_{2.5}O_4$	-11.6	-30.17	-25.5	(3)

If AA and BB interactions are ignored altogether as is done here, it is suggested from the J_{AB} values that $J_{AB}(Fe^{3+} - Fe^{3+})$ is stronger than $J_{AB}(Fe^{3+} - Fe^{2+})$. It has been argued[3,4] (as seen in Table 1) that J_{AA} and J_{BB} may be of comparable magnitude to J_{AB}. It, however, appears unlikely that $J_{BB}(Fe^{3+} - Fe^{3+})$ is so large as deduced in Ref. 3. An estimate of $J_{BB}(Fe^{3+} - Fe^{3+})$ of only -1.02°K, is directly available from the paramagnetic scattering study[7] of the completely normal $ZnFe_2O_4$ where this (J_{BB}) is the only exchange constant opertive. Additional investigations would be required to satisfactorily resolve these points. The deduced value of J_{AB} however is fairly correct as it does not sensitively depend on the choice of J_{AA} and J_{BB}.

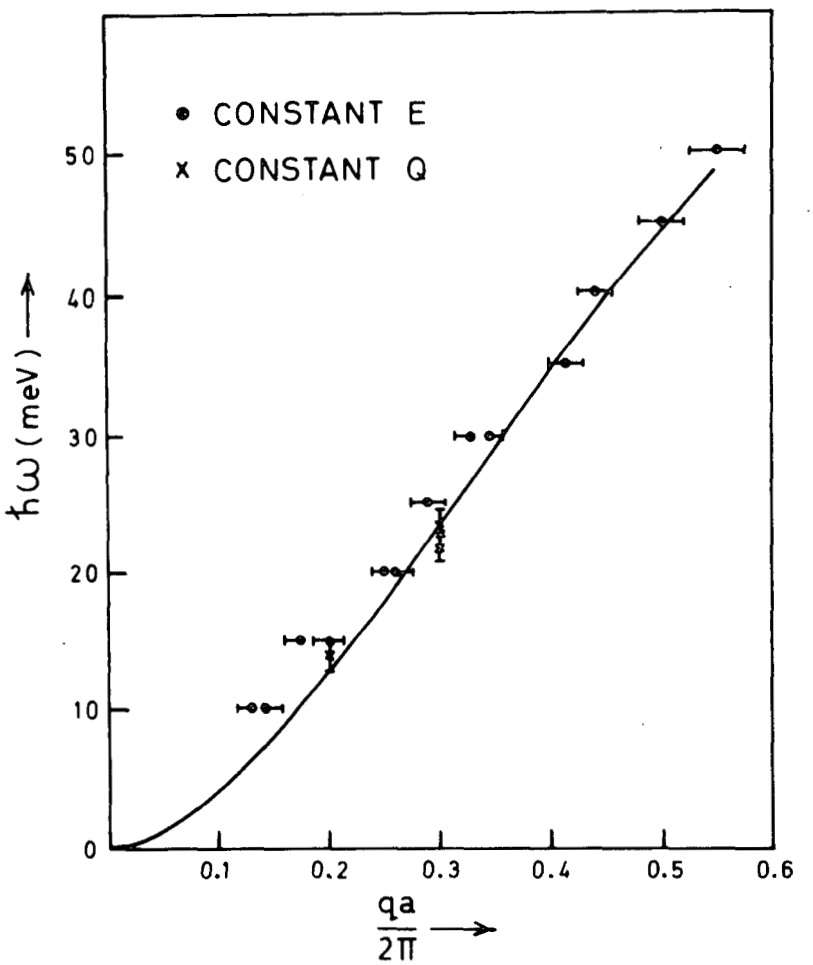


Fig. 1. Spin Wave Dispersion in $Li_{0.13}Fe_{2.87}O_4$

REFERENCES

1. B.N. Brockhouse and H. Watanabe, Inelastic Scattering of Neutrons in Solids and Liquids, IAEA, 2, p.297, 1963.
2. H. Watanabe and B.N. Brockhouse, Phys. Letts. 1, 189, (1962).
3. A. Wanic, T. Riste and O. Steinsvoll, Int. J. Magnetism 3, 349 (1972).
4. K.T. Moglestue, Neutron Inelastic Scattering, IAEA, 2, p.117, 1963.
5. M.L. Glasser and F.J. Milford, Phys. Rev. 130, 1783 (1963).
6. T.A. Kaplan, Phys. Rev. 109, 782 (1958).
7. N.S. Satya Murthy, L. Madhav Rao, M.G. Natera and S.I. Youssef, Ferrites, Proceedings of the International Conference, p. 64, 1970.

SPIN WAVES IN FERRIMAGNETIC $ErFe_2$

J. J. Rhyne
Institute for Materials Research, National Bureau of Standards
Washington, DC 20234

N. C. Koon and J. B. Milstein
Naval Research Laboratory, Washington, DC 20375
and National Bureau of Standards

H. A. Alperin
Naval Surface Weapons Center, White Oak, MD 20910
and National Bureau of Standards

ABSTRACT

Spin excitations in a single crystal of the rare earth Laves phase compound $ErFe_2$ have been studied using inelastic neutron scattering. Measurements were made in the ordered state at room temperature (Curie temperature = 574K) and revealed one acoustic and two optic modes. The lower optic mode is non-dispersive with energy of 5 meV, and is nearly degenerate with the acoustic mode at the zone boundary. Dispersion in this mode is controlled by the rare earth-rare earth exchange interaction which was found to be nearly zero for this compound. The upper optic mode exhibits a gap of 8.75 meV at the zone center and has a wave-vector dependence defined by the Fe-Fe exchange and which is approximately equal to that in Fe metal. A nearest neighbor spin wave model has been developed for which the calculated spin wave energies are in excellent agreement with those observed for all three modes. The model also predicts three additional optic modes (two are degenerate) at energies above 100 meV which are not significantly populated.

INTRODUCTION

The group of compounds RFe_2, where R is a heavy rare earth, crystallize in the close packed Laves phase or $MgCu_2$ structure. These compounds have high Curie temperatures (T_c>550K) and show extraordinarily large magneto-elastic interactions[1]. The iron moments are ferrimagnetically aligned, and are antiparallel to the R moment (ferrimagnetic order). The iron moment as determined from both bulk measurements[1] and neutron scattering[2] on polycrystalline samples shows an anomalous reduction from

the expected $2\mu_B$ to approximately $1.6\mu_B$. The rare earth moments have their free ion values.

In this paper we will discuss the results of an experimental and theoretical investigation of spin waves in $ErFe_2$. The results will be compared to measurements on the analogous compound $Ho_{.88}Tb_{.12}Fe_2$[3]. Inelastic scans along three principal axis directions were made at room temperature (T_c for $ErFe_2$ = 574K)[4] on a single crystal approximately 0.5 cm^3 using a triple axis spectrometer at the National Bureau of Standards Reactor. Fixed incident energies of 13 and 35 meV obtained from the 002 and 004 reflections of a curved pyrolytic graphite monochrometer were used with a variety of collimation conditions to optimize resolution and intensity for the modes examined. Flat graphite was used as an analyzer.

EXPERIMENTAL RESULTS

$ErFe_2$ has 6 atoms per unit cell with the Er atoms arranged on sites of tetrahedral symmetry and the Fe atoms on octahedral sites. One thus expects six spin wave branches, one acoustic and five optic. As the results in Figure 1 show only three of these branches have energies easily studied by neutron scattering. The model calculation discussed later predicts the remaining three modes (two are degenerate) to have energies of approximately 200-300 meV. The data in Figure 1 for spin waves propagating in the [q,q,o] and [q,q,q] directions show isotropic spectra consisting of (1) an acoustic mode with no measurable anisotropy energy gap, (2) a very flat optic mode of energy 5.1 meV degenerate with the acoustic mode at the zone boundary and (3) a highly dispersive higher optic mode starting from an energy gap of 8.75 meV. This latter mode has quadratic dispersion ($\hbar\omega=D|q|^2$) in the q range shown with D=240 meV-A^2 only slightly smaller than pure iron metal[5] (D=280 meV-A^2) and would represent the iron acoustic mode in the absence of rare earth spins and the R-Fe exchange interaction. This mode is shown over only a small portion of the Brillouin zone due to the very high energy transfers involved. The model calculation given an energy of 172 meV at the zone boundary. The acoustic mode in $ErFe_2$ is not purely quadratic (even

at small q) in contrast to that reported for $Ho_{.88}Tb_{.12}Fe_2$. The vanishing dispersion in the lower optic mode is a consequence of negligible Er-Er exchange in this compound; rather the Er simply sits in the molecular field from the iron spins. Data were also taken in the [q,o,o] direction which again indicated no evidence of a dependence of the dispersion on propagation direction.

MODEL CALCULATION

A nearest neighbor interaction spin-wave model has been applied to explain the data of Figure 1. The Hamiltonian included exchange and crystal field terms (the latter are negligible at room temperature) and had the form

$$H = \sum_{n,m} \sum_{j,j} 2J_{ij}^{nm} \vec{S}_i^n \cdot \vec{S}_j^m + H_{c.f} \qquad (1)$$

where J_{ij}^{nm} describes the interaction between the i'th ion of spin S_i in cell n with the j'th ion of spin S_j in cell m (i and j thus range from 1 to 6 and n, m were restricted to only nearest neighbors). The spin wave energies were calculated from Fourier transforms of the equations of motion for the spin raising and lowering operators $S^{\pm}=S_x \pm iS_y$ (Note: S for the rare earth site is replaced by the total momentum J) as follows (omitting crystal field terms):

$$\hbar\omega(q)\ S_i^+(q) = -2\sum_{j=1}^{6} \{S_i^Z J_{ij}(q) S_j^+ - S_j^Z J_{ij}(o) S_i^+ \} \qquad (2)$$

$$\text{where } J_{ij}(q) = \sum_{mj} J_{ij}^{nm} \exp\ [i\vec{q}\ (\vec{r}_{mj} - \vec{r}_{ni})] \qquad (3)$$

and the six equivalent relations for S^-. In fitting the spectra the spins on the Er and Fe atoms were fixed at 3.6 μ_B and 0.66 μ_B respectively as obtained from a combination of neutron diffraction and bulk magnetization data[1-2]. At the zone center the energies of the two optic modes are given simply by $\omega_1^{op}=24J_{Er\text{-}Fe}S_{Fe}^Z$ and $\omega_2^{op}=12J_{Er\text{-}Fe}(S_{Er}^Z-2S_{Fe}^Z)$ respectively. These relations and the known values of S^Z thus allowed the rare earth-iron exchange constant $J_{Er\text{-}Fe}=-0.32$ meV to be determined. The remaining exchange constant $J_{Fe\text{-}Fe}=30$ meV was adjusted to obtain the

correct dispersion in the higher optic mode. The corresponding values for $Ho_{.88}Tb_{.12}Fe_2$ were J_{R-Fe}=-0.42 meV and J_{Fe-Fe}=+23 meV with J_{R-R} equal to zero in both cases to an accuracy of approximately ±.01 meV as determined from the maximum dispersion in the lower optic mode. Within the restricted q-range of the higher energy data, this model fits the experimental results extremely well. Its success in predicting accurately the E and q dependence of the remaining magnon branches is not known.

These results on $ErFe_2$ plus the previous study on $Ho_{.88}Tb_{.12}Fe_2$[3] allow one to check the dependence of the effective exchange constant $\mathcal{J}_{R-Fe}$ on the Landé "g" factor of the rare earth (R). Including the effects of strong spin-orbit interactions, the effective Hamiltonian for the rare earth-iron exchange can be written[6]

$$H = 2\sum_{ij} \mathcal{J}'_{ij} \quad (g_J-1) \quad J_i \cdot s_j \equiv 2\sum_{i,j} \mathcal{J}_{i,j} J_i \cdot s_j$$

and summed over appropriate sites, where J_i is the total angular momentum of the rare earth ion, and s_j is the Fe spin.

The $\mathcal{J}'_{ij}$ is the bare exchange interaction between the rare earth and the iron spins and physically arises from an interaction between the local 4f spin and the iron exchange-polarized conduction bands. Thus $\mathcal{J}'_{ij}$ is expected to be independent of the particular rare earth ion and then the effective exchange constant $\mathcal{J}_{R-Fe}$ given in Figure 1 should scale as g_J-1 [$\mathcal{J}_{ij} \equiv (g_J-1)\mathcal{J}'_{ij}$] from one rare earth to another.

For the $ErFe_2$ and $Ho_{.88}Tb_{.12}Fe_2$ compounds the ratio of g_J-1 is: $(g_J-1)_{Er}/(g_J-1)_{Ho_{.88}Tb_{.12}}$ =.71 while the ratio of the lower optic mode energies (proportional to the $\mathcal{J}_{R-Fe}$ assuming the same $\langle S_Z \rangle_{Fe}$) is 0.68, confirming within experimental uncertainty the predicted relationship.

Lower temperature measurements on $ErFe_2$ at 4K and 77K show a significant renormalization of the spin wave energies greatly in excess of that calculated for conventional crystal field effects and point to a strong contribution of magneto-elastic origin. This study will be reported separately[7].

REFERENCES

1. A. E. Clark, A.I.P. Conf. Proc. Series 18, 1015 (1974).
2. J. J. Rhyne, to be published; M. O. Bargouth and G. Will, Journal de Physique C1 32, 675 (1971).
3. R. M. Nicklow, N. C. Koon, C. M. Williams, and J. B. Milstein, Phys. Rev. Letters 36, 532 (1976). (Note: Due to a difference in definition of the Hamiltonian, exchange constants quoted in this reference are larger by a factor of two than those in the present paper.)
4. E. Burzo, Z. Angew, Phys. 32, 127 (1971).
5. H. A. Mook and R. M. Nicklow, Phys. Rev. B 7, 336 (1973).
6. A similar analysis was used in interpreting Mössbauer data by Atzmony, Dariel, Bauminger, Lebenbaum, Nowik and Ofer, Phys. Rev. Letters 28, 244 (1972).
7. To be published in proceedings of the International Conference on Magnetism, Amsterdam, 1976.

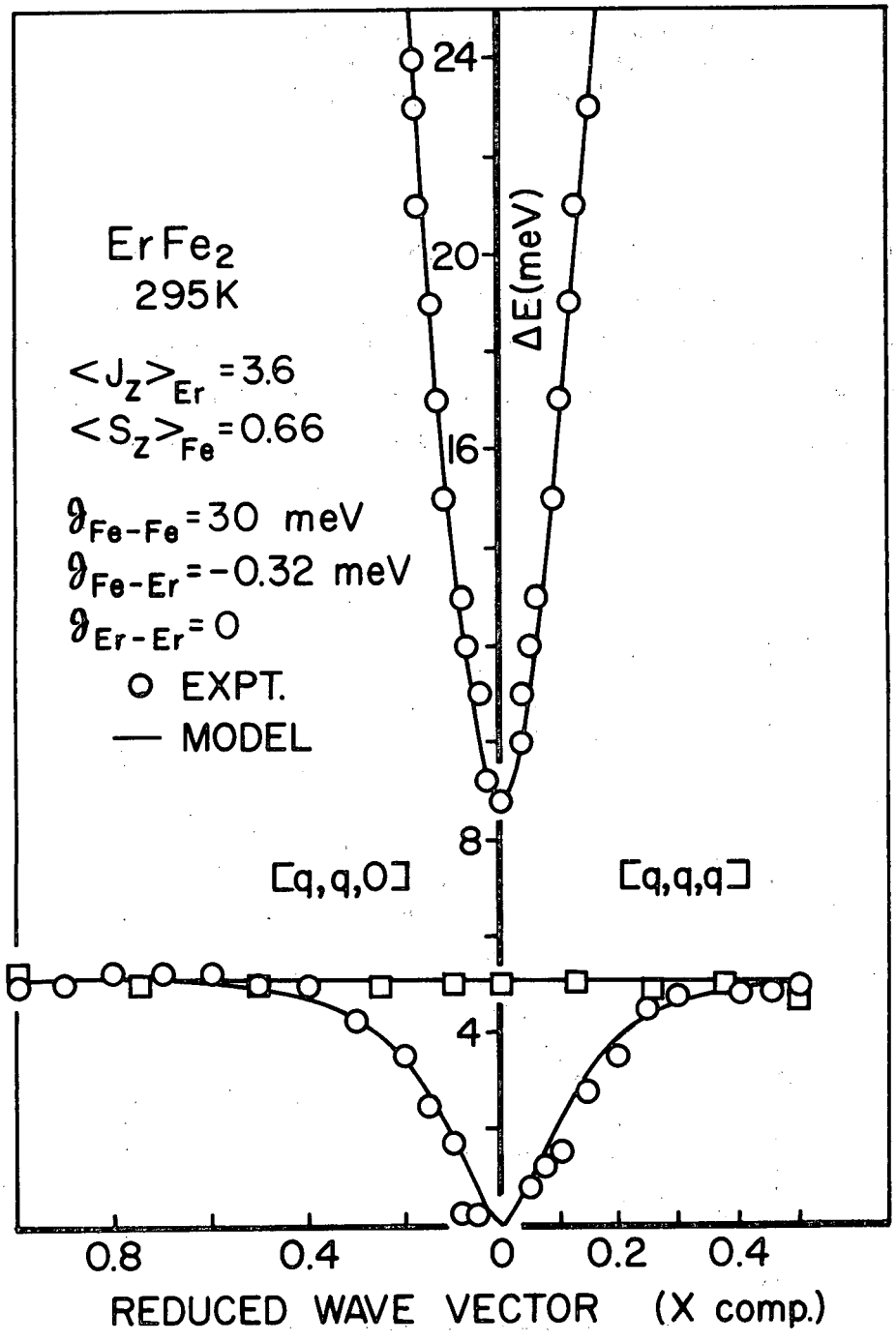


Fig. 1, Magnon dispersion of $ErFe_2$ along [q,q,0] and [q,q,q] symmetry directions. The acoustic mode was measured about the (111) and (220) lattice reflections, the lower optic mode at (200), and the higher optic mode at (220) and (222) reflections. The solid line is the result of a nearest neighbor spin wave calculation described in the text.

SPIN WAVE DISPERSION IN Tb-Y ALLOYS†

N. Wakabayashi and R. M. Nicklow
Solid State Division, Oak Ridge National Laboratory
Oak Ridge, Tennessee 37830

ABSTRACT

The alloys Tb_cY_{1-c} ($0.05 \lesssim c \lesssim 0.85$) have spiral magnetic structures with the moments confined in the plane parallel to the basal plane of the hexagonal lattice. The spin wave dispersion curves along the c*-direction have been measured for alloys with c = 0.1, 0.5, 0.76, and 0.85. Some of the results are shown in Fig. 1. In the mean lattice approximation the

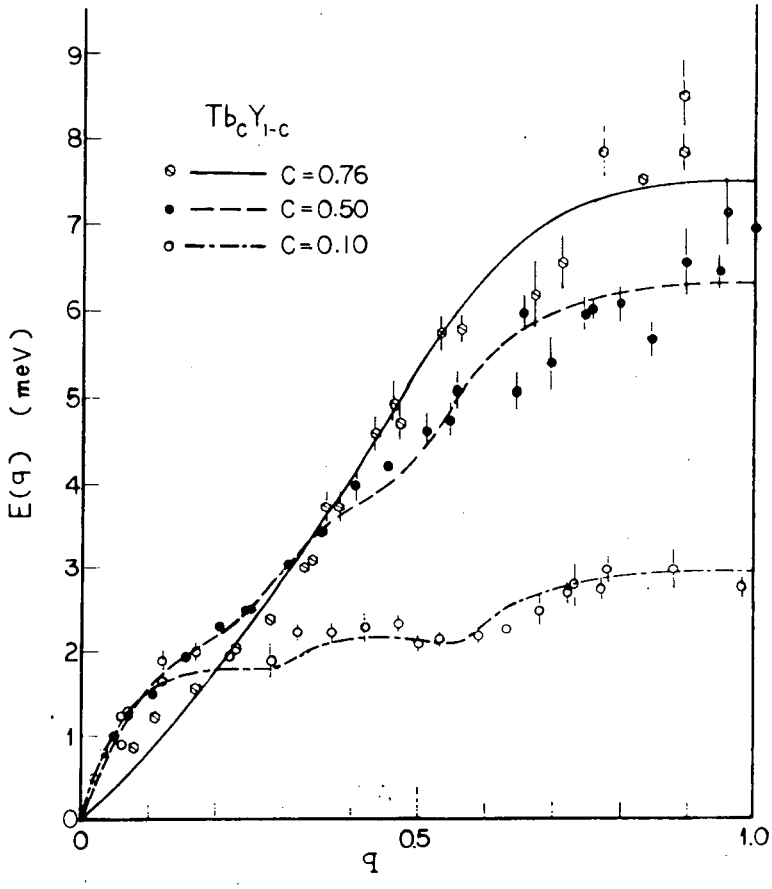


Fig. 1. Spin wave dispersion curves for Tb-Y alloys along the c*-direction.

†Operated by Union Carbide Corporation for the USERDA.

dispersion relation along the c*-direction is given[1] by

$$E(q) = J([cJ(q_o) - \frac{1}{2}\{J(q_o+q) + J(q_o-q)\}][cJ(q_o) - cJ(q) + 2B])^{1/2} \quad (1)$$

where J is the angular momentum and is equal to 6 for Tb, c is the concentration of the magnetic atoms. B is the axial crystal field anisotropy constant, and q_o is the wave vector that characterizes the spiral structure. $J(q)$ is the Fourier transform of the RKKY exchange interaction and is proportional to the generalized susceptibility $\chi(q)$ of the conduction electrons. The most straightforward analysis of the data can be carried out by expanding $J(q)$ in a Fourier series with the Fourier coefficients as the fitting parameters. However, since the RKKY interaction is rather long-ranged, a large number of coefficients may be needed in order to reproduce the experimental results. An alternative approach which we have explored is to assume a certain functional form for $\chi(q)$, and hence for $J(q)$, containing only a few adjustable parameters. The microscopic calculations of $\chi(q)$ for Y seem to indicate the existence of a prominent peak due to the nesting of the Fermi surface. This peak may be retained to some extent in the alloys. Therefore, $\chi(q)$ may be assumed to be similar to the susceptibility function for a one-dimensional system but modified owing to the incomplete nesting. One functional form that simulates the nesting is

$$\chi(q) \propto \frac{2k_F q}{q^2+(\gamma q^2)^2} \log\left[\frac{(2k_F+q)^2+(\gamma q^2)^2}{(2k_F-q)^2+(\gamma q^2)^2}\right] \quad (2)$$

where γ is a measure of the incompleteness of the nesting. The data have been fit by $J(q)$ given by

$$J(q) = P\sum_{\tau}\chi(q+\tau) \quad (3)$$

where χ is given by Eq. 1 and τ is a reciprocal lattice vector. P, γ, and k_F are the fitting parameters of the model. Best fits were obtained for B = 0.25 $\pm$ 0.02 meV. The values for the parameters determined by the fit are given in Table 1, and the $J(q)$'s are shown in Fig. 2. The spin wave

energies calculated from the model are shown in Fig. 1 by the lines. Although the functional form for $\chi(q)$ given by Eq. 2 gives reasonable fits as indicated by χ^2 in Table 1, it cannot reproduce the second peak known to exist in $J(q)$ near $q = 0.8$ for pure Tb. Thus it is necessary to introduce more parameters in the model, which may not be any more advantageous than the straightforward Fourier series analysis. The result of the latter analysis will be reported elsewhere.

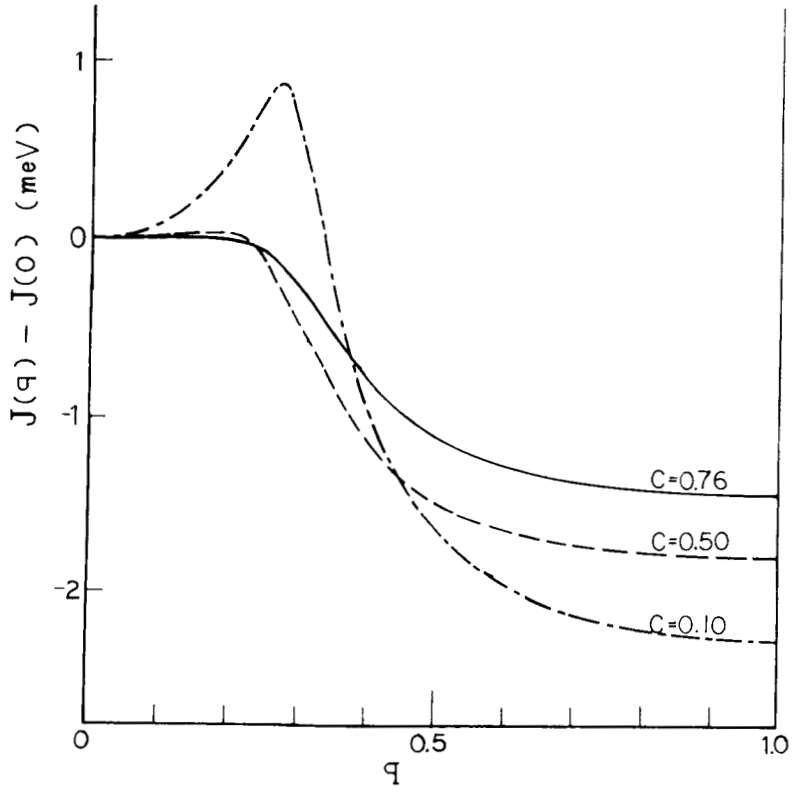


Fig. 2. Exchange function for Tb-Y alloys.

TABLE 1. MODEL PARAMETERS AND χ^2

c	P	$2k_F$	γ	χ^2
0.10	2.54	0.30	0.50	2.2
0.50	1.84	0.33	1.43	1.3
0.76	1.51	0.46	1.53	1.9

1. N. Wakabayashi and R. M. Nicklow, Phys. Rev. B10, 2049 (1974).

THEORETICAL CALCULATION OF THE EXCHANGE INTEGRAL FOR EUROPIUM

J. F. Cooke and H. L. Davis
Solid State Division, Oak Ridge National Laboratory*
Oak Ridge, Tennessee 37830

ABSTRACT

Results are presented of *ab initio* calculations of the exchange integral $J(\vec{q})$ for metallic europium. These calculations are based on the s-f exchange interaction between the localized 4f electrons and the conduction electrons. Reasonably good agreement is found between the calculational and experimental values of the interlayer turn angle existing in europium's spiral-spin configuration. Interestingly, it is found that band structure matrix elements are responsible for the spiral-spin configuration observed in europium, rather than density-of-states effects arising from Fermi surface nesting.

INTRODUCTION

As has been inferred from a wide variety of studies,[1] the s-f exchange interaction between the localized 4f electrons and the conduction electrons is thought to be the basic ingredient in any proper theoretical description of the magnetic properties of the rare-earth metals. As shown by the work of Ruderman, Kittel, Kasuya, and Yosida (RKKY),[1] this direct s-f exchange coupling leads to a long-range, indirect interaction between the localized 4f moments which, in turn, is thought to be responsible for the wide variety of magnetic ordering and related phenomena which have been observed in the rare-earth metals. However, practically all attempts to use the RKKY model to "explain" the magnetic properties of rare-earth metals have either invoked phenomenological parameters or performed calculations where some band structural details were drastically oversimplified. Although sometimes proving to be useful for correlating experimental information, such semiempirical uses of

---

*Operated by Union Carbide Corporation for the USERDA.

the RKKY model do not really serve to provide definitive tests of the model's quantitative validity. In fact, the very nature of the s-f exchange interaction probably implies that definitive tests of the RKKY model must necessarily include results from the calculations of experimental verifiable quantities from realistic, rare-earth electronic band structures. To such an eventual end, we present here preliminary results from a research program motivated to furnish calculational tests of the RKKY model. The results presented herein pertain to europium, which we specifically chose for our initial investigations because it possesses the calculational simplifications of zero orbital moment and the bcc lattice structure.

THE EXCHANGE INTEGRAL $J(\vec{q})$

In its simplest form, the RKKY model reduces to an isotropic Heisenberg model having an exchange integral $J(\vec{q})$. This $J(\vec{q})$ is defined in terms of the s-f exchange matrix element and the relevant metal's electronic band structure; i.e., in principle, theoretical predictions of $J(\vec{q})$ are calculable directly from band structural information. To have quantities to compare with theory, neutron diffraction experiments may be used to obtain empirical information about $J(\vec{q})$. Extensive experimental $J(\vec{q})$ information may be obtained by analyzing spin-wave dispersion curves, but, if these are not available, some partial information can be inferred from any knowledge concerning the metal's magnetic structure. For example, spin-wave curves are not presently available for europium, so empirical $J(\vec{q})$ information is not available from this technique. However, europium is known[2] to order in a spiral-spin configuration, so $J(\vec{q})$ should have its maximum value at a $\vec{q}$ corresponding to the spiral wave vector. In summary, since the possibility exists to obtain RKKY $J(\vec{q})$ predictions which may be compared with empirical information, $J(\vec{q})$ represents a quantity of fundamental importance in tests of the validity of the s-f exchange model for the rare-earth metals.

Europium has zero orbital moment and only one atom per unit cell (bcc structure). Using these simplifications, the RKKY model's theoretical expression for $J(\vec{q})$ reduces to[3]

$$J(\vec{q}) = \frac{2}{N} \sum_{n,n',\vec{k}} |I_{nn'}(\vec{k},\vec{k}+\vec{q})|^2 \frac{f_{n\vec{k}} - f_{n'\vec{k}+\vec{q}}}{\varepsilon(n'\vec{k}+\vec{q}) - \varepsilon(n\vec{k})} , \quad (1)$$

where the $\vec{k}$ sum is on N $\vec{k}$ values in the total Brillouin zone (BZ), $\varepsilon(n\vec{k})$ is the energy of an electron in band n with wave vector $\vec{k}$, and $f_{n\vec{k}}$ is the Fermi occupation number. $I_{nn'}(\vec{k},\vec{k}+\vec{q})$ is the s-f exchange matrix element, which we have taken in this initial work to be of the unscreened form

$$7\, I_{nn'}(\vec{k},\vec{k}+\vec{q}) = \sum_{m=-3}^{+3} \iint \psi^*_{n\vec{k}}(\vec{r}_1)\phi^*_{fm}(\vec{r}_2) \frac{1}{r_{12}} \phi_{fm}(\vec{r}_1)\psi_{n'\vec{k}+\vec{q}}(\vec{r}_2) d^3r_1 d^3r_2. \quad (2)$$

Here the $\psi_{n\vec{k}}$ are band wave functions, while the ϕ_{fm} are the 4f orbitals.

As may be seen from Eqs. (1) and (2), in order to obtain theoretical predictions for $J(\vec{q})$ detailed calculational tasks must be performed. Not only must electronic band structure calculations be done to obtain the $\psi_{n\vec{k}}$, $\varepsilon(n\vec{k})$, and $f_{n\vec{k}}$ factors, but the BZ sum in Eq. (1) also requires extensive numerical calculations. Some aspects of the numerical techniques and procedures used in our calculations are briefly discussed below.

CALCULATIONAL DETAILS

The required band structure features were calculated by use of a crystal potential generated from a lattice superposition of atomic charge densities. The charge densities were obtained from a relativistic Hartree-Fock-Slater calculation for europium in the $4f^7 6s^2$ configuration. This potential was used in conjunction with the nonrelativistic KKR method to obtain a first principles europium band structure at 91 $\vec{k}$ points in the irreducible 1/48-th of the BZ. These KKR results then were fitted to a second-neighbor, s-p-d Slater-Koster model, with the fit resulting in a rms deviation of 4 mRy between the KKR and Slater-Koster bands. The Fermi energy was determined by using QUAD techniques applied to the Slater-Koster bands. For comparison, the band structure used in our investigation is quite similar to an europium band structure obtained by Freeman and Dimmock[4] using the nonrelativistic APW method. At the same time, the Fermi surface obtained in our work has topology similar to the one calculated by Andersen and Loucks[5] by the relativistic APW method.

The s-f matrix elements of Eq. (1) were evaluated using conduction band wave functions and 4f orbitals obtained[6] from atomic Hartree-Fock calculations. The band wave functions we employed were a combination of Slater-Koster, s-p-d expansion coefficients and radial functions obtained by integration of the radial equation which contains the crystal potential. The n and n' sums of Eq. (1) were each performed over the six s,d hybridized bands of europium's electronic structure. The required BZ integration was performed using the tetrahedron method.[7,8] The results presented in this report were obtained using 1024 tetrahedra in the irreducible 1/48-th of the BZ. However, from work presently in progress where a larger number of tetrahedra are being used, there are indications that the results for 1024 tetrahedra are numerically converged to within a few percent for those $|\vec{q}|$ greater than about 0.2 $(2\pi/a)$. To date, we have performed $J(\vec{q})$ calculations for $\vec{q}$ along only the [100] direction.

RESULTS AND DISCUSSION

In order to investigate the role played in $J(\vec{q})$ by the s-f matrix elements, we have evaluated $J(\vec{q})$ by using both matrix elements obtained from the band structure wave functions via Eq. (2) and a constant matrix element approximation [i.e., arbitrarily setting $I_{nn'}(\vec{k},\vec{k}+\vec{q}) = 1$]. The results obtained using constant matrix elements are given in Fig. 1, while those obtained using matrix elements calculated from band wave functions are given in Fig. 2. An inspection of these figures dramatically illustrates the importance of considering the inclusion of matrix elements in any $J(\vec{q})$ calculation, and clearly shows that the constant matrix element approximation is inadequate for europium.

The $J(\vec{q})$ of Fig. 1 is almost constant with $|\vec{q}|$, while the one of Fig. 2 shows a pronounced maximum at $|\vec{q}| \simeq 0.375\ (2\pi/a)$. Thus, matrix elements are more important in producing structure in europium's $J(\vec{q})$ than density of states effects arising from Fermi surface nesting. That is, if nesting were an important effect some structure would appear in Fig. 1. So we conclude that nesting effects are not responsible for the spiral-spin configuration found experimentally in europium's magnetic structure. It is to be noted that this conclusion is diametric to speculations of

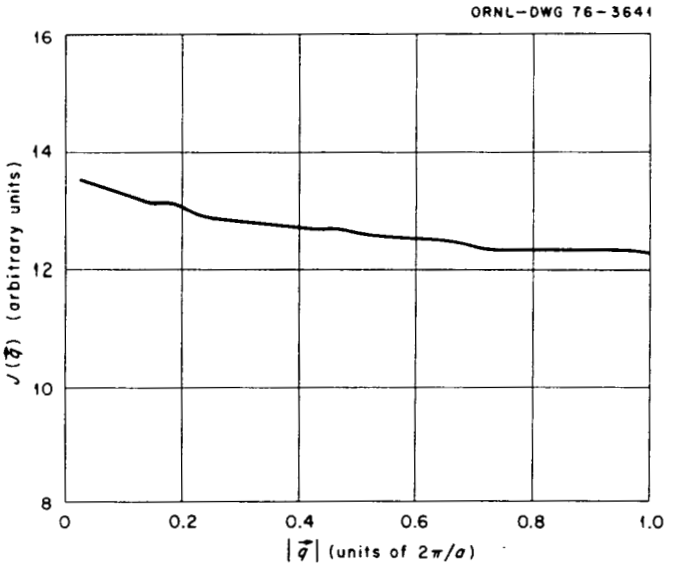


Fig. 1. Exchange integral along the [100] direction calculated using the constant matrix element approximation.

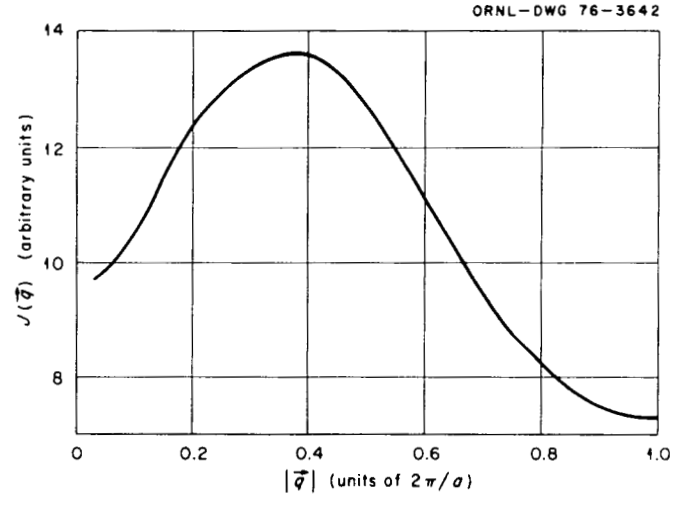


Fig. 2. Exchange integral along the [100] direction as obtained using matrix elements calculated from band structure wave functions.

Andersen and Loucks,[5] who attempted to account for the spiral-spin configuration by nesting arguments. In this regard, it is interesting that Lindgård *et al.*[9] have concluded that matrix elements are at least as important as Fermi surface nesting in determing the $\vec{q}$ dependence of gadolinium's $J(\vec{q})$.

Nereson *et al.*[2] have obtained polycrystalline neutron diffraction data which show europium is antiferromagnetic below 91°K. These authors also deduced from their data a model which implies a helical spin arrangement where the moments are parallel to, and the screw axis normal to a cube face. The interlayer turn angle was found to vary only slightly with temperature, and had a value of 50° per layer at 4.2°K. A moot, but perhaps interesting, point is that the constant matrix element calculation shown in Fig. 1 would imply europium is ferromagnetic, since its maximum occurs at $\vec{q} = 0$. However, the results of Fig. 2 (matrix elements included) have a maximum at $|\vec{q}| = 0.375\ (2\pi/a)$, which corresponds to a spiral with a turn angle of 67°. Furthermore, we have found that arbitrarily lowering the Fermi energy by 0.01 Ry, but keeping the bands fixed, produces a calculated turn angle equal to the experimental value of 50°. Thus, it appears that very modest changes in the electronic band structure could produce complete agreement between experimental and calculational values of the turn angle. So given the uncertainties present in band structure calculations and the lack of precise experimental information concerning europium's bands, we conclude that our calculations have yielded reasonably good agreement with presently available experimental information concerning europium's $J(\vec{q})$. This conclusion adds support to the view that the RKKY model is capable of providing an eventual quantitative description of magnetic ordering in rare-earth metals.

REFERENCES

1. See the articles and their references in Magnetic Properties of the Rare-Earth Metals, edited by R. J. Elliot (Plenum, London, England, 1972).
2. N. G. Nereson, C. E. Olsen, and G. P. Arnold, Phys. Rev. 135, A176 (1964).
3. T. A. Kaplan and D. H. Lyons, Phys. Rev. 129, 2072 (1963).
4. A. J. Freeman and J. O. Dimmock, Bull. Am. Phys. Soc. 11, 216 (1966). See Fig. 6-20 of A. J. Freeman, Chap. 6 of reference 1 above.
5. O. K. Andersen and T. L. Loucks, Phys. Rev. 167, 551 (1968).
6. C. F. Fischer, Rept. Dept. Math., Univ. of British Columbia, 1968.

7. G. Lehmann and M. Taut, Phys. Status Solidi B 54, 469 (1972).
8. J. Rath and A. J. Freeman, Phys. Rev. B 11, 2109 (1975).
9. P.-A. Lindgård, B. N. Harmon, and A. J. Freeman, Phys. Rev. Letters 35, 383 (1975).

SPECTRAL DENSITY FUNCTIONS FOR AMORPHOUS SOLIDS*

D. G. Hall†
Department of Physics and Astronomy
The University of Tennessee, Knoxville, Tennessee 37916

and

Metals and Ceramics Division, Oak Ridge National Laboratory
Oak Ridge, Tennessee 37830

and

J. S. Faulkner
Metals and Ceramics Division, Oak Ridge National Laboratory
Oak Ridge, Tennessee 37830

ABSTRACT

The spectral density function $A(\vec{Q},\omega)$, proportional to the imaginary part of the single-particle Green's function $G(\vec{Q},\omega)$, is calculated exactly for a one-dimensional model of an amorphous solid. In addition to a Hamiltonian that describes electrons in the tight-binding approximation or spin waves, we also treat one that describes phonons. The insight gained from the model calculation is applied to recent neutron scattering results of Mook et al.

In a recent paper, Mook, Wakabayashi, and Pan reported neutron inelastic scattering measurements on the amorphous ferromagnet Co_4P.[1] Some results of their measurements are shown in Fig. 1(a) where the neutron scattering intensity is plotted as a function of $\vec{Q}$ for several energies. At the highest energy shown, there exists a three-peaked structure which becomes two-peaked at lower energy and merges into a single peak at an energy which we shall call E_o. Below E_o, one finds a small broad structure independent of energy and centered near the first peak in the liquid structure factor S(Q) (at Q = 3.13 Å^{-1}). In

*Research sponsored by the Energy Research and Development Administration under contract with the Union Carbide Corporation.

†Under appointment to the Graduate Laboratory Participation Program administered by ORAU for ERDA.

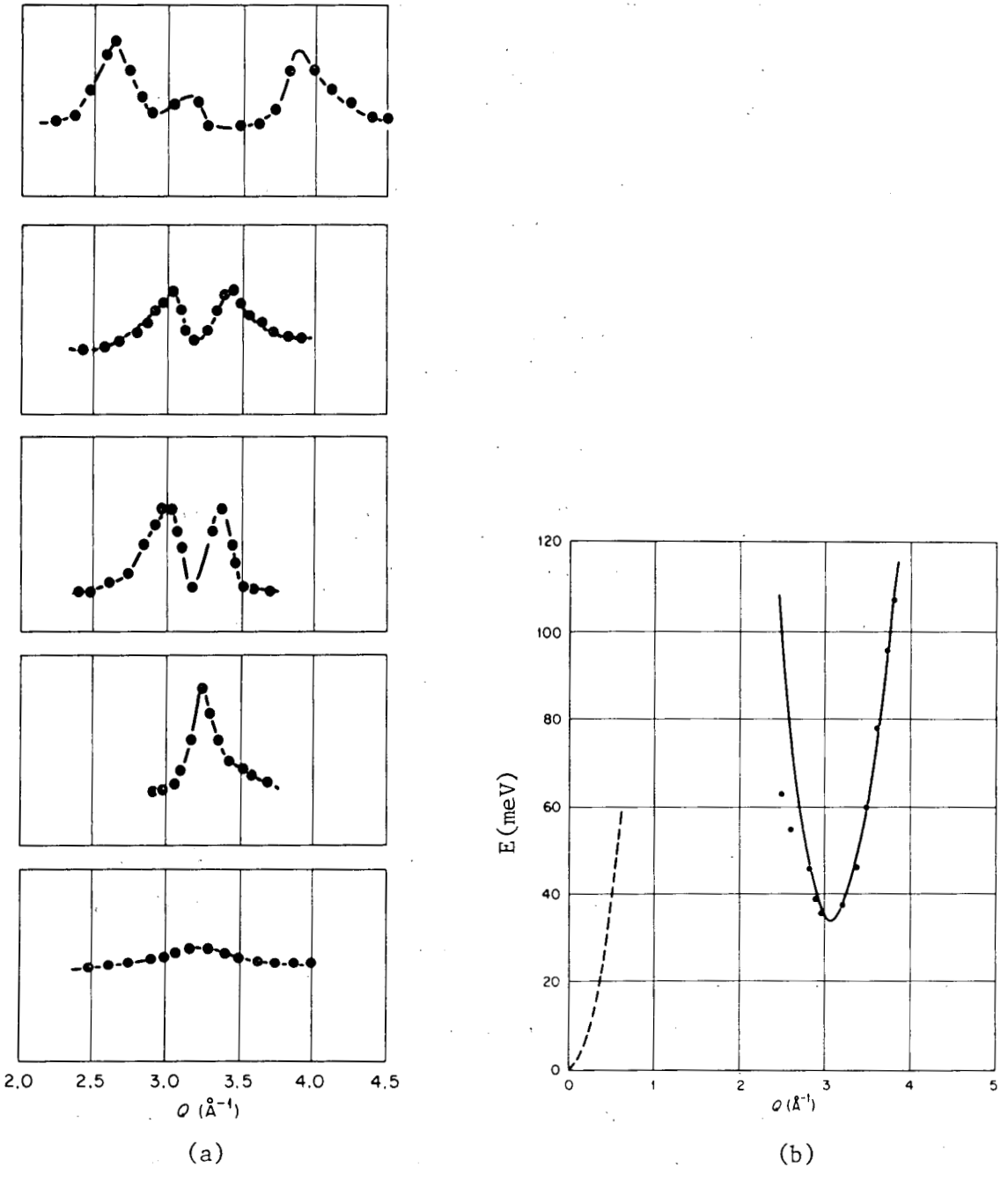


Fig. 1. (a) Measured Neutron Scattering Intensity for Five Energies as a Function of Q, from Mook et al. (b) Dispersion relation obtained from analysis suggested by Mook et al.

analyzing this data, Mook et. al. suggested that if one were to ignore the small central peak situated between two stronger peaks and to neglect the small structure below E_o, the data might be plotted as shown in Fig. 1(b). Plotted in this way, the dispersion relation is

reminiscent of that associated with rotons in liquid helium. The natural question to pose is whether the observations are best explained by the introduction of a new magnetic excitation, or as a manifestation of the effects of disorder upon the spin-wave spectrum of a magnetic system. To address this question, we have performed exact calculations of the spectral density function $A(\vec{Q},\omega)$ for a one-dimensional model of an amorphous solid. The spectral density describes the character of the single-particle excitations of the model system and can be used to gain insight into the effects of disorder. In what follows, we discuss the model, the significance of the spectral density, and the results of the calculations.

The configuration averaged spectral density $\langle A(\vec{Q},\omega)\rangle$ is defined by

$$\langle A(\vec{Q},\omega)\rangle = -\frac{1}{\pi}\,\mathrm{Im}\langle G(\vec{Q},\omega)\rangle \tag{1}$$

where $G(\vec{Q},\omega)$ is the Fourier Transform in space and time of the single-particle Green's function, and $\langle\ldots\rangle$ indicates an average over the statistical ensemble. For the duration of this paper, the brackets will be omitted as we shall always be referring to the averaged spectral density. Our method for calculating $A(\vec{Q},\omega)$ follows the formalism developed by Halperin[2] and leads to an exact result. The details of the calculation will not be presented here. We calculate the spectral density for excitations described by two similar Hamiltonians: (1) that for a system of coupled harmonic oscillators appropriate to a study of lattice vibrations and (2) a tight-binding Hamiltonian which has been used for a simplified description of electrons or spin waves. The former Hamiltonian is given by

$$H_v = \sum_n \frac{p_n^2}{2m} + \frac{1}{2}\sum_n \beta_{n+1}(U_{n+1} - U_n)^2 \tag{2}$$

where p_n and U_n are the momentum and displacement operators for the atom of mass m at site n, and β_{n+1} is the force constant coupling the displacements at sites n+1 and n. The latter Hamiltonian is given by

$$H_T \psi(n) = K_n \psi(n) + M_n \psi(n-1) + M_{n+1} \psi(n+1) \tag{3}$$

where $\psi(n)$ gives the probability amplitude for finding an excitation on the site n, K_n is the diagonal matrix element, and M_n is the off-diagonal matrix element coupling sites n and n-1. Both β_n and M_n are assumed to decrease exponentially with the spacing d_n between sites n and n-1. The ordered system dispersion relations for the above Hamiltonians are

$$\omega(Q) = 2\left|\sin(Q/2)\right| \tag{4}$$

and

$$E(Q) = 2 \sin^2(Q/2) \tag{5}$$

respectively, in our units.

The distribution of sites in our model is governed by the so-called "hard-rod" distribution function for the classical one-dimensional fluid.[3] N identical atoms are distributed on a line of length $N\ell$ where ℓ is the average equilibrium interatomic spacing. Each site is centered on a hard (impenetrable) rod of length a with $a < \ell$. The minimum atomic separation a and the average separation ℓ completely specify the distribution. To characterize the level of structural disorder in the model system, we introduce the short-range order parameter $\alpha = a/\ell$. $\alpha = 1$ corresponds to the limit of perfect order while $\alpha = 0$ corresponds to the random limit. In what is to follow, the average spacing ℓ is set equal to unity.

The role of the spectral density in neutron scattering can be demonstrated by considering the dynamic form factor $S(\vec{Q},\omega)$ for scattering from lattice vibrations.[4] If one expands $S(\vec{Q},\omega)$ and neglects those terms which describe the excitation of two or more phonons, one obtains

$$S(Q,\omega) = Ne^{-2W(\vec{Q})}\left[I(\vec{Q})\delta(\omega) + Q^2 A(\vec{Q},\omega)\right] \tag{6}$$

where $I(\vec{Q})$ gives the strength of the contribution to $S(\vec{Q},\omega)$ from elastic scattering and $2W(\vec{Q})$ is the Debye-Waller factor. It is clear from Eq. (6) that $A(\vec{Q},\omega)$ gives the inelastic scattering contribution to $S(\vec{Q},\omega)$ from single-particle excitations.

For constant ω (or constant E), the ordered-system spectral density consists of δ-functions at the positions $Q = Q(\omega)$ [or $Q = Q(E)$] determined from the appropriate dispersion relation [Eq. (4) or (5)]. In Fig. 2 we show the results of the calculation for the vibrational system

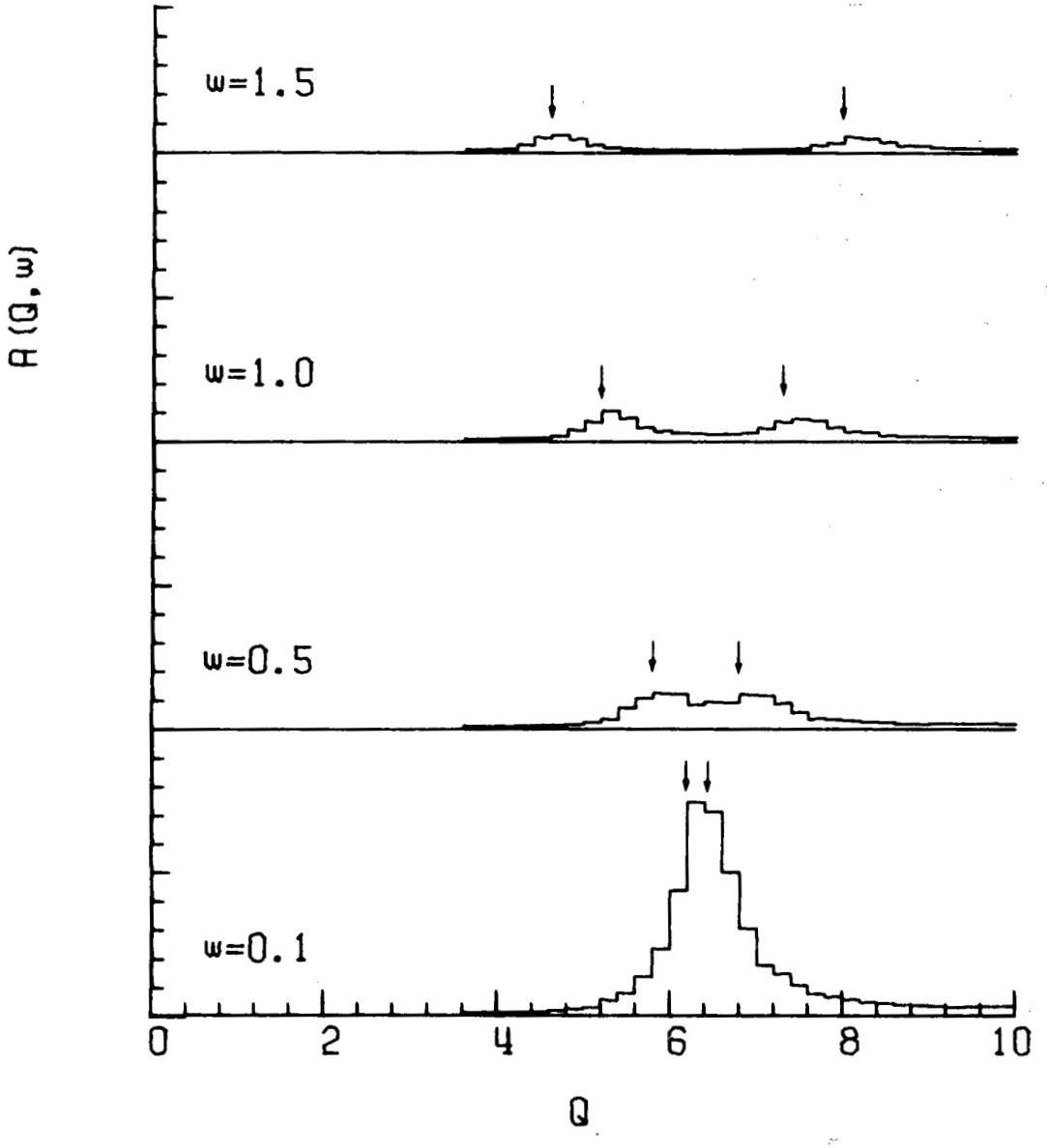


Fig. 2. Calculated $A(Q,\omega)$ for the Vibrational System for $\alpha = .85$ and Four Values of ω.

for $\alpha = .85$. Shown in that figure are plots of $A(Q,\omega)$ as a function of Q for four values of fixed ω. In the figure only the peaks in $A(Q,\omega)$ in the second zone are displayed [as in Fig. 1(a)]. It will be noted that the δ-function behavior characteristic of the ordered system has yielded to broadened structures located near the values of $Q(\omega)$ determined from Eq. (4) and indicated by arrows. At $\omega = .10$, it is no longer possible to distinguish two distinct structures and at $\omega = .50$ the two peaks have nearly merged into a single structure. That the peak in $A(Q,\omega)$ is large for small ω is a feature peculiar to the vibrational system and does not depend upon the dimensionality of the system. In Fig. 3 are the results of our calculation for the tight-binding system with $\alpha = .85$. As for the phonon system, A(Q,E) in Fig. 3 for the lowest energy shown can no longer be distinguished as two distinct peaks. Unlike the phonon system, however, the lowest energy A(Q,E) does not consist of a single strong peak, but rather a small broad structure. At higher energies, the excitation peaks in A(Q,E) are fairly sharp, though still broadened from the δ-function behavior of the ordered-system spectral density.

Based on the results of our model calculation, it appears quite likely that the structures below the energy minimum E_o shown in Fig. 1(b) are real and should not be neglected. Our investigations for $\alpha < 0.85$ reveal that these structures persist though we do not present those results here. From a comparison of Fig. 1(a) and Fig. 3 we conclude that the neutron scattering data shown in Fig. 1 is understandable as a manifestation of the effects of structural disorder upon ordinary spin-wave excitations. From Fig. 2 we see that a similar experiment on phonons should give a large peak below the "minimum".

REFERENCES

1. H. A. Mook, N. Wakabayashi, and D. Pan, Phys. Rev. Lett. 34, 1029 (1975).
2. B. I. Halperin, Phys. Rev. 139, A104 (1965).
3. Z. W. Salzburg, R. W. Zwanzig, and J. G. Kirkwood, J. Chem. Phys. 21, 1098 (1953).

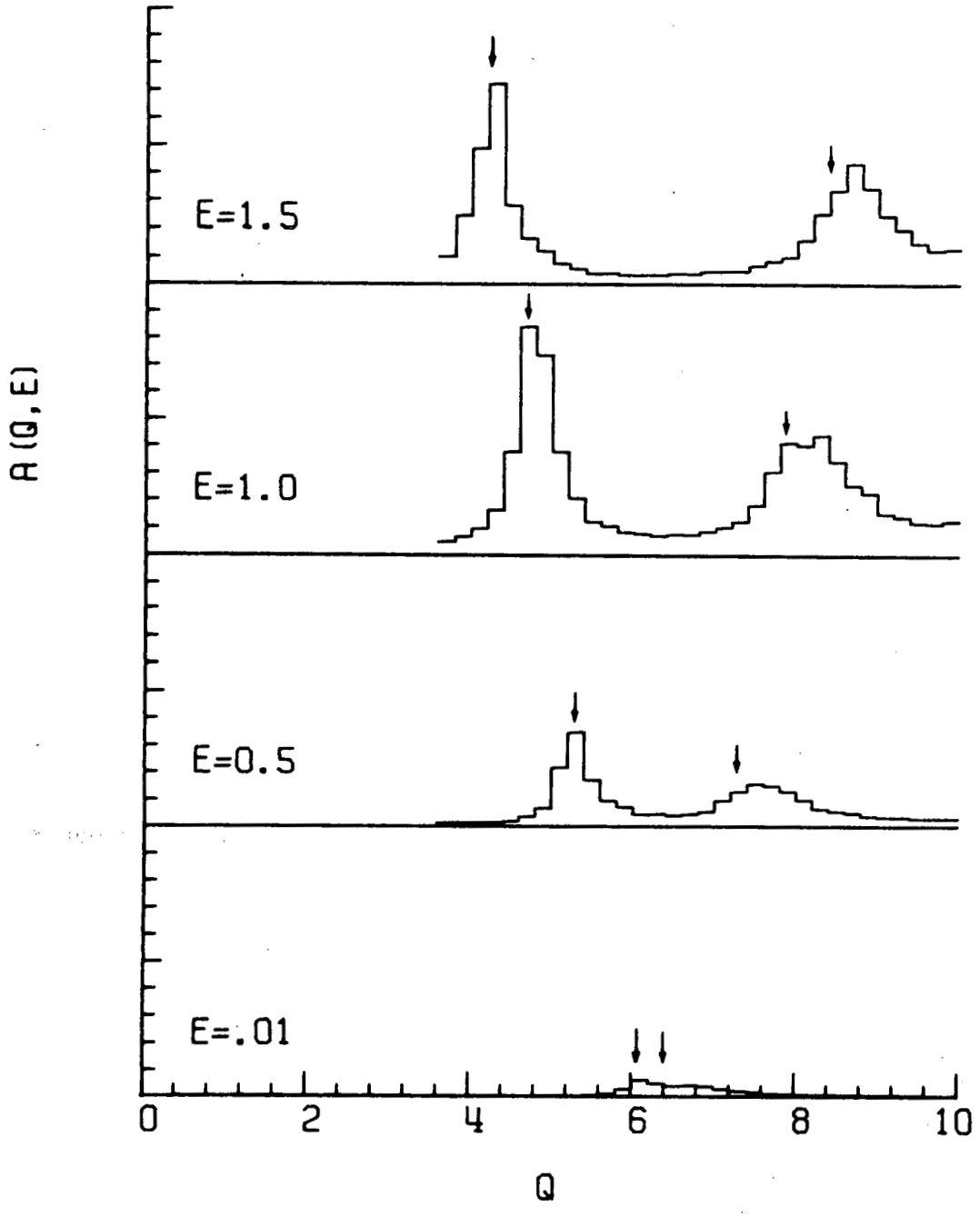


Fig. 3. Calculated A(Q,E) for the Tight-Binding System for α = .85 and Four Values of E.

CONF-760601--7

POLARIZATION DEPENDENCE OF MAGNETIC NEUTRON SCATTERING

M. Blume
Brookhaven National Laboratory*
Upton, New York 11973

and

State University of New York+
Stony Brook, New York 11794

ABSTRACT

The polarization dependence of magnetic neutron scattering is shown to depend on the imaginary part of the symmetric generalized susceptibility $\chi_s^{\alpha\beta} = \frac{1}{2}(\chi^{\alpha\beta}(Q,\omega) + \chi^{\beta\alpha}(Q,\omega))$ as well as on the real part of the antisymmetric susceptibility $\chi_a^{\alpha\beta} = \frac{1}{2}(\chi^{\alpha\beta}(Q,\omega) - \chi^{\beta\alpha}(Q,\omega))$. The latter term contains the spin-wave contributions to the polarization dependent scattering, along with other effects which are a consequence of the presence of a magnetic field or a spiral structure.

The polarization dependence of magnetic neutron scattering has been thoroughly discussed in literature[1,2] and the experimental results are well understood. It is the purpose of this note only to point out that the polarization dependent terms in the magnetic cross-section can be interpreted in terms of the real part of the antisymmetric part of the generalized magnetic susceptibility tensor. The polarization independent terms are of course a measure of the imaginary part of the symmetric part of that tensor. Since the derivations given here are extensions of well-known results, only sufficient detail to follow the procedure is written down. The magnetic scattering cross-section can be written as

---

*Work supported by U.S. Energy Research and Development Administration

+Work supported by the National Science Foundation

$$\frac{d^2\sigma}{d\Omega d\omega} = \frac{k'}{k}\left(\frac{\gamma e}{\hbar c}\right)^2 T^{\alpha\beta} \cdot \frac{1}{2\pi}\int_{-\infty}^{\infty} dt e^{-i\omega t} \langle M^{\alpha}(-\underline{K}o) M^{\beta}(\underline{K}t)\rangle, \qquad (1)$$

where $M^{\beta}(\underline{K}t)$ is the spatial Fourier transform of the magnetization density operator, $T^{\alpha\beta}(\alpha,\beta = x,y,z)$ is a 3x3 tensor, discussed below, and the other symbols have their usual meanings. For an unpolarized neutron beam, $T^{\alpha\beta} \equiv T_1^{\alpha\beta} = \delta^{\alpha\beta} - \hat{K}^{\alpha}\hat{K}^{\beta}$, and the scattering cross-section has the Van Hove form. For a polarized beam, the standard form becomes[1] $T = T_1^{\alpha\beta} + iT_2^{\alpha\beta}$, where $T_1^{\alpha\beta} = T_1^{\beta\alpha}$ and $T_2^{\alpha\beta} = -T_2^{\beta\alpha}$, with

$$T_1^{\alpha\beta} = \delta^{\alpha\beta} - \hat{K}^{\alpha}\hat{K}^{\beta} \qquad (2)$$
$$T_2^{\alpha\beta} = \epsilon^{\mu\nu\gamma} P^{\gamma} \{\delta^{\mu\alpha}\delta^{\nu\beta} - \delta^{\nu\beta}\hat{K}^{\mu}\hat{K}^{\alpha} - \delta^{\mu\alpha}\hat{K}^{\nu}\hat{K}^{\beta}\}$$

Here $\epsilon^{\mu\nu\gamma}$ is the antisymmetric tensor of third rank, and a summation convention is used for repeated indices. Also, $\underline{P}$ is the polarization vector of the incident neutron beam. It is seen from these expressions that the polarization dependent terms are antisymmetric in the indices α and β.

The generalized magnetic susceptibility is given by

$$\chi^{\alpha\beta}(\underline{K}\omega) = i\int_{o}^{\infty} dt e^{-i\omega t} \langle [M^{\alpha}(\underline{K}t),\ M^{\beta}(-\underline{K}o)]\rangle, \qquad (3)$$

the symmetric and antisymmetric parts are defined by

$$\chi_s^{\alpha\beta}(\underline{K}\omega) = \tfrac{1}{2}(\chi^{\alpha\beta}(\underline{K}\omega) + \chi^{\beta\alpha}(\underline{K}\omega)),$$

$$\chi_a^{\alpha\beta}(\underline{K}\omega) = \tfrac{1}{2}(\chi^{\alpha\beta}(\underline{K}\omega) - \chi^{\beta\alpha}(\underline{K}\omega)),$$

and the real and imaginary parts of each by

$$\chi = \mathrm{Re}\,\chi - i\,\mathrm{Im}\,\chi.$$

The flucutation-dissipation theorem then enables us to write[3]

$$\frac{1}{2\pi}\int_{-\infty}^{\infty} dt e^{-i\omega t} \langle M^{\alpha}(-\underline{K}o) M^{\beta}(\underline{K}t)\rangle$$

$$= \frac{1}{\pi} \frac{\text{Im } \chi_s^{\alpha\beta}(\underline{K}\omega)}{1 - e^{-\beta\omega}} + \frac{1}{i\pi} \frac{\text{Re } \chi_a^{\alpha\beta}(\underline{K}\omega)}{1 - e^{-\beta\omega}}$$

$$+ \langle M^{\alpha}(-\underline{K})\rangle \langle M^{\beta}(\underline{K})\rangle \delta(\omega). \qquad (4)$$

Substituting (4) in (1), we obtain the expression for the cross-section:

$$\frac{d^2\sigma}{d\Omega d\omega} = \frac{k'}{k}\left(\frac{\gamma e}{\hbar c}\right)^2 \frac{1}{\pi}\left\{T_1^{\alpha\beta} \frac{\text{Im } \chi_s^{\alpha\beta}(\underline{K}\omega)}{1 - e^{-\beta\omega}}\right.$$

$$\left. + T_2^{\alpha\beta} \frac{\text{Re } \chi_a^{\alpha\beta}(\underline{K}\omega)}{1 - e^{-\beta\omega}}\right\} + \left(\frac{\gamma e}{\hbar c}\right)^2 \delta(\omega)\ (T_1^{\alpha\beta} + iT_2^{\alpha\beta}) \langle M^{\alpha}(-\underline{K})\rangle$$

$$\times \langle M^{\beta}(\underline{K})\rangle \qquad (5)$$

Terms involving T_2 are polarization dependent, while those involving T_1 are independent of polarization.

The term with the factor $\delta(\omega)$ in (5) is the Bragg scattering, and the term involving T_2 leads to polarization effects in magnetic spirals. The part involving Re $\chi_a^{\alpha\beta}$ is the inelastic term which contains polarization dependent contributions to spin-wave scattering and to inelastic crystal field scattering.

It should be mentioned that both terms in the inelastic cross-section involve the dissipative parts of the susceptibility, since, for the antisymmetric term, the real and imaginary parts interchange the dispersive and dissipative roles played by the corresponding terms in the symmetric part.

The antisymmetric part of the susceptibility vanishes for a magnetically disordered system unless a magnetic field is present, so that "sloppy spin waves" would not give the same polarization effects as would ordinary spin waves.

Similar, but more complex, results for the form of the polarization of the scattered beam can be derived.

REFERENCES

1. M. Blume, Phys. Rev. 130, 1670 (1963).
2. W. Marshall and S. W. Lovesey, Theory of Thermal Neutron Scattering, Oxford University Press (Oxford, 1971), p. 324 et seq., and references contained therein.
3. Ibid., p. 231 et seq.

THE DYNAMICS OF THE ONEDIMENSIONAL FERROMAGNETIC CHAIN SYSTEM $CsNiF_3$

M. Steiner fuer
Hahn-Meitner-Institut für Kernforschung
Postfach 39 01 28, D 1000 Berlin 39, FRG

ABSTRACT

By means of inelastic neutron scattering the existence of spin-waves far above the Neèl temperature has been proven and their dispersion relation and the influence of the planar anisotropy has been studied in $CsNiF_3$. According to the onedimensionality dispersion exists along q_c, the chain direction only. The anisotropy leads to two different types of spin-waves, the IPC-peak, which is broad and similar to that measured in isotropic systems, and the unique OPC-peak, the width of which is limited by the experimental resolution. The temperature dependence of both peaks has been studied up to 25K. Dilution of the system influences the sharp OPC-peak only.

INTRODUCTION

The strong interest, which has been focussed on phase transitions in the past, was not only devoted to the spatial dependence of the correlation function, but also to the time dependence of this function. In threedimensional magnetic systems the study of this time dependence is much more difficult than the study of the spatial dependence of the correlation function. The critical region is so small in such systems, that a detailed study of the collapse of the propagating modes is nearly impossible. In onedimensional magnetic systems the critical region is very large, thus the

study of the dynamic properties in the critical region in detail is possible. Especially the possible existence of spin-waves in a nonordered system and the influence of the degree of short range order on the spin-waves may be studied. As a model system, which has been used for the study, serves $CsNiF_3$, which has been shown to be a onedimensional ferromagnetic chain system with planar anisotropy (see the review of Steiner et al [1]) for $T \gg 4K$. The spin-waves in $CsNiF_3$ have been studied by means of inelastic neutron scattering for $4K \leq T \leq 25K$ using the IN2 triple axis spectrometer at the HFBR of ILL in Grenoble.

RESULTS

Dispersion-relation

Constant Q-Scan at 4.9K revealed well defined spin-waves for all accessible Q values in the first Brillouin-Zone around the origin of reciprocal space. From these results the dispersion curves shown in fig. 1 were deduced [2]. The onedimensionality of the system is reflected in the fact that dispersion only exists along q_c, whereas q_a or q_b does not influence the energy of the spin-wave. In other words: The only q-component which determines the spin-wave energy is the distance from the planes 1 = o, 2 ... , which build up the reciprocal space of a onedimensional ferromagnetic chain as shown in fig. 1 too. Since the magnetic chains run along c, q_c is the only momentum-transfer-component, which determines the spin-wave energy. The solid line is the result of least square fit of the dispersion relation, caculated by Villain [3] 1973

$$\hbar\omega = 2S \left\{ (2J - 2J \cos \pi \ q_c) \ (2J - 2J \cos \pi \ q_c + A) \right\}^{1/2}$$

to the experimental results with the following values

$$J/k_B = (\ 11.8 \pm 0.03\ )K\ ,\ A/k_B = (4.9 \pm 1)K$$ [4]:

The planar anisotropy does not lead to an anisotropy gap at $q_c = 0$ in a ferromagnetic chain.

$\vec{Q}$ - Dependence at 4.9K

The q_a-dependence of the spin-wave with $q_c = 0.35$ is shown in fig. 2, demonstrating the change in the line shape from $q_a = 0$ to $q_a = 0.4$. At $q_a = 0$ only the S^x and S^y - components of $\vec{S}$ contribute, whereas at $q_a = 0.4$ S^z contributes too. At $q_a = 0$ the line is a Lorentzian line with $\delta\nu/\nu = 0.29$, whereas at $q_a = 0.4$ the line consists of the Lorentzian line as for $q_a = 0$ plus a line, which is given by the resolution of the instrument alone. The solid lines in fig. 2 are the result of a least squares fit of the described line shape to the experiment yielding an intensity ratio sharp line to broad line of 1/5 [4]. Thus one concludes that there are two types of spin-waves in $CsNiF_3$, one which is due to $\langle S^x S^x + S^y S^y \rangle$, the in plane correlation part IPC, and another, which is due to $\langle S^z\ S^z \rangle$, the out of plane correlation part OPC. The difference between both is due to the anisotropy and has been found in theory as well [5,6]. The agreement between theory and experiment is quite good

$$\left(\frac{\delta\nu}{\nu}\right)_{\text{Villain}} = 0.3 \qquad \left(\frac{\delta\nu}{\nu}\right)_{\text{exp.}} = 0.29$$

$$\frac{\text{Intensity IPC}}{\text{Intensity OPC}_{\text{Villain}}} = 4{,}5 \qquad \frac{\text{Intensity IPC}}{\text{Intensity OPC}_{\text{exp.}}} = 5$$

The physical background of the two spin-waves is: Due to the anisotropy the fluctuations, which are responsible for the correlationlength ξ , are bound to the a-b-plane. Thus the IPC does not represent a single spin-wave but a bundle of

such, whose extension in q_c is roughly given by $1/\xi$ as shown in fig. 3. This is the same situation as in isotropic systems. On the contrary the OPC is unique to planar systems, since his width is given by the lifetime τ_k of the spin-waves. Thus the experiments show that the lifetime of a spin-wave in a paramagnetic system with onedimensional short range order is so long, that it can't be measured by usual neutron spectroscopy : $\tau^{-1} \leq 10^{11}$ Hz.

Temperature dependence

From the physics outlined above it follows that the width of the IPC, being proportional to $1/\xi$, should be proportional to T. This was found experimentally as shown in fig. 4 a. Similar agreement with theory was found for the weak energy renormalization as shown in fig. 4 b. More interesting is the behaviour of the OPC, since that reflects the lifetime τ_k of the spin-wave. Theoretically it is expected, that this peak should disappear very rapidly with temperature [6]. As can be seen in fig. 5 a, the experimental and theoretical results agree very well. The found weak energy renormalization of fig. 5 b is in accordance with theory as well. The reason for the disappearance of the OPC is, that the width increases rapidly with temperature, thus its intensity becomes unmeasurable small. This increased width couldn't be measured since the calculated widths were still to small to be detected.

CONCLUSION

The measurements show, that the planar anisotropy leads to a unique spin-wave peak in the energy spectrum. This OPC reflects in his line-width the true lifetime τ_k of the ex-

citation. It was found, that this lifetime is surprisingly long regarding the fact, that the system possesses only short range order. The OPC enables thus to study small effects on the lifetime of the spin-wave in such systems. In a recent experiment Steiner and Dorner [7] were able to show, that a small diamagnetic dilution (2% Mg) increases the width of the OPC by a small but measurable amount, whereas the JPC remains unchanged.

REFERENCES

1. M. Steiner, J. Villain, C.G. Windsor, Adv. Phys. in press
2. M. Steiner, B. Dorner, Sol. State Comm. 12, 537 (1973)
3. J. Villain, J. Phys. C6, L97 (1973)
4. M. Steiner, B. Dorner, J. Villain, J. Phys. C8, 165 (1975)
5. J. Villain, J. Phys. Paris 35, 27 (1974)
6. J. Loveluck, S.W. Lovesey, J. Phys. C8, 3857 (1975)
7. M. Steiner, B. Dorner, to be published

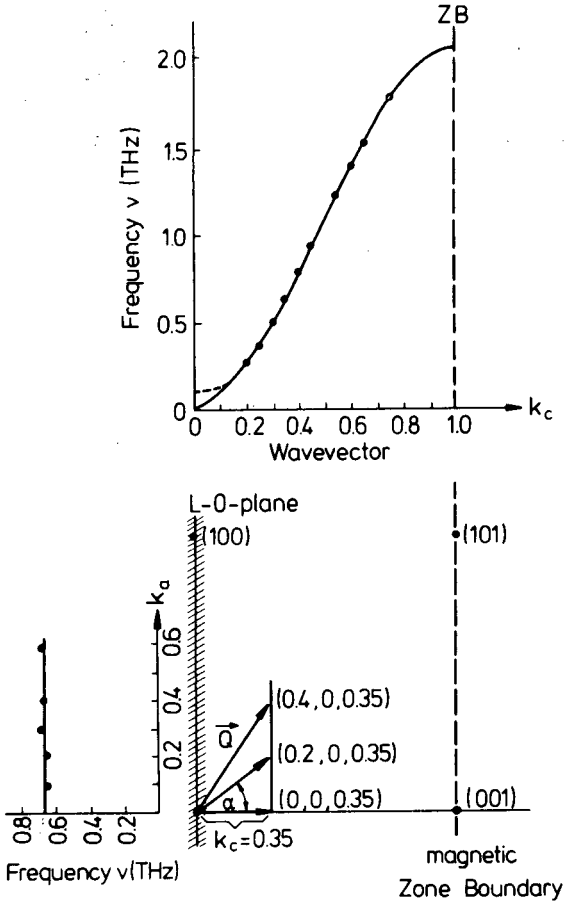


Fig.1: Reciprocal space and dispersion curves in $CsNiF_3$

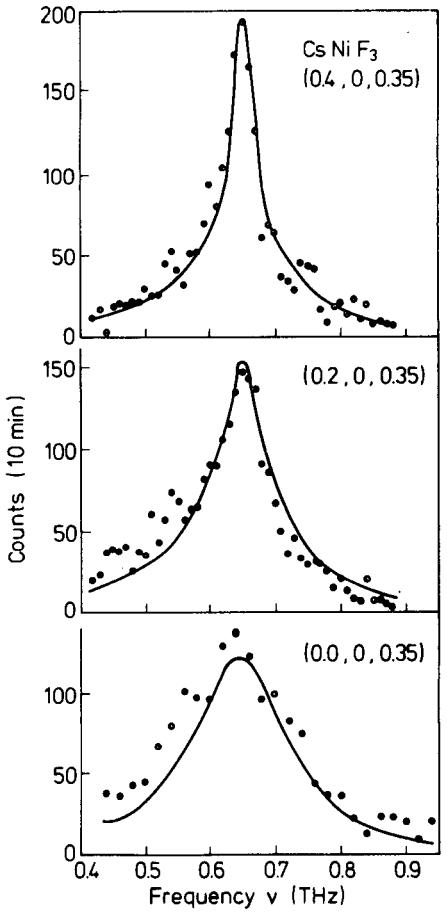


Fig.2: q_a-dependence of the spin-waves in $CsNiF_3$

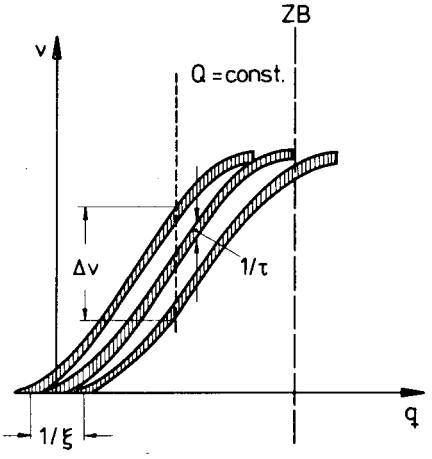
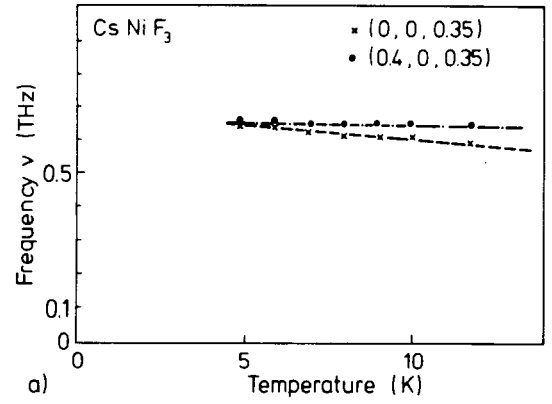


Fig.3: Schematic representation of the different origins for the spin-wave linewidth



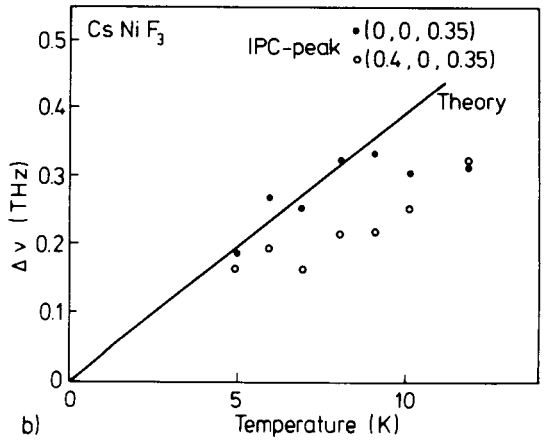
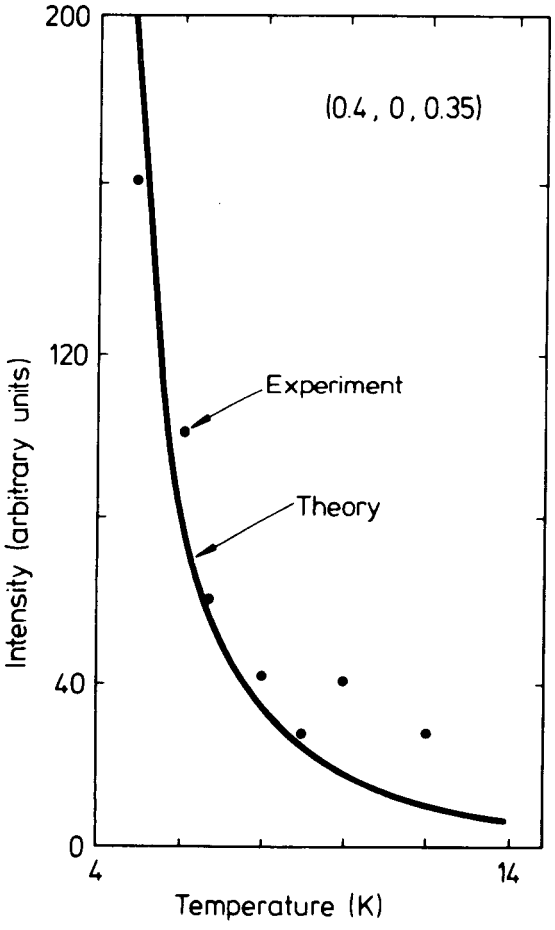


Fig.4: Temperature dependence of a) the spin-wave energy b) the spin-wave linewidth



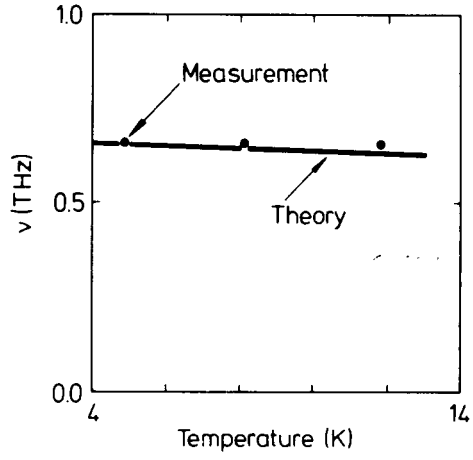


Fig.5: Temperature dependence of the OPC: Comparison between theory and experiment a) intensity b) energy

ELEMENTARY EXCITATIONS IN SOME 3d METAL ALLOYS

K. Mikke and J. Jankowska
Institute of Nuclear Research, ŚWIERK
05-400 Otwock, Poland

ABSTRACT

Our inelastic neutron scattering work performed in the last few years for some ferromagnetic and antiferromagnetic 3d metal alloys is presented. For Ni-Fe alloys with Fe concentration from 5% to 65% the exchange stiffness constant D decreases with a much faster rate than in SWR measurements. The effect of atomic ordering on the value of D is demonstrated. There is a fair agreement of the data with latest band model calculations. In the invar range the observed decrease of D confirms the theoretical predictions. In Ni-Co alloys the value of D increases slightly in violent contrast to predictions based on the CPA-RPA approximation and to SWR data. For Ni-V and Ni-Cr D decreases fast with V and Cr concentration. In the Ni-Fe 50% alloy a pronounced decrease of magnon intensities was observed at higher temperatures and higher energy transfers. Magnetic excitations were investigated in several chromium alloys. The most striking effect is the disappearance of magnetic excitations in the Cr-Al alloy below 0.8 T_N.

INTRODUCTION

The main topics of the present studies were the magnetic excitations in ferromagnetic Ni-based alloys and in antiferromagnetic chromium alloys. All data were obtained by the triple axis spectrometry mostly in the constant energy mode with energy transfers from 5 to 34 meV. Corrections to the measured peak positions were computed by a program folding the dispersion relation with the spectrometer resolution function. In our studies of the concentration dependence of the exchange stiffness constant in

Ni-Fe alloys special attention was paid to possible influence on spin dynamics of atomic ordering, the transition from strong to weak ferromagnetism and the invar anomaly. The data for Ni-Co alloys when combined with those for Ni-Fe were meant to provide a validity test of the CPA-RPA theory in describing Ni alloys containing Fe and Co. In antiferromagnetic chromium alloys our studies were mainly devoted to Cr-Al system which displays a very anomalous behaviour.

EXPERIMENTAL RESULTS AND DISCUSSION

Concentration Dependence of Spin Waves in Ni-Based Alloys

In view of continuing difficulties in applying the band model to weak ferromagnetic 3d metal the choice of strong ferromagnet nickel as the matrix seemed desirable for a more systematic survey of spin dynamics in alloy systems, although iron would be much more favourable from the experimental point of view.

The corrected magnon peak positions were fitted to a parabolic dispersion relation $E = Dq^2$ and the value of the exchange stiffness constant was extracted for each composition. These data for Ni-based alloys are summarized in figure 1, where: ○ , are data for Ni-Fe at 295 K; ⊗ , data for Ni-Fe at 85 K; x , data for Ni-Fe at $T \gg T_C$; △ , data for Ni-Co at 295 K; ⊡ , data for Ni-V at 295 K and ● , data for Ni-Cr at 85 K. The full curve is the best fit to spin wave resonance data for Ni-Fe [1]. For the reason of clarity the

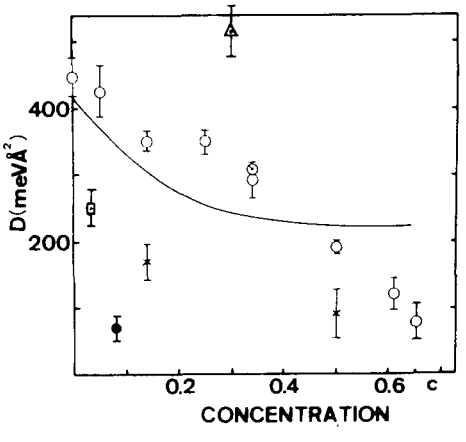


Fig.1. D(c) in Ni alloys.

figure does not contain the data by other authors which were recently summarized [1,2,3]. Our Ni-Fe data are following the trend found in small angle scattering experiments but most of our values fall lower. Together with an additional recent result of D = 340 ± 10 meVÅ^2 for c = 0.21, not displayed in fig. 1, our data cannot be satisfactorily fitted by one smooth curve. This shape of our D(c) curve led us to consider more carefully the phenomena occuring in the Ni-Fe system. At c = 0.25 a number of physical properties change appreciably and this is usually associated with the transition from weak to strong ferromagnetism [4]. In the invar region (c from 0.65 to 0.75) many physical properties display an unusual behaviour [5]. Finally the atomic ordering processes should be taken into account in particular in the region of c = 0.25 and c = 0.5. Strong tendency for atomic ordering in Ni-Fe alloys of both Ni_3Fe and NiFe type is well known [6,7]. Slow cooling inherent to the growing techniques of our single crystal samples favours a considerable degree of ordering. A simple calculation of the contribution of ordering to the value of D in terms of the Heisenberg model was made in the zeroth order approximation with only the nearest neighbour interaction [8] and the results are summarized in fig. 2.In the lower part of figure 2 open circles denote the experimental data obtained from D values extrapolated to 0 K. Upper solid line refers to maximum ordering and lower one to a disordered alloy. ΔD - the increment of D due to ordering is shown in the upper part of figure 2. The best fit was found when ordering effects were included and the resulting values for the exchange interaction constants were J_{11} = 65.6 meV this value was computed from the results by Mook et al.[9], J_{12} = 22.8 ± 1.4 meV and J_{22} = - 5.8 ± 1.2 meV. There was no need to assume the variation of J_{12} with composition.

The effect of atomic ordering on the value of D was

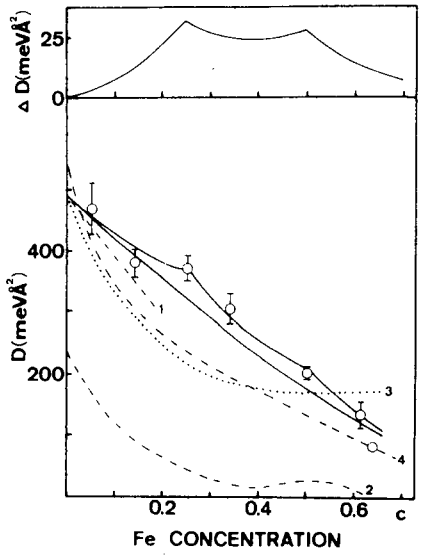


Fig.2. D(c) in Ni-Fe alloys.

studied recently in more detail. Following the known procedures [7] three Ni_3Fe samples cut from the same ingot were exposed to different thermal treatment. One sample was left as grown for reference. The other was treated for maximum ordering and the third one quenched to produce the maximum attainable disorder. The value of D was increased from 345 meVÅ^2 for the sample "as grown" up to 390 meVÅ^2 for the annealed sample and decreased down to 305 meVÅ^2 for the quenched sample. The details of this work shall be published elsewhere.

The effect of ordering on the D values has not yet been treated in terms of the band model. A few calculations were tried for a disordered alloy and the results are shown in fig. 2 by dashed lines: 1 - Yamada and Shimizu [10], shifted to initial (c = 0) experimental value; 2 - Wakoh [2]; 3 - Edwards and Hill [11]; 4 - Riedinger and Nauciel-Bloch [12]. In their extended work Edwards and Hill [13] raised doubts regarding the validity of the RPA even for Ni-Fe alloys. Since within RPA-CPA no essential differences are expected between Ni-Fe and Ni-Co alloys the D(c) dependence for Ni-Co should provide decisive arguments on the applicability of present theories. We have performed such studies and the triangle in fig. 1 is our result for $Ni_{.69}Co_{.31}$ alloy. Together with the data for three other crystals with lower content of Co, which will be reported in detail elsewhere, they indicate a slow increase of D(c). These results are completely different from SWR data [14] where a fast decrease of D was found and e.g. for 31% Co the value of D was only

130 meVÅ^2.

Our earlier measurements of spin waves in $Ni_{.97}V_{.03}$ in the energy transfer range 5-10 meV have now been extended up to 30 meV. Room temperature data are shown in fig. 3. The vertical bar indicates the range of our earlier measurements. At room temperature we have obtained D = 250 ± 20 meVÅ^2 and at 85 K D = 320 ± 30 meVÅ^2. These values are considerably reduced compared to pure Ni, which is presumably caused by strong perturbation by V impurity in nickel matrix. Another expected effect of this perturbation was the lowering, compared to pure nickel, of the Stoner splitting and thus lowering of magnon energies at which their intensity suddenly decreases. We could not find this effect up to 30 meV. For the $Ni_{.92}Cr_{.08}$ alloy which is paramagnetic at room temperature the measurements were made at 85 K and D = 70 ± 15 was found.

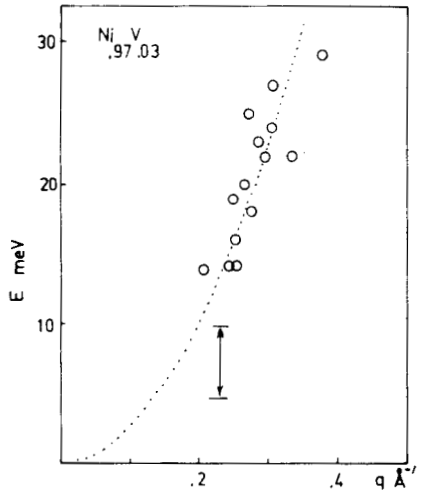


Fig. 3. Dispersion relation of spin waves in Ni-V alloy.

Temperature Dependence of Magnetic Excitations in $Ni_{.5}Fe_{.5}$

Spin wave intensities for [100] direction were measured at room temperature, 630 K and 800 K. A pronounced decrease of these intensities at higher temperatures and higher energy transfers was observed. The ratios of integrated spin wave intensities at 630 K and 800 K to those at room temperature are shown in fig. 4 by filled and open circles correspondingly. These data are in marked contrast

to those for pure nickel and iron [15] where a similar decrease was temperature independent. It took place at much higher energies and was explained in terms of intersection of spin wave spectrum with the Stoner band. If the same explanation is applied our results mean that in a Ni-Fe alloy the Stoner band is temperature dependent.

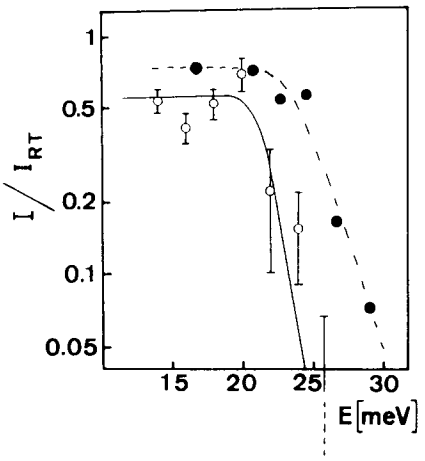


Fig.4. The ratio of integrated intensities at higher temperature to those at room temperature, as a function of spin wave energy.

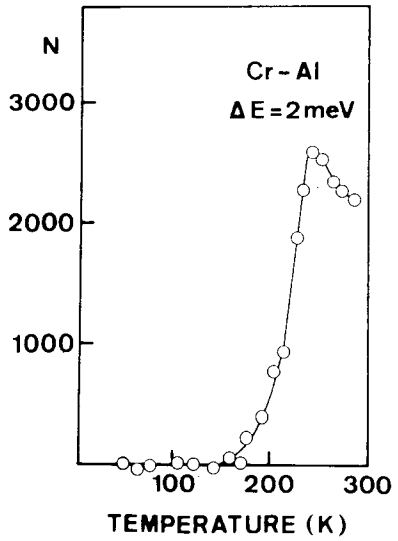


Fig.5. Temperature dependence of magnetic excitation intensity.

Spin Density Waves and Magnetic Excitations in Cr(1.5% Al)

From the temperature variation of elastic neutron scattering around (100) point the transition temperatures were found to be: $T_N = 238 \pm 5$ K and $T_{SF} = 66 \pm 3$ K, and the SDW wavevector $\vec{Q} = 0.952\ \vec{\tau}_{100}$ at 4.2 K. T_N is much lower than for pure Cr and this confirms the presence of a dip in the T_N dependence on Al concentration contrary to neutron scattering data for powdered samples. The most striking effect is the disappearance of magnetic excitations in Cr-Al alloy below 0.8 T_N fig. 5 .

REFERENCES

1. T. Maeda, H. Yamauchi and H. Watanabe, J. Phys. Soc. Japan 35, 1635 (1973).
2. S. Wakoh, J. Phys. Soc. Japan 30, 1068 (1971).
3. H. Hennion, B. Hennion, A. Castets and D. Tocchetti, Solid State Commun. 17, 899 (1975).
4. I.A. Campbell, J. Phys. F.: Metal Phys. 4, L181 (1974)
5. E.P. Wohlfarth, Phys. Rev. 10B, 3010 (1974).
6. M.F. Collins, R.V. Jones and R.D. Lowde, J. Phys. Soc. Japan 17, Suppl. B-III, 19 (1962).
7. W.I. Gomankow, I.M. Puzey, A.A. Loschmanov and J.I. Maltzev, Izw. Akad. Nauk USSR: Metally 1, 160 (1971).
8. K. Mikke, J. Jankowska and A. Modrzejewski, J. Phys. F: Metal Phys. 6, 631 (1976).
9. H.A. Mook, R.M. Nicklow, E.D. Thompson and H.K. Wilkinson, J. Appl. Phys. 40, 1450, (1969).
10. H. Yamada and M. Shimizu, J. Phys. Soc. Japan 28, 327 (1970).
11. D.M. Edwards and D.J. Hill, J. Phys. F.: Metal Phys. 3, L162 (1973).
12. R. Riedinger and M. Nauciel-Bloch, J. Phys. F.: Metal Phys. 5, 732 (1975).
13. D.M. Edwards and D.J. Hill, J. Phys. F.: Metal Phys. 6, 607 (1976).
14. M. Hinoul and J. Witters, Solid State Commun. 10, 749 (1972).
15. J.W. Lynn, Phys. Rev. B11, 2624 (1975).
16. A. Kallel and F. de Bergevin, Solid State Commun. 5, 955 (1967).

THE GENERALISED SUSCEPTIBILITY OF $Mn_{73}Ni_{27}$

B.Hennion
Centre d'Etudes Nucleaires de Saclay, Paris, France

M.T.Hutchings, R.D.Lowde, M.W.Stringfellow
Atomic Energy Research Establishment, Harwell, England

and D.Tocchetti
Institut Laue-Langevin, Grenoble, France

ABSTRACT

The inelastic magnetic scattering from a crystal of disordered antiferromagnetic $Mn_{73}Ni_{27}$ has been surveyed up to energy transfers of approximately one-sixth of an eV by use of the IN1 spectrometer at the hot source of the Laue-Langevin Institute, Grenoble. The results are presented as a plot of the generalised perpendicular susceptibility. A spin wave contribution is conspicuously present, with maximum energy in the region of 0.16 eV and showing everywhere an intrinsic line breadth of the order of 30%.

We present here a preliminary account of an experiment in which the magnetic neutron inelastic scattering from a crystal of disordered $Mn_{73}Ni_{27}$ was surveyed and the results converted into a map of the generalised susceptibility.

Our study is part of an investigation of the face-centred-cubic 3d-transition metal alloys, which occupy about half the first transition-element row of the periodic table. This is a range of materials including many steels, stainless steels, the invars, & a class of alloys undergoing an important type of martensitic transformation. Much about their behaviour is not well understood, but it is believed that many of their anomalous properties are associated with a tendency to develop antiferromagnetism.

The subject of itinerant-electron antiferromagnetism is itself by no means fully worked out. Features of the generalised susceptibilities $\chi(\underline{K})$ have been explained on one-electron band theory, particularly by the school of Yamashita & Asano;[1] the basic input for the work rested heavily on neutron diffraction investigations, also largely contributed by Japanese

teams, especially those of Ishikawa & Adachi.[2] We have pursued the present investigation with the idea of extending this research into the area of electron dynamics, and to this end shall in a later publication compare our measurements of $\chi(\underline{K},\omega)$ with calculations based on the discussion by Young.[3]

According to Hicks et al,[4] our crystal must be a type 1 antiferromagnet with alternate {001} type sheets of "up" & "down" spins pointing along the c axis; the spin direction is confirmed in our experiment by the behaviour of the $(1+\check{K}_z^2)$ factor in the cross-section for spin-wave scattering.

Three features of the situation particularly influenced our approach to this study. Firstly, it is a characteristic of itinerant-electron magnets that the energy of the collective magnetic excitations is high, this resulting from the fact that the responsible electrons mostly travel through the crystal at velocities approaching the Fermi velocity, which as it turns out gives rise to magnons themselves of high velocity. Now to make neutron-scattering measurements at the high energies involved and at low enough momentum transfer to avoid serious intensity losses due to the form factor, incident neutron energies up to at least half an eV are desirable. We have accordingly made use of the IN1 spectrometer at the Laue-Langevin Institute, Grenoble, which employs the neutron beam from a source at 2000 K in the high-flux reactor. We were, moreover, privileged to do the work at a time when the world's largest beryllium monochromating crystal was installed thereon, kindly loaned by the Oak Ridge National Laboratory; this (thanks to its high atomic density) gives exceptionally strong reflexions & enables one to use the spectrometer for runs with incident energy up to $\frac{1}{2}$eV.

A second important technical point is that the IN1 spectrometer is equipped with a composite pyrolytic-graphite crystal analyser in the form of a flat slab, with the [002] direction vector lying in the plane of the slab. Used at high outgoing energies, as in the present experiment, such an analyser lies physically almost perpendicular to the neutron beam & can therefore be operated over a range of Bragg angles going down to the smallest required (4.43° in our case) without calling into play any correction factor for its geometrical "aspect".

Thirdly it can occur with itinerant-electron antiferromagnets - as apparently it does here - that the spin wave energy "line" is at virtually all energies massively broadened by interaction with the single-particle modes. The problem is therefore not to determine the position of a sharp spectrum line in the scattering but to take careful measurements of a gently varying intensity distribution. Using a triple-axis spectrometer, this is something normally regarded as very difficult; but we have made a serious attempt to do it, since there was one factor militating very strongly in our favour. The outstanding difficulty in a normal case is that competing effects other than the inelastic process sought are frequently able to produce a response in the counter, distorting the curves obtained. Among these may be counted unsuspected Bragg reflexions or even phonons shining onto the analyser crystal and its support, and intense phonons which surprisingly often present themselves at the analyser at a wave-vector acceptable in one of its orders of reflexion. However, a great saving virtue in our experiment was that these effects were almost entirely absent. From the point of view of nuclear scattering the alloy was, as near as could be fabricated, a null matrix. Therefore coherent nuclear scattering could be largely ignored, while the coherent magnetic scattering was strong only for the innermost few Bragg reflexions hkl because of the form factor. In these circumstances, and with an extremely carefully designed experiment, we have found it possible to obtain significant curves free, so far as we can determine, of spurious contributions.

Our results for the c-axis direction are illustrated in fig.1, which gives a general view of the susceptibility by exhibiting suitably transformed versions of curves hand-drawn through the original data sets. Two of the original data sets are shown in figs 2 & 3. A remarkable feature of the data is the great intrinsic linewidth observed, from which it would follow that the magnons suffer from exceptionally strong interactions, which for various reasons may be suspected to be mainly with the single-particle excitations. At 70 meV, for example, it would be fair to say that the entire Brillouin zone is involved in the interaction. To display this effect with the minimum of disturbance from instrumental limitations an analysis has been carried out by fitting to the data spectra generated by

convolving the resolution function of the instrument with cross-sections corresponding to sharp excitations having the phenomenological antiferromagnetic dispersion law $\hbar\omega = \sqrt{(c^2+d^2K^2)}$. In order to take into account in a simple manner the physical line broadening, each observed magnon

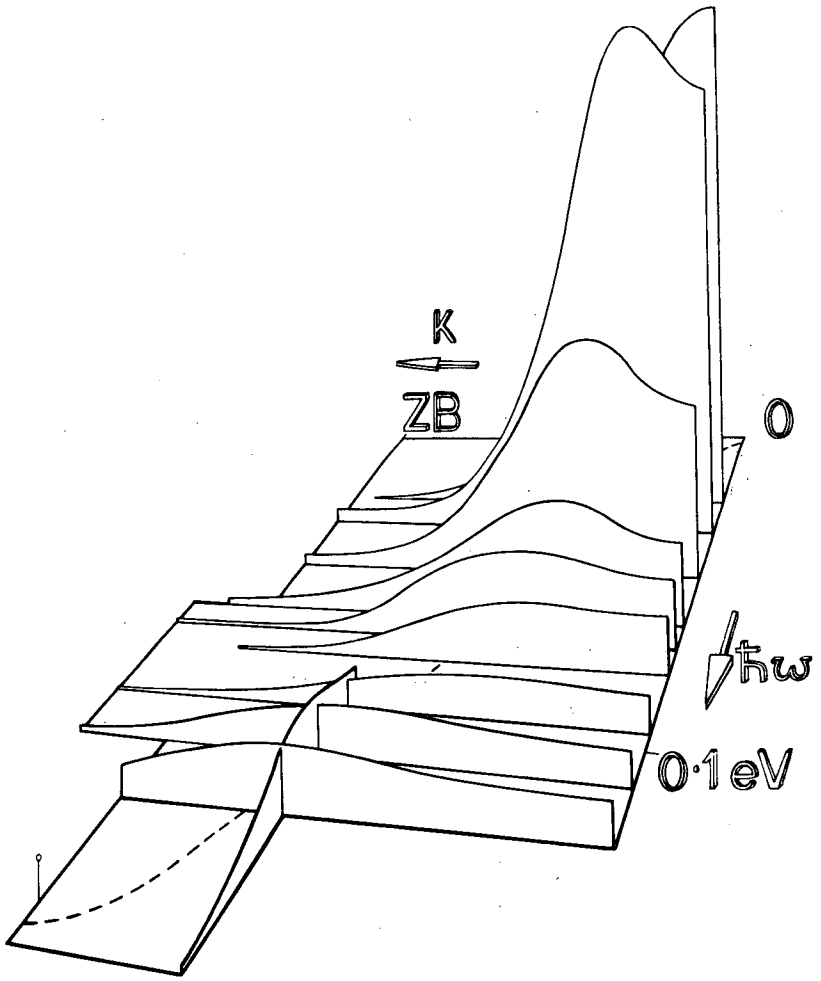
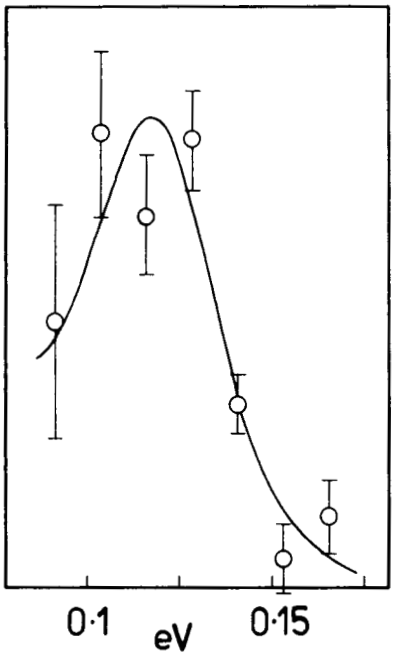


Figure 1. The reduced perpendicular susceptibility $\chi^{\perp}(K,\omega)$ (the perpendicular susceptibility $\chi_0^{\perp}(K,\omega)$ divided by the square of the form factor) for the [001] direction in $Mn_{73}Ni_{27}$ as measured by neutron scattering at the hot source triple-axis spectrometer IN1 at Grenoble. Shown in perspective is a montage of several sections of a surface, plus a single point in the lower left corner. The individual graphs are taken from curves hand-drawn through the points of a series of triple-axis-spectrometer surveys after correction for multitudinous factors converting the counting rates to the susceptibility. Their shapes are slightly distorted in different ways by the resolution function of the instrument and a deconvolution process as in fig.3 would be necessary to derive sections that could be expected to match more exactly. Plotted along the base plane is a best-fitting spin wave dispersion law derived from the deconvoluted distribution.



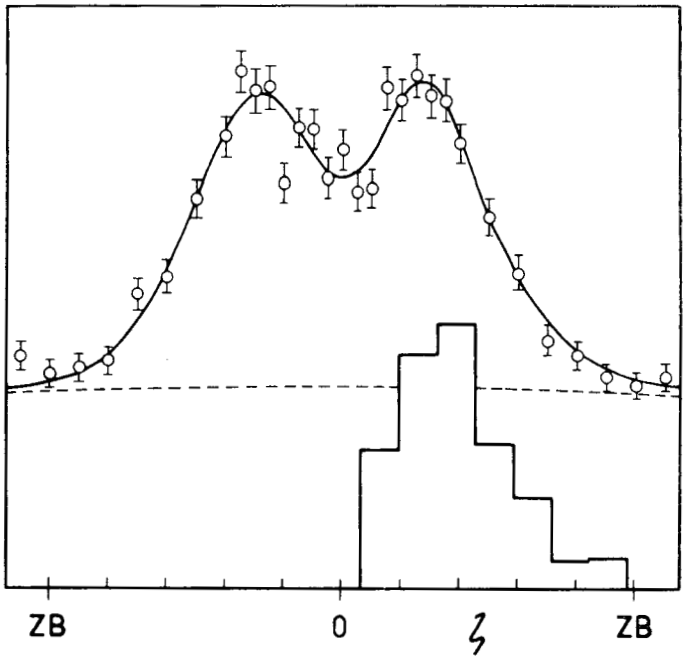


Figure 2 (above, left). A "constant-Q" survey of the magnon intensity at $0.65K_{max}$ in the c direction, again after conversion to a susceptibility. The peak of the distribution corresponds to a counting rate of 2.6 min^{-1}.

Figure 3 (above, right). A constant-energy survey of the magnon peak for the c direction at 65 meV. The background level is shown by a dashed line; the continuous line is the best-fit curve of a model described in the text. The histogram, obtained by correcting the data for resolution effects, indicates the true line shape of a 65 meV magnon.

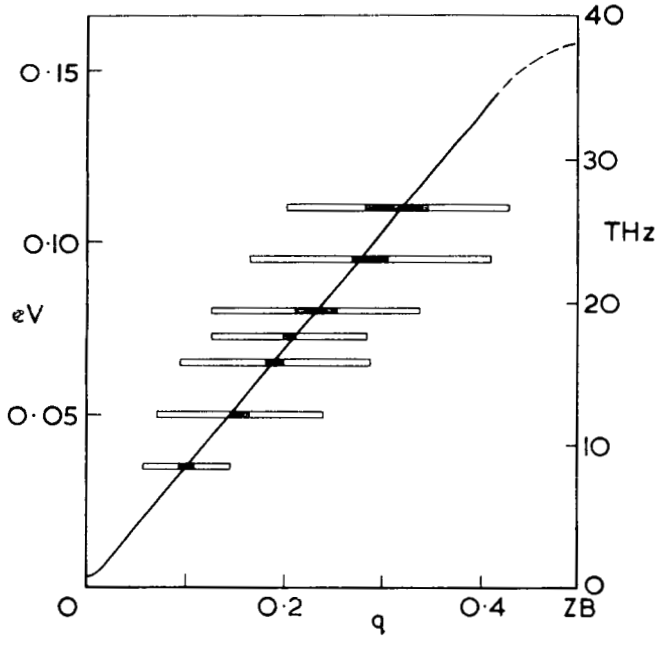


Fig.4. The measured dispersion relation for spin waves travelling in the c direction. Filled rectangular blocks represent our observed values of ζ and their statistical uncertainties; the wider error bars give the standard deviations of the line shape histograms and demonstrate the great intrinsic "width" of these excitations.

spectrum was assumed to consist of the sum of spectra arising from a set of dispersion laws of different slopes. The weights to be attached to the individual spectra were then treated as variables to be determined by a linear least squares fit to the data. The results of this analysis are presented in fig.3 for the 65 meV scan; the continuous line represents the best fit to the data points, while the histogram gives the weights attached to individual spectra and represents effectively the line shape of the magnon as a function of reduced wave vector ζ.

The dispersion relation deduced from analysis of our data up to 0.11 eV is shown in fig.4, where the wider bars on the points indicate the standard deviations in K of the intrinsic line shape. Over this whole energy range the results show a linear dispersion law with a slope of 201 ± 3 meV Å. There is, however, an "anisotropy gap" of 3.0 ± 0.3 meV. The long-wavelength magnon velocity of $\sim$31 km sec^{-1} defined by the linear portion of the curve may be compared with the approximate value of 47 calculated from first principles for pure f.c.c. manganese by Gillan.[5] It is substantially less, in fact, than the corresponding values for some well-known itinerant-electron antiferromagnets such as NiS (67) & Cr ($\sim$150), and less even than the 34 km sec^{-1} appropriate to NiO; but it does border on the region of numbers associated with itinerant-electron antiferromagnetism.

The experimentally indicated width of the magnon line is roughly constant at about 30%. This proportion is rather larger than Gillan's approximate theoretical $\sim$15%; but it is, of course, reasonable that an alloy should give a broader line than a pure element. The fundamental reason for the substantial linewidth is as follows. According to standard theories of antiferromagnetism,[3] the phenomenon is caused by a kind of self-consistent splitting of the electron energy band structure. Now in a practical case there will normally be some bands that are not so completely split that one split-off part rises wholly above the Fermi surface while the other sinks wholly below. Thus there will normally be "magnetised" bands at the Fermi surface, so that just as in a paramagnet a probe will be able to interact with a single-particle excitation at simultaneously low K and ω. Although there are various other

contributions to the magnon linewidth which remain to be assessed theoretically, we believe that the broadening observed in the present experiment is essentially a verification of this effect.

A more complete account of the investigation will be published shortly.

REFERENCES

1. S.Asano & J.Yamashita, Progr.Theor.Phys. 49, 373 (1973).
2. See particularly the review by Y.Ishikawa: Sci.Rep.Tohoku.Univ. 58, 151 (1975), and references therein.
3. W.Young, J.Phys.F 6, 829 (1976).
4. T.J.Hicks, A.R.Pepper & J.H.Smith, J.Phys.C 1, 1683 (1968).
5. M.J.Gillan, J.Phys.F 3, 1874 (1973).

INFLUENCE OF THE ORDER-DISORDER TRANSITION IN Fe_3Al ON THE LOW-ENERGY SPIN WAVES

E. Frikkee
Reactor Centrum Nederland
Petten (N.H.), The Netherlands

K. Mikke
Institute of Nuclear Research
Swierk, Poland

ABSTRACT

To investigate the influence of the order-disorder transition in Fe_3Al at T_c = 824 K on the properties of the low-energy spin waves, neutron inelastic scattering experiments were performed on an annealed Fe_3Al single crystal between 298 K and 873 K. To distinguish magnons in the ordered and disordered phases, a comparison was made between observations in the (111) and (220) Brillouin zones. At room temperature the dispersion relation was found to be isotropic, $E(\vec{q}) = Dq^2$, with D = 132±7 meV Å^2. In the ordered phase below T_c the dispersion relation along [111] remains quadratic when the temperature is increased, until the magnons become unobservable above 773 K. In the (220) zone excitations with wave vectors $q > 0.27$ Å^{-1} were still observable above T_c. These excitations are tentatively interpreted as magnons in completely disordered regions with dimensions < 25 Å.

INTRODUCTION

According to the phase diagram for the Fe-Al system, alloys with compositions close to stoichiometric Fe_3Al may exist in three phases[1]. In the α_1 phase below T_c = 824 K Fe_3Al has the DO_3-type structure[2]. As shown in fig. 1, there are two different types of Fe atoms in this structure. The Fe(I) atoms are surrounded by eight Fe(II) atoms as nearest neighbours, whereas Fe(II) atoms have four Al atoms and four Fe(I) atoms as nearest neighbours.

In the α_2 phase, between T_c and T_c^* = 1049 K, Fe_3Al has a partially disordered, B2-type structure with a simple cubic primitive cell,

in which an Fe atom is situated at the centre and the corners are statistically occupied by Fe and Al atoms. The transition to a completely disordered phase occurs at T_c^*. Above this temperature all atoms are distributed at random over the lattice sites, which results in the body-centred cubic, A2 structure (α phase).

The magnetic properties of Fe_3Al are strongly affected by the degree of order. Firstly, the magnetic moments of the Fe atoms in Fe-Al alloys are found to decrease very rapidly if the number of Al nearest neighbours (n) becomes larger than 4[3]. In the ordered α_1 phase, which is ferromagnetic, the moments of Fe(I) (n = 0) and Fe(II) (n = 4) are $2.18\pm0.10\ \mu_B$ and $1.50\pm0.10\ \mu_B$, respectively[4]. Secondly, the exchange interaction between the Fe atoms depends on the distribution of the Al atoms over the lattice sites. When the Al concentration is increased from 25 to 33 at.%, a gradual change from ferromagnetic to antiferromagnetic behaviour is observed[5]. In order to explain these results, Sato and Arrott have introduced an interaction model involving direct ferromagnetic exchange interaction between nearest-neighbour Fe atoms and a 180° antiferromagnetic super-exchange interaction between two Fe atoms separated by an Al atom[6]. According to this model the ferromagnetic interactions dominate in the α_2 phase of stoichiometric Fe_3Al, but the Mössbauer spectra observed by Cser et al.[7] between 780 K and 920 K for a sample containing 24.3 at.% Al indicate that this phase is probably paramagnetic. Also in the completely disordered α phase the ferromagnetic interactions are strongest. However, for Fe_3Al the transition temperature T_c^* is higher than the Curie temperature in the α phase[1], and ferromagnetic order has only been realized by rapid cooling from the paramagnetic α phase[8].

The present investigation of the low-energy spin waves in Fe_3Al was undertaken to study the influence of the order-disorder transition at T_c on the dynamical properties of the spin system. A similar investigation has been carried out by Van Dijk for specific branches of the phonon dispersion relation[9]. A comparison will be made with previous experimental work at room temperature[10,11], and with theoretical predictions for the spin-wave dispersion relation for small wave vectors in the three

phases[12].

EXPERIMENTS

Neutron inelastic scattering experiments were carried out by means of a triple-axis spectrometer at the HFR reactor in Petten. Curved pyrolytic graphite (0002) and zinc (0002) were used as monochromators to select incident neutrons with energies of 20.18 meV and 37.61 meV, respectively. In both cases curved pyrolytic graphite was used as analyzer. Horizontal collimators in the combinations 20'-30' for E_o = 37.6 meV and 40'-60' for E_o = 20.2 meV were mounted in front of the monochromator and analyzer, respectively. For these combinations a separation of magnons and phonons in the frequency range 1 THz < ν < 2.5 THz could be made. The measurements were performed on an annealed sample, containing 24.9±0.2 at.% Al, at fixed temperatures between 298 K and 873 K. The crystal, which was used previously for an investigation of the phonon dispersion relation[9,13], was mounted in a vacuum furnace with the [T10] direction vertical.

To investigate the effect of increasing disorder on the energy and life-time of the magnons, a systematic comparison was made between magnons in the (111) and (220) Brillouin zones corresponding to the DO_3 superstructure. Because the transition at T_c between the α_1 and α_2 phase is of second order, both phases will coexist within a large temperature range. Well below T_c short-range (B2) disorder will start to develop, while an appreciable amount of short-range (DO_3) order persists up to at least 900 K [9]. The choice of the zones (111) and (220) was based on the general consideration that long wave length acoustic excitations in a lattice with a particular structure are only observable in the vicinity of the reciprocal lattice points corresponding to that structure (see fig. 2). Therefore, the (111) zone was selected for the observation of long wave length magnons in the DO_3 structure. If magnons exist in the B2 structure, one should obviously try to observe them in the (002) or (222) zone. However, the small value of the magnetic structure factor in these zones[4] is a serious drawback, and therefore the (220) zone was chosen instead. In the selected zones constant-ν scans

were performed along the [111] and [110] directions, respectively, to avoid the scattering by acoustic transverse phonons.

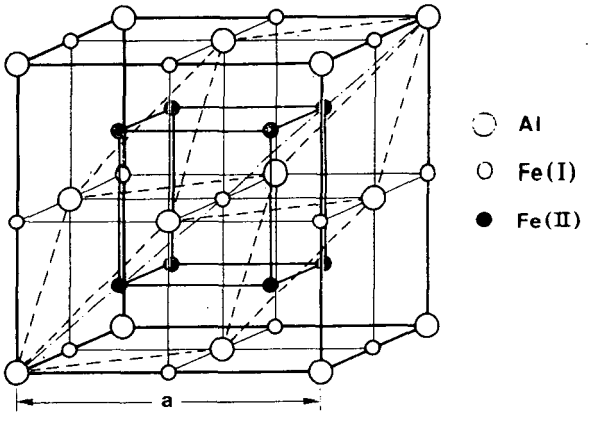


Fig. 1. DO_3 structure of ordered Fe_3Al. The dashed edges indicate the primitive cell.

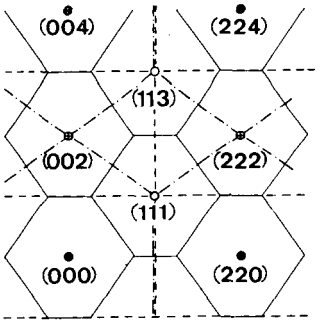


Fig. 2. Reciprocal lattice points and zone boundaries in the $(\bar{1}10)$ plane for the three structures of Fe_3Al.
○ ⊕ ● ——— : DO_3 (α_1)
⊕ ● – – – – : B2 (α_2)
● – . – . – : A2 (α)

RESULTS

In the vicinity of the reciprocal lattice point (111) the dynamic structure factors for inelastic scattering by the acoustic magnons and longitudinal phonons are approximately equal (see fig. 3). The inelastic scattering by phonons and magnons decreases rapidly for $T > 673$ K, as the transition temperature $T_c = 824 \pm 1$ K is approached, and is no longer observable at 873 K. Between 298 K and 773 K the magnon dispersion relation remains quadratic, $E(q) = Dq^2$, in the investigated frequency range 1.0 THz $< \nu \leq$ 2.5 THz. The observed values of the stiffness constant D are listed in table 1.

Although the observation of the magnons in the (220) zone is complicated by the strong neutron-phonon scattering (cf. fig. 3), systematic differences in comparison with the magnons in the (111) zone could be detected. For $T \geq 573$ K the observed peak positions cannot be fitted by a quadratic dispersion relation. In the scans for $\nu = 1.0$ THz and 1.5 THz the positions of the neutron groups do not change with temperature, the

intensity decreasing rapidly for T > 573 K. On the other hand, the magnons with $\nu \geq 2$ THz remain clearly observable, and persist above T_c where the stiffness parameter D appears to become constant (cf. fig. 3 and table 1).

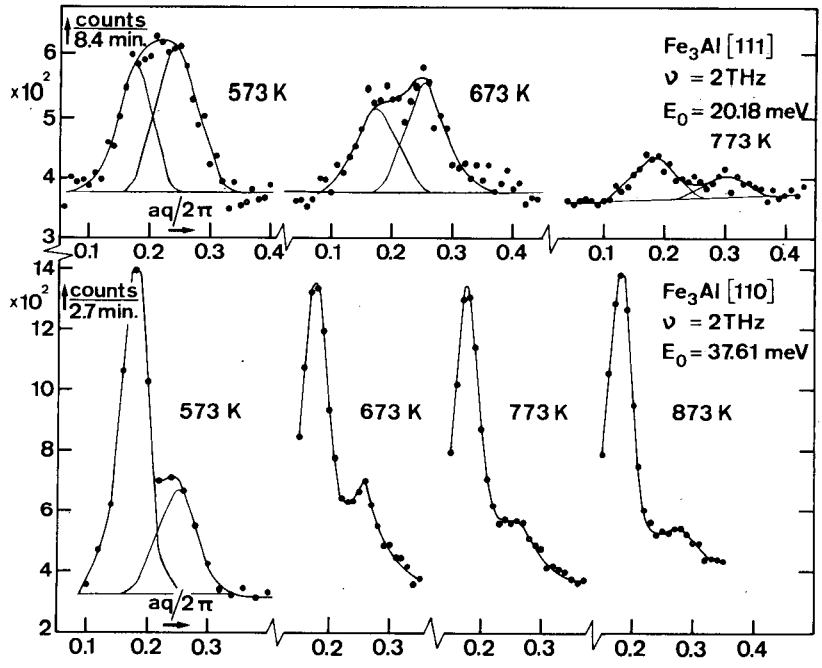


Fig. 3. Constant-ν scans in the (111) and (220) zones performed at various temperatures. The maxima at small q values are due to longitudinal phonons.

Table 1. Observed values of the stiffness parameter D(T) in Fe_3Al.

T(K)	zone (111) direction [111] 1 THz < ν < 2.5 THz	zone (220) direction [110] ν < 2 THz	$\nu \geq$ 2 THz
298	133.0±6.5 [a]	131±11	
423	131 ±8		
573	126 ±8	131±11	109±6
673	111 ±7	131±11	102±5
773	74 ±10	-	96±5
873	-	-	95±5

[a] D in units meV $Å^2$

DISCUSSION

When the magnons in the $\alpha_1(DO_3)$-phase of Fe_3Al, observed in the (111) zone, are compared with those in α-Fe[14,15], two significant differences may be noticed. In the first place, the renormalization of the magnons in Fe_3Al is much smaller than in Fe. If the temperature dependence of D(T) is assumed[16] to be described by $D(T) = D(0) - D_2T^{5/2}$, the value $D(0) = 134.5 \pm 8$ meV Å^2 is obtained by extrapolation of the results for $T \leq 573$ K. The decrease in D(T) between T = 0 K and $T/T_c = 0.7$ is only 6.3%, whereas this renormalization effect is 40.4% in Fe at the same value of T/T_c [14]. Secondly, the magnons in the α_1 phase of Fe_3Al are not observable above the transition temperature, in contrast to the observation of magnons with $\nu = 2$ THz in Fe, even at $T/T_c = 1.4$.[15] This different behaviour of the magnons in Fe_3Al may be due to the close relation between magnetic and chemical order in the DO_3 structure. From the smooth variation with temperature of the intensity of the (111) reflection, which contains an appreciable magnetic contribution[4], it may be concluded that the Curie temperature in the DO_3 structure coincides with T_c.

The anomalous behaviour of the magnons observed in the (220) zone, i.e. the different temperature dependence of D(T) for $\nu < 2$ THz and $\nu \geq 2$ THz, is most likely due to the fact that in the vicinity of the (220) reciprocal lattice point long wave length excitations in different coexisting phases are observed simultaneously. In this case the properties of the excitations will depend on the size of the regions having different structures, and the observed modes should therefore be distinguished by their wave vectors q. Comparison with the results in the (111) zone shows that the excitations with $q > 0.27$ Å^{-1} ($\nu \geq 2$ THz) observed for $T \geq 773$ K must be ascribed to the α_2 or α phase. As the excitations are only observable above a minimum value of q, and the scattered intensity is approximately independent of temperature, it seems probable that these are magnons in completely disordered (α phase) regions with dimensions < 25 Å. The coexistence of two phases $\alpha+\alpha_1$ and $\alpha+\alpha_2$ in alloys with less than 25 at.% Al at temperatures below T_c* has been observed previously[1]. Extrapolation of the magnetic transition

curve for the α phase towards larger Al concentration shows that for $T \leq 873$ K ferromagnetic order may be expected in these α-phase regions. If this interpretation is correct the excitations should not be observable in the (222) zone. Additional experiments in this zone are in progress.

Comparison with previous experimental results[10,11] shows considerable differences between the D-values in the $\alpha_1(DO_3)$ phase. The value D(0) = 102±1.5 meV Å^2 was obtained by means of small-angle scattering on a polycrystalline sample containing 25 % Al [10]. Secondly, measurements with the so-called diffraction method[11] on a single crystal with 26.5 % Al in the range $0.24\ Å^{-1} < q < 0.33\ Å^{-1}$ in the (220) zone yielded the value D(295) = 83±4 meV Å^2. From the present investigation it may be concluded that the disagreement between the previous and the present D values for $T \leq 298$ K cannot be explained by anisotropy, extrapolation to T = 0 [10] or differences between magnons in different zones. A possible explanation for the small value of D in the 26.5 % Al alloy seems that D decreases rapidly with increasing Al concentration above 25 %, because (1) the magnetic moments decrease[11] and (2) antiferromagnetic interactions become more important.[6]

On the other hand, the experimental results may be compared with calculations by Elk[12], which yield the values D(0) = 110±7 meV Å^2, 190 meV Å^2 and 232 meV Å^2 in the DO_3, B2 and A2 structure, respectively. The former value is in reasonable agreement with the extrapolated value D(0) = 134.5±8 meV Å^2 for the present crystal with 24.9±0.2% Al. The latter two values are obviously much larger than the experimental result $D(T > 773\ K) = 95±5$ meV Å^2 in the (220) zone. However, the decrease of D(T) for increasing T has not been taken into account in the calculations. Unfortunately, an experimental determination of D(0) for the A2 structure is not possible, because the α phase cannot be retained during quenching. Experiments on the B2 structure in a quenched sample will be performed later.

REFERENCES

1. P.R. Swann, W.R. Duff, and R.M. Fisher, Met. Trans. 3, 409 (1972).
2. A.J. Bradley and A.H. Jay, Proc. Roy. Soc. A136, 210 (1932).
3. G.P. Huffman and R.M. Fisher, J. Appl. Phys. 38, 735 (1967), M.J. Besnus, A. Herr, and A.J.P. Meyer, J. Phys. F5, 2138 (1975).
4. S.J. Pickart and R. Nathans, Phys. Rev. 123, 1163 (1961).
5. A. Arrott and H. Sato, Phys. Rev. 114, 1420 (1959).
6. H. Sato and A. Arrott, Phys. Rev. 114, 1427 (1959).
7. L. Cser, J. Ostanevich, and L. Pál, Phys. Stat. Sol. 20, 581 (1967).
8. C. Sykes and H. Evans, J. Iron Steel Inst. 131, 225 (1935).
9. C. van Dijk, Second Conference of the Condensed Matter Division of the European Physical Society, Budapest (1974).
10. B. Antonini and M.W. Stringfellow, Proc. Phys. Soc. 89, 419 (1966).
11. B. Antonini, F. Menzinger, and A. Paoletti, J. de Phys. C1, 1188 (1971).
12. K. Elk, Phys. Stat. Sol. 38, 297 (1970).
13. C. van Dijk, RCN-129 (1970), Phys. Letters 32A, 255 (1970).
14. M.W. Stringfellow, J. Phys. C1, 950 (1968).
15. J.W. Lynn, Phys. Rev. B11, 2624 (1975).
16. W. Marshall and S.W. Lovesey, Theory of Thermal Neutron Scattering, p. 267, Clarendon Press, Oxford, 1971.

MAGNON-PHONON-HYBRIDISATION IN $FeCl_2$

K.R.A. Ziebeck[+], J.G. Houmann[x]
[+]Institut Laue-Langevin, 156X Centre de Tri, 38042-Grenoble Cédex, France
[x]Danish AEC Research Establishment, Risø, Roskilde, Denmark

ABSTRACT

High resolution inelastic neutron scattering measurements have been performed on the metamagnet $FeCl_2$ using the Risø cold source triple axis. The purpose of these measurements was to confirm the existence of strong hybridised modes in the antiferromagnetic phase of $FeCl_2$. Constant Q surveys made in the |100| direction without an applied magnetic field established the splitting at the nominal point of intersection $K_x = 0.17$ to be 0.32 meV. The application of a 8.9 KG field parallel to the c axis raised the degeneracy of the magnons enabling both polarisations to be identified. From the observed magnon energy gap at $K_x = 0$ the gyromagnetic ratio g was estimated to be 4·01±0.2 in close agreement with the value 4.14 obtained by resonance experiments. Furthermore the applied field permitted a more precise investigation of the hybridised modes by contributing an additional splitting. Detailed measurements made in the |100| direction showed that the hybridisation takes place only between the magnons and the low energy $TA_\perp$ (Σ_2) phonon in agreement with theory.

INTRODUCTION

The primitive cell of $FeCl_2$ is rhombohedral with space group D^5_{3d} and contains one molecular unit. For convenience the system may be characterised by the triple hexagonal cell with parameters a = 3.583 Å and c = 17.45 Å. Susceptibility and specific heat measurements Starr et al[1] and Trapeznikowa and Schubnikow[2] indicated that below 23.5 K the system becomes ordered antiferromagnetically. These assertions were substantiated by the neutron diffraction measurements of Wilkinson et al[3] who determined the ordered moment to be 4.5 μ_B per Ferrous ion and noted that the spins were aligned along the c axis. The magnetic unit cell has an edge doubled in the c direction.

Thus antiferromagnetic $FeCl_2$ is composed of hexagonal sheets of

ferromagnetically aligned Ferrous ions with a strong anisotropy fixing the moments in the C direction. The anisotropy energy is approximately 2 meV. A very weak antiferromagnetic interaction exists between the hexagonal planes so that the overall order is antiferromagnetic. Moreover the exchange interaction in the plane is dominated by nearest neighbour coupling. Birgeneau et al[4] have shown that magnons with wave vectors parallel to c exhibit negligible dispersion but "in plane" magnons can be described by simple spin wave theory.

$$H = -J \sum_{1\delta} \underline{S}_1 . \underline{S}_{1+\delta} + D\Sigma_1 (S_1^z)^2$$

At 4.2 K a field of 10.6 KG applied parallel to the c axis overcomes the inter layer exchange to produce a ferromagnet.

MAGNON-PHONON COUPLING

The possibility of magnon-phonon coupling in $FeCl_2$ was first suggested by Laurence and Petitgrand[5] (1973) to explain the pronounced dip at 17 K in the thermal conductivity in the hexagonal plane. The nature of the coupling was discussed by Lovesey (1974)[6] and is analogous to that in FeF_2 Lovesey (1972)[7]. The hybridised modes arise from a modulation of the orbital motion of the single electron outside the half filled closed shell of the Fe^{2+} ion by the ligand crystal field. The six chlorine ions surrounding each ferrous ion do not form a regular octahedra so that the symmetry of the crystal field is orthorhombic D_{2h}. The modulation of the orbital motion is transmitted to the spins via the spin orbit coupling. The static component of the field gives rise to the large single ion anisotropy and the component linear in the displacements of the ferrous and ligand ions from their equilibrium positions creates the magnon-phonon coupling. Confirmation of this mechanism for the Ferrous compounds is given by the absence of magnon-phonon coupling in MnF_2 in which the Mn^{2+} ions are in an S state.

For the $|100|$ direction group theory dictates that only the low energy $TA_\perp$ phonon (Σ_2) will couple with the magnon modes Cracknell[8] (1974). In the absence of a magnetic field, the hybridised modes at

the nominal point of intersection $K_x = 0.17$ Å^{-1} are separated by some 0.33 meV. Moreover the unperturbed magnon is situated midway between the hybridised modes. Thus to resolve the three features requires an energy resolution better than 0.16 meV. However a magnetic field applied parallel to the c direction lifts the degeneracy of the magnons and increases the separation of the hybridised modes. The splitting of the magnon modes is given by $2\ g\mu_B H$ where $g = 4.14$. Therefore the application of a 10 KG field increases the splitting by a further 0.44 meV.

The model[6] predicts three modes :

ω_0 mode : - Σ_2 magnon at $K_x = 0$ changing to TA Σ_2 phonon at the zone boundary.

ω_1 mode : - Σ_1 magnon the zone centre which becomes Σ_2 magnon at M.

ω_2 mode : - Σ_2 TA phonon at $K_x = 0$ changing to Σ_1 magnon at the zone boundary.

EXPERIMENTAL

High resolution neutron scattering experiments were performed using the Risø cold source triple axis TAS1 and a single crystal 500 mm^3 kindly loaned by Professor D. Bloch of C.N.R.S.. The instrument was operated in the constant K_f mode with an outgoing neutron wavevector of $K_f = 1.553$ Å^{-1} and a cooled Be filter inserted before the graphite analyser. The incident neutron wave vector was focused onto the specimen by a vertically curved tunable graphite monochromator. The collimators employed, following the outgoing beam were 55', 38', 140' and 66'. The $FeCl_2$ crystal was sealed in a thin walled aluminium can under a helium atmosphere and mounted in a cryomagnet. Measurements were recorded at 4.2 K with and without a field of 10 KG. The orientation of the crystal was such that the c axis subtended an angle of 27.19° to the field. In this configuration the (105) magnetic reciprocal lattice point was brought into the scattering plane which was defined by the vectors $|105|$ $|100|$. Thus the magnon dispersion and the possibility of magnon-phonon coupling was investigated in the $|100|$ direction i.e. for the Σ modes. For measurements with a vertical field of 10 KG the component along the c axis was 8.895 KG.

RESULTS AND DISCUSSION

The optimum arrangement for the experiment would be a (hol) scattering plane and a horizontal field applied parallel to the c axis. However the requirements of good resolution when coupled with physical constraints necessitated a non standard orientation. Despite this, the optimum magnetic reciprocal lattice point (105) was brought into the scattering plane whilst retaining the |100| symmetry direction.Since the magnon dispersion was investigated from the 105 Γ point the phonon modes detected could only arise from magnon phonon coupling. In the absence of a field the splitting was determined to be 0.33 meV, in good agreement with the theoretical prediction. The application of a magnetic field with component of 8.895 KG along the c axis lifted the degeneracy of the magnons and enabled an unambiguous identification of the modes. This appears to be the first observation of such magnon-phonon coupling in which the modes have been separated by an applied field. In figure (1) the hybridised excitations are shown for the |100| direction at 4.2 K with a vertical field of 10 KG. A typical excitation as measured is shown in figure (2). From the magnon energy gap at $K_x = 0$ the gyromagnetic ratio g was estimated to be 4.01±0.2 which is in good
the value 4.14 obtained by resonance experiments. Despite the efficacy of the applied field in permitting the identification of the modes it is not certain to what extent such a field modifies the selection rules. It may be expected that these will remain unchanged so long as the magnetic structure is not significantly modified. This was borne out by the experiment which indicated that the coupling in the |100| direction was only between the magnons and the low energy $TA_1(\Sigma_2)$ phonon.

REFERENCES

1. Starr, Bitter and Kaufmann, Phys. Rev. 58, 977 (1940)
2. O. Trapeznikowa and L. Schubnikow, Physik Z. Sowjetunion 7, 66 (1935)
3. M.K. Wilkinson, J.W. Cable, E.O. Wollan and W.C. Koehler, Phys. Rev. 113(2) 497 (1959)
4. R.J. Birgeneau, W.B. Yelon, E. Cohen and J. Makovsky, Phys. Rev. B, 5(7), 2607 (1972)

5. G. Laurence and D. Petigrand, Phys. Rev. B 8, 2130 (1973)
6. S.W. Lovesey, J. Phys. C. 7, 2049 (1974)
7. S.W. Lovesey, J. Phys. C. 5, 2769 (1972)
8. A.P. Cracknell, J. Phys. C. 7, 4323 (1974)

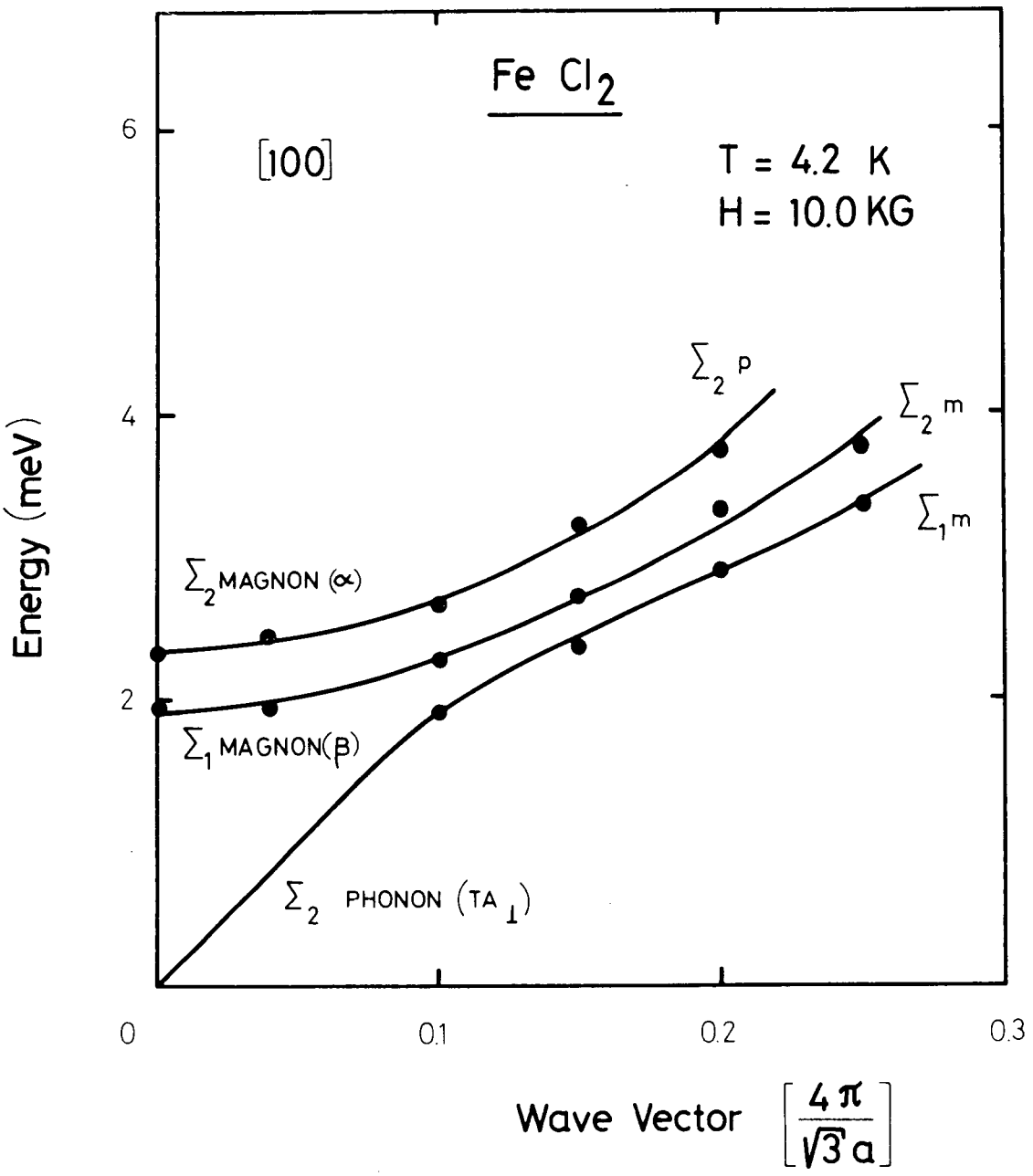


Fig. 1. The Dispersion Relation of the hybridised Modes in the |100|

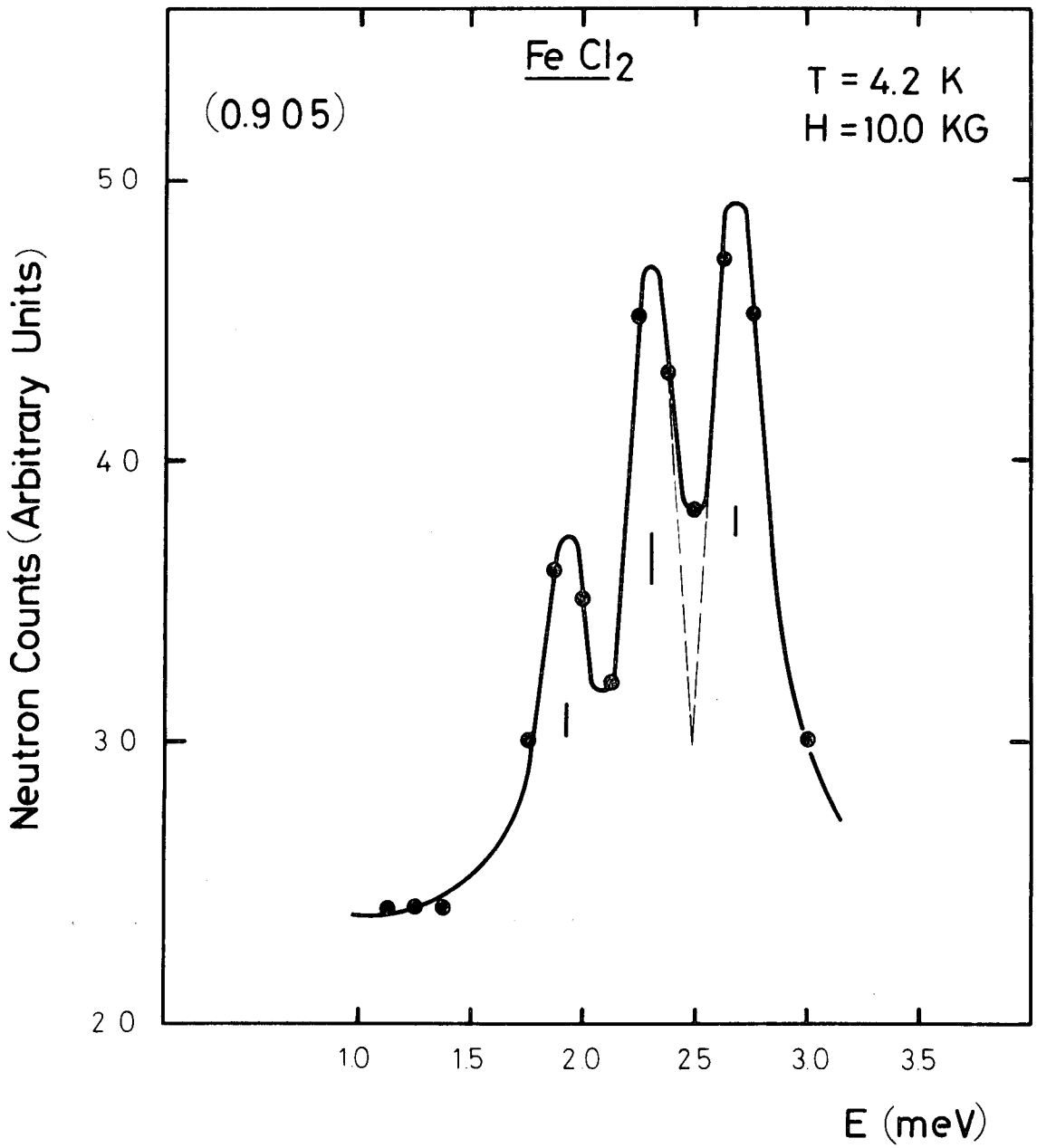


Fig. 2. A typical neutron group

STATIC AND DYNAMIC RESPONSE FUNCTIONS FOR A CLASSICAL PARAMAGNET IN AN APPLIED FIELD

S. W. Lovesey and J. M. Loveluck
Institut Laue-Langevin
156X Centre de Tri, 38042 Grenoble Cedex, France

INTRODUCTION

We shall develop a formalism which describes the response of a classical paramagnet, subject to an applied magnetic field, to a spatial- and time-dependent perturbation, with particular emphasis on the static and dynamic response functions measured by neutron scattering.

For paramagnetic systems, which do not support long-range magnetic order, an understanding of the fluctuations induced by the perturbation is crucial. For a spatially varying, static perturbation, an appropriate description is obtained as a generalisation of the theory of thermodynamic fluctuations, by the introduction of local thermodynamic variables and corresponding response functions, which reduce, in the long-wavelength limit, to familiar thermodynamic quantities. It is shown that the effects of coupling between the energy and magnetisation densities, caused by the magnetic field, can be fully included by a renormalisation of the energy density, and features in the response functions, attributable to this coupling, are readily identified; this is illustrated explicitly by calculations for a one-dimensional Heisenberg magnet, with the anti-ferromagnetically-coupled chain leading to particularly striking results.

Dynamic aspects of the response are studied within the framework of the Mori approach to irreversible thermodynamics. It is found that modifications, due to the magnetic field, of both the dynamical equations and the thermodynamic quantities entering the theory, can be included by a multi-variable description, with a judicious choice of variables, and the renormalisation of the energy density, referred to above. The novelty of the resulting equations necessitates innovations in the determination of approximate solutions, and these are found to exhibit rather striking

features (in particular, in the collective mode behaviour) which can be attributed to the applied magnetic field. The classical Heisenberg chain again provides a useful model to illustrate the consequences of the theory, since it combines the features that: (a) required static correlation functions can be calculated exactly; and (b) strongly-developed short-range order, at low temperatures, enhances effects which may be marginal in three-dimensional systems.

An analogy can be drawn between the description of classical paramagnets and that of a monatomic classical fluid. While this analogy is useful, in particular, in discussing static fluctuations, it is not complete, and there are important differences between the dynamic properties of the two systems, which can be traced to the absence of a kinetic energy term in the Hamiltonian of the magnetic system. The usefulness, and limitations, of this analogy are discussed more fully in two forthcoming publications by the authors[1], which also include a more detailed analysis of the results obtained for the classical Heisenberg chain.

WAVELENGTH-DEPENDENT THERMODYNAMIC VARIABLES AND RESPONSE FUNCTIONS

A description of thermodynamic fluctuations in magnetic systems is readily constructed, using a Gibbs distribution which is canonical in the internal energy E and the magnetisation, M, parallel to the applied field; this procedure being analogous to the use of an isothermal-isobaric ensemble for the more familiar case of a fluid. A natural generalisation of this description, to include local fluctuations, suggests, as basic local thermodynamic variables, $M_{\underline{k}}$, the k-th Fourier component of the magnetisation density, and $\varepsilon_{\underline{k}}$, the corresponding Fourier component of a renormalised energy density, defined by

$$\varepsilon_{\underline{k}} = E_{\underline{k}} - (E_{\underline{k}}, M_{\underline{k}}^{*}) M_{\underline{k}} / \chi_t^z(k) \qquad (1)$$

In Eq. (1), $\chi_t^z(\underline{k})$ is the wavelength-dependent isothermal susceptibility, which determines the elastic neutron cross-section, and is related to the magnetisation fluctuations by

$$\chi_t^z(\underline{k}) = (M_{\underline{k}}, M_{\underline{k}}^{\ddagger}) \tag{2}$$

The bracket notation in (1) and (2) is defined by

$$(A,B) = \beta\{\langle AB\rangle - \langle A\rangle\langle B\rangle\}, \tag{3}$$

in terms of which $M_{\underline{k}}$ and $\varepsilon_{\underline{k}}$ are orthogonal. To complete the thermodynamic description, a second pair of orthogonal variables, conjugate to the first pair, is introduced: a local field, $H_{\underline{k}}$, and a local entropy, $\delta_{\underline{k}}$, the latter being a more useful quantity than the corresponding enthalpy, which is naturally suggested by the "isothermal-isobaric" ensemble, since this would include fluctuations in the applied field.

The fluctuations in these four local thermodynamic variables determine the four basic response functions of the system, via the relation (2) together with

$$\chi_s(k) = (H_{\underline{k}}, H_{\underline{k}}^{\ddagger})^{-1} \tag{4}$$

$$C_h(\underline{k}) = T(\delta_{\underline{k}}, \delta_{\underline{k}}^{\ddagger}) \qquad \text{and} \qquad C_m(\underline{k}) = (\varepsilon_{\underline{k}}, \varepsilon_{\underline{k}}^{\ddagger})/T,$$

which reduce, respectively, to the isentropic susceptibility and the specific heats at constant field and constant magnetisation, in the long-wavelength ($k \to 0$) limit.

The quantities $M_{\underline{k}}$, $H_{\underline{k}}$ and $\varepsilon_{\underline{k}}$, $\delta_{\underline{k}}$ can be regarded as the basic local "mechanical" and "thermal" variables for a paramagnet and the functions χ_t, χ_s, C_m, C_h are then a measure of the response of the paramagnet to fluctuations in these four variables.

A one-dimensional Heisenberg magnet is defined by the energy density

$$E_{\underline{k}} = -\frac{J}{2} \sum_{\ell,\delta} \exp(ik\ell)\, \underline{S}_{\ell} \cdot \underline{S}_{\ell+\delta}, \tag{5}$$

where J is the exchange coupling for nearest neighbour spins, $\underline{S}_{\ell}$ and $\underline{S}_{\ell+\delta}$ (taken as unit vectors for the classical model) and $\delta = \pm 1$ if we measure lengths in units of the lattice spacing. For this model, the

response functions introduced above can be expressed in terms of static spin correlation functions, which can be evaluated exactly, using a transfer matrix technique similar to that described by Loveluck et al.[2], and, also, analytic expressions can be obtained yielding good approximations in the limits of both high and low temperatures. For ferromagnetic coupling ($J>0$), the most accurate approximations at low temperature are obtained using a semi-classical spin-wave theory[1]. We now describe some of the results obtained from these calculations. All response functions calculated are per spin, and we use reduced units of temperature and field, defined by $T^{*}= T/|J|$ and $h^{*}= h/|J|$ respectively, where h is the magnetic field, in units of $g\mu_B$.

For ferromagnetic coupling, the wave-vector dependence of $\chi_t^z(k)$ is not radically affected by the magnetic field, but its magnitude decreases with h^{*}. More interesting effects, associated with a change from anti- to ferromagnetic character, are observed in antiferromagnetically coupled chains. This is most clearly illustrated in the behaviour, as a function of field, of suitably defined inverse correlation lengths κ_α and κ_α^{*} measured, respectively, with respect to the zone centre and zone boundary. Typical behaviour of these quantities is shown, for $T^{*}= 0.10$, in Fig. 1. An approximate solution for the spin correlation functions (results denoted by solid circles in Fig. 1) suggests that, for low temperatures, the magnetic character of the system changes at $h^{*}= 2\sqrt{2}$, and the numerical results support this conclusion. A change in local magnetic order occurs for much smaller fields ($h^{*}\sim 1$ for $T^{*}= 0.1$), and this is reflected, in particular, in a maximum, for this value of h^{*}, in $\chi_t^z(\pi)$ as a function of field. The ratio $\gamma(k)$ of the wavevector-dependent specific heats is a measure of the coupling between the energy and magnetisation densities induced by the magnetic field. In Fig. 2 we show $\gamma(0)$ as a function of h^{*}, for both ferro- and antiferromagnetic coupling, at two values of T^{*}. For the ferromagnetic chain $\gamma(0)$ is seen

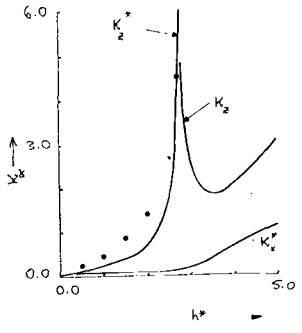


Fig. 1 Inverse correlation lengths for an antiferromagnetic chain.

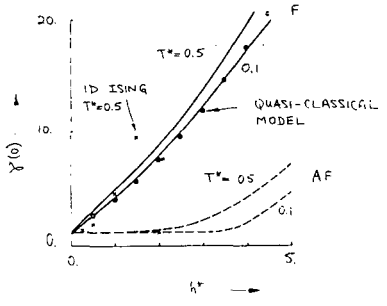


Fig. 2 $\gamma(0)$ for ferro (F) and antiferromagnetic (AF) coupling.

to be strongly field dependent, with a rather weak temperature dependence, quite modest fields producing significant deviations from the zero field value of unity. The quasi-classical spin wave result (solid circles) is seen to be a good approximation for small T^*, but the result is temperature independent. For an antiferromagnetic chain the numerical results indicate negligible coupling between the energy and magnetisation densities ($\gamma(0) \sim 1.0$) until field strengths are attained which are sufficient to evoke the change of magnetic character. Also shown in Fig. 2 are results, denoted by (×), for an antiferromagnetic Ising chain. The dramatic field dependence for this model reflects an oscillation in $C_h(0)$, as a function of h^*; a similar, but much weaker, oscillatory behaviour was found for the classical antiferromagnetic chain, and the results for the Ising chain indicate that this behaviour is not peculiar to the classical model.

DYNAMICAL EQUATIONS AND THE RESPONSE FUNCTION FOR ONE-DIMENSIONAL HEISENBERG CHAINS

The formalism of Mori[3] expresses the equation of motion for time dependent correlation functions in the form of a generalised Langevin equation, and it was recognised by Mori that this scheme encompasses a situation whose description requires a number of dynamical variables. Expressed in terms of a column vector, our initial choice of variables is

$$A = \mathrm{col}(M_{\underline{k}}, \dot{M}_{\underline{k}}, \varepsilon_{\underline{k}}) \tag{6}$$

this choice being motivated by the following considerations:

(a) the requirement that the equations of motion be valid in the hydrodynamic regime, which suggests the inclusion of basic conserved variables (see, for example, Copley and Lovesey[4]);

(b) the inclusion of effects of the magnetisation-energy density

coupling on thermodynamic properties, via the renormalisation of the energy density $E_{\underline{k}} \rightarrow \varepsilon_{\underline{k}}$, suggested in the previous section;

(c) the objective of obtaining a good approximation to the equation of motion for the magnetisation density autocorrelation function, which suggests the inclusion of $\dot{M}_{\underline{k}}$, but not $\dot{\varepsilon}_{\underline{k}}$, in our choice of variables, so that magnetisation fluctuations are included in higher order than energy fluctuations.

With this choice of variables, a straightforward application of the Mori formalism enables us to obtain a formally exact expression for the matrix

$$\Phi(t) = (A(t),A^{\ddot{}}).\ (A,A^{\ddot{}})^{-1} \tag{7}$$

We are particularly interested in the matrix element of $\Phi(t)$ which corresponds to the magnetisation density relaxation shape function, and this can be written, in terms of its Laplace transform, as

$$\tilde{F}(\underline{k},s) \equiv (\tilde{\dot{M}}_{\underline{k}},M_{\underline{k}})/\chi_t^z(k) = \left\{ s + \frac{\omega_o^2}{s+\tilde{K}(\underline{k},s)} \right\}^{-1} \tag{8}$$

where, within certain approximations to be discussed below, the "memory function" K is given by

$$\tilde{K}(\underline{k},s) = \tilde{\theta}_2^2(s) + \frac{\omega_o^2(\underline{k})\ \{\Gamma(\underline{k})-1\}}{s + \tilde{\theta}_3^2(s)} \tag{9}$$

where we have introduced

$$\Gamma(\underline{k}) = 1 + \frac{|(\dot{M}_{\underline{k}},\dot{\varepsilon}_{\underline{k}}^{\ddot{}})|^2 (M_{\underline{k}},M_{\underline{k}}^{\ddot{}})}{(\varepsilon_{\underline{k}},\varepsilon_{\underline{k}}^{\ddot{}})(\dot{M}_{\underline{k}},\dot{M}_{\underline{k}}^{\ddot{}})^2}, \quad \omega_o^2(k) = \frac{(\dot{M}_{\underline{k}},\dot{M}_{\underline{k}}^{\ddot{}})}{\chi_t^z(\underline{k})} \tag{10}$$

and

$$\theta_2^2(t) = k^2(\hat{\sigma}_{\underline{k}}(t),\hat{\sigma}_{\underline{k}}^{\ddot{}})(\dot{M}_{\underline{k}},\dot{M}_{\underline{k}}^{\ddot{}})^{-1}, \quad \theta_3^2(t) = k^2(\hat{q}_{\underline{k}}(t),\hat{q}_{\underline{k}}^{\ddot{}})(\varepsilon_{\underline{k}},\varepsilon_{\underline{k}}^{\ddot{}})^{-1} \tag{11}$$

which are expressed in terms of the non-conserved parts, $\hat{\sigma}_{\underline{k}}$ and $\hat{q}_{\underline{k}}$, of the fluxes $\sigma_{\underline{k}}$ and $q_{\underline{k}}$ associated with the continuity equations for $E_{\underline{k}}$ and $\dot{M}_{\underline{k}}$. These non-conserved fluxes, following a similar analysis

of a classical fluid by Schofield[5], are defined to be orthogonal to the basic variables $M_{\underline{k}}$, $E_{\underline{k}}$ and $\dot{M}_{\underline{k}}$, and describe damping processes, in contrast to the conserved parts, which form the secular components of the associated continuity equations. In the limit of long wavelengths and times, the autocorrelation functions of the non-conserved fluxes determine transport coefficients, through Kubo relations.

The approximation we have introduced in Eq. (9) is to neglect terms involving correlations between $\hat{\sigma}_{\underline{k}}(t)$ and $\hat{q}_{\underline{k}}(t)$, which should be satisfactory since these terms can be shown to vanish both in the hydrodynamic and instantaneous limits. As noted above, the secular behaviour of the dynamical variables has been separated out, by the decomposition of the associated fluxes, with the result that $\theta_2^2(t)$ and $\theta_3^2(t)$ depend only on the non-conserved components of the fluxes, and can be expected to decay rapidly in time. These considerations lead us to adopt the simple exponential approximations

$$\theta_2^2(t) = \theta_2^2(0)\exp\{-|t|/\tau_2\} \ , \quad \theta_2^2(t) = \theta_3^2(0)\exp\{-|t|/\tau_3\}, \tag{12}$$

which should be appropriate in the limit of short times, and therefore useful in the interpretation of neutron scattering experiments. A straightforward calculation shows that

$$\theta_2^2(0) = \omega_\ell^2(\underline{k}) - \omega_o^2(\underline{k})\Gamma(\underline{k}) \ , \quad \theta_3^2(0) = \omega_e^2(\underline{k}) - \omega_o^2(\underline{k})\{\Gamma(\underline{k})-1\}, \tag{13}$$

where

$$\omega_\ell^2(\underline{k}) = (\ddot{M}_{\underline{k}},\dddot{M}_{\underline{k}})(\dot{M}_{\underline{k}},\ddot{M}_{\underline{k}})^{-1} \quad \text{and} \quad \omega_e^2(\underline{k}) = (\dot{\varepsilon}_{\underline{k}},\ddot{\varepsilon}_{\underline{k}})(\varepsilon_{\underline{k}},\ddot{\varepsilon}_{\underline{k}})^{-1} \tag{14}$$

The relaxation times τ_2 and τ_3 entering Equs. (12) are related to integrals of autocorrelation functions, which are approximated by simple, plausible forms suggested by physical arguments. The procedure is guided by experience gained from previous studies of dynamic behaviour[6,8] (involving a three-pole approximation and a single relaxation time), but incorporates an elementary approximation to the energy autocorrelation function, which conforms with our aim of a higher order treatment of magnetisation fluctuations, and is consistent with the fact that much

stronger short-range order is required to support collective energy-density excitations.

For classical Heisenberg chains, the correlation functions entering the above description can be evaluated, in a manner analogous to that used in the calculation of static response functions, and we now present some of the numerical results of such calculations.

For both ferromagnetic and antiferromagnetic coupling it is found that an applied magnetic field has dramatic effects on the spin dynamics, although it does not introduce qualitatively different structure into the relaxation function. The more basic effects of the applied field are summarised, for the ferromagnetically coupled chain, in Fig. 3 and, for antiferromagnetic coupling, in Fig. 4, which give the frequency, ω_k, and width, Δ_k, of the peak in $F(k,\omega)$ corresponding to collective mode behaviour, for $T^{*}=0.10$, and several values of h^{*} (indicated alongside each curve), including $h^{*}=0.0$ (broken lines).

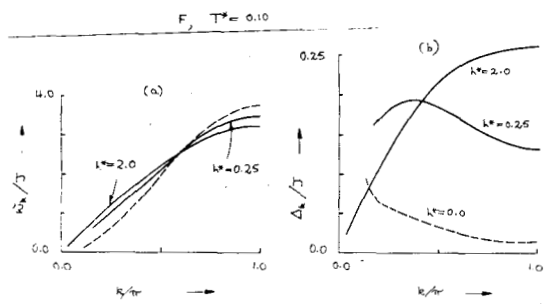


Fig. 3 Collective mode behaviour for a ferromagnetic chain.

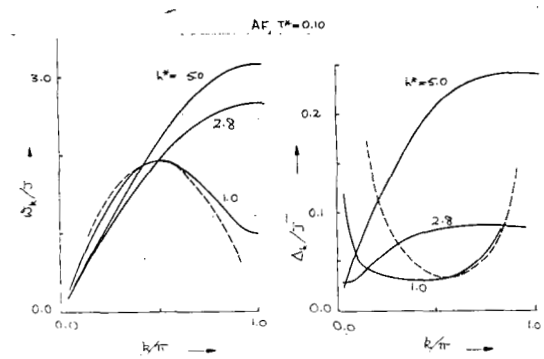


Fig. 4 Collective mode behaviour for an antiferromagnetic chain.

For ferromagnetic coupling, the frequency of the collective mode is seen to be relatively insensitive to the magnetic field, but there is a significant increase in the width, with a complete change in the wavevector dependence for large fields. These effects are accompanied by a reduction in intensity of the collective mode, with a corresponding increase in intensity at small ω. The broadening of the collective mode, for large fields, as the zone boundary is approached, is in sharp contrast to the zone boundary narrowing predicted for isotropic and easy-plane one-dimensional magnets (Lovesey[6], Villain[7], and Loveluck and Lovesey[8]),

and resembles the behaviour of a weakly interacting magnon gas, indicating the high degree of magnetic order induced by the magnetic field.

For antiferromagnetic coupling, the results illustrated by Fig. 4 show that, as for the static response functions, the dynamic behaviour of the system is not significantly modified by an applied magnetic field, except for large values of $h^{\ddagger}$ which result in a change in magnetic character, as is clear from comparison of the curves corresponding to large values of $h^{\ddagger}$ in Figs. 3 and 4. Again, for low temperatures, the onset of this change to ferromagnetic character appears to occur at $h^{\ddagger} \sim 2\sqrt{2}$, as suggested by the semi-classical spin-wave approximation.

The semi-classical spin-wave model, with its attendant computational tractability, affords a means of investigating more sophisticated theories of the dynamic properties, and the authors intend to pursue this possibility.

REFERENCES

1. S.W. Lovesey and J.M. Loveluck, submitted to J. Phys. C.
2. J.M. Loveluck, S.W. Lovesey and S. Aubry, J. Phys. C 8, 3847 (1975).
3. H. Mori, Prog. Theor. Phys. 33, 423 and 34, 399 (1965).
4. J.R.D. Copley and S.W. Lovesey, Repts. Prog. Phys. 38, 461 (1975).
5. P. Schofield, Proc. Phys. Soc. 88, 149 (1966).
6. S.W. Lovesey, J. Phys. C 7, 2008 (1974).
7. J. Villain, J. de Physique 35, 27 (1974).
8. J. M. Loveluck and S. W. Lovesey, J. Phys. C 8, 3857 (1975).

INVESTIGATION OF SPIN DYNAMICS OF DILUTE MAGNETIC ALLOYS BY DIFFUSE NEUTRON SCATTERING

M. Loewenhaupt, H. Scheuer[+] and W. Schmatz
Institut für Festkörperforschung der Kernforschungsanlage
D-517 Jülich, West-Germany

[+]Sonderforschungsbereich 125, Fehlordnung in Metallen, Aachen-Jülich-Köln, Universität zu Köln, D-5000 Köln, West-Germany

ABSTRACT

Spin relaxation rates of dilute magnetic systems in zero external field have been studied by time of flight spectrometry of unpolarized neutrons. The magnetic scattering was obtained from a difference measurement of doped and undoped samples. In case of large background due to nonmagnetic scattering the choice of special energy windows was necessary for the detection of the magnetic scattering. The data have been analyzed in terms of one or two Lorentzians around $\hbar\omega = 0$.

Neutron scattering experiments were performed on the Kondo system CuFe for concentrations between 600 and 4800 ppm Fe and in the temperature range 15 K to 300 K. The measured absolute values and the temperature dependence of the spin relaxation rates of the Fe single magnetic impurities in the Cu metallic host are found to agree well with theoretical calculations by Götze and Schlottmann and with recent NMR experiments below T_k by Alloul.

The spin glass system AuFe was investigated in the concentration range of 5 to 15 at.% Fe for temperatures between 3 K and 300 K. We found a more complex relaxation behaviour because of the additional interactions between the magnetic moments in this more concentrated system. We observed two species of magnetic moments with different relaxation rates: a fast relaxation rate of $1/\tau = 16 \cdot 10^{12}$ cps ($\hat{=}$ 10.5 meV) for uncoupled single spins and a slower one of $1/\tau = 2.6 \cdot 10^{12}$ cps ($\hat{=}$ 1.7 meV) for spin clusters.

Quasielastic neutron scattering is the most direct method to measure the spin relaxation time for well-localized magnetic moments above the ordering temperature. In noble metals with 3d-magnetic impurities spin relaxation is caused either by the interaction of the local moment with the conduction electrons or by exchange interactions to other magne-

tic moments in the neighbourhood. Normally both interactions are strong. They lead to characteristic relaxation times τ in the range between $5 \cdot 10^{-11}$ sec and $5 \cdot 10^{-13}$ sec. A simple approximation is to assume that the spin-spin correlation of the localized magnetic moment is an exponential decay, i.e. $\langle S_\alpha(o) S_\alpha(t) \rangle \sim \exp(-t/\tau)$. The Fourier transform of this gives the scattering cross-section

$$\frac{d^2\sigma}{d\Omega\, d\omega} \sim S(S+1)\, \frac{1}{\pi}\, \frac{1/\tau}{\omega^2 + (1/\tau)^2}\, |F_d(\kappa)|^2 \qquad (1)$$

where $\hbar\omega = E_o - E_1$ is the neutron energy transfer, S is the spin quantum number and $F_d(\kappa)$ is the 3d form factor. Thus $2\hbar/\tau$ is the energy linewidth of the quasielastic neutron scattering observed at such a system. With the values of τ given above this ranges from 0.3 to 30 meV. Fortunately energy-transfers in this range are well-observable with neutrons, they partly even allow rather relaxed energy resolution which is absolutely necessary for small concentrations of 3d magnetic impurities. We measured successfully the quasielastic scattering of 600 ppm Fe in Cu which seems us at the moment the absolute lower limit of a single impurity concentration ever studied with neutrons. This low concentration was necessary to keep the indirect Fe-Fe magnetic interaction at such a low energy level that our values obtained could be compared with recent theories for a single impurity Kondo state. In current work also the quasielastic scattering of the spin-glass alloy $Au_{1-x}Fe_x$ for concentrations x = 0.05, 0.11 and 0.15 is investigated at temperatures from 3 K to 300 K. The high neutron absorption of gold compensates partly the advantage of having higher concentrations in this system. It is the main purpose of this paper to describe the experimental procedure and its difficulties in this type of studies.

For the study of nonmagnetic point defects two very similar low resolution time-of-flight spectrometers /1,2/ have been developped: the DNS in Jülich and the D7 in Grenoble.

Both instruments are connected with guide tubes to the cold source of the respective reactor. The incident wavelengths can be varied from 4 to 10 Å at the DNS and from 3 to 6 Å at the D7. At the DNS the beam is monochromatized with a mechanical velocity selector (halfwidth $\Delta\lambda/\lambda$ = 15 %) and afterwards chopped with a Fermi chopper (duty cycle 1:14; 11000 rpm). For the D7 a graphite monochromator and a disc chopper (duty cycle 1:60; 7000 rpm) is used. The total time-of-flight resolution as measured by elastic scatterers is for the D7 a factor five better than for the DNS. The sample-detector distance is 80 and 130 cm for the DNS and D7 respectively. In both cases about 30 detectors cover about 0.3 steradian solid angle in the horizontal plane. (The vertical divergence is 0.2 radian approximately.)

The quasielastic scattering of the 600 ppm Fe in Cu was observable only in narrow energy windows left and right from the elastic scattering: The elastic scattering is dominated totally by the incoherent elastic scattering of Cu ($\sigma_{inc,Cu} \simeq 550$ mbarn). Further for high energy transfers at least at higher temperatures the coherent one-phonon scattering dominates. Three examples of time-of-flight (TOF) spectra with one counter at the D7 for a pure Cu-sample are shown in Fig. 1a. The phonon scattering is between channels 20 and 40, the elastic scattering is centered at channel 80. In Fig. 1b the same spectra are shown a factor 100 enlarged. The differences in scattering rate between the Cu (600 ppm Fe)-sample and the pure Cu-sample integrated over 24 counters and 5 TOF--channels are shown in Fig. 1c. As one sees the difference is only a small fraction of the scattering even in these favourable windows. Thus the whole experiment was at the very limits of experimental possibilities.

The scattering rate of the pure Cu-sample in the energy windows shown in Fig. 1b consists of the overall background, the incoherent inelastic scattering and the tails of the

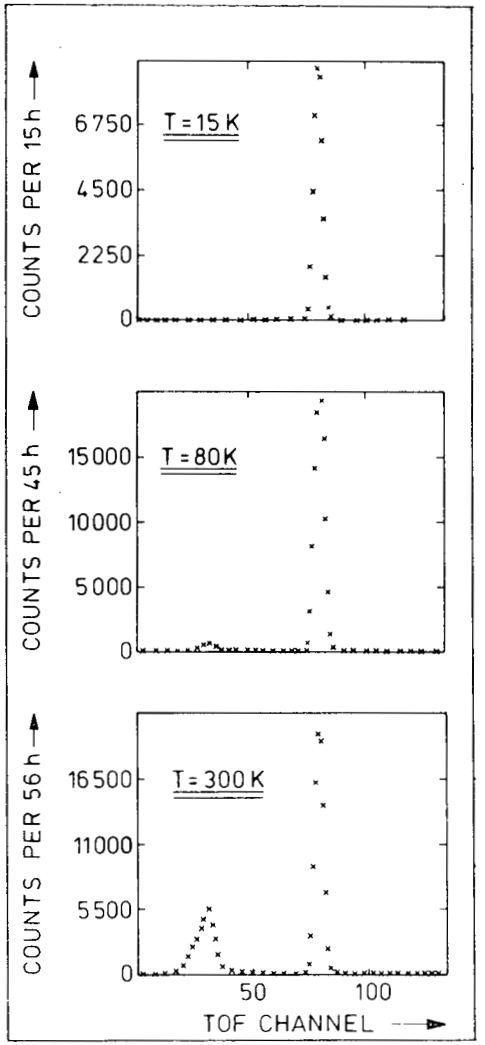


Fig.1a: TOF-spectra of one counter at D7 and a scattering angle of 63° for the pure Cu-reference sample.

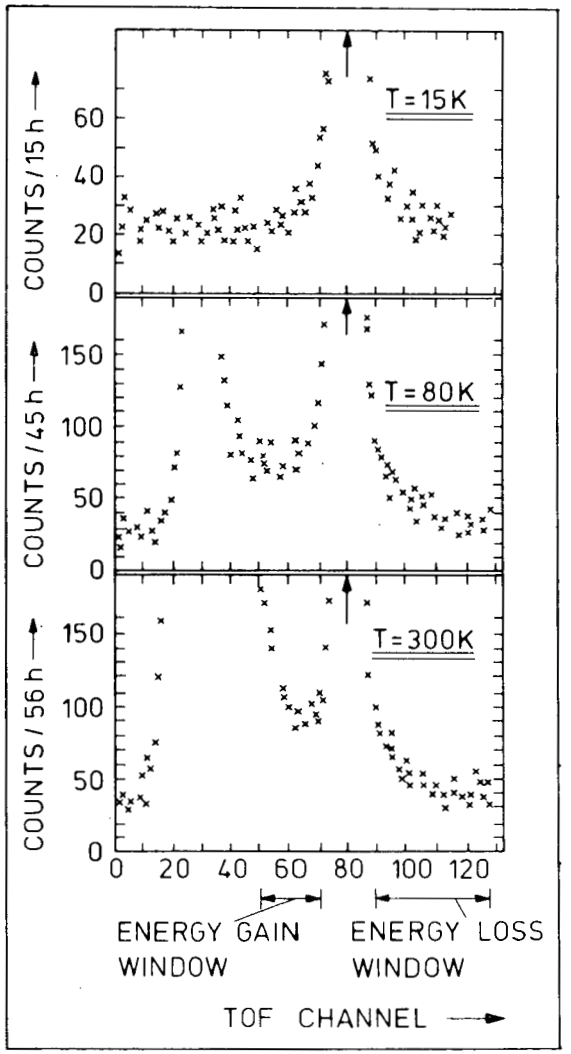


Fig.1b: Same as 1a, but vertical scale enlarged by a factor 100.

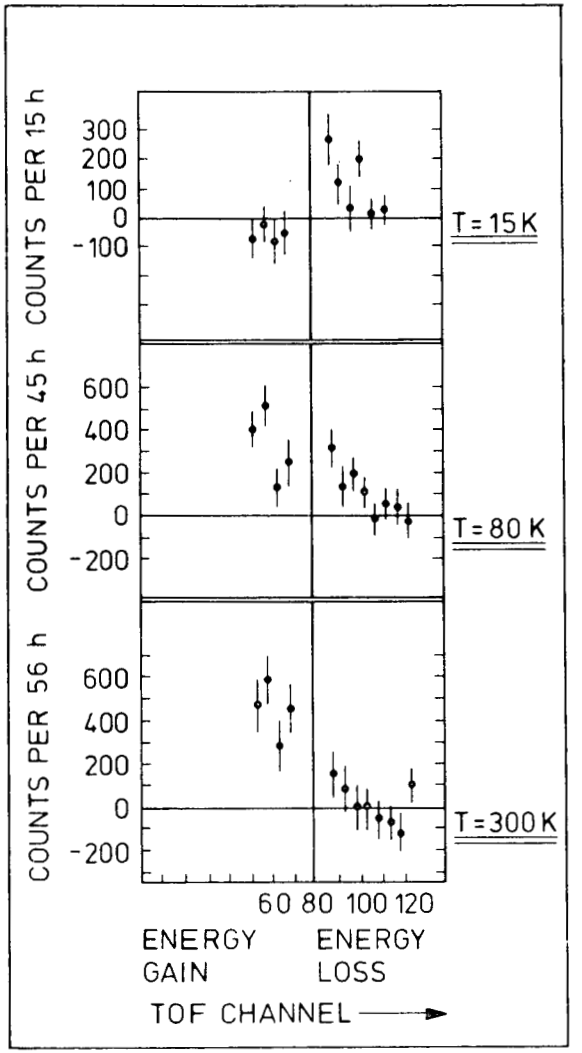


Fig.1c: Difference of TOF-spectra of CuFe 600ppm and Cu (each point is the sum over 24 counters and 5 TOF-channels!).

elastic scattering and the coherent one-phonon scattering. The latter vanishes of course for T → 0 K. All this types of background scattering are exactly the same for the Cu (Fe 600 ppm) and the Cu-reference sample because the samples have had within ± 0.02 mm the same diameter and the same measuring position. They have been prepared very similar (10 h heat treatment at 950°C and rapid quench in cold water) so that also the grain size was approximately the same. Bragg-scattering has been excluded by the use of long-wavelength neutrons. After all care and considerations we have been very confident to ascribe the difference in scattering in the special energy windows solely to the quasielastic magnetic scattering of the Fe-impurities. The results are presented in the table. With the assumption of S = 3/2 the values give after some discussion /3,4/ the spin relaxation line-width Γ/2 as shown in Fig. 2. The result is in good agreement with theoretical calculations by Götze and Schlottmann /5/ and the values are evidently above the Korringa relaxation rates. The Korringa values are typical for a local magnetic moment without Kondo effect and they are pro-

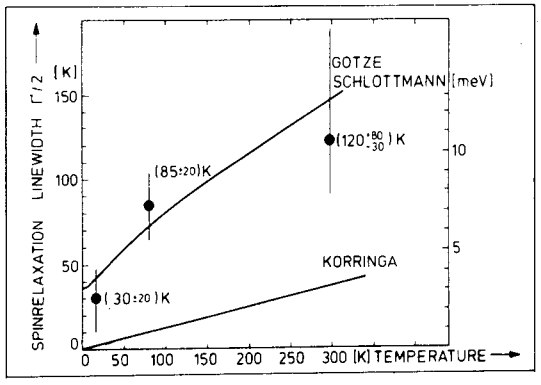


Fig.2: Spin relaxation linewidth of CuFe as function of temperature.

portional to T. Recent NMR experiments /6/ confirm after some initial difficulties /7,8/ the neutron result. For the specialist we complete this part of the paper by the correct scattering cross-section used for the data evaluation /3/

$$\frac{d^2\sigma}{d\Omega\, d\hbar\omega} = \frac{2}{3} c \left(r_e \gamma_N\right)^2 \frac{k_1}{k_0} S(S+1) \left[1 - \exp\left\{-\frac{\hbar\omega}{k_B T}\right\}\right]^{-1} \frac{\hbar\omega}{k_B (T+T_K)} \times$$

$$\times \frac{1}{\pi} \frac{\Gamma/2}{(\hbar\omega)^2 + (\Gamma/2)^2} \left|F_d(k)\right|^2 \qquad (2)$$

In Fig. 3 the results for 4800 ppm Fe in Cu are shown. They have already much better accuracy. At this concentration and at 300 K the relaxation rate $\Gamma/2$ is 10.3 meV in good agreement with the value for 600 ppm Fe. At 80 K there is evidence for two characteristic relaxation rates: $\Gamma/2$ = 7.3 meV would be the same as for the 600 ppm Fe-sample and therefore due to single impurities. The smaller relaxation rate $\Gamma/2$ = 1 meV could be due to interacting Fe-impurities. More precise experimental data are however required to come to more conclusive results.

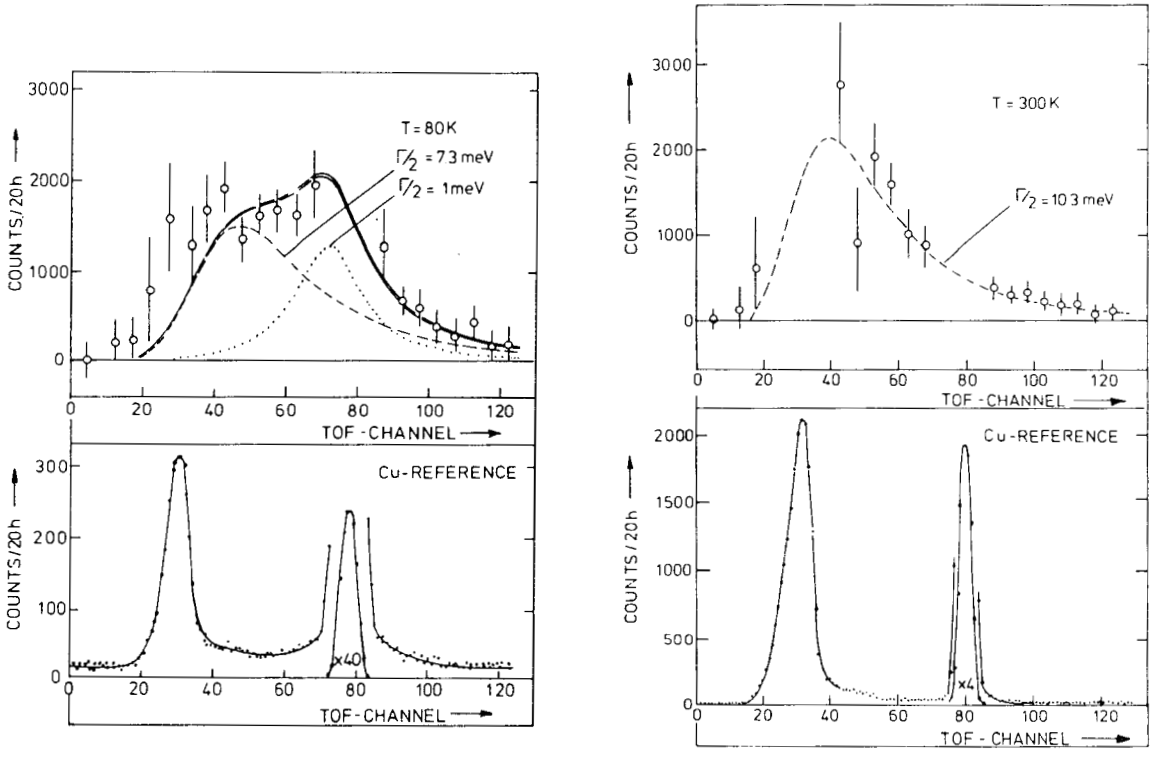


Fig.3: Above: difference of TOF-spectra of CuFe 4800 ppm and Cu for T = 80 K and T = 300 K (each point is the sum over 24 counters and 5 TOF-channels!). Below: TOF-spectra of one counter at D7 and a scattering angle of 61° for the pure Cu-reference sample.

As an example in Fig. 4 the difference in the TOF-spectra of an $Au_{0.855}Fe_{0.145}$-sample and a pure Au-sample is shown, proper corrections for different thickness and absorption induced. The spectrum can be decomposed into three individual contributions: i) an elastic line (dotted) with the same halfwidth as the calibration scatterer Vanadium, ii) a broad

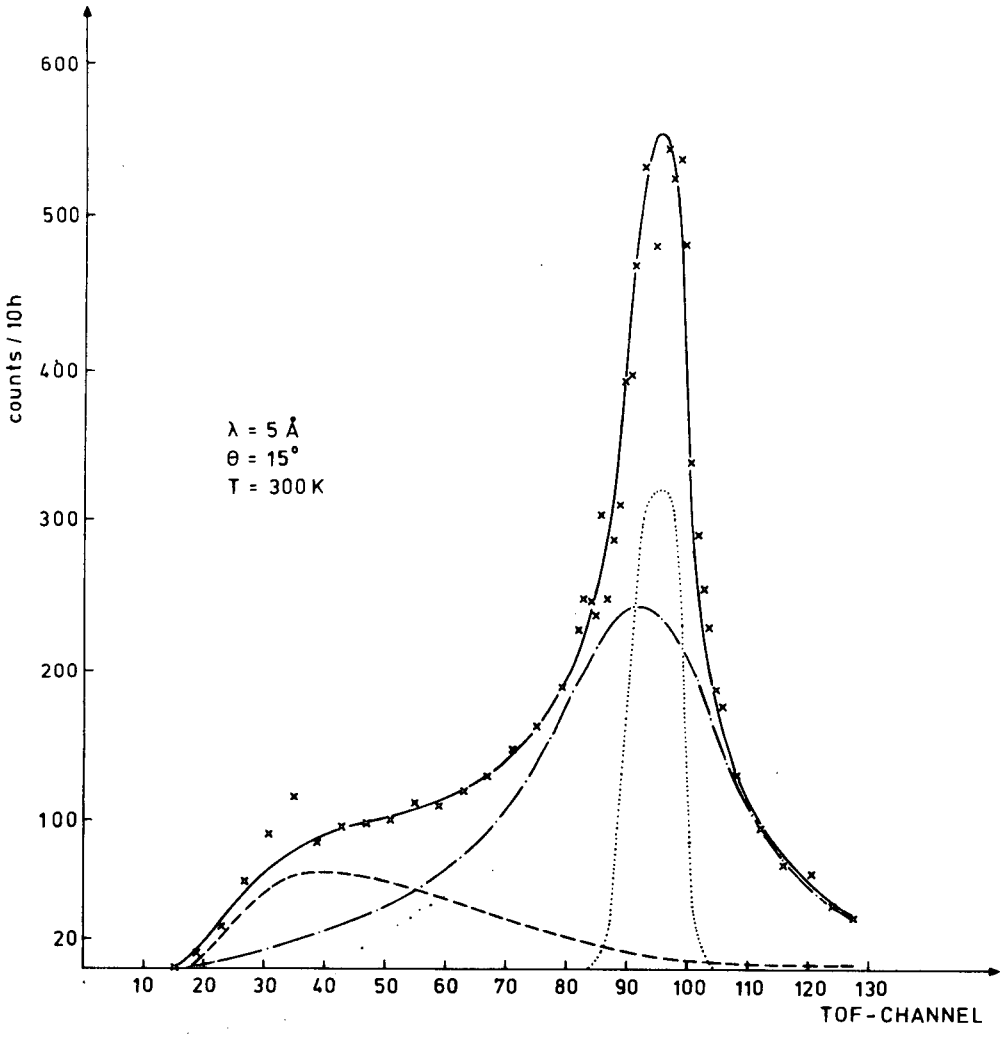


Fig.4: Difference of TOF-spectra of AuFe 14.5 at.% and Au for one counter (scattering angle 15°) at T = 300 K.

quasielastic line with a value of about 10 meV for $\Gamma/2$ and iii) a narrow quasielastic line with $\Gamma/2 \simeq 2$ meV. The narrow line vanishes rapidly for increasing scattering angle (not shown here!). From the data one can see that the slow relaxation process has a correlation size of about 10 Å and only a small fraction of Fe atoms estimated to about 5 to 10 % is involved in this. The fast relaxation rate of 10 meV is nearly independent of κ and the intensity is proportional to $|F_d(\kappa)|^2$. This process is therefore a single site behaviour.

TABLE

Difference of the neutron scattering cross sections for 600 at. ppm Fe in Cu and pure Cu for different energy windows and temperatures in μbarn per steradian, Cu atom and energy window, averaged over a k-range from 0.5 to 2 Å^{-1}. The value in brackets with * refers to 2800 at.ppm, the other values in brackets to 4800 at.ppm Fe in Cu, but reduced to a nominal concentration of 600 at.ppm.

experiment	energy window	energy transfer in meV	T=15K	T=80K	T=300K
Grenoble	gain	0.85 to 4.22	4±12	36±4	68±10
				(32±2)	(39± 2)
Grenoble	loss	0.87 to 1.87	23±12	16±4	10± 8
				(15±2)	(12± 2)
Jülich	loss	2.76 to 3.31			3± 2
					(4± 2)*
				(7±1)	(6± 1)

REFERENCES

/1/ G. Bauer, E. Seitz, W. Just, J. Appl. Cryst. 8 (1975) 162

/2/ W. Just, W. Schmatz, G. Bauer, Proc. Conf. on Neutron Diffraction, Petten, 1975; Report Reactor Centrum Nederland RCN-234 (Petten)

/3/ M. Loewenhaupt, W. Just, Phys. Lett. 53A (1975) 305

/4/ M. Loewenhaupt, J. Magn. and Magn. Mat. (1975), in press

/5/ W. Götze, P. Schlottmann, J. Low Temp. Phys. 16 (1974) 87

/6/ H. Alloul, Phys. Rev. Lett. 35 (1975) 460

/7/ H. Alloul, P. Bernier, Proc. of LT13, Boulder (1973)

/8/ P. Bernier, Thèse d'Etat (1975) Orsay

A STUDY OF CRYSTAL-FIELD SPLIT LEVELS OF Pr^{3+} IN PrF_3 BY INELASTIC NEUTRON SCATTERING

N. Shamir and M. Melamud
Department of Physics, Nuclear Research Center - Negev,
P.O.Box 9001, Beer Sheva, Israel

and

H. Shaked
Department of Physics, Nuclear Research Center - Negev,
P.O.Box 9001, Beer Sheva, Israel
Department of Physics, Ben-Gurion University of the Negev,
P.O.Box 2513, Beer Sheva, Israel

ABSTRACT

Transitions between crystal-electric-field (CEF) split energy levels of Pr^{3+} in PrF_3 were measured by inelastic neutron scattering. The measurements were performed on a powder sample using the recently constructed triple-axis spectrometer KANDI III at the IRR-2 reactor. The energy-transfer neutron spectrum was measured at 4.2K, 80K and 300K. The quality of the data is similar to previously obtained data at 20K, 80K and 300K using neutron time of flight, at the IBR-30 pulsed reactor. A set of gaussians was fitted to the measured spectrum at 4.2K in order to obtain the splitting of the energy levels of Pr^{3+} and the line intensities due to transitions from the ground level to the higher ones. Estimates of relative magnitudes of the matrix elements for the transitions were derived from the measured intensities at 4.2K and 80K.

INTRODUCTION

Inelastic neutron scattering (INS) is useful in studying low lying (up to $\sim$ 100 meV) energy levels of paramagnetic ions in crystals, and magnetic dipole transitions between them. These transitions are induced by the interactions between the magnetic moment of neutrons and that of the ion. The rare earth ions are the most extensively studied by this method (especially in intermetalic compounds). This is so because exchange interactions (which cause broadening of the energy width of the neutron

group) are small between these ions, since their unpaired (4f) electrons are shielded by the outer electrons. Pr^{3+} in PrF_3 is an example of these characteristics and is the subject of the present work.

There are several solutions in the literature (Table 1) for the crystallographic structure of PrF_3 .

Table 1. Crystallographic data for PrF_3. n is the number of formula units per unit cell.

	Space group	n	Pr^{3+} site symmetry	Lattice constants a ; b	Reference
1	$P6_3/mcm$	6	C_{2v}	7.075; 7.233	1
2	$P6_3/mmc$	2	D_{3h}	4.085; 7.238	2
3	$P\bar{3}c1$	6	C_2 [a]	7.078; 7.239	3,9
4	$P6_3/mcm$	6	C_{2v}		4
5			C_2		5
6			C_{2v}		6
7			C_2		7
8	$P6_3/mcm$	6	C_{2v}		8

[a] Deduced from the data in Ref. 3, 9.

Consequently, the site symmetry of the Pr^{3+} ion is ambiguously known. (This point symmetry, of course, plays a dominant role in the way the levels are split). Our elastic neutron diffraction pattern from a powder sample confirms the lattice constants given in Ref. 1 and 3 (Table 1), which are in agreement with a unit cell containing six formula units (n=6). Good single crystal diffraction data is required in order to determine the space group unambiguously.

The compound PrF_3 was studied by X-rays,[1-3] NMR,[4] optical methods,[6-9] and by INS time-of-flight method.[5] We present here an INS study of PrF_3, performed on a triple-axis neutron-spectrometer.

EXPERIMENTAL

The measurements of the energy-transfer neutron spectra were performed using the recently constructed triple-axis neutron-spectrometer KANDI III at the IRR-2 reactor, on a powder sample of PrF_3. An incident beam of λ=1.36Å neutrons was used, with the sample at 4.2K, 80K and 300K (Fig. 1). The spectra were measured at a fixed take-off angle of 10°.

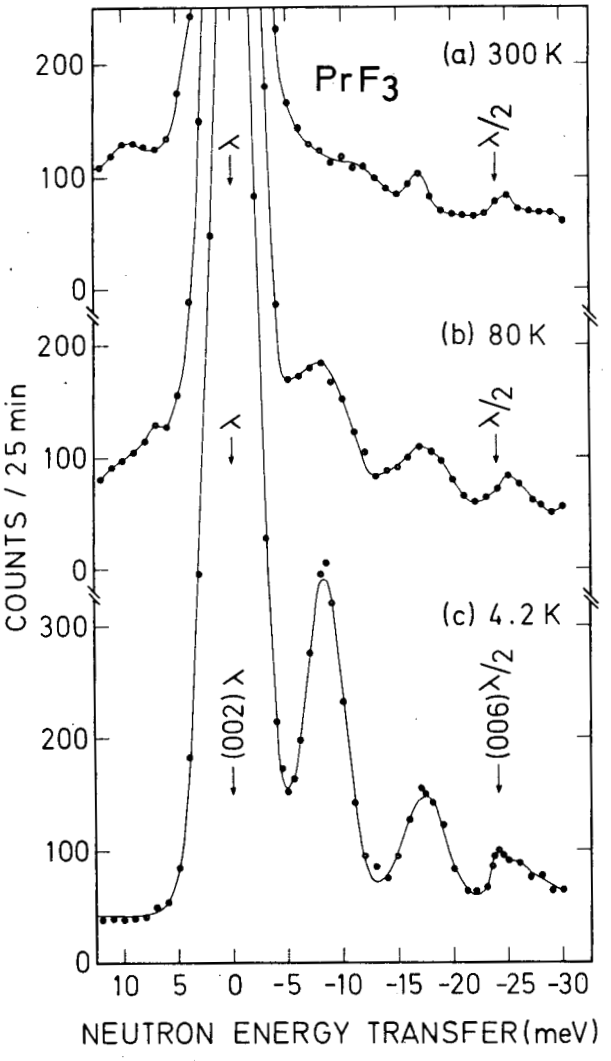


Fig. 1. Energy transfer spectra of neutrons scattered from a PrF_3 powder sample. The elastic reflections of λ from the (002) and of $\lambda/2$ from (006) planes of the analyzer are indicated. The solid line in (c) was obtained by the gaussians fit, while in (a) and (b) it is only a guide to the eye.

Beside the zero-transfer neutron groups (002)λ and (006)$\lambda/2$, three neutron groups of energy loss and one neutron group of energy gain are observed (Fig. 1). These data are similar to that observed at 20K, 80K and 300K by Feldmann *et al.*[5] using the neutron time-of-flight technique, at the IBR-30 pulsed reactor.

A study of the Pr^{3+} form factor was started by varying the take-off angle at the sample but has not been completed due to mechanical difficulties.

ENERGY LEVELS AND TRANSITION PROBABILITIES

In order to determine the energies of the CEF levels and the intensities of the transitions between them, for Pr^{3+}, a set of gaussians was fitted by a least-square-analysis computer-program to the 4.2K spectrum (solid line in Fig. 1(c)). The $\lambda/2$ contribution to the third neutron group was subtracted. As in the data of Feldmann *et al.*[5] and in contrast to optical data,[6] no evidence was found for the existence of two energy levels in the vicinity of 8 meV. This point was explored with an incident beam of 1.6Å neutrons (giving better energy resolution) and the least-square program with two gaussians around 8 meV. The best fit however, came out always with a single gaussian. Our data leads, therefor, to three indistinguishable alternatives:

(a) There is only one level in the vicinity of 8 meV.

(b) The two levels are so close (< 0.2 meV) that even gaussians fitting analysis can not separate them.

(c) The transition probability to one of the levels is too small to be observed.

In order to be able to make calculations and to be consistent with optical data we base our analysis on alternative (b). The energies of the CEF levels given in Fig. 2 are deduced from the fit.

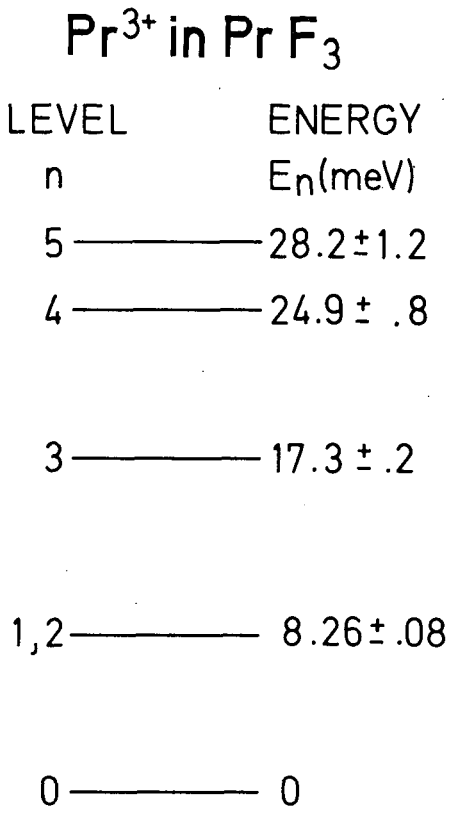


Fig. 2. Low lying levels in the ground term $^2H_4$ of Pr^{3+} (f^2) in PrF_3, as obtained from the gaussians fit of the neutron energy transfer spectrum at 4.2K.

The thermal neutron cross section for a system of N non- interacting ions in the small Q approximation is equal to:[10]

$$\frac{d^2\sigma}{d\Omega d\omega} = N\left(\frac{1.91e^2}{2mc^2}\, g_J\right)^2 F^2(Q)\, \frac{k_f}{k_i} \exp(-2W) \cdot I \qquad (1a)$$

where

$$I = \frac{1}{Z} \sum_{n,m} \exp\left(-\frac{E_n}{k_B T}\right) \left| \langle m|\vec{J}_\perp|n\rangle \right|^2 \delta(E_n - E_m - \hbar\omega) \qquad (1b)$$

Z is the partition function, F(Q) is the form factor, k_i and k_f are the wavenumbers of the incoming and outgoing neutrons respectively, exp(-2W) is the Debye-Waller factor, E_j and $|j\rangle$ are the eigenvalues and eigenfunctions of the crystal field Hamiltonian, $\vec{J}_\perp$ is the component of the total angular momentum operator perpendicular to Q and the remaining symbols have their usual meaning.

The relative magnitudes of the matrix elements are calculated from

the observed intensities of the neutron energy groups at 4.2K and 80K. The observed intensity is calculated from Eq. (1) where the δ function is replaced by a gaussian distribution of width ρ in order to account for instrumental resolution and intrinsic linewidth. As the count was performed in constant ΔE steps we have:

$$I_{obs} = A \cdot \sum_{\substack{\text{const.} \\ \Delta E}} \int_{\substack{\text{detector} \\ \text{area}}} R^{max}(E,\theta)\, E_{ff}(E)\, \frac{d^2\sigma}{d\Omega d\omega}\, \frac{dE}{d\theta}\, d\theta \qquad (2)$$

where A is a constant, $R^{max}(E,\theta)$ is the reflectivity of the pyrolitic graphite analyzer,[11] $E_{ff}(E)$ is the efficiency of the detector and E is the scattered neutron energy. Following Eq. (1) we obtain:

$$I_{obs} = B \cdot \sum_{\substack{\text{const.} \\ \Delta E}} \int_{\substack{\text{detector} \\ \text{area}}} R^{max}(E,\theta)\, E_{ff}(E)\, F^2(Q)\, k_f$$

$$\times \exp\left(-\frac{E_n}{k_B T}\right) \left| \langle m|\vec{J}_\perp|n\rangle \right|^2 \exp\left(-\frac{(E+E_n-E_m)^2}{2\rho^2}\right) \frac{dE}{d\theta}\, d\theta \qquad (3)$$

where B is a constant. Assuming that the functions in the integrand do not vary much within the energy width of a neutron group, we replace them by their mean values and obtain:

$$I_{obs} = B\, R^{max}(E,\theta)\, E_{ff}(E)\, F^2(Q)\, k_f \exp\left(-\frac{E_n}{k_B T}\right) \left| \langle m|\vec{J}_\perp|n\rangle \right|^2$$

$$\times \frac{dE}{d\theta} \cdot \sum_{\substack{\text{const.} \\ \Delta E}} \exp\left(-\frac{(E+E_n-E_m)^2}{2\rho^2}\right) \int_{\substack{\text{detector} \\ \text{area}}} d\theta \qquad (4)$$

Since the detector area is a constant, the summation over constant ΔE steps gives a normalized gaussian area which is also a constant. Hence, following Eqs. (1) and (4):

$$I = C \frac{I_{obs}\, d\theta/dE}{F^2(Q)\, k_f\, R^{max}(E,\theta)\, E_{ff}(E)} \qquad (5)$$

where C is a constant of the experiment. F(Q) was approximated to the form factor given by Marshall and Lovesey:[12]

$$F(Q) = \exp[-3.285(Q/4\pi)^2]$$

The I_{obs} and corresponding normalized I at 4.2K and 80K are given in Table 2.

Table 2. I_{obs} (counts/25 min) and normalized I at 4.2K and 80K.

Energy transfer (meV)	4.2K I_{obs}	4.2K I	80K I_{obs}	80K I
8.26	-	-	530 ± 100	.17 ± .04
- 8.26	1306 ± 40	1	886 ± 110	.68 ± .09
-17.3	512 ± 20	.64 ± .05	400 ± 30	.51 ± .05
-24.9	130 ± 25	.32 ± .08	63 ± 15	.16 ± .04
-28.2	125 ± 15	.47 ± .07	63 ± 15	.24 ± .07

The calculation of the relative magnitudes of the matrix-elements was carried out according to Eq. (1) and Table 2, taking into account that the 80K line at -8.26 meV contains the $0 \to 1$, $0 \to 2$ and $1 \to 3$, $2 \to 3$ transitions, and the -17.3 line contains the $0 \to 3$, $1 \to 4$, $1 \to 5$, $2 \to 4$, $2 \to 5$ transitions we obtain from the 4.2K intensities:

$$\langle 1|\vec{J}_\perp|0\rangle + \langle 2|\vec{J}_\perp|0\rangle = 1$$

$$\langle 3|\vec{J}_\perp|0\rangle = .80 \pm .04$$

$$\langle 4|\vec{J}_\perp|0\rangle = .57 \pm .04$$

$$\langle 5|\vec{J}_\perp|0\rangle = .69 \pm .04$$

the 80K intensities yield:

$$\langle 4|\vec{J}_\perp|0\rangle = .53 \pm .06$$

$$\langle 5|\vec{J}_\perp|0\rangle = .64 \pm .06$$

in good agreement to the 4.2K values. From these values and the remaining 4.2K and 80K energy loss intensities we evaluate:

$$\langle 3|\vec{J}_\perp|1\rangle + \langle 3|\vec{J}_\perp|2\rangle = .77 \pm .06$$

$$\langle 4|\vec{J}_\perp|1\rangle + \langle 5|\vec{J}_\perp|1\rangle + \langle 4|\vec{J}_\perp|2\rangle + \langle 5|\vec{J}_\perp|2\rangle = .28 \pm .03$$

and the calculation of the energy gain intensity from these values yields the value $.22 \pm .04$ in good agreement with the value of $.17 \pm .04$ obtained from the measured intensity.

REFERENCES

1. I. Oftedal, Z. Physik. Chem. B13, 190 (1931).
2. R.W.G. Wyckoff, Crystal Structures, Vol. 2, second edition, Interscience Publishers, New York, 1964 .
3. F.H. Spedding and D.C. Henderson, J. Chem. Phys. 54, 2476 (1971).
4. M.L. Afanasiev, S.P. Habuda and A.G. Lundin, Acta Cryst. B 28, 2903 (1972).
5. K. Feldmann, K. Hennig, L.P. Kaun, B. Lippold, S. Matthies, W. Matz, B.N. Savenko and D. Welsch, Phys. Stat. Solidi (b) 70, 71 (1975).
6. E.V. Sayre and S. Freed, J. Chem. Phys. 23, 2066 (1955).

7. D.J. Newman and M.M. Curtis, J. Phys. Chem. Solids 30, 2731 (1969).
8. E.Y. Wong, O.M. Stafsudd and D.R. Johnston, J. Chem. Phys. 39, 786 (1963).
9. R.P. Lowendens, J.F. Parrish and C.H. Perry, Phys. Rev. 182, 913 (1969).
10. P.G. De Gennes, in Magnetism III, p. 115, T. Rado and H. Suhl editors, Academic Press, 1963.
11. T. Riste and K. Otnes, Nuclear Inst. & Methods 75, 197 (1969).
12. W. Marshall and S.W. Lovesey, Theory of Thermal Neutron Scattering, p. 164, Oxford University Press, 1971.

INELASTIC NEUTRON SCATTERING MEASUREMENTS ON $CeAl_3$ AND $Ce_{.8}Th_{.2}$*

A. S. Edelstein and R. Majewski
University of Illinois, Chicago, Illinois 60680 and
Argonne National Laboratory, Argonne, Illinois 60439

S. K. Sinha, T. Brun and C. A. Pelizzari
Argonne National Laboratory, Argonne, Illinois 60439

H. R. Child
Oak Ridge National Laboratory, Oak Ridge, Tennessee 37830

ABSTRACT

Inelastic neutron scattering measurements have determined that the spectrum of $Ce_{.8}Th_{.2}$ at 170K consists of a single quasi-elastic peak of width $\Gamma \simeq 12$ meV. Besides a narrower quasi-elastic peak the spectrum of $CeAl_3$ also shows a crystal field splitting of approximately 5 meV. The temperature dependence of the width Γ of the quasi-elastic peak for each system is best fitted by a model which includes an intrinsic relaxation mechanism as well as the Korringa mechanism. The magnitude of Γ also indicates the hybridization of the Ce moment with the conduction electrons.

Inelastic neutron scattering measurements provide valuable information about the dynamics of magnetic systems. Except for elastic measurements, neutrons probe the system in a time 10^{-12} - 10^{-13} sec. This is quite different from susceptibility measurements which average $\langle S(o)S(t)\rangle$ over a time proportional to T^{-1}. Inelastic neutron measurements can determine 1) the spatial distribution of the moment,[1] 2) crystal field (CF) splittings,[2] 3) the fractional occupancy of a localized configuration[3] η and 4) the spin-lattice relaxation time T_1 of the local moment.[4]

In this paper we report on time of flight neutron scattering measurements made at the Argonne CP-5 reactor on polycrystalline powder

*Work performed under the auspices of the U. S. Energy Research and Development Administration.

samples of $CeAl_3$ and $Ce_{.8}Th_{.2}$. $CeAl_3$ has a hexagonal DO_{19} structure while $Ce_{.8}Th_{.2}$ undergoes a phase transition with decreasing temperature from a fcc phase (the γ phase) to another fcc phase (the α phase) with a smaller lattice constant.

Previous diffuse scattering measurements[3] made without an energy analysis have determined that the fractional occupancy η of the localized 4f' configuration of Ce in $CeAl_3$ only decreased slightly, if at all, with decreasing temperature for $11 \leq T \leq 295$ K. Similar measurements[3] made on $Ce_{.8}Th_{.2}$ indicate a large decrease in η at the α-γ transition at T = 140 K but it is interesting that $\eta = 0.4 \pm 0.1$ at 11 K in the "non-magnetic" α state. The alloy $Ce_{.8}Th_{.2}$ is certainly a configuration fluctuation (CF) system, while it is not clear that $CeAl_3$ is a CF system because η decreases at most only slightly. The γ-α transition can also be induced at 300 K by applying approximately 7 kbars pressure to Ce. Buras, Rainford and Lebech[4] have performed inelastic neutron scattering measurements at 300 K on Ce under pressure to study η and T_1.

The present measurements yield 1) the qualitative temperature dependence of T_1 in $CeAl_3$ and 2) T_1 of $Ce_{.8}Th_{.2}$ at 170°K. The measurements were made using a statistical chopper.[5] The initial energy of the neutrons was 4.83 meV. Our detectors were arranged so that $3.9° < \theta < 170°$ and $0.1\ \mathring{A}^{-1} < Q < 3.0\ \mathring{A}^{-1}$. Corrections were made for the spurious oscillations in the spectra arising from the small imperfections in the correlation chopper. This was done by subtracting from the data a suitably normalized, decorrelated spectrum of the elastic peak of vanadium. The energy dependence was, within experimental error, the same in each detector group. In Fig. 1 the Im $\chi(\omega)/\omega$ for $Ce_{.8}Th_{.2}$ at 170 K is plotted versus $\hbar\omega$, the energy gained by the neutron. The function Im $\chi(\omega)$ was obtained by summing over all detectors groups and neglecting the slight Q dependence of the form factor over this Q range. The small ω region of the quasi-elastic peak shown in Fig. 1 can be fitted to a single Lorentzian of width $\Gamma \approx 12$ meV. Measurements were also performed on $Ce_{.8}Th_{.2}$ at 40 K. Because of poorer counting statistics at this temperature we have only determined an approximate value for Γ of 8 meV.

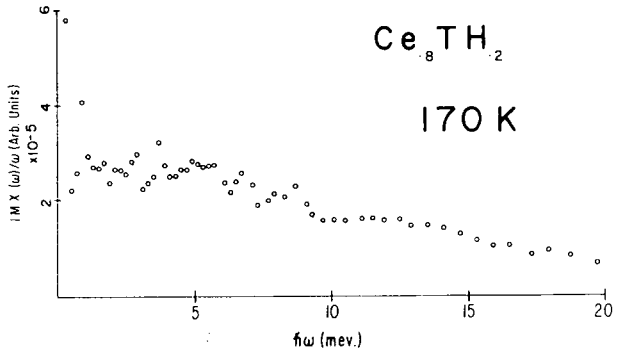


Fig. 1. Im $\chi(\omega)/\omega$ versus $\hbar\omega$ for $Ce_{.8}Th_{.2}$ at 170 K.

Using the same incident neutron energy, and only changing our detector angles to avoid Bragg peaks, we have also performed inelastic neutron scattering measurements on $CeAl_3$ at T = 79.5, 40, 20 and 6.2 K. The results of those measurements are shown in Fig. 2 and 3.

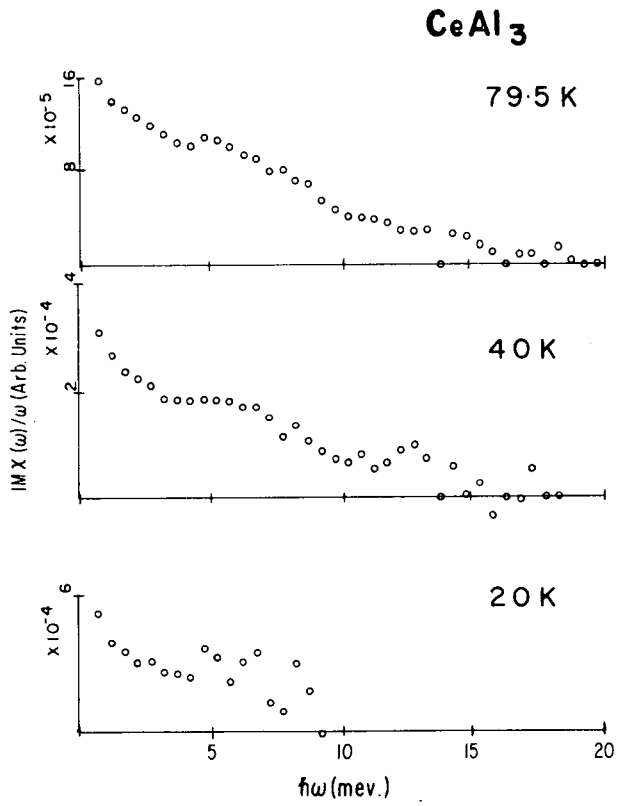


Fig. 2. Im $\chi(\omega)/\omega$ versus $\hbar\omega$ for $CeAl_3$ at 79.5, 40 and 20 K.

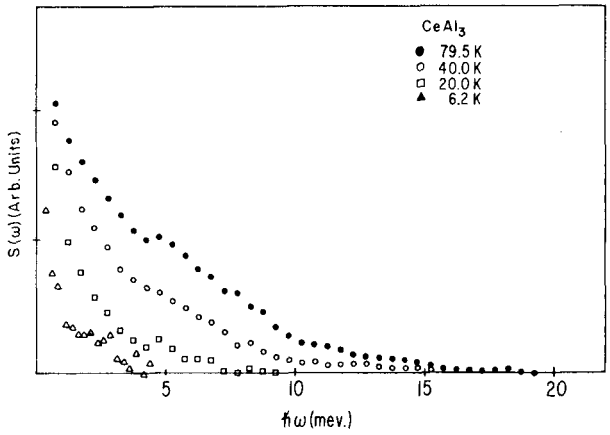


Fig. 3. Unsymmetrized scattering function $S(\omega)$ versus $\hbar\omega$ for $CeAl_3$ at 79.5, 40, 20 and 6.2 K.

In Fig. 2 we again plot Im $\chi(\omega)/\omega$ versus $h\omega$, the neutron's energy gain, while in Fig. 3 we plot the unsymmetrized scattering function $S(\omega)$. Again the intensity in each detector group showed the same energy dependence and all groups were added. In this case the spectrum consists of a central quasi-electric peak and one crystal field peak. Because of the hexagonal symmetry the crystal field splits the levels into three doublets $J = \pm 1/2, \pm 3/2, \pm 5/2$. The peak observed in Fig. 2 and 3 at approximately 5 meV corresponds to the splitting between two of these doublets.

By fitting the central quasi-elastic peak of Im $\chi(\omega)/\omega$ to a Lorentzian, we determined the width of Γ as 3.74 ± 0.6, 2.65 ± 0.5, 1.97 ± 0.5 and 0.4 ± 0.4 meV at T = 79.5, 40, 20 and 6.2 K respectively. The spin lattice relaxation time T_1 is given by h/Γ. The most appropriate theory for treating T_1 is that of Gotze and Schlottmann.[6] In their theory, which does not include interactions between the localized spins, there is an intrinsic relaxation time $T_{int} \approx 0.67\ h/kT_{sf}$ (where T_{sf} is the spin fluctuation temperature) which persists at T = 0 when the Korringa process no longer contributes. The temperature dependences of our widths is shown in Fig. 4. The data on the compound $CeAl_3$ is not very well fitted by a simple Korringa law, T_1T = const. If one uses the approximate value for Γ of $Ce_{.8}Th_{.2}$ at 40 K of then $Ce_{.8}Th_{.2}$ also does not obey a Korringa law. For $CeAl_3$, the temperature dependence of

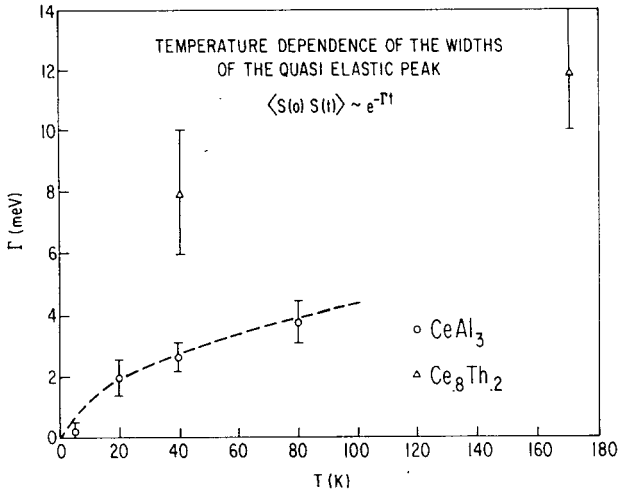


Fig. 4. Width of the quasi-elastic peak Γ versus temperature.

Γ is consistent with a model in which T_{sf}, decreases at low temperatures. This in turn is consistent with the suggestion made by Cornut and Coqblin[7] that higher crystal field levels have higher fluctuation temperatures since one would expect T_{sf} to decrease as the spins condensed into the lowest doublet with decreasing temperature.

REFERENCES

1. M. H. Dickens, C. G. Shull, W. C. Koehler and R. M. Moon, Phys. Rev. Letters 35, 595 (1975).
2. A. H. Millhouse and A. Furrer, Solid State Commun. 15, 1303 (1974).
3. A. S. Edelstein, H. R. Child and C. Tranchita, Phys. Rev. Letters 36, 1332 (1976).
4. B. Buras, B. D. Rainford and B. Lebech, these conference proceedings.
5. K. Sköld, Nuclear Inst. and Methods 63, 114 (1968).
6. W. Gotze and P. Schlottmann, J. Low Temp. Phys. 16, 87 (1974).
7. B. Cornut and B. Coqblin, Phys. Rev. B5, 4541 (1972).

SOME EXPERIMENTS ON NEUTRON INELASTIC SCATTERING AT THE PULSED REACTOR IBR-30

K. Hennig[+)], L. Kaun, B. Lippold, W. Matz
Laboratory of Neutron Physics, Joint Institute for Nuclear Research
Dubna, USSR

ABSTRACT

The crystal field splitting of the $^3H_4$ ground state of the Pr ion in polycrystalline $PrFeO_3$, $PrGaO_3$, $PrAl_2$, and Pr_3Al has been investigated by inelastic scattering of thermal neutrons. At several temperatures the transitions between the crystalline field levels have been measured by using the time-of-flight technique with a beryllium-filter in front of the detector. From the experiments the energy level scheme for each compound has been deduced. By the same method the inelastic scattering on hydrogen solved in Pr_3Al and La has been studied. For high energy transfer ($\sim$100 meV) a harmonic oscillator type behavior of the spectra has been observed.

In principle two different kinds of powerful neutron sources are available for neutron scattering experiments, stationary and pulsed sources. The pulsed reactor IBR-30 in Dubna has been already used for investigations in nuclear and solid state physics for many years. More details about this reactor are given in reference (1). The maximum mean thermal power is 30 kW. Because of the generation of periodic neutron pulses the IBR-30 is especially appropriate for using the time-of-flight method.

In order to perform inelastic neutron scattering experiments on polycrystalline samples the method of inverted geometry[2] has been used in our investigations. Here a white incident neutron beam on the sample is used. Therefore, this method has an extremely high luminosity and is an adequate one even for reactors with a small mean power.

A schematic representation of our TOF-spectrometer is given in Fig. 1. In a good approximation, the neutron energy transfer ΔE in one scattering event can be calculated from the expression for the total time-of-flight

+) Central Institute for Nuclear Research, Rossendorf, GDR

$$N\tau = \alpha\{\frac{L_1}{(E_c + \Delta E)^{1/2}} + \frac{L_2}{E_c^{1/2}}\},$$

where N - channel number, τ - channel width, $\alpha = (m_n/2)^{1/2}$ with m_n - neutron mass, L_1 and L_2 - flight paths, and E_c - cut-off-energy of the filter material.

We have used this method for the determination of the $^3H_4$ ground state splitting of the paramagnetic ion Pr^{3+} which results from the crystalline electric field in some materials. For cubic point symmetry of the Pr^{3+} ion in the lattice the free ion ground state splits into four sublevels. In cases of lower symmetry up to nine sublevels are possible[3].

The differential cross section for paramagnetic neutron scattering in the dipole approximation can be written in the form[4]

$$\frac{d^2\sigma}{d\Omega d\omega} = C\cdot\frac{k_f}{k_i} f^2(\kappa) \sum_{n,m}\rho_m |\langle n|J_\perp|m\rangle|^2 \delta(\frac{E_n - E_m}{\hbar} - \omega),$$

where $C = (1.91e^2 g_J/2m_n c^2)^2$ with g_J the Lande factor, k_f and k_i - outgoing and incident neutron wave vector, $f(\kappa)$ - magnetic atomic form factor, $\vec{\kappa} = \vec{k}_i - \vec{k}_f$ scattering vector, ρ_m - population of the energy level E_m, $|n\rangle$, $|m\rangle$ - eigenfunctions describing the crystal field levels E_n, E_m, $J_\perp$ - the component of the total angular momentum operator perpendicular to $\vec{\kappa}$.

Our first experiments have been carried out on insulators. In Figs. 2 and 3 are shown the TOF-spectra for $PrFeO_3$ and $PrGaO_3$. From this the crystal field level scheme given in Table 1 has been derived for both substances[5]. The point symmetry of Pr^{3+} is C_s and, therefore, 9 levels should be found. The fact that only six levels could be detected can be explained by small energy differences of some levels (the resolution in energy of the spectrometer is about 14% in the region from ΔE = 10 to 100 meV) and by small transition probabilities.

The main advantage of neutrons in comparison with other methods becomes evident in investigations of metals and metallic compounds. In Figs. 4 and 5 are given the TOF-spectra of $PrAl_2$ and Pr_3Al obtained with

the above described method. $PrAl_2$ has a cubic Laves phase structure. The substance orders ferromagnetically at T_c about 34K[6]. The direction of the ferromagnetic order is the <100> direction. Thus, four transitions between the crystal field levels within the split ground state $^3H_4$ in the paramagnetic region (T > 34K) must be expected. On the other hand, for temperatures below T_c the degeneracy of the $^3H_4$ state of Pr^{3+} is completely lifted. When the direction of the ferromagnetic ordering is taken in the <100> direction the dependence of the splitting as a function of the internal magnetic field on the Pr ion site has been calculated within the molecular field approximation in reference (7). From our measurements carried out in Dubna and at the HFR in Grenoble (I.L.L.) we have deduced the parameter set given in Table 2.

Pr_3Al shows a more complicated structure than $PrAl_2$. Below 600K exists a so called α - Pr_3Al phase of hexagonal structure. The substance orders ferromagnetically at T_c about 16K[8]. In Table 3 are given five transitions found from our experiments. Because of the point symmetry C_{2v} of the Pr ion the ground state degeneracy is completely lifted. Therefore, more transitions should be expected than are observed. This can be explained due to either small transition probabilities between some levels or the finite energy resolution of the spectrometer. On the other hand, another explanation can be given in which it is assumed that the Pr and the Al ions have the same point charges. Such an assumption has been made in a similar way in reference (9) for the cubic case. This means that the Pr ion now "feels" a hexagonal surrounding and the possible number of transitions between them[10]. Taking into account the splitting under the influence of a magnetic field[10] the results can be described with the value of the parameter x about 0.6. This yields a level scheme given in Table 4.

In Fig. 5 are shown some transitions with relatively high energies ΔE. It is of interest that these transitions follow the rule ΔE, $2\Delta E$, $3\Delta E$ as clearly seen for T = 300K. Measurements by the NMR-method indicate the existence of hydrogen in this material. Therefore, this high energy transition can be attributed to states of bound (or solved) hydrogen. The same situation has been found for rare earth metals. In

Fig. 6 the results for La are shown (3 - 5 atomic percent hydrogen). From these experiments it can be deduced that the hydrogen "feels" a harmonic potential and fromthe point of view of phonons it means that for this case the Einstein model is adequate[11].

The last results show that the simple inverted geometry spectrometer in connection with a pulsed neutron source like IBR-30 is a good one for investigation of processes with high energy transfer ($300 > \Delta E > 20$ meV). Therefore, we think that this method is especially useful for investigations of crystal field level splitting in metallic compounds of the actinides - where the splittings are expected to be much higher than in the rare earth compounds - and of metals with solved hydrogen.

ACKNOWLEDGEMENTS

We would like to thank Drs. Yu. M. Ostanevich and L. Cser for many helpful discussions.

REFERENCES

1. И.М.Франк Проблемы физики элементарных частиц и атомного ядра (ЭЧАЯ) 2, выпуск 4, Москва 1972, стр.807

2. А.Байорек, Т.А.Мачехина, К.Парлински, Ф.Л.Шапиро Препринт ОИЯИ, Р-1899, Дубна, 1964

K. Parlinski, M. Sudnik-Hrynkiewicz, A. Bajorek, T. A. Janik and W. Olejarczyk, Research Applications of Nuclear Pulsed Systems, IAEA, Vienna, 1967, p. 179.

3. E. Fick and G. Joos, Handbuch der Physik, Band XXVIII/II, Springer-Verlag, 1957, p. 205; K. R. Lea, M. J. M. Leask and W. P. Wolf, J. Phys. Chem. Solids 23, 1381 (1962).

4. P. G. DeGennes in Magnetism, Vol. 3, p.115, Academic Press, New York and London (1963).

5. K. Feldmann, K. Hennig, L. Kaun, B. Lippold, M. M. Lukina, S. Matthies, W. Matz and E. Warming, Phys. Stat. Sol. (B) 72, 817 (1975).

6. N. Nereson, C. Olsen and G. Arnold, J. Appl. Phys. 39, 4605 (1968).

7. K. Hennig and S. Matthies, Preprint JINR, E17-9535, Dubna, 1976.

8. K. H. Mader and W. E. Wallace, J. Less-Common Metals 16, 85 (1968).

9. R. J. Birgeneau, J. Als-Nielsen and E. Bucher, Inelastic Scattering of Neutrons (Proc. Symp. Grenoble, 1972) IAEA, Vienna, 1972.

10. E. Segal and W. E. Wallace, J. Solid State Chem. 2, 347 (1970); J. Solid State Chem. 6, 99 (1973).

11. И.И.Гуревич, Л.В.Тарасов Физика нейтронов низких энергий, Москва, 1965, стр.107

Table 1. Energy level scheme for $PrFeO_3$ and $PrGaO_3$ (obtained from neutron scattering). The energies are given in meV.

Denotation of the energy levels	0	1	2	3	4	5
$PrFeO_3$	0	2.0±0.1	14.7±0.4	23.2±0.5	36±1	58±2
$PrGaO_3$	0	4.7±0.1	10.7±0.3	20.0±0.4	37±1	65±2

Table 2. Energy level scheme and crystal field parameter set for $PrAl_2$ (obtained from neutron scattering).

Energy level scheme in the paramegnetic region:

$\Gamma_3(0)$, $\Gamma_5(8.2\text{meV})$, $\Gamma_4(15\text{ meV})$, $\Gamma_1(36\text{ meV})$

LLW - parameters[3]: $x = -0.58 \pm 0.02$

$W = -(0.48 \pm 0.02)$ meV

Molecular field: $H_M = (480 \pm 50)$ kOe

Crystal field parameters: $B_4 = (47\pm4)\cdot10^{-4}$ meV

$B_6 = -(156\pm12)\cdot10^{-6}$ meV

Table 3. Transition energies for α-Pr_3Al found from the neutron scattering experiments.

Temperature (K)	Energy ΔE of the transitions in meV
300	(4.2±0.2), (7.6±0.2), (11.1±0.4), (17.3±0.3), (21.2±0.5), (100±5), (202±6), (309±10)
80	(4.3±0.2), (8.1±0.2), (11.1±0.2), (27.0±0.5), (100±5), (197±6)
11	(3.2±0.2), (6.1±0.2), (9.2±0.2), (28.5±0.5), (102±5)

Table 4. Energy level scheme for α-Pr_3Al

$\Gamma_{52}(0)$, $\Gamma_6(4.2\text{ meV})$, $\Gamma_1(6.3\text{ meV})$, $\Gamma_{51}(8.0\text{ meV})$, $\Gamma_3(17.3\text{ meV})$, $\Gamma_4(27\text{ meV})$

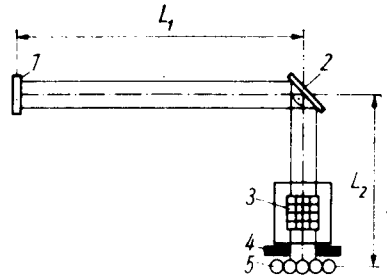


Fig. 1. Schematic representation of the experimental arrangement: 1 moderator, 2 sample, 3 beryllium filter, 4 shielding, 5 counter.

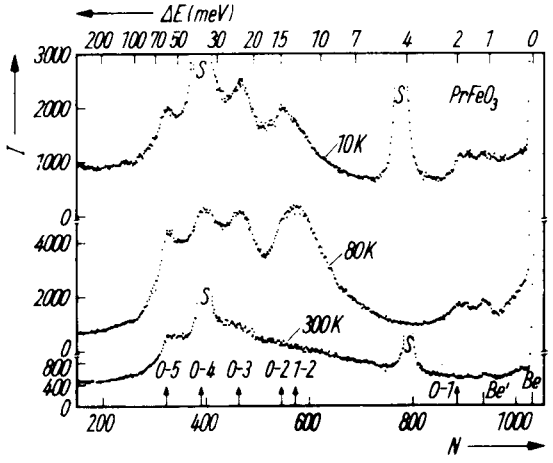


Fig. 2. TOF-spectra for $PrFeO_3$ at 10, 80, and 300 K. The arrows indicate the maxima due to transitions between crystal field levels. S denotes the so called satellites which are typical for the IBR type reactor. The spectrum for 80 K without satellites is a result of two measurements at different satellite positions. I are the counts per channel for the measuring time of about 35 h, ΔE is the energy transfer, N is the channel number with a width of 32μs, Be is the beryllium cut-off, and Be' is the beryllium pre-cut-off.

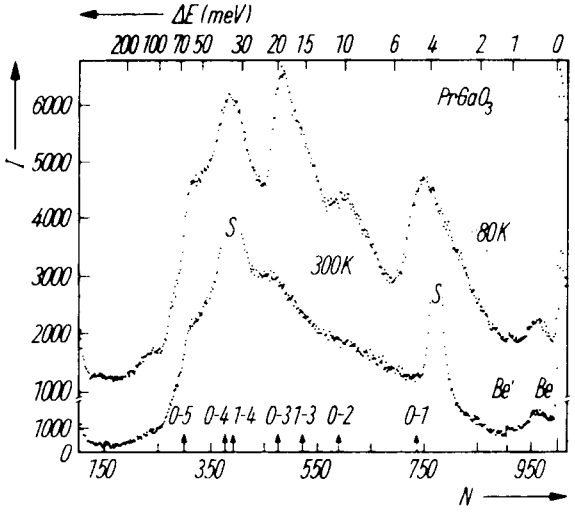


Fig. 3 TOF-spectra for $PrGaO_3$ at 80 and 300 K. The spectra are measured for the period of time of about 35 h. The meaning of the symbols is the same as in Fig. 2.

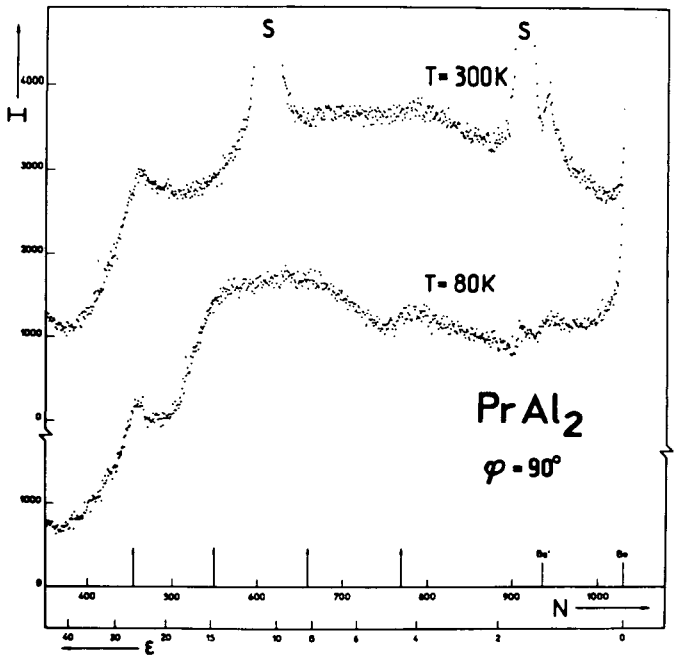


Fig. 4. TOF-spectra of inelastically scattered neutrons on $PrAl_2$ at a scattering angle $\phi = 90°$ for a period of time of 80 h. ε is the energy transfer in meV. The meaning of the other symbols is the same as in Fig. 2.

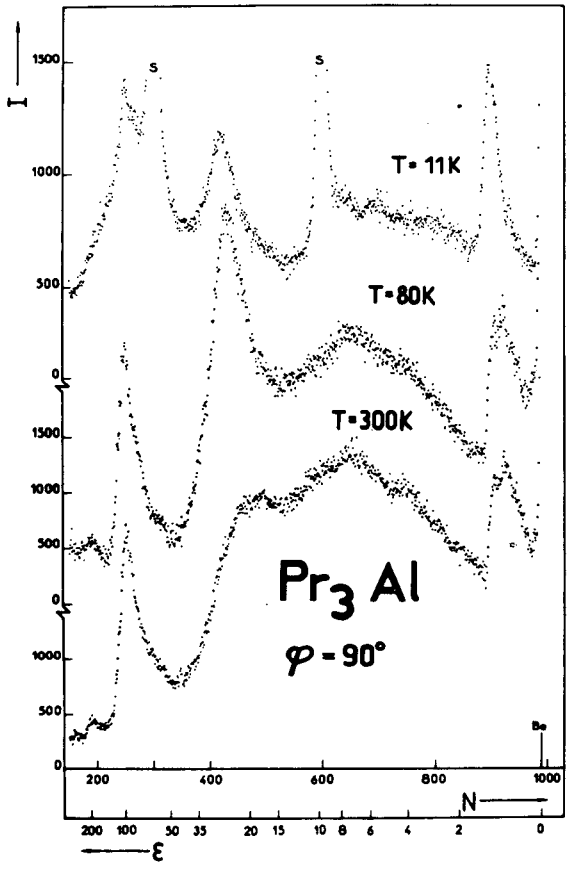


Fig. 5. TOF-spectra of inelastically scattered neutrons on α-Pr_3Al at a scattering angle ϕ =90° for periods of time of 80 h (300 K), 70 h (80 K), and 13 h (11 K). ε is the energy transfer in meV. The meaning of the other symbols is the same as in Fig. 2.

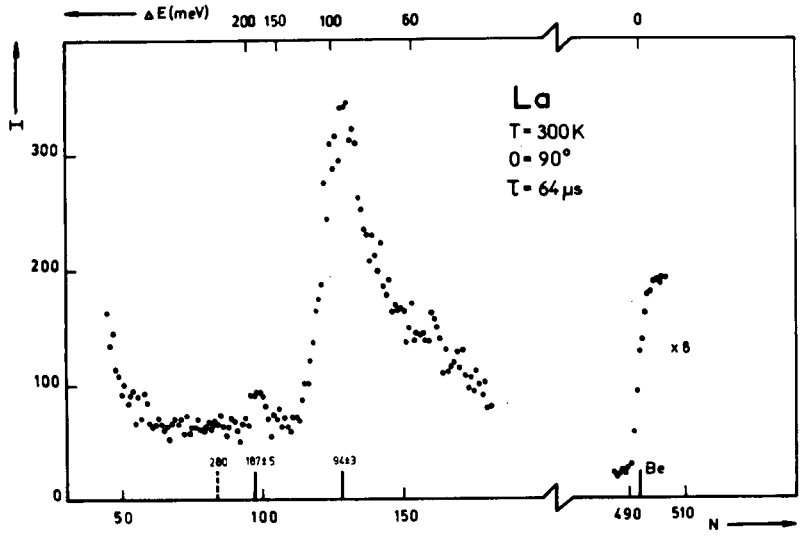
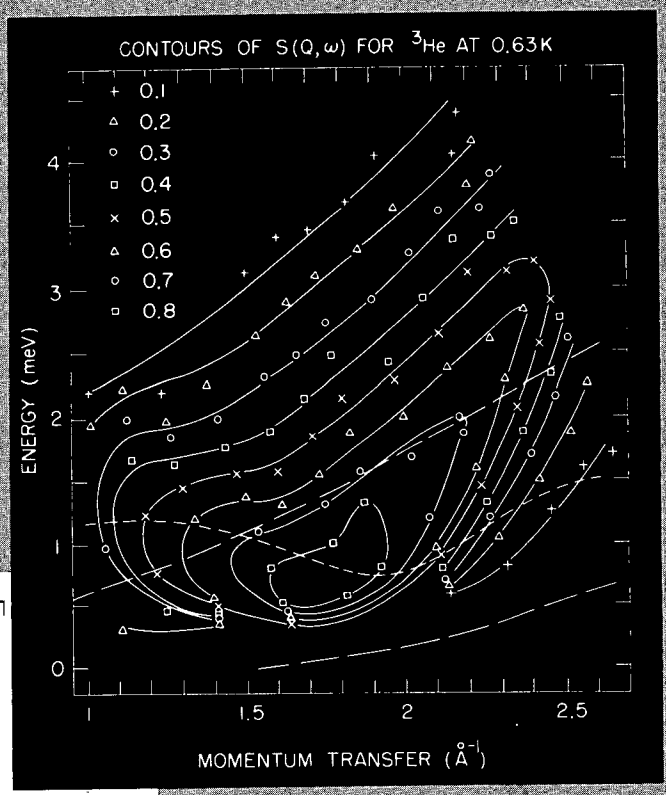
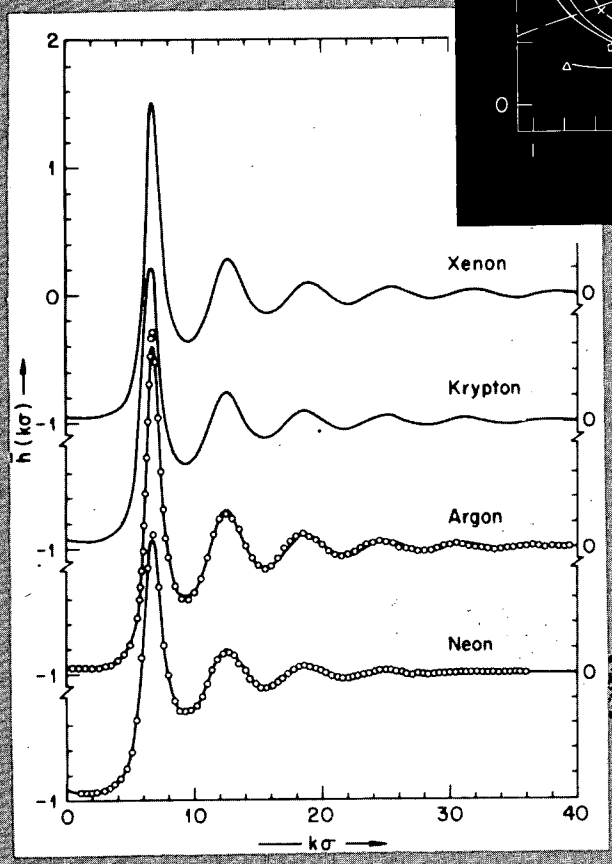


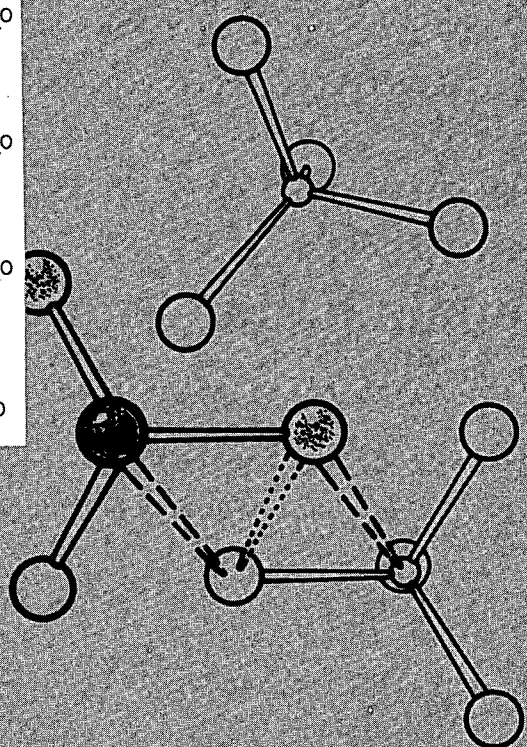
Fig. 6. TOF- spectra of inelastically scattered neutrons on La for a period of time of 2 h. The meaning of the other symbols is the same as in Fig. 2.


John Cooke
Mike Wilkinson
Jens Haumann

LIQUIDS AND GASES







CONF-760601--1

STRUCTURE OF LIQUIDS

A. H. Narten
Chemistry Division, Oak Ridge National Laboratory*
Oak Ridge, Tennessee 37830

ABSTRACT

The structure of most liquids is completely described by probability functions of position and orientation. Knowledge of the pair correlation function and the intermolecular potential is sufficient in principle for the calculation of all thermodynamic properties by standard methods of statistical mechanics. The Fourier transform of the pair correlation function is closely related to the liquid structure function which can be obtained from the experimentally accessible static scattering cross section.

For monatomic fluids the agreement between experiment and the general theory is, to this date, quite satisfactory. For molecular liquids the situation is not so clear. The pair correlation function is now a function of more than one variable and cannot possibly be mapped by a single one-dimensional diffraction experiment. Hence, it is necessary to combine results from several diffraction experiments (neutrons, x-rays) with theoretical considerations to obtain information about orientational correlations in molecular fluids.

INTRODUCTION

It is important to realize at the outset that the term "structure," as used in studies of the liquid state, usually means something quite different from the same word used to describe crystalline solids.

The structure of a crystalline solid is specified by the symmetry of the space group and by the mean atomic positions in the unit cell, together with estimates of the amplitudes of thermal vibration of each of the nuclei. The periodicity of the lattice allows one to construct a model of the unit cell which is representative of the entire crystal.

*Operated by Union Carbide Corporation for the USERDA.

In a liquid there is no such periodicity. The short-range ordering, or structure, found in liquid materials is completely described by probability functions of position and orientation. If we choose the symbol X_i to denote the set of all coordinates needed to specify the position and orientation of a particle, and we let dX_2 be the volume of a differential volume element in the coordinate space of particle 2, then we may define a pair correlation function $g(X_1,X_2)$ so that $\rho g(X_1,X_2)dX_2$ is the average number of particles at X_2 in the volume element dX_2 when another particle is at X_1. Hence, the function $g(X_1,X_2)$ is a measure of the local particle density in the vicinity of any origin particle in a fluid of bulk density ρ. In principle, knowledge of the pair correlation function $g(X_1,X_2)$ and of the pair potential $V(X_1,X_2)$ is sufficient for the prediction of all equilibrium properties of fluids through standard methods of statistical mechanics.[1] While this sounds very simple, it is feasible only for the simplest types of fluids.

For monatomic fluids (Ar,Na) the pair correlation function depends only on the scalar distance between the atoms, and we usually write the function as $g(r)$. The atom pair correlation function of a monatomic fluid can be obtained from a single diffraction experiment using thermal neutrons, x-rays, or electrons. If the interatomic potential function $V(r)$ is known, the function $g(r)$ can also be obtained from computer experiments involving the Monte Carlo or the molecular dynamics method, and from molecular theory. For simple fluids such as argon the agreement between experiment, computer simulation, and the general theory is quite satisfactory.

For molecular fluids the situation is not so clear. Even for the simple case of linear molecules the function $g(X_1,X_2)$ now depends on four relative coordinates of the two molecules, and a single diffraction experiment does not provide enough information to determine a function of four or more variables. For fluids with nearly spherical molecules a multipole expansion of molecular properties leads to a rapidly converging series the coefficients of which can be determined from one or two diffraction experiments.[1] This approach is promising for the

analysis of x-ray diffraction data because many non-spherical molecules have a very nearly spherical distribution of electron density. An example is liquid water, for which the pair correlation function for molecular centers has been derived from a single x-ray diffraction experiment.[2]

The expansion method appears less promising for the analysis of neutron diffraction data, because the molecular neutron scattering density is highly non-spherical and the resulting series does not converge. An alternate approach, which has been the traditional one, is to describe the structure of molecular fluids in terms of atom pair correlation functions, $g_{\alpha\beta}(r)$. In this picture, the functions $g_{\alpha\beta}(r)$ are related to the probability of finding an atom of type β of some molecule at a scalar distance r from an atom of type α of some different molecule. Knowledge of all atom pair correlation functions is not sufficient for a complete description of the structure of a molecular fluid. This may be visualized by considering a fluid with homonuclear diatomic molecules such as N_2 which is described by a single atom pair correlation function, $g_{NN}(r)$. Clearly, the function $g_{NN}(r)$ does not tell us whether the N_2 molecules are aligned or perpendicular to each other.

Despite these limitations, the description of liquid structure in terms of atom pair correlation functions will be adopted in this discussion because the experimental determination of these quantities is feasible for many liquids of practical interest. This will be discussed in the next section.

DIFFRACTION EXPERIMENTS

The purpose of diffraction experiments is to determine the static scattering function S(k) which is related to the dynamic scattering function $S(k,\omega)$ by the expression[3]

$$S(k) = \int_{-\infty}^{\infty} S(k,\omega)d\omega \ , \qquad (1)$$

where $\hbar\omega$ represents the energy transfer and the integration has to be

carried out at constant value of the wave vector change $\underset{\sim}{k}$. In conventional diffraction experiments a detector is used to count the scattered radiation at a preset angle θ, and the measured cross section may be written as

$$\left(\frac{d\sigma}{d\Omega} \right)_\theta = \int_{-\infty}^{\omega_0} (k_s/k_0)\varepsilon(k_s)S(k,\omega)d\omega \qquad (2)$$

with ω_0 the angular frequency of incident radiation, $\underset{\sim}{k}_0$ and $\underset{\sim}{k}_s$ the wave vector of incident and scattered radiation (magnitudes $2\pi/\lambda_0$ and $2\pi/\lambda_s$, respectively) and $\varepsilon(k_s)$ the detector efficiency. Eq. (2) differs from Eq. (1) because constant θ does not imply constant $\underset{\sim}{k}$, the detector sensitivity depends on the scattered wave vector, and the frequency has an upper limit, ω_0. However, all these effects can be accounted for by a method introduced by Placzek.[4] One expands the integrand in Eq. (2) in a series about the elastic values, and the resulting expression[1,5] is of the general form

$$\left(\frac{d\sigma}{d\Omega} \right)_\theta = \varepsilon(k_0)S(k) + \text{corrections} \quad . \qquad (3)$$

For most fluids the main contribution to the corrections comes from center of mass motion terms, and in the "static approximation" these dynamic corrections are completely neglected. For x-ray scattering the corrections in (3) are negligibly small, but for thermal neutrons they can be of sizeable magnitude.

The computed dynamic corrections for neutron scattering from CCl_4 molecules are shown in Fig. 1. The dashed curves represent the "self" part of the corrections, which is due to the recoil of neutrons from individual uncorrelated atoms, and depends only on the experimental parameters and on the scattering amplitudes and masses of the nuclides in the sample. In addition, there is a "distinct" contribution due to recoil from different atoms in the same molecule which depends on the mean intramolecular distances and their vibrational amplitudes.[5] As a consequence, the total corrections (solid lines) are modulated by coherence effects. The upper part of Fig. 1 shows a comparison of the

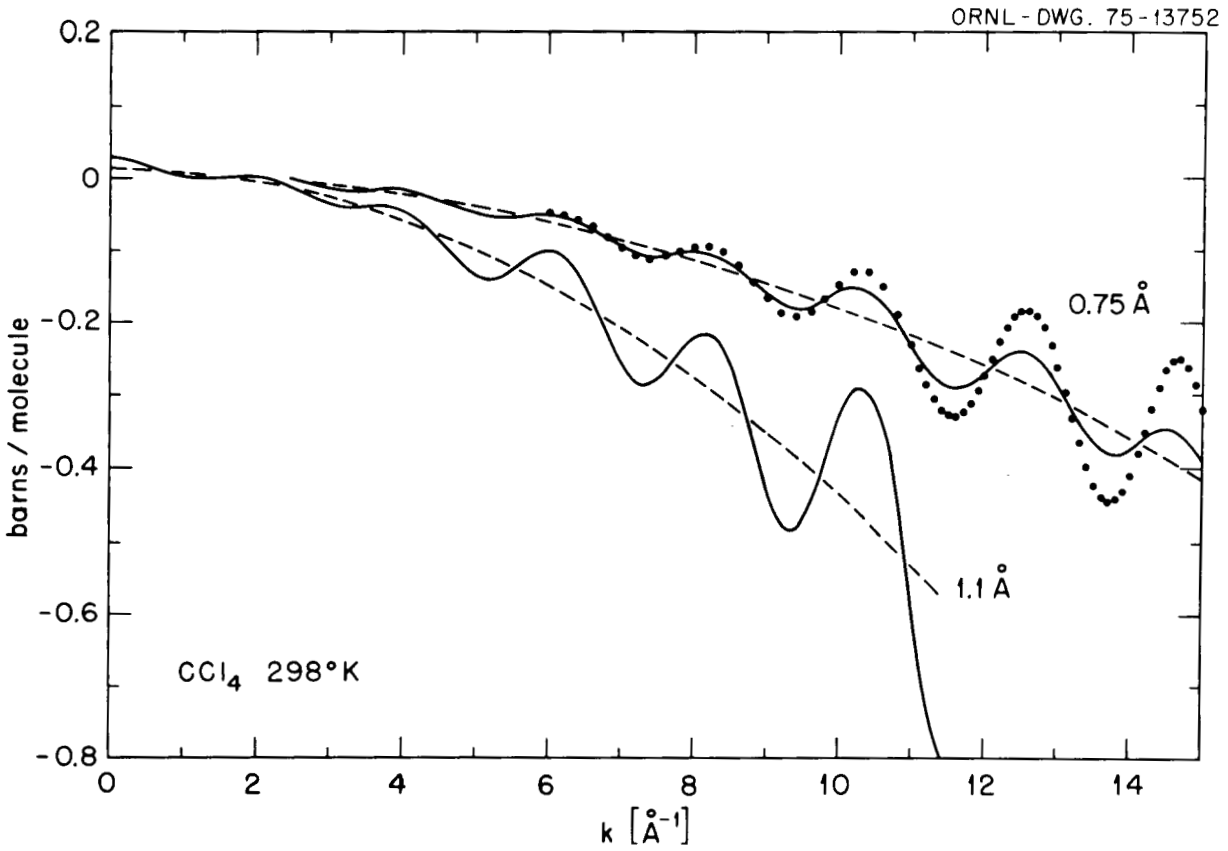


Fig. 1. Dynamic corrections for neutron scattering from CCl_4 molecules. The points have been computed for rigid and the solid lines for vibrating molecules. The dashed curves describe the "self" part of the corrections.

dynamic corrections computed for rigid (points) and for vibrating CCl_4 molecules (solid line). Dynamic corrections for neutron scattering from a number of diatomic molecules are shown in Fig. 2.

A comparison between the computed dynamic corrections and measured neutron cross sections[6] for liquid CCl_4 is shown in Fig. 3. The measured cross sections (points) show the characteristic fall-off below the asymptotic value expected for independent atoms in the static approximation (dashed line), and the two data sets measured with two different incident neutron wavelengths do not match in the region of overlap $8.8\ Å^{-1} \lesssim k \lesssim 9.8\ Å^{-1}$. This behavior is well described by the computed curves (solid lines), which represent the sum of the static

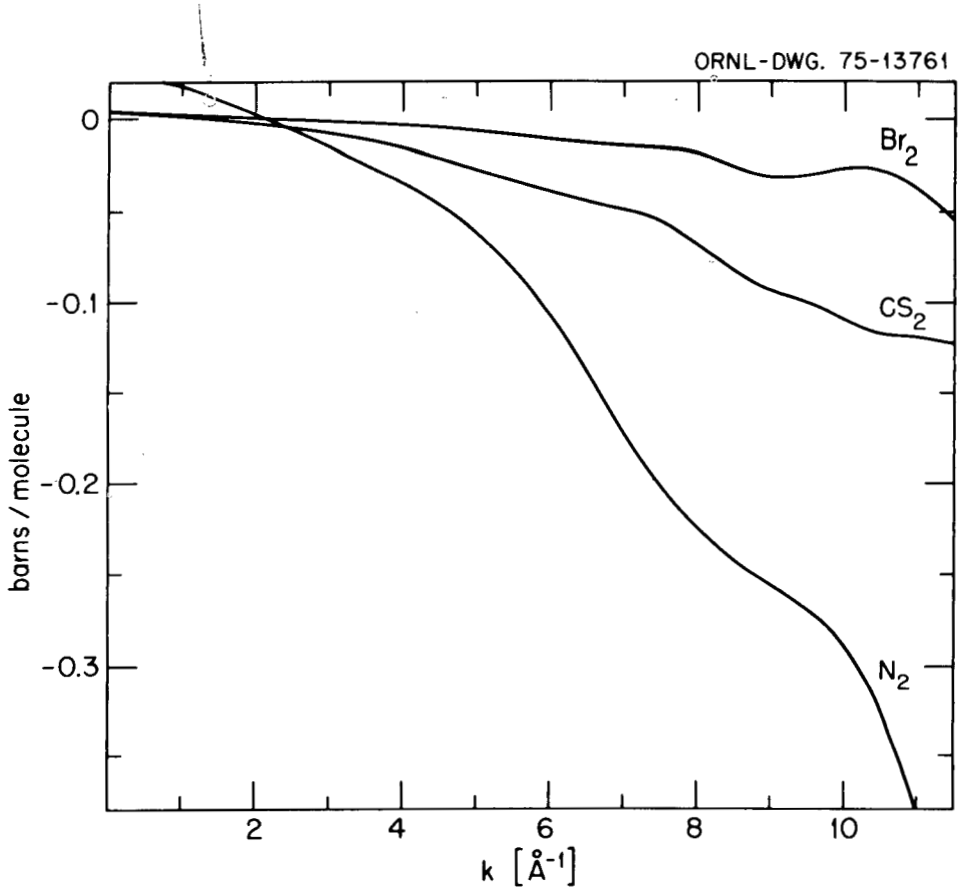


Fig. 2. Dynamic corrections computed for some linear molecules (1 Å neutrons).

self-scattering and the dynamic corrections. The oscillations in the computed curves are very nearly in phase with the oscillations of the measured cross sections, but the amplitudes are reversed. Hence, the effect of the recoil of neutrons scattered from different atoms in the CCl_4 molecule is a damping of the oscillations of the measured cross sections.

A comparison between the computed dynamic corrections and measured neutron cross sections[7] for liquid D_2O is shown in Fig. 4. In this case, the fall-off below the static self-scattering (dashed curve) predicted by the computed corrections (solid line) is much larger than found experimentally (points). The main reason for this is the failure of the Placzek expansion which converges only if the ratio of the neutron mass to the atomic mass is small.

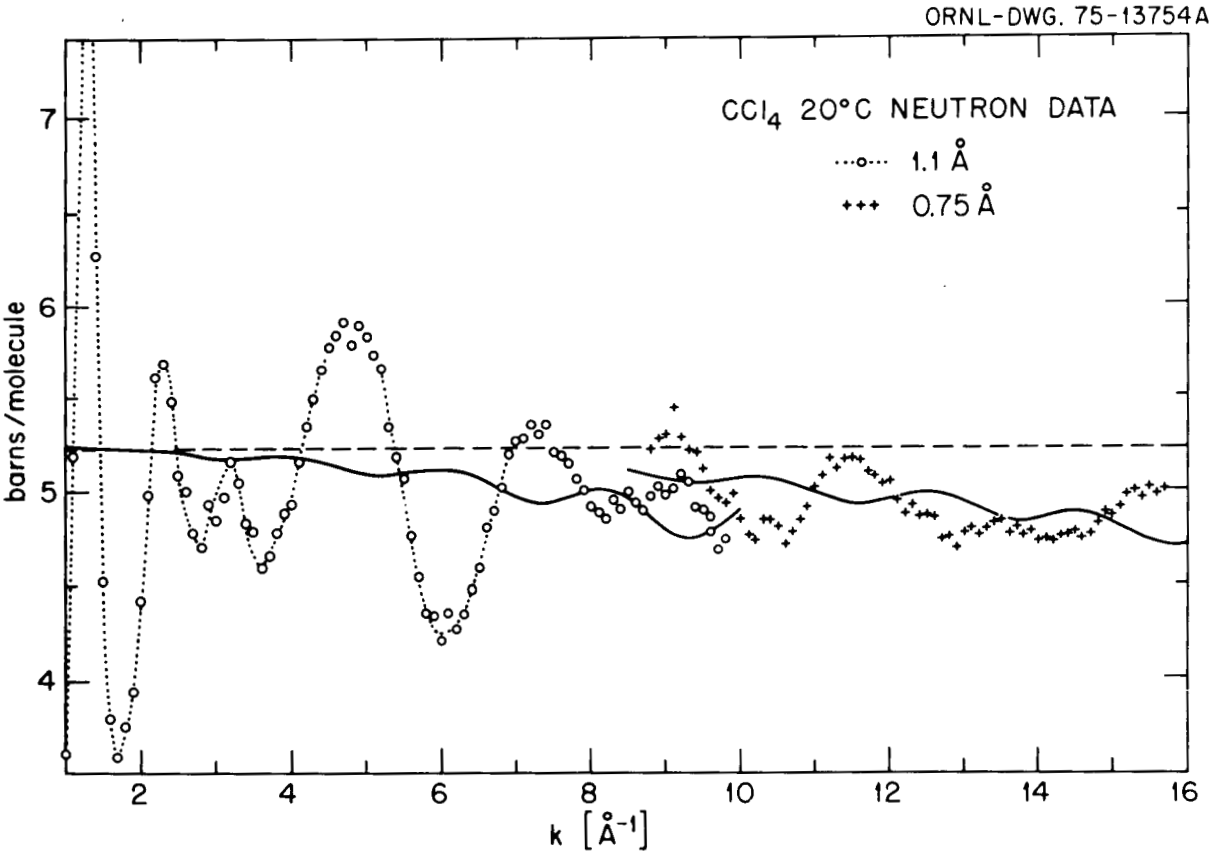


Fig. 3. Measured neutron cross sections (points) and computed dynamic corrections (solid lines) for liquid CCl_4. The dashed curve describes the scattering from uncorrelated atoms in the static approximation. (Reproduced from Ref. 6.)

We conclude that, for fluids with heavy nuclides, the static scattering function S(k) can be determined with good accuracy from the scattering cross section $\left(\frac{d\sigma}{d\Omega}\right)_\theta$ measured in conventional diffraction experiments using continuous neutron sources such as nuclear reactors. The situation is not so clear for scattering experiments with pulsed neutron sources. For this case, the relationship between the measured cross sections and the static scattering function is quite complex,[8] and a satisfactory theory has yet to be developed.

The application of neutron diffraction to fluids with light nuclides such as water and aqueous solutions has been hampered by our inability to account for the dynamic corrections in a satisfactory

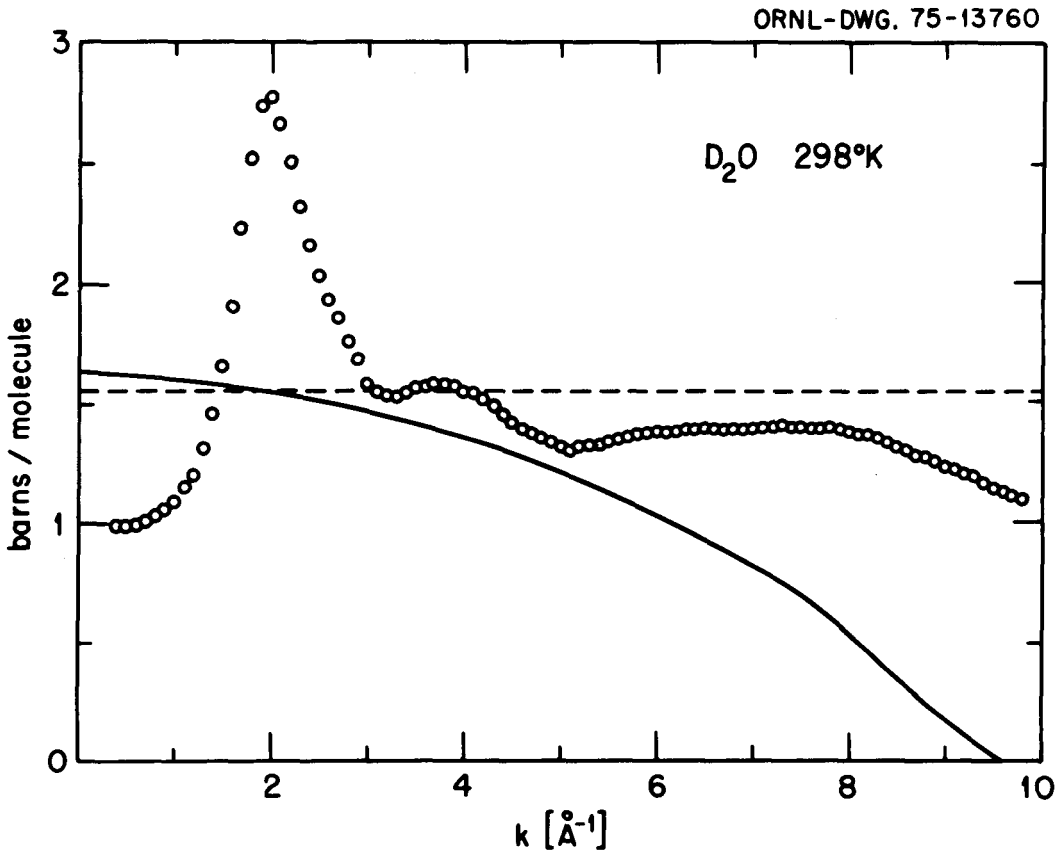


Fig. 4. Measured neutron cross sections (points) and computed dynamic corrections (solid line) for liquid D_2O (1.1 Å neutrons).

manner. Here, the approach has been to treat one or more of the constants in the theoretical expressions as adjustable parameters which are then determined by more or less well-established criteria.

DATA ANALYSIS

Structure Functions

The static coherent scattering function S(k) is related to the liquid structure function H(k) by the expression

$$H(k) \equiv [S(k) - S_s(k)]M(k) ,$$

with $S_s(k) = \sum_\alpha b_\alpha^2$, $M(k) = [\sum_\alpha b_\alpha]^{-2}$, b_α the coherent scattering factor of

atom α, and summation over a stoichiometric unit characteristic of the sample.

For monatomic fluids the liquid structure function is directly related to the Fourier transform of the atom pair correlation function describing the liquid structure. Fig. 5 shows the structure function of liquid Ga.[9] The curve derived from neutron diffraction (xxx) is in excellent agreement with the curve obtained from x-ray diffraction (circles). This agreement indicates, again, that recoil effects can be accounted for with good accuracy in the case of neutron scattering.

For molecular fluids the function H(k) may be written as the sum of two terms, namely

$$H(k) = H_m(k) + H_d(k) \ .$$

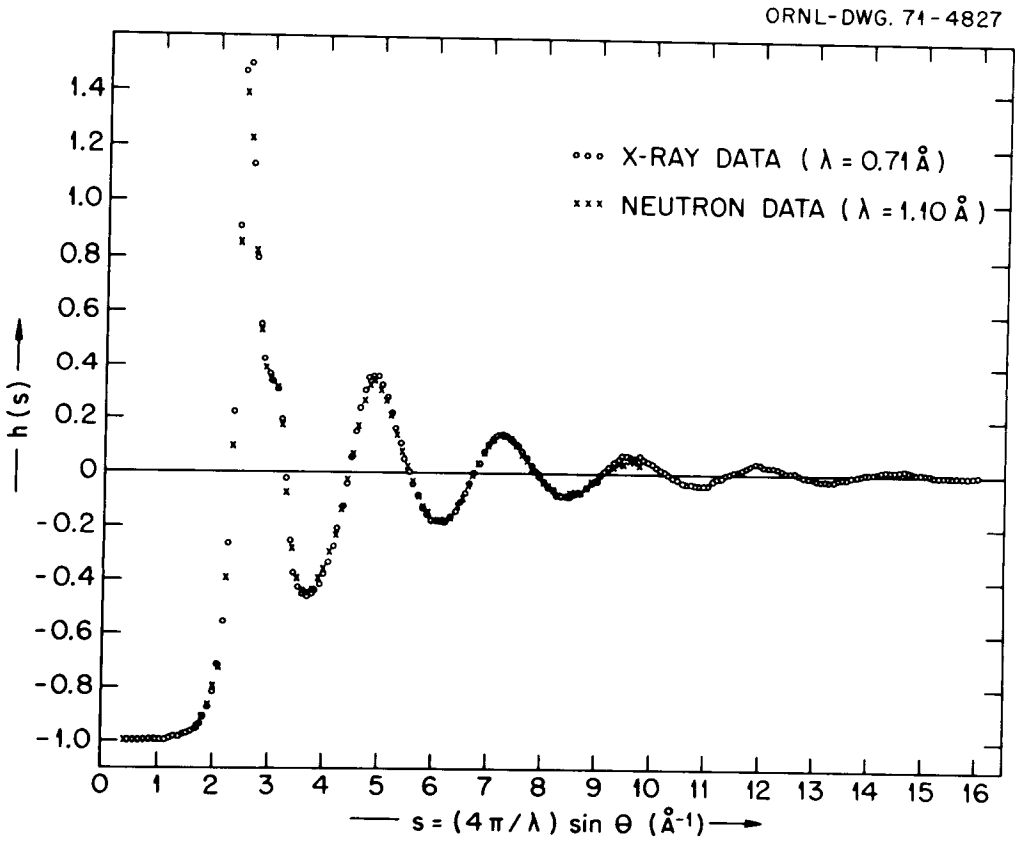


Fig. 5. Structure functions for liquid Ga at 20°C derived from neutron and from x-ray diffraction. (Reproduced from Ref. 9.)

The term $H_m(k)$ depends only on the structure of individual, uncorrelated molecules. The distinct structure function $H_d(k)$ contains the contributions from atom pairs in different molecules, i.e., the liquid structure. Structure functions for liquid CCl_4 are shown in Fig. 6. The agreement between the function $kH(k)$, derived from the neutron data shown in Fig. 3, and the function $kH_m(k)$, computed from the known molecular structure,[6] is satisfactory for values of $k \gtrsim 8$ Å^{-1}. The distinct structure function $H_d(k)$ is related to the atom pair correlation functions $g_{\alpha\beta}(r)$ by the expression

$$H_d(k) = M(k)\sum_{\alpha}\sum_{\beta} b_\alpha b_\beta 4\pi(\rho_\alpha\rho_\beta)^{\frac{1}{2}}\int_0^\infty r^2 j_0(kr)h_{\alpha\beta}(r)dr \ ,$$

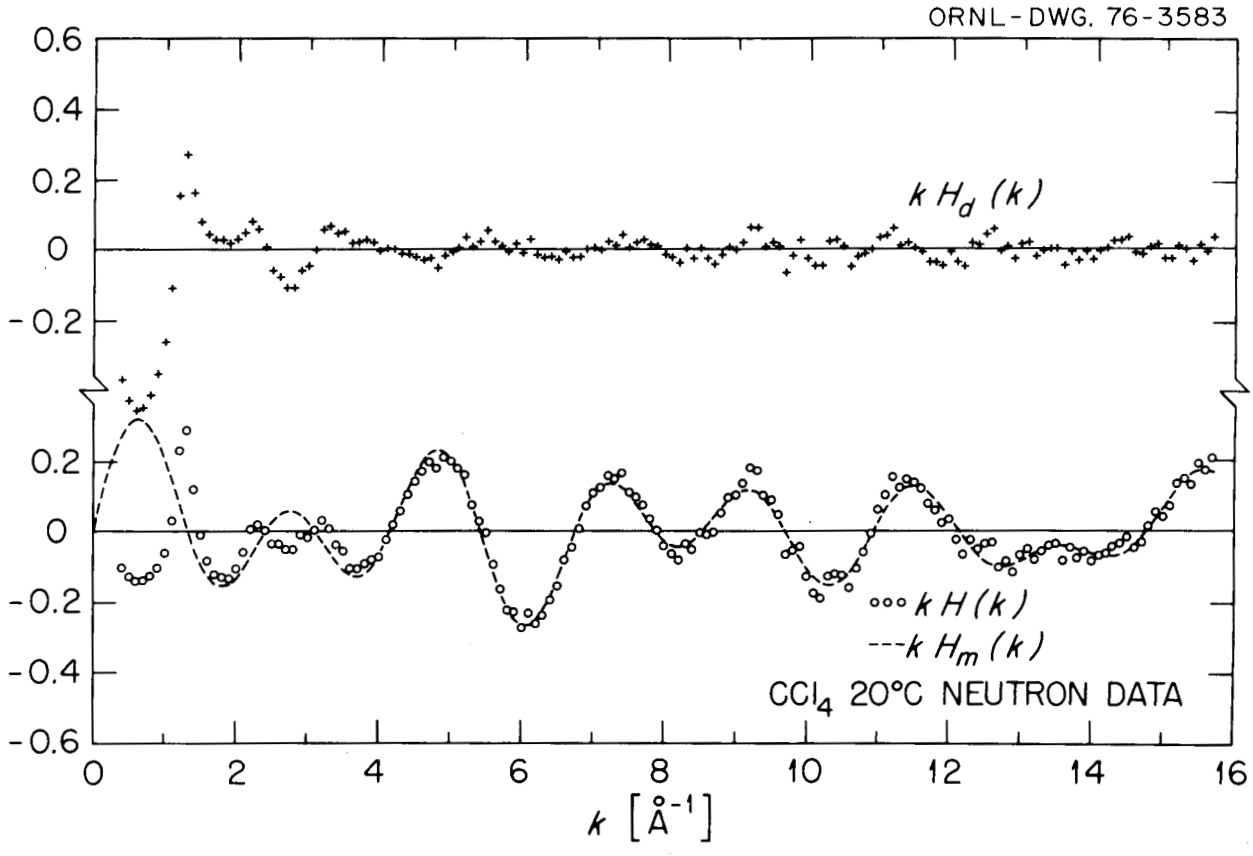


Fig. 6. Weighted structure functions for liquid CCl_4 derived from neutron diffraction (points) and computed for uncorrelated molecules (dashed curve). (Reproduced from Ref. 6.)

with $h_{\alpha\beta}(r) = g_{\alpha\beta}(r) - 1$, $j_0(x) = \sin x/x$, and ρ_α the bulk number density of atom α. To determine the three atom-pair correlation functions which describe the structure of a molecular fluid with two different kinds of atoms, an equal number of diffraction experiments involving different scattering factors are necessary. For CCl_4 this could be done by combining results from x-ray and from neutron diffraction, the latter with both $C^{35}Cl_4$ and $C^{37}Cl_4$. This has not yet been done. However, x-ray and neutron diffraction data on liquid CCl_4 of normal isotopic abundance have been analyzed[6] to yield two of the three correlation functions, namely $g_{CCl}(r)$ and $g_{ClCl}(r)$. This is possible because the C-C interactions contribute less than 2% to both the neutron and x-ray scattering in CCl_4. These results will be discussed in the next section.

Correlation Functions

Atom pair correlation functions have been derived from diffraction data for many homoatomic[10] and for a few heteratomic fluids.[11] Fig. 7 shows a typical example of the atom pair correlation function for a liquid metal, namely Ga.[9] This function has the limiting values

$$g(r) \longrightarrow 1 \quad \text{as} \quad r \longrightarrow \infty$$

$$g(r) \longrightarrow 0 \quad \text{as} \quad r \longrightarrow 0 \, .$$

The latter result expresses the fact that two atoms cannot occupy the same position at the same time. The correlation functions, and hence the structure, of monatomic fluids can often be described in terms of a random close packing of hard spheres.

Atom pair correlation functions have been determined[1] for a few molecular fluids with homonuclear diatomic molecules (N_2, O_2, Br_2) and for two fluids with heteronuclear molecules (H_2O and CCl_4). Fig. 8 shows two of the three atom pair correlation functions descriptive of the structure of liquid CCl_4. These curves yield directly some valuable insight into the average arrangement of CCl_4 molecules in the liquid. The maximum at 4.9 Å in $g_{CCl}(r)$ corresponds to four C···Cl (and Cl···C) neighbors per molecule. The intermolecular C···Cl distance of 4.9 Å is shorter than the sum of the C-Cl bond length (1.77 Å)

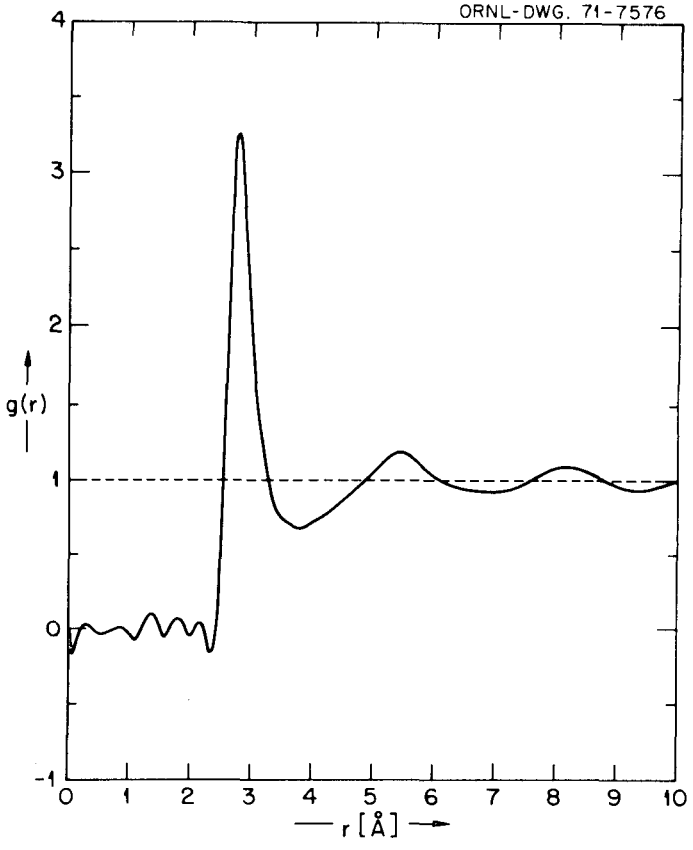


Fig. 7. Atom pair correlation function of liquid Ga obtained by Fourier inversion of the curves shown in Fig. 5. (Reproduced from Ref. 9.)

and the van der Waals diameter of a chlorine atom (3.6 Å), namely 5.4 Å. This means that each of four neighboring molecules has one of its chlorine atoms nestled into one of the four hollows of the central molecule. At the same time, the central molecule has one of its chlorine atoms located in a hollow of the nearest neighbor, giving rise to the Cl···Cl contact distance of 3.8 Å (Fig. 8). One possible way of interlocking four CCl_4 neighbors with a central molecule is shown in Fig. 9 (only three of the four neighbors are shown). This interlocking gives rise to pronounced orientational correlations between CCl_4 molecules in the liquid. It does not imply tetrahedral coordination. In fact, the molecules in liquid CCl_4 are more nearly close packed, and one can construct models[12] of liquid CCl_4 having 12 neighbors in a first

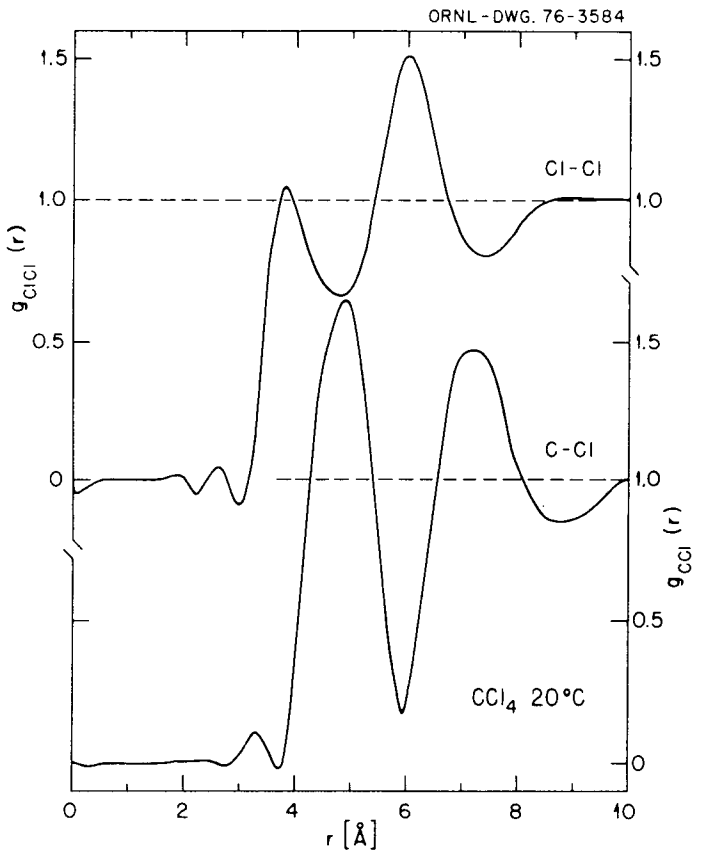


Fig. 8. Intermolecular atom pair correlation functions for liquid CCl_4 derived from neutron and x-ray diffraction. (Reproduced from Ref. 6.)

coordination shell of about 6 Å. The diffraction data tell us that the orientation of only four of these neighbors is strongly correlated with that of a central molecule.

MODELS OF LIQUID STRUCTURE

Less direct methods of interpreting diffraction data from liquids involve the use of model potentials, and statistical mechanical or computer simulation methods for generating structure and correlation functions. If the calculated quantities agree with the experimental results, it is assumed that the model potential is sufficiently realistic for the prediction of other properties by these methods. In cases of disagreement, the experimental data serve as a valuable guide for the improvement of the model potential and/or the theory.

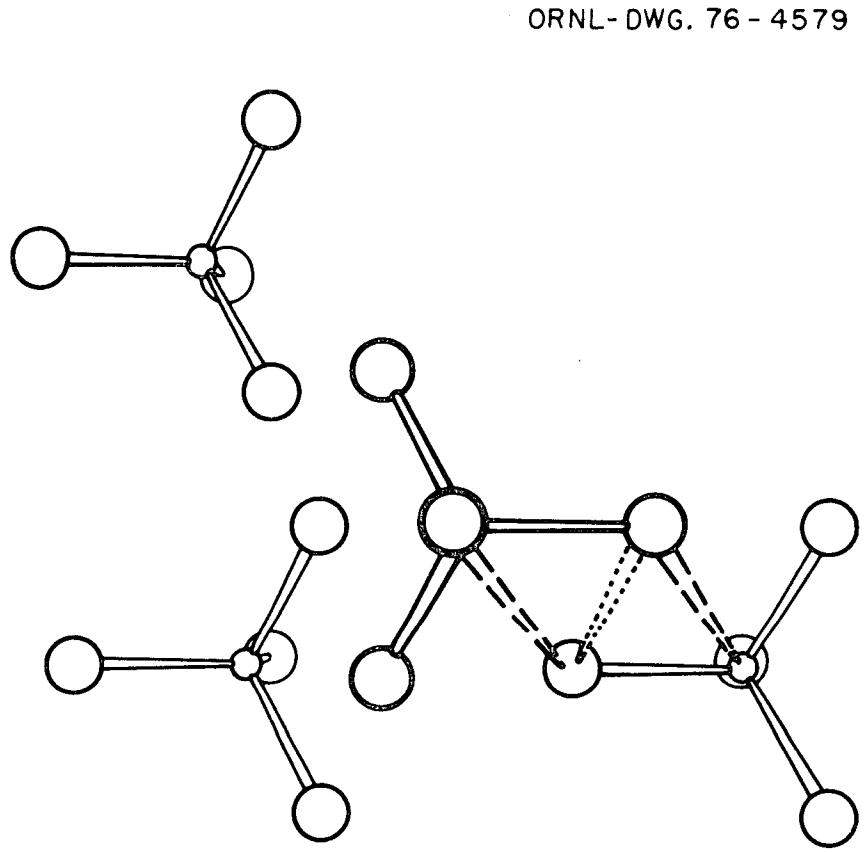


Fig. 9. Orientational correlation between pairs of neighboring molecules in liquid CCl_4 inferred from the atom pair correlation functions shown in Fig. 8. (Reproduced from Ref. 6.)

It has already been mentioned that the agreement between results from experiment, computer simulation and the general theory is quite satisfactory for atomic fluids. As an example, we show in Fig. 10 structure functions for Lennard-Jones (12/6) fluids in four different states which correspond to those of neon, argon, krypton, and xenon near their respective triple points. The solid curves have been computed[13] using molecular theory in the so-called mean spherical approximation (MSA). The circles represent experimental results for neon[14] and argon.[15] Fig. 11 shows the corresponding pair correlation functions. The solid and dashed curves have been computed[13] using two different versions of the MSA, and the circles represent results from computer simulations[16] using the molecular dynamics method.

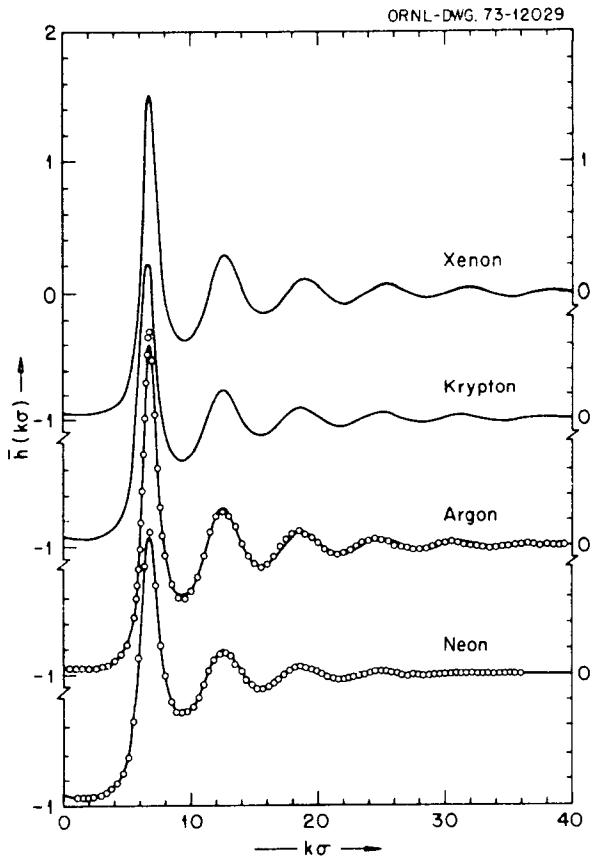


Fig. 10. Structure functions for Lennard-Jones fluids. Solid lines calculated from a 12/6 potential, circles derived from neutron diffraction. (Reproduced from Ref. 13.)

For molecular fluids the situation is not so clear. The only successful theoretical approach to this date has been the so-called reference interaction site model (RISM).[12] This model assumes that the correlations between molecules are determined primarily by the short range, repulsive forces of the intermolecular potential. These repulsive interactions are modelled as hard core interactions by assuming molecules as composed of overlapping hard spheres which are rigidly fused together. The pair correlations produced by these interactions are determined from an approximate integral equation which is solved in a computationally convenient variational form. Structure functions predicted by the RISM theory[12] for liquid CS_2 and CSe_2 are shown in Fig. 12 (solid lines). Also shown are results from neutron diffraction

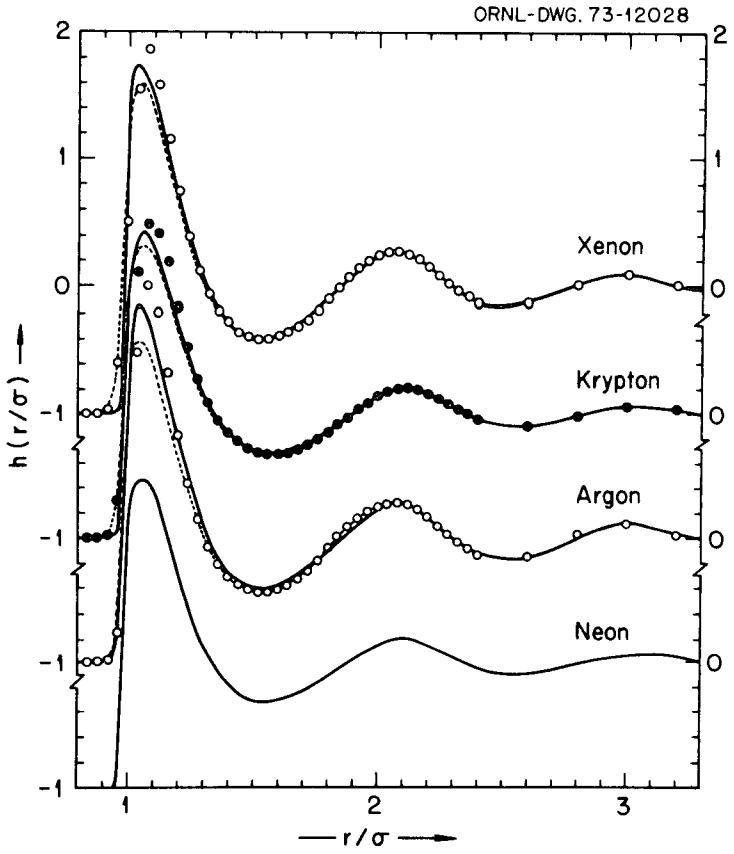


Fig. 11. Correlation functions for Lennard-Jones fluids. Solid and broken lines calculated from MSA, circles from molecular dynamics. (Reproduced from Ref. 13.)

(points).[17] The two sets of curves are in moderately good agreement. The overall discrepancy of ∿20% is quite typical of the present state of the art, and it is not clear whether it is due to deficiencies in the model or in the data. This serves to illustrate an important point, namely that diffraction data of high accuracy are needed to test the structural predictions of theoretical models.

Even if accurate diffraction data are available, it will not always be possible to test the predictions of theoretical models because the data may be insensitive to certain aspects of the model. As an example, we show in Fig. 13 atom pair correlation functions for the molecular centers of liquid CCl_4 computed from three different models. The dashed curves are predicted from a one-center hard sphere model, the solid line

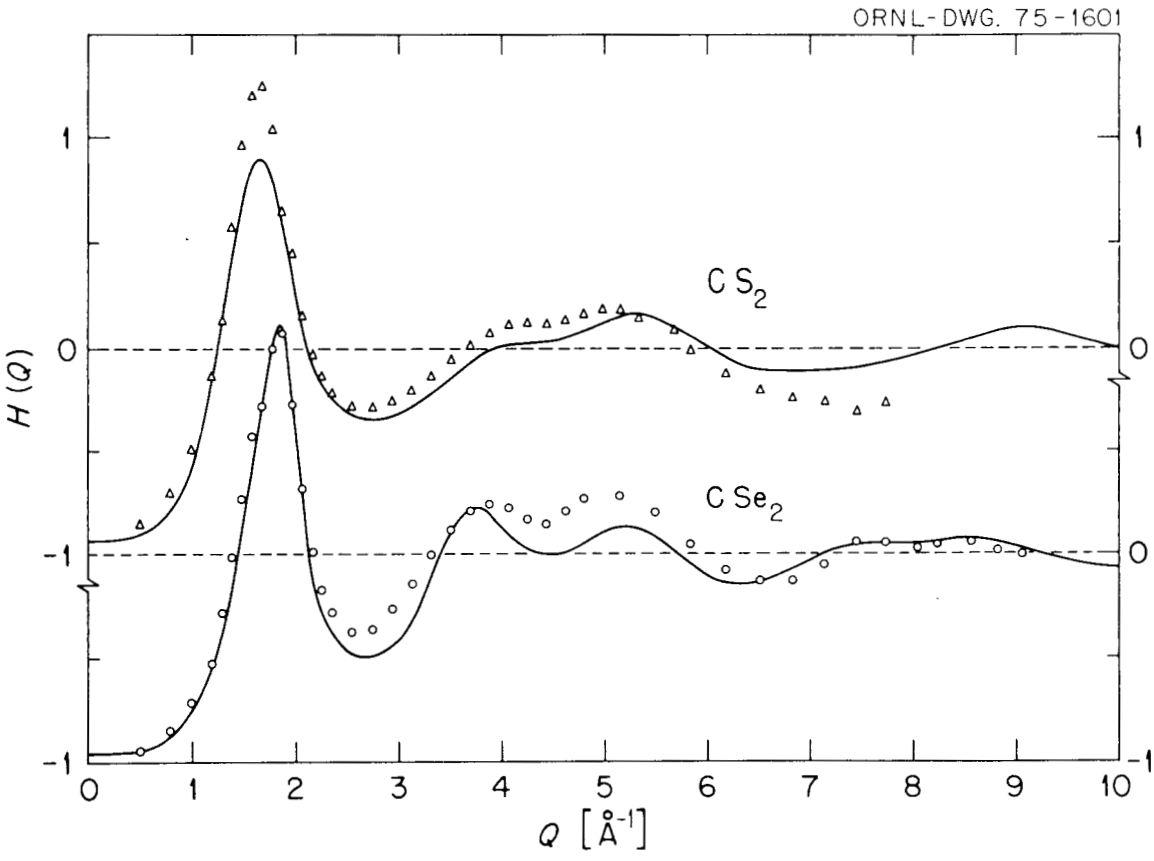


Fig. 12. Structure functions for liquid CS_2 and CSe_2 derived from neutron diffraction (points) and from RISM theory (solid curves). (Reproduced from Ref. 1.)

is from a RISM liquid of appropriate molecular dimensions, and the points are from a computer simulation (Monte Carlo) using atom-atom potentials derived from crystallographic data.[1] Only the one-center hard sphere model can be eliminated by comparison with diffraction data because it does not predict the orientational correlations present in liquid CCl_4. We cannot distinquish between the other two models, because the functions $g_{CCl}(r)$ and $g_{ClCl}(r)$ predicted by both the RISM theory and the computer simulation are very similar, and the diffraction data are very insensitive to contributions from C-C interactions.

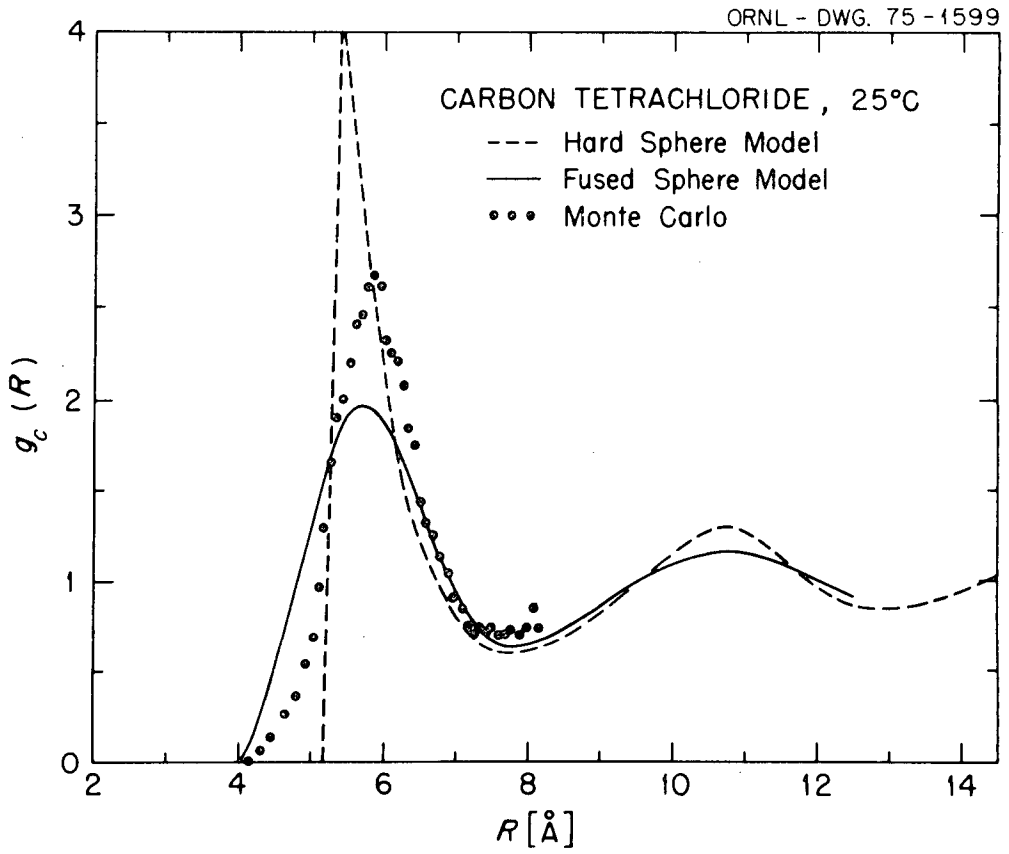


Fig. 13. Correlation functions for molecular centers in liquid CCl_4 computed from three different models. (Reproduced from Ref. 1.)

CONCLUSIONS AND OUTLOOK

The structural information accessible from diffraction data on liquid materials is limited in principle. Only for monatomic fluids the atom pair correlation function obtainable from experiment provides a complete structural description. For molecular fluids, the atom pair correlation functions do not provide a complete description of the orientational correlations, and a sizeable experimental effort is required for a precise determination of these quantities.

In practice, then, it will always be useful, and often necessary, to combine data from neutron and x-ray diffraction with results from theoretical models of liquid structure. The diffraction data serve as a sensitive test of potential energy models through statistical

mechanical theory and as a guide for the improvement of these models. Once a realistic force law has been established, the liquid material can be modelled, in complete microscopic detail, by the method of molecular dynamics. The data provided by such a computer experiment can then be used to calculate a variety of liquid properties. Unlike laboratory experiments, the computer simulations can easily be extended to very high temperatures and pressures.

We are confident that these methods will be recognized as powerful tools for the understanding and description of liquid materials in general. Important applications to energy transfer media (liquid metals) and catalytic fuel conversion systems (molten salts) are sure to follow.

REFERENCES

1. L. Blum and A. H. Narten, Adv. Chem. Phys., in press.
2. A. H. Narten and H. A. Levy, J. Chem. Phys. 55, 2263 (1971).
3. L. Van Hove, Phys. Rev. 95, 249 (1954).
4. G. Placzek, Phys. Rev. 86, 377 (1952).
5. L. Blum and A. H. Narten, J. Chem. Phys. 64, 2804 (1976).
6. A. H. Narten, J. Chem. Phys., in press.
7. A. H. Narten, J. Chem. Phys. 56, 5681 (1972).
8. J. G. Powles, Mol. Phys. 26, 1325 (1973).
9. A. H. Narten, J. Chem. Phys. 56, 1185 (1972).
10. P. W. Schmidt and C. W. Tompson, in Simple Dense Fluids, H. L. Frisch and Z. W. Salsburg, Eds., Academic Press, New York, 1968, p. 78.
11. D. I. Page and K. Mika, J. Phys C: Solid St. Phys. 4, 3034 (1971); F. G. Edwards, J. E. Enderby, R. A. Howe, and D. I. Page, ibid., 8, 3483 (1975).
12. L. J. Lowden and D. Chandler, J. Chem. Phys. 61, 5228 (1974).
13. A. H. Narten, L. Blum, and R. H. Fowler, J. Chem. Phys. 60, 3378 (1974).
14. L. A. De Graaf and B. Mozer, J. Chem. Phys. 55, 4967 (1971).
15. J. L. Yarnell, M. J. Katz, R. G. Wenzel, and S. H. Koenig, Phys. Rev. A7, 2130 (1973).

16. L. Verlet, Phys. Rev. 159, 98 (1967).

17. K. Suzuki and P. A. Egelstaff, Can. J. Phys. 52, 241 (1974).

DYNAMICS OF SIMPLE FLUIDS

P. A. Egelstaff
University of Guelph
Ontario, Canada

ABSTRACT

The history of inelastic neutron scattering by liquids will be outlined and the steps in the development of modern experimental techniques will be discussed: parallel improvements in data handling and analysis have taken place. While useful results have been obtained, many published experiments should be viewed as setting the stage for future sophisticated work.

The dynamics of a simple fluid may be discussed at a microscopic level through the Van Hove space-time correlation functions. While these functions are a rich source of information, it is difficult either to make neutron inelastic scattering measurements of the required accuracy or to develop theoretical models of the required depth. Precise measurements and appropriate theories are required to extract information of real interest. A number of basic rules have been exploited during the past decade or so, and the use of these to set the stage for an 'in-depth' investigation will be reviewed.

The relative significance of experiments on gases and liquids, and some possible future experiments, will be discussed.

HISTORICAL INTRODUCTION

Speculations concerning the movement of atoms and molecules in fluids have an established place in the history of science. In his book Kinetic Theory of Liquids, Frenkel[1] discusses many of these views. At the time his book was written there were almost no techniques for studying the motion of atoms and molecules by direct methods. After thirty years, Frenkel's book is still an excellent background text in this field and this illustrates how ideas about microscopic processes may be inferred by applying general theories to macroscopic data. Since then several techniques such as depolarized light scattering and nuclear magnetic resonance have provided information on molecular

motions. However, because of the large wavelengths or times used in these experiments, one has to infer individual molecular modes through the application of models. Then with the advent of inelastic neutron scattering, it became possible to study the motion of individual atoms and molecules on the relevant time and distance scales, namely times of approximately 10^{-12} seconds and distance of 1 - 2 A. The process of inelastic neutron scattering was discovered by Fermi[2] in 1934 in his celebrated experiments on thermal neutrons. The first experiments reporting energy changes on scattering were published in 1951[3], but all the early work was concerned with solids. Experiments on liquids were not carried out until the mid-fifties and in the past twenty years the field was developed rapidly in size, in precision and in theoreticl understanding.

The theory of fluids is a many body theory and as such is expressed in terms of many particle correlation functions. Specific configurations which make some contribution are easy to visualise in terms of physical arrangements of the atoms, but the statistical content of the same physical idea is difficult to present in a quantitative form. Perhaps for this reason it was many years before the general theory of fluids was expressed in terms of correlation functions. The pioneering work of Kirkwood[4] took place in the thirties and it is only now, some forty years later, that a fairly complete theory is available. At the time that inelastic scattering of neutrons became popular the elements of this theory were in place. The basic assumption was that the pair potential together with the pair correlation function, describing the relative positions of two atoms, would be sufficient to calculate many properties to a first approximation. A reasonable knowledge about pair potentials was obtained initially through an analysis of macroscopic data on gases and improved by studying other properties. In addition the technique of X-ray diffraction was used to obtain a general survey of pair correlation functions for many kinds of liquids. A number of theories of this function were developed too. Thus work on neutron scattering began from the point of view that these two basic pieces of information (the pair potential u(r) and the pair

correlation g(r)) were available, and that the job of inelastic scattering was to examine fluids from a deeper point of view.

The theory of neutron scattering by general systems was developed by a group working with George Placzek at Princeton during the late forties and early fifties. Placzek's[5] paper of 1952 contains most of the basic ideas, although the problem he addressed in this paper was not of long term interest. The paper of Wick[6] should be mentioned here also. The ideas of this group were brought together in the now famous paper of Van Hove[7]. In this paper Van Hove presented the theory of neutron scattering in terms of the basic correlation functions of interest in the general theory of fluids. By taking a broad point of view he was able to consolidate the knowledge of the previous twenty years and lay the foundation for the next twenty years. In expressing the neutron scattering data in terms of time dependent correlation functions Van Hove illuminated the field, but at the same time he presented the difficulties in a deceptively simple form. His greatest contribution was to steer people's thoughts in the right direction rather than to solve their problems. The work of Placzek's school, culminating in the paper of Van Hove, may be summarized in the series of equations given below.

The neutron cross section (per atom) for a system of atoms in thermal equilibrium is:

$$\frac{d^2\sigma}{d\Omega d\omega} = \frac{k}{k_o}\left[b_{coh}^2\, S(Q,\omega) + b_{incoh}^2\, S_s(Q,\omega)\right] \qquad (1)$$

where b_{coh} and b_{incoh} are the neutron-nucleus scattering lengths, and hQ and h are the momentum and energy transferred in the scattering process. The scattering law, S(Q,), is defined as:

$$S(Q,\omega) = \frac{1}{2\pi}\int e^{i(\underline{Q}.\underline{r} - \omega t)}\,[G(\underline{r},t) - \rho]\, d\underline{r}\, dt \qquad (2)$$

and the space time correlation function $G(\underline{r},t)$ as:

$$G(r,t) = \frac{1}{N} \left\langle \sum_{ij} \int dr' \; \delta\left[\underline{r} + \underline{r}_i(o) - \underline{r}\right] \delta\left[\underline{r}' - \underline{r}_j(o)\right] \right\rangle \quad (3)$$

The theoretical usefulness of the intermediate scattering function $I(Q,t)$ was clearly demonstrated in these papers, where:

$$I(Q,t) = \int e^{i\omega t} \, S(Q,\omega) d\omega \quad (4)$$

In the incoherent case we have:

$$S_s(Q,\omega) = \frac{1}{2\pi} \int e^{i(\underline{Q}.\underline{r} - \omega t)} \, G_s(\underline{r},t) d\underline{r} \, dt$$

and $G_s(\underline{r},t)$ is defined as the i=j term in $G(\underline{r},t)$. Throughout these equations $\underline{r}_i(t)$ is the position vector of the ith atom at time t.

The lowest frequency moment is given by:

$$\int \omega \, S(Q,\omega) d\omega = \int \omega \, S_s(Q,\omega) d\omega = \frac{\hbar Q^2}{2m} \quad (5)$$

and in the classical limit we find:

$$\int \omega^2 \, S(Q,\omega) d\omega = \int \omega^2 \, S_s(Q,\omega) d\omega = Q^2 \, \frac{kT}{M} \quad (6)$$

Placzek[5] derived expressions for quantum moments up to the fourth for both the self and coherent scattering laws. It was pointed out later that this determined the classical moments up to the eighth, since the coefficient of $(i\hbar t)^n$ gives the classical coefficient of t^{2n} in the time expansion of $I(Q,t)$.

The above equations are readily extended to mixtures and to molecular systems by adding up an appropriate combination of terms (eg. Vineyard[8]), and in this case each pair correlation function joins a given pair of atoms (like or unlike). However, in many cases it is worth introducing a model into the problem in order to simplify it.

Thus in the case of molecules it is frequently assumed that each molecule is a rigid body, and in this case there is a simple generalisation of Van Hove's formulae which has been given by Egelstaff et al.[9]. For such cases it is important to remember that the moment theorems need to be modified as was first pointed out by de Gennes[10].

In this paper we give a brief review of the theoretical ideas, then we discuss the development of experimental techniques for inelastic scattering and the kinds of techniques which should be developed in the future. Following this, we will review studies of atomic fluids and finally molecular fluids. These fields have grown extensively and cannot be covered properly in a short review; thus only selected references will be given.

EARLY THEORETICAL MODELS

To proceed from these general results to predictions requires a model. The papers by Vineyard[8] and de Gennes[10] introduced new models and summarised some older ideas. In this regard it is worth recalling the paper of Lamb[11] on the self-correlation function seen in neutron resonance absorption. Lamb's equation may be written as follows:

$$\sigma_a(\omega) = \int \sigma_{BW}(\omega')\ S_s(\omega - \omega')d\omega' \qquad (7)$$

where σ_a is the observed absorption cross section and σ_{BW} is the theoretical Breit-Wigner expression for this cross section. Thus Lamb's models are models of the self-correlation function of Van Hove. These three papers emphasised that at high momentum transfer the scattering was similar to that from a perfect gas and at intermediate values of Q the detailed dynamics could be observed, while at very low momentum transfer the self term was dominated by self-diffusion effects and the coherent term was dominated by collective effects. Vineyard in particular had a convenient physical picture of the transition between these regimes. The work of de Gennes however

quickly showed that Vineyard's picture, although physically appealing, was inadequate.

At this time the self correlation function was studied extensively. Vineyard suggested that it was almost a Gaussian function of r, and consequently it was only necessary to determine the mean square displacement as a function of time. Many models of this quantity followed, at short times they tended to $\frac{kTt^2}{M}$ and at long times to 2Dt (where D is the diffusion coefficient). A number of models of the diffusion process were used to predict the form of $S_s(Q,\omega)$ at low momentum transfer.

A little later a number of papers were published in which the equations for macroscopic motion were generalised to large values of the wave vector and frequency (e.g. Kadanoff and Martin[12] and Zwanzig[13]). These equations were intended to cover both the self and coherent terms of Van Hove and expressed the neutron scattering in terms of generalised transport coefficients (discussed below). While these ideas were physically appealing they merely changed one function into another of similar complexity. However, they have the advantage of allowing our knowledge about frequency moments to be incorporated naturally into the theory. From equations (1 - 6), some of the higher moments and one of these models it was possible to calculate the neutron inelastic scattering cross section with reasonable accuracy if the pair potential and the pair correlation function were known. The original information concerning these functions soon proved inadequate and neutron diffraction experiments began to be used to extend our knowledge about them. New theoretical methods and computer similation techniques were developed to derive a pair correlation function if given a pair potential. With these improvements the same basic assumptions have been continued through almost all subsequent work. It was realised that if the pair theory of fluids was valid the success of this approach would move attention to the sixth moment and to triplet correlation functions. However most authors preferred to neglect or roughly approximate these functions so that they could present a result in a convenient form, and this was

sufficient for comparison with the experiments which were available at that time.

The past ten years has seen an extensive development of these theoretical ideas and experiments based upon them and the review by Copley and Lovesey[14] gives a summary of the present state of affairs.

THE DEVELOPMENT OF EXPERIMENTAL TECHNIQUES

The earliest experiments on the inelastic scattering of neutrons involved the use of absorbers to measure energy changes (Egelstaff[3], Brockhouse and Hurst[15]) with such coarse resolution that only the main ideas could be checked. Subsequently these groups began to develop spectrometers for inelastic scattering measurements. These instruments involved the two basic techniques of Bragg reflection and of time-of-flight analysis. The triple axis spectrometer using Bragg reflection to analyse both incident and scattered neutrons was developed at Chalk River[16], while the multi-angle time-of-flight technique was developed at Harwell[17]. In addition various combinations of the two methods have been used such as the rotating crystal[16] and the crystal-chopper approaches. At the same time as these developments were taking place the filter/chopper technique was in use at Brookhaven. Although this technique was quite useful in the period of low neutron fluxes, because of its limited scope it is no longer used.

In the early experiments using absorbers[15,18], a range of corrections was applied. These corrections included multiple scattering, sample absorption and resolution. However, when the new spectrometers were constructed and detailed spectra became available, these techniques were temporarily set aside by many experimentalists, because of the difficulty in extending the older methods to cases involving several more variables.† Later the full range of corrections was reapplied in most inelastic scattering experiments (Copley and Lovesey[13]).

The experimental objectives have oscillated between two views. On the one hand attempts have been made to measure a very large part

of the complete function $S(Q,\omega)$, while on the other hand attempts have been made to define a significant region of $S(Q,\omega)$ and to measure that only. Both ideas have their merit and are still employed. Experimental data are taken in the form of intensities as a function of time-of-flight or of angular settings. Theoretical models have been converted to this form (resolution and multiple scattering effects added) and compared directly to these data. In contrast data are also converted to $S(Q,\omega)$ or to some intermediate stage and then compared to models. Different authors have pressed the advantages of these differing methods; the present reviewer believes that they are not significantly different as vehicles for the comparison of experiment and theory. For example, the differences between old and new results due to improved spectrometers and improved versions of theoretical models are greater than that due to the form of presentation.

It is frequently useful for experimentalists to compare models and data in an experimental space. An example of this kind is time-of-flight data, where a theoretical model for the correlation function is often broadened with the experimental resolution before comparing to the data. An example of this type will given later. Nevertheless it would be useful if all data were converted to $S(Q,\omega)$ whether the results are in the form of constant angle, constant ω or constant Q.

For theoretical reasons it is important to obtain both precise and absolute measurements of the Van Hove scattering function. For this purpose, very stable equipment capable of measuring broad energy spectra is required. Experiments have been performed with each of the techniques listed above. Many experimentalists have believed that the multi-angle time-of-flight technique can offer high efficiency, stability and reliable absolute and relative scattering cross-sections. However data handling was difficult until on-line computers were available (Hall and Egelstaff[9]). Modern equipment of this kind includes for example, the IN4 spectrometer at Grenoble, the correlation chopper at Oak Ridge and the time-of-flight spectrometer at the Argonne National

Laboratory. Three axes spectrometers at Chalk River, Risø and Julich have been used successfully for work on liquids, and offer the advantage of built in techniques for measuring spectra at constant momentum transfer. This is useful as it is one of the conventional forms for comparison with theoretical models. The range of Q which can be covered by these instruments is approximately 0.05 to $20A^{-1}$ and the ω resolution is sufficient to resolve fluid spectra.

In the future we are likely to see special instruments developed for particular regions. For example, the low momentum transfer region where the neutron scattering can be described by hydrodynamic models requires special attention. Enough work has been done with some of the above spectrometers to illustrate this need. Also techniques to improve stability are needed, because some important (theoretically expected) effects are of the order of a few % of $S(Q,\omega)$ and stability in the ¼% range for a period of several weeks is needed in order to study them properly. Finally, the very high momentum transfer region has been examined in a number of experiments, including experiments using accelerator pulsed neutron sources. Techniques are difficult here due to the low fluxes available, but a variety of interesting effects have been discovered during the approach to free particle behaviour. New methods (and the revision of nuclear physics techniques) will be needed to study both atomic and molecular liquids in this region.

---

† At this time substantial resources were devoted to studying reactor moderators and both experimental and theoretical techniques were advanced, (see Egelstaff and Poole "Experimental Neutron Thermalization", Pergamon Press 1969). It was some years before these advances, especially the experimental ones, were incorporated into the general liquid state field.

THEORETICAL MODELS AND EXPERIMENTAL DATA ON ATOMIC SYSTEMS

Theoretical models of atomic fluids have been based frequently on the following pattern. The overall shape of $S(Q,\omega)$ - i.e. its functional form - has been taken from a physical model. For example the Langevin equation or the hydrodynamic equations have been used for the self and coherent correlation functions respectively. Then the coefficients appearing in these equations have been modified to give the correct short time behaviour, that is to give the lowest few frequency moments of $S(Q,\omega)$ correctly. To improve a theory more mements may be included or the theoretical basis for the functional form may be improved.

(a) The Self Term

In the case of the self-term, the effect being studied is a generalised diffusion of the atoms: at very low momentum transfer the diffusion coefficient is the only parameter of importance, while at very high momentum transfer the atoms behave as though they were in a perfect gas. In between the collision effects are of varying importance. Brockhouse[16] developed and used empirical models incorporating these effects.

Vineyard[8] suggested that the self-correlation function for fluids is approximately Gaussian in r since some ideal models have this property. In this case we have:

$$S_s(Q,\omega) \simeq \frac{1}{2\pi} \int \exp - \left\{\frac{Q^2 W(t)}{2}\right\} . \, e^{i\omega t} \, dt \qquad (8)$$

and

$$W(t) = \left\langle [\underline{r}(t) - \underline{r}(o)]_Q^2 \right\rangle$$

A model for W(t) based on the idea of Brownian motion, but modified to give the correct analytical properties, was suggested by Egelstaff and Schofield[20],

$$W(t) \simeq DQ^2 \left[(t^2 + c^2)^{\frac{1}{2}} - c \right] \tag{9}$$

where D is the diffusion constant and c is a relaxation time. The derivative $\partial^2 W/\partial t^2$ is the velocity autocorrelation function, so that this function is determined by two parameters. If the second and fourth moments of $S_s(Q,\omega)$ are to be satisfied then c and D have the values:

$$D = c \frac{kT}{M} \; ; \; c = \left[\frac{3m}{\langle \nabla^2 U \rangle} \right]^{\frac{1}{2}} \tag{10}$$

where $\langle \nabla^2 U \rangle$ is the thermally averaged Laplacian of the potential energy (U) with respect to the position of one atom. It can be measured through the isotopic separation effect in argon, and even for the liquid the numberical value of D is nearly correct (e.g. Egelstaff[21]).

Nelkin and Ghatak[2] have developed a binary collision model for $G_s(r,t)$, using a linearised Boltzmann equation to describe the collision dynamics. In this case the expression for $S_s(Q,\omega)$ includes small non-Gaussian terms outside the approximation (8). But if their diffusion coefficient is determined by the fourth moment of S_s a result essentially the same as (10) is obtained, and the calculated scattering law has nearly the same magnitude and shape as that calculated from (8) and (9). Thus both a "first principles" approach and an "ad hoc" approach are forced to be nearly the same through fitting the above theoretical pattern.

Ruijgrok[23] and Kadanoff and Martin[12] developed expressions for $S_s(Q,\omega)$ from ideas concerning the propagation of disturbances through the system. This idea has been used by many authors and we quote the example of Lovesey[25] who based his approximation on the continued fraction representation of a generalised Langevin equation. His result is (in terms of c at equation 10):

$$S_s(Q,\omega) = \frac{1}{\pi} \frac{\tau S_2(2S_2 + c^{-2})}{[\omega\tau(\omega^2 - 3S_2 - c^{-2}]^2 + (\omega^2 - S_2)^2} \qquad (11)$$

and $\tau^{-1} = (2S_2 + c^{-2})^{\frac{1}{2}}$ and S_2 is the second moment of $S_s(Q,\omega)$. This expression satisfies the lowest two classical moments and contains information from the next moment. Lovesey shows that it gives results essentially the same as those obtained by the former method.

By adjusting the parameter c in equation (9) or (11) it has been possible to fit data on an inert system (i.e. argon[24]) and a liquid metal (i.e. sodium[25]). The data may be fited over extensive ranges of momentum and energy transfer, the fit being satisfactory for both the shape of the curve and the absolute intensity. These data are shown in Fig. 1 and 2. The significance of the parameter is related to the momentum transfer range studied. For example, Cocking[25] has fitted the self-correlation function for sodium to the model of Egelstaff and Schofield[20] to obtain the step time, c, in the diffusion process. Lovesey[24] has fitted the self-correlation data on liquid argon obtained by Sköld et al.[26], and relates c to the mean square force seen by an atom in the liquid.

The goodness of fit may be better than the approximations used so that it has become necessary to tighten up the way in which the model is employed. The parameter, c, should be given by equation (10) using a measured value of $\langle\nabla^2 U\rangle$. This will display the real differences between the model and the data. It is important that if a theoretical value of $\langle\nabla^2 U\rangle$ is used it should reflect the real situation, thus for argon the correct pair potential and the three body terms should be used in the calculation rather than the customary practice using only the L-J potential.

In terms of the theoretical pattern described at the beginning of this section, it is necessary to consider the relationship between ΔS (the difference between rigorous model and data) and the higher frequency moments. To do this properly involves some knowledge of

3-body forces and 3-body correlation functions which, unfortunately, is not available yet. An experimental method by means of which these terms can be displayed is to measure the pressure derivative of $S_s(Q,\omega)$. This possibility has been discussed by Egelstaff et al.[27] and Chen et al.[28]. One way to see the implications of this method is to take the pressure derivative of equation (8), when the leading term becomes proportional to $\langle\nabla^2 U\rangle$. Consequently the magnitude of this quantity is related to the unknown parameters, in contrast to $S_s(Q,\omega)$ itself.

(b) The Coherent Term

Theoretical and experimental work on the coherent correlation function has been fairly extensive. Vineyard[8] attempted to relate its behaviour to the self correlation function, but his model did not satisfy the second frequency moment. De Gennes[10] pointed out that the frequency width of the coherent correlation function should vary with momentum transfer in a way that was proportional to the inverse of the structure factor. This effect was observed by Brockhouse and Pope[29] in the case of lead and has been found later in many other experiments. This paper is the most notable experimental one of the period. It describes the first attempt to study G(r,t) over an extensive range, including a number of experimental corrections.

A variety of other models have been suggested. Some of these, such as that due to Kerr[30] have related the self and total correlation functions in the manner of Vineyard, while others have looked for formal expressions, e.g. Zwanzig[31] or Kadanoff and Martin[12] or Boley[32]. In the former case the agreement with experiment has not been satisfactory while in the latter case agreement with experiment is obtained only if some arbitrary parameters are included in the theory and adjusted to fit the data.

The choice of function, to use as a vehicle to compare theory with experiment, is an open matter. In addition to the coherent correlation function it has been suggested that a current-current or a force-force correlation function be used. If the system is stationary

these are derived from Van Hove's function by multiplying by factors ω^2 or ω^4 respectively, while other functions of theoretical interest may be obtained by multiplying either by ω or $1/\omega$. Some authors have argued that a particular feature in one function is evidence for a particular result. For example in the study of phonons in solids the phonon appears as a δ-function in Fourier frequency space, and so would appear as a δ-function in each of the above five quantities. It is the appearance of the δ-function which identifies the phonon rather than the choice of representation. The experimental data on fluids consists of continuous curves and to attach physical significance to them requires some theoretical assumption: thus if the fitted model is based on collective modes the result is expressed in these terms, or if the fitted model is based on kinetic effects the result is expressed in those terms.

Several theoretical approximations give rise to the same kind of analytical expression for $S(Q,\omega)$. These include hydrodynamic, visco-elastic, memory function and continued fraction methods among others. This common expression, sometimes called the "three pole formula", reduces to three lines when the damping is small. It is:

$$S(Q,\omega) = \frac{1}{\pi} \frac{kT.M^{-1}\, Q^4\, R\{\Gamma(Q,\omega)\}}{\left|Q^2 kT(MS(Q))^{-1} - i\omega Q^2 \Gamma(Q,\omega) - \omega^2\right|^2} \tag{12}$$

where $\Gamma(Q,\omega)$ is a complex damping function, and its real part in the $Q \to o$ limit, is the Fourier transform of the stress-stress correlation function. Equation (12) satisfies the zero and second moments of $S(Q,\omega)$ for any choice of Γ. If we denote the nth frequency moment of $S(Q,\omega)$ by S_n, then Γ also has the properties:

$$\left.\begin{aligned} \frac{Q^2}{\pi} \int_{-\infty}^{+\infty} \Gamma(Q,\omega)\, d\omega &= \frac{S_4}{S_2} - \frac{S_2}{S_o} = \Gamma_o \\ \frac{Q^2}{\pi} \int_{-\infty}^{+\infty} \omega^2\, \Gamma(Q,\omega)\, d\omega &= \frac{S_6}{S_2} - \left[\frac{S_4}{S_2}\right]^2 = \Gamma_2 \end{aligned}\right\} \tag{13}$$

We shall consider a model in which Γ is forced to satisfy these moments, but not all theoreis are required to do this within the framework of equation (12). If the self term is determined by moments of S up to the fourth (e.g. equation 10), then an equivalent approximation for the coherent term is to use moments up to the sixth. For example, in the $Q \to o$ limit, these approximations are equivalent to a representation of the velocity or stress autocorrelation functions respectively by two moments only.

Egelstaff[21] has suggested the following approximation for Γ:

$$\left.\begin{aligned} \text{let} \quad \frac{\Gamma(Q,\omega)}{\frac{1}{\pi}\int_{-\infty}^{+\infty}\Gamma(Q,\omega)d\omega} &= \int_0^\infty e^{i\omega t}\, M(Q,t)dt \\ \text{and assume:} \quad M(Q,t) &\simeq \exp - \left\{\left(t^2/\tau^2(Q) + 1\right)^{\frac{1}{2}} - 1\right\} \end{aligned}\right\} \tag{14}$$

Thus from (13) we find:

$$\tau(Q) = \left(\Gamma_2/\Gamma_o\right)^{-\frac{1}{2}} \tag{15}$$

So that $S(Q,\omega)$ is completely specified by the model and three moments.

If equations (12) - (15) are to be used properly it is necessary to know both the pair and higher order potentials and the pair and higher correlations function. Unfortunately only the pair functions are known adequately. A common procedure is to approximate all unknowns in terms of pair functions, and then to use an effective pair potential in place of the real one. The errors so introduced are not yet understood properly.

The first experiment to be interpreted through equation (12) was that of Cocking and Egelstaff[33] on lead. They did not know the values of Γ_o and Γ_2 and so used empirical forms for Γ. In this way they were

able to show that the expression (12) was better than other models proposed at that time, and that $\Gamma(Q,\omega)$ behaved similarly to $1/S(Q)$ as suggested by (13). Figure 3 presents one of their curves compared to equation (12), and also to a model with no adjustable parameters but which satisfies the zero and second moment. The difference between this model and the data represents the quantity which Cocking and Egelstaff were fitting by their models of $\Gamma(Q,\omega)$. Their best model did not fit the data properly. Other and better models have been developed since then. A comparison - given in figure 4 - between one of their figures and an analogous figure from Copley and Lovesey[13], who fitted the data of Copley and Rowe[34] on liquid rubidium, illustrates this improvement. Although the first curve is cross-section v.s. time-of-flight and the second $S(Q,\omega)$ v.s. ω there is no ambiguity in interpretation. If Q_o is the position of the principal maximum in $S(Q)$, Cocking and Egelstaff[33] claimed to see peaks in $S(Q,\omega)$ up to $0.8\ Q_o$, and this has been correctly criticised as an overstatement (Copley and Lovesey[13]). When converted to $S(Q,\omega)$ their data showed a weak maximum at $0.6\ Q_o$ ($Q \simeq 1.3A^{-1}$), at a point similar to the limit of $0.7\ Q_o$ ($Q \simeq 1A^{-1}$) observed by Copley and Rowe[34] for liquid rubidium.

The careful data of Sköld *et al.*[26] on argon have been fitted with equation (12) using information on the second and fourth moments. Furtado *et al.*[35] have fitted the same data with a kinetic model based on hard sphere dynamics. The two methods are equally successful-fig. 5.

Lovesey[25] makes an approximation for $\tau(Q)$ which is equivalent to writing $\Gamma_2 \simeq \Gamma_o^2$ in (15). Other approximations have been suggested by Akcasu and Daniels[35] and by Machida and Murase[37]. Rowe and Sköld analyse their experimental data on argon using an exponential form for $M(Q,t)$ i.e. $t \gg \tau$. In this case an experimental $\tau(Q)$ is obtained which is compared to the various theoretical values in Fig. 6. All theories give the correct order of magnitude, but differ in detail. Other experiments, notably the extensive work on neon[39,40] have been interpreted in an analogous way. We prefer to wait for a proper evaluation of (15) (using realistic potentials and triplet functions) before commenting on whether these differences are due to the rough

approximations made for S_4 and S_6 or due to the structure of the theory.

Again it may be useful to measure quantities, such as the pressure derivative[27] of $S(Q,\omega)$ which may throw light on uncertain features of present theories. Groome et al.[41] have discussed this area.

MOLECULAR FLUIDS

Some of the earliest neutron inelastic scattering experiments involved molecular fluids. Many of these contained hydrogen; since hydrogen is a strong scatterer and the scattering is largely incoherent these experiments were felt to be fairly simple to interpret. However, the data were largely uninterpretable because of the inherent complexity of the problems being studied and because of the natural limitations of the early data. After this phase, experimentalists tended to study small molecules, such as homonuclear diatomic molecules, or simple tetrahedylmolecules (e.g. methane). This work has been carried out both on gases and on liquids. By making the assumption that the molecules are rigid we can obtain the following formulae[9]; the scattering law is inserted into (1) to obtain the cross-section per molecule if the b's in (1) are interpreted as molecular scattering lengths.

$$S(Q,\omega) = \frac{1}{2\pi} \int e^{i(\underline{Q}.\underline{r} - \omega t)} \, d\underline{r}dt \left\langle G(\underline{r},\Omega_1,\Omega_2,t) \; F(\underline{Q},\Omega_1) \; F(\underline{Q},\Omega_2) \right\rangle_{\Omega_1\Omega_2} \quad (16)$$

where $F(\underline{Q},\Omega_i) = \frac{1}{\sum_\alpha b_\alpha} \sum b_\alpha \exp(i\underline{Q}.\underline{r}_{ci\alpha})$, $\underline{r}$ is the position vector joining the centres of molecules 1 and 2, and $\underline{r}_{ci\alpha}$ is the position vector for the αth nucleus in the ith molecule relative to the molecular centre, and Ω_i is the angular orientation of this molecule, The correlation function G is now a function of position, time and the angular orientations Ω_1,Ω_2 of two molecules. The self term correlates the positions and orientations of one molecule at two different times. A common approximation is to assume that the

positions and orientations are uncorrelated (sometimes called the free rotation approximation) when the angular averaging in (16) can be simplified e.g. Sears[42]. In dense systems this approximation is not valid and specific models are required.

Another case has been studied by Hudson et al.[43], namely the relationship between molecular potential functions and the spectrum of incoherently scattered neutrons. The internal modes of the molecule can give rise to spectral features which may be observed in fluids as well as solids. This question will not be discussed here.

Because the study of molecules is a much more complicated topic than the study of atomic systems it seems desirable to explore the gas phase before the liquid since the theoretical interpretation is more straightforward. In addition, gas phase studies can provide information about intermolecular forces. This is important because our knowledge of the anisotropic part of molecular forces is not yet complete.

Methane has been studied in both liquid and gas phases[44,45]. In both cases it rotates fairly freely so that the scattered distribution may be analysed in the free rotation approximation. Figure 7 shows a comparison between the theory and experiment from the work of Randolph et al.[44] The translational broadening of the spectra is such that the individual quantum peaks cannot be observed and only a broad classical type distribution is seen. The theory gives a reasonable fit to the data without adjustable parameters being required.

Postal and Chen[46] have studied hydrogen gas and an example of their work is given at Fig. 8. In this case, they compared their data with a generalised Enskog theory. The collision dynamics was shown to follow the predictions of previous molecular dynamics studies of Alder et al.[47]. Further experiments of this kind are likely to provide very detailed information on this topic. The above examples are illustrations of incoherent scattering by gases and we now turn to examples of coherent scattering. Hawkins and Egelstaff[48] studied the pressure dependence of the spectra from nitrogen gas. They assumed that the molecules rotated freely in the gas and compared the

results to theories of the three-body correlation function for atomic systems. An example of their results is given at Fig. 9, from which it can be seen that their predictions are approximately correct, but that improved models of the triplet function are required.

Carneiro and McTague[49] have studied the scattering law for liquid nitrogen near its triple point. Weiss and Levesque[50] compare these data to the predictions of their molecular dynamics study using a site-site model of the nitrogen potential. Figure 10 shows this comparison. They concluded that at liquid densities the dynamics of nitrogen molecules is similar to that for hard spheres. However since the structure of liquid nitrogen is not sensitive to the intermolecular potential[51], it is possible that only the finer details of the dynamics will prove to be sensitive to the potential used in the calculations.

DISCUSSION

It is useful to consider the question, 'what has inelastic neutron scattering achieved over the past twenty years?' When a new method is discovered, which is capable of giving a wealth of detailed information if the experimental techniques were perfected, then a long period of development must follow. The field of fluids has been developing at the same time, and therefore the new area must keep up with the rest of the field as well as develop within its own boundaries. Contrasting developments will occur which will stimulate new theoretical ideas and lead to experimental improvements.

One of the most noticeable developments has been the improvement in the range and power of numerical experiments carried out on computers. The field of molecular dynamics allows predictions to be made for the inelastic neutron scattering cross-section on the basis of given interaction potentials, and in addition allows theoretical models to be tested without recourse to real experiments. Better theories then become available to interpret data, so that the results of an inelastic neutron scattering experiment can be predicted to a fair accuracy.

The neutron experiments have acted in some ways as a catalyst. While the theorists have been trying to find better ways of describing many-body correlation functions, several techniques have provided better input data for such theories and the neutron field has provided better data on the Van Hove correlation function to test them. This combined effort has led to movement on a broad front so giving a much better over-all understanding of the field. Thus the principal thing neutron inelastic scattering has done in the past twenty years is to contribute towards this broad forward movement.

It may be argued that all previous work has been devoted to including the trivial data about fluids in the theory, and to improving the experimental data to the point where the difference between such a theory and an experiment can be detected. At this stage we can begin to approach the heart of the problem. The best neutron techniques must be used over wide regions of the liquid and gas phases, and the results compared to the predictions of theoretical models using realistic intermolecular forces and three-body correlation functions. It is likely that the gas phase data will prove quite important in this respect since the density may be varied over a significant range. In contrast at liquid densities, close to the triple point, the hard core interaction is sufficiently important that only one part of the problem can be illuminated.

It is probable that this technique has developed to the stage where it could spearhead future developments. A number of good neutron spectrometers are now available: spectrometers which are capable of achieving results which were once thought impossible. In addition experimentalists know how to collect the careful and accurate data needed for this purpose. It has been emphasised in this paper that our general knowledge, especially concerning frequency moments, allows good predictions of $S(Q,\omega)$ to be made. Measurements need to be substantially better than these predictions, and to cover broad regions of phase space extending from the gas to the liquid regions. Thus more accurate data must be obtained more quickly and analysed more readily than in the past. This will put great demands on the

experimentalists and theorists alike but may lead to a proper understanding of many-body systems.

REFERENCES

1. Frenkel, J. "Kinetic Theory of Liquids", U.S.S.R. (1943), O.U.P. (1946).
2. Fermi, E. et al. Ric. Sci. 5, 380, (1934).
3. Egelstaff, P. A. Nature 168, 290, (1951).
4. Kirkwood, J. G. J. Chem. Phys. 3, 300, (1935).
5. Placzek, G. Phys. Rev. 86, 377, (1952).
6. Wick, G. C. Phys. Rev. 94, 1228 (1954).
7. Van Hove, L. Phys. Rev. 95, 249 (1954).
8. Vineyard, G. H. Phys. Rev. 110, 999, (1958).
9. Egelstaff, P. A., Gray, C. G., Gubbins, K. E. and Mo, K. C. J. Stat. Physics 13, 315 (1975).
10. de Gennes, P. G. Physica 25, 825 (1959).
11. Lamb, W. E. Phys. Rev. 55, 190 (1939).
12. Kadanoff, L. D. and Martin, P. C. Ann. Phys., N. Y., 24, 419 (1963).
13. Zwanzig, R. Phys. Rev. 133, A50 (1964).
14. Copley, J. R. D. and Lovesey, S. W. Rep. Prog. Phys. 38, 461 (1975).
15. Brockhouse, B. N. and Hurst, D. G. Phys. Rev. 88, 542 (1952).
16. Brockhouse, B. N. In "Inelastic Scattering of Neutrons in Solids and Liquids" p. 113, I.A.E.A. (Vienna) (1960), and Suppl. Nuovo Cimento 9, 45 (1958).
17. Egelstaff, P. A., Cocking, S. J. and Alexander, T. K. In "Inelastic Scattering of Neutrons in Solids and Liquids" p. 165, I.A.E.A. (Vienna) (1960).
18. Egelstaff, P. A. and London, H. Proc. Roy. Soc. 242, 374 (1957).
19. Hall, J. W. and Egelstaff, P. A. Nucl. Inst. Meth. 92, 51 (1971).
20. Egelstaff, P. A. and Schofield, P. Nucl. Sci. Engng. 12, 260 (1962).
21. Egelstaff, P. A. Ann. Rev. Phys. Chem. 24, 159 (1973).
22. Nelkin, M. S. and Ghatak, A. Phys. Rev. 135, A4 (1964).
23. Ruijgrok, Th. W. Physica 29, 617 (1963).
24. Lovesey, S. W. J. Phys. C. Solid St. Phys. 6, 1856 (1973).
25. Cocking, S. J. Adv. Phys. 16, 189 (1967).

26. Sköld, K. et al. Phys. Rev. A6, 1107 (1972).
27. Egelstaff, P. A., Gray, C. G. and Gubbins, E. E. Phys. Letts. 37A, 321 (1971).
28. Chen, S. H. et al. In "Molecular Motions in Liquids" - Reidel Pub. Co. Ed. J. Lascombe, 507 (1974).
29. Brockhouse, B. N. and Pope, N. K. Phys. Rev. Lett. 3,259 (1959).
30. Kerr, W. C. Phys. Rev. 174, 316 (1968).
31. Zwanzig, R. In "Lectures in Theoretical Physics, Boulder Vol. III." Ed. Britton, Downs and Downs, (N. Y. Interscience) (1961).
32. Boley, C. D. Phys. Rev. A. 11, 328 (1975).
33. Cocking, S. J. and Egelstaff, P. A. Phys. Letts. 16, 130 (1965) and J. Phys. C. Solid. St. Phys. 1, 507 (1968).
34. Copley, J. R. D. and Rowe, J. M. Phys. Rev. A9, 1656 (1974).
35. Furtado, P. Mazenko, G. F. and Yip, S. Phys. Rev. 12, 1653 (1976).
36. Akcasu, A. Z. and Daniels, E. Phys. Rev. A2, 962 (1970).
37. Machida, M. and Murase, C. Prog. Theor. Phys. 50, 1 (1973).
38. Rowe, J. M. and Sköld, K. In "Neutron Inelastic Scattering", 413, I.A.E.A. (Vienna) (1972).
39. Buyers, W. J. L. et. al. Phys. Rev. A 11, 697 (1975).
40. Bell, H. et al. Phys. Rev. A. 11, 316 (1975).
41. Groome, L., Gubbins, K. E. and Dufty, J. Phys. Rev. A13, 437 (1976).
42. Sears, V. F. Can. J. Phys. 44, 1279 (1966).
43. Hudson, B. Warshal, A. and Gordon, R. G. J. Chem. Phys. 61, 2929 (1974).
44. Randolph, P. D. et al. Phys. Rev. 124, 460 (1961).
45. Harker, Y. D. and Brugger, R. M. J. Chem. Phys. 42, 275 (1965).
46. Postol, T. A. and Chen, S. H. Phys. Rev. Letts.
47. Alder, B. J. Gass, D. M. and Wainwright, T. E. J. Chem Phys. 53, 3813 (1970).
48. Hawkins, R. K. and Egelstaff, P. A. Mol. Phys. 29, 1639 (1975).
49. Carneiro, K. and McTague, J. P. Phys. Rev. A11, 1744, (1975).
50. Weiss, J. J. and Levesque, D. Phys. Rev. A13, 450 (1976).
51. Egelstaff, P. A. Physikalische Blatter 12, 635 (1975).

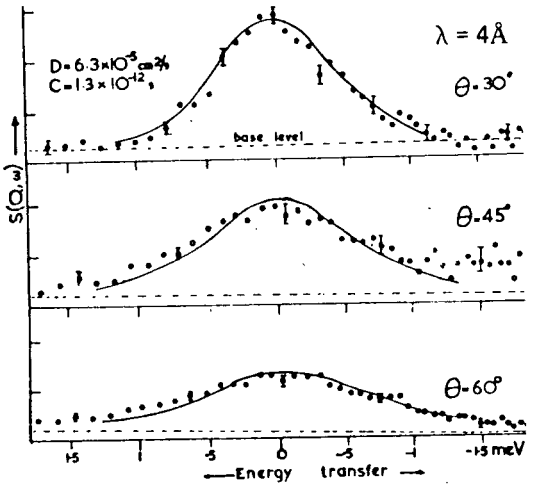


Fig. 1. Liquid Sodium[25], full line equations (8) and (9).

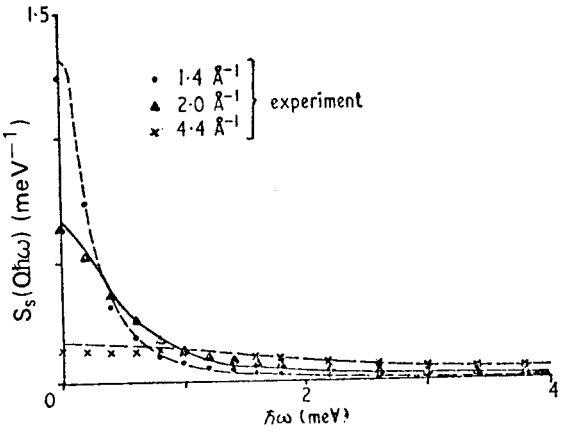


Fig. 2. Liquid Argon[24], full line equation (11).

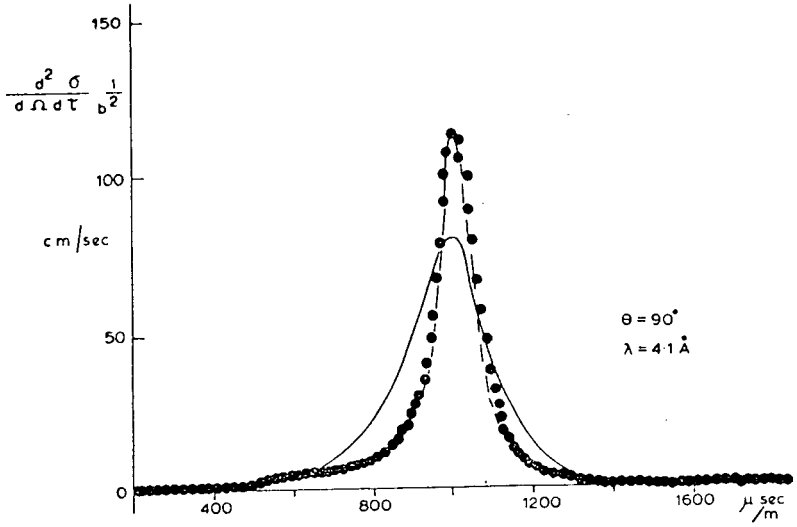


Fig. 3. Liquid Lead[33], full line is gas formula with mass weighted by $S(\alpha)$, dashed line equation (12) with $\Gamma_0 = 6S_2/S_0$; $2\tau^{-1} = (S_2/S_0)^{1/2}$.

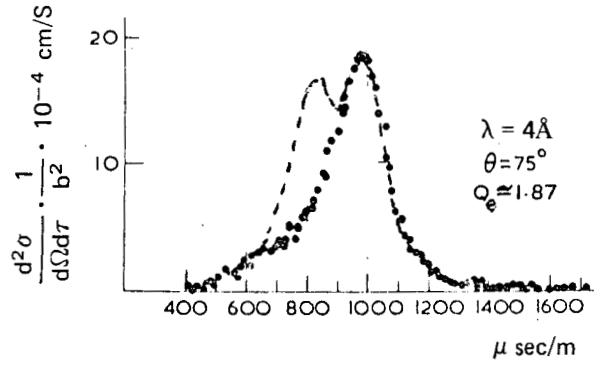


Fig. 4(a). Liquid Lead[33], dashed line as for figure 3. Ratio of Q/Q_0 is same as for 4b.

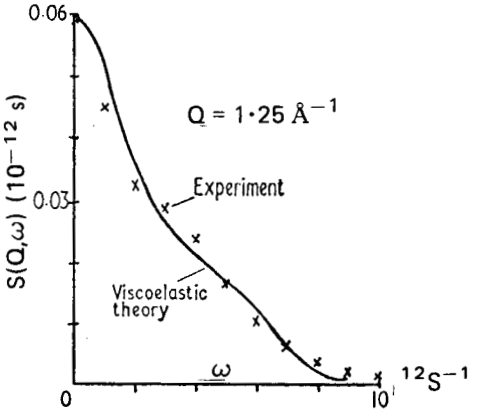


Fig. 4(b). Liquid Rubidium[13,34], full line equation (12), with $\Gamma_2 = \Gamma_0^2$.

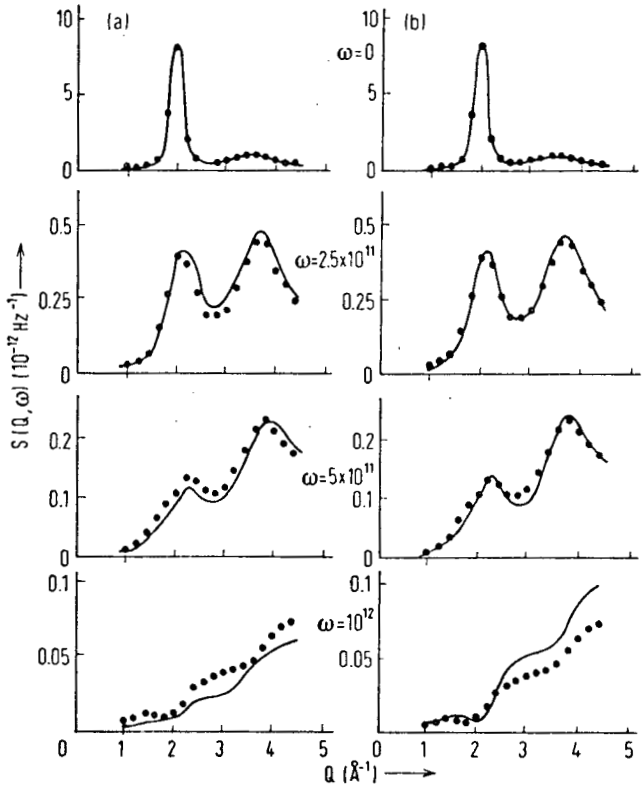


Fig. 5 Liquid Argon[26], (a) fitted to equation 12 or (b) to kinetic theory[35]. τ(Q) of figure 6 corresponds to (a).

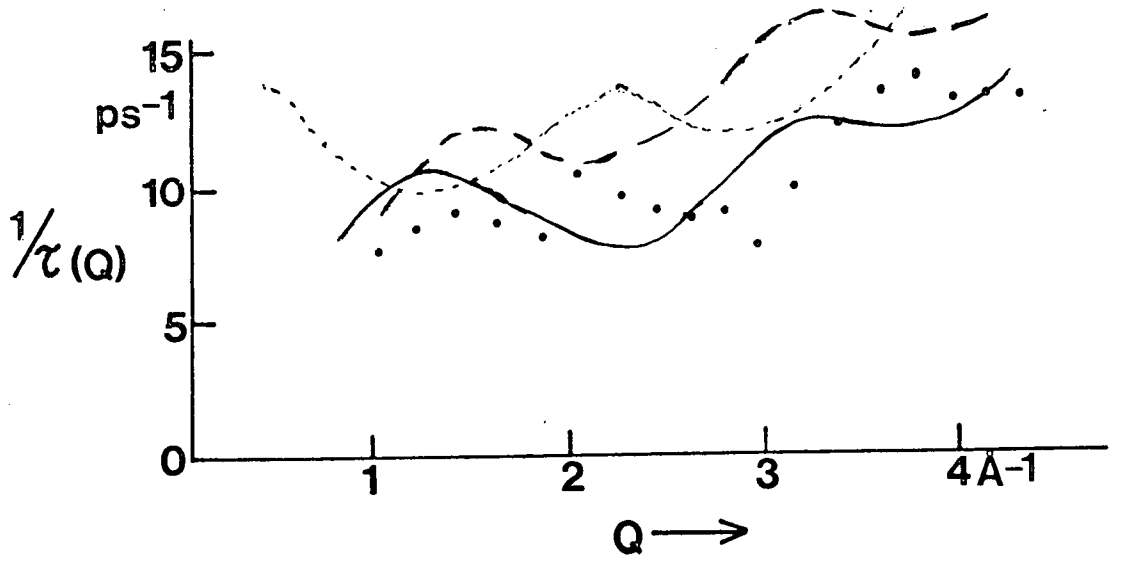


Fig. 6. τ(Q) for argon - points compared with theoretical curves. Refs. 25 - full line, 35 - dashed line and 37 (for the L-J fluid) - dotted line.

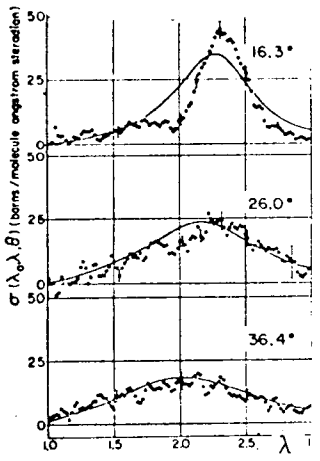


Fig. 7. Differential cross section of methane gas[44] at 21°C and 100 p.s.i. Full line is free rotation theory.

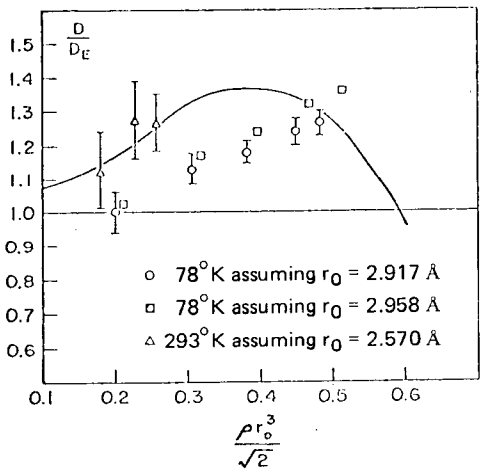


Fig. 8. Ratio of diffusion constant for hydrogen molecules[46] to Enskog value, as a function of density.

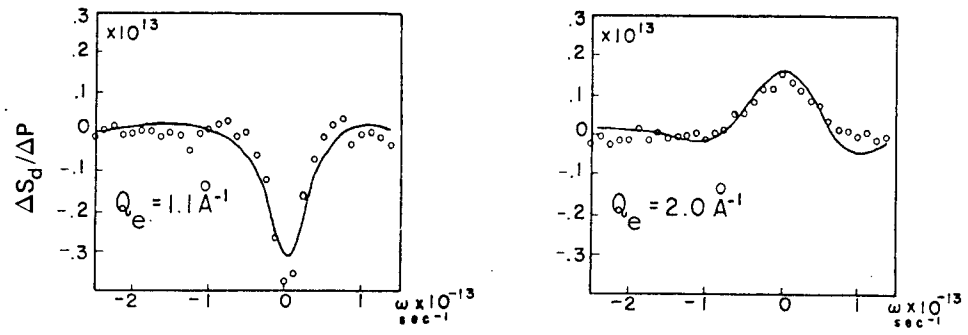


Fig. 9. Isothermal pressure derivative of S_d for nitrogen gas at 22°C and 3,500 p.s.i.[48] Full line is based on a model for the time dependent-3-body correlation function.

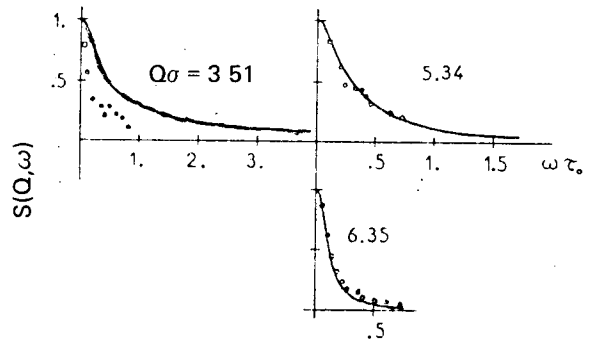


Fig. 10. Experimental scattering law for liquid nitrogen[49] - points, compared to molecular dynamics results[50] - full line. The discrepancy of $Q\sigma = 3.51$ may be due to an error in substracting incoherent scattering.

CONF-760601--10

NEUTRON SCATTERING FROM QUANTUM LIQUIDS

R. A. Cowley*
Brookhaven National Laboratory†
Upton, New York 11973

ABSTRACT

Recent neutron scattering measurements on the quantum liquids ^{4}He and ^{3}He are described. In the Bose superfluid there is a well-defined excitation for wave vectors less than 3.6 $\AA^{-1}$. In the Fermi liquid measurements are much more difficult because of the large absorption cross section, but measurements at the Institute Laue-Langevin have shown that there are no well-defined excitations at 0.63 K for wave vectors between 1.0 and 2.6 $\AA^{-1}$. The difference between these results is due to the existence of particle-hole excitations in the Fermi liquid into which collective excitations can decay. Because of the simplicity of the excitations in ^{4}He, it has become a testing ground for the effects of the interactions between the excitations. Measurements are described which show that while roton-roton interactions are attractive at small wave vectors they are repulsive at larger wave vectors. The scattering at large momentum transfer in ^{4}He has been measured, but its interpretation is still open to question.

INTRODUCTION

Ever since the start of neutron scattering experiments, quantum liquids have been chosen for study so that now at least nine laboratories have engaged in this work. There are two quantum liquids which can be studied with neutron scattering: the Bose liquid, ^{4}He, and the Fermi liquid, ^{3}He. Since the theory of Fermi and Bose liquids plays such an important role throughout theoretical physics, the hope of testing these

---

* Permanent address: Department of Physics, University of Edinburgh, Scotland.

† Work performed under the auspices of the U. S. Energy Research and Development Administration.

theories with experimental results provides the stimulus for all this effort.

The Bose liquid, ^{4}He, becomes superfluid below 2.1 K and has excellent neutron scattering properties, and so has received by far the largest amount of attention. The results obtained in this liquid confirm the existence at low temperatures of well-defined excitations as originally suggested by Landau. They have been reviewed in detail[1] and are described in outline in the next section.

The Fermi liquid, ^{3}He, becomes superfluid only below 2 mK and has a large neutron absorption cross section (1.2×10^4 barns for neutrons with a wavelength of 4 Å). This large absorption cross section discouraged many of us from attempting to measure the scattering from liquid ^{3}He until recently. The development of the high flux reactor at the Institute Laue-Langevin with its cold source providing a very high flux of low energy neutrons, together with the existence of a high flux time-of-flight spectrometer, IN5, on a low background position at the end of a curved guide tube made the experiment possible.[2,3] In the third section the results are described and compared with those obtained from the Bose liquid.

Besides the intrinsic interest in superfluid ^{4}He, it has also become a model system with which to test the theories of the interactions between elementary excitations. This is because liquid ^{4}He is isotropic and so the dispersion relation for the excitations and their interactions are simpler in liquid ^{4}He than in solids. As a result the theory of sound attenuation in liquid ^{4}He is now far better understood than in solids. Another point of interest is that Raman scattering

measurements[4] have shown that two-roton bound states exist, and some recent neutron scattering experiments have been performed to elucidate the nature of roton-roton interactions in more detail. The results of these experiments[5-7] are described in the third section.

The neutron scattering from liquid ^{4}He at large momentum transfers is discussed in the fourth section. Despite the considerable effort which has been devoted to this experiment and to the theory of the experiment, there has still not been a wholly convincing experiment showing that there is a macroscopic occupation of the zero momentum state in the superfluid, or theoretical interpretation of the results.

There are several aspects of the neutron scattering from quantum liquids which I do not have either the time or space to review. Work on mixtures of liquid ^{3}He and ^{4}He will be reported at this meeting as well as work on ^{4}He at 4.2 K where it behaves more like a classical liquid. Finally the recent work by L. Passell and collaborators on thin films of ^{4}He has yielded some very interesting results.

SCATTERING FROM SUPERFLUID ^{4}He

The neutron scattering from ^{4}He nuclei is wholly coherent so that the scattered intensity gives directly the Van Hove correlation function, $S(Q,\omega)$; the Fourier transform with respect to time of the time correlation function for density fluctuations with wave vector $|\vec{Q}|$. At low temperatures it is convenient to divide $S(Q,\omega)$ into two parts: one is the scattering from well-defined excitations, and the other the remaining scattering which is distributed smoothly in frequency and wave vector

$$S(Q,\omega) = Z(Q)\ \delta(\omega-\omega(Q)) + S^{II}(Q,\omega)$$

Measurements have been reported[1] of the frequency of the excitations, $\omega(Q)$, and of their intensity. These frequencies are shown in Fig. 1 and at small Q, they increase linearly with Q, reach a maximum, then a minimum, the roton minimum, and then increase in frequency again. These results are in excellent accord with the dispersion relation for the excitations proposed by Landau to explain the macroscopic properties of superfluid ^{4}He.

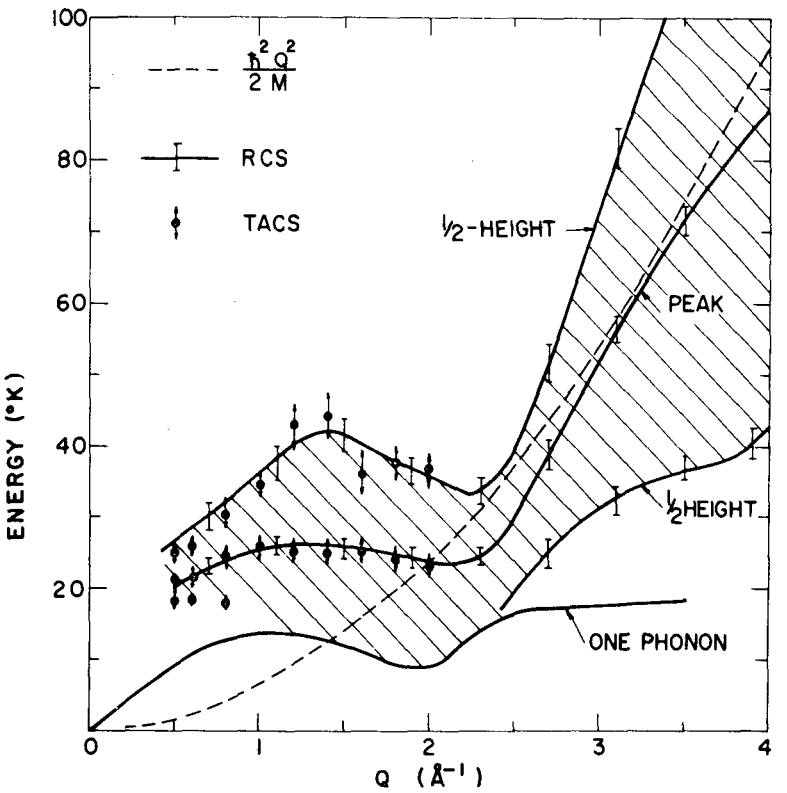


Fig. 1. The energy-wave vector dependence of the scattering in ^{4}He at 1.1 K. The single excitation dispersion relation is shown and the peak and half-height of the broad scattering, $S^{II}(Q,\omega)$.

The frequency dependence of the broad scattering is also shown in Fig. 1. At small wave vectors this scattering has a frequency close

to twice the frequency of the roton minimum and is similar in form to that expected from multi-phonon scattering in a solid.[5,6] At larger wave vectors the intensity of the single excitations decreases rapidly and the mean frequency of the broad component approaches the free particle frequency $\frac{\hbar Q^2}{2M}$.

SCATTERING FROM LIQUID ^{3}He

The scattering from liquid ^{3}He is considerably more difficult to measure than that from liquid ^{4}He because of the large neutron absorption cross section. As the mean free path of the neutrons in the liquid is only 0.05 mm the scattering from the liquid is considerably less than the scattering from the specimen container and from the radiation shields surrounding the specimen. As a result precautions[3] need to be taken so that neutrons could not be scattered by the radiation shields directly into the counters of the time-of-flight spectrometer, and so that the scattering from the front of the specimen cassette could be subtracted as accurately as possible. A typical result[3] showing the scattering from the ^{3}He at 0.63 K is shown in Fig. 2.

The scattering from the ^{3}He was corrected for counter efficiency, for the changing absorption of the scattered neutron beam and converted from a time-of-flight distribution to an energy distribution. Some of the results are shown in Fig. 3 and clearly do not show the sharp peaks characteristic of the scattering from superfluid ^{4}He, in this momentum and energy range.

The results[3] are summarized by the contour map shown in Fig. 4. At the smallest frequency transfers the scattering by the ^{3}He is

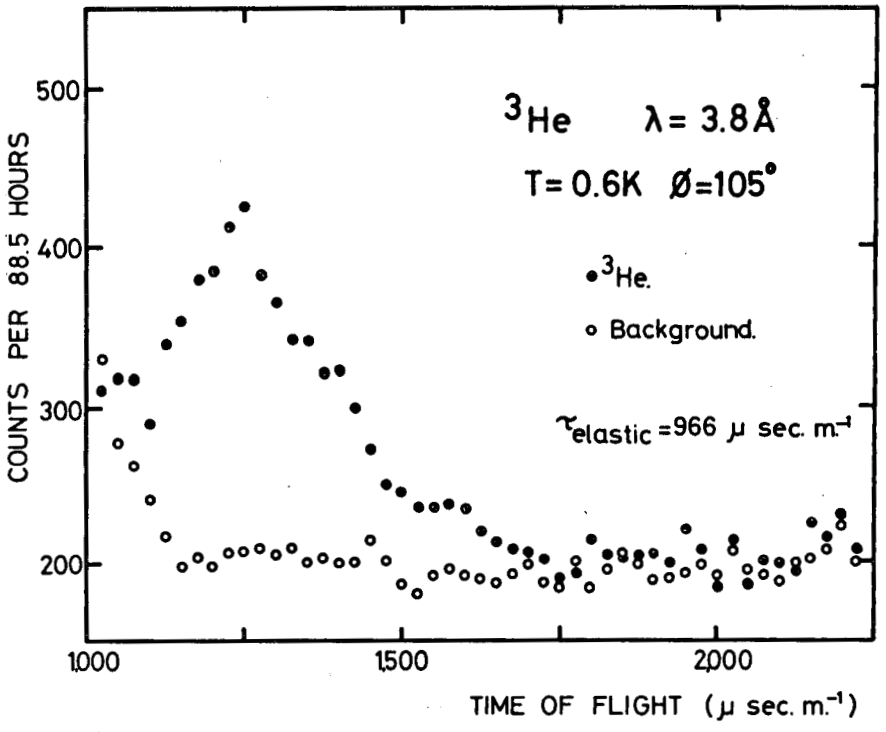


Fig. 2. The time-of-flight spectrum from liquid ^{3}He at 0.63 K and the background from the empty cassette at 0.63 K.

obscured by the more intense scattering from the specimen cassette , while at the larger frequency transfers the results become more uncertain because of the conversion from a time-of-flight to an energy distribution. Measurements were also made[2] of the scattering at 1.3 K under somewhat different conditions, but qualitatively no temperature dependence was observed.

The interpretation of the scattering from liquid ^{3}He requires more care than that from liquid ^{4}He. Because the nuclear spin of the ^{3}He is 1/2, a neutron and a ^{3}He nucleus may form either a triplet or singlet intermediate state. The scattering lengths of these states are different so that the scattering observed with unpolarized neutrons is

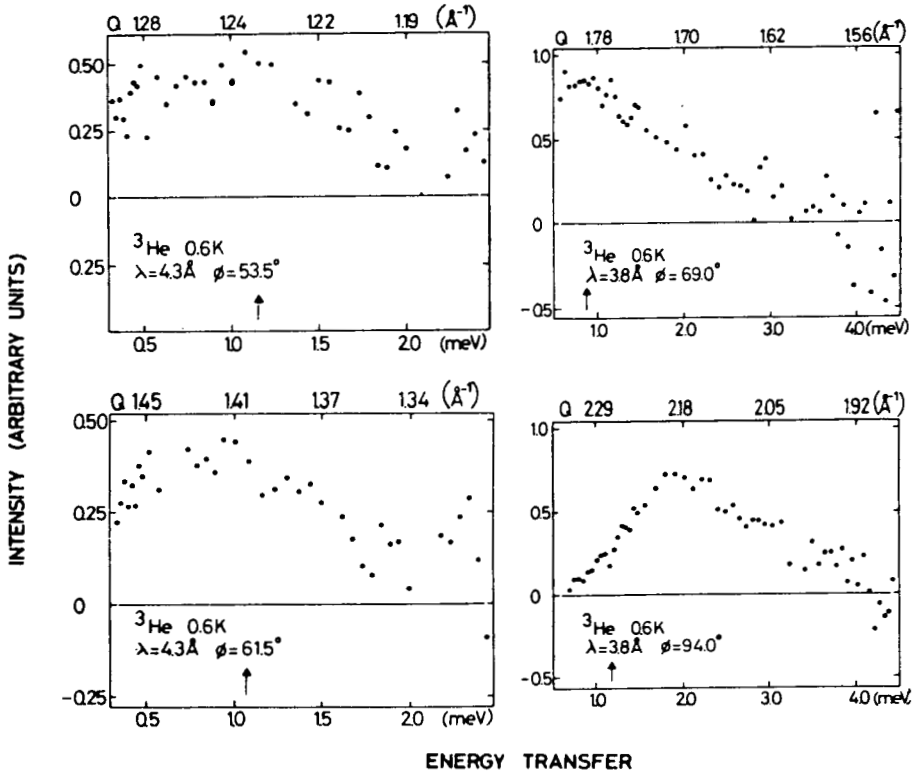


Fig. 3. Intensity scattered from liquid ^{3}He at 0.63 K and 1.0 atm. The large uncertainties at the larger frequency transfers arise from the conversion from time-of-flight distributions to energy distributions.

given by

$$I = \sigma_c S(Q,\omega) + \sigma_I T(Q,\omega) \quad ,$$

where σ_c and σ_I are the coherent and incoherent scattering cross sections, and S and T are the Van Hove number density and spin density correlation functions. At present the ratio σ_I/σ_c is experimentally unknown but Sears and Khanna[8] have estimated it to be about 0.25. Until this ratio is known accurately it is clearly impossible to develop a

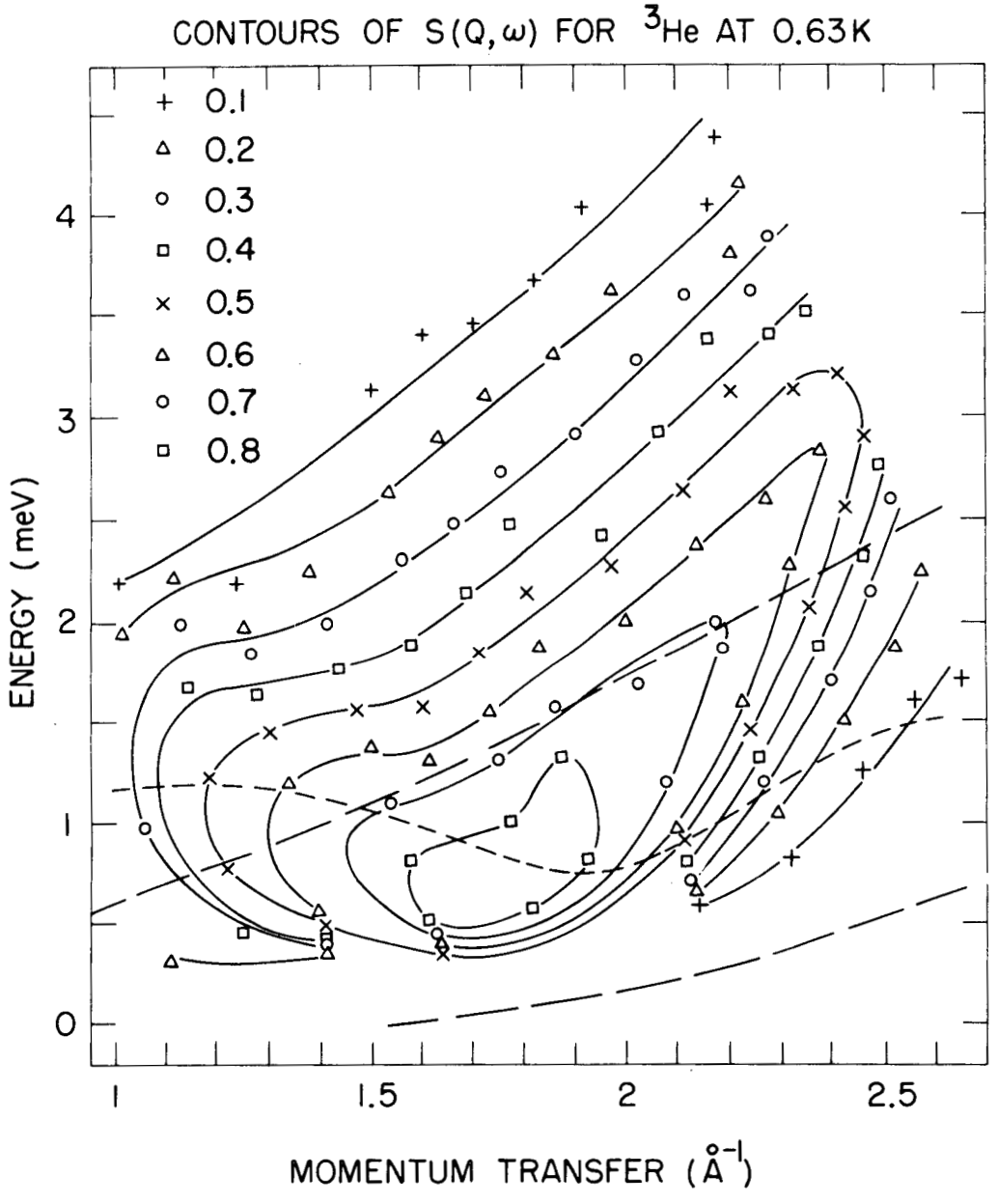


Fig. 4. Intensity contours[3] for the scattering from liquid ^{3}He at 0.63 K and 1.0 atm. The small dotted line gives the dispersion relation for ^{4}He and the large dotted lines the boundaries of the particle-hole continuum assuming that the effective mass of the ^{3}He atoms is 3M.

completely quantitative theory of the neutron scattering from liquid ^{3}He.

Some aspects of the results may however be discussed without a

detailed model. Firstly the differential neutron scattering from liquid ^{3}He and superfluid ^{4}He are qualitatively different. The latter shows well-defined excitations whereas the former does not. Since the structure factor S(Q) is very similar in ^{3}He to that in ^{4}He, this difference illustrates the difficulty of constructing theories of liquids based purely upon the static properties. The difference also and more importantly shows the correctness of the reasoning by Landau and by Feynman that the superfluid property of ^{4}He is intimately connected with the absence of low frequency excitations, apart from the long wavelength phonons, in the Bose fluid. Since scattering is not observed at frequencies below the well-defined excitations, it is not possible for these excitations to decay with conservation of energy and momentum.

In the Fermi liquid there are many low frequency excitations associated with the creation of single particle-hole excitations. These low frequency excitations scatter neutrons and also provide a damping mechanism for any collective excitations. In Fig. 4 the region in frequency-wave vector space for which the single particle-hole excitations occur is shown assuming that the effective mass of the ^{3}He is that deduced from macroscopic measurements[9], three times the base mass. Comparison of this region with the experimental results suggests that for $Q > 2.0$ $\mathring{A}^{-1}$ the scattering is described by a somewhat smaller effective mass, 2.5 M. This reduction is effective mass is to be expected because at large enough wave vectors the scattering will approximate that of bare ^{3}He atoms. Fig. 4 also shows that broad scattering is observed outside the particle-hole continuum. Within the random phase

approximation[9] only well-defined collective modes are expected outside this region. One possibility for this discrepancy is that the boundaries of the particle-hole continuum are incorrect. This would arise if the single particle energies deviated strongly from a parabola. The results do however suggest that the effective mass does not alter greatly over the momentum range of our measurements so that although the upper frequency limit of the continuum may be increased somewhat, it seems unlikely that it can be increased sufficiently to account for the observed broad scattering. Thermal broadening of the continuum boundary is probably small at 0.63 K for frequency transfers of 1 meV.

A more likely explanation of our results can be obtained by considering Landau's arguments in superfluid ^{4}He. He suggested that the excitations would decay into pairs of excitations if the process is allowed by energy and wave vector conservation. In the case of ^{3}He collective excitations with $Q \sim 1.7$ $\mathring{A}^{-1}$ are broadened by the interaction with the particle-hole continuum. Any collective excitations with $Q \sim 1$ $\mathring{A}^{-1}$ and frequencies comparable to these in liquid ^{4}He are then able to decay into pairs of excitations with $Q \sim 1.7$ $\mathring{A}^{-1}$. This mechanism would then allow zero sound excitations in liquid ^{3}He to decay even when their frequency is outside the particle-hole continuum. If this suggestion is correct it implies that the simple random phase approximation is not an adequate description of liquid ^{3}He, and that in addition to particle-hole excitations a more complete theory needs to include the effects of two particle-two hole and other complex excitations.

Various variants of the random phase approximation have been compared with the experimental results[3], but fail to give a satisfactory

description of the measurements. Calculations by Lovesey[10] of the scattering $S(Q,\omega)$ based on the continued fraction method does give a reasonable description of the measurements.[3]

INTERACTIONS BETWEEN THE EXCITATIONS IN LIQUID ^{4}He

Because of the simplicity of the dispersion relation in liquid ^{4}He it provides an excellent model system on which to study the effects of the interactions between the excitations. In this section I wish to discuss the information which has been obtained on the interactions between the rotons. Pitaevskii[11] investigated the effect on the dispersion relation, $\omega(Q)$, of the decay of an excitation into pairs of rotons. If the rotons are non-interacting he showed that the dispersion relation $\omega(Q)$ could not exceed 2Δ, where Δ is the roton frequency. He predicted that at large Q the dispersion relation would have the form

$$\omega(Q) = 2\Delta - A \exp\left(-B/(Q_c - Q)\right) , \qquad (1)$$

where A, B and Q_c are constants. This limiting behavior is a direct result of the isotropy of the dispersion relation in the liquid which gives rise to a singularity in the two-roton density of states at a frequency of 2Δ. This prediction has been shown[1,5] to give a good description of the dispersion relation for $2.2 < Q < 2.8$ $\mathring{A}^{-1}$ at 1.1 K and 1.0 atm.

Raman scattering measurements on liquid ^{4}He measure largely the two-roton density of states with a total wave vector, Q=0. Careful measurements of the shape of the scattering[4] have shown that the density

of states is not that given by non-interacting rotons but corresponds to the density of states to be expected from pairs of rotons which attract one another. This attraction leads to a two-roton bound state with a frequency $2\Delta-\delta$ where δ is the binding frequency of the bound state.

The effect of the interaction between the rotons on the neutron scattering was discussed by Zawadowski et al.[12] If the interactions are attractive the maximum frequency of the elementary excitations is $2\Delta-\delta$, the two-roton bound state frequency. This development has recently been tested by measurements[5,6] of the pressure dependence of the excitations with a wave vector of 1.1 $\mathring{A}^{-1}$. The results are shown in Fig. 5 and show that while the intensity in the excitation peak decreases with increasing pressure the frequency is clearly above 2Δ for pressures larger than 20 atm.

Measurements[7] have also been performed for large wave vectors as a function of pressure. Whereas at the vapor pressure the frequencies[1] lie close to 2Δ, at 24 atm the frequencies are clearly larger than 2Δ as shown in Fig. 6. Both of these observations of frequencies in excess of 2Δ are inconsistent with the predictions of theories with non-interacting or attractively interacting rotons. They are consistent, however, if the interactions between the rotons are repulsive in character, and the magnitude of the interaction may be estimated from the observed line shapes.[7] The results are shown in Fig. 7 where they are compared with estimates of the roton-roton interaction based on the theory developed by Lee.[13]

The observation of repulsive interactions between pairs of rotons

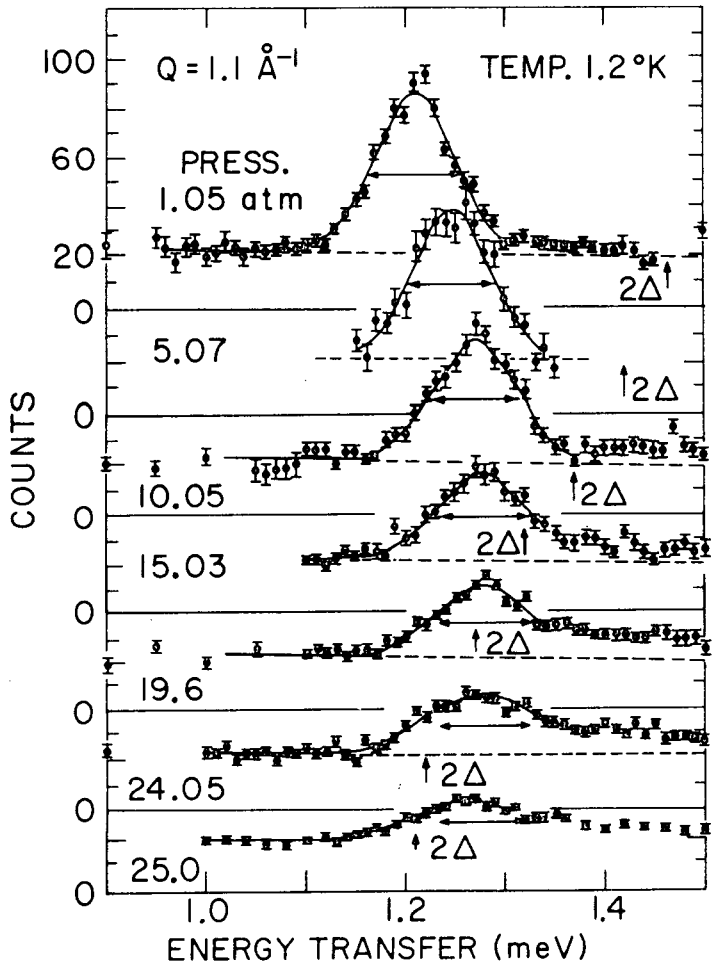


Fig. 5. Pressure dependence[5] of the excitation frequency for Q = 1.1Å^{-1} in ^{4}He at 1.2 K.

by neutron scattering is not inconsistent with the results of the Raman scattering. In the latter case the interaction is between pairs of rotons with total wave vector Q=0, whereas Q is much larger in the neutron scattering measurements. In fact Woerner and Stephen[14] have pointed out that a large part of the attractive part of the interaction in the Raman scattering measurements may arise from interactions with pairs of phonons. This attractive mechanism is absent in the neutron scattering case because the small wave vector of the phonons prohibits

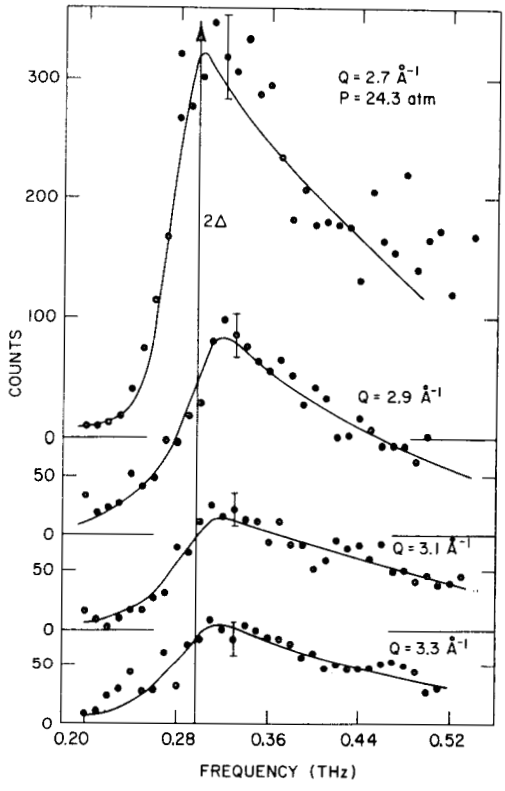


Fig. 6. Neutron scattering distributions[7] for increasing wave vector at 24 atm and 1.1 K. The solid curves show fits to the line shapes based on repulsive roton-roton interactions.

this process for the larger wave vector transfers involved in the neutron scattering.

LARGE MOMENTUM TRANSFER SCATTERING IN ^{4}He

The interest in the nature of the scattering from liquid ^{4}He at large Q was stimulated by the work of Hohenberg and Platzman[15] who pointed out that as $Q \to \infty$ the scattering is given by

$$S(Q,\omega) = \sum_{\vec{p}} n(\vec{p})\,\delta\left(\omega - \frac{\hbar}{2M}(Q^2 + 2\vec{Q}\cdot\vec{p})\right) \qquad (2)$$

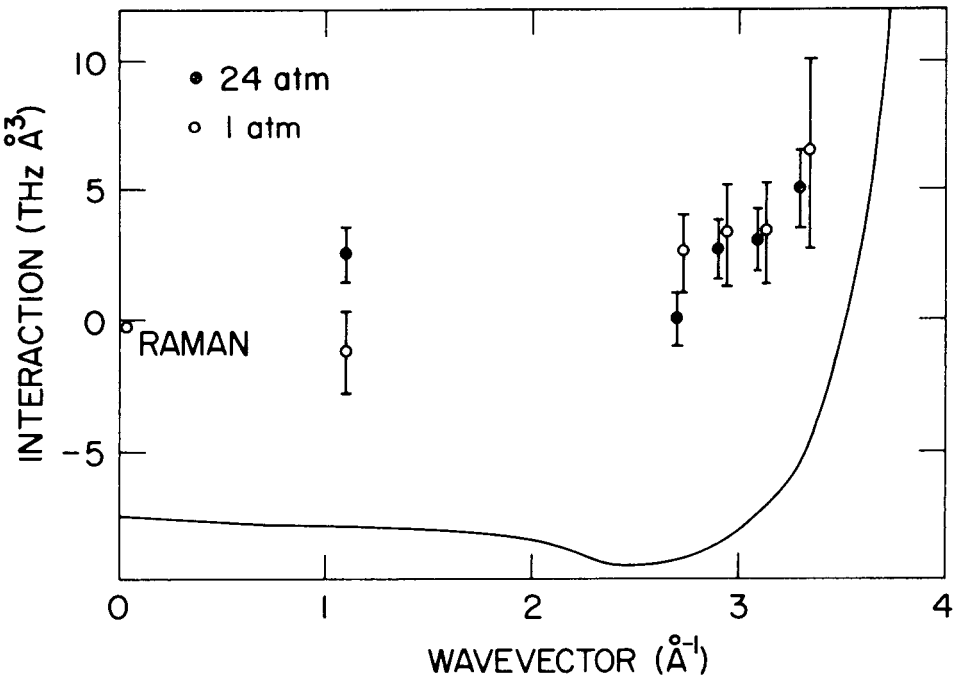


Fig. 7. The roton-roton interactions as deduced from measurements[7,4] and calculated using the theory of Lee.[13]

where $n(\vec{p})$ is the number of particles with wave vector $\vec{p}$ in the ground state. The superfluid properties of ^{4}He are believed to be intimately related to the macroscopic occupation of the zero momentum state and the observation of a sharp peak corresponding to n(0) would confirm this connection.

There have now been several attempts[1,16-19] to study the scattering at large Q, but none of the measurements has convincingly demonstrated a well-defined component coming from the condensate fraction. Several experiments have been analyzed using Eq. (2) to obtain n(p) and two of the most recent results are shown in Fig. 8. The experimental results are clearly not in detailed agreement with one another. In particular Mook[18] interprets the peak at small p as an indication of a macroscopic occupation of the condensate and estimates

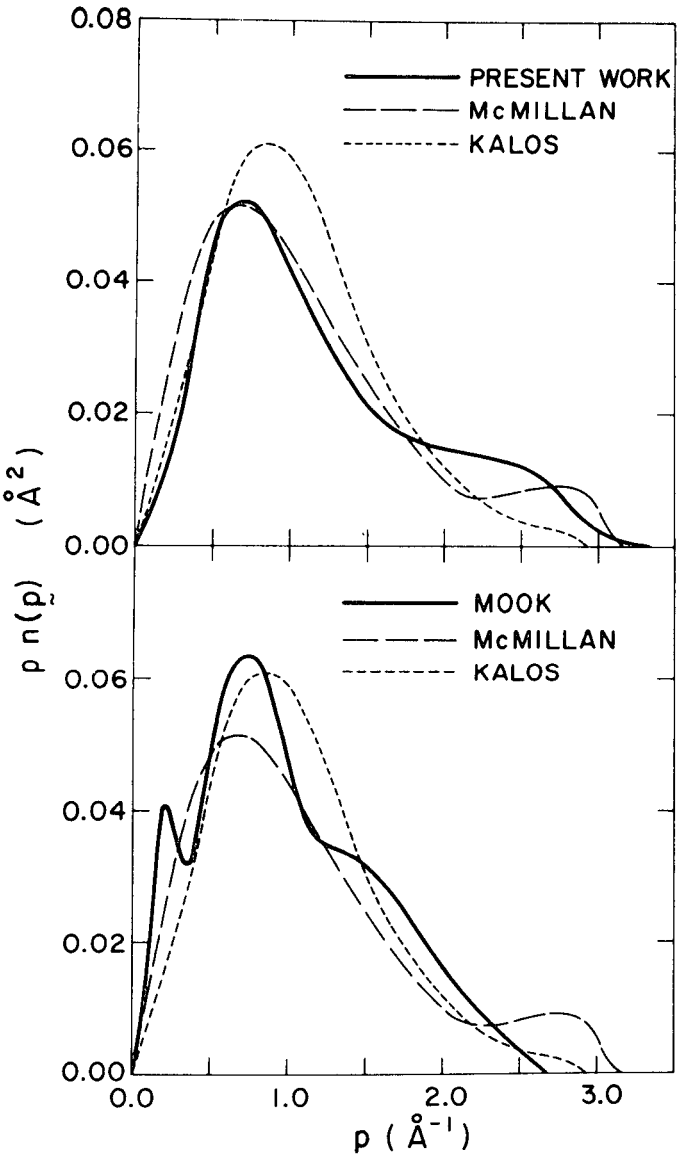


Fig. 8. The momentum distribution at 1.2 K deduced from constant Q measurements[19] with Q = 10.0 $Å^{-1}$ (upper diagram) and from time-of-flight measurements[18] with Q ≈ 14 $Å^{-1}$. The results are compared with theoretical calculations by McMillan[20] and by Kalos et al.[21]

n(0) = 0.018 ± 0.01. No indication of this structure is found in the other experiment. We may conclude, however, that if Eq. (2) is valid for the interpretation of these experiments that the value of n(0) is at least an order of magnitude less than most theoretical estimates.

Unfortunately there are indications that Eq. (2) may not be adequate. In Fig. 9 the width of the scattering[19] is shown for increasing wave vector. This tends to oscillate in a way which seems to be correlated with the oscillations in the He atom-atom scattering cross section.[22] If this is a correct interpretation it implies that the

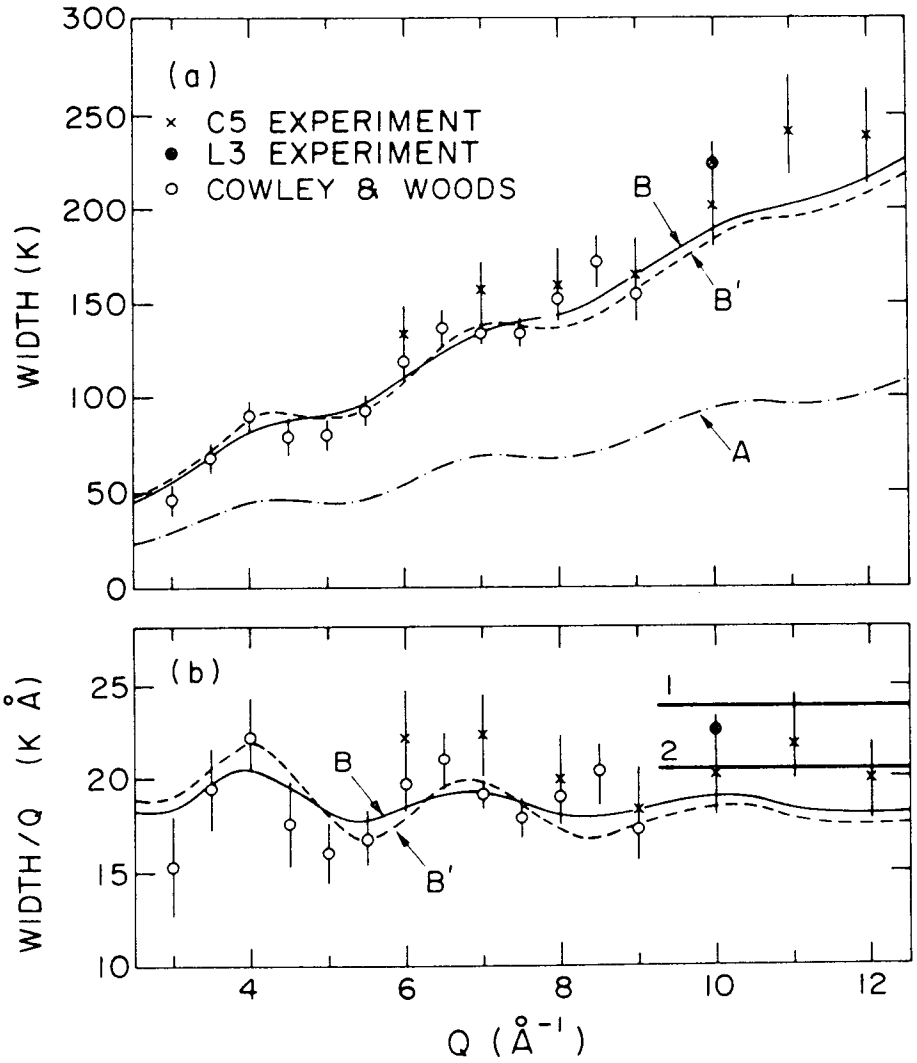


Fig. 9. The full widths[19] at half maximum of the scattered neutron distributions at 1.1 K. Curve A is the width of the scattering expected due to collisions of the excited helium atom with the bulk. Curve B and B' are this width convoluted with Gaussian and Lorentzian distibutions for $n(\vec{p})$ chosen to give approximately the measured width. The heavy solid lines 1 and 2 are the theoretical width calculated using Kalos et al's[21] and McMillan's[20] $n(\vec{p})$ respectively.

collisions which are neglected in the derivation of Eq. (2) play an important role for these wave vectors. Unfortunately estimates of the validity of Eq. (2) based on moments suggest that it should be much more accurate in this momentum range than the above considerations. Clearly further theoretical work and further experiments are required before we can be confident of any value for n(0).

ACKNOWLEDGMENTS

The experimental work discussed in this paper in which I have been involved was performed either at the Institute Laue-Langevin (^{3}He) or at the Chalk River Nuclear Laboratories (^{4}He) for whose facilities I am very grateful. I am indebted to my collaborators, in particular to P. A. Hilton, P. C. Martel, R. Scherm, A. J. Smith, W. G. Stirling, E. C. Svensson and A. D. B. Woods without whom the experiments would not have been performed.

REFERENCES

1. A. D. B. Woods and R.A. Cowley, Rep. Progr. Phys. 36,1135(1973).
2. R. Scherm, W. G. Stirling, A. D. B. Woods, R. A. Cowley, and G. J. Coombs, J. Phys. C 7, L34 (1974).
3. W. G. Stirling, R. Scherm, P. A. Hilton, and R. A. Cowley, J. Phys. C (in press).
4. T. J. Greytak, R. Woerner, J. Yan, and R. Benjamin, Phys. Rev. Lett. 25, 1547 (1970); C. A. Murray, R. Woerner, and T. J. Greytak, J. Phys. C 8, L90 (1975).
5. E. H. Graf, V. J. Minkiewicz, H. Bjerrum Møller, and L. Passell, Phys. Rev. A 10, 1748 (1974).

6. E. C. Svensson, P. Martel, V. F. Sears, and A. D. B. Woods (to be published).

7. A. J. Smith, R. A. Cowley, A. D. B. Woods, W. J. Stirling and P. Martel(to be published).

8. V. F. Sears and F. C. Khanna, Phys. Lett. 56 B, 1 (1975).

9. D. Pines and P. Nozieres, The Theory of Quantum Liquids, Benjamin (1975).

10. S. W. Lovesey, J. Phys. C 8, 1649 (1975).

11. L. P. Pitaevskii, Sov. Phys. JETP 9, 830 (1959).

12. A. Zawadowski, J. Ruvalds, and J. Solana, Phys. Rev. A 5, 399 (1972).

13. D. K. Lee, Phys. Rev. 162, 134 (1967).

14. R. L. Woerner and M. J. Stephen, J. Phys. C 8, L464 (1975).

15. P. C. Hohenberg and P. M. Platzman, Phys. Rev. 152, 198 (1966).

16. O. K. Harling, Phys. Rev. A 3, 1073 (1971).

17. H. A. Mook, R. Scherm, and M. K. Wilkinson, Phys. Rev. A 6, 2268 (1972).

18. H. A. Mook, Phys. Rev. Lett. 32, 1167 (1974).

19. P. Martel, E. C. Svensson, A. D. B. Woods, V. F. Sears, and R. A. Cowley, J. Low Temp. Phys. 23, 285 (1976).

20. W. L. McMillan, Phys. Rev. 138, A442 (1965).

21. M. H. Kalos, D. Levesque, and L. Verlet, Phys. Rev. A 9, 2178(1974).

22. R. Feltgen, H. Pauly, F. Torello, and H. Vehmeyer, Phys. Rev. Lett. 30, 820 (1973).

SHORT WAVELENGTH COLLECTIVE DENSITY EXCITATIONS IN MONATOMIC LIQUIDS

S.W. Lovesey[+], J.W.E. Lewis[§]
[+]Institut Laue-Langevin, 38042 Grenoble, France.
§Rutherford Laboratory, Oxfordshire, U.K.

ABSTRACT

There has been considerable speculation in the past as to the conditions which must be met for a monatomic liquid to support a short wavelength, collective density excitation (cde). Computer simulation and neutron scattering studies have shown that liquid rubidium (1), near the solidification line, can support a cde whose wavevector is about two-thirds of the wavevector at which the main peak in the structure factor occurs. On the other hand, extensive studies of a Lennard-Jones liquid (2) near the triple point show that this system does not possess sufficient correlation amongst the atoms for it to support a cde. These results have often been taken as evidence in favour of the idea that the features necessary for a liquid to support a short wavelength cde is a soft-core potential since a hard-core potential results in large angle scatterings of the atoms that are particularly effective in distroying correlated motions. As a first step toward clarifying the role of the potential in establishing the conditions necessary for a liquid to support a short wavelength cde, we have performed computer simulation studies using 256 particles interacting via a generalised L-J potentials. We find that, at high densities, the r dependences of the potential must be weakened significantly before a short wavelength cde contributes a peak in the spectral density $S(k,\omega)$ at non-zero ω. Softening the core potential is not in itself sufficient to establish highly correlated motions of the atoms. The analysis of our data suggests that a short wavelength cde can exist, at high densities, if

$$\gamma_G = -\frac{r_o}{6}\,(U'''/U'')_{r_o} < 2$$

where U'' and U''' are the second and third derivatives, respectively, of the two-particle potential, and r_o is the position of the main minimum in the potential.

(1) Rahman A 1974 Phys. Rev. Lett. 32, 52
(2) Levesque D et al 1973 Phys. Rev. A7, 1690.

NEUTRON DIFFRACTION STUDIES OF TETRACHLORIDE LIQUIDS AND LIQUID MIXTURES

J. H. Clarke, J. C. Dore and G. W. Stanton
Physics Laboratory, The University of Canterbury, Kent, England

ABSTRACT

Neutron diffraction measurements have been made for CCl_4, $SiCl_4$, $TiCl_4$, $GeCl_4$, $SnCl_4$ and special mixtures of $SiCl_4/TiCl_4$ and $SnCl_4/TiCl_4$ using steady state and pulsed neutron facilities. A wide Q-range has been obtained by using short wavelength neutron (λ = 0.5 Å) for the reactor measurements at ILL (Grenoble) and the large angle detector bank (150°) on the total scattering spectrometer at the Harwell Electron Linac. The differential scattering cross-sections show significant oscillation amplitudes up to values of 30 A^{-1} and have been analysed in terms of the structure of individual molecules in the liquid.

INTRODUCTION

Neutron diffraction techniques have been used extensively for the study of simple liquids such as the rare gas liquids and liquid metals but have not been widely applied to the study of molecular liquids. The importance of molecular orientation effects has been emphasised in an analysis of earlier data for tetrahedral molecules by Egelstaff, Page and Powles[1]. However, the diffraction pattern is dominated by intra-molecular contributions so that the analysis is difficult unless an accurate determination of the molecular form-factor can be established. The relatively recent development of TOF diffraction methods using an accelerator-driven pulsed neutron source has provided new possibilities for investigating the high-momentum transfer region. Work has already been carried out for a number of linear molecular species[2,3] and we here present a preliminary report on the investigation of a range of tetrachloride liquids and mixtures.

THE MOLECULAR FORM FACTOR

The structure factor for molecular liquids $S_m(Q)$ may be written[1]:-

$$S_m(Q) = N_m \left[\sum b_i \right]^{-2} \sum_i \sum_j < \bar{b}_i \bar{b}_j \exp(i\underline{Q}.\underline{r}_{ij}) >$$

where N_m is the number of molecules in the system, $\bar{b}_i$ is the coherent scattering length averaged over isotopes and $\underline{r}_{ij}$ is the vector distance between nuclei $\underline{r}_i$ and $\underline{r}_j$. It can be shown[1] that in the high Q-value limit

$$S_m(Q) \rightarrow f_1(Q)$$

where $f_1(Q)$ is the molecular form-factor. The differential coherent scattering cross-section per molecule in the high Q-value limit is given by

$$\left[\frac{\partial \sigma_{coh}}{\partial \Omega} (\lambda, \theta) \right] = < \left| \sum_i \bar{b}_i \exp(i\, \underline{Q}.\underline{r}_i) \right|^2 > = f_1(Q) \left(\sum \bar{b}_i \right)^2 .$$

Q is the scattering vector and, for elastic scattering, is given by

$$Q = \frac{4\pi}{\lambda} \sin \theta/2.$$

For tetrachlorides with molecular constitution $XC\ell_4$ we have

$$\left[\frac{\partial \sigma_{coh}}{\partial \Omega} (\theta, \lambda) \right] = \bar{b}_X^2 + 4\bar{b}_{C\ell}^2 + 12\bar{b}_{C\ell}^2 \, j_o(Qr_{C\ell C\ell}) \exp(-\gamma_{C\ell C\ell} Q^2) + 8\bar{b}_X \bar{b}_{C\ell} \, j_o(Qr_{XC\ell}) \exp(-\gamma_{XC\ell} Q^2)$$

where $j_o(Qr)$ is a spherical Bessel function and the exponential term is a Debye-Waller Factor to allow for vibrational effects.

The tetrachlorides molecules have central atoms with b values which range from -3.3 fm to +8.4 fm and therefore provide a suitable system for investigation. The differential scattering cross-section contains two oscillatory terms of different periodicity since $r_{C\ell C\ell} = (2\sqrt{2}/\sqrt{3})\, r_{XC\ell}$. It is also possible to utilise the negative scattering length of titanium to greatly reduce one of these oscillatory terms by mixing $TiC\ell_4$ with one of

the other tetrachlorides.

For a mixture of tetrachlorides labelled α and β with relative number densities ω_α and ω_β, the high Q-value cross-sections will be:-

$$\left[\frac{\partial\sigma_{coh}}{\partial\Omega}(\theta,\lambda)\right]_{\alpha,\beta} = \omega_\alpha\left[\frac{\partial\sigma_{coh}}{\partial\Omega}(\theta,\lambda)\right]_\alpha + \omega_\beta\left[\frac{\partial\sigma_{coh}}{\partial\Omega}(\theta,\lambda)\right]_\beta$$

where $\omega_\alpha + \omega_\beta = 1$, which may be re-written as:-

$$\begin{aligned}\left[\frac{\partial\sigma_{coh}}{\partial\Omega}(\theta,\lambda)\right]_{\alpha\beta} = {} & \omega_\alpha\bar{b}_\alpha^2 + \omega_\beta\bar{b}_\beta^2 + 4\bar{b}_{C\ell}^2 + 8\omega_\alpha\bar{b}_\alpha\bar{b}_{C\ell}j_o(Qr^\alpha_{XC\ell})\exp(-\gamma^\alpha_{XC\ell}Q^2) \\ & + 8\omega_\beta\bar{b}_\beta\bar{b}_{C\ell}j_o(Qr^\beta_{XC\ell})\exp(-\gamma^\beta_{XC\ell}Q^2) \\ & + 12\omega_\alpha\bar{b}_{C\ell}^2\, j_o(Qr^\alpha_{C\ell C\ell})\exp(-\gamma^\alpha_{C\ell C\ell}Q^2) \\ & + 12\omega_\beta\bar{b}_{C\ell}^2\, j_o(Qr^\beta_{C\ell C\ell})\exp(-\gamma^\beta_{C\ell C\ell}Q^2)\ .\end{aligned}$$

To minimise the oscillatory part of the cross-term (in $r_{\alpha C\ell}$ and $r_{\beta C\ell}$) we may adjust the mixture such that

$$\omega_\alpha b_\alpha = -\omega_\beta b_\beta\ .$$

The partial cancellation of certain interference contributions which, in this case, is achieved by chemical substitution is similar to the more usual technique of isotropic substitution. The cross-section now becomes:-

$$\left[\frac{\partial\sigma_{coh}}{\partial\Omega}(\theta,\lambda)\right] = 4\bar{b}_{C\ell}^2 + \omega_\alpha\bar{b}_\alpha^2 + \omega_\beta\bar{b}_\beta^2 + i(Q)$$

where i(Q) is an interference function given by

$$i(Q) = 8\omega_\alpha \bar{b}_\alpha \bar{b}_{C\ell} \left[j_o(Qr^\alpha_{XC\ell}) - j_o(Qr^\beta_{XC\ell}) \right]$$

$$+ 12\omega_\alpha \bar{b}^2_{C\ell} \left[j_o(Qr^\alpha_{C\ell C\ell}) - \frac{b_\alpha}{b_\beta} j_o(Qr^\beta_{C\ell C\ell}) \right].$$

Since $\bar{b}_{C\ell} = +9.58$ fm is greater than $\bar{b}_\alpha$ for the liquids studied the second term dominates the interference pattern but because $r^\alpha_{C\ell C\ell} \neq r^\beta_{C\ell C\ell}$ the two oscillatory contributions become out of phase as the Q-value is increased. This leads to a partial cancellation and creates a 'molecular beat' effect in the oscillations of the form-factor for the mixture. The first terms also show this effect but since the magnitude is much smaller it will not be seen in the diffraction pattern.

EXPERIMENTAL PROCEDURE

The data were collected on a two-axis diffractometer (D4) at the High Flux Beam Reactor, Institut Laue Langevin Grenoble and also from the total scattering spectrometer (TSS) at the Electron Linear Accelerator (LINAC) Harwell. Cylindrical thin walled vanadium containers of 5 mm internal diameter were used for the reactor measurements, and due to the fixed geometry of the TSS it was possible to use plate samples of 4 mm thickness for the linac measurements. The data reduction followed the usual procedure[4].

ANALYSIS

The observed diffraction patterns show good agreement (Fig. 1) with the predictions of the calculated form-factors although there is some discrepancy in absolute amplitudes which is being further investigated. The 'beat effect' is clearly observed in the results for the mixtures (Fig. 2) and the Q-range was such that the amplitude of the envelope for the oscillations was seen to increase after passing through a minimum. Distinct oscillations were observed up to, and in some cases exceeding, a Q-value of 30 $\mathring{A}^{-1}$.

A preliminary analysis of the data has been made using a χ^2 fitting routine to determine the bond lengths and the results are compared with accepted values in Table 1. A similar procedure was adopted for the mixtures with two independent bond-length parameters; because of the 'beat effect', the fitting is particularly sensitive to bond-length differences. The values obtained were found to be consistently larger than the accepted values by about 1%, but for $GeCl_4$ the difference was much larger. This effect has also been observed in recent X-ray diffraction[6] for $GeCl_4$ which indicates that the accepted value is probably too small. A more detailed analysis will be presented later.

Table 1. A comparison of bond lengths of tetrachlorides and tetrachloride mixtures (distances in Å)

LINAC DATA	CCl_4	$SiCl_4$	$GeCl_4$	$SnCl_4$	$TiCl_4$	$SiCl_4/TiCl_4$	$SnCl_4/TiCl_4$
Neutron Diffraction	1.79	2.03	2.13	2.30	2.19	2.03/2.19	2.30/2.19
Accepted Values	1.77	2.01	2.08	2.29	2.17	-	-

ACKNOWLEDGEMENTS

This work has been carried out with the support of the Neutron Beam Research Committee of the SRC. Two of us wish to thank the SRC (JHC and GWS) and A.E.R.E. Harwell (JHC) for financial support.

REFERENCES

1. P. A. Egelstaff, D. I. Page and J. G. Powles, Mol. Phys. 20, 881 (1971)
2. J. C. Dore, G. Walford and D. I. Page, Mol. Phys. 29, 565 (1975)
3. G. Walford, J. H. Clarke and J. C. Dore, Paper , this conference.
4. J. H. Clarke, J. C. Dore, G. Walford and R. N. Sinclair, Mol. Phys. 31, 883 (1976).
5. C. T. Rutledge and G. T. Clayton, J. Chem. Phys. 63, 2211 (1975).

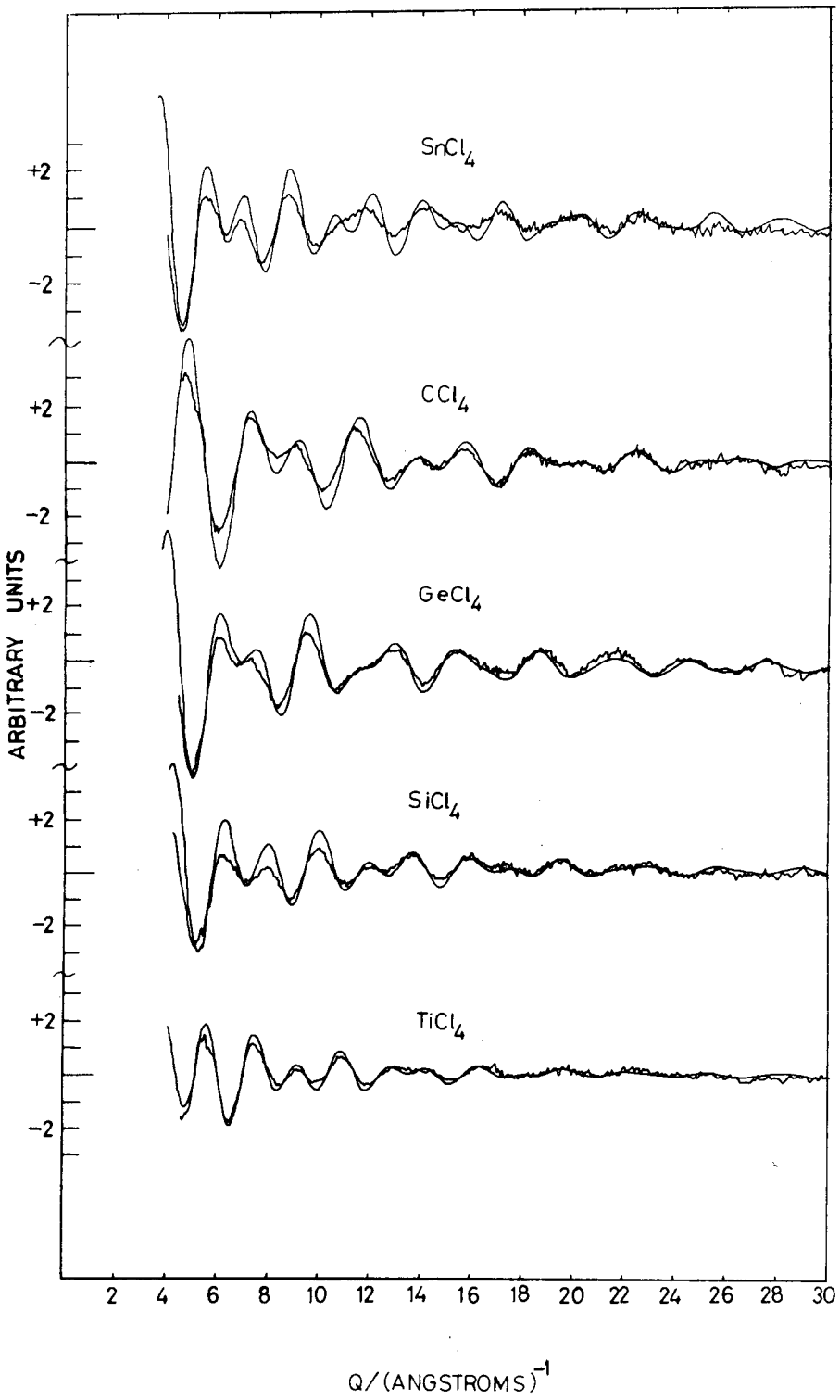


Fig 1. Interference Functions of the tetrachlorides compared with calculated values.

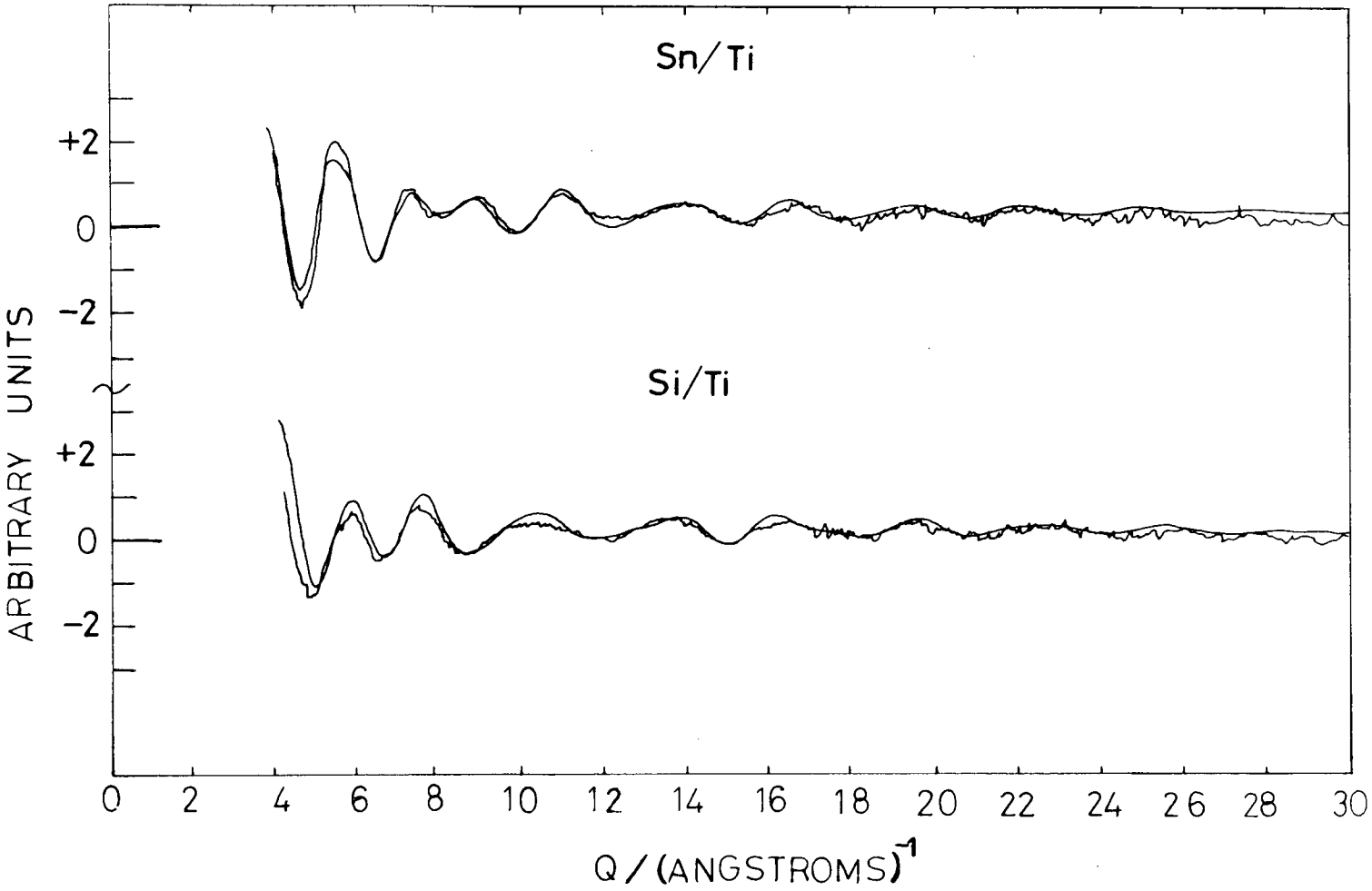


Fig 2. Interference Functions of the tetrachloride mixtures compared with calculated values.

OBSERVATION OF ENHANCED SELF DIFFUSION IN HIGH DENSITY GASEOUS HYDROGEN BY INCOHERENT NEUTRON SCATTERING*

T. A. Postol, S. H. Chen
Massachusetts Institute of Technology
Cambridge, Massachusetts 02139
and
K. Sköld**
Solid State Science Division
Argonne National Laboratory
Argonne, Illinois 60439

ABSTRACT

Incoherent quasi-elastic scattering of neutrons from hydrogen gas at room temperature and 78°K in a range of pressures from 100 to 2000 atm. has been measured. Part of the data which lie in the hydrodynamic regime have been analyzed to obtain the self-diffusion coefficient as a function of density. We observe an enhancement of the measured self-diffusion coefficients over that of the equivalent hard sphere Enskog values.

Recently a series of computer molecular dynamic studies of hard sphere systems by Alder et al[1],[2] demonstrated convincingly that the test particle motion in a dense fluid deviates considerably from what one expects from the well known hard sphere Enskog theory.[3] The computer study shows that for density $nr_0^3/\sqrt{2}$ (relative to the close pack density) less than 0.5 the velocity autocorrelation function (VAF) of the test particle decay monotonically to zero with a time constant which is appreciably larger than the Enskog value $\tau_E = D_E/v_0^2$. We denote the thernal speed $v_0 = (k_B T/M)^{\frac{1}{2}}$,

$$D_E = \frac{3}{8}\sqrt{\frac{k_B T}{\pi M}}\,\frac{1}{nr_0^2}\,\frac{1}{g(r_0)} \qquad (1)$$

where M is the molecular mass, n the number density, r_0 the hard sphere diameter and $g(r_0)$ the pair correlation function at contact. Physically, the motion of the test particle, in the Enskog description, is characterized by a series of uncorrelated binary collisions which lead to an exponential decay of the VAF. The uncorrelated collision description fails to account for the fact that a test particle can undergo repeated

collisions with a given particle of the medium under the collective influence of all other particles. These correlated collisions produce persistent correlations in the VAF in two ways. In the intermediate time regime corresponding to 3 to 10 collisions (measured in collision time $\tau = 2\tau_E/3$) the hard sphere VAF shows enhancement over the Enskog VAF by as much as 0.02.[1] At long times, where 20 or more collisions occur, hydrodynamic effects dominate the dynamical behavior of the tagged particle and the VAF decays as $t^{-3/2}$.[2] Theoretically, the intermediate and long time effects come from "ring collision terms" which are not contained in the Enskog memory function of the generalized Boltzmann-Lorentz equation.[4] However, in terms of an observable effect, the intermediate time phenomenon produces an enhancement of the diffusion coefficient (which is proportional to the area under the VAF) over that of D_E by as much as 34% while the long time tail effect contributes only a negligible amount to this enhancement. It is well known that the quasi-elastic spectrum of incoherently scattered neutrons is directly related to the generalized diffusion coefficient.[5] For this reason, neutron scattering is a particularly powerful technique for the study of single particle motions in dense fluids.

These measurements were made by the time of flight technique using the Argonne Thermal Neutron Time of Flight Spectrometer (TNTOFS).[6] 4.54 meV incident neutrons were chopped with a pseudorandom statistical chopper and scattered neutrons were detected (simultaneously) at 15 angles. Complete multiple scattering calculations were performed using the code of Copley[7] and the multiple scattering was found to be always less than 2% of the signal even at the extreme wings and at the highest density.

Typical spectra for three different densities at 78°k and $\Theta = 13.80°$ are presented in Fig. 1. The graphs are in absolute scale with the container scattering subtracted. Multiply scattered neutrons are not plotted because their intensity was insignificant. The solid line is a fitted curve which is the convolution of a Lorentzian function with the measured resolution of the spectrometer. The fit is good showing that the data is properly in the hydrodynamic regime.

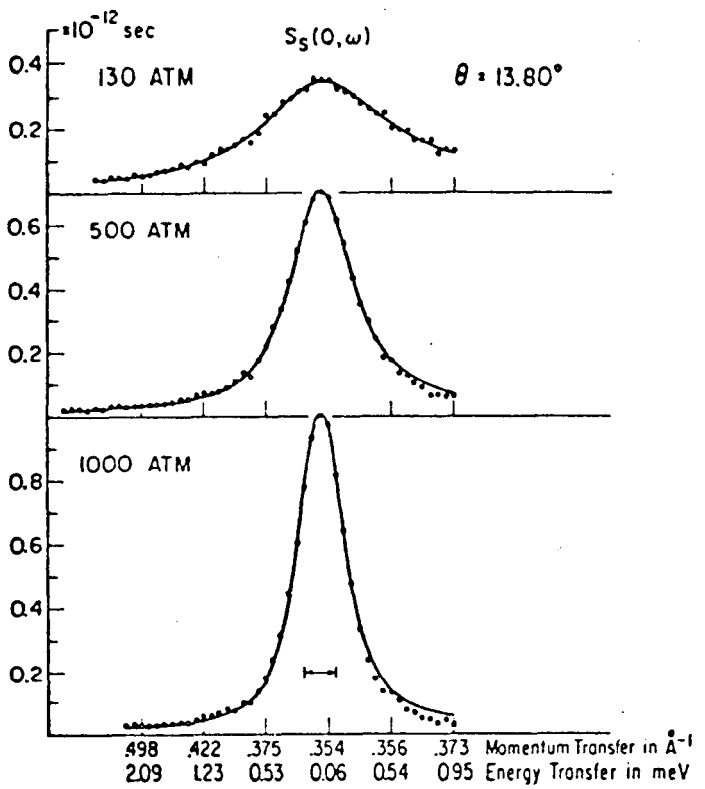


Fig. 1. Self part of the dynamic structure factor of hydrogen gas at 78°K. The corresponding densities are are indicated in Table 1. Note the data is not presented in constant Q form.

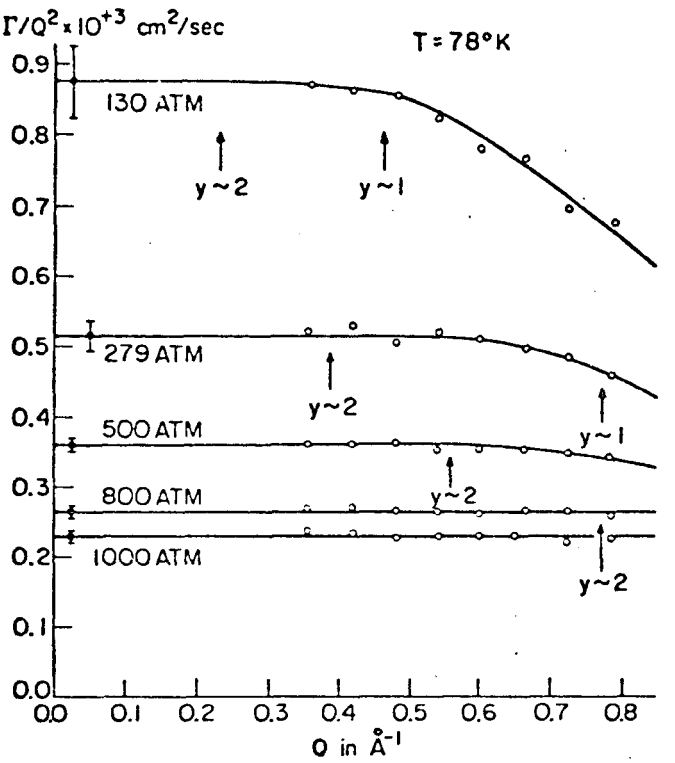


Fig. 2. HWHM Γ of $S_s(Q,\omega)$ divided by Q^2 as function of Q. For $y \geq 2$ the is expected to be accurately given by DQ^2. Therefore, the intercept of the solid line at Q=0 gives D.

Fig. 2 is a plot of the extracted full width at half maximum divided by Q^2 for 8 values of Q. The Q dependence of the diffusion coefficient in the lower density data is due to deviations from hydrodynamics and will be discussed in detail elsewhere. The parameter $y = v_0/\sqrt{2}DQ$ [8] is a kinetic theory parameter which is the ratio of the wavelength of fluctuation being observed to the collision mean free path of particles in the fluid. When $y \lesssim 1$ kinetic theory must be used to interpret the data and when $y \gtrsim 2$ the hydrodynamics description is adequate.

The diffusion coefficients at 500, 800 and 1000 atmospheres and 78°K were all measurable to within 1-3% accuracy since most or all of the data at a given density were within the hydrodynamic regime. The data at 1000, 1504 and 1946 atmospheres and 293°K (not shown in Fig. 2) are considerably less accurate because of problems with intense container scattering. The solid lines in Fig. 2 are our extrapolation of the data to Q=0 and the solid points with error bars the estimate of the diffusion coefficients.

Table 1. Summary of the experimentally measured self diffusion coefficients and the Enskog diffusion coefficients as computed from Eq.(1).

T(K°)	P(atm.)	$n(10^{22}cm^{-3})$	$nr_o^3/\sqrt{2}$	$D(10^{-3}cm^2/sec)$	D_E
293	1000	1.49	0.1788	1.97 ± 0.19	1.743
	1504	1.89	0.1680	1.46 ± 0.13	1.148
	1946	2.14	0.2569	1.20 ± 1.10	0.946
	130	1.15	{0.2012(a) 0.2106(b)	0.88 ± 0.05	{0.876(a) 0.858(b)
	279	1.74	{0.3052 0.3187	0.52 ± 0.03	{0.455 0.440
78	500	2.16	{0.3795 0.3957	0.36 ± 0.01	{0.303 0.290
	800	2.55	{0.4471 0.4673	0.27 ± 0.01	{0.213 0.201
	1000	2.74	{0.4809 0.5011	0.23 ± 0.01	{0.179 0.169

$T_c = 33°K$ $\quad n_c = 0.939 \times 10^{22}$ $\quad T_t = 13.8°K$ $\quad n_t = 2.30 \times 10^{22}$

(a) For $r_o = 2.917Å$ (b) For $r_o = 2.958Å$

In Table 1 we compare our measured value of the diffusion coefficients to that of the hard sphere Enskog value calculated according to equation (1). We also plot in Fig. 3 the ratio of the measured to the Enskog diffusion coefficients as a function of density. The hard sphere diameter of 2.917Å was arrived at from a measured value of the low density diffusion coefficient at 85°K and using equation (1).[10] An alternative hard sphere diameter of 2.958Å was derived from the equation of state measurements of Michels et al.[11] The high temperature hard sphere diameter of 2.57Å was derived from low density room temperature diffusion data.[10] We put $g(r_0) = (1-0.5\eta)/(1-\eta)^3$ where $\eta = \pi n r_0^3/6$, which is consistent with the best molecular dynamics equation of state of hard spheres.[12] We clearly observe a consistent shift towards greater enhancement compared to the Enskog value as the density increases.

In conclusion, we have measured the spectrum of incoherently scattered neutrons at eight densities and two temperatures. We find that the density dependence of the measured diffusion coefficients substantially deviate from the Enskog Kinetic Theory consistent with predictions of Alder et al which is indicated by the solid line in Fig. 3.[1]

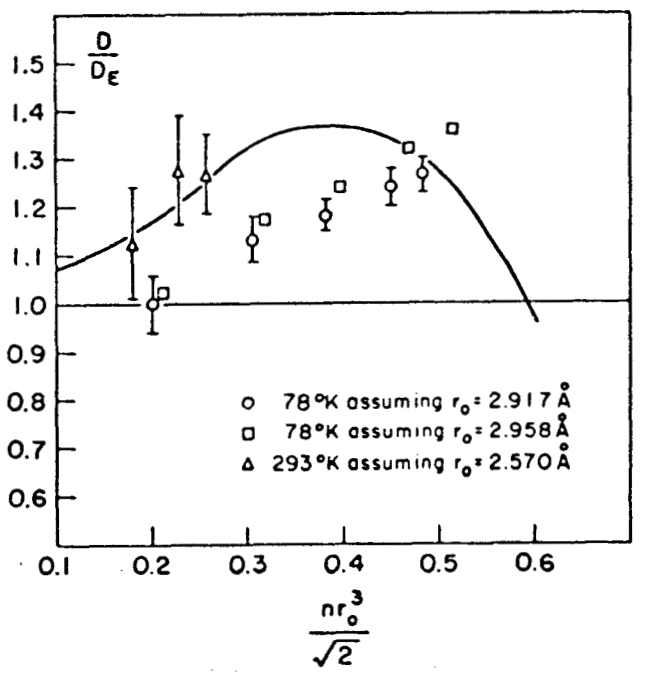


Fig. 3. D/D_E plotted as function of the reduced density. The solid line is taken from Alder et al[1] which represents enhancement of the hard sphere system.

The agreement between our experiment and the molecular dynamics experiment should not be expected to be quantitative because hydrogen molecules are not hard spheres and there is no unique way of assigning an equivalent hard sphere diameter to them. Thus the attractive part of the intermolecular potential as well as the soft repulsive core should reflect itself in the temperature dependence of D and r_0 in a way which is not present in the hard sphere computer data. Details of the experimental method and data analysis with kinetic theory[9] and generalized hydrodynamic theory will be presented elsewhere.

REFERENCES

1. B.J. Alder, D.M. Gass, and T.E. Wainwright, J.Chem.Phys. 53, 3813 (1970).
2. B.J. Alder and T.E. Wainwright, Phys.Rev. 1A, 18 (1970); B.J. Alder and T.E. Wainwright, Phys. Rev.Lett. 18, 988 (1967).
3. S. Chapman and T.G. Cowling, The Mathematical Theory of Non-Uniform Gases, 3rd ed., Cambridge U.P., London (1970).
4. G.F. Mazenko, Phys.Rev. 7A, 209, 222 (1973); J.R. Dorfman and E.G.D. Cohen, Phys.Rev.Lett. 25, 1257 (1970).
5. L. van Hove, Phys.Rev. 95, 249 (1954); R. Zwanzig, Phys.Rev. 133, A50 (1964).
6. R. Kleb, G.E. Ostrowski, D.L. Price and J.M. Rowe, Nuclear Inst. and Meth. 106, 221 (1973).
7. J.R.D. Copley, Comp.Phys.Comm. 7, 289 (1974).
8. S.H. Chen, Y. Lefevre and S. Yip, Phys.Rev. A8, 3163 (1973).
9. I.M. De Schepper, "Generalized Hydrodynamics for the Diffusion Process", Ph.D. Thesis, University of Nijmegen (1974) and private communications.
10. American Institute of Physics Handbook, McGraw-Hill, 2nd Ed. p. 2-236.
11. A. Michels et al, Physica 26, 393 (1960).
12. L. Verlet and J.J. Weis, Phys.Rev. A3, 939 (1972).

* Research supported by ERDA AT(11-1)3352. The authors gratefully acknowledge the generous help and hospitality of the Solid State Division of Argonne National Laboratory.

** On leave from AB Atomenergi, Studsvik, Sweden.

NEUTRON SCATTERING FROM DILUTE AND MODERATELY DENSE GASES

J. W. Dufty, L. J. Groome and K. E. Gubbins
Chemical Engineering and Physics Departments,
University of Florida, Gainesville, Florida 32611

and

P. A. Egelstaff
Physics Department, University of Guelph, Guelph,
Ontario, Canada

ABSTRACT

The dynamic and static structure factors, and also their pressure derivatives, for dilute and moderately dense gases are studied theoretically and experimentally. The density region of particular interest is that corresponding to the zeroeth and first order terms in a density expansion of the distribution function. For the static structure factor, the lowest order term provides direct information about the intermolecular pair potential, while the next higher term involves both the pair and triplet potentials. The corresponding terms in the expansion of the dynamic structure factor provide information about the two- and three-body dynamics. Theoretical and Monte Carlo calculations are presented, and compared with available data on krypton.

INTRODUCTION

With the advent of more powerful neutron sources and spectrometers it is now possible to obtain precise neutron scattering data for dilute and moderately dense gases. By taking accurate data at several density points along an isotherm it is possible to estimate the first few terms in a density expansion of the static and dynamic structure factors.[1] This improved experimental situation has prompted us to examine the theory of the structure factor for such gases, and also to carry out computer simulation. The theory is reviewed in the next section. This is followed by a description of the results for the static structure factor for noble gases (experiment and simulation), and a description of

kinetic modeling for the dynamic structure factor.

GENERAL THEORY

Static Structure Factor

A density expansion of the static structure factor yields (for monatomic molecules):

$$S(k) = 1 + \rho \int [g(r)-1]\, e^{i\underline{k}\cdot\underline{r}} d\underline{r} = 1 + \rho B(k) + \rho^2[B^2(k) + C_1(k) + C_2(k)] + \ldots \quad (1)$$

where

$$B(k) = \int f(r)\, e^{i\underline{k}\cdot\underline{r}}\, d\underline{r} \quad (2)$$

$$C_1(k) = \iint f(r)\, f(s)\, f(\underline{r}-\underline{s})\, e^{i\underline{k}\cdot\underline{r}}\, d\underline{r}d\underline{s} \quad (3)$$

$$C_2(k) = \iint [f(r)-1][f(s)-1][f(\underline{r}-\underline{s})-1][e^{-\Delta u(\underline{r},\underline{s})/kT} - 1]\, e^{i\underline{k}\cdot\underline{r}}\, d\underline{r}d\underline{s} \quad (4)$$

with $f(r) = e^{-u(r)/kT} - 1$, and $u(r)$ is the pair potential while $\Delta u(\underline{r},\underline{s})$ is the three-body potential. Thus, $B(k)$ contains complete information about the pair potential, while $C_2(k)$ provides an average over the triplet potential.

Dynamic Structure Factor

The dynamic (self-) structure factor, $S_s(k,\omega)$ may also be expanded in the density, from knowledge of the corresponding virial expansion of the generalized kinetic collision operator. A direct expansion of $S_s(k,\omega)$ in ρ does not lead to a uniform approximation with respect to ω (e.g. it is not valid for small ω). More appropriately the density expansion is carried out holding $\alpha \equiv \omega^{-1}\rho$ constant. The result is then uniformly good for all ω, at sufficiently low density,

$$S_s(k,\omega) = S_s^{(o)}(k,\omega) + \rho\, S_s^{(1)}(k,\omega) + \ldots \tag{5}$$

where

$$S_s^{(o)}(k,\omega) \equiv -2\ \mathrm{Im}\ \omega^{-1}(1,R1) \tag{6}$$

$$S_s^{(1)}(k,\omega) \equiv -2\ \mathrm{Im}\ \omega^{-1}(1,R\hat{M}^{(1)}R1) \tag{7}$$

$$R(k,\omega) \equiv [1 - \omega^{-1}\underline{k}\cdot\underline{v} - i\alpha\hat{M}^{(o)}]^{-1} \tag{8}$$

The scalar product (A,B) is defined to be $(A,B) \equiv \int d\underline{v}\phi(v)A^*(v)B(v)$, and $\phi(v)$ is the Maxwell-Boltzmann distribution. The operators $\hat{M}^{(o)}$ and $\hat{M}^{(1)}$ are the leading terms in the virial expansion of the generalized kinetic collision operator[2],

$$\hat{M}(k,\omega) = \hat{M}^{(o)}(k,\omega) + \rho\hat{M}^{(1)}(k,\omega) + \ldots \tag{9}$$

The operator $\hat{M}^{(o)}(k,\omega)$ is a generalization of the usual Boltzmann (Lorentz) operator,

$$\hat{M}^{(o)}(k,\omega) \equiv -(m^2\phi(v))^{-1}\int_0^\infty dt\ e^{-i\omega t}\int d\underline{v}_2\ d\underline{r}_{12}\ \underline{F}(r_{12})\cdot\vec{\nabla}_v\ S_{-t}(12)$$

$$f_o(1,2)\vec{F}(r_{12})\cdot\vec{\nabla}_{v_1} \tag{10}$$

where $\vec{F}(r)$ is the interatomic force, $f_o(12)$ is the low density equilibrium two-particle distribution function, and $S_t(12)$ is the two-particle time development operator. A similar expression may be obtained for $\hat{M}^{(1)}(k,\omega)$ in terms of three-body collision dynamics[2], but is somewhat lengthy and will not be given here. Thus $S_s^{(o)}(k,\omega)$ contains the information regarding binary collision dynamics, while $S_s^{(1)}(k,\omega)$ provides a measure of the triplet dynamics.

STATIC PROPERTIES

In this section we discuss some Monte-Carlo calculations of g(r) at densities where the attractive part of the potential is important. This region can be shown to be $\rho \lesssim 2\rho_c$, where ρ_c is the critical density. Egelstaff et al.[3] have computed g(r) by Monte-Carlo methods using the L-J potential, the Barker[4] potentials and the Axilrod-Teller three-body potential. At low density the main feature of g(r) is a large peak positioned at $r_m \simeq$ the potential minimum. To some extent the curve can be characterized by the amplitude of this peak. Figure 1 shows the value of $g(r_m)$ as a function of density for krypton gas at room temperature calculated from the Barker potential using the virial expansion or Monte Carlo methods. Similar data for the Barker plus Axilrod-Teller potentials are given in Figure 1. These curves dip in the neighborhood of ρ_c, showing that critical fluctuations affect the pair correlations to some degree. The calculations using a two plus three body potential show that the size of the dip is increased and because the Axilrod-Teller potential is repulsive the sign of this effect is expected.

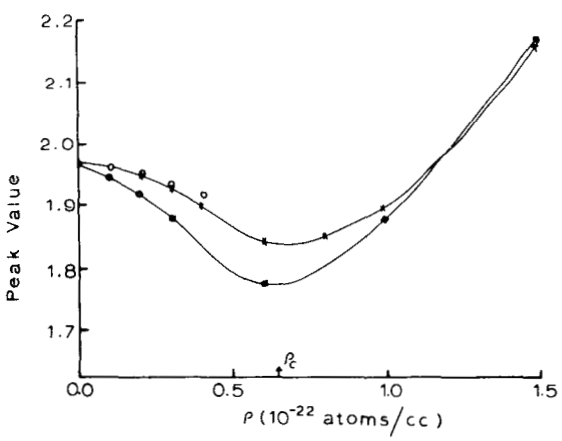


Fig. 1. $g(r_m)$ as a function of density. Comparison of Barker (o virial series, x Monte-Carlo), and Barker plus Axilrod-Teller (● virial series, ☒ Monte-Carlo).

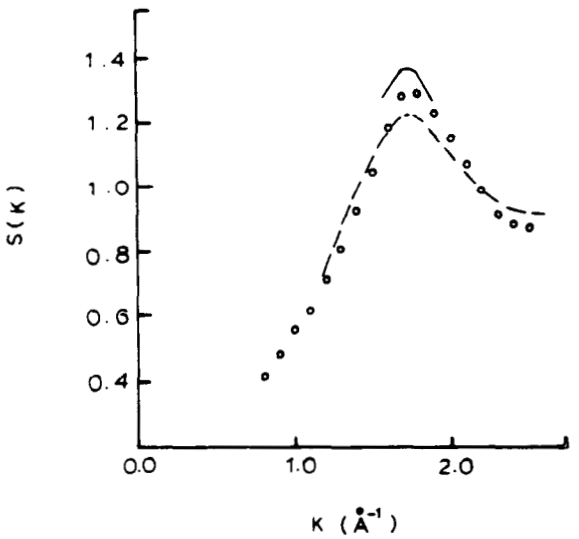


Fig. 2. Structure factor of krypton at 218 K and $\rho=0.8\rho_c$. (o experimental values[5], dashed and full lines are Monte-Carlo for L-J and Barker potentials, respectively).

Calculations of this type should be Fourier transformed, as shown in Eq. (1), and compared to experiments on S(k). The only published experiments are those of Winfield and Egelstaff[5] on krypton gas near the C.P. Figure 2 is a comparison of one of their data sets with the pair-potential calculations, for L-J and Barker potentials. The sensitivity of this region to choice of potential and the need for very accurate data is clear. It seems probable that the two plus three body calculation would give better agreement, but is not available yet. It is also apparent that the observed peak position is at a higher value of k than the calculated one, but it is not yet clear whether this is due to a small error in the two body or the three body potential.

KINETIC MODEL FOR $S_s(k,\omega)$

Insofar as the collision dynamics of $\hat{M}^{(o)}$ and $\hat{M}^{(1)}$ can be measured only through $S^{(o)}(k,\omega)$ and $S^{(1)}(k,\omega)$, it is important to have an accurate means of calculating these functions from the properties of $\hat{M}(k,\omega)$. Present calculations have generally made use of "kinetic modeling" techniques, based on a formal spectral decomposition of the collision operator,

$$\hat{M}(k,\omega) = \sum_{\alpha} \lambda_{\alpha} P_{\alpha} \tag{11}$$

where P_{α} are projection operators onto the eigenfunctions (possibly improper) of $\hat{M}$ and λ_{α} are the corresponding eigenvalues. An approximation of order N consists of assuming $\lambda_{\alpha} = \lambda_N$ for all $\alpha \geq N$. Present calculations[6] have been limited to hard spheres and used a kinetic model with N>30. This is less practical for generalized collision operators for real potentials.

An optimization of usual kinetic modeling involving more tractable calculations is being studied. For example, the structure factor $S_s(k,\omega)$ may be written

$$S_s(k,\omega) = -2\mathrm{Im}\,\frac{1}{\omega}\,[(1,R_N 1) + (1,R_N[\hat{M}-\hat{M}_N]R)]$$

$$R_N(k,\omega) \equiv [1-\omega^{-1}\underline{k}\cdot\underline{v}-i\alpha\hat{M}_N]^{-1} \tag{12}$$

and $\hat{M}_N$ is the order N kinetic model. The optimization consists of replacing the eigenvalue λ_N by a function $\lambda(k,\omega)$ which is determined by minimizing the second term in Eq. (12). This minimization may be chosen in a variety of ways, for example using standard variational principles. The most elementary choice, however, is simply to require this term to be at least of second order in $(\hat{M}-\hat{M}_N)$, i.e.,

$$(1,R_N[\hat{M}-\hat{M}_N]R_N\ 1) = 0 \tag{13}$$

or, more explicitly,

$$\lambda(k,\omega) = (1,R_N\mathcal{P}_N\hat{M}\,\mathcal{P}_N R_N\ 1) \,/\, (1,R_N\mathcal{P}_N R_N) \tag{14}$$

Here $\mathcal{P}_N = 1-\sum_{\alpha}^{N-1} P_\alpha$. The structure factor is then approximately given by the first term in Eq. (12). It is hoped in this way $\lambda(k,\omega)$ may better sample the spectrum of $\hat{M}$ so that lower order kinetic models may be used. To test these ideas a calculation of $S_s(k,\omega)$ from a Fokker-Planck kinetic equation was considered. (This example was chosen because the exact solution may be obtained for comparison). Calculations were performed using a standard kinetic model of N=2 and the corresponding optimized kinetic model (OKM) of the same order using Eq. (14). Figure 3 shows a comparison of $R(x,y) = kv_o S_s(k,\omega)$ with the exact result for a typical value of k in the difficult transition region between hydrodynamic and free particle limits (here $x=\omega/kv_o$, $y=4\rho^*/kr_o$, v_o is the thermal velocity and ρ^* is the reduced density.) The agreement of the OKM is even better at other k values and clearly represents an improvement of the N=2 kinetic modeling. Figure 4 shows a comparison of the half width at half maximum (HWHM) as a function of k and indicates, as noted, that the approximation is uniformly good for all k. Present results suggest that accurate values for $S_s(k,\omega)$ from the low density Boltzmann kinetic equation should result for the optimized kinetic model with N=2 or 3. These calculations are in progress.

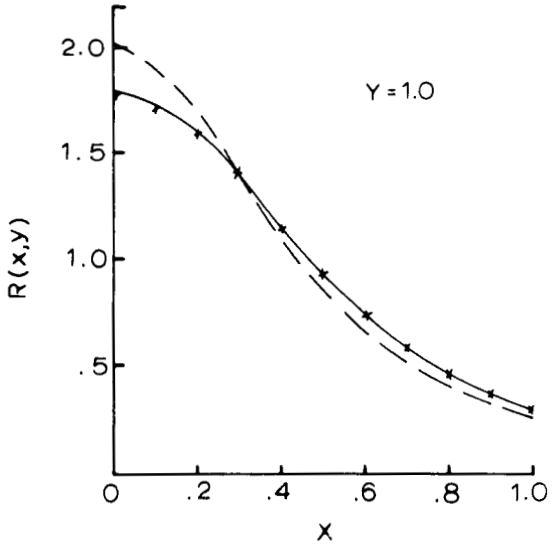


Fig. 3. R(x,y) for y=1.0. Comparison of exact result —, OKM x, and N=2 kinetic model ---.

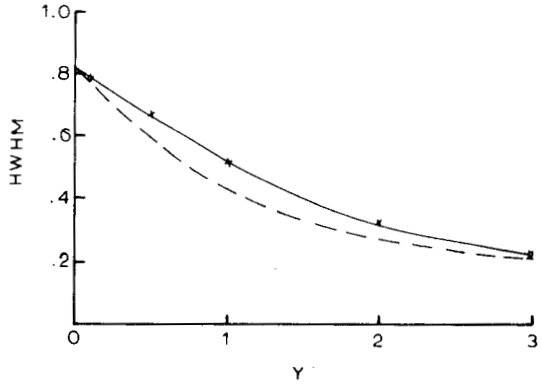


Fig. 4. Half width of R(x,y) at half maximum as a function of y.

ACKNOWLEDGEMENT

We thank the National Science Foundation for financial support of this work.

REFERENCES

1. P. A. Egelstaff, D. Litchinsky, J. B. Suck and W. Glaeser, to be published.
2. C. D. Boley and R. C. Desai, Phys. Rev. 7, 1700 (1973).
3. P. A. Egelstaff, S. S. Wang, S-D Wang, R. McPherson, R. L. Henderson, and A. Teitsma, to be published (1976).
4. J. A. Barker, R. O. Watts, J. K. Lee, T. D. Schafer, and Y. T. Lee, J. Chem. Phys. 61, 3081 (1974).
5. D. J. Winfield and P. A. Egelstaff, Can J. Phys. 51, 1965 (1973).
6. G. Mazenko, T. Wei, and S. Yip, Phys. Rev. 6, 1981 (1972).

NEUTRON DIFFRACTION STUDIES OF LIQUIDS AT HIGH MOMENTUM TRANSFER

J. H. Clarke, J. C. Dore and G. Walford
Physics Laboratory, The University of Canterbury, Kent, England

ABSTRACT

Time-of-flight techniques have been developed for use with pulsed neutron sources. The high intensity of epithermal neutrons enables measurements to be made for a wide range of Q-values (< 60 $\AA^{-1}$). The features of a new total scattering spectrometer installed at the Harwell Electron Linac are described briefly and the advantages of the method illustrated by recent measurements on liquid carbon suboxide.

INTRODUCTION

The current use of time-of-flight diffraction for structural studies has been reviewed by Buras[1]. The main development in recent years has centred on the new pulsed neutron facilities associated with accelerator beams. Earlier work at the Harwell Electron Linac has been previously described[2] and a critical comparison of reactor and linac techniques for liquid studies has also been presented[3]. The purpose of the present paper is to examine these new developments in terms of the specific information that is obtained from the data concerning the structural properties of molecules for the liquid phase. This information is useful for general considerations but has a particular importance for the accurate determination of the contribution from inter-molecular terms which is directly related to the structural arrangement of the molecules in the liquid.

The initial studies have concentrated on diatomic species (e.g. N_2, O_2 and Br_2) which represent the simplest case of molecular liquids. It is therefore interesting to extend the study to more complex systems and the linear molecule, carbon suboxide (C_3O_2) was chosen for this investigation. Other work on a range of tetrachloride liquids is presented in a separate paper[4].

EXPERIMENTAL

A schematic diagram of the TSS spectrometer at the Harwell Electron Linac is shown in Fig. 1. The main feature of the previous instrument, the wide angle detector bank at a scattering angle of 150°, which is arranged in a time-focusing configuration, has remained unchanged. An automatic sample changer has been fitted into the sample well and operates inside a chamber which may be evacuated to reduce air scattering. The overall performance of the spectrometer has been considerably improved by the reduction of background levels. A discussion of resolution and intensity factors has been presented elsewhere[2,3].

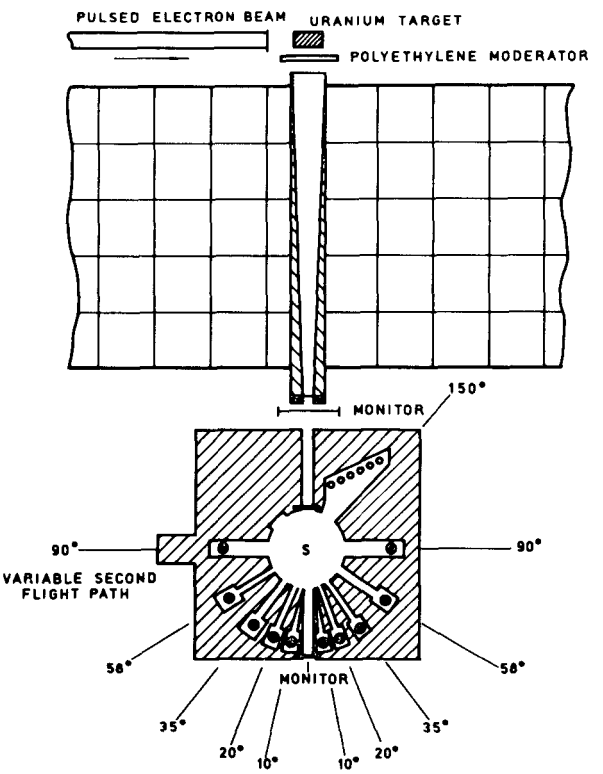


Fig. 1. The TSS spectrometer at the Harwell Electron Linac

The TOF measurements for each detector are made for 'sample plus container', 'empty container', 'standard vanadium sample', 'background' and also a powdered nickel sample. The data aquisition is controlled by a PDP 11/10 on-line computer. The vanadium measurements are used to deter-

mine the shape of the incident neutron spectrum and the nickel powder measurements are used to calibrate the time-of-flight scale. Data reduction methods are carried out with the programme LINDA[5] which corrects for absorption, multiple-scattering and other experimental features. For measurements on liquid carbon-suboxide, a thin-walled aluminium container of 8.0mm internal diameter was attached to a Peltier device and the liquid condensed at -42°C from the vapour phase. Since the instrument has fixed-angle detectors, the cylindrical sample configuration conventionally used in reactor experiments is not necessary, so that it is sometimes convenient to use plate samples. This is particularly useful for situations where the diffraction pattern has only small oscillation amplitude as the overall count rate can be considerably improved by use of a wide area beam. This method was used for the study of tetrachloride liquids[4] which were held in a thin-walled vanadium plate container.

THEORY

At high values of momentum-transfer ($\hbar Q$), the liquid structure factor $S_m(Q)$, which is obtained from the diffraction pattern corresponds to the molecular form factor $f_1(Q)$ which characterises the structure of a single molecular unit[6]. For C_3O_2, we may write

$$S_m(Q) \rightarrow f_1(Q) = \frac{1}{(3b_c+2b_o)^2}\left\{3b_c^2 + 2b_o^2 + \sum_{i\neq j} b_i b_j j_o(Qr_{ij})\exp(-\gamma_{ij}Q^2)\right\} \quad (1)$$

where b_c and b_o are the coherent scattering lengths for C and O, r_{ij} represents the molecular bond-length for atoms i and j, and the exponential term corresponds to Debye-Waller factor allowing for intramolecular vibrations. There are six oscillatory terms corresponding to the different atom pairs but only two independent bondlengths corresponding to the nearest neighbour C=O and C=C bonds.

RESULTS AND ANALYSIS

The linac data has been combined with reactor data to give the $S_m(Q)$ curve shown in Fig. 2. Significant oscillations are seen to extend to

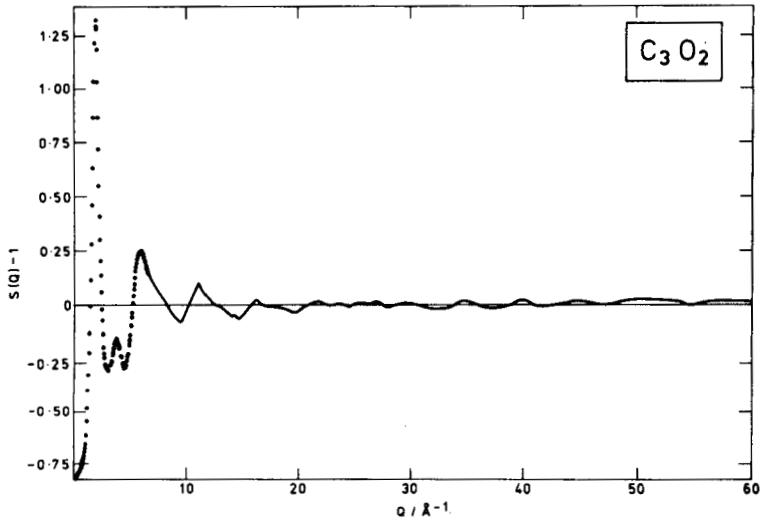


Fig. 2. Combined reactor and linac data for liquid carbon suboxide

60 $Å^{-1}$. The distribution function d(r) in real space is obtained from the Fourier transform:-

$$d(r) = 4\pi r\rho_o[g(r) - 1] = \frac{2}{\pi}\int_0^\infty Q\, i(Q) \sin Qr\, dQ \qquad (2)$$

where i(Q) is the oscillatory part of the diffraction pattern and the other symbols have their usual meaning. In practice the data are terminated at some point, Q_{max} so that the integral can only be evaluated for a certain Q-value range. The truncation of the data leads to a decrease in the spatial resolution which is given approximately by $\Delta r \sim 2\pi/Q_{max}$ and is dependent on the shape of any modification function used in the transform procedure.

The transform of the i(Q) data for C_3O_2 is shown in Fig. 3 for three termination points at 40, 50 and 60 $Å^{-1}$. The improvement in resolution is clearly apparent from the shape of the first interatomic peak at

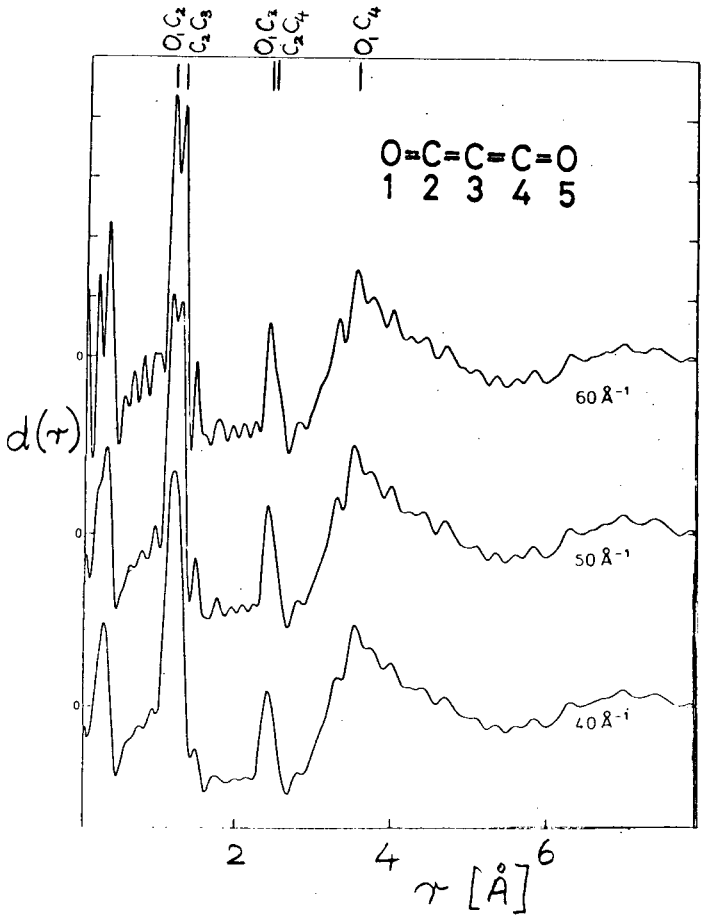


Fig. 3. The Fourier transform of the liquid carbon suboxide data showing the effect of different truncation points in Q.

$\sim$ 1.2 Å which is split into two distinct components corresponding to CO and CC bond-lengths when the wider Q-range is used. Another peak is clearly visible at 2.5 Å which has an asymmetric structure due to two overlapping peaks. The distribution also contains many ripples which probably result from statistical uncertainties in the original $S_m(Q)$ data. These high frequency components in the transform cannot exist in the real liquid and are often removed using refinement techniques based on iterative procedures. However, in this case, it is not clear how this method might be applied without destroying the excellent resolution obtained for the intramolecular terms. The derived bond-lengths are found to be in excellent agreement with electron diffraction measurements[7] on the vapour phase after application of a molecular recoil correction[8]; the results are listed in Table 1.

Table 1. A comparison of molecular parameters for C_3O_2 (distances in Å)

	bond	O_1-C_2	C_2-C_3	O_1-C_3	C_2-C_4	O_1-C_4	O_1-O_5
liquid (neutron diffraction)		1.16(5)	1.29(8)	2.44	(2.55)	3.59	-
vapour (electron diffraction)		1.162	1.288	2.444	2.48	3.63	4.75

CONCLUSION

The importance of diffraction measurements over a wide Q-value range is well illustrated in this example. Since the O_1-C_2 and C_2-C_3 bonds differ by only 0.13 Å, the oscillatory terms in the form factor are out of phase in the region of 25 $Å^{-1}$ which results in almost complete cancellation. The high Q-value data are therefore required to provide sufficient information in the region of 50 $Å^{-1}$ where the oscillations are in phase but even a $Q_{max} \sim 60$ $Å^{-1}$ is insufficient to resolve the closer O_1C_3 and C_2C_4 bonds. The features discussed here for liquids will also apply to the study of amorphous solids.

REFERENCES

1. B. Buras, Report 75-B, Copenhagen University and Pelten Conference (1975).
2. R. N. Sinclair et al, Nuc. Inst. & Meth. 117, 445 (1974).
3. J. C. Dore and J. H. Clarke, Nuc. Inst. & Meth., to be published.
4. J. H. Clarke, J. C. Dore and G. W. Stanton, paper , this conference.
5. J. H. Clarke, A.E.R.E. Report R8121, (1976).
6. J. G. Powles, Advances in Physics 22, 1 (1973).
7. M. Ianimoto, K. Kuchitsu and Y. Morris, Bull. Chem. Soc. Jap. 43, 2776 (1970).
8. J. C. Dore, J. H. Clarke and G. Walford, paper , this conference.

ACKNOWLEDGEMENTS

Two of us wish to thank the Science Research Council (JHC & GW) and the Atomic Energy Research Establishment (JHC) for financial support.

LOW FREQUENCY MOLECULAR VIBRATIONS IN 1-BROMOPENTANE AND 1,5-DIBROMOPENTANE BY NEUTRON INELASTIC SCATTERING*

Y. P. Sharma, H. R. Danner and H. Kim
Departments of Physics and Chemistry
University of Missouri
Columbia, MO 65201

ABSTRACT

The torsional and bending fundamentals in solid 1-bromopentane and 1,5-dibromopentane are determined from measurements of their incoherent neutron spectra. These modes appear between 50 and 500 cm^{-1} and are assigned on the basis of a normal coordinate analysis in which only intramolecular valence force fields for each molecule are used. Comparison with similar measurements on pentane shows that replacing the end hydrogen atoms with the heavier bromine atoms drastically alters the nature of the skeletal motions.

INTRODUCTION

Recent incoherent neutron scattering measurements[1] have shown that the low frequency intramolecular vibrations in the solid n-paraffins can be described reasonably well using a relatively simple model requiring a minimal number of force constants. These measurements have been extended to other closely related compounds in order to further test the model. In the present paper the neutron spectra of 1-bromopentane and 1,5-dibromopentane have been measured to determine the effect of tying down first one and then both ends of a paraffin chain with a heavy atom.

*Work supported by the National Science Foundation.

Except for the case of propyl bromide[2], where a complete spectral assignment has been made, the low frequency infrared studies of the bromo-alkanes[3-6] have been limited to the band characterization of the C-Br stretching modes. These stretching modes are observed in the region from 500 cm^{-1} to 700 cm^{-1} and their frequencies are sensitive to the conformational structure of the molecule. Data on the skeletal torsion and bending vibrations, which occur at lower frequencies and are even more sensitive to the molecular structure, are rare in the literature. Since the predominant conformation in solid propyl bromide is TT (trans-trans) in which the bromine atom lies in the plane of the carbon backbone, we have assumed that TT is the predominant conformation in both solid 1-bromopentane and 1,5-dibromopentane.

EXPERIMENTAL

The neutron spectra presented in this study were measured at a scattering angle of 27° using the cold-neutron, time-of-flight spectrometer[7] at the Missouri University Research Reactor. This instrument utilizes the full cold spectrum (0-5.2 meV) transmitted by a refrigerated beryllium filter as the incident beam and post pulse modulation to analyze the scattered beam. The energy resolution of the spectrometer (which is limited by the time resolution at large energy transfers and by the uncertainty of the incident energy at low energy transfers) varies from 4 to 7% over the range of energy transfers (50 - 500 cm^{-1}) considered.

Reagent grade samples were used as obtained from the manufacturer (Matheson, Coleman and Bell) and contained in a thin (0.03 cm), large diameter (15 cm) holder fabricated with very thin (0.008 cm) stainless steel windows. In each case the sample was cooled into its solid phase using a helium-atmosphere, liquid nitrogen cryostat.

The experimental time-of-flight spectra for 1-bromopentane and 1,5-dibromopentane are shown in Figures 1 and 2, respectively. The spectra have been corrected for background (using measurements from the empty holder), chopper transmission, detector efficiency and the

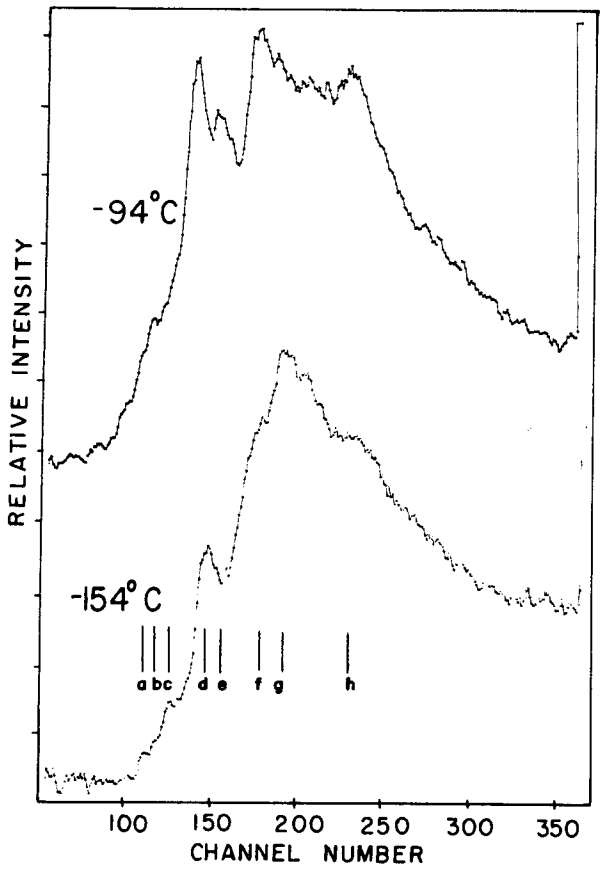


Fig. 1. Neutron spectra of solid 1-bromopentane.

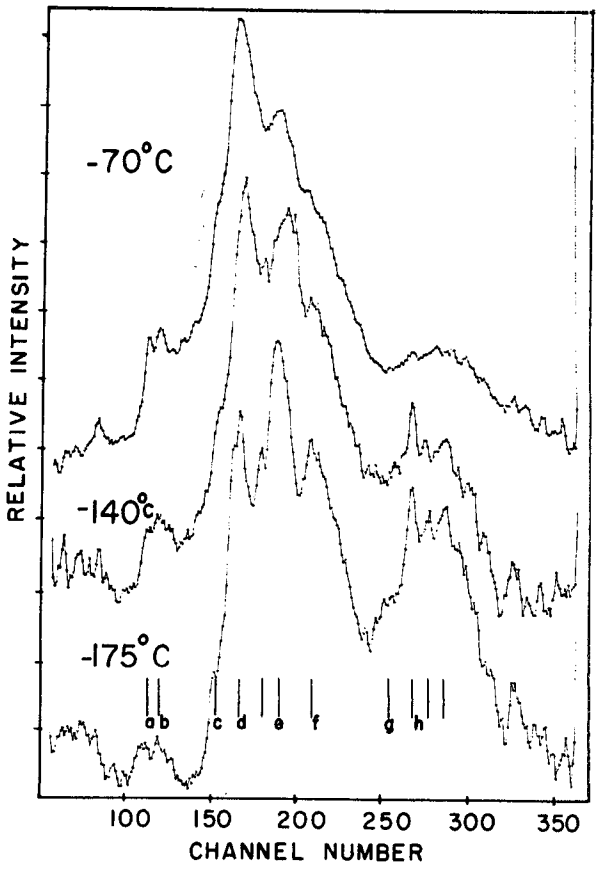


Fig. 2. Neutron spectra of solid 1,5-dibromopentane.

attenuation of the scattered beam due to air and aluminum scattering. The data as presented have been smoothed over three points. Finally the spectra have been measured at several temperatures to aid in distinguishing adjacent bands by changing their relative populations.

SPECTRAL ASSIGNMENTS

Most of the structure observed in the neutron spectra of both solids is due to the CCC and CCBr skeletal bending modes, and to torsional librations around the C-C single bonds. In order to assign the observed bands to specific normal modes, we have calculated the normal frequencies using the set of valence force constants that was used to assign the observed bands in the n-paraffins together with three additional constants, which determine the relative motion of the bromine atoms. The values of the latter were adjusted to reproduce the

assigned skeletal frequencies of propyl bromide[2] and butyl bromide[3]. These frequencies, along with the values adopted for all of the force constants, are listed in Table 1.

This set of force constants was then used to calculate the normal frequencies of 1-bromopentane and 1,5-dibromopentane. The frequencies calculated for both solids are compared in Table 2 with the frequencies of the observed bands in the neutron spectra. In the case of 1-bromopentane, the end-methyl torsional band, which appears as a sharp band at 240 cm^{-1} in all of the solid n-paraffin spectra, is identified easily at 234 cm^{-1}. The two higher bands at 420 cm^{-1} and 330 cm^{-1} (labeled a and c in Fig. 1) are assigned to the upper pair of skeletal bending modes. The rest of the bands at lower frequencies are assigned by their proximity to the calculated values.

In the spectrum of 1,5-dibromopentane we do not observe the end-methyl torsion band in the frequency range 230-240 cm^{-1}. The bands at 415 cm^{-1} and 361 cm^{-1} (labeled a and b in Fig. 2.) are assigned to the upper pair of skeletal bending modes, while the bands at 181 cm^{-1} and 177 cm^{-1} (labeled d in Fig. 2. and only partially resolved at the lowest temperature) are assigned to the two highest torsional modes. This latter assignment is consistent with the fact that bands associated with torsional modes generally appear sharper in our data than bands due to bending modes. The sharp band at 49 cm^{-1} is assigned to the lowest torsional mode. As before the rest of the labeled bands are assigned by their proximity to calculated frequencies.

The calculations and assignments presented are considered preliminary. For example, we have left unassigned three relatively sharp peaks at 40, 44 and 148 cm^{-1} in the low temperature spectrum of 1,5-dibromopentane; these may be due to excited and/or overtone bands of the lowest torsional or they may be due to intermolecular vibrations which we have not considered. However the overall agreement between observed and calculated frequencies is very encouraging, particularly in view of the fact that the model employs a minimum number of force constants whose values were predetermined from previous infrared and

Table 1. Frequencies (in cm^{-1}) of 1-bromopropane and 1-bromobutane to adjust the bromine valence force constants.

	Propyl Bromide		Butyl Bromide	
	Observed[2]	Calculated*	Observed[3]	Calculated*
Stretching	645	649	643	643
Bending	311	298	397	389
	220	226	228	257
Torsion	220	234	169	161
	133	132		

*the values of the force constants are:

k_r (C-C)	= 4.5 mdyn/A	H'_δ (HCCH)	= 0.0103 mdynA/rad
k_r (C-H)	= 4.7 "	H'_δ (HCCC)	= 0.0103 "
k_r (C-Br)	= 2.3 "	H''_δ (CCCC)	= 0.055 "
H_α (HCH)	= 0.55 mdynA/rad	H'''_δ (BrCCC)	= 0.035 "
H_β (HCC)	= 0.65 "	H'''_δ (BrCCH)	= 0.035 "
$H_{\alpha'}$ (BrCH)	= 1.0 "	H_ω (CCC)	= 1.05 "
$H_{\beta'}$ (BrCC)	= 1.0 "	$H_{\omega\omega'}$ (CCC)	= 0.5 "

Table 2. Observed and calculated frequencies (in cm^{-1}) of n-pentane, 1-bromopentane and 1,5-dibromopentane.

	n-pentane		1-bromopentane			1,5-dibromopentane		
	Observed	Calc.	Observed		Calc.	Observed		Calc.
Bending	450	428	420	(a)*	417	415	(a)*	413
	386	381	330	(c)	354	361	(b)	342
	180	177	198	(e)	197	210	(c)	207
			121	(g)	123	131	(e)	142
						59	(g)	67
Torsion	240	241	234	(d)	240	181	(d)	185
		238			171	177	(d)	161
	136	139	140	(f)	135	100	(f)	95
		122	75	(h)	70	49	(h)	54

*Refers to band labels used in Figures 1 and 2.

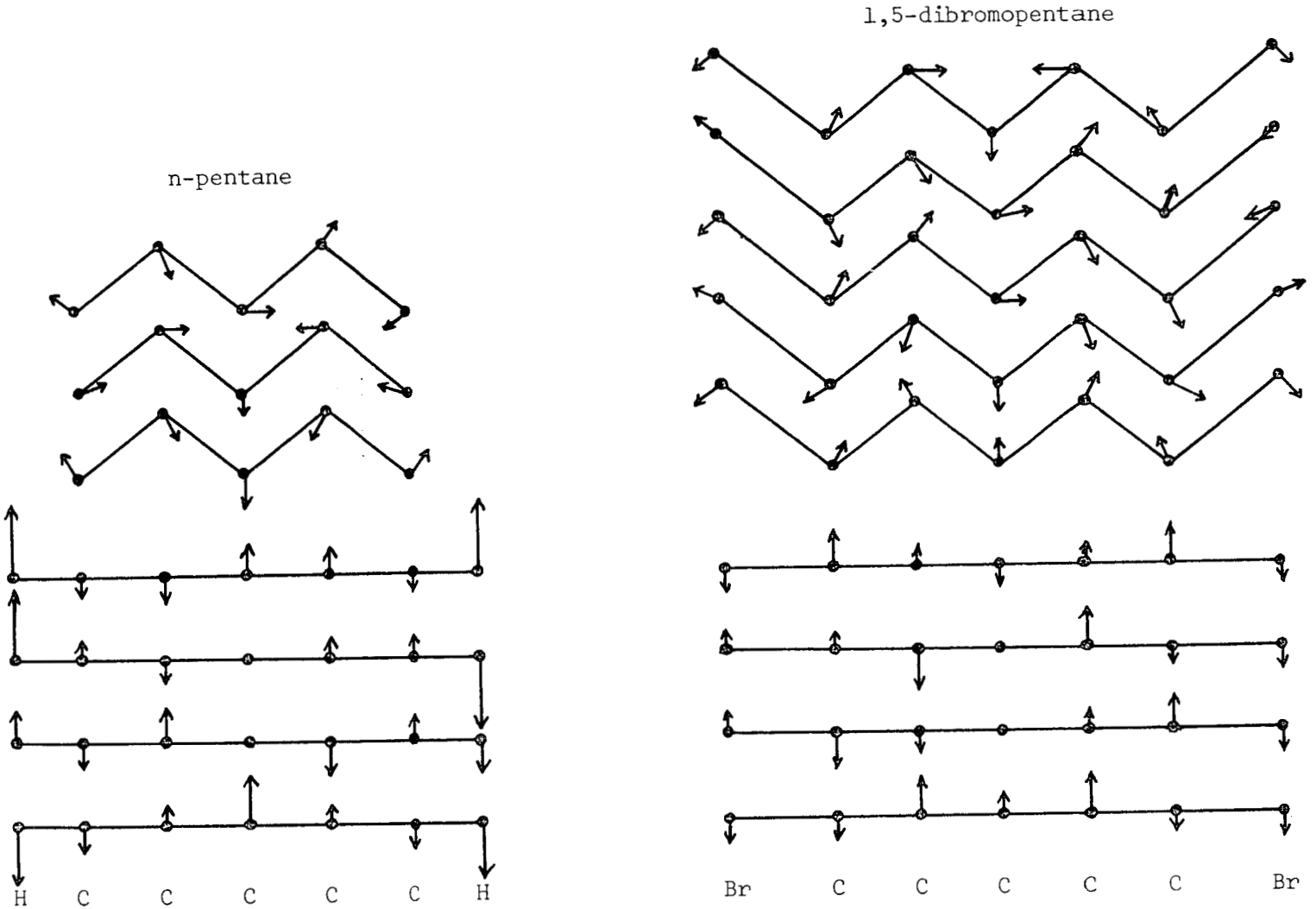


Fig. 3. Approximate relative amplitudes of the skeletal bending (upper) and skeletal torsion (lower) normal modes in n-pentane and 1,5-dibromopentane.

neutron spectra. Moreover, the calculated amplitudes of the motions of the individual atoms in the various normal modes are quite reasonable. Fig. 3 shows a comparison of the relative amplitudes of motion of the atoms in the skeletal bending and torsion modes in n-pentane and 1,5-dibromopentane.

REFERENCES

1. K.W. Logan, H.R. Danner, J.D. Gault and H. Kim, J. Chem. Phys. 59, 2305 (1973).
2. M. Hayaski, K. Ohno and H. Murata, Bull. Chem. Soc. Jap. 46, 2332 (1973).
3. T. Fujiyama, Bull. Chem. Soc. Jap. 45, 3016 (1972).
4. F.F. Bentley, N.T. McDevitt and A.L. Rozek, Spectrochim. Acta 20, 105 (1964).
5. N.T. McDevitt, A.L. Rozek, F.F. Bentley and A.P. Davidson, J. Chem. Phys. 42, 1173 (1965).
6. J.J. Shipman, V.L. Folt and S. Krimm, Spectrochim. Acta 18, 1603 (1962).
7. J.D. Gault, Ph.D. thesis, University of Missouri, Columbia, MO (1970).

THE DYNAMICS OF LIQUID ^{3}He

H.R. Glyde
Physics Department, University of Ottawa
Ottawa, Ontario, Canada K1N 6N5

F.C. Khanna
Atomic Energy of Canada Limited
Chalk River Nuclear Laboratories
Chalk River, Ontario, Canada K0J 1J0

ABSTRACT

The particle density and spin density correlations appearing in the dynamic form factor, $S(Q,\omega)$, of liquid ^{3}He are calculated within a simple RPA model employing Landau parameters to describe the quasi-particle interaction. The purpose is to investigate the temperature dependence of these correlations and the importance of the incoherent scattering of neutrons from liquid ^{3}He.

INTRODUCTION

Recent pioneering experiments[1] of neutron inelastic scattering from liquid ^{3}He have stimulated new interest in the dynamics of normal liquid ^{3}He. The experiments measure a dynamic form factor[2]

$$S(Q,\omega) = (\sigma_c/\sigma_T)\ S_c(Q,\omega) + (\sigma_i/\sigma_T)\ S_i(Q,\omega)$$

having a coherent, $S_c(Q,\omega)$, and an incoherent, $S_i(Q,\omega)$, part weighted by their respective cross sections $\sigma(\sigma_T = \sigma_c+\sigma_i)$. Here

$$S_c(Q,\omega) = \frac{1}{N}\int dt\ e^{-i\omega t} \langle\rho(-Q,0)\rho(Q,t)\rangle$$

and

$$S_i(Q,\omega) = \frac{3}{N}\int dt\ e^{-i\omega t} \langle G_z(-Q,0)G_z(Q,t)\rangle$$

are the form factors for the density, $\rho = \rho_\uparrow + \rho_\downarrow$, and spin-density, $G_z = \frac{1}{2}(\rho_\uparrow - \rho_\downarrow)$, correlations respectively, where $\rho_\uparrow(\rho_\downarrow)$ is the density of ^{3}He having spin parallel (anti-parellel) to the z axis.

Pines and Nozières[3] investigated $S_c(Q,\omega)$ in detail - particularly in the limit of non-interacting ^{3}He where both $S_c(Q,\omega)$ and $S_i(Q,\omega)$ become equal to the non-interacting value $S_0(Q,\omega)$. Aldrich[4] and Pines[5] have considered $S_c(Q,\omega)$ within the random phase approximation (RPA) employing an extension of the Landau theory to describe the quasi-particle interaction, $v(Q)$. Stirling et al.[1] also presented an RPA theory of $S_c(Q,\omega)$ taking $S_i(Q,\omega) = S_0(Q,\omega)$. All this work considers T = 0°K only.

THE MODEL

Here we present a simple RPA model of both $S_c(Q,\omega)$ and $S_i(Q,\omega)$, which is similar but less sophisticated than that of Aldrich, and consider T between 0.05 K and 0.63 K. To parameterize, we interpret the spin symmetric interaction, $v^s(Q)$, appearing in $S_c(Q,\omega)$ and the spin antisymmetric interaction, $v^a(Q)$, appearing in $S_i(Q,\omega)$ as scattering amplitudes and replace them by the corresponding Landau amplitudes[3],

$$v^s(Q) = A^s(Q) \sim \frac{2\varepsilon_F \Omega_0}{3} [F_0^s + F_1\lambda^2]$$

$$v^a(Q) = A^a(Q) \sim \frac{2\varepsilon_F \Omega_0}{3} [F_0^a + F_1\lambda^2]$$

Here ε_F is the Fermi energy, Ω_0 is the volume per particle, and $\lambda = (\omega/Q)/v_F$ is the ratio of the phase velocity to Fermi velocity. The model thus contains 3 parameters $F_0^s = 0.91$, $F_0^a = -2.0$ and $F_1 = 2.03$ dictated by other experiments with an effective mass $m^*/m = (1 - F_1/3)^{-1} = 3.1$. Scattering from single particle-hole excitations only is included and with this parameterization exactly 1/2 of the Placzek (f) sum rule is accounted for. To calculate the dynamic susceptibility of non-interacting ^{3}He appearing in the RPA expression, we have used the finite temperature result derived by Khanna and Glyde[6].

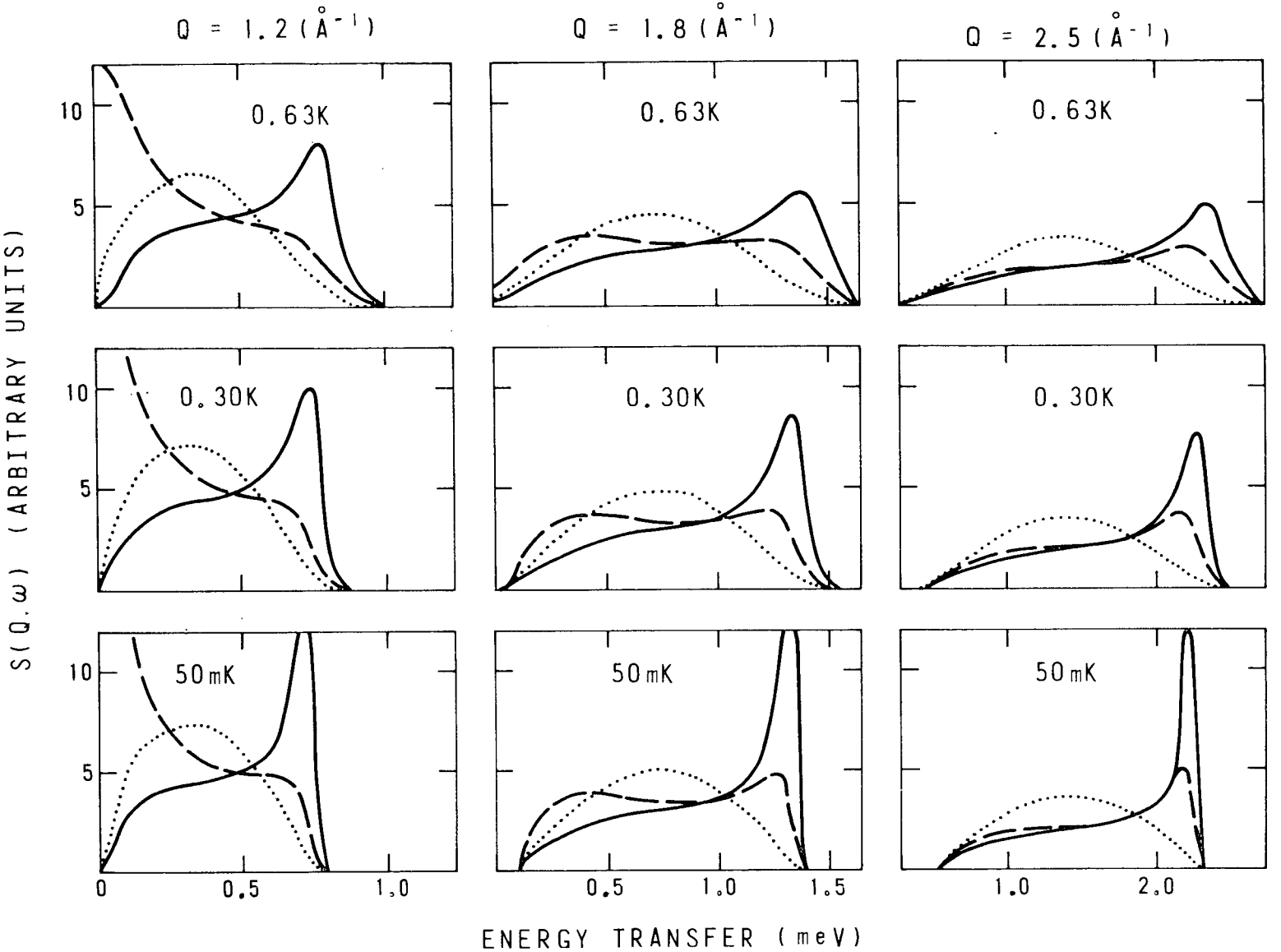


Fig. 1. The dynamic form factors $S_0(Q,\omega)$ ····, $S_c(Q,\omega)$ ——, and $S_i(Q,\omega)$ ----.

THE RESULTS

Figure 1 shows the $S_0(Q,\omega)$, $S_c(Q,\omega)$ and $S_i(Q,\omega)$ for three wave vectors Q and at three temperatures. There we see that decreasing the temperature sharpens the structure of $S(Q,\omega)$. The incoherent part $S_i(Q,\omega)$ makes a large contribution at small $\hbar\omega$ for low Q since at small $\hbar\omega$ the $v^a(Q)$ is negative. At high Q, where $\hbar\omega$ is correspondingly larger, $F_1\lambda^2$ dominates making $v^a(Q)$ positive so that $S_i(Q,\omega)$ has a form similar to $S_c(Q,\omega)$.

The present model shows a zero sound mode outside the single particle-hole spectrum for $Q \lesssim 0.4$ $\mathring{A}^{-1}$. The peaks in $S_c(Q,\omega)$ in Fig. 1 correspond to a damped zero sound resonance within the single particle-hole spectrum. At T = 0.63 K which is a high temperature (compared to the reduced Fermi energy at 1.6°K) the resonance is even further damped. The appearance of a zero sound mode depends strongly on the parameterization. If $v^s(Q)$ had been chosen so that the whole Placzek (f) sum rule was contained in the single particle-hole spectrum, a zero sound mode would exist up to $\sim Q = 3.0$ A^{-1}. Clearly, a more realistic theory must allow the contribution to the Placzek sum rule from the single particle-hole scattering to vary with Q.

Figure 2 shows the sensitivity of the total $S(Q,\omega)$ to different ratios of (σ_i/σ_T) to (σ_c/σ_T). Sears and Khanna[7] estimate a ratio of 1.2/4.9. Clearly a larger incoherent part would increase the scattering at low $\hbar\omega$ for low Q but would have little effect at large Q.

Figures 3 and 4 compare the total $S(Q,\omega)$ (converted to constant scattering angle scans) with experiment at T = 0.63 K using $(\sigma_i/\sigma_T)/(\sigma_c/\sigma_T)$ = 1.2/4.9. We note first that there is considerable scattering at large energy transfer not described by the theory. This could be explained by (1) multi particle-hole scattering not included here and (2) a smaller effective mass at large Q than the value of 3.1 used here. Also a finite instrumental resolution would smear out the peaks transferring some scattering to higher $\hbar\omega$. The instrumental resolution in the present experiments[1] is $\sim$0.35 meV.

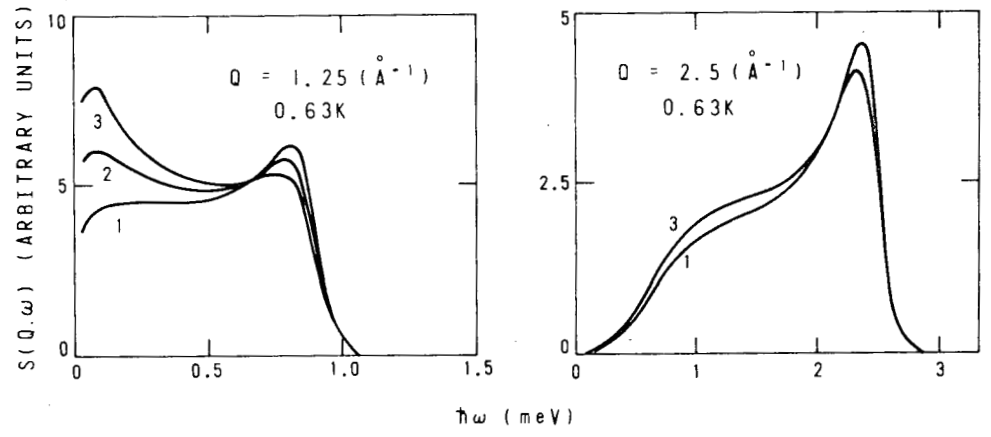


Fig. 2. The total $S(Q,\omega)$ for ratios of $(\sigma_i/\sigma_T)/(\sigma_c/\sigma_T)$ of (1) 0.2/0.8; (2) 0.35/0.65 and (3) 0.5/0.5.

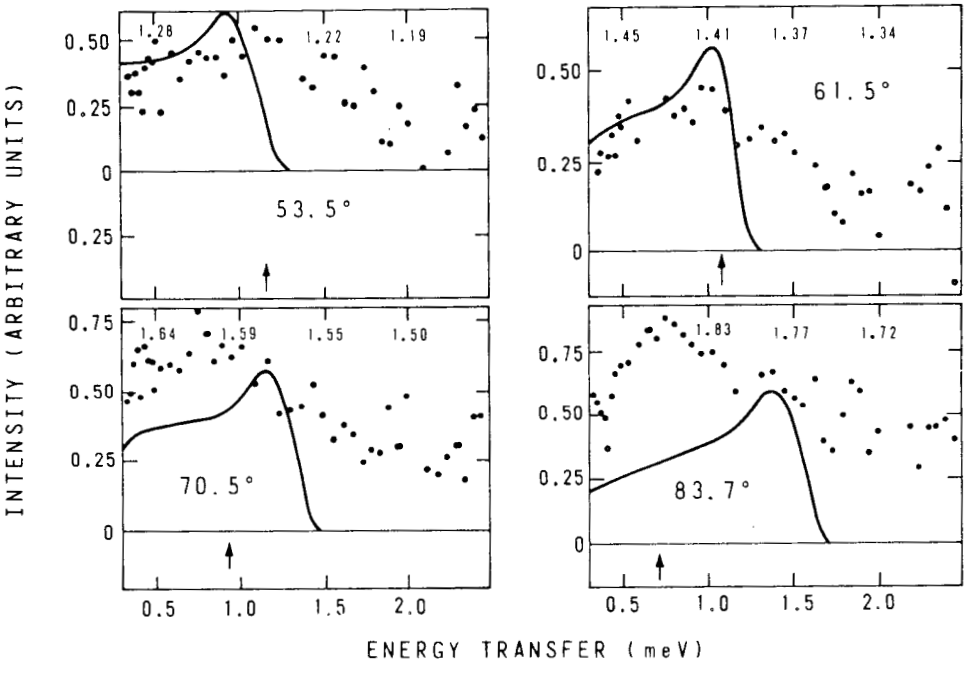


Fig. 3. The single particle-hole intensity (solid lines) compared with experiment (1) for incident wavelength of 4.3 Å and scattering angles noted. The corresponding Q (in $Å^{-1}$) are marked at the top of each figure. The arrow marks the ^{4}He one phonon peak position.

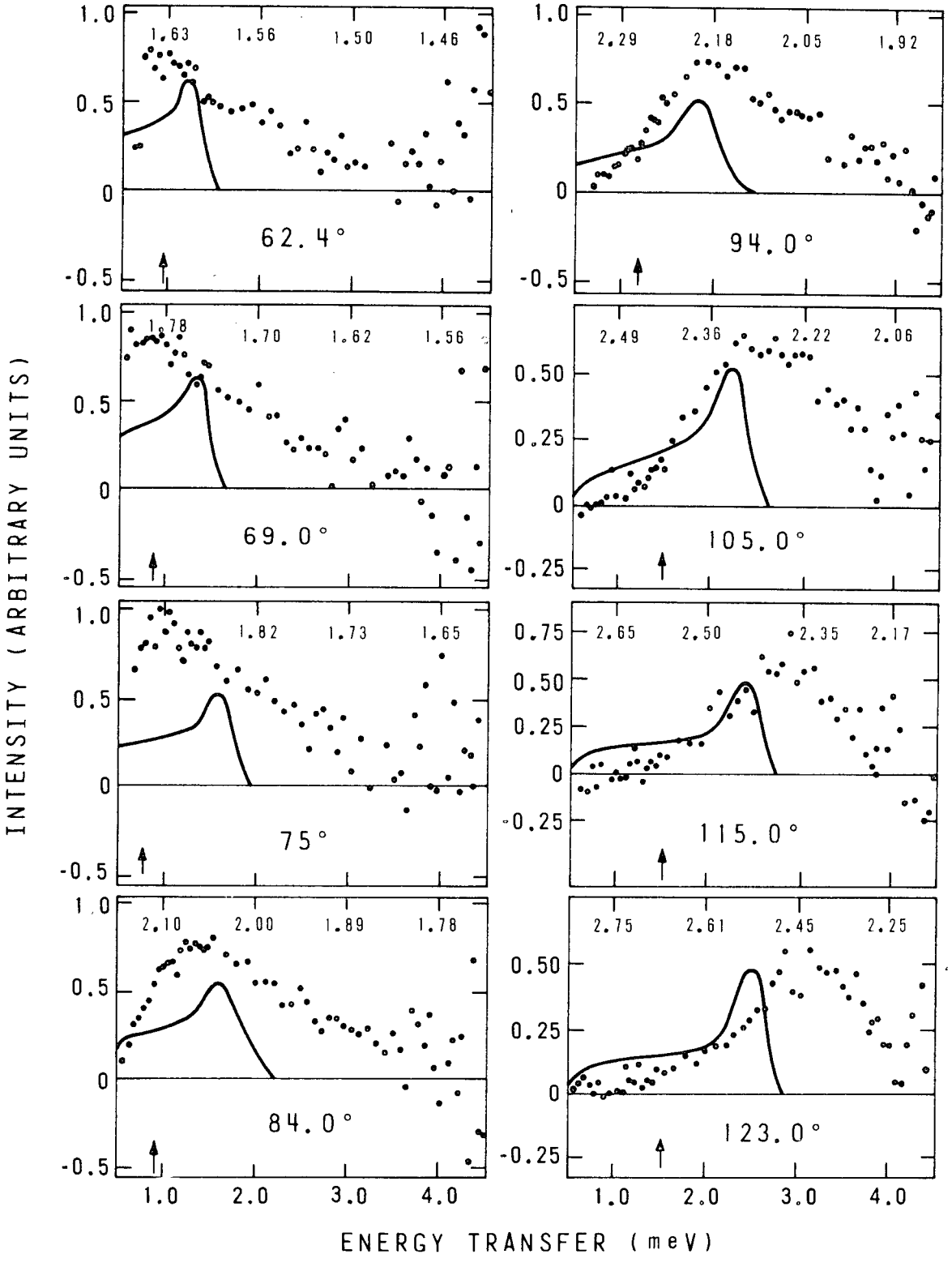


Fig. 4. Same as Fig. 3 for incident wavelength of 3.8 Å.

The present results suggest that experiments at low temperature with improved resolution would be interesting to study zero sound modes and resonances, and at low Q to isolate the incoherent part.

H.R. Glyde acknowledges the NRC (Canada)-CNRS (France) exchange program for support of a visit to the Institut Laue-Langevin.

REFERENCES

1. W.G. Stirling, R. Scherm, P.A. Hilton and R.A. Cowley, J. Phys. C. (in press); R. Scherm, W.G. Stirling, A.D.B. Woods, R.A. Cowley, G.J. Coombs, J. Phys. C 1, L341 (1974).

2. V.F. Turchin, Slow Neutrons, Israel Program for Scientific Translations, (1965), p.108.

3. D. Pines and P. Nozières, Theory of Quantum Liquids, Benjamin (1966).

4. C.H. Aldrich III, Ph.D. Thesis, University of Illinois (unpublished).

5. D. Pines in Quantum Fluids, (Ed. D.F. Brewer) North Holland (1965).

6. F.C. Khanna and H.R. Glyde, Can. J. Phys. 54, 648 (1976).

7. V.F. Sears and F.C. Khanna, Phys. Lett. 56B, 1 (1975).

NEUTRON SCATTERING STUDY OF ELEMENTARY EXCITATIONS IN LIQUID HELIUM-3*

K. Sköld,† C. A. Pelizzari, R. Kleb, and G. E. Ostrowski
Solid State Science Division, Argonne National Laboratory, Argonne, IL 60439

ABSTRACT

The neutron inelastic scattering function of liquid helium-3 at 0.015 K has been measured for wave vectors in the range 0.8 $\text{Å}^{-1} \leq q \leq 2.2\ \text{Å}^{-1}$. For $q \leq 1.3\ \text{Å}^{-1}$ the spectrum shows a two-peak structure and the peaks are identified as quasiparticle excitations and zero sound excitations, respectively. By comparing the measured structure factor with the x-ray structure factor the spin-dependent scattering cross-section and the corresponding structure factor are determined. It is conjectured that the quasiparticle excitations at small values of q are seen through the spin-dependent scattering.

The importance of neutron inelastic scattering results for liquid ^{3}He has long been recognized[1] but the large neutron absorption cross-section of the ^{3}He nucleus has discouraged experimental efforts in the past. However, recent development of high flux reactors and experimental techniques has made such measurements feasible and a series of experiments at ILL in Grenoble have been reported by Scherm, et al.,[2] and Stirling, et al.[3,4] The lowest temperature of the Grenoble measurement was 0.63 K and in all cases the spectra consisted of a broad peak with no discernible structure. In particular, no structure consistent with a well defined zero sound mode was observed. In the present letter we report measurements of the neutron inelastic scattering function for liquid ^{3}He at (0.015 ± 0.005) K and for wave vectors in the range $0.8\ \text{Å}^{-1} \leq q \leq 2.2\ \text{Å}^{-1}$.

The measurements were made at the CP-5 reactor at Argonne National Laboratory.[5] This is a rather modest flux reactor and to overcome the experimental difficulties associated with the large absorption in the

---

*Work performed under the auspices of the U. S. Energy Research and Development Administration.

†On leave from AB Atomenergi, Studsvik, Sweden.

sample, the statistical chopper time-of-flight technique was used.[6] In order to fully utilize the advantage of the statistical modulation technique great care was taken to suppress scattering of the modulated beam other than by ^{3}He. In order to avoid systematic errors it is also very important that an accurate correction for the extraneous scattering be applied. The sample arrangement which was used in the present study was designed with these criteria in mind and will be described in detail in a forthcoming paper. The sample was cooled in a ^{3}He-^{4}He dilution refrigerator[7] and the sample temperature was monitored by two carbon resistors attached to the sample container.

Time-of-flight spectra were measured in 15 separate groups of detectors at scattering angles between 30.4° and 106.7°; the incident neutron energy was 4.82 meV. Data were collected for 10 days with liquid ^{3}He in the container and for an equal length of time with the container empty. The scattering observed with the container after normalization to equal incident flux as measured by a beam monitor. Standard correction procedures were used to transform the time-of-flight spectra to the scattering function at constant angle.[8]

It is clearly more advantageous to represent the scattering function at a constant value of q rather than at a constant angle of scattering. Standard interpolation procedures[8] were employed to obtain thescattering function at values of q in the range $0.8\ \text{Å}^{-1} \leq q \leq 2.2\ \text{Å}^{-1}$. Examples of S(q,E) at selected values of q are shown in Fig. 1.

The data are normalized such that the experimental scattering function is:

$$S(q,E) = S_c(q,E) + \frac{\sigma_I}{\sigma_c} S_I(q,E) \qquad (1)$$

where σ_I and σ_c measure the spin dependent and the coherent scattering respectively;[9] we take $\sigma_c = (4.9 \pm 0.9)$ barns.[10]

Before discussing the detailed features of S(q,E) it is useful to assess the reliability of the results by evaluation of the energy moments.

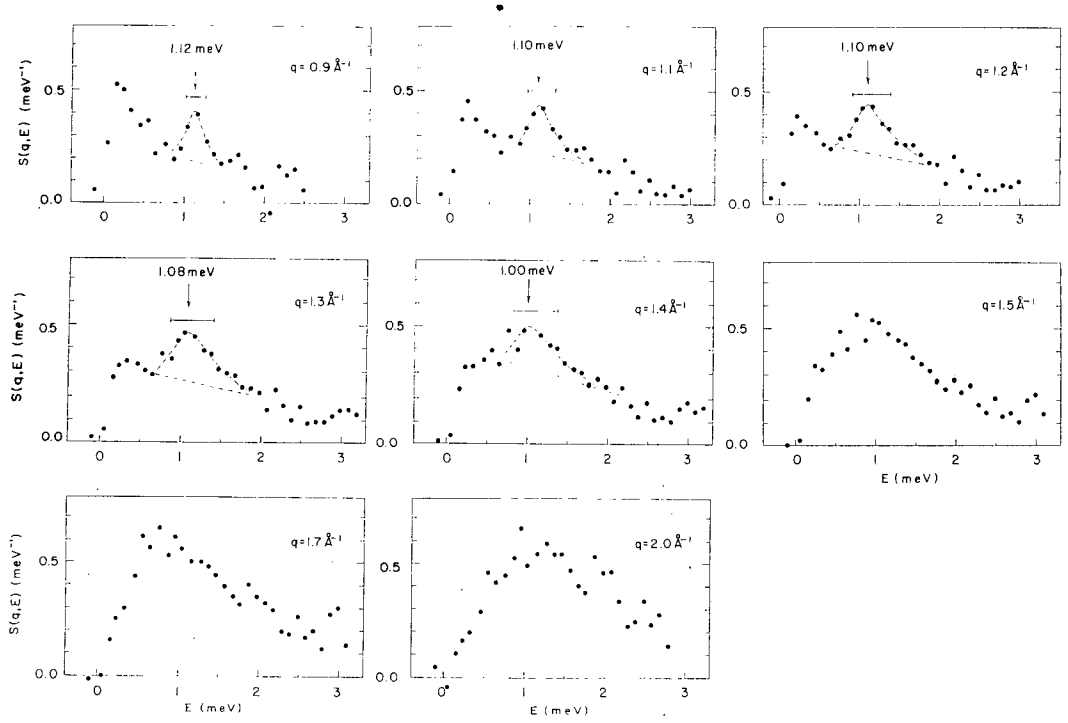


Fig. 1 S(q,E) at selected values of q normalized such that it represents $S(q,E) + (\sigma_I/\sigma_c)S_I(q,E)$ on an absolute scale.

In the present case the 0th and the 1st moments are of particular interest. The moments were evaluated by numerical integration of S(q,E) and of $E \cdot S(q,E)$ at each value of q. Figures 2a and 2b show examples of the accumulated integrals in the two cases as a function of the limit of integration. The 0th moment, which is the structure factor S(q), shows adequate convergence for $q \leq 1.8$ $\mathring{A}^{-1}$ and should therefore be reliably determined in this region of q. The estimated uncertainties are obtained from the fluctuation in the level of the accumulated integrals at large E as shown by the horizontal lines in Figs. 2a and 2b. The resulting structure factor is shown in Fig. 2c. The determination of the 1st moment is shown in Fig. 2b and the result in Fig. 2d. For obvious reasons the reliability of the result is much lower in this case. In particular we would expect that the integration is not carried out to large enough energies at large values of q in this area.

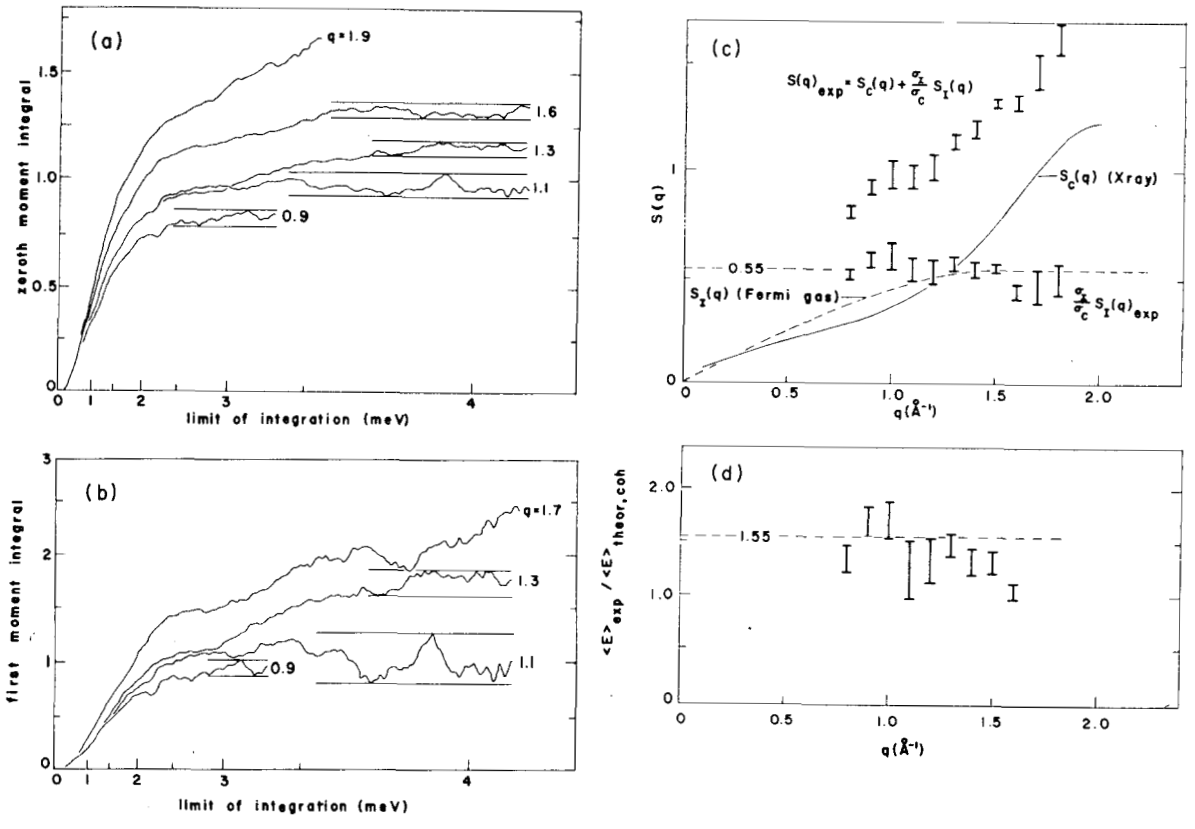


Fig. 2 (a) Examples of the accumulated 0th moment integral as a function of the limit of integration. The horizontal lines show the estimated uncertainties in the integral for values of q for which the integral shows adequate convergence. (b) Same as (a) for the 1st moment integral. (c) Experimental structure factor together with the x-ray structure factor by Hallock[11] and the difference between the neutron and the x-ray results. Also shown is the spin-dependent structure factor for a noninteracting Fermi gas. (d) Experimental first moment divided by $\hbar^2q^2/2m$.

In Fig. 2c we show S(q) together with $S_c(q)$ from x-ray measurements by Hallock[11] and the difference which is then $\sigma_I/\sigma_c \cdot S_I(q)$. We note that $S_I(q)$ is essentially constant and, if we assume that it has reached the limiting value of 1, we find that $\sigma_I \approx 0.55\,\sigma_c$. From this and the value for σ_c given above we obtain $\sigma_I = (2.7 \pm 0.6)$ barns. This is the first experimental determination of σ_I and is considerably larger than the value (σ_I = 1.2 barns) estimated by Sears and Khanna.[12] The result for the first moment divided by the theoretical value ($h^2q^2/2m$) is shown in Fig. 2d. To be consistent with the value for σ_I obtained above the ratio should be 1.55 and we note that it is in acceptable agreement with this

value at small q where we should expect that the first moment is determined with reasonable accuracy.

The experimental S(q,E) shown in Fig. 1 has several interesting features. First of all we see a well defined peak at E $\approx$ 1.1 meV for $q \leq 1.4$ Å^{-1} which we identify as the zero sound mode. This is in fact the first experimental observation of zero sound under circumstances where the Landau theory does not apply. The existence of such a mode in liquid ^{3}He was predicted over a decade ago by D. Pines.[13] The vertical arrows in Fig. 1 show the estimated peak positions and the horizontal lines above each peak show the estimated halfwidths. The estimates are obtained from the dashed curves which are fitted to the experimental points by eye. The results are shown in Fig. 3 together with the particlar-hole continuum for $m^* = 3\ m_o$ and the linear dispersion curve for $c_o = 194$ m/s.[14] The results clearly show that zero sound exists as a well defined excitation in the region where it does not intersect the continuum. We also note that the width of the peak is consistent with the experimental resolution width (i.e., the intrinsic width of the mode is small) for $q \leq 1.1$ Å^{-1} but that the peak broadens rapidly as the mode approaches the edge of the continuum. The results further show that at $q = 0.8$ Å^{-1} the zero sound mode lies above the linear dispersion curve. This implies the existence of a region with positive dispersion for $q < 0.8$ Å^{-1} in agreement with recent calculations by Aldrich.[15]

Another interesting feature of the scattering function is the intense peak at small energies for small values of q. The shape of the peak is similar to that expected for quasiparticle excitations with $m^* = 3\ m_o$. However, recent calculations[15] indicate that the spectral weight in $S_c(q,E)$ for quasiparticle excitation is negligible for $q \lesssim 1.2$ Å^{-1}. In view of the result obtained above for $S_I(q)$ and σ_I, the peak at small energies may represent quasiparticle excitations seen through the spin-dependent scattering.[16] This would in fact be a fortunate circumstance as it gives a possibility for study of the quasiparticle excitation in a region of q where it is well separated from the zero sound mode. We hope to elucidate this question by measurements at smaller values of q which are now in progress.

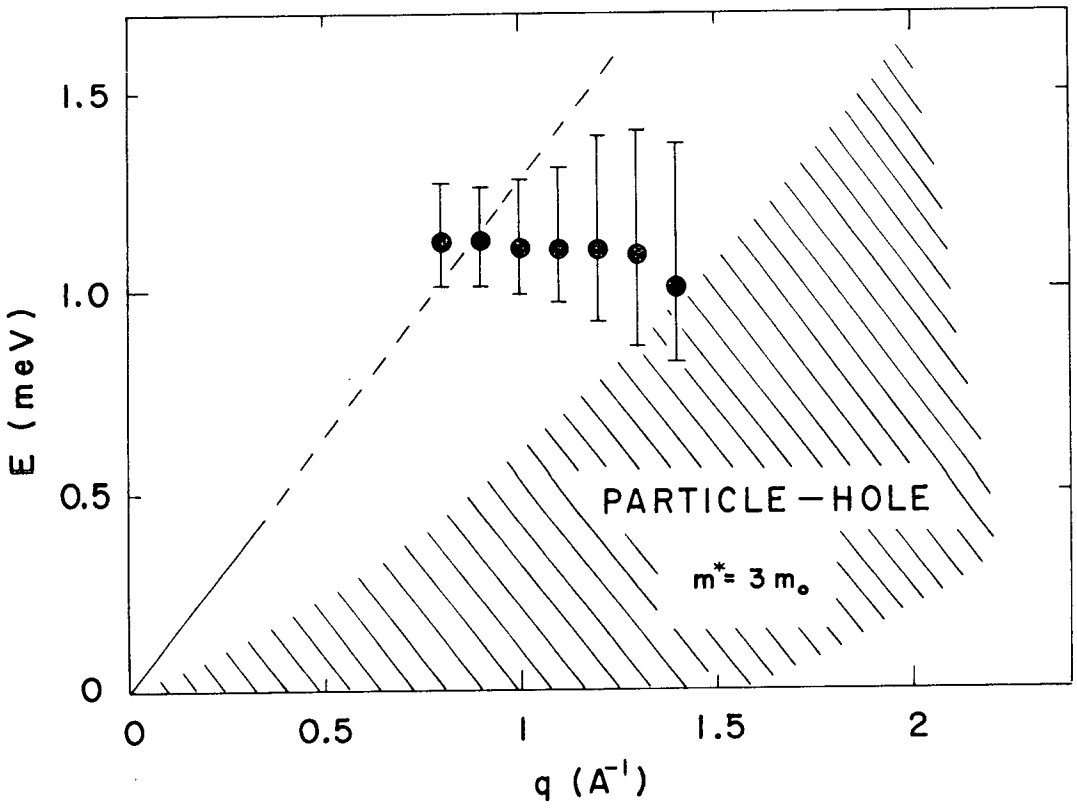


Fig. 3 Peak position versus q(o) for the zero sound mode and estimated half height contours (vertical lines) together with the linear zero sound dispersion curve for c_o = 194 m/s[13] and the quasiparticle continuum for m^* = 3 m_o.

We would like to acknowledge useful discussions with Drs. D. L. Price, J. M. Rowe, J. E. Robinson, G. F. Mazenko, P. Vashishta, and J. B. Ketterson. We are also indebted to the Argonne Research Reactor Operations Division for their cooperation and to Mr. T. Erickson for technical assistance.

REFERENCES

1. D. Pines and P. Nozières, The Theory of Quantum Liquids (Benjamin, 1966).
2. R. Scherm, W. G. Stirling, A. D. B. Woods, R. A. Cowley, and G. J. Coombs, J. Phys. C: Solid State Phys. 7, L341 (1974).
3. W. G. Stirling, R. Scherm, F. Volino, and R. A. Cowley, Proc. of LT-14 Helsinki (1975), Vol. 1, p. 76.

4. W. G. Stirling, R. Scherm, P. A. Hilton, and R. A. Cowley, J. Phys. C: Solid State Phys. (to be published).
5. R. Kleb, G. E. Ostrowski, D. L. Price, and J. M. Rowe, Nucl. Instr. Meth. 106, 221 (1973).
6. K. Sköld, Nucl. Instr. Meth. 63, 114 (1968): and D. L. Price and K. Sköld, Nucl. Instr. Meth. 82, 208 (1970).
7. The ^{3}He-^{4}He dilution refrigerator is manufactured by S.H.E. Corporation, San Diego, California.
8. J. R. D. Copley, D. L. Price, and J. M. Rowe, Nucl. Instr. Meth. 107, 501 (1973).
9. V. F. Sears, J. Phys. C 9, 409 (1976).
10. T. A. Kitchens, T. Oversluizen, L. Passell, and R. A. Schermer, Phys. Rev. Letters 32, 791 (1974).
11. R. B. Hallock, J. Low Temp. Phys. 9, 109 (1972).
12. V. F. Sears and F. C. Khanna, Phys. Letters 56B, 1 (1975).
13. D. Pines, Quantum Fluids, Proc. Sussex University Symposium, August 16-20, 1965 (North-Holland, 1966), p. 257; and D. Pines, Many-Body Theory, Part 1, 1965 Tokyo Summer Lectures in Theoretical Physics, (Syokabō, Tokyo, and Benjamin, New York, 1966), p. 36.
14. W. R. Abel, A. C. Anderson, and J. C. Wheatley, Phys. Rev. Letters 17, 74 (1966).
15. C. H. Aldrich, Polarization Potentials and Elementary Excitations in Strongly Interacting Quantum Liquids, Ph.D. Thesis, University of Illinois, Urbana (1974).
16. It has been brought to our attention that this result has been obtained from a RPA-type calculation by H. R. Glyde and F. C. Khanna (to be published).

Note added in proof: The moments of $S(q,E)$ shown in Fig. 2 are improperly scaled. The correct value for the ratio σ_T/σ_c is 0.28 (not 0.55) and the correct value for σ_T is (1.4 ± 0.3) b, in fair agreement with the theoretical prediction of Sears.

EXCITATION SPECTRUM OF ^{3}He-^{4}He MIXTURES

P.A. Hilton
University of Edinburgh, Edinburgh, U.K. and

W.G. Stirling and R. Scherm
Institut Laue-Langevin, Avenue des Martyrs, Grenoble, France.

ABSTRACT

The form of the excitation spectrum of a dilute (6%) ^{3}He-^{4}He mixture has been studied by neutron inelastic scattering. The observed energy spectra show two principal features, a single phonon-roton peak and, at lower energies, a broader peak arising from the ^{3}He quasiparticle-quasihole continuum. Our results indicate a continuum which lies below the ^{4}He single phonon dispersion curve. The measurements were made at 0.6, 1.0 and 1.5K and cover wavevector transfers in the range 0.8 to 2.0 $\AA^{-1}$. We have also determined the shifts in energy and increased linewidths of the single phonon excitations relative to those of pure ^{4}He.

INTRODUCTION

In a forthcoming publication[1], we report the results of a neutron inelastic scattering experiment on ^{3}He-^{4}He mixtures . As well as observing scattering from the single phonon-roton excitations, we also observed scattering attributable to excitations arising from the particle hole continuum in these mixtures. However, we could not resolve this latter scattering at wavevector transfers close to the ^{4}He roton minimum as here the scattering is dominated by the roton excitations. We also found that the shifts in energy, $\delta\hbar\omega = \hbar\omega$ (mixture) - $\hbar\omega(^4\text{He})$, of the single phonon-roton excitations at the roton minimum were practically independent of ^{3}He concentration for concentrations up to 25% ^{3}He in ^{4}He.

Pitaevskii[2] has suggested that in ^{3}He-^{4}He mixtures, the particle-hole continuum could deviate from a quadratic form and in fact have a minimum, similar to the ^{4}He roton minimum. Following this suggestion Varma[3] and

Stephen and Mittag[4] have used a ^{3}He energy spectrum of the form $\hbar\omega(k) = \hbar^2k^2/2m_3^*$ at small wavevectors and $\hbar\omega(k) = \Delta_3 + \hbar^2 (k-k_3)^2/2\mu_3$ for wavevectors close to the ^{4}He roton minimum ; here Δ_3 is taken as approximately 5K, k_3 is a wavevector slightly smaller than that of the ^{4}He roton minimum, and μ_3 is an effective mass. These workers find that with such a spectrum the previous transport property measurements[5,6,7], which indicate a marked decrease in the energy of the roton minimum Δ with concentration, can be reconciled with Raman[8] and neutron[1,10] scattering experiments which, on the contrary, indicate that Δ is practically independent of ^{3}He concentration.

We have therefore repeated our previous measurements on a 6% ^{3}He-^{4}He mixture at improved experimental resolution, in order to attempt to determine whether the particle hole continuum in the mixture has a form quadratic in wavector and intersects the ^{4}He phonon-roton spectrum, or whether it lies below the ^{4}He spectrum and exhibits a minimum similar to the ^{4}He roton minimum.

Bartley et al[11] have calculated that as the temperature of the mixture is decreased the behaviour of the shifts $\delta\hbar\omega$ in the phonon-roton excitation spectrum can also be considered to indicate the class of particle hole continuum present. More specifically they find that close to the roton minimum there should be a positive contribution to the phonon shift, which increases as the temperature decreases, when using a "roton" type continuum. This differs significantly from the low temperature effects of the quadratic continuum for which the phonon shift near the roton minimum becomes more negative as the temperature decreases. Thus we have also performed measurements as a function of temperature in the range $0.6K < T < 1.5K$.

EXPERIMENT

The measurements were performed on the IN5 cold neutron time of flight spectrometer at the I.L.L., essentially as described in references 1 and 12. An incident wavelength of 5.50 Å was used, giving an elastic energy resolution (FWHM) of 0.16 meV and a typical ^{4}He phonon-roton linewidth of 0.12 meV. A total of 400 ^{3}He detectors was arranged in 8 groups at angles of scatter from 44° to 131°, corresponding to k(elastic) from 0.86 to 2.08 $Å^{-1}$. The same continuous flow ^{3}He cryostat and the same sample holder were used as for our previous ^{3}He and ^{3}He-^{4}He measurements. Measurements were made at three temperatures 0.60, 1.04 and 1.55K. Subsequent data analysis consisted of the subtraction of the measured background scattering and the conversion from a time of flight scale to an energy scale, with corrections for detector efficiency. Allowance was made for the energy,concentration,and angular dependence of the ^{3}He absorption and the effect of the Jacobian factor.

RESULTS

The energy spectra of the mixture for the lowest temperature investigated are shown in Fig. 1. It is clear that the spectra at lower wavevector transfers consist of two distinct components, a phonon-roton peak and a broader peak at lower energy, which we believe arises from excitations within the particle-hole continuum. This latter peak is apparent up to wavevector transfers of the order 1.7 $Å^{-1}$, but above this value it becomes extremely difficult to resolve scattering from the particle hole continuum as in this region the energy spectra are dominated by "roton" excitations. (S(k) has its maximum at $\simeq$ 2.0 $Å^{-1}$). As a function of k the behaviour of the phonon-roton peaks in the mixtures is essentially the same as in pure ^{4}He ; however we do observe slight shifts in energy and increases in linewidth of these peaks, the magnitude of which increase as the temperature is increased. Unfortunately as the scattering from the particle hole continuum is so weak, apart from an apparent broadening with increasing T, we cannot describe quantitatively its temperature dependence.

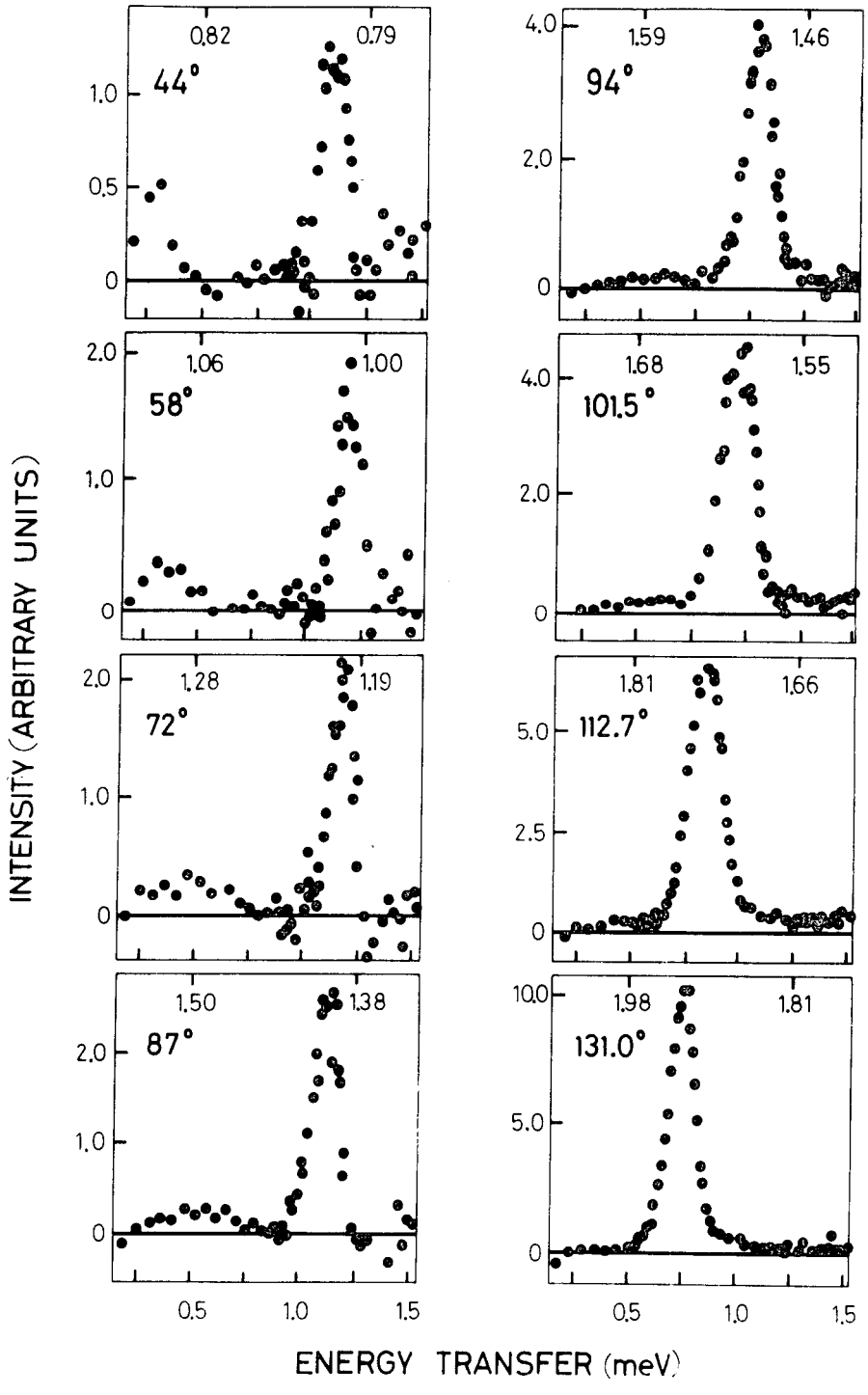


Fig. 1. Energy spectra of 6% ^{3}He-^{4}He at 0.6K.
The figures at the top are values of k($\AA^{-1}$).

However, since a major aim of the experiment was to attempt to distinguish between the two proposed forms of the particle-hole continuum in the mixture, the energy spectra were examined carefully to extract the energies of the "continuum" peaks, up to the highest possible values of wavevector transfer. The positions thus obtained are shown as the open circles of Fig. 2, where the "error bars" represent the full widths at half maximum of these peaks. The solid circles give the positions of the corresponding phonon-roton peaks while the triangles show the lower limit of effects due to the phonon-roton peaks, i.e. where the signal and background counts become equal. Also shown in this figure are two possible forms for the particle-hole continuum. The dashed lines show a continuum, calculated for a 6% mixture, of the form $\hbar\omega\ (k) = \hbar^2k^2/2m_3^*$, where $m_3^* = 2.34\ m_3$. The dot-dash lines represent a continuum which is quadratic for $k \gtrsim 1.2\ \text{Å}^{-1}$ but has a form $\hbar\omega\ (k) = \Delta_3 + \hbar^2\ (k - k_3)^2/2\mu_3$ for larger k (after Aldrich[13]). We can see that our measurements certainly appear to deviate from the quadratic case and are better described by the latter of the two models for the particle-hole continuum. However, we are unable to say whether or not the continuum exhibits a minimum as a function of energy as we were unable to resolve scattering from the continuum for $k \lesssim 1.7\ \text{Å}^{-1}$. It is interesting to note that the particle-hole continuum in pure ^{3}He appears to have a similar form (cf. Fig. 7 of reference 12) to that described above.

Our results for the phonon-roton excitations have been fitted to Voigt functions, the convolution of a Gaussian and a Lorentzian (using the Gaussian positions and widths obtained from pure ^{4}He), in order to extract the shifts in energy, $\delta\hbar\omega$ and increases in linewidth, 2Γ, of these excitations in the mixture. For the 1.5K data, we used ^{4}He data taken also at this temperature. The results are summarised in Fig. 3 where for the sake of clarity, error bars have only been shown on selected points. The measured shifts are always negative and small, becoming more negative as the temperature increases, and there is some evidence for a small peak in the shift as a function of k at about $1.7\ \text{Å}^{-1}$. This behaviour seems to be reflected in the measurement of Γ, which also appears to peak close to $1.7\ \text{Å}^{-1}$. As might be expected Γ increases as the temperature is

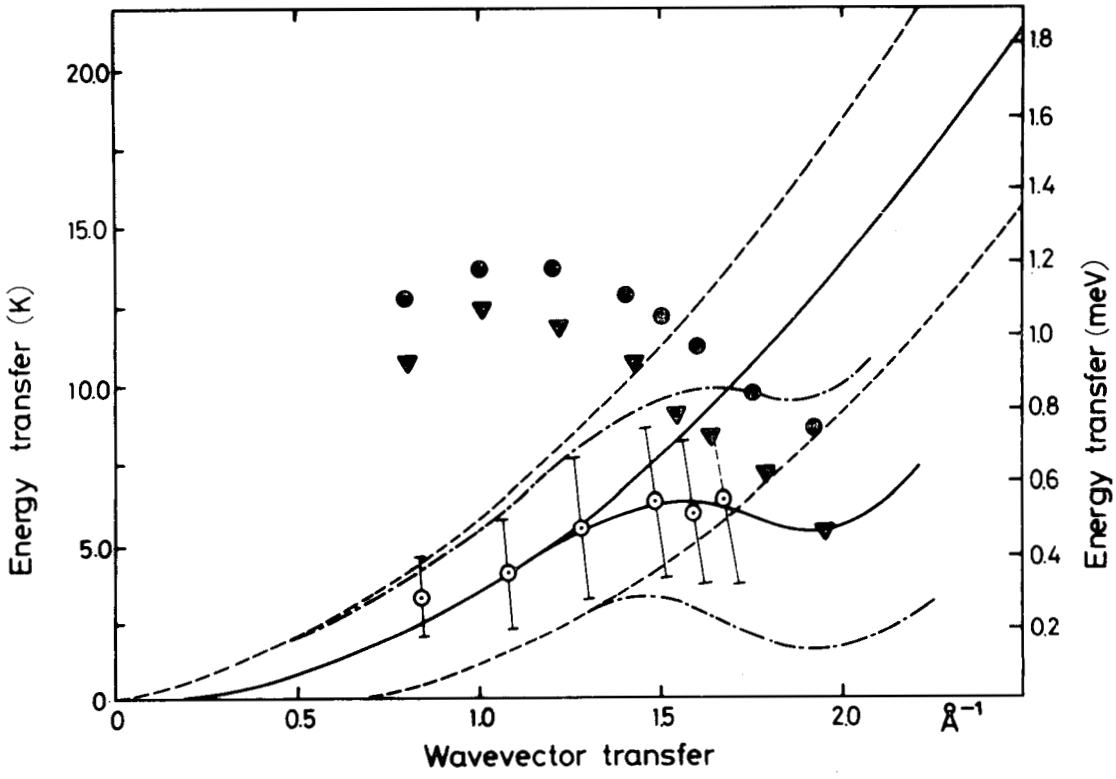


Fig. 2. Experimental and theoretical excitation spectra of 6% ^{3}He-^{4}He.

increased.

According to the calculations of Bartley et al[11] for a "roton-like" continuum, the shifts near the ^{4}He roton minimum should be positive, increasing with decreasing temperature. For a quadratic continuum they predict negative shifts which become more negative as the temperature decreases. Our measurements do not agree with either prediction as the shifts near the roton minimum are negative but become less negative as the temperature decreases. Thus the phonon-roton shifts do not clarify the situation, but nevertheless, from Figure 2, we can see that a continuum lying below the ^{4}He dispersion curve is indicated. We cannot, however, say if it exhibits a "roton-like" minimum.

REFERENCES

1. P.A. Hilton, W.G. Stirling and R. Scherm, to be published.

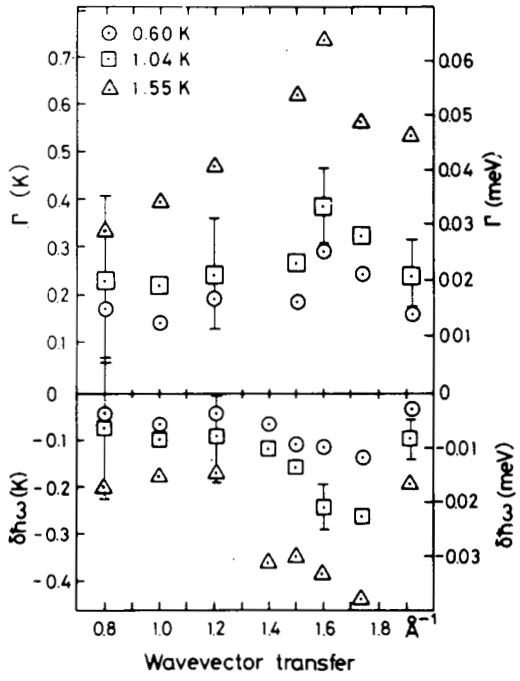


Fig. 3. Increases in half width Γ and shifts in energy δħω of phonon-roton excitations in 6% ^{3}He-^{4}He.

2. L.P. Pitaevskii, Proc. of U.S.-Soviet Symposium on Condensed Matter, Berkley, California, 1973.
3. C.M. Varma, Phys. Lett. 45A, 301, 1973.
4. M.J. Stephen and L. Mittag, Phys. Rev. Lett. 31, 923, 1974.
5. B.N. Essel'son, Yu. Z. Kovdrya and V.B. Shikin, Soviet Phys. JETP 32, 37, 1971.
6. N.E. Dyumin, B.N. Essel'son, E. Yu. Rodovskii and I.A. Serbin, Soviet Phys. JETP 29, 406, 1969.
7. V.I. Sobolevand, B.N. Esel'son, Soviet Phys. JETP 33, 132, 1971.
8. R.L. Woerner, D.A. Rockwell and T.J. Greytak, Phys. Rev. Lett. 30, 1114, 1973.
9. C.M. Surko and R.E. Slusher, Phys. Rev. Lett. 30, 1111, 1973.
10. J.M. Rowe, D.L. Price and G.E. Ostrowski, Phys. Rev. Lett. 31, 510, 1973.
11. D.L. Bartley, V.K. Wong and J.E. Robinson, J. Low Temp. Phys. 17, 551, 1974.
12. W.G. Stirling, R. Scherm, P.A. Hilton and R.A. Cowley, J. Phys. C : Solid State Phys. 9, 1643, 1976.
13. C.H. Aldrich, Ph. D. Thesis, University of Illinois, Urbana, 1974.

THE DYNAMIC STRUCTURE FACTOR OF NONSUPERFLUID LIQUID ^{4}He

A.D.B. Woods, E.C. Svensson, and P. Martel
Chalk River Nuclear Laboratories
Atomic Energy of Canada Limited
Chalk River, Ontario, Canada, K0J 1J0

ABSTRACT

Neutron-scattering measurements are combined with X-ray measurements of S(Q) and with the requirements of the first-moment theorem and the detailed-balance condition to yield absolute values of the resolution-broadened $S(Q,\nu)$ for non-superfluid ^{4}He at SVP and T = 4.2 K. The results are discussed in terms of various model calculations.

INTRODUCTION

Inelastic neutron scattering has been used to study[1,2] many aspects of the dynamic structure factor, $S(Q,\omega)$, of various liquids including superfluid ^{4}He, but there are few cases where extensive results in terms of $S(Q,\omega)$ have been published. In this paper we present analysis of measurements[3] of neutron scattering from nonsuperfluid ^{4}He at the saturated vapor pressure (SVP) and T = 4.2 K for Q in the range 1.0 nm^{-1} to 26.0 nm^{-1}. The resulting resolution-broadened $S(Q,\nu)$* and functions of Q related to its frequency moments are compared with model calculations.

*In this paper experimental results are presented in terms of the frequency, ν, while general arguments are often discussed in terms of the angular frequency, $\omega = 2\pi\nu$, which is used in most theoretical papers.

ANALYSIS

The scattered-neutron energy distributions of Ref. 3, for which $2.0\ nm^{-1} \leq Q \leq 26.0\ nm^{-1}$, were obtained with a triple-axis crystal spectrometer having two analysing units. Two overlapping series of measurements were carried out under slightly different experimental conditions. There were thus four independent, but similar, spectrometer calibration constants each of which applied to measurements at about 10 different values of Q. In addition, more recent measurements at higher resolution (the width in frequency of the elastic peak from vanadium was 0.02 THz compared with 0.04 THz for the measurements of Ref. 3) at a nominal value of Q of $1.0\ nm^{-1}$ ($1.0_5\ nm^{-1}$ when corrected for vertical divergence) were included in the analysis.

The measurements were first corrected for fast-neutron background and scattering from the empty specimen holder with appropriate allowance being made for the transmission of the helium specimen. Most of the resultant scattered-neutron energy distributions contained a small residual background of undetermined origin (see Fig. 1 of Ref. 3). In our analysis the background was assumed to be independent of frequency except in those cases where the residual intensity at $\nu = -0.30$ THz (i.e. neutron energy gain at $h\nu = 3.43$ kT) was sufficiently high that this assumption was untenable.

The average calibration constant, a, and the residual background levels were then determined by applying the following conditions in which $I(Q,\nu)$ is the observed detector count rate per unit incident flux:

$$S(Q,\nu) = a\ I(Q,\nu)\ , \tag{1}$$

$$\int S(Q,\nu)d\nu = S(Q)\ , \tag{2}$$

$$2\pi \int \nu\ S(Q,\nu)d\nu = \frac{\hbar Q^2}{2M}\ , \tag{3}$$

and

$$S(Q,-\nu) = e^{-h\nu/kT}\ S(Q,\nu)\ . \tag{4}$$

The values of S(Q) used in Eq. (2) were averaged X-ray results[4,5].

With few exceptions this condition was satisfied to better than 1%. The first-moment condition, Eq. (3), was generally satisfied to better than 0.5% while Eq. (4) could readily be satisfied to any desired degree of precision.

RESULTS

Figure 1 shows resolution-broadened $S(Q,\nu)$, determined as described in the previous section, for several values of Q. At $Q = 1.0_5$ nm^{-1}, $S(Q,\nu)$ consists of a quasielastic Rayleigh component with shoulders corresponding to Brillouin components centered at $\nu = cQ/2\pi$, where c is the velocity of sound. At larger Q there is no distinct structure in $S(Q,\nu)$.

Lovesey[6] has discussed neutron scattering from liquid ^3He in terms of the function

$$\tilde{R}'(Q,i\omega) = \frac{\pi(1 - e^{-\hbar\omega/kT})}{\omega} S(Q,\omega) \tag{5}$$

which is even in ω and for which the sum rules are particularly simple. The expressions

$$\omega_o^2 = \frac{\int_{-\infty}^{\infty} \omega^2 \tilde{R}'(Q,i\omega)\, d\omega}{\int_{-\infty}^{\infty} \tilde{R}'(Q,i\omega)\, d\omega} \tag{6}$$

and

$$\omega_\ell^2 = \frac{\int_{-\infty}^{\infty} \omega^4 \tilde{R}'(Q,i\omega)\, d\omega}{\int_{-\infty}^{\infty} \omega^2 \tilde{R}'(Q,i\omega)\, d\omega} \tag{7}$$

follow directly from the relations given by Lovesey.

Evaluation of ω_ℓ^2 from experimental determinations of $S(Q,\omega)$ is considered[1] to be a formidable problem and has not often been attempted, largely because of the sensitivity of the fourth moment to $S(Q,\omega)$ at large ω where the accuracy of the results is usually lowest. While the use of the constant-Q method[7] avoids many otherwise difficult corrections, two other circumstances are also of importance: 1. when, as in this case, $\hbar\omega >> kT$ Eq. (7) depends more on the third moment of $S(Q,\omega)$

than on the fourth as in a classical system, and, 2. as a result of the type of analysis employed the high-ω behaviour of $S(Q,\omega)$ is more determined by the requirements of Eq. (3) than by statistics and poorly-known corrections. Figure 2 shows values of $\nu_o(Q)$ and $\nu_\ell(Q)$ derived from our $S(Q,\nu)$ and $\nu_\ell(Q)$ calculated from the Lennard-Jones potential and equations (2.11) and (2.12) of Ref. 6. The poor agreement between the experimental and calculated $\nu_\ell(Q)$ persists even when the parameters of the Lennard-Jones potential are varied.

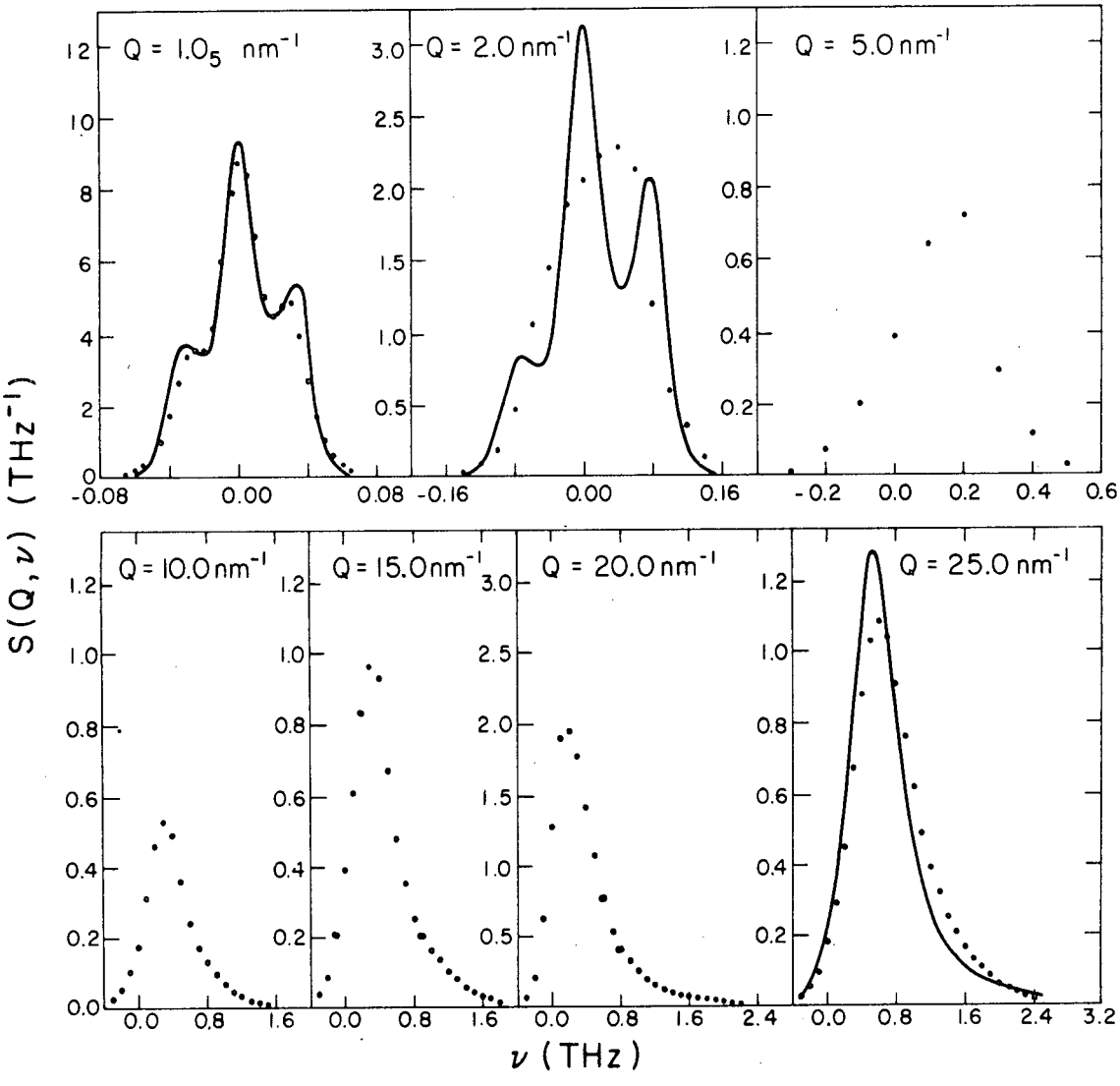


Fig. 1. Resolution-broadened $S(Q,\nu)$ for ^{4}He at SVP and T = 4.2 K. The solid lines are resolution-broadened $S(Q,\nu)$ calculated as described in the text.

MODELS

Calculations of $S(Q,\nu)$ were carried out on the basis of hydrodynamic and memory-function models. The curves shown in Fig. 1 for $Q = 1.0_5$ nm^{-1} and 2.0 nm^{-1} were calculated from the memory-function model of Sears[8] modified to include the detailed-balance factor as it occurs in Eq. (5) and the resolution of the spectrometer. The parameters ω_o and ω_ℓ were taken from Fig. 2, $S(Q)$ was chosen to give the observed integrated intensity and the other parameters were assigned their thermodynamic values.

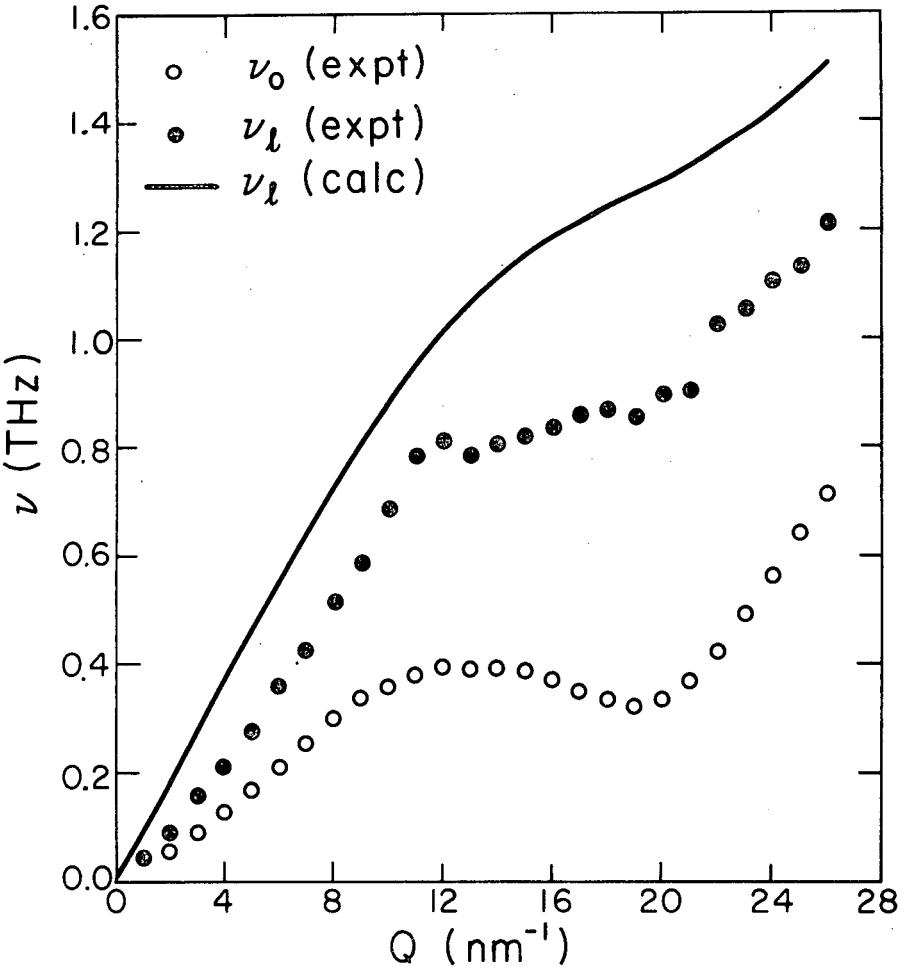


Fig. 2. The isothermal and high-frequency dispersion laws for ^{4}He at SVP and T = 4.2 K.

The agreement between calculation and experiment is excellent at $Q = 1.0_5$ nm^{-1} but poor at $Q = 2.0$ nm^{-1} where the model predicts three distinct peaks which do not occur in the experimental $S(Q,\nu)$. The agreement between theory and experiment can be improved in all models if the parameters are given arbitrary values. Even at $Q = 25$ nm^{-1}, Fig. 1 shows that reasonably good agreement with simple hydrodynamic theory can be obtained if the value of the viscosity parameter is taken to be ~25% of its thermodynamic value. Dasannacharya et al.[9] have discussed their recent neutron scattering results in terms of the hydrodynamic model and conclude that even at $Q \sim 1.0$ nm^{-1} a good fit can be obtained only when the parameters differ from their thermodynamic values.

CONCLUSIONS

The dynamic structure factor, $S(Q,\nu)$, for liquid ^{4}He at SVP and $T = 4.2$ K, when determined by a combination of neutron-inelastic-scattering measurements and various theoretical requirements, allows a determination of the isothermal and high-frequency dispersion laws, $\omega_o(Q)$ and $\omega_\ell(Q)$. The high-frequency dispersion law does not agree with calculations based on a Lennard-Jones potential. While hydrodynamic and memory-function models of $S(Q,\nu)$ show reasonable agreement with experiment at very small Q, agreement at larger Q can be obtained only when the parameters of the models assume arbitrary values.

ACKNOWLEDGEMENTS

Discussions with Dr. V.F. Sears are gratefully acknowledged.

REFERENCES

1. J.R.D. Copley and S.W. Lovesey, Rep. Prog. Phys. 38, 461 (1975).
2. R.A. Cowley and A.D.B. Woods, Can. J. Phys. 49, 177 (1971) and A.D.B. Woods and R.A. Cowley, Rep. Prog. Phys. 36, 1135 (1973).
3. A.D.B. Woods, P. Martel and E.C. Svensson in Low Temperature Physics - LT 14 (ed. M. Krusius and M. Vuorio), p. 187, Vol. 1, North-Holland, Amsterdam, 1975.
4. W.L. Gordon, C.H. Shaw and J.G. Daunt, J. Phys. Chem. Solids 5, 117 (1958).
5. R.B. Hallock, Phys. Rev. A 5, 320 (1972).
6. S.W. Lovesey, J. Phys. C 8, 1649 (1975).
7. B.N. Brockhouse in Inelastic Scattering of Neutrons in Solids and Liquids, p. 113, International Atomic Energy Agency, Vienna, 1961.
8. V.F. Sears, Can. J. Phys. 48, 616 (1970).
9. B.A. Dasannacharya, A. Kollmar and T. Springer, Phys. Lett. 55A, 337 (1976).

LOW-MOMENTUM-TRANSFER NEUTRON SCATTERING FROM LIQUID ^{4}He AT T = 4.2 K AND P = 2.5 MPa

E.C. Svensson, W.G. Stirling*, A.D.B. Woods and P. Martel
Chalk River Nuclear Laboratories
Atomic Energy of Canada Limited
Chalk River, Ontario, Canada, K0J 1J0

ABSTRACT

The inelastic scattering of neutrons from liquid ^{4}He at T = 4.2 K and P = 2.5 MPa has been studied for momentum transfers in the range $1.53 \leq Q \leq 6.0$ nm^{-1}. In general, the scattered-neutron energy distributions consist of single peaks centred at the frequencies expected from ultrasonic sound-wave measurements, although hydrodynamic theory does not give an adequate description of the results.

The study of neutron scattering from liquid ^{4}He I in the low-momentum-transfer region is of interest because of the possibility of observing the transition from the first-sound to the zero-sound mode of propagation and of testing the applicability of hydrodynamic theory to quantum systems. Pines[1] proposed that the excitations observed[2] in He I could be interpreted as zero-sound modes. In measurements at T = 2.3 K and SVP we have recently[3] obtained evidence for a transition from the first-sound to the zero-sound mode of propagation near $Q = 2.5$ nm^{-1}. Dasannacharya et al.[4] have recently studied the neutron scattering from ^{4}He I at 4.2 K and SVP for $0.6 \leq Q \leq 2.0$ nm^{-1}. They find that the results can be reasonably well described by hydrodynamic theory but only if the parameters are allowed to vary significantly from their thermodynamic values. In this paper we report the results of low-Q measurements at T = 4.2 K and P = 2.5 MPa.

In this experiment, a triple-axis crystal spectrometer at the NRU reactor was operated in its constant-$|\vec{Q}|$ mode[5]. The monochromator was Si(111), and a (002) pyrolitic graphite analyser was set so as to reflect scattered neutrons of energy 1.134 THz. Quartz and beryllium

*Permanent address: Institut Laue-Langevin, Grenoble, France.

filters were placed in the incident and scattered beams, respectively. The resolution at the elastic position was 0.04 THz (FWHM). The specimen was cylindrical, 5 cm in diameter and 5 cm high, and contained horizontal cadmium discs 1 mm thick and spaced 11 mm apart. The transmission of the specimen was approximately 90%. Because of the vertical divergence of the neutron beams, a nominal Q of 1.5 nm^{-1} was actually 1.5_3 nm^{-1}. For $Q \geq 2.0$ nm^{-1} the corrections for vertical divergence were <1%.

Figure 1 shows the scattered-neutron distributions for various values of Q. The arrows show the frequencies $\nu = cQ/2\pi$, where c is the ultrasonically determined[6] first-sound velocity, 360 $m \cdot s^{-1}$. Except for $Q = 6.0$ nm^{-1} the arrows agree, within the estimated error, with the centroids of the peaks.

Figure 2 shows the "dispersion relation" obtained from the experimental results shown in Fig. 1. The agreement with the velocity-of-sound line (solid line) indicates that, except possibly for $Q \gtrsim 6.0$ nm^{-1} the excitations propagate as first sound at T = 4.2 K and P = 2.5 MPa. In contrast, measurements[3] at T = 2.3 K and SVP show a marked increase in velocity near $Q = 2.5$ nm^{-1} which is interpreted as indicating the transition from the first-sound to the zero-sound mode of propagation.

The dashed curves in Fig. 1 represent resolution-broadened $S(Q,\nu)$ calculated from hydrodynamic theory[7] using the thermodynamic values of the parameters. The agreement with the observed $S(Q,\nu)$ is inadequate at all values of Q. At $Q = 1.5_3$ nm^{-1} the position of the peak is reasonably well predicted but the calculated width is much smaller than observed. At larger values of Q the positions of the calculated peaks do not agree with experiment. (The calculated peaks are centred at frequencies significantly less than $cQ/2\pi$ because of the damping which arises mainly from the viscosity.) The agreement between theory and experiment could of course be improved by allowing, as was done by Dasannacharya et al.[4], the velocity-of-sound and viscosity parameters to deviate from their thermodynamic values.

The authors would like to thank R.S. Campbell, H.F. Nieman, D.C. Tennant and M.M. Potter for invaluable technical assistance.

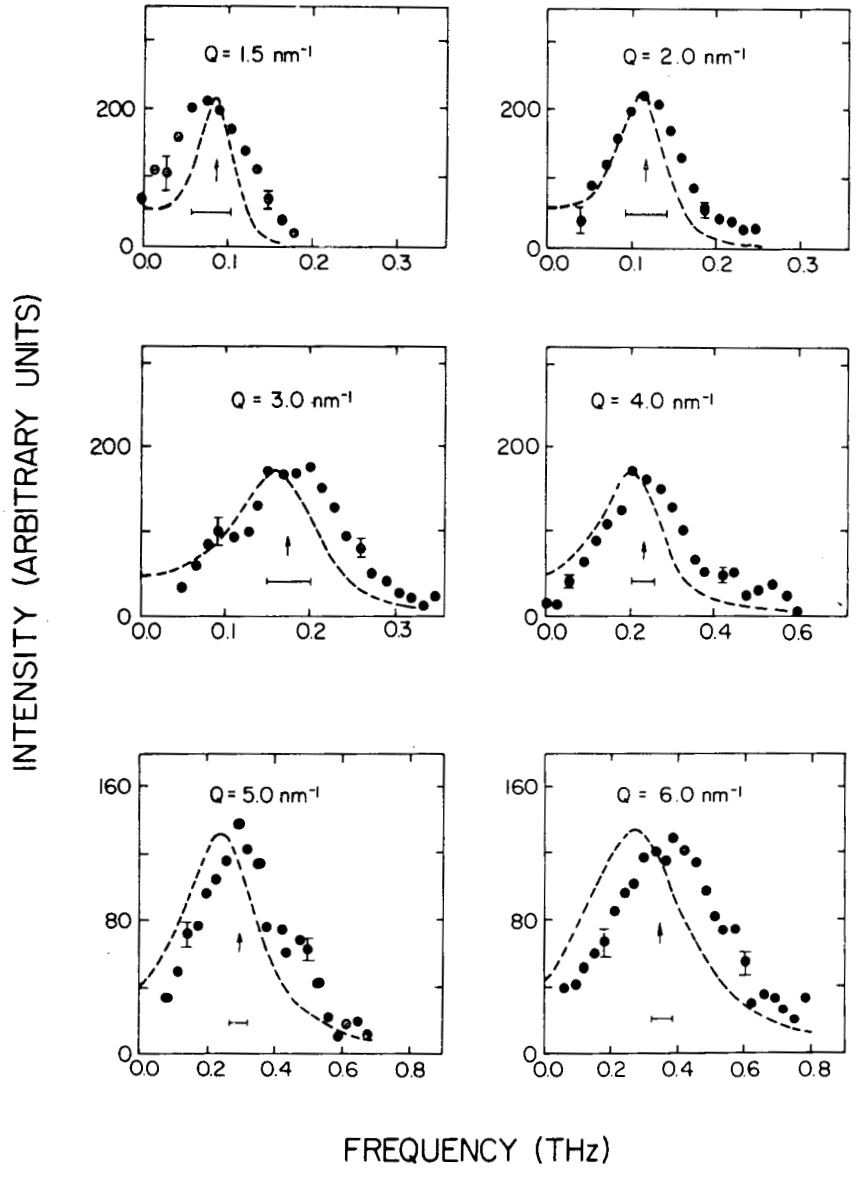


Fig. 1. Scattered-neutron distributions for ^{4}He I at T = 4.2 K and P = 2.5 MPa. The fast-neutron background and the scattering from the empty specimen chamber have been subtracted and all distributions are normalized to the same number of counts/point in the incident-beam monitor and hence represent resolution-broadened $S(Q,\nu)$. The horizontal bars give the calculated resolution widths (FWHM) and the arrows indicate the frequencies $\nu = cQ/2\pi$. The dashed curves are resolution-broadened $S(Q,\nu)$ calculated from hydrodynamic theory.

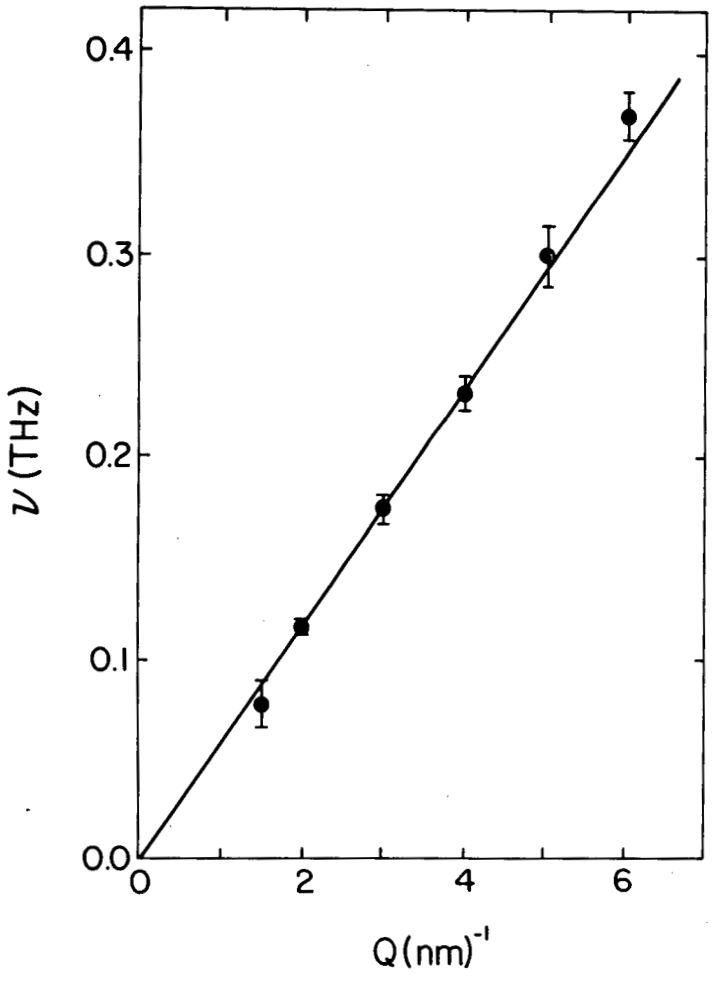


Fig. 2. The low-Q part of the "dispersion relation" for ^{4}He I at T = 4.2 K and P = 2.5 MPa. The solid line gives $\nu = cQ/2\pi$, where c = 360 m·s^{-1}, is the first-sound velocity (Ref. 6).

REFERENCES

1. D. Pines, in Quantum Fluids (edited by D.F. Brewer) p. 257, North-Holland, Amsterdam, 1966.
2. A.D.B. Woods, Phys. Rev. Lett. 14, 355 (1965).
3. A.D.B. Woods, E.C. Svensson and P. Martel, to be published.
4. B.A. Dasannacharya, A. Kollmar and T. Springer, Phys. Lett. 55A, 337 (1976).
5. B.N. Brockhouse, in Inelastic Scattering of Neutrons in Solids and Liquids, p. 113, International Atomic Energy Agency, Vienna, 1961.
6. K.R. Atkins and R.A. Stasior, Can. J. Phys. 31, 1156 (1953).
7. See, e.g., V.F. Sears, Can. J. Phys. 48, 616 (1970).

NEUTRON DIFFRACTION STUDIES OF HEAVY WATER

J. H. Clarke, J. C. Dore and G. Walford
Physics Laboratory, The University of Canterbury, Kent.

ABSTRACT

Neutron diffraction measurements have been made for liquid heavy water D_2O at 0.35 and 0.70 Å. The liquid structure factor $S_m(Q)$ has been derived and the high Q-value region has been analysed to give information on the molecular parameters.

INTRODUCTION

The structure of liquid heavy water has been the subject of two previous experimental studies[1,2] using neutron diffraction techniques. The small discrepancies in the two data sets are sufficient to give substantial differences in the interpretation of the measured liquid structure factor. Due to the importance of water to a wide range of topics in physics, chemistry and biology, it seemed desirable to extend the investigation and to examine the accuracy of both the experimental and analytic corrections which are applied to the raw data in order to extract the required structural information.

THEORY

On the basis of the static approximation, the molecular structure factor $S_m(Q)$ may be written in terms of the coherent differential scattering cross-section per molecule as[3]:-

$$S_m(Q) = \left(\sum b_i\right)^{-2} < \sum_i \sum_j b_i b_j \exp\left(iQr_{ij}\right) > = \frac{d\sigma}{d\Omega_{coh}}(\theta,\lambda) \qquad (1)$$

where Q is the scattering vector

$$Q = \frac{4\pi}{\lambda} \sin \theta/2 \qquad (2)$$

for a wavelength λ and scattering angle θ; b_i is the coherent scattering length and r_{ij} the distance between scattering centres. Unfortunately there are important departures from the static approximation due to the small masses of the constituents relative to the neutron mass. Corrections for the various inelasticity effects are complex and difficult to evaluate but Powles[3] has shown that, with certain assumptions, the formalism originally developed by Placzek may be applied to molecular liquids. The differential scattering cross-section is separated into self- and interference-contributions rather than the more conventional coherent and incoherent expressions. The self-terms which include contributions from spin- and isotopic-incoherence contain no structural information but the cross-section decreases with scattering angle for constant incident energy due to the inelasticity effects. In terms of the momentum transfer for elastic scattering (Q_{el}), the first order Placzek correction gives[3]:-

$$\frac{d\sigma_{self}}{d\Omega}(\theta,\lambda) = \sum_n N_n \bar{b}_n^2 \left[1 - \alpha_d \frac{M_n}{M_{eff}} \left(\frac{\lambda}{(4\pi)}\right)^2 Q_{el}^2\right] \qquad (3)$$

where α_d is a constant depending on the detector efficiency. The experimentally-determined interference function has an oscillatory pattern and does not exhibit Placzek corrections but for light molecules the effective momentum transfer is reduced to recoil of the molecule in the scattering process. This phenomenon has been clearly demonstrated in the extensive work on liquid nitrogen[4] and shows that the application of a simple kinematic correction to the Q-scale is necessary to provide satisfactory agreement with the known molecular bond-lengths. We may approximate the effective recoil mass by the molecular mass M_{mol}^{eff} so that

$$\left(\frac{Q_{eff}}{Q_{el}}\right)^2 = 1 + C_E(\theta) - 2\sqrt{C_E(\theta)}\cos\theta \qquad (4a)$$

where

$$C_E(\theta) = \frac{M_n}{(M_{mol}^{eff} + M_n)} \left\{\cos\theta + \left[\left(\frac{M_{mol}}{M_n}\right)^2 - \sin^2\theta\right]\right\} \qquad (4b)$$

causing a non-linear correction to the Q-scale of the diffraction pattern. This recoil correction increases with scattering angle for $M_{eff}^{mol} \square 20$ is approximately 4% at 140°; the change in the Q-scale is therefore different for different incident neutron wavelengths.

A weighted radial-distribution function d(r) is readily obtained from a Fourier transform of the corrected interference function i(Q) using

$$d(r) = 4\pi\rho_o r[g(r) - 1] = \frac{2}{\pi}\int_0^\infty Q\, i(Q)\sin Qr\, dQ \qquad (5)$$

where g(r) is a weighted pair correlation function ρ_o is the mean number density. The main contribution to the diffraction pattern is from the molecular unit which, for heavy water, has the following form-factor

$$F_1(Q) = \frac{1}{(b_O + 2b_D)^2}\left[b_O^2 + 2b_D^2 + 4b_O b_D\, j_o(Qr_{OD})e^{-\gamma_{OD}Q^2} + 2b_D^2\, j_o(Qr_{DD})e^{-\gamma_{DD}Q^2}\right] \qquad (6)$$

where b_D and b_O are the coherent scattering lengths for deuterium and oxygen respectively and the Debye-Waller terms arise from vibrational motion with parameters γ_{DD} and γ_{OD} which are proportional to the mean square amplitude. Inter-molecular terms which characterise the structure of the liquid are significant only for Q-values below about 10 $Å^{-1}$.

EXPERIMENTAL PROCEDURE AND DATA REDUCTION

The sample (99.8% D_2O) was contained in a vanadium cylinder of 5 mm internal diameter. Measurements of the scattered intensity were made with a conventional two axis diffractometer (D4) at incident wavelengths of 0.35 and 0.70 Å. Experimental corrections for container scattering, absorption, multiple-scattering and hydrogen contamination were made in the usual way and the cross-sections were normalised to an absolute scale by comparison with the scattering from a standard vanadium bar. The incident neutron wavelength was calibrated by Bragg scattering from a powdered nickel

sample. The data is shown in Fig. 1, illustrating the importance of the Placzek corrections.

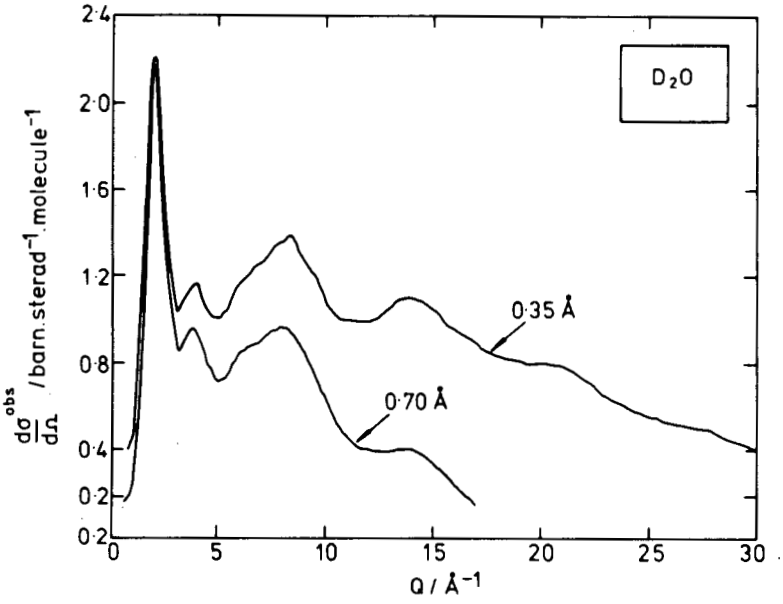


Fig. 1. Diffraction data for liquid D_2O using 0.35 and 0.70 Å neutrons.

Although the self and interference contributions cannot be separately determined a knowledge of the approximate molecular form-factor enables the oscillatory term to be calculated and subtracted from the observed data. This procedure enables the cross-section for the self-terms to be determined and gives the curves exhibited in Fig. 2. These show the expected behaviour but indicate that a first-order correction with terms in Q^2 is unsatisfactory at high Q-values, particularly as the curve approaches the calculated free-atom limit shown in the diagram by an arrow.

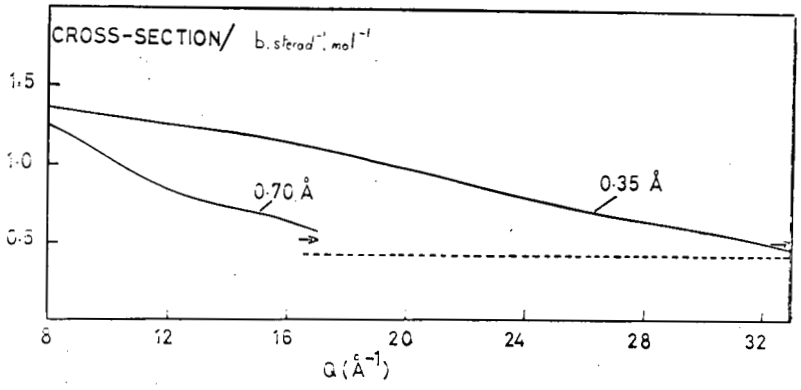


Fig. 2. The derived cross-section for self-terms in the scattering from D_2O (see text for details).

STRUCTURAL INFORMATION

The interference function for the different wavelengths was evaluated using the parameters required to fit the self-contribution and shows a shift in the oscillatory pattern for the two different wavelengths. Application of a recoil correction using an effective mass M_{eff}^{mol} of 20 a.m.u. gives a Q-scale correction which brings the oscillations into much closer agreement, as shown in Fig. 3; the molecular form-factor (Equation 6) is also shown with parameters given for the vapour phase[5]. Analysis of the neutron data gives the value 0.98 ± .001 Å for the OD bond which is intermediate between the accepted values for ice (1.011 Å) and vapour (0.958 Å) although there is some current controversy over these values[6]. The results are therefore in satisfactory agreement and give confidence in the correction procedure. A Fourier transform of the Placzek-corrected $S_m(Q)$ values gives the d(r) function shown in Fig. 4. The sharp peaks at small distances arise from intra-molecular terms but the presence of further structure peaks at higher values gives some indication that hydrogen-bonding is playing an important role in the orientational correlation of neighbouring molecules. The inter-molecular information given by the data has yet to be evaluated in detail.

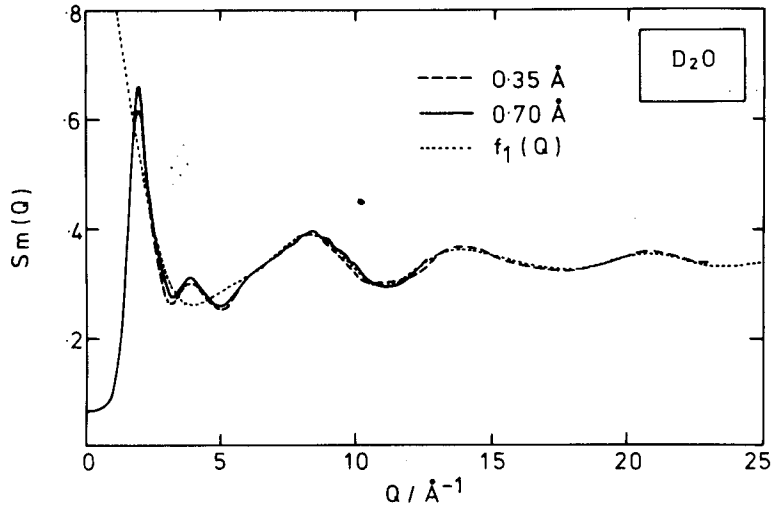


Fig. 3. The structure factor for liquid D_2O after corrections.

EXPERIMENTAL

The neutron scattering experiments have been performed on the diffractometer "D4" at the HFR of the Institute Laue-Langevin at Grenoble. The incident wave length was 0,696 Å and the angular range of 1,2 - 140° was investigated in 0,1° steps. It is estimated that spectrometer resolution contributes less than 3% to the width of the main diffraction peak of S(Q).

Liquid aluminum was held in a container made of a polycristalline Al_2O_3 tube with 0,5 mm wall thickness and sealed by graphite plugs. The sample diameter and sample height were about 10 mm and 47 mm respectively. In an additional run a graphite container of the same dimensions was used, taking advantage of the fact that graphite has its main diffraction peak at a different position. The sample was heated by a cylindrical vanadium heating element of a diameter of about 30 mm and a wall thickness of 0,1 mm, contained in a vacuum furnace. The setting accuracy of the temperature was of the order of $\pm$ 2°C and the stability about $\pm$ 0,5°C.

In addition to the sample runs at 680, 720, 760, 800, 840°C two measurements on the empty container have also been performed at 700 and 780°C. The empty furnace has been measured at 750°C.

DATA EVALUATION

In evaluating the scattering intensity of the sample, furnace scattering may be neglected. Attenuation has been allowed for in both sample and container by using the Paalman-Pings factors [21]. Inasmuch as in a scattering experiment using a diffractometer S(Q) cannot be measured directly, the results were calculated using Placzek's correction [22] in the extended form [23] by Yarnell et al. applicable to arbitrary detector efficiencies. In our case a He3 detector with 94% efficiency for 0,7 Å neutrons was used. The contribution of multiple scattering has been calculated at 9% and was found to be practically angle-independent [24].

The structure factor for a coherent scatterer is given by

$$S(Q) = A\,(I_s(Q) - M_{eff}) - f(Q) \qquad (1)$$

where $I_s(Q)$ is the corrected sample intensity, M_{eff} the effective multiple scattering of the sample-container arrangement and A a normalization factor; M_{eff} and A are assumed to be angle-independent.

A and M_{eff} have been evaluated by using the compressibility limit of S(Q) for $Q \to 0$ and the normalization integral corresponding to $g(r)=0$ for $r \to 0$. A value of 11,2 $\pm$ 0,8 % for M_{eff} has been obtained.

No resolution correction has been applied.

RESULTS

Fig. 1 shows the structure factors of liquid Al at 680, 720, 760, 800 and 840°C. The dashed curves are given as a guide for the eye. The points representing raw data show the difficulties in subtracting the container scattering and the concomitant experimental and statistical errors.

Fig. 2 shows the sample intensity obtained in a run using a graphite container. The measuring time for each point was extended by a factor of 8 in order to achieve a higher statistical accuracy. The data have been collected along the right-hand side of the first maximum of S(Q) at 680°C. Graphite has been used because of its smaller diffraction peaks in that range. In agreement with our previous results [17] no shoulder on the main diffraction peak was observed.

In Fig. 3 the pair correlation function g(r) is shown for all the temperatures measured. The position and width of the first maximum change very little. The coordination number, obtained by integrating $4\pi r^2 \rho_o g(r)$ up to r = 3.6 Å is 10.9 at 680°C and decreases to 10.7 at 840°C.

The temperature dependence of the first maximum of S(Q) is given in Fig. 4 together with the results of some of the other experiments. While the X-ray data of Ref. 8 give higher values, the agreement with Ref. 7 and Ref. 17 is satisfactory. In the temperature range between 700 and 760°C, the peak height seems to remain unchanged.

Within the statistical error, the decrease of the first maximum can be described [16] by

$$\frac{S(T)}{S(T_m)} = 0{,}443 + 0{,}557\,\frac{T_m(K)}{T(K)} \qquad (4)$$

where T_m is the melting temperature. The error bars correspond to one single experimental point. The position of the first diffraction maximum does not shift within the observed temperature range.

DISCUSSION

The general form of S(Q) reveals that liquid aluminum behaves like a simple liquid; between 680 and 840°C the overall shape of S(Q) appears to change very little as a function of temperature. However Fig. 4 shows that the change in the amplitudes of S(Q) with temperature is not monotonic over the measured temperature range. This behaviour was reproduced in $\Delta S(Q)/\Delta T$ over the whole Q-range within the statistical error of the data. A comparison of S(Q) with a hard sphere model shows the well-known deviations of a system interacting via an effective pair potential with a soft core.

For an investigation of the viscosity discontinuity, the statistical and systematic error (background substraction) of the structure factor would have to be improved by a factor of about 3.

An investigation of the scattering law for liquid aluminum is underway and has already been carried out in the low Q-range.

ACKNOWLEDGEMENT

We are indebted to Dr. W. Knoll and Dr. H. Egger for their support at ILL and Dr. M. Suda for doing most of the computer work.

This work has been funded by the Austrian Ministry of Science and Research.

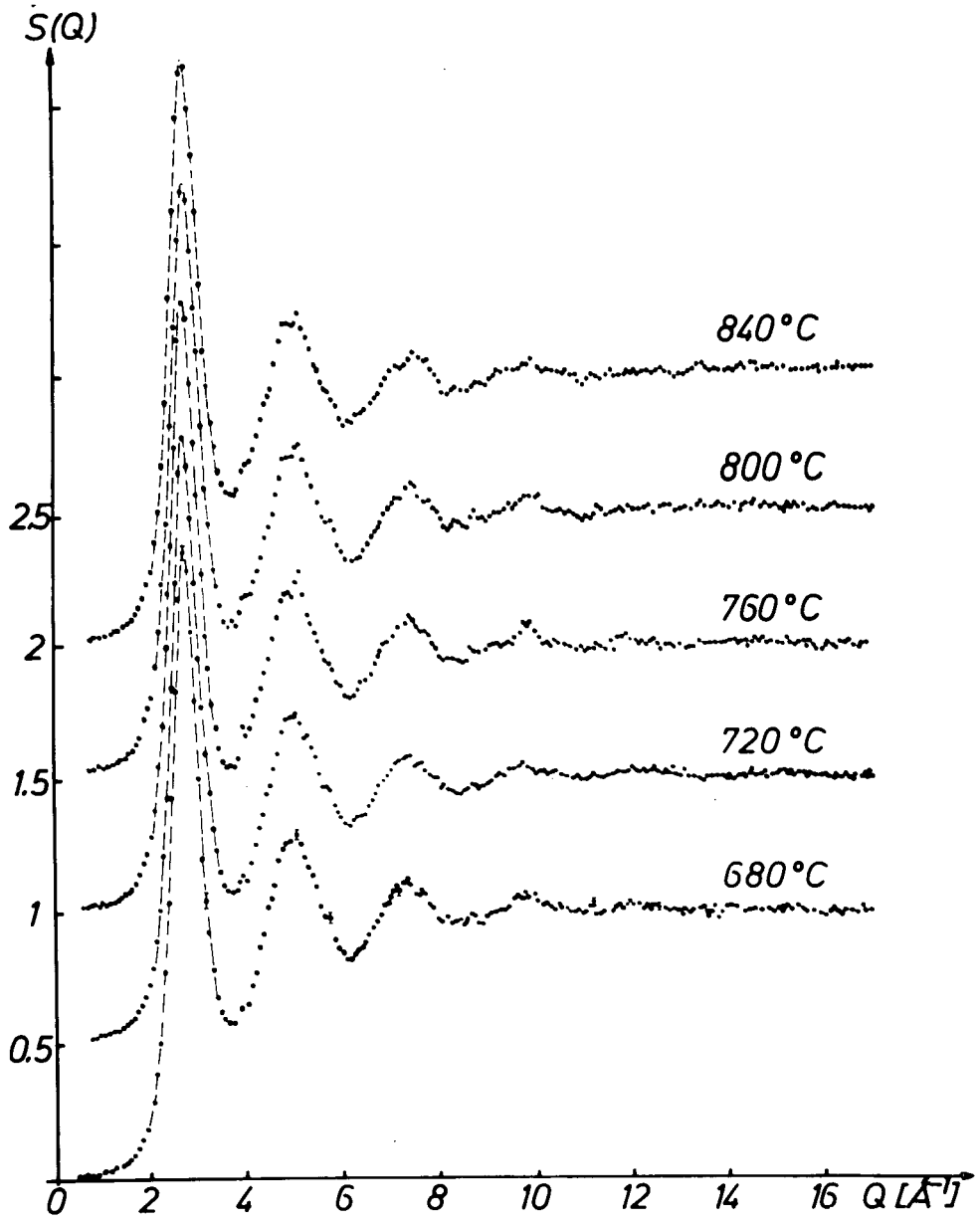


Fig. 1. Structure factor S(Q) for liquid aluminum at different temperatures

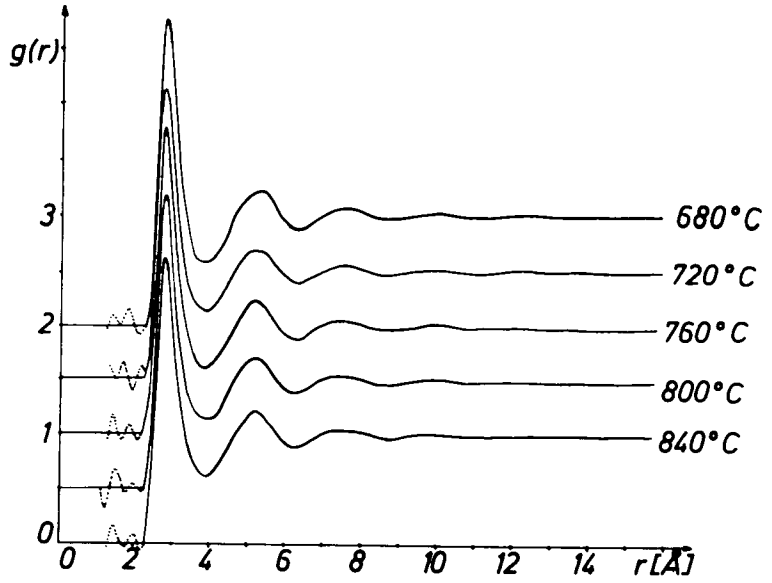


Fig. 3. Pair correlation function g(r) of liquid Al at different temperatures

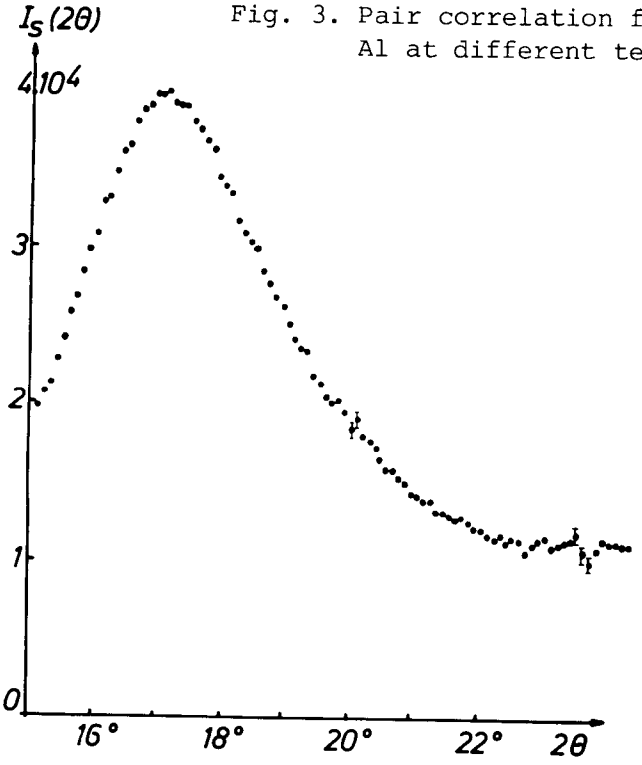


Fig. 2. Derived scattering intensity (counts/7 min.) of liquid Al vs. scattering angle around the main diffraction peak at 680°C.

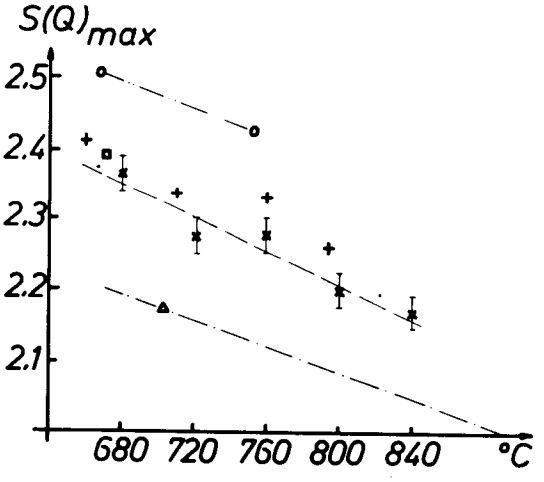


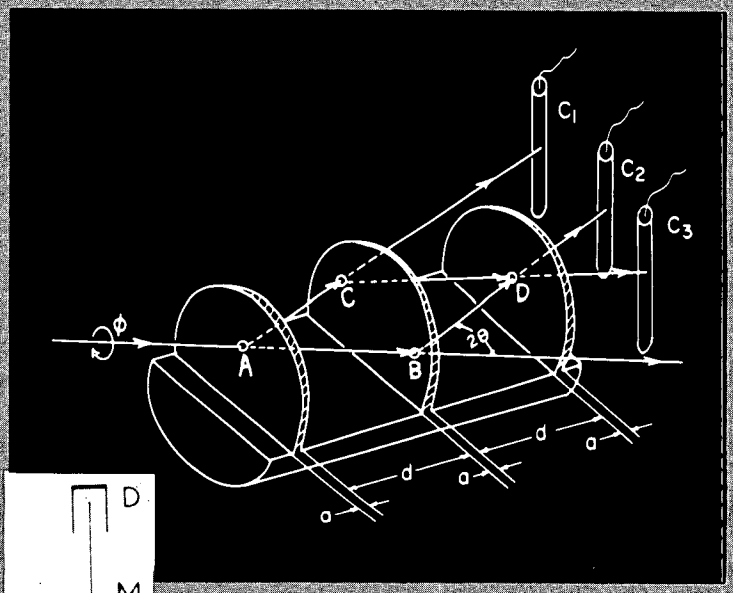
Fig. 4. Variation of the main peak height of S(Q) with temperature obtained by different authors: ○[8], □[7], △[16], +[17] and this work (x)

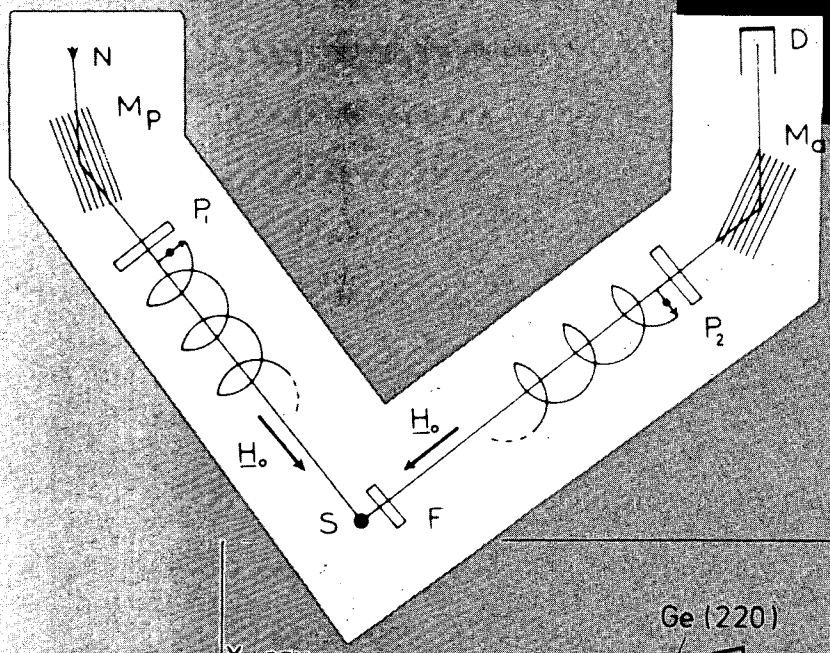
REFERENCES

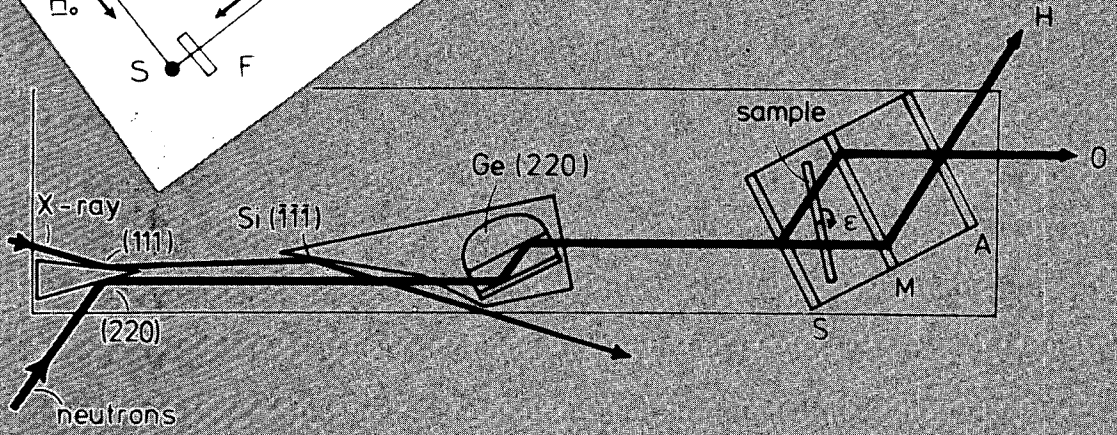
1. C. Gamertsfelder, J. Chem. Phys. 9, 450 (1941)
2. P. J. Black and J. A. Cundall, Acta Cryst. 19, 807 (1965)
3. Ia. I. Dutchak and N. M. Klim, Fizika (USSR) 10, 140 (1968)
4. Y. Waseda and K. Suzuki, Phys. Stat. Sol. 49b, 339 (1972)
5. G. I. Batalin, W. P. Kazimirow and B. F. Dmitruk Metalli (USSR) 1, 88 (1972)
6. G. D. Scott, Nature 188, 908(1960) and 194, 956 (1962)
7. H. Ruppersberg and H. J. Seemann, Z. Naturforsch. 20a, 104 (1965)
8. R. R. Fessler, R. Kaplow and B. L. Averbach, Phys. Rev. 150, 34 (1966)
9. H. Ruppersberg and H. Wehr, Phys. Lett. 40A, 31 (1972)
10. R. Hezel, Thesis, Univ. Stuttgart 1968
11. R. Hezel and S. Steeb, Z. Naturforsch. 25a, 1085 (1970)
12. A. I. Bublik and A. G. Buntar, Kristallogr. (USSR) 3, 32 (1958)
13. E. S. Levin, P. W. Geld and W. P. Jakubchik, Metalli (USSR) 5, 80 (1975)
14. K. E. Larsson, U. Dahlborg and D. Jovic, Inelastic Scattering of Neutrons, p. 117, vol. II, IAEA, Vienna, 1965
15. H. Okazaki, K. Iida and S. Tamaki, J. Phys. Soc. Japan 29, 1396 (1970)
16. J. M. Stallard and C. M. Davis, Phys. Rev. A8, 368 (1973)
17. O. J. Eder, B. Kunsch and G. Pressl, Proc. 6th Int. Conf. on Light Metals Leoben, Vienna 1975, p. 130, Aluminium-Verlag, Düsseldorf, 1976
18. F. Lihl and A. Schwaiger, Z. Metallkde 58, 777 (1967)
19. F. Lihl, E. Nachtigall and A. Schwaiger, Z. Metallkde 59, 213 (1968)
20. W. Z. Kisunko, J. A. Novochatski, W. J. Archarow and B. F. Below, Metalli (USSR) 2, 176 (1975)
21. H. H. Paalman and C. J. Pings, J. Appl. Phys. 33, 2635 (1962)
22. G. Placzek, Phys. Rev. 86, 377 (1952)
23. J. L. Yarnell, M. J. Katz, R. G. Wenzel and S. H. Koenig, Phys. Rev. A7, 2130 (1973)
24. We are grateful to Dr. D. I. Page for this calculation


Mike Wilkinson
Dan Stevens
Werner Schmalz

NEUTRON OPTICS AND TECHNIQUES







NEUTRON SMALL-ANGLE SCATTERING: EXPERIMENTAL TECHNIQUES AND APPLICATIONS

W. Schmatz
Institut für Festkörperforschung der Kernforschungsanlage
D-517 Jülich, West-Germany

ABSTRACT

Neutron small-angle scattering is applied today in very different scientific fields. The success of this technique is based on the availability of high intensity cold neutron sources as well as on the optimization of the small-angle scattering equipment itself. Cold neutron sources, guide tubes, multidetectors and on-line data handling are the most important components.

The best instrument is D11 at Grenoble with a maximum length of 80 m and the enormous through-flow of about 50 experiments a year. The design of this instrument benefitted from the experience obtained with the Jülich instrument. Wavelengthes used range between 20 Å and 4 Å. Scattering vectors are between 1 $Å^{-1}$ and $3 \cdot 10^{-4}$ $Å^{-1}$.

A special advantage of neutron small-angle scattering is the H-D contrast used mainly in biology and polymer science with considerable success for structural problems. In solid state physics fluctuations in magnetization - e.g. flux lines in type II-superconductors, magnetic domains and particles, spin-glasses - are of major interest. However, there are also numerous cases of fluctuations in chemical composition and in density where neutrons have been used with advantage compared to X-rays, for which still the problem of double Bragg-scattering is rather restrictive.

INTRODUCTION

During the last fifteen years, small-angle scattering of neutrons has developed into an important method for the investigation of structural problems in solid-state physics, chemistry and biology. There are two major reasons for this: First, with high flux reactors, cold neutron sources, guide tubes, multidetectors, on-line data handling and an optimization of the experimental layout a well-developed and

very efficient technique became available. Secondly, with the total growth of material science there was also an increase of the number of problems which can be favourably investigated by neutron small-angle scattering. Long-wavelength fluctuations in density and composition can be studied partly in competition with and partly in ways supplementary to X-rays. Especially in cases where X-ray scatterers have problems with double Bragg-scattering neutrons are favourable. A domain of neutron scattering solely is magnetic scattering by long-wavelength magnetic fluctuations and the investigation of polymers and biopolymers by use of the H-D contrast.

This paper is adressed mainly to new-comers in the field and therefore written in rather simple terms. After a short description of the basic scattering laws mainly the experimental techniques will be described, followed by a short review of applications with the exception of biology which is treated at the same conference by Schoenborn. For a more detailed description of the whole subject we can refer to a review article written at the end of 1972 /1/ with about twice the volume of the present article. References given there will only in special cases show up here again. Recent work, however, is listed and shortly described here, at least in the attempt to obtain completeness. Thus the present paper is a self-contained description of the field as well as a supplement to the earlier review. A section 'Future Developments?' is added at the end as a challenge.

SCATTERING THEORY

The scattering cross-section per atom for a sample with N atoms in a volume V is

$$\frac{d\sigma}{d\Omega} = \frac{1}{N} \left| \int_V e^{i\underline{\chi}\underline{r}} \varrho(\underline{r})\, d\underline{r} \right|^2 \qquad (1)$$

where $\varrho(\underline{r})$ is the scattering length density defined by

$$\varrho(\underline{r}) = \sum_{i=1}^{N} b_i \, \delta(\underline{r} - \underline{r}_i). \qquad (2)$$

b_i is the coherent scattering length of the nucleus i at position $\underline{r}_i$. $\underline{\varkappa}$ is the scattering vector. For small scattering angles its absolute value is simply $2\pi\vartheta/\lambda$ where ϑ is the scattering angle and λ the neutron wavelength. The term neutron small angle scattering describes scattering experiments in an angular range of 0.5 to $5 \cdot 10^{-4}$ radian using wavelengths from 5 to 20 Å. This defines a $\varkappa$-range from 0.5 to 10^{-4} $Å^{-1}$ approximately. With atomic distances of 2 to 3 Å the phase factor $\exp(i\,\underline{r})$ in eq. (1) varies from atom to atom considerably only for the highest $\varkappa$-values in the above-mentioned $\varkappa$-range. For $\varkappa < 0.1$ $Å^{-1}$ it varies so little that $\varrho(\underline{r})$ can be regarded as a continuous function of $\underline{r}$.

Equation (1) can easily be evaluated for numerous cases either analytically or with computers. A comprehensive treatment is given in older text-books /2,3,4/. As a very simple example we give the Guinier-approximation for a sphere of volume V in vacuo with a scattering length density $\varrho = N \cdot b/V$:

$$\frac{d\sigma}{d\Omega} = \frac{1}{N}(\varrho \cdot V)^2 \cdot e^{-\varkappa^2 R_K^2/5} = N b^2 \cdot e^{-\varkappa^2 R_K^2/5}. \qquad (3)$$

R_K is the radius. As equation (3) shows the forward scattering cross-section ($\varkappa = 0$) per atom is a factor N higher for an ensemble of N atoms than for N atoms randomly arranged. This amplification makes small angle-scattering so sensitive. However in competition to the coherent scattering of equation (1) we have spin- and isotope incoherent scattering which at low concentrations of heterogenities limits in many cases the sensitivity, especially at high $\varkappa$-values. Extreme cases are vanadium with $\sigma_{inc} = 5.1$ barn and $\sigma_{coh} = 4 \cdot b^2 = 0.03$ barn on the one hand and lead with $\sigma_{inc} = 0.002$ barn

and σ_{coh} = 11.5 barn on the other hand. When the sphere of N atoms moves by diffusion the elastic scattering of equation (3) is broadened into a quasielastic scattering with an energy half-width $\Delta E_{1/2} = 2\hbar D_s \varkappa^2$ where D_s is the diffusion coefficient. In most cases the neutron energy E is considerably larger than $\Delta E_{1/2}$ and eq. (1) can be used.

The scattering cross-section for unpolarized neutrons by magnetic heterogeneities is given by

$$\frac{d\sigma}{d\Omega} = \frac{1}{N} \cdot \gamma^2 \cdot \left(\frac{e}{\hbar c}\right)^2 \cdot \left| \underline{\tilde{M}}^{\perp}(\underline{\varkappa}) \right|^2 \qquad (4)$$

where $\gamma = -1.91$ and $\underline{\tilde{M}}^{\perp}$ is the component of $\underline{\tilde{M}}$ perpendicular to $\underline{\varkappa}$. $\underline{\tilde{M}}$ is the Fourier transform of the magnetization $\underline{M}$:

$$\underline{\tilde{M}} = \int \underline{M}(\underline{r}) e^{i \underline{\varkappa} \underline{r}} d\underline{r} \qquad (5)$$

For a collinear spin system $d\sigma/d\Omega$ is zero for $\underline{\varkappa}$ parallel to $\underline{M}$. Often it is reasonable to introduce a magnetic scattering length

$$\underline{b}_{mag,i} = \gamma \cdot \frac{e}{\hbar c} \int_{atom\ i} \underline{M}(\underline{r})\, d\underline{r} \qquad (6)$$

per atom i which allows to proceed in the same way as for nuclear scattering (equations (1) and (2)).

For polarized neutrons we have in addition interference between nuclear and magnetic scattering and their use also makes it reasonable to ask for neutron spin-flip and non-spin-flip scattering. For a careful listing of the corresponding scattering cross-section we refer to /5,6,7/. Little use of polarized neutron techniques has been made in small angle scattering up-to now.

EXPERIMENTAL TECHNIQUES

For a small sample of illuminated area F, homogeneous thickness D and transmission $\exp(-\Sigma_{tot} \cdot D)$ the neutron intensity I_D counted by a detector element seen with the solid angle $\Delta\Omega_1$ from the sample is given by

$$\Delta I_D = I_o \cdot F \cdot \frac{d\Sigma}{d\Omega} \cdot D \cdot e^{-\Sigma_{tot} \cdot D} \cdot \Delta\Omega_1 \cdot E \qquad (7)$$

I_o is the neutron flux per unit area incident on the sample. $\Sigma_{tot} = N_v \cdot \sigma_{tot}$ is the total macroscopic neutron scattering cross-section including absorption and scattering, whereby N_v is the number of atoms per unit volume and σ_{tot} the average total cross-section per atom. Similarly $d\Sigma/d\Omega = N_v \cdot d\sigma/d\Omega$ where $d\sigma/d\Omega$ is the total scattering cross-section per atom and unit solid angle. E is the wavelength-dependent detector efficiency.

Normally no energy-analysis of the scattered beam is performed and elastically, quasielastically and inelastically scattered neutrons are counted undiscriminated. Nevertheless consideration of the features of inelastic scattering at small scattering angles is often necessary. For this purpose κ,ω--scattering diagrams are useful where $\hbar\omega = E_o - E_1$ the energy transfer to the scattering system and $\hbar\kappa = \hbar(\underline{k}_o - \underline{k}_1)$ the momentum transfer. E_o and E_1 are the neutron energies before and after scattering respectively. $\underline{k}_o$ and $\underline{k}_1$ are the corresponding wave vectors whereby $|\underline{k}| = 2\pi/\lambda$. The κ,ω region covered for an incident energy E_o is the dashed area shown in Fig. 1. The limiting curves at the left and right of the dashed area are the scattering curves for the scattering angles equal to zero and 180° respectively. Small angle scattering is confined to a region very near to the $\vartheta = 0$ scattering curve. To incorporate coherent one-phonon scattering in the same diagram the phonon dispersion relations can be drawn as done schematically in Fig. 2. One sees that for neutron ve-

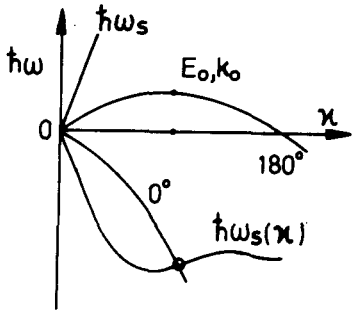


Fig.1: $\varkappa,\omega$-diagram.

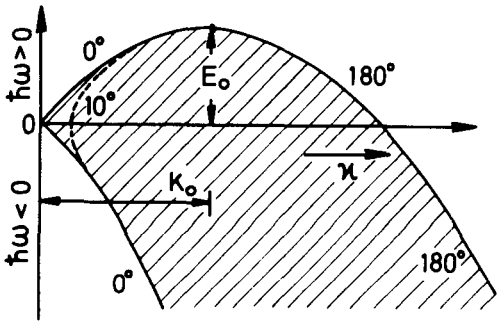
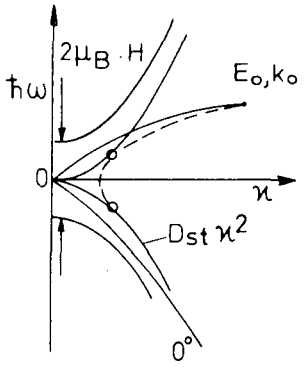


Fig.2: Phonon scattering.

locities v_N very much smaller than the sound velocity v_S no energy loss scattering for neutrons ($\hbar\omega > 0$) is possible and energy gain scattering occurs for very high $\varkappa$-values, which means neutron gain considerably in energy and momentum. One sees also that the crossing point of the scattering line and the dispersion relation changes only very little for a variation of the scattering angle in the small-angle scattering range. One has small changes also for the collection of all coherent multiphonon and incoherent phonon scattering along the scattering curves. This is because the main contribution is also for energy transfers around $k_B \cdot T$ or $k_B \cdot \Theta_D$ with T and Θ_D the sample- and the Debye-temperature respectively. We learn that in most cases inelastic scattering contributions are nearly constant within the small angle-scattering region and they occur with considerable energy transfer. Following the elastic scattering by weak scatterers toward high $\varkappa$--values - as we did recently for the critical scattering from an Al-Zn-alloy - demands separation of the phonon scattering. This can easily be done for instance by a time-of-flight analysis at moderate scattering angles according to the scattering behaviour discussed above.

As has been known since the very early days of neutron scattering a special situation exists for spin-wave scattering in ferromagnets. Because of the quadratic dispersion law ($\omega = D_{st} q^2$) there is for every neutron wavelength a critical angle below which spin wave scattering occurs at small $\varkappa$'s

and ω's (see Fig. 3). This critical angle can be lowered by an energy gap $2\mu_B \cdot H$ between the $\omega > 0$- and $\omega < 0$-part of the



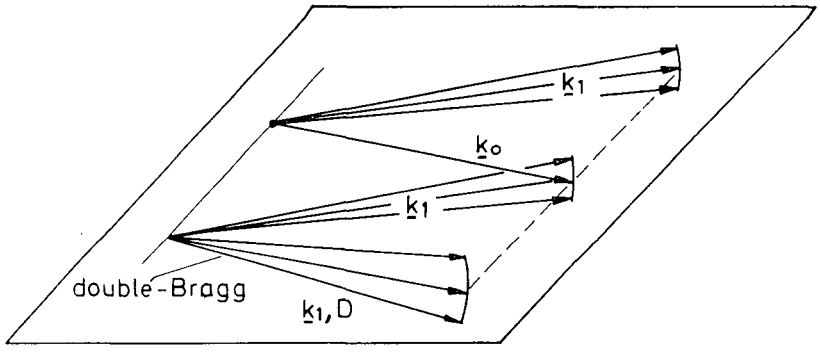


Fig.3: Spin-wave scattering. Fig.4: Double Bragg scattering.

spin-wave dispersion. H can be an applied field or an effective field as arises for instance from magnetic anisotropy. For high values of H and of the spin-wave stiffness D_{st} the spin-wave dispersion curves and the $\vartheta = 0$ scattering curve can be well-separated.

In addition to the single scattering process included in equation (1) double or even multiple scattering processes may occur. The most famous example is double Bragg scattering. The mechanism is explained in Fig. 4 for the case of a single crystal with high mosaic spread as many metal crystals have. Double Bragg scattering is avoided easily by the use of neutrons with wavelengths longer than twice the maximum lattice plane spacing d_{max}. One has to be sure that this holds for all wavelengths of the incident neutron spectrum. In case of single crystals one may use shorter wavelengths if an incident beam direction is chosen such that none of the Ewald spheres touches a reciprocal lattice point. For normal metal crystals it is easy to have $\lambda > 2d_{max}$; there is some danger however that experimenters might forget double Bragg scattering going to materials with large unit cells. A very weak double scattering may even arise for amorphous substances

and liquids if k_o exceeds $\varkappa_m/2$ where $\varkappa_m$ is the $\varkappa$-value for which the structure factor has its first maximum.

Another case of a double scattering process is given for scatterers containing a considerable amount of hydrogen where most of the scattering is incoherent elastic or quasielastic. If the sample scatters more than 20 % of the incident beam serious corrections might be necessary in corresponding the scattering of standard and sample especially if one is interested in the tails of the scattering law. The corrections are kept to a minimum if sample and standard have the same value for $N_H \cdot D$ where N_H is the number of hydrogen atoms per unit volume and D is the sample thickness.

The absolute value of $d\sigma/d\Omega$ can be obtained quite easily by calibration with vanadium or a thin polyethylene foil ($\Sigma_{tot} \cdot D < 0.1$) within an accuracy somewhere between 5 and 10 % depending on the effort. The transmissions $\exp(-\Sigma_{tot} D)$ must be measured separately. Keeping collimation fixed the calibration is done for high intensities without changing the detector position. In case of highly collimated beams it is advisible to put the detector near to the collimator exit (0.5 to 1 m) and to take into account the increase of the acceptance angle $\Delta\Omega_1$.

For weak scatterers some care is necessary for background corrections. One has to measure without sample the background for the open collimator, for the collimator closed at the entrance, at the exit and at both the entrance and the exist. The last three measurements should result the same[x] overall background which has to be subtracted unattenuated. The additional counting rate one has for the open collimator has to be subtracted only after multiplying by the sample transmission. Background determination and calibration have to be done repeatedly in the course of an experiment,

[x] If not, the experimenter should think about what happened.

because there always are slight if not even severe changes.

For a given scattering law to be investigated a proper resolution has to be applied. The $\underline{\varkappa}$-resolution can be decomposed into three mutually perpendicular directions: the radial resolution $\delta\varkappa_r$ parallel to $\underline{\varkappa}$, the parallel resolution $\delta\varkappa_{\parallel}$ parallel to the incident beam and the azimuthal resolution $\delta\varkappa_\varphi$ which is perpendicular to $\underline{\varkappa}$ and the incident neutron beam direction.

The resolution elements $\delta\varkappa_r$, $\delta\varkappa_{\parallel}$ and $\delta\varkappa_\varphi$ as well as all other resolution elements δx to be used later are root mean square values. The $\underline{\varkappa}$-resolution depends on finite geometrical elements, i.e. the finite sizes of collimator entrance and exit and of the detector elements. It also depends on the wavelength resolution. Monochromators used in small angle scattering are normally mechanical velocity selectors for which the typical wavelength spectrum is triangular in shape with some roundings at the corners which increase with decreasing angular resolution (Fig. 5). Normally the resolution $\Delta\lambda/\lambda_m$ is between 0.05 and 0.2 and most problems need no better resolution as we know from our experience in Jülich and Grenoble. A special case exists for high wavelength- and moderate angular resolution if one tries to obtain this with a mechanical velocity selector. The resulting resolution element is shown in Fig. 6. For neutrons scattered into a direction parallel to the velocity selector slits one has optimal focussing condition.

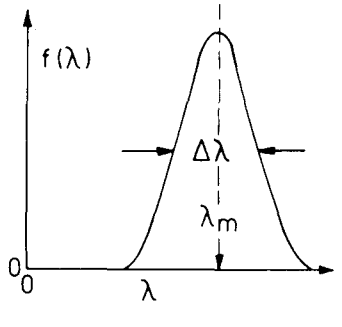


Fig.5: Wavelength spectrum.

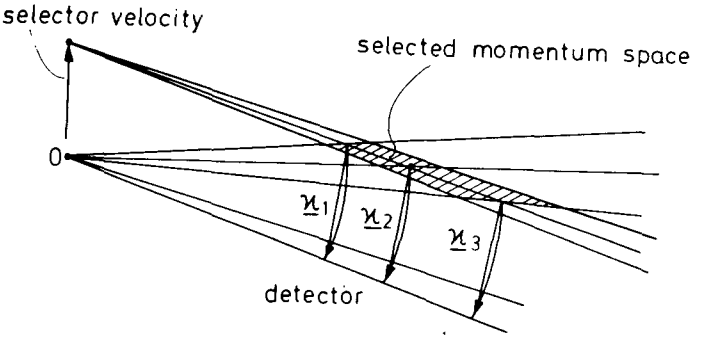


Fig.6: Special focussing condition.

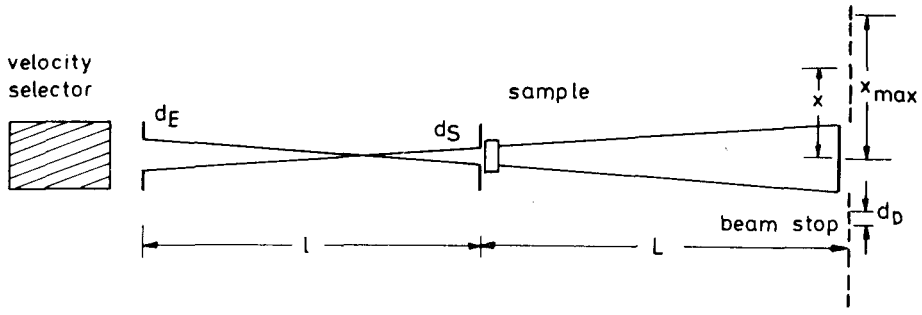


Fig.7: Schematical sketch for resolution elements.

Using the geometrical data of Fig. 7 we get with the assumption of a homogeneously illuminated collimator after a simple calculation

$$\left(\frac{\delta\lambda_r}{\lambda_r}\right)^2 = \frac{1}{12}\left[\left(\frac{d_D}{x}\right)^2 + \left(\frac{d_E}{x}\right)^2\left(\frac{L}{l}\right)^2 + \left(\frac{d_S}{x}\right)^2\left(1+\frac{L}{l}\right)^2 + 2\cdot\left(\frac{\Delta\lambda}{\lambda}\right)^2\right] \quad (8)$$

Because the intensity at the detector is proportional to d_D, d_E, d_S and $\Delta\lambda$ it is reasonable that each of the four terms in eq. (8) gives approximately the same contribution. To obtain this, a good choice is L = l, $d_D = d_E = 2d_S$ and $\sqrt{2}\,\Delta\lambda/\lambda = d_D/x$. If a multidetector is used the condition above should be chosen for $x = x_{max}/2$. Thus, for $x > x_{max}/2$ the wavelength resolution is below and for $x < x_{max}/2$ it is above its optimal value. However such small misadjustments can easily be tolerated. We know from computer experiments /9/ that even a 30 % change in the resolution condition changes very little the quality of the final result. We now give an example: Assume we have a multidetector with d_D = 1 cm and x_{max} = =32 cm (D11). With a sample size of 1 cm we choose d_E = 2 cm and take the counting rate of the detector elements together, which gives an effective value d_D = 2 cm. Thus $\Delta\lambda/\lambda = (d_D/(x_{max}/2))/\sqrt{2} \simeq 0.09$ is a proper choice. With a maximum length of L = l = 40 m (D11 in Grenoble) the medium scatter-

ing angle with this optimal condition is $\vartheta = 16/4000$ radian which gives for $\lambda = 20$ Å a $\varkappa$-value of $9.2\ 10^{-3}$ Å^{-1}. Lattice spacings of 5000 Å can be well resolved!

Assuming 'point' geometry, i.e. the same geometrical resolution elements in both directions perpendicular to the incident neutron beam we obtain for the azimuthal resolution $(\delta\varkappa_\varphi/\varkappa_r)^2$ the same expression as for $(\delta\varkappa_r/\varkappa_r)^2$ if the contribution of the wavelength resolution is set to zero.

For a horizontal neutron beam and long neutron flight paths one has to take into account gravity effects. Depending on the direction of $\underline{\varkappa}$ this influences $\delta\varkappa_r$ or $\delta\varkappa_\varphi$. Below the primary beam gravity acts so as to defocus. Focussing by gravity can be obtained above the primary beam with a proper arrangement of the collimator slits relative to the detector /10/.

The parallel resolution $\delta\varkappa_{\parallel}$ finally is given by a wavelength and an angular distribution again. For point geometry it is

$$\left(\frac{\delta\varkappa_{\parallel}}{\varkappa_r}\right)^2 = \left(\frac{\varkappa_r}{k_0}\right)^2 \cdot \left(\frac{\delta\varkappa_r}{\varkappa_r}\right)^2 \qquad (9)$$

The resolution element $\delta\varkappa_{\parallel}$ is a factor ϑ smaller than $\delta\varkappa_r$. Using actual numbers, spacings of 5000 Å x 4000/8 = 0.25 mm could thus made be observable! $\delta\varkappa_{\parallel}$ is also roughly a factor k/k_0 smaller than $\delta\varkappa_\varphi$. Both these resolution elements are perpendicular to $\underline{\varkappa}$. For high resolution therefore one should put the direction to be investigated parallel to the incident beam if possible. Unfortunately, there is no way to improve $\varkappa_r$ without considerable intensity loss.

The development of two-dimensional multidetectors favoured in general the use of point-geometry. The essential advantage was the simultaneous registration of the two-dimen-

sional scattering pattern (Fig. 8a). An alternation to point-geometry is slit geometry. For instance for an isotropic scatterer one has two possibilities: either one keeps point-geometry and one collects the counting rates of all detector elements with nearly the same distance from the central beam (Fig. 8b) or one opens the primary beam in one direction and takes together detector elements in just this direction (Fig. 8c). The latter procedure is evidently better if one

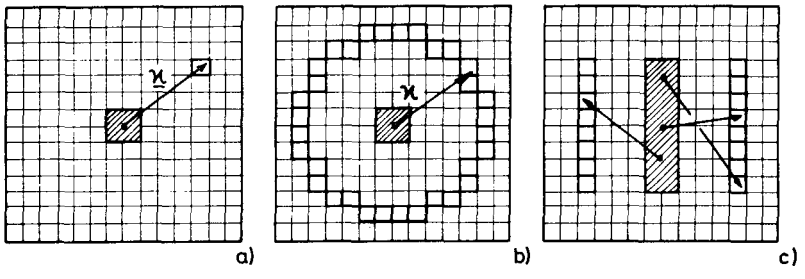


Fig.8: Different counting arrangements.

has a long thin sample which cannot properly be illuminated in point-geometry. A tendency towards the use of slit geometry exists also for experimenters using position sensitive wire counters. These counters have a spatial resolution down to 5 mm along their axis whereas their extension perpendicular to the axis is 2.5 or 5 cm. On the other hand such position-sensitive counters offer a cheep multidetector solution. At the ILL a multidetector is in development of size 64x64 cm^2 with detector element sizes of 0.5x1 cm^2. This will be suitable both for extreme slit and for 'point'-geometry.

A schematic sketch of an optimal layout is shown in Fig. 9: The machine has some maximum length between 20 and 80 m. The sample position is kept fixed at the middle of this distance. The detector can be put at various positions inside the vacuum tube behind the sample. The collimator length is changed by replacing neutron guide tubes with collimator

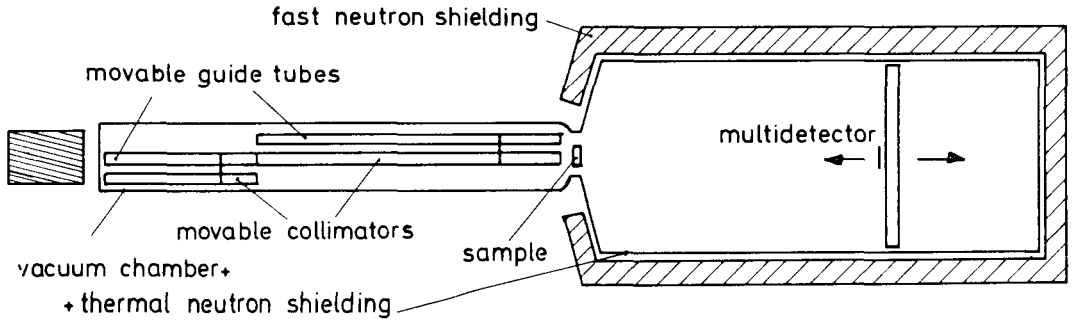


Fig.9: Important components of a small angle scattering set-up.

pieces or vice versa. The velocity selector is placed before the total set-up. (Focussing as in Fig. 6 is however not possible in this case.) The total apparatus is shielded carefully against thermal neutrons by cadmium. Additional shielding of the detector against fast neutrons might be necessary. An optimum choice of the sample thickness is advisible. This is given by $D = 1/\Sigma_{tot}$. Finally one can optimize within limits the neutron wavelength. For devices connected to a cold source the optimum wavelength ranges between 6 and 20 Å whereas at beam holes without cold source the proper choice is between 4 and 8 Å in most cases /11/. Small angle scattering experiments are in many cases possible at low flux reactors ($\simeq 5 \cdot 10^{12}$ n/sec cm^2) without cold source.

DENSITY AND COMPOSITIONAL FLUCTUATIONS

Typical density or compositional fluctuations investigated by neutron small angle scattering are: voids, precipitates, dislocations, radiation damaged zones, surface inhomogeneities, cracks, pores and any other types of inhomogeneities.

As an example we present the scattering curve (Fig. 10) obtained from a fast-neutron-irradiated aluminium-single-cry-

stal /12/. The sample contained voids with a volume fraction of 0.7 % and an average diameter of about 400 Å. For high $\varkappa$-values (10^{-2} to 10^{-1} Å^{-1}) the scattering cross-section has had extremes for $\underline{\varkappa}$ parallel to the [11$\bar{1}$]- and the [100]-crystallographic direction /13/. This special behaviour is caused by the shape of the voids, which are truncated octahedrons

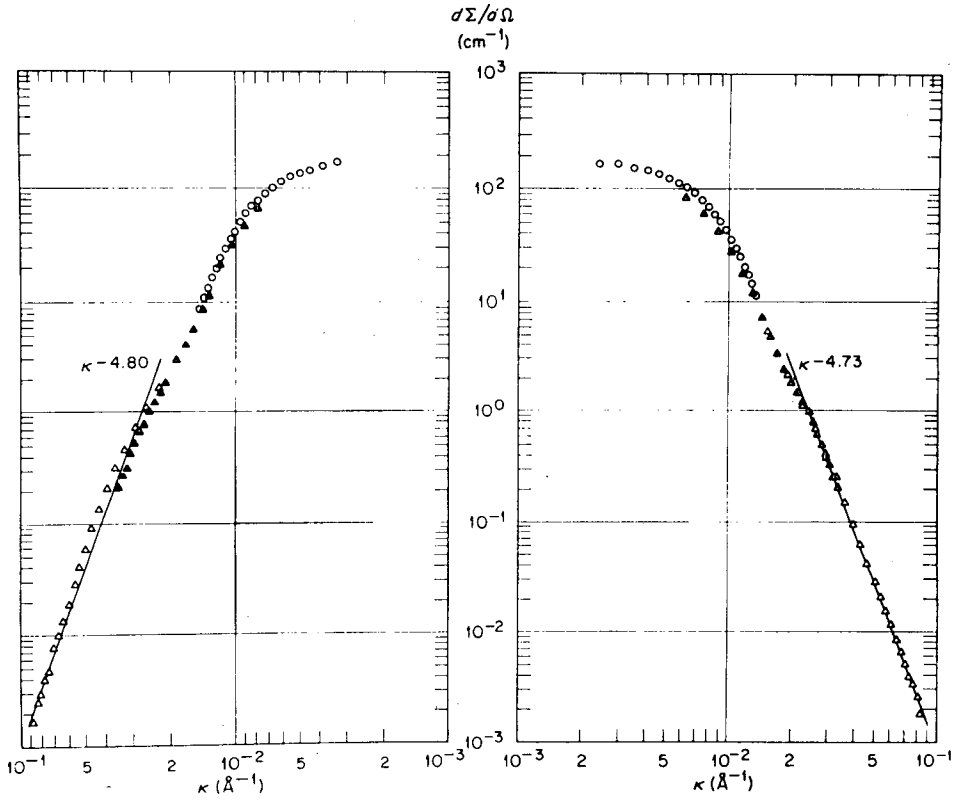


Fig.10: Typical scattering curve for specimen Al-5 as recorded at 12 (o), 5(▲), and 2(△)m specimen-to-detector distances by Detector D1 on the left- and right-hand sides of the detector. Detector centre-line displacement from the beam axis is 1 cm.

with (111)- and (100)-surfaces. The many decades covered in Fig. 10 for $d\Sigma/d\Omega$ clearly demonstrate the sensitivity of the method and a few more general remarks should be made about this:

The beam intensity I_o for the 5m-experimental run in Fig. 10 was 2.5×10^4 n/sec cm^2 for a wavelength of 8 Å, $\Delta\lambda/\lambda_m = 0.2$ and a collimation of the incident beam $\Delta\Omega_o$ =

$= 4.4 \times 10^{-5}$ steradian /14/. The illuminated sample volume F·D was 7.5 cm^3 and the detector area 1000 cm^2 ($E \simeq 0.7$). From these data the number of counted neutrons within 4 hours results as about $2 \cdot 10^6$ as the reader can easily recalculate. We see the volume fraction could even be as low as 10^{-5} and still the voids would be detectable! The sensitivity decreases as 1/R for constant volume fraction because $d\sigma/d\Omega$ increases as R^3 however the product $\Delta\Omega_0 \cdot \Delta\Omega_1$ decreases with $1/R^4$. For $R < 100$ Å $\Delta\Omega_0$ is no more determined by the resolution because the incident beam is already collimately sufficiently by the guide tube. Thus for $R < 100$ Å the sensitivity is proportional to R. In addition for small R's the incoherent elastic scattering may lower the sensitivity.

Recently at D11 it became evident that neutrons are even small-angle scattered by long-wavelength surface imperfections. From measurements on polycrystalline samples of aluminium, aluminium alloys and vanadium of different grain size and after various etching and annealing treatments it was concluded that surface inhomogeneities contributed to the scattering /15,16/. The surfaces S deduced from the scattering power in the asymptotic $\varkappa^{-4}$ region have been found to be comparable to the real surface /15/. It is an open question now whether the unexplained scattering from polycrystalline copper arises really from grain boundaries or from surface inhomogeneities correlated with the grain size.

We end this section by listing heterogeneities of various systems studied within the last few years or being under study: agglomerates of quenched-in thermal vacancies in a stochiometric β'-NiAl compound /17a/; concentration fluctuations of an $Al_{0.6}Zn_{0.4}$-alloy above the incoherent critical point (351 °C) and between the coherent and incoherent (325 °C) critical point /18/; concentration fluctuations in the Nb-D system above the incoherent critical point /19/; concentration fluctuations and possibly spinodal decomposition in a

$(Cu65)_{0.435}(Ni62)_{0.565}$-alloy /20/ (the average coherent scattering length is zero for this special composition, the difference in scattering length very large); possibly $Al_{12}Fe_3Si$--precipitates in Al(Si,Fe)-alloys /16/; precipitates in the Al-Mg-Zn alloy system /21/ (combined X-ray and neutron small angle scattering experiments allow to determine solubility limits in ternary alloys in favourable cases /22/); precipitates in $Al_{1-x}Mg_x$ ($7\ \% < x < 13\ \%$) alloys /23,24,25/; precipitates in Al-Zn alloys /17b,26/; dislocation arrangements in coldworked nickel- /27,28/ and iron-/29/ single crystals; spinodal decomposition in an $(Al_2O_3)_x$-$(SiO_2)_{1-x}$ liquidus-quenched system ($x \simeq 0.2$ to 0.4) /30/; clusters in silicon single crystals /17c/; damage zones in a fast-neutron irradiated GaAs single crystal /17d/; needle-like Cu-rich zones in a $CeCo_{3.5}Cu_{1.5}$-alloy /31/ and compositional fluctuations in a SiO_2-12mol% Na_2O glass /32/. The listing could be enriched by taking systems studied on the border line between diffuse and small angle scattering as for instance liquid alloys. Recent reviews on dislocation scattering /33/ and about studies of defect structures /34,35/ should be mentioned.

MAGNETIC INHOMOGENEITIES IN THE SOLID STATE

The studies on possible coexistence of ferromagnetism and superconductivity ($Ce_{0.8}Tb_{0.2}Ru_2$) and on the cluster structures of an invar alloy ($Fe_{0.65}Ni_{0.35}$), both mentioned in /1/, have been continued and completed /36/. For $Fe_{0.65}Ni_{0.35}$ /37/ a broad maximum in the scattering as a function of temperature has been observed with its center about 50 °C below T_c (225 °C).

Superparamagnetic clusters have been studied in Co-Ca--alloys /38/. For very fine nickel particles (average diameter about 70 Å) by small-angle scattering with 1.2 Å polarized neutrons either 3 to 4 magnetic dead layers or 2 layers

of reversed magnetization have been found at the surface /39/. From small-angle diffraction it was concluded that MnSi has at 4.2K a helical spin structure with a period of 68 unit cells in the [111]-direction /40/. Also for FeGe a helical spin structure with about 700 Å repetition length has been found /17e/. The critical scattering of nickel becomes anisotropic by external stress for T approaching T_c at values of $(T-T_c)/T_c$ below 10^{-3} /41/. Current interest in spin glass systems has also led to some studies at $Au_{1-x}Fe_x$ alloys. For $x > 0.15$ the scattering peaks at temperatures known as Curie temperatures from other measurements. At all concentrations however there is below T_c and below 50 to 100 K a continuous increase of scattering with decreasing temperature which seems to be characteristic for spin glasses /42/. There are drastic changes of the magnetic scattering near the freezing temperature at very small scattering angles for $x < 0.15$ /43/. Scattering by Bloch walls is a complicated phenomena because it can no more be handled solely in simple first Born approximation. For a ⟨110⟩ - 90° Bloch wall in an Fe(2.5 % Si) single crystal the problem has been tackled both theoretically and experimentally /44,45/.

FLUX-LINES IN TYPE-II SUPERCONDUCTORS

Earlier work as reviewed in /1/ has been continued by analyzing the form factors of flux-lines in Nb as a function of temperature and magnetic flux /46/ and by investigation of the perfection of the flux line lattice and its correlation to the metal lattice for Nb with various crystal orientations and for $Pb_{1-x}Tl_x$ /47,48/. Recent reviews are concerned with the work of the Saclay group /49/, the morphology of the flux-line lattice /50/ and with the whole subject /51/.

The experiments in Jülich have now been concentrated

on the use of the excellent resolution $\delta\varkappa_{\parallel}$ mentioned before, for flux-lines oriented parallel or nearly parallel to the incident neutron beam (Fig. 11a).

By supplying a transport current $\underline{j}$ perpendicular to the flux lines /52/ and to the scattering vector $\underline{\varkappa}$ (Fig. 11a) the flux line lattice moves with the velocity $\underline{v}_L \parallel$ to $\underline{\varkappa}$. Within the moving coordinate system the incident neutrons have the velocity $\underline{v}_o'$ (Fig. 11b). If the Bragg-condition was fulfilled for the velocity pair $\underline{v}_o, \underline{v}_1$ for the flux-lines at rest the sample has to be turned around an axis parallel to $\underline{j}$ with an angle $\Delta\varphi = |\underline{v}_L| / |\underline{v}_o|$ in order to obtain again the Bragg-condition, which in Fig. 11b holds then for the velocity pair $\underline{v}_o', \underline{v}_1'$. The idea sounds simple but the experiment was very difficult because at motion the flux-lines were bent parabolically and therefore the initially narrow rocking curve was broadened to an extent much higher than the velocity shift $\Delta\varphi$. As shown in Fig. 11c the final result for v_L agreed well with the velocity calculated from the fundamental equation $\underline{E} = -(\underline{v}_L \times \underline{B})$, where $\underline{B}$ is the magnetic flux density and $\underline{E} \parallel \underline{j}$ the electric field vector. This experiment is the first one in which the flux line velocity was measured.

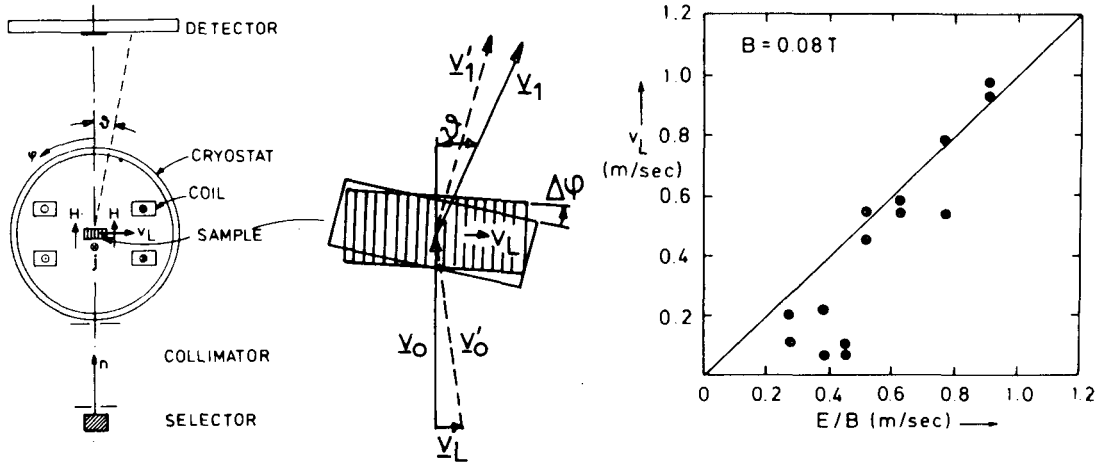


Fig.11: Direct observation of current-induced flux flow; a) experimental set-up, b) sketch for the Bragg-condition, c) result.

The same geometry as in Fig. 11a (however with $\underline{j} = \underline{0}$) was used to determine the bending of flux-lines by the presence of pinning centres /53/. Disc-shaped precipitates of Nb_2N in Nb have been chosen as pinning centres. Nuclear small angle scattering at room temperature was used in addition to measure diameter ($\simeq$ 3500 Å), thickness ($\simeq$ 500 Å) and number densities (1.3×10^{11} to 1.3×10^{12} cm^{-3}) of the precipitates. Acting as pinning centers they cause a mean square fluctuation $(\delta\varphi)^2$ of the flux lines relative to the field direction, which was measured by the broadening of the rocking curves. The experiments are the first microscopic proof of current pinning theories. The geometry of Fig. 11a was also used to decide whether a transport current is carried in the bulk of type II superconductor or at its surface.

POLYMERS IN THE SOLID STATE

Solid polymers offer quite a special problem for diffractionist. X-ray techniques give no information on the configuration of the polymer chain molecules because for X-rays a chain molecule on a long-wavelength scale (10 — 500 Å) has no contrast to its neighbouring molecules. Such a contrast however exists for neutrons for samples with a small fraction of deuterated molecules in an undeuterated matrix or vice versa. The scattering lengths of H and D are -0.38×10^{-12} cm and $+0.65 \times 10^{-12}$ cm respectively and they differ so much that within the last few years the problem of polymer configuration could be tackled quite successfully. For polymers in the glassy state - PMMA /55/ and polystyrene /56,57/ - the scattering curves and their dependence on the molecular weight was fully in agreement with the predictions of Flory's random coil model. This holds even for the assymptotic scattering (χ^{-2}) of polystyrene. Also the scattering data for polyethylene in the melt /58/ are consistent with the random coil

model. Current studies are concerned with the configuration of chain molecules in partially crystalline polyethylene /59/, with polymer networks and with the confermation of stretched molecules. Considerable progress is to expect.

FUTURE DEVELOPMENTS?

The number of applications in materials science and especially in biology is still increasing and a second instrument at the ILL (M. Roth, D17) is under construction to take off part of the pressure at D11. By the use of multidetectors also small or medium flux reactor can successfully compete. Well-developped equipments are in Jülich and in Saclay. Activities are growing up at various places, e.g. for FIAT at Pisa, at Geesthacht (GKSS) and at Aldermaston (University of Reading). There is special interest in non-destructive material testing /60/. After a preliminary series of experiments at turbine blades, fatigued copper, creep fatigued steel, fast neutron-irradiated steel, welded steel and other materials, neutron small angle scattering has a good chance to be applied in an increasing extent for technological problems.

Quite undevelopped is small angle inelastic scattering. The technique of very long-wavelength neutrons (50 to 300 Å) as developped for instance by Steyrl at the FRM offers new possibilities. With an easy calculation along the guide lines given in /61/ one can show that for inelastic scattering problems the intensity goes as $1/k_o$ even for 1/v absorbers. Diffusive motion of macromolecules might be investigated with very long wavelength neutrons.

It would be desirable that polarized neutron technique or even polarization analysis is introduced in small angle scattering techniques. Finally, I think that in case when enough sample volume is available scattering intensities

could be enhanced by building huge 'point' focussing mirrors (size 30 m x 1 m), which would allow to illuminate a sample area of 0.1 m^2. Such an effort would require of course a first class problem.

ACKNOWLEDGEMENT

First of all I have to thank Dr. J. Schelten who accompanied me for many years. He is now the far more active scientist in this field. I have to thank also many other collegues, especially Dr. K. Ibel, Dr. G. Kostorz, Dr. M. Roth, Dr. Julia Higgins and Dr. O. Schärpf. Looking far back I am also deeply indebted to Prof. Maier-Leibnitz and to Prof. Springer who supplied the activities and participated for many years beginning as early as 1961.

REFERENCES

1. W. Schmatz, T. Springer, J. Schelten and K. Ibel, J. of Appl. Cryst. 7, 96 (1974).
2. A. Guinier and G. Fournet (1955) Small Angle Scattering of X-rays, New York: John Wiley.
3. A. Guinier (1963), X-ray Diffraction, San Francisco, W.H. Freeman.
4. W.W. Beeman, P. Kaesberg, J.W. Anderegg and M.B. Webb (1957). In Handbuch der Physik, edited by S. Flügge, 32, Berlin and New York:Springer-Verlag.
5. I.I. Gurwich and L.V. Tarasov (1968), "Low Energy Neutron Physics" (R.I. Sharp and S. Chomet, eds.), p. 541, North-Holland Publ. Amsterdam.
6. W. Schmatz (1973). In Treatise on Materials Science and Technology 2, edited by H. Herman, pp. 105-229, New York: Academic Press.
7. W. Marshall and S.W. Lovesey (1971). Theory of Thermal Neutron Scattering, edited by W. Marshall and P.H. Wilkinson, Oxford: Clarendon Press.
8. K. Ibel (1975). Proceedings of the Neutron Diffraction Conference, Petten 1975. Reactor Centrum Nederland, Report RCN-234, p. 15, also submitted to J. of Appl. Cryst. 1976.
9. O. Glatter, private communication.

10. K. Ibel, W. Schmatz and T. Springer, Atomkernenergie 17, 15 (1971).
11. W. Schmatz, to be published as JÜL-Report.
12. R.W. Hendricks, J. Schelten and W. Schmatz, Phil.Mag. 30, 819 (1974).
13. R.W. Hendricks, J. Schelten and G. Lippmann, to be submitted to Phil. Mag.
14. J. Schelten and R.W. Hendricks, J. of Appl. Cryst. 8, 421 (1975).
15. M. Roth, to be submitted to J. of Appl. Cryst.,
16. G. Kostorz, ILL Scientific Report 75 K 250S, Grenoble 1975.
17. ILL-Annex to the Annual Report 1975, Grenoble 1976: a) J.E. Epperson, D. Berner, C. Ruano and G. Kostorz, exp. no. 07-03-040; b) D. Allen, G. Kostorz and R.J. Stewart, exp. no. 07-03-035; c) E.W.J. Mitchell, R.J. Stewart, R. Beddoe, S. Messoloras and G. Kostorz, exp. no. 07-03-025; d) E.W.J. Mitchell, R. Beddoe, S. Gupta, G. Kostorz and R.W.J. Stewart, exp. no. 07-03-011 A/42; e) C. Wilkinson, J.B. Forsyth and F. Sinclair, exp. no. 05-02-055 A.
18. D. Schwahn, Dissertation an der Ruhr-Universität Bochum.
19. N. Stump and W. Münzing, private communication.
20. J. Vrijen and C. van Dyjk, Reactor Centrum Nederland Report, RCN-75-054.
21. J.E. Epperson, V. Gerold and G. Kostorz, current work.
22. V. Gerold, submitted to J. of Appl. Cryst.
23. J.M. Raynal, M. Roth, M. Bernole, P. Guyot and R. Graf, C.R. Acad. Sci. Paris, Série B 277, 225 (1973).
24. M. Roth and J.M. Raynal, J. Appl. Cryst. 7, 219 (1974).
25. J.M. Raynal and M. Roth, J. Appl. Cryst. 8, 535 (1975).
26. S.A. Messoloras, P.H.D. Thesis University of Reading.
27. W. Vorbrugg and O. Schärpf, Phil. Mag. 32, 629 (1975); W. Vorbrugg, Phil. Mag. 32, 643 (1975).
28. H. Scheuer, Dissertation Dr. rer. nat. an der Ruhr-Universität Bochum, 1976.
29. G. Göltz, Dissertation Dr. rer. nat. an der Universität Stuttgart, 1976.
30. C.M. Jantzen, D. Schwahn, W. Schmatz and H. Herman, Verhandlungen der Deutschen Physikalischen Gesellschaft 7, 594 (1976).
31. J.H. Wernick, Ann. Rev. Mat. Sci. 2, 607 (1972).
32. M. Roth and J. Zarzycki, J. Non-Cryst. Solids 16, 93 (1974).
33. W. Schmatz, Rivista del Nuovo Cimento 5, 398 (1975).
34. G. Bauer, E. Seitz and W. Just, J. Appl. Cryst. 8, 162 (1975).
35. G. Kostorz, Proceedings of the 61st Enrico Fermi Summer School, Varenna 1974.
36. S. Roth, K. Ibel and W. Just, J. Appl. Cryst. 7, 230 (1974).

37. S. Komura, G. Lippmann and W. Schmatz, Proceedings of the Neutron Diffraction Conference, Petten 1975, Reactor Centrum Nederland Report RCN-234, p. 89.
38. R. Cywinski, J.G. Boeth and B.D. Rainford, J. Phys. F, to be published.
39. M. Sato and K. Hirakawa, J. of the Phys. Soc. of Japan 36, 1467 (1975).
40. Y. Ishikawa, K. Tajima, D. Bloch and M. Roth, submitted to Solid State Communications.
41. F. Söttge, K. Stierstadt, G. Göltz and K. Ibel, submitted to Solid State Communications.
42. A.P. Murani, S. Roth, P. Radhakrishna, B.D. Rainford, B.R. Coles, K. Ibel, G. Göltz and F. Mezei, J. Phys. F: Metal Phys. 6, 425 (1976).
43. A.P. Murani, private communication.
44. O. Schärpf and R. Seifert, Proc. of the Neutron Diffraction Conference, Petten 1975, Reactor Centrum Nederland Report RCN-234, p. 90.
45. O. Schärpf and H. Strothmann, Conference on Neutron Scattering, Gatlinburg 1976.
46. R. Kahn and P. Thorel, Low Temp. Phys. LT13, 3, 64 (1973).
47. M. Roger, R. Kahn and J.M. Delrieu, Physics Letters 50 A, 291 (1974).
48. R. Kahn and G. Parrette, Sol. State Commun. 13, 1839 (1973).
49. P. Thorel, R. Kahn, Y. Simon and D. Cribier, Journal de Phys. 34, 447 (1973).
50. J. Schelten, Proceedings of the Int. Discussion Meeting on Anisotropy Effects in Superconductors, Wien, April 1976, ed. by R. Baker, Plenum Publishing Company Limited, London, 1976.
51. J. Schelten, Habilitationsschrift an der Ruhr-Universität Bochum, 1976.
52. J. Schelten, H. Ullmaier and G. Lippmann, Phys. Rev. B12, 1772 (1975).
53. G. Lippmann, J. Schelten and W. Schmatz, Phil. Mag. 33, 475 (1976).
54. J. Schelten and D.M. Kroeger, Conference on Neutron Scattering, Gatlinburg 1976.
55. R.G. Kirste, W.A. Kruse and K. Ibel, Polymer 16, 120 (1975).
56. G.D. Wignall, D.G.H. Ballard and J. Schelten, Europ. Polymer J. 10, 861 (1974).
57. J.P. Cotton et al., Macromolecules 7, 863 (1974).
58. G. Lieser, E.W. Fischer and K. Ibel, Polymer Letters Edition 13, 39 (1975).
59. J. Schelten, G.D. Wignall, D.G.H. Ballard and W. Schmatz, Kolloid-Z. 252, 749 (1974a).
60. P. Pizzi and H. Walther, J. Appl. Cryst. 7, 230 (1974). C.P. Galotto, P. Pizzi, H. Walther, V. Angelostro, N.Cherullo and G. Cherubini, to be published in Nucl. Instr. and Methods.
61. H. Maier-Leibnitz, Nukleonik 8, 861 (1966).

NEUTRON INTERFEROMETRY

S. A. Werner
Physics Dept., University of Missouri-Columbia
Columbia, Missouri 65201

R. Colella and A. W. Overhauser
Physics Dept., Purdue University
W. Lafayette, Indiana 47907

C. F. Eagen
Scientific Research Staff, Ford Motor Company
Dearborn, Michigan 48121

ABSTRACT

In this paper we review our work using a neutron interferometer, and discuss our ongoing and planned experiments in neutron interferometry at the University of Missouri Research Reactor (MURR). The basic theory of the neutron interferometer is discussed. Two experiments of direct relevance to fundamental physics are described:

1. Observation of the quantum-mechanical phase shift of neutrons caused by their interaction with the Earth's gravitational field.
2. Observation of the sign reversal of the wave function of a fermion produced by its precession of 2π radians in a magnetic field.

INTRODUCTION

Neutron interferometry is one of the newest developments in neutron scattering. It is particularly important because we now have an instrument which is sensitive to the relative phases of neutron waves, while all other instruments are amplitude sensitive only. There are currently two groups which are actively engaged in neutron interferometry. There will undoubtedly be many more as time passes. The group working at the Institute Laue-Langevin has performed some very interesting experiments recently. Some of their results will be discussed in another paper at this conference.[1] Our group began experiments at the University of Michigan reactor about a year and a half ago. We now have a beam port at the 10 MW University of Missouri Research Reactor (MURR). The flux at this

beam port is at least a factor of 10 higher, which will permit us to enormously extend and refine our experiments.

The basic design of our interferometer is the same as that first developed by Bonse and Hart[2] for x-rays in 1965. That this design would work as a neutron interferometer was first shown by Rauch, Treimer and Bonse[3] in 1974. A schematic drawing of our interferometer is shown in Fig. 1. It was fabricated from a 5 cm diameter, dislocation-free, single crystal of silicon. The material between the three upright plates was cut away using a diamond saw. The surfaces of the crystal were strongly etched to remove work damage resulting from the cutting operation.

THEORY OF THE NEUTRON INTERFEROMETER

A nominally monoenergetic thermal neutron beam is directed along the line AB (Fig. 1) and is coherently split near point A by Bragg reflection in the first Si slab. These two coherent beams are again split at points B and C in the second slab. Two of these beams overlap and interfere near point D in the third Si slab. We use the (220) reflection in our experiments.The outgoing interfering beams are detected using two high pressure (40 atm.) He^3, 1/4 inch diameter, neutron detectors (labelled C_2 and C_3). We also detect the non-interfering beam directed along the line AC with detector C_1. The distances $\underline{a}$ and $\underline{d}$ are 0.2 cm and 3.5 cm respectively.

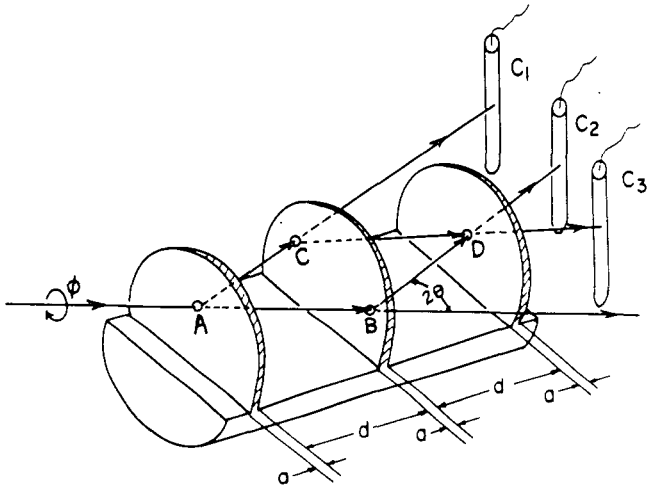


Fig.1. Schematic diagram of the neutron interferometer.

If the beam traversing the path ACD is phase shifted (by a nuclear, magnetic or gravitational interaction) relative to the beam traversing

the path ABD, the expected intensities observed at detectors C_2 and C_3 are

$$I_2 = \gamma - \alpha \cos\beta \qquad (1)$$

and

$$I_3 = \alpha(1 + \cos\beta). \qquad (2)$$

The phase shift is β; α and γ are constants which depend upon the incident flux, the crystal structure and the scattering length of Si. We will derive these intensity relationships here.

We first briefly review the results of the dynamical theory of diffraction for the symmetric Laue case as shown in Fig. 2. Call the incident wave ϕ, the wavefunction inside the crystal ψ, and the wave emerging from the back face of the crystal χ. The incident plane wave

$$\phi(\vec{r}) = \Phi e^{i\vec{k}_o \cdot \vec{r}} \qquad (3)$$

gives rise to 4 internal waves, such that[4]

$$\psi(\vec{r}) = \psi_o^\alpha e^{i\vec{K}_o^\alpha \cdot \vec{r}} + \psi_o^\beta e^{i\vec{K}_o^\beta \cdot \vec{r}} + \psi_G^\alpha e^{i\vec{K}_G^\alpha \cdot \vec{r}} + \psi_G^\beta e^{i\vec{K}_G^\beta \cdot \vec{r}} . \qquad (4)$$

The internal incident wave vectors $\vec{K}_o^\alpha$ and $\vec{K}_o^\beta$ differ from the external incident wave vector $\vec{k}_o$ by a small wave vector normal to the crystal surface. The internal diffracted wave vectors are related to the incident wave vectors by Bragg's Law:

$$\vec{K}_G^{\alpha,\beta} = \vec{K}_o^{\alpha,\beta} + \vec{G} , \qquad (5)$$

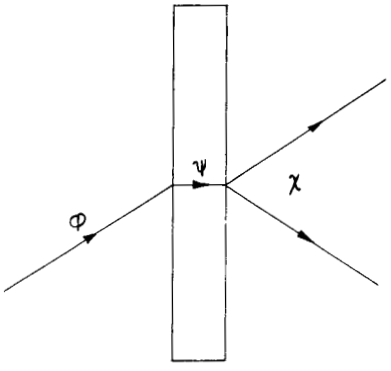


Fig.2. Perfect crystal, Laue case geometry.

where $\vec{G}$ is the reciprocal lattice vector of interest. The indices α and β correspond to the two brances of the dispersion surface (solutions of the secular determinant). The wave function given by Eq. (4) is a solution of the Schrödinger equation (for a single neutron) containing the periodic potential of the crystal corresponding to the reciprocal lattice vector $\vec{G}$ of interest. Continuity of the neutron wave function across the incident boundary then determines the amplitudes $\psi_o^{\alpha,\beta}$ and $\psi_G^{\alpha,\beta}$.

The wave function $\chi(\vec{r})$ emerging from the back face of the crystal is the sum of two coherent plane waves:

$$\chi(\vec{r}) = \chi_o e^{i\vec{k}_o \cdot \vec{r}} + \chi_G e^{i\vec{k}_G \cdot \vec{r}} \quad . \tag{6}$$

This wave function satisfies the Schrödinger equation in free space. The amplitudes χ_o and χ_G and the wave vector $\vec{k}_G$ are determined by continuity of the neutron wave function across the back face of the crystal. The results are

$$\chi_o = \left[i \frac{\eta \sin\xi}{\sqrt{\eta^2 + p^2}} + \cos\xi \right] e^{-i\delta_o} \Phi \tag{7}$$

and

$$\chi_G = \left[i \frac{k_o}{v_G} \frac{p^2}{\sqrt{\eta^2 + p^2}} \sin\xi \right] e^{-i\delta_G} \Phi \quad . \tag{8}$$

Here

$$\xi \equiv a\sqrt{\eta^2 + p^2}/2 \cos\theta_B \ , \tag{9}$$

$$\delta_o \equiv a\left[\frac{v_o}{k_o} + \eta\right]/2 \cos\theta_B \ , \tag{10}$$

$$\delta_G \equiv \delta_o + 2k_o a\Delta\theta \sin\theta_B \ . \tag{11}$$

The crystal thickness is a, θ_B is the nominal Bragg angle, and $\Delta\theta$ is the angular deviation of the incident wave vector $\vec{k}_o$ from the nominal Bragg condition. The quantities p and η are given by

$$p \equiv \frac{|v_G|}{k_o} \quad , \tag{12}$$

and

$$\eta \equiv k_o \Delta\theta \sin 2\theta_B \ . \tag{13}$$

The Fourier components of the neutron-crystal interaction potential v_G are related to the structure factors F_G by

$$v_G = 4\pi F_G / V_{cell} , \tag{14}$$

where V_{cell} is the volume of a unit cell. The wave vector of the diffracted wave is given by

$$\vec{k}_G = \vec{G} + \vec{k}_o + 2 k_o \Delta\theta \sin\theta_B \hat{n} \ , \tag{15}$$

where $\hat{n}$ is a unit vector normal to the crystal surface.

These formulas allow us to calculate the amplitudes of the waves

emerging from the back face of the crystal as a function of $\Delta\theta$. For a fixed wavelength significant diffracted intensity $|\chi_G|^2$ occurs over a very narrow range of $\Delta\theta$, of the order of a second of arc. In practice, the incident beam is always much more divergent than this; consequently the intensities of interest will involve an integration over $\Delta\theta$.

Using these results it is an easy matter to derive an expression for the waves emerging from the third plate of the interferometer. Define the transmission coefficient $T(\Delta\theta)$ and the diffraction coefficient $D(\Delta\theta)$ as the amplitude ratios χ_o/Φ and χ_G/Φ respectively. With these definitions, it is then easy to see that the wave function in the region of detector C_2 is

$$U_2(\vec{r}) = \Phi \Big\{ D(\Delta\theta)e^{i\vec{k}_G\cdot\vec{r}_C}\, D(-\Delta\theta)e^{i\vec{k}_o\cdot(\vec{r}_D-\vec{r}_C)}\, T(\Delta\theta)$$

$$+T(\Delta\theta)e^{i\vec{k}_o\cdot\vec{r}_B}\, D(\Delta\theta)e^{i\vec{k}_G\cdot(\vec{r}_D-\vec{r}_B)}\, D(-\Delta\theta)e^{i\beta}\Big\}\, e^{i\vec{k}_o\cdot(\vec{r}-\vec{r}_D)}\,, \qquad (16)$$

and the wave function in the region of detector C_3 is

$$U_3(\vec{r}) = \Phi \Big\{ D(\Delta\theta)e^{i\vec{k}_G\cdot\vec{r}_C}\, D(-\Delta\theta)e^{i\vec{k}_o\cdot(\vec{r}_D-\vec{r}_C)}\, D(\Delta\theta)$$

$$+T(\Delta\theta)e^{i\vec{k}_o\cdot\vec{r}_B}\, D(\Delta\theta)e^{i\vec{k}_G\cdot(\vec{r}_D-\vec{r}_B)}\, T(-\Delta\theta)e^{i\beta}\Big\}\, e^{i\vec{k}_G\cdot(\vec{r}-\vec{r}_D)}. \qquad (17)$$

The origin of coordinates is taken to be point A. After some algebra we find

$$|U_2|^2 = |\Phi|^2\,[1 + \cos\beta]\; 2\; A(x,\varepsilon) \qquad (18)$$

and

$$|U_3|^2 = |\Phi|^2\,[B(x,\varepsilon) - 2A(x,\varepsilon)\cos\beta]. \qquad (19)$$

Here

$$A(x,\varepsilon) = \frac{1}{(x^2+1)^3}\sin^4\xi\,\left\{x^2 + \cos^2\xi\right\}, \qquad (20)$$

and

$$B(x,\varepsilon) = \frac{1}{(x^2+1)^3}\sin^2\xi\,\left\{(x^2+\cos^2\xi)^2 + \sin^4\xi\right\}. \qquad (21)$$

These functions are dependent on the dimensionless parameters

$$x \equiv \eta/p = \left[\frac{k_o^2 \sin 2\theta_B V_{cell}}{4\pi|F_G|}\right]\Delta\theta\,, \qquad (22)$$

and

$$\varepsilon \equiv \frac{pa}{2\cos\theta_B} = \frac{2\pi|F_G|a}{V_{cell}k_o\cos\theta_B} \quad . \tag{23}$$

From Eq. (9) we see that

$$\xi = \varepsilon\sqrt{x^2 + 1} \quad . \tag{24}$$

Since the beam incident on the interferometer is divergent, we must integrate these expressions over angle. This is equivalent to integrating over the scaled angular variable x. We, thus, see that expression for α and γ in Eqs. (1) and (2) are

$$\alpha = I_o \frac{4\pi|F_G|}{k_o^2 \sin 2\theta_B V_{cell}} 2\int_{-\infty}^{\infty} A(x,\varepsilon)dx \ , \tag{25}$$

and

$$\gamma = I_o \frac{4\pi|F_G|}{k_o^2 \sin 2\theta_B V_{cell}} \int_{-\infty}^{\infty} B(x,\varepsilon)dx \ , \tag{26}$$

where I_o is the incident beam intensity. The integrals appearing in (25) and (26) are shown in Fig. 3. For our experiments a = 0.2 cm, λ = 1.445 Å,

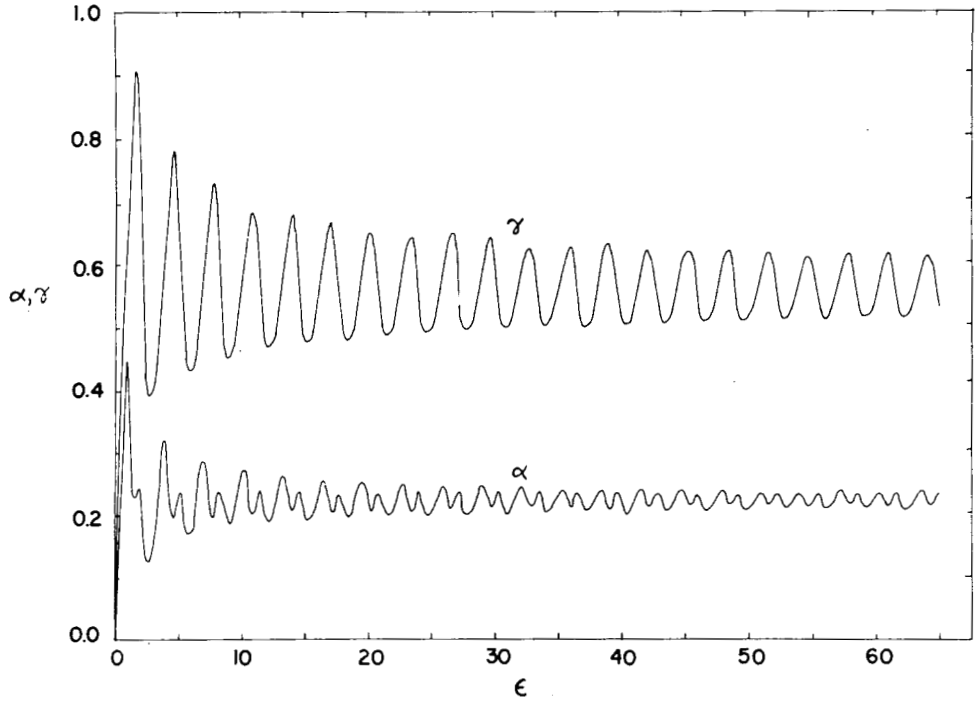


Fig.3. Dependence of α and γ on ε , in units of $4\pi|F_G|I_o/k_o^2 \sin 2\theta_B V_{cell}$.

Si scattering length $b = 0.42 \times 10^{-12}$cm, using the (220) reflection, we get $\varepsilon = 32.8$, and $\gamma/\alpha \approx 2.6$ as observed.

In the theory of the neutron interferometer given by Rauch and Suda[5], an average over the pendellösung interference fringes is performed before the integration over $\Delta\theta$, i.e. the integrands in(25) and (26) are averaged over ε. It is difficult to see the justification for this. This problem does not arise for the x-ray interferometer, since the β branch intensity is strongly absorbed and can be ignored.

GRAVITATIONALLY INDUCED QUANTUM INTERFERENCE

In most phenomena of interest in physics, gravity and quantum mechanics do not simultaneously play an important role. We have carried out such an experiment for which the outcome necessarily depends upon both the gravitational constant and Planck's constant.[6,7]

It is well-known that potentials cause phase shifts. To see this, consider a free neutron, having momentum $\vec{p}_o$, which encounters a region of space where its potential energy is V. The neutron's momentum then becomes $\vec{p}$, such that its total energy E_o is conserved; thus

$$\frac{p_o^2}{2m} = \frac{p^2}{2m} + V. \tag{27}$$

If V/E_o is small, we can solve this equation for the shift in momentum

$$\frac{\Delta p}{p_o} = \frac{\Delta k}{k_o} = -\frac{1}{2}\frac{V}{E_o} \quad . \tag{28}$$

The phase shift caused by the potential is then

$$\beta = \Delta k s = -\frac{1}{2} k_o s \frac{V}{E_o} \quad , \tag{29}$$

where s is the distance over which the neutron feels the new potential V.

For a neutron moving in the gravitational field of the Earth, the potential is

$$V = m_g g H \quad , \tag{30}$$

where H is the height above some reference level and g is the acceleration

due to gravity. The subscript g on the neutron mass indicates that this is the gravitational mass. Consider now the passage of a neutron through the interferometer which has been turned by an angle ϕ about the incident beam line AB, out of the horizontal plane. If we let H_o be the perpendicular distance between the lines CD and AB, then the potential energy difference between these two paths is

$$V = m_g g H_o \sin \phi \quad . \tag{31}$$

Thus, using Eq. (29) we find the neutron phase shift along the path ACD relative to ABD:

$$\beta = q_{grav} \sin \phi \tag{32}$$

where

$$q_{grav} = -2\pi \, m_i m_g \left[\frac{g}{h^2}\right] \lambda_o S H_o \quad , \tag{33}$$

and S is the distance between A and B or C and D, m_i is the inertial mass, and λ_o is the neutron wavelength. Thus, by rotating the interferometer through an angle ϕ, the phase β will change and the intensities I_2 and I_3 will be expected to oscillate. Our first results are shown in Fig. 4.

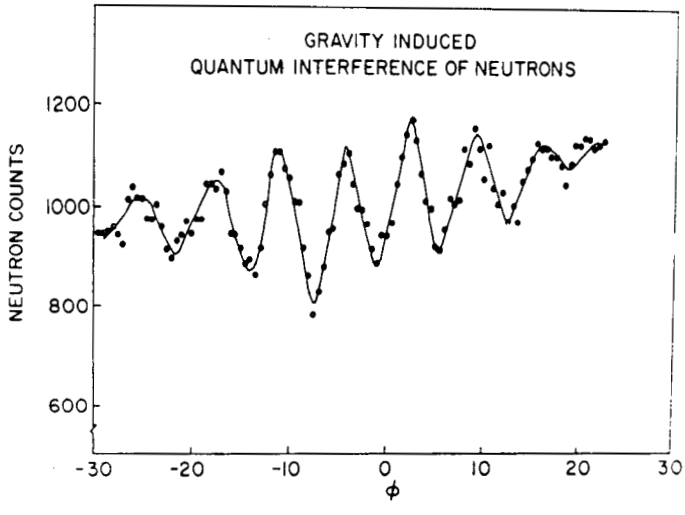


Fig.4. The difference count I_2-I_3 as a function of the interferometer rotation angle ϕ.

By Fourier transforming this data we find that the oscillation frequency is

$$q_{grav}(\text{exp}) = 54.3 \tag{34}$$

while the formula (33) predicts

$$q_{grav}(\text{theory}) = 59.6 \tag{35}$$

We believe that this discrepancy is due to the effect of bending of the interferometer under its own weight, and not that we have assumed the inertial mass m_i and the gravitational mass m_g are equal. We know that the effects of bending are important from our tests of this interferometer using x-rays. We are now setting up an x-ray source on the neutron beam line at MURR

in order to in situ null out the effects of bending.

The importance of a precision experiment cannot be underestimated, since it is the first time that the principle of equivalence ($m_i = m_g$) has been tested in the quantum limit.

There is an additional effect which a precision experiment can detect. Since the experiment is done in the frame of the rotating Earth (a non-inertial frame), an additional term must be added to the Hamiltonian. The correct Hamiltonian is

$$H = \frac{p^2}{2m_i} + m_g g z - \vec{\omega} \cdot \vec{r} \times \vec{p} \ , \tag{36}$$

where $\vec{\omega}$ is the angular frequency of the Earth's rotation. The canonical momentum $\vec{p}$ is obtained from Hamilton's equation

$$\dot{\vec{r}} = \frac{\partial H}{\partial \vec{p}} \ . \tag{37}$$

We get

$$\vec{p} = m_i \dot{\vec{r}} + m_i \vec{\omega} \times \vec{r} \ . \tag{38}$$

The phase shift is obtained by integrating $\vec{p}$ around the interferometer path ACDBA. We get

$$\beta = \frac{1}{\hbar} \oint \vec{p} \cdot d\vec{\ell} = q_{grav} \sin\phi + \frac{2m_i}{\hbar} \vec{\omega} \cdot \vec{A} \ , \tag{39}$$

where $\vec{A}$ is the normal area of the parallelogram ACDBA. The additional term resulting from the Coriolis force depends on the latitude and the interferometer orientation with respect to the North-South longitude line. The magnitude of this term is about 2% of the phase shift due to gravity. Thus, a precision experiment is necessary to detect this effect.[8]

PHASE SHIFT DUE TO SPIN PRECESSION

It is well known that the operator for rotation through 2π radians for a fermion causes a reversal of the sign of the wave function. We have directly observed this effect for neutrons precessing in a magnetic field using the neutron interferometer.[9] Essentially the same experiment has been successfully carried out by the I.L.L. group.[10] This experiment was first suggested by Bernstein.[11]

A schematic diagram of the experiment is shown in Fig. 5. A monoenergetic, unpolarized neutron beam (λ = 1.445 Å) is split at point A of the interferometer. The one beam passes through a dc magnetic field on path AC. The relative phase of the two beams where they recombine and interfere at point D is varied by adjusting the magnetic field $\vec{B}$.

If we take the Hamiltonian for the neutron of momentum $\vec{p}$ and magnetic moment $\vec{\mu}$ to be

$$H = p^2/2m - \vec{\mu} \cdot \vec{B} \quad , \tag{40}$$

it is easy to show that the phase shift to first order in $\vec{B}$ is

$$\beta = \pm 2\pi \, g_n \mu_N m\lambda B\ell \, /h^2 \, . \tag{41}$$

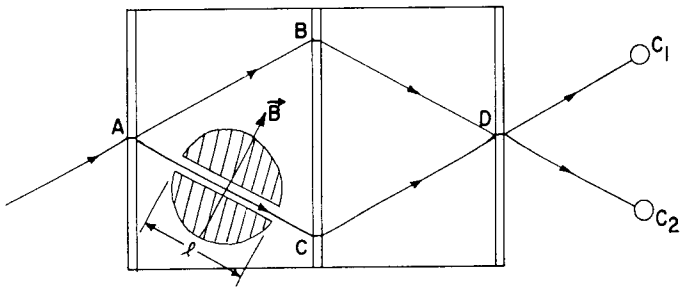


Fig.5. On path AC the neutrons are in a magnetic field B(0 to 500 G) for a distance ℓ(2 cm).

The ± signs are for spin-up and spin-down neutrons; g_n is the neutron magnetic moment in nuclear magnetons (=-1.91), μ_N is the nuclear magneton, and ℓ is the distance over which the neutron is in the magnetic field.

Since the experiment is done with unpolarized neutrons, we must add the contributions of spin-up and spin-down neutrons. There is always a residual phase shift δ in the interferometer due to various causes, including gravity. The counting rates at detectors C_2 and C_3 are expected to be

$$\begin{aligned} I_2 &= I_2(\uparrow) + I_2(\downarrow) \\ &= \left[\frac{1}{2}\gamma - \frac{1}{2}\alpha \cos(\delta+\beta)\right] + \left[\frac{1}{2}\gamma - \frac{1}{2}\alpha \cos(\delta-\beta)\right] \\ &= \gamma - \alpha \cos\delta \cos\beta \quad , \end{aligned} \tag{42}$$

and

$$I_3 = I_3(\uparrow) + I_3(\downarrow)$$

$$= \frac{1}{2}\alpha\,[1 + \cos(\delta+\beta)] + \frac{1}{2}\alpha\,[1 + \cos(\delta-\beta)]$$

$$= \alpha\,[1 + \cos\delta\,\cos\beta]. \qquad (43)$$

We have taken β to be defined by the plus sign in Eq. (41) in these expressions. Thus, if the phase δ is fortuitously $\pi/2$, $3\pi/2$,..., there will be no observable effect of the magnetic field on the intensities.[12] We circumvent this problem by first rotating the interferometer about the line AB, thus using the effect of gravity to set the phase at a maximum or minimum of $I_2 - I_3$ which insures that $\delta = 0, \pi \cdots$.

Eq. (41) predicts that the field required for a precession of 4π (complete period) is

$$B\ell = 272/\lambda\ , \qquad (44)$$

where B is in gauss, ℓ in cm, λ in angstroms. For our magnet and interferometer, the effective

$$\langle B\ell \rangle = 2.7\ B_{gap}[G\cdot cm] \qquad (45)$$

where B_{gap} is the field in the magnet gap.

Some of our first results are shown in Fig. 6. The main oscillation period is found to be 68 ± 2 G. This leads to

$$\langle B\ell \rangle = 265/\lambda\ . \qquad (46)$$

The agreement of this result with theory (Eq. 44) is within the experimental errors we are willing to assign to the measurement of the effective $B\ell$. The modulation of the interference pattern is found to be due to the noncollinear fringing fields from the magnet. This effect can be understood quantitatively by integrating the equations of motion of the neutron spin around the interferometer.

It is clear that we have observed the complete rotation symmetry demanded by the spinor character of the neutron wave function. Future experiments will be devoted to improving the accuracy.

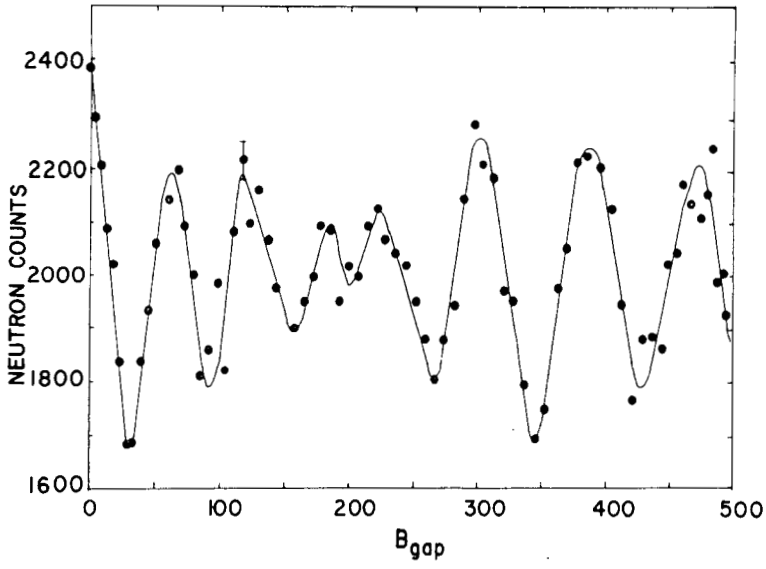


Fig.6. The difference count I_2-I_3 as a function of magnetic field.

THE FUTURE

It is clear to us that the potential applications of neutron interferometry are considerable. We would like to give a glimpse here of some of the experiments we are planning to carry out in the near future.

Precision measurement of the neutron-nuclear scattering lengths of various isotopes is the most obvious application of neutron interferometry. An accurate measurement of the energy dependence of the real part of the scattering length in the vicinity of a low-lying Breit-Wigner resonance, say in cadmium,samarium or lutetium, would be a first, providing data of great importance in isotopic differential labeling in neutron crystallography. To carry out such an experiment, it is necessary to be able to continuously vary the energy of the incident beam. We are currently installing a double crystal (Be) monochromator assembly at our beam port at MURR. The conventional type of triple-axis monochromator assembly will probably be inadequate for this application, since the interferometer must be vibration isolated from the reactor hall.

The phase problem in neutron crystallography can be solved if two coherent beams are aligned so as to simultaneously reflect from a single crystal.[13] The most obvious scheme is to remove the third slab of the

interferometer and place the sample crystal at point D. Simultaneous reflection of the beams incident along BD and CD requires the reciprocal lattice vector $\vec{G}$ of interest in the sample crystal to be of the same length as the reciprocal lattice vector used in the Si beam splitters. This problem can be circumvented by using two separate Si crystals at points B and C. By using the (311) or (111) reflections in these crystals and the (220) reflection in the first slab, and adjusting the incident wavelength, we can simultaneously satisfy the Bragg condition in the sample crystal for $+\vec{G}$ and $-\vec{G}$ for a wide range of reciprocal lattice vectors. This then allows the forward scattered beams to overlap and interfere with the Bragg scattered beams in free space, a condition which is necessary to determine the phase of a structure factor F_G. There are several technical problems which must be overcome to make this scheme work.

We would like to acknowledge the very useful discussions we have had with many of our colleagues, in particular, F. Belinfante, G. W. Ford and J. Huang.

This work was supported in part by Ford Motor Company, the Univeristy of Missouri Research Council, the Materials Research Laboratory (Purdue) program GH33574 A1, and National Science Foundation under contract No. GH41884.

REFERENCES

1. The group working at the I.L.L. consists of H. Rauch, A. Zeilinger, G. Badurek and A. Wilfing from Atominstitut der Oesterreichen Hochschulen, Vienna and W. Bauspiess and U. Bonse from Institut für Physik, Universität Dortmund.
2. U. Bonse and M. Hart, Appl. Phys. Lett. 6, 155 (1965).
3. H. Rauch, W. Treimer and U. Bonse, Phys. Lett. 47A, 369 (1974).
4. For an excellent review of the dynamical theory of diffraction see B. W. Batterman and H. Cole, Rev. Mod. Phys. 36, 681 (1964).
5. H. Rauch and M. Suda, Phys. Stat. Sol.(A) 25, 495 (1974).
6. A. W. Overhauser and R. Colella, Phys. Rev. Lett. 33, 1237 (1974).

7. R. Colella, A. W. Overhauser and S. A. Werner, Phys. Rev. Lett. 34, 1472 (1975).
8. This effect was discussed by Lorne A. Page, Phys. Rev. Lett. 35, 543 (1975).
9. S. A. Werner, R. Colella, A. W. Overhauser and C. F. Eagen, Phys. Rev. Lett. 35, 1053 (1975).
10. H. Rauch, A. Zeilinger, G. Badurek, A. Wilfing, W. Bauspiess and U. Bonse, Phys. Lett. 54A, 425 (1975).
11. H. J. Bernstein, Phys. Rev. Letts. 18, 1102 (1967).
12. The importance of the residual phase was pointed out to us by M. A. Horne and A. Shimony.
13. The theory of scattering of two coherent neutron beams has recently been worked out by M.C.Li, Phys.Rev. B8,3150 (1975). A scheme, which appears to us to be difficult to implement, has recently been proposed by C.C.Chiu and H.Y.Chiu, Bull.Am.Phys.Soc. Series II,vol.21, p668 (1976), and a paper to be published.

RECENT DEVELOPMENTS IN POLARISED NEUTRONS

John B. Hayter
Institut Laue-Langevin, 156X Centre de Tri, 38042 Grenoble Cedex, France

ABSTRACT

In recent years there has been a striking diversification in the application of polarised neutrons to systems with no electronic magnetism, encompassing fields from chemistry to nuclear physics, concurrently with advances in more conventional areas, such as polarised diffuse scattering and magnetic domain topography.

This paper reviews some of these recent developments. The concept of precessing polarisation, central to many of them,is discussed at length. Emphasis has been placed on those new techniques which are emerging to study generally non-magnetic systems. These include neutron spin-echo, in which precessing polarisation is used to label each neutron with its own velocity change on scattering; in-beam NMR, where the polarised neutron is captured to produce an oriented nucleus; and resonance modulated diffraction, which uses magnetic resonance techniques to modulate the structure-factors during polarised neutron diffraction from hydrogenous materials.

New techniques of producing polarised white beams are also briefly reviewed.

INTRODUCTION

Since the neutron is a spin 1/2 particle, its cross-section for scattering from a target system with a preferred axis will in general depend on the relative orientation of this axis and the neutron spin. In certain cases this dependence may be so strong that the cross-section is significant only for one incident spin state, and this is of course the basis of many neutron beam polarising devices. More generally, analysis of the usually less-than-total polarisation created in the scattered beam (for example, by magnetic inelastic scattering) can give considerable information about the structure of the target system. Alternatively, if the incident beam is polarised, measurement of the cross-section as a

function of the incident beam polarisation provides us with extra information on preferred axis systems.

The latter is the experimentally simpler situation, and for many years represented the main use of polarised neutrons, as a tool for studying magnetic structures. There is, however, more information to be gained from such an experiment if the polarisation of the scattered neutrons is also analysed. In particular, the scattered beam polarisation may be changed from its initial (non-zero) value even if the target system has no preferred axis at all. In this case the actual cross-section is independent of the initial polarisation.

Neutron Spin Spectroscopy

A thorough investigation of the possibilities offered by such an experiment was made at Oak Ridge at the end of the last decade by Moon, Riste and Koehler[1]. These authors showed that, for many cases, it is sufficient to measure the cross-sections connecting the neutron spin-states before and after scattering, rather than analysing the final polarisation as such; for this reason they suggested the technique be termed "neutron spin spectroscopy" rather than polarisation analysis.

The technique used at Oak Ridge employs an incident beam polarised parallel or anti-parallel to a guide field whose direction in space remains constant across the sample; each incident neutron is thus in one of two possible spin eigenstates which we will denote by $|+\rangle$ and $|-\rangle$. After scattering, the beam is analysed by a flipper-polarising crystal combination, aligned parallel to the incident spin direction. Such an analyser effectively measures the Zeeman energy of the neutron by acting as a perturbation which transfers the neutron spin to one of its eigenstates. For parallel polariser and analyser directions, the available incident (i) and scattered (f) eigenstates will be the same, and hence we will be concerned with four transition probabilities : $|+\rangle_i \rightarrow |+\rangle_f$, $|+\rangle_i \rightarrow |-\rangle_f$ and their converses. (We can say the incident neutrons were in defined states, because the polariser acts as an analyser on the unpolarised beam arriving from the reactor).

These transition probabilities are the four partial cross-sections,

designated (++), (+-), (-+) and (--), which were calculated by Moon, Riste and Koehler and measured by them for a number of systems. Evidently, we may consider that (++) and (--) give the probability of non-spin-flip on scattering, while (+-) and (-+) give that for spin-flip, since we analyse the scattered beam in a direction parallel or antiparallel to the incident spin direction. (That is, we identify $|+>_i$ with $|+>_f$, and $|->_i$ with $|->_f$).

The theory of such measurements is by no means new[2], but the importance of an analysis in these terms is that it shows how to extract extra (and often unique) information from the system under study at a minimum cost in added experimental complexity. The technique is particularly important because of a second reason : neutron spin spectroscopy as outlined above is useful in investigating many systems which have no preferred axis. While we shall look at this point in a little more detail below, for the present it suffices to remark that if there is a neutron-spin/nuclear-spin interaction, the effect on the partial cross-sections may not average to zero even if the nuclear spins are randomly oriented.

Neutron spin spectroscopy therefore extends the use of polarised neutrons beyond their conventional application in the study of (aligned) electronic magnetism.

This concept forms the basis for many of the recent developments in polarised neutrons which will be reviewed in this paper. These may use the neutron-nuclear spin interaction in spin-dependent scattering, for example to separate coherent from incoherent scattering or to modulate structure factors, especially in hydrogenous materials. Alternatively, the neutron may have no spin interaction with the sample : we may still use its interaction with a suitably time-dependent (in the neutron's frame) external field to determine fine structure in the scattered energy spectrum, as in the neutron analogue of NMR spin-echo. Yet another possibility is simply to absorb the polarised neutron to produce a polarized nucleus, which can be used to study, for example, its own recoil defect - "in-beam" NMR.

The method of measuring partial cross-sections effectively analyses the component of the scattered polarisation in the incident polarisation direction. In some systems of interest, for example spiral magnetic structures, it is useful to measure the vector polarisation which may be created from an unpolarised incident beam, or which is not parallel or antiparallel to the incident polarisation.

Such measurements have been termed generalised polarisation analysis (although "polarisation analysis" would suffice). They have been made experimentally feasible by the use of spin-turn devices, which may be used to turn individual spin components into the analysis direction; the polarisation vector on scattering may then be reconstructed. These methods have also opened the way to new techniques in magnetic domain topography[3].

Since such spin-turn devices are critical to many of the new developments, we shall review their action in some detail.

NEUTRON SPIN-TURN DEVICES

Rather paradoxically, many of the new polarised neutron techniques, which were made possible by the availability of high-flux neutron beams, require us to consider the motion of individual neutrons. We first consider the interaction of a neutron, magnetic moment $\underline{\mu}$, with a constant magnetic field $\underline{H}$. For just the magnetic part of the interaction we then have the Hamiltonian

$$\hat{V} = -\gamma\mu_N \, \hat{\underline{\sigma}} \cdot \underline{H} \qquad (1)$$

$\gamma\mu_N = -1.913\,\mu_N$ is the gyromagnetic ratio of the neutron, μ_N is the nuclear magneton and the components of $\hat{\underline{\sigma}}$ are the Pauli matrices. (The origin of $\underline{\mu}$ is not a true magnetic dipole, and we should use the magnetic induction $\underline{B}$, rather than $\underline{H}$. We shall only consider the free-space case).

We may consider a neutron, whether in a field or not, as completely polarised; its polarisation is described by a vector $P = 2\langle\hat{\underline{s}}\rangle = \langle\hat{\underline{\sigma}}\rangle$, where $\langle\ \rangle$ denotes an expectation value. Clearly, for a single neutron $|P| = 1$. If the density matrix[4] is $\hat{\rho}$, we have

$$\hat{\rho} = \frac{1}{2}\,(\underline{1} + \underline{P} \cdot \underline{\hat{\sigma}}) = \frac{1}{2}\begin{pmatrix} 1 + P_z & P_x - iP_y \\ P_x + iP_y & 1 - P_z \end{pmatrix} \qquad (2)$$

If we choose a representation in which $\hat{V}$ is diagonal ($\underline{H}$ parallel to z) then we have for the time evolution of the matrix elements $\rho_{\ell m}$ the standard result[5]

$$\rho_{\ell m}(t) = \rho_{\ell m}(0)\,\exp\left[\overline{i(E_m - E_\ell)t/\hbar}\right] \qquad (3)$$

where the E_ℓ are eigenvalues of the energy under the interaction $\hat{V}$. (Note that the trace of $\hat{\rho}$ is unaffected).

Eqs. (2) and (3) together immediately give the time evolution of the individual polarisation components :

$$\begin{aligned} P_x(t) &= \cos(\omega_L t)\,P_x(0) - \sin(\omega_L t)\,P_y(0) \\ P_y(t) &= \sin(\omega_L t)\,P_x(0) + \cos(\omega_L t)\,P_y(0) \\ P_z(t) &= P_z(0) \end{aligned} \qquad (4)$$

That is, the polarisation vector precesses about the applied field direction with a frequency

$$\omega_L = (E_m - E_\ell)/\hbar = 2\,|\gamma\mu_N H|/\hbar \qquad (5)$$

which is just the Larmor frequency which would be calculated for a classical system[6].

Since many polarisers use neutron optical techniques, it is useful to arrive at Eq. (4) in a slightly different way.

The eigenstates E_ℓ represent different values of the neutron wave-vector k, with k_+ and k_- corresponding to $|+\rangle$ and $|-\rangle$. We may therefore define two refractive indices for the region on which $\hat{V}$ acts :

$$n_\pm = k_\pm/k \qquad (6)$$

The appropriate values are easily calculated to be[7]

$$n_{\pm} = 1 \mp \lambda^2 m \left| \gamma\mu_N H \right| / 4\pi^2\hbar^2 \qquad (7)$$

where m is the neutron mass and λ the wavelength.

If the neutron wave-function is initially $\psi = \alpha_1 \left| + \right> + \alpha_2 \left| - \right>$, then after travelling a distance z it will be

$$\begin{aligned} \psi(z) &= \alpha_1 (0)\, e^{ikzn_+} \left| + \right> + \alpha_2(0)\, e^{ikzn_-} \left| - \right> \\ &= e^{ikzn_+} \left\{ \alpha_1(0) \left| + \right> + e^{ikz\Delta n}\, \alpha_2(0) \left| - \right> \right\} \end{aligned} \qquad (8)$$

where $\Delta n = n_- - n_+$.

That is, there is an accumulated phase-angle $kz\Delta n$. If v is the neutron velocity, the time-evolution of this angle is then $\omega = kv\Delta n$, which is seen (using eq. (7)) to be the previous result.

Eq. (8) is important because it shows that, in a region of Zeeman splitting, 2π precession angle only corresponds to $\pm\ \pi$ in phase shift for the components of the wave-function. As pointed out recently by Mezei[8], this means that care should be exercised in interpreting so-called "4π" or spinor experiments, when a change in Zeeman energy is involved. (In the above case, 4π precessions correspond to 2π maximum phase change).

As mentioned in the introduction, a neutron in a fully polarised beam will be aligned with the field. We may use the adiabatic approximation to state that, if the field $\underline{H}$ evolves in time, the polarisation vector $\underline{P}$ will follow this evolution provided it is slow (in the neutron's frame of reference) compared with the frequency ω_L.

Spin-turn devices are designed to turn $\underline{P}$ out of the direction of $\underline{H}$. Until recently, these have been used solely to flip neutrons (that is, turn them 180°). The most common device has been the radio-frequency (r.f.) flipper, which effectively performs a magnetic resonance experiment on the neutron. We shall discuss later why such a flipping

technique is not useful for general spin-turn devices.

For the latter, we use interactions which can no longer be represented as a constant part plus a small perturbation.

The most generally useful form is a magnetic field which changes direction in space as a step-function. Using co-ordinates in the neutron's centre-of-mass frame, we may write the Hamiltonian as

$$\begin{aligned} \hat{V} &= \hat{V}_o \qquad (t \leqslant 0) \\ \hat{V} &= \hat{V}_1 \qquad (t > 0) \end{aligned} \tag{9}$$

where both $\hat{V}_o$ and $\hat{V}_1$ are independent of time.

Since the neutron wave-function is required to be continuous in time, it will not change across the abrupt transition (although the basis set for its description may alter).

In practice, the transition cannot be made instantaneous, but it can be fast enough for us to assume that the above argument holds for the constancy of the wave-function. This is the "sudden" approximation. We will briefly describe two common applications.

The Leningrad Flipper[9]

This device is shown schematically in Fig. 1. The beam passes axially through two coils with opposed fields, so that the (solenoidal) guide field changes sign in a very short distance, and we may apply the sudden approximation. The neutron polarisation vector remains unchanged in the laboratory frame while the field reverses, so that the spin is effectively flipped with respect to the field. There have been other devices giving a similar effect[10], for example the Dabbs' foil[11]; the present geometry has the advantage of putting no material in the beam.

The major advantage of the Leningrad flipper is that it works for a large range of wavelengths without tuning. There are certain disadvantages. To provide a flipping plane over the area of a normal beam requires sophisticated coil design and construction, and the device is very sensitive to stray fields. The coils are also rather inductive, so that the

method is not particularly suited to the flipper-chopper applications which are becoming increasingly useful in, for example, polarised diffuse scattering[12].

The Mezei Spin-Turn Coil

Mezei[13] proposed using a flat rectangular coil as a device for turning the neutron spin to any general angle with respect to the guide field, $\underline{H}_o$. Passing a direct current through the coil generates an interior field $\underline{H}_1$, which adds to $\underline{H}_o$ within the volume of the coil; outside, $\underline{H}_o$ remains unchanged.

We apply the sudden approximation to the neutron's passage into and out of the coil. The net field inside, $\underline{H}_o + \underline{H}_1$, makes an angle θ with the guide field $\underline{H}_o$. A neutron polarisation vector parallel to $\underline{H}_o$ outside the coil will thus be at an angle $-\theta$ with respect to the net field on sudden entry to the coil. (This is equivalent to saying that we change the basis set while the wavefunction remains constant). The polarisation will then precess about this net field direction, according to Eq. (4), during the time of passage through the coil.

Figure 2(a) shows a practical application of this idea to turn the neutron polarisation by $\pi/2$ with respect to $\underline{H}_o$, by choosing $\underline{H}_o \cdot \underline{H}_1 = 0$ and $|H_o| = |H_1|$. Precession takes place inside the coil about an axis which makes an angle $\pi/4$ with $\underline{H}_o$. If the coil thickness is chosen with respect to the neutron velocity so that the transit time corresponds exactly to π in Larmor precession angle about this axis, on exit the neutron polarisation has turned $\pi/2$ with respect to $\underline{H}_o$.

Neutron spin-flip, corresponding to a spin-turn of π, may be achieved using two such coils immediately in series. To emphasize the generality of the spin-turning action of the Mezei coil, however, Fig. 2(b) shows the use of a single coil as a flipper. The relative magnitudes and directions of $\underline{H}_o$ and $\underline{H}_1$ are chosen so that the net field in the coil is perpendicular to $\underline{H}_o$; a Larmor precession of π about the net field in this case gives a spin-turn of π, corresponding to spin-flip.

Since we may track the motion of each component of the polarisation,

it is easy to follow the action of a Mezei coil on a neutron with initial polarisation in some general direction with respect to $\underline{H}_o$. In the particular cases above, taking $\underline{H}_o$ parallel to z, a $\pi/2$ turn transforms $\underline{P}$ according to

$$(P_x, P_y, P_z) \rightarrow (P_z, -P_y, P_x) \tag{10}$$

while a π turn gives

$$(P_x, P_y, P_z) \rightarrow (-P_x, P_y, -P_z) \tag{11}$$

The $\pi/2$ turn thus projects the component of the polarisation along the coil axis into the direction of $\underline{H}_o$. This is useful in polarisation analysis, where each component in turn of a generalised polarisation may be projected onto the analyser direction.

Mezei coils have the advantage of simplicity (and therefore low cost), low inductance for fast switching applications, and are unrestricted in beam size; the rectangular coil must simply be larger than the beam. The only disadvantage is the necessity to tune them to a given neutron velocity. This is not,however, a drastic restriction. For a beam with a peaked (Gaussian or triangular) wavelength distribution, for example, a wavelength spread $\Delta\lambda/\lambda \sim \pm 10$ % still gives an integrated flipping efficiency of order 98 %.

PRECESSING POLARISATION

So far, we have discussed individual neutrons. In a neutron beam, we define the beam polarisation $\overline{\underline{P}}$ as the vector average of the N spins in the beam :

$$\overline{\underline{P}} = \frac{1}{N} \sum_{i=1}^{N} \underline{P}_i \tag{12}$$

Conventionally, linearly polarised beams have been the only cases of importance. In these, the polarisation may be considered to measure the

excess of one spin state over the other : $\underline{\bar{P}} = [(N_+ - N_-)/(N_+ + N_-)]\,\underline{h}$ where $N_\pm$ gives the number of neutrons in the appropriate spin state, and $\underline{h}$ is a unit vector in the direction of the applied field.

In many of the recent techniques using polarised neutrons, it is preferable to remain with eq. (12) as the definition and to continue to treat each neutron as polarised. An important case is the action of a $\pi/2$ spin-turn device on a linearly polarised beam : on exit, $\underline{\bar{P}}$ is a vector which rotates at the Larmor frequency in the guide field, and we say the beam has precessing polarisation.

It is important to note, in this connexion, the difference in action between a π spin-turn coil and a conventional r.f. flipper. The former is described by a time dependent Hamiltonian of the form $\underline{\hat{H}}_o(t)$, while that for the latter is $\underline{\hat{H}}_o + \underline{\hat{H}}_1(t)$ where $|H_1| << |H_o|$; this is most easily handled in a rotating frame, unlike the case described by Eq. (9). The r.f. flipper works in the regime of time-dependent perturbation theory[14], and the small perturbation $\underline{\hat{H}}_1(t)$ only couples significantly when it has a frequency component in resonance with a transition between energy eigenvalues.

The theory of such a device has been thoroughly treated elsewhere[6] and will not be discussed here; it will be sufficient to give a simple example to demonstrate the point. Consider a beam of neutrons with precessing polarisation rotating in a plane perpendicular to the guide field, which we take as the z-direction.

At the entrance to the flipper, let the polarisation be $(\bar{P}_x, \bar{P}_y, 0)$.

On exit from a Mezei flipper, this will transform, according to Eq. (11), to $(-\bar{P}_x, \bar{P}_y, 0)$.

If we do the same calculation for an r.f. flipper, following the individual x and y spin components, the final polarisation has a time-average value of zero; the precessing polarisation has been destroyed. This is because, for the time the neutrons are in the flipper, the transformations described by Eqs. (4) have initial conditions which are themselves time-dependent in the rotating frame.

If we wish to measure precessing polarisation, the operator nature of $\hat{\underline{s}}$ means we must measure each component of $\langle \underline{s} \rangle$ in turn. The technique is to use spin-turn devices to project these components one-by-one onto the guide-field (and hence analyser) direction. The value of $\underline{P}$ is then known at the spin-turn position, and knowing the guide field geometry and strength we may reconstruct $\underline{P}$ at the point of scattering. This is a quite general feature of precessing polarisation : until we force a transition to an eigenstate by making a measurement, we may predict the vector $\underline{P}$ at any point in a spectrometer which has a known field configuration. The latter may have discontinuities, provided they conform to the general characteristics outlined above for spin-turn devices. In particular, if we know $\underline{P}$ for a given neutron at one point in the spectrometer, we can predict its value after passage through such a discontinuity.

NEUTRON SPIN-ECHO

Consider a linearly polarised neutron beam, which passes through a uniform magnetic guide field and is detected by a spin analyser aligned in the direction of the polarisation. At some point in the uniform guide field $\underline{H}_o$ (parallel to z) we apply a $\pi/2$ spin turn, after which the polarisation will precess about $\underline{H}_o$. At a later point, we apply a second $\pi/2$ turn. According to the previous discussion, this will project the x-component of the precessing polarisation onto the analyser direction. It is clear that for a monochromatic beam, it is possible to arrange for the precessing polarisation to be in the x-direction at the point of the second spin-turn, by placing this at an appropriate distance from the first. That is, the transit time τ_o between the two spin-turns is such that $\omega_L \tau_o$ is an integral multiple of 2π, where ω_L is the Larmor frequency in $\underline{H}_o$.

Under fixed geometrical conditions, linear variation in transit time (i.e. in neutron wavelength) will therefore give a sinusoidal variation in the intensity transmitted by the analyser, and this may be used as an extremely sensitive measure of changes in the beam velocity.

For a polychromatic beam, such an arrangement will only be tuned for

certain wavelength, and for a transit time τ the x-component of the polarisation at the second coil will in general be given by $\cos(\omega_L \tau/\tau_o)$. If the analyser and detector integrate with equal efficiency over all wavelengths in the beam, the detected intensity will therefore be proportional to the Fourier transform of the wavelength distribution.

It is possible, however, to focus all of the x-components back into the same direction at the second spin-turn coil, by reversing the precessing polarisation at the midpoint between the coils. Under this condition, the net precession angle accumulated during transit may be made zero for all transit times, and the original polarisation is recovered at the analyser. (We assume the spin-turn device works over the range of velocities involved).

This is the spin echo focussing action, proposed by Mezei[13].

The direction of precessing may be reversed by reversing the field at the midpoint, or by reversing the spin direction with respect to the field. (In the latter case, general spin-flipping devices must be used; thus, as discussed earlier, an r.f. flipper would not work). Either case is equivalent to a π spin-turn, and the complete pulse sequence $\pi/2 - \pi - \pi/2$ is a direct analogue of NMR spin-echo[15].

The major application of neutron spin-echo is in the measurement of very small energy transfers. These may be relative to some finite energy transfer, as in inelastic line-width measurements, or relative to zero; we shall only consider the latter (quasielastic) case here.

The experimental arrangement is shown in Fig. 3. P_1 and P_2 are coils giving $\pi/2$ turns, and F is a π-turn coil. The line integrals of the guide field in the regions P_1F and FP_2 are made equal, so that the focussing effect discussed above applies, providing the sample scatters purely elastically. We assume that the sample has either no effect on the precessing polarisation, or that it transforms it according to Eq. (11), in which case the flipper F would be unnecessary. (Other cases may be handled; they complicate the discussion but make no fundamental difference).

Assuming that, for a fixed momentum transfer $\underline{Q}$, the probability of energy transfer ω on scattering is $S(\underline{Q},\omega)$, it may be shown (see ref. 13 for details) that the measured x-component of the polarisation is to a good approximation

$$P_x = \int_{-\infty}^{\infty} S(\underline{Q},\omega) \cos(\omega T) d\omega \qquad (13)$$

where T, which has the dimension of time, depends linearly on the number of precessions in FP_2, and hence may be controlled by varying $|H_o|$.

We thus measure the Fourier transform of $S(\underline{Q},\omega)$ on a timescale which overlaps with NMR; the equivalent energy resolution is of order 10^{-8} ev.

The ability to measure with very high energy resolution at low momentum transfers makes neutron spin-echo a particularly interesting technique for the investigation of many problems in colloid and macromolecular chemistry[16].

IN-BEAM NMR

Absorption, rather than scattering, of cold polarised neutrons is useful in nuclear physics to study parity non-conservation. The techniques involved are also useful in certain problems of solid state physics and chemistry. As an illustration, we shall briefly consider a method now becoming practical as a result of the availability of high-flux polarised beams.

When a neutron is absorbed by a nuclide to form a new nucleus, the reaction passes through an intermediate excited state which decays immediately to the ground state by a γ-ray cascade. If the created nuclide has some measurable property distinguishable from those in the original sample, it may be used as a local probe of its own γ-induced recoil defect.

Classical NMR may be used as the measurement technique, but it requires the creation of order 10^{19} probe nuclei for sufficient sensitivity; bulk radiation damage is therefore significant.

If the created nucleus is β-active, however, the same information may be obtained with an enormous increase in sensitivity. Absorption of

polarised neutrons creates polarised nuclei from which the β-decay will normally have an asymmetric distribution due to parity violation; the asymmetry may be used to monitor the nuclear polarisation. The sensitivity is such that between 10^2 and 10^6 activated nuclei in equilibrium are sufficient[17]. (Transient effects may also be observed, using a chopped beam). There is thus no bulk damage, and the probe nuclei are extremely isolated.

An example is the study[18] of (n,γ) induced defects in CaF_2 :

$$^{19}F + n_{pol} \longrightarrow {}^{20}F^{x}_{Pol} \xrightarrow{\gamma's} {}^{20}F_{Pol} \xrightarrow{\beta^-} {}^{20}Ne^{x}_{Pol} \xrightarrow{\gamma} {}^{20}Ne \quad (14)$$

At temperatures below 75K, the defects created were stable, and their electric field gradients caused quadrupolar splitting of the NMR line. This cas measured[18] and the defects assigned to $^{19}F^-$ interstitials in normally empty lattice positions.

The method is being extended to observe chemical effects, for example[19] the influence of hydrogen bonding on the form of ions such as HF_2^-.

RESONANCE MODULATED DIFFRACTION

Magnetic resonance techniques may also be coupled with polarised neutron diffraction. This new technique, termed resonance modulated diffraction,is of interest in the crystallography of hydrogen containing compounds because, under certain conditions, the proton may be considered as a "heavy-atom" in neutron diffraction.

The poor signal-to noise ratio inherent in diffraction from hydrogenous systems is largely a result of the nuclear spin incoherence of the protons. If these nuclear spins are polarised by a technique such as dynamic nuclear polarisation[21], a considerable enhancement is observed in the brightness of a Bragg reflection, together with a diminution of the incoherent background. The primary effect is therefore analogous to deuteration of the sample; the total enhancement, however, is very much larger, and the proton scattering length becomes of heavy-atom proportions.

The technique may be considerably extended by using more explicitly the spin dependence of the neutron-proton interaction.

The cross-section for coherent scattering from a polarised nuclear system may be written[22]

$$\frac{d\sigma^{\pm}}{d\Omega} = \left| \sum_{\nu} \exp(i\underline{Q}.\underline{R}_{\nu}) < \{ a_{\nu} \} \pm \frac{1}{2} \underline{d}_{\nu} > \right|^2 \qquad (15)$$

where the incoming neutron polarisation is parallel (+) or anti-parallel (-) to the nuclear magnetisation. Here $\{a_{\nu}\}$ is the coherent scattering length for the nucleus of spin $\underline{I}_{\nu}$ at site ν, and $\underline{d}_{\nu} = 2I_{\nu}(a_{\nu}^{+} - a_{\nu}^{-}) \times \underline{P}_{\nu}/(2I_{\nu} + 1)$; $a_{\nu}^{\pm}$ are the usual spin dependent scattering lengths, and the nuclear polarisation $\underline{P}_{\nu} = <\underline{I}_{\nu}>/I_{\nu}$.

In a conventional nuclear diffraction experiment, $P_{\nu} = 0$ and $d\sigma^{+}/d\Omega = d\sigma^{-}/d\Omega = |F(\underline{Q})|^2$, $F(\underline{Q})$ being the usual nuclear structure factor.

If we now polarise the nuclei, the structure factor becomes spin-dependent. This allows us to measure a second polarised structure factor,

$$|F_d(\underline{Q})| = \left| \sum_{\nu} \exp(i\,\underline{Q}.\underline{R}_{\nu}) d_{\nu} \right| \qquad (16)$$

and also the <u>phased</u> difference $|F(\underline{Q}) - F_d(\underline{Q})|$.

By using magnetic resonance techniques to polarise the protons, we may thus measure, for example, difference Patterson functions of the form $\sum_{\underline{Q}} |F(\underline{Q}) - F_d(\underline{Q})|^2 \exp(i\underline{Q}.\underline{r})$. Since the phase differences are known, there will be no induced noise peaks; further, since only protons contribute non-zero terms to $F_d(\underline{Q})$, all cross-term peaks represent vectors starting or ending on a proton.

Experimentally, this represents a very nice situation, since at each momentum transfer $\underline{Q}$, we use the same scattering geometry, sample and wavelength, merely changing the applied resonant frequency to extract the different terms.

So far, experiments have only been done using low temperature (1°K) techniques, which induce a high equilibrium nuclear polarisation. Fast

spin-relaxation times at higher temperatures mean that non-equilibrium techniques[23] may have to be employed to extend the method to materials which cannot be cooled.

BROAD-SPECTRUM NEUTRON POLARISERS

In much of the previous discussion, it has been assumed that it is possible to produce a white beam of cold polarised neutrons. In practice this has been an extremely difficult problem, which only now is nearing an efficient solution. Since the new techniques of neutron polarisation have recently been reviewed[24], we shall restrict the present comments to a few remarks on the use of neutron optics.

In a magnetic medium, the neutron refractive index depends on the neutron spin state relative to the magnetic induction. By a suitable choice of material, the refractive index can be made to differ from unity for only one spin state; a mirror of this material will then act as a polariser.

Alloys of iron : cobalt are most often used. In bulk, this material is hard to magnetise sufficiently, but the use of thin (1000 Å) films evaporated under a field overcomes this problem. Spurious reflections from the substrate (which lower the polarisation at small angles) may be avoided by first evaporating an anti-reflecting layer, or by using a substrate with zero coherent scattering length. Both methods have been used successfully[25,26], as shown in Fig. 4. The incoherent substrate used in this case is a thin (20 μ) plastic film, which allows construction of very compact polarising guides using a bent soller-type construction.

The more fundamental problem of mirror reflection is that the critical angle (θ^{x}) is very small and depends linearly on wavelength. Typically, θ^{x} is about 30' at 6 Å, and the divergence limitation is severe at short wavelength.

This problem should be resolved by the "supermirror" idea of Mezei[27]. An evaporated film construction is used which is analogous to the multi-layer interference coatings used in light optics. An enhancement of the critical angle by a factor of at least 3 should be possible, so that mirror

polarisers would become useful at short wavelength; at long wavelength, they would also provide wide divergence analysers. The problem of producing intense white polarised beams with reasonable divergence thus appears to be solved.

CONCLUSION

The recent developments in polarised neutrons are a generalisation of the idea of magnetic neutron scattering, to any neutron scattering experiment in which a magnetic interaction (not necessarily electronic) is used to extract more information). The magnetic interaction involved may not even be with the sample, but purely with the spectrometer, as is the case in neutron spin-echo.

These new techniques are extending the usefulness of polarised neutrons to many new areas, particularly in chemistry. In other more conventional areas, new techniques of polarised neutron production should make possible many experiments which were previously limited by flux, especially in magnetic inelastic scattering.

It is a pleasure to acknowledge discussions with my colleagues F. Mezei and S.W. Lovesey during the writing of this review.

REFERENCES

1. R.M. Moon, T. Riste and W.C. Koehler, Phys. Rev. 181, 920 (1969).
2. O. Halpern and M.R. Johnson, Phys. Rev. 55, 898 (1939). For a recent review, see reference 22 and papers cited therein.
3. M. Schlenker and C.G. Shull, J. Appl. Phys. 44, 4181 (1973); M.Th. Rekveldt, Z. Physik 259, 391 (1973); A.I. Okorokov, V.V. Runov, V.N. Volkov and A.G. Gukasov, Preprint F.T.I.-106, Leningrad (1974).
4. W. Marshall and S.W. Lovesey, Theory of Thermal Neutron Scattering, p. 326, Clarendon Press, Oxford, 1971.
5. L.I. Schiff, Quantum Mechanics, p. 140, Edn. 2, McGraw-Hill, N.Y.,1955
6. A. Abragam, The Principles of Nuclear Magnetism, Chap. 2, Clarendon Press, Oxford, 1961.

7. I.I. Gurevich and L.V. Tarasov, Low-Energy Neutron Physics, p. 54, North-Holland, Amsterdam, 1968.
8. F. Mezei, private communication.
9. G.M. Drabkin, E.I. Zabidarov, Ya. A. Kasman, A.I. Okorokov and V.A. Trunov, Preprint FTI-183, Leningrad (1969); idem Sov. Phys. JETP 29, 261 (1969).
10. E. Majorana, Nuovo Cimento 9, 43 (1932).
11. J.W.T. Dabbs, private communication referred to in R. Haas, L.B. Leipuner and R.K. Adair, Phys. Rev. 116, 1221 (1959).
12. F. Mezei, Unpublished Lecture, I.L.L. Grenoble (1975).
13. F. Mezei, Z. Physik 255 , 146 (1972).
14. L.I. Schiff, op.cit. Chap. VIII.
15. H.Y. Carr and E.M. Purcell, Phys. Rev. 94, 630 (1954).
16. J. Higgins, Ed., Proceedings of Chemistry Information Meeting, I.L.L. Grenoble (1975).
17. H. Ackermann and P. Heitjans, private communication.
18. D. Dubbers, H. Ackermann, H. Grupp, M. Grupp, P. Heitjans and H.J. Stoeckmann, Proceedings of International Meeting on Hyperfine Interactions, Uni. of Leuven, Belgium (1975).
19. J.A. Smith and T.C. Waddington, private communication.
20. J.B. Hayter, G.T. Jenkin and J.W. White, Phys.Rev.Letts.33,696 (1974).
21. C.D. Jeffries, Dynamic Nuclear Orientation, Wiley, New York, 1963.
22. R.I. Schermer and M. Blume, Phys. Rev. 166 , 554 (1968).
23. M. Goldman, Spin Temperature and NMR in Solids, Clarendon Press, Oxford, 1970.
24. J.B. Hayter, Proceedings of Neutron Diffraction Conference, Petten, RCN-234, p. 137 (1975).
25. G.M. Drabkin, A.I. Okorokov, A.F. Shchebetov, N.V. Borovikova, A.G. Gukasov, A.I. Yegorov, V.V. Runov, Preprint, FTI-183, Leningrad (1975).
26. J.B. Hayter, J. Penfold and W.G. Williams, work in progress.
27. F. Mezei, submitted to Comm. on Physics.

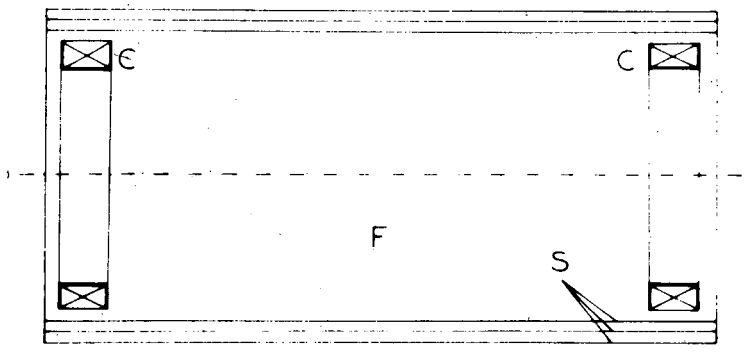


Fig. 1. Leningrad flipper. C : coils with opposed axial fields. S : magnetic shielding. F : flipping plane.

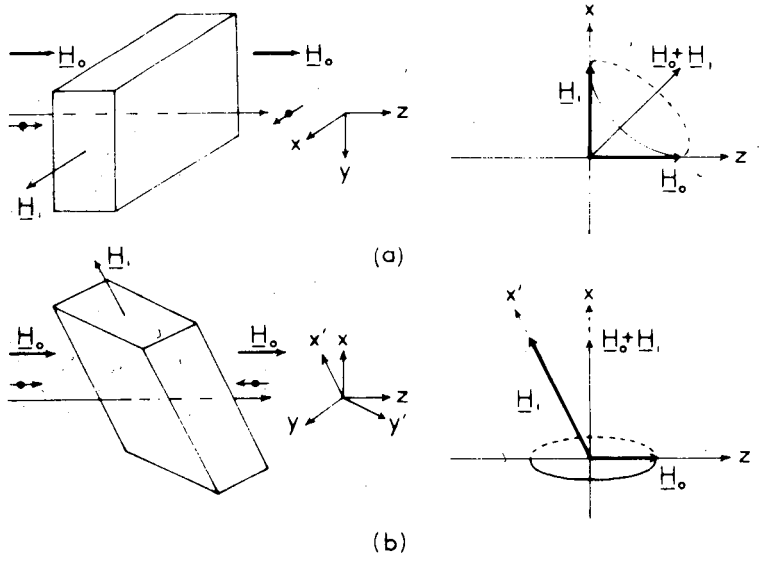


Fig. 2. Mezei spin-turn coils and their action. (a) $\pi/2$ turn. (b) π-turn. Dotted arrows represent neutron spins.

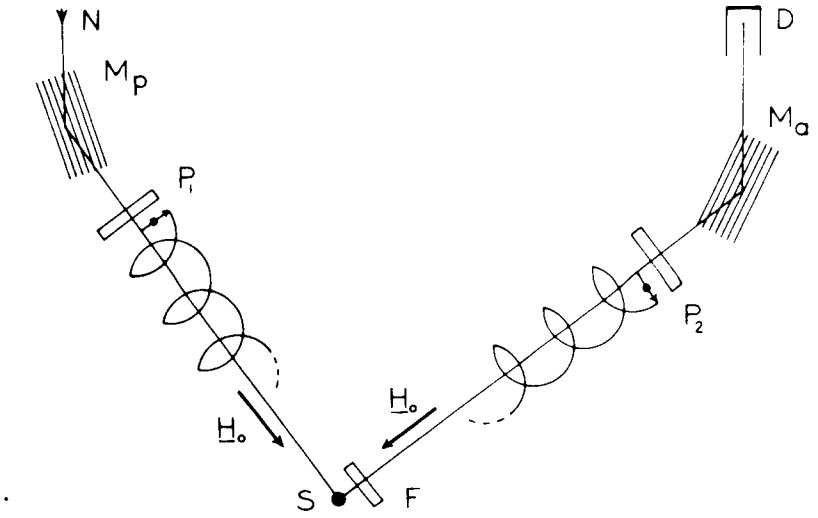


Fig. 3. Spin-echo experiment. N : unpolarised incident beam. M_p, M_a : polariser and analyser. P_1,P_2 : $\pi/2$ spin turn coils. F : π spin turn coil. S : sample. D : detector. The guide field H_o (shown solenoidal here) rotates adiabatically.

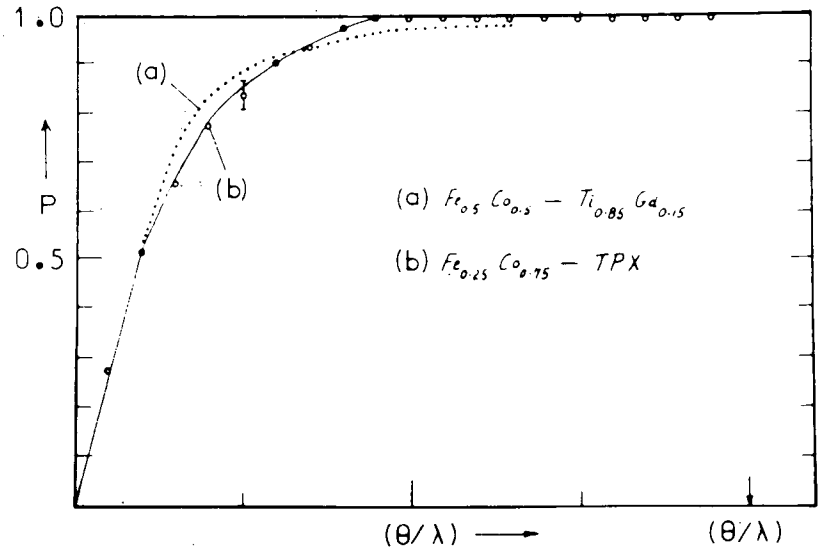


Fig. 4. Polarisation vs (glancing angle/wavelength) for magnetised thin-film mirrors. (a) anti-reflecting substrate[25]; (b) 20 μ plastic TPX film substrate[26].

THE PERFECT CRYSTAL NEUTRON INTERFEROMETER: A TOOL FOR NOVEL AND PRECISE MEASUREMENT[ßß]

W. Bauspiess[ß], U. Bonse[+] and H. Rauch[o]

[+]Institut für Physik, University of Dortmund, D-4600 Dortmund 50, Postfach 50 05 00, Germany (BRD)

[o]Atominstitut der Österreichischen Hochschulen, Wien, Austria

[ß]Institut Laue-Langevin, Grenoble, France

ABSTRACT

After the first successful realization of a crystal-diffraction neutron interferometer[1,2] the instrument has been further developed to be capable of accurate measurement of phases of neutron waves. The results of the application of the interferometer to the precision measurement of coherent scattering lengths of a number of materials will be presented. In these measurements the neutron wavelength effectively used in the interferometer was defined by a Si-Ge bicrystal combination acting as a monochromator of suitable wavelength resolution. Furthermore the effects of simultaneous phase shifts and spin rotation on neutron waves was measured. The influence of vibrations, thermal disturbances, mechanical stresses and errors of geometry on the phase pattern was investigated and minimized. The energy flow within the instrument was measured and compared with theoretical energy distributions[3] calculated from the dynamical theory of neutron diffraction adapted to the case of three consecutive diffracting crystal plates. It was found that even with an incident beam of very limited width there may be a nonuniform phase distribution across the outgoing beams resulting in a considerable loss of fringe contrast. Neutron interferometers with geometries avoiding most of the phase inhomogeneities will be discussed.

[ßß]Supported by the Bundesminister für Forschung und Technologie KNF-FV-4 DO 1T and by Fonds zur Förderung der Wissenschaftlichen Forschung - project 1178.

INTRODUCTION

Along the design principles of X-ray interferometers[3,4] the first perfect crystal neutron interferometer was developed and successfully put into operation by the end of 1973[1,2]. Lateron similar single crystal neutron interferometers were operated by Colella et al.[5] and by Kikuta et al.[6] Presently all crystal neutron interferometers are of the triple Laue case (LLL) type shown in Fig. 1. By dynamical diffraction occuring in crystal wafers S, M, and A the neutron wave is split into two coherent parts, conducted over separated beam paths I and II and superimposed again in either outgoing beam O and H. Phase shifts or rotations of the neutron spin introduced over path I or II result in intensity modulations and polarization effects in beams O and H. The essential feature is that changes of the neutron wave function including spin - and not only of the intensity of the neutron wave - become physical observables. Thus it is clear that a number of new and important experiments in the fields of fundamental nuclear and particle physics and of solid state physics are now within reach.

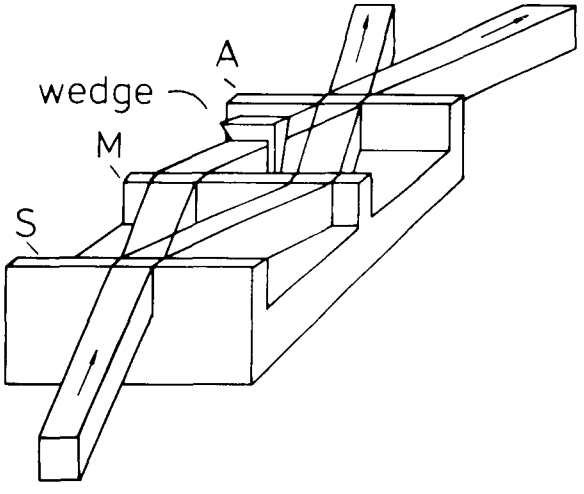


Fig. 1. LLL Neutron Interferometer

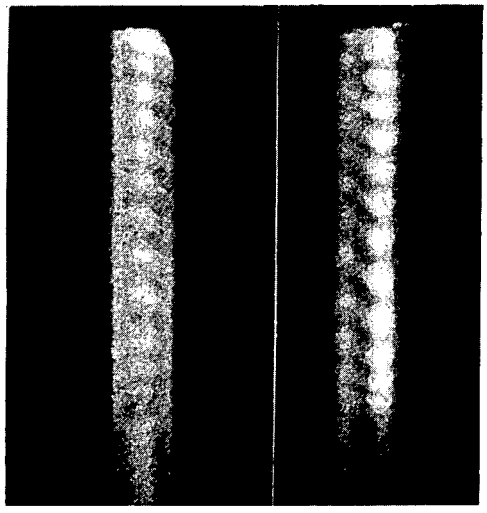
Among those experiments which have been at least started so far we list the precise measurement of coherent scattering lengths[2], the measurement of the influence of precipitations in alloys and of magnetic domains on the interference pattern[7], the gravitationally induced phase shift of neutron waves[5], the change of sign of a neutron spinor wave function for rotations of 2π and odd multiples of it[8,9], and the combined measurement of phase shift and spin rotation phenomena[10]. There is no doubt that further novel experiments with the neutron interferometer will be performed in the near future. To the benefit of such experiments in past and future

we shall discuss some functional and quantitative aspects of the instrument and report on first precision measurements performed with it.

FORMATION OF THE PHASE PATTERN

For the performance of precision phase measurements a detailed understanding of the formation of the fringe pattern and of the factors affecting contrast, stability and reproducibility of fringes is essential. Contrary to the X-ray case, with neutrons absorption is practically zero in silicon and germanium, materials from which interferometers are conveniently manufactured. As a consequence both types of dynamical wavefields contribute to the fringe pattern and may give rise to rather complicated Pendellösung effects which might perhaps destroy the phase sensing ability of the LLL interferometer altogether.

From a spherical wave treatment of the zero absorption interferometer[11] ist was learnt that at least in the O beam there is spacial phase homogeneity provided certain 'ideal' geometries are guaranteed, e.g. that crystals, S, M, and A have equal thickness $t_S=t_M=t_A$ and that S and A have equal distance $z_S=z_A$ from M. Another ideal geometry would consist of $z_S=z_A$ and $2t_S=t_M=2t_A$. In the latter case a favourable focussing of the intensity in the exit beams is observed. A four-wafer geometry appears to assure good imaging properties allowing the formation of a topographic phase contour of the sample.



H O

Fig. 2. 'Chessboard' Pattern in O and H Exit Beam

The spacial phase homogoneity and the contrast of fringes is impaired not only by geometric misfits but also crystal imperfections. An example of a somewhat unforeseen complication are the O and H beam patterns of a wedge sphaped sample

shown in Fig. 2. The patterns were obtained with an incident beam only 0.3 mm wide. On transmission through the wafers of the interferometer the beam is spread out over a region at the exit surface which is about 8.5 mm wide. As expected horizontal fringes caused by the sample wedge are seen. What is unexpected however is for instance the occurrence of two separated fringe systems in the left and the center part of the O-beam which are shifted against each other by roughly a half fringe spacing. According to the theory[11] there should be no phase difference between two lacations at the same height in the beam. Apart from not being understood at present the observed horizontal phase variation necessarily decreases fringe contrast if - as is the case in the conventional set-up - the full cross section of the beam is measurd in recording interference fringes.

PRECISION MEASUREMENT OF COHERENT SCATTERING LENGTHS

A sample containing N_i nuclei per unit volume of type i each with a coherent scattering length b_{ci} has an averaged specific scattering $\sum_i N_i b_{ci}$ which can be determined experimentally according to

$$\sum_i N_i b_{ci} = 2\pi \lambda^{-1} D_{\lambda s}^{-1} \qquad (1)$$

where λ is the neutron wavelength and $D_{\lambda s}$ the so-called λ-thickness of the sample material, i.e. the thickness of a sample layer which introduces an optical path change of one wavelength. In an interferometric measurement $D_{\lambda s}$ is determined directly from the fringe period p. $D_{\lambda s}$ is related to the refractive index n as

$$D_{\lambda s} (1-n) = \lambda \qquad (2)$$

from which n can be calculated if needed. Hence for a precise determination of $\sum_i N_i b_{ci} D_{\lambda s}$ and λ have to be measured exactly.

MEASUREMENT OF THE λ-THICKNESS $D_{\lambda S}$

The sample consists of a plano-parallel plate placed between crystalls S and A of the interferometer (Fig. 1). By rotation of the sample about a vertical axis the optical path length for one beam is increased while it is decreased for the other. We call the angle of rotation ε with $\varepsilon=0$ for the symmetric position. The path difference x within the sample of beam I and beam II is then given by

$$x = Df(\varepsilon) = D\ (\mathrm{cosec}\ (\Theta-\varepsilon) - \mathrm{cosec}\ (\Theta+\varepsilon)) \qquad (3)$$

where D is the sample thickness and Θ the Bragg angle of the reflexion used in the interferometer. From (3) we calculate the phase difference φ caused by a rotation

$$\varphi = 2\pi D\ (D_{\lambda s}^{-1} - D_{\lambda e}^{-1})\ f\ (\varepsilon) \qquad (4)$$

$D_{\lambda e}$ is the λ-thickness of the environment of the sample (e.g. air). With varying phase shift the coherent intensity $I_{O,H}$ of the exit beams O and H is modulated in a sinusodial manner proportional to

$$\sin\ (2\pi D\ (D_{\lambda s}^{-1} - D_{\lambda e}^{-1})\ f\ (\varepsilon)) + 1 \qquad (5)$$

The period p of this modulation is extracted from the recorded data. With p we calculate

$$D_{\lambda s} = pD\ (1 + pDD_{\lambda e}^{-1})^{-1} \qquad (6)$$

Since usually $D_{\lambda e} \gg D$

$$D_{\lambda s} \approx pD \qquad (7)$$

is often a good approximation. If the measurement is made in air at 20°C and 760 torr then $D_{\lambda e} = 15.7$cm at $\lambda = 1.8\text{Å}$ and for a precision measurement the correction has to be taken into account.

The average maximum number of oscillations which can be measured with solid samples is for the present set-up at the HFR in Grenoble of the order of 25. Together with a phase resolution of about 10^{-2} we measure p with a relative error of $5_{\%} 10^{-4}$. With some care taken in the sample preparation it is possible to determine D to 10^{-4} so that D_{λ_s} in the end is obtained with a relative error of roughly $5_{\%} 10^{-5}$. This is a preliminary limit. The precision can be increased with the new and more elaborate instrument which is presently being installed in Grenoble.

MEASUREMENT OF THE NEUTRON WAVELENGTH

The interferometer is located at a thermal neutron guide. Very good monochromacy and wavelength definition is achieved by employing in the incident beam a monochromator crystal combined with a silicon-germanium bicrystal as described below. The total arrangement is shown in Fig. 3.

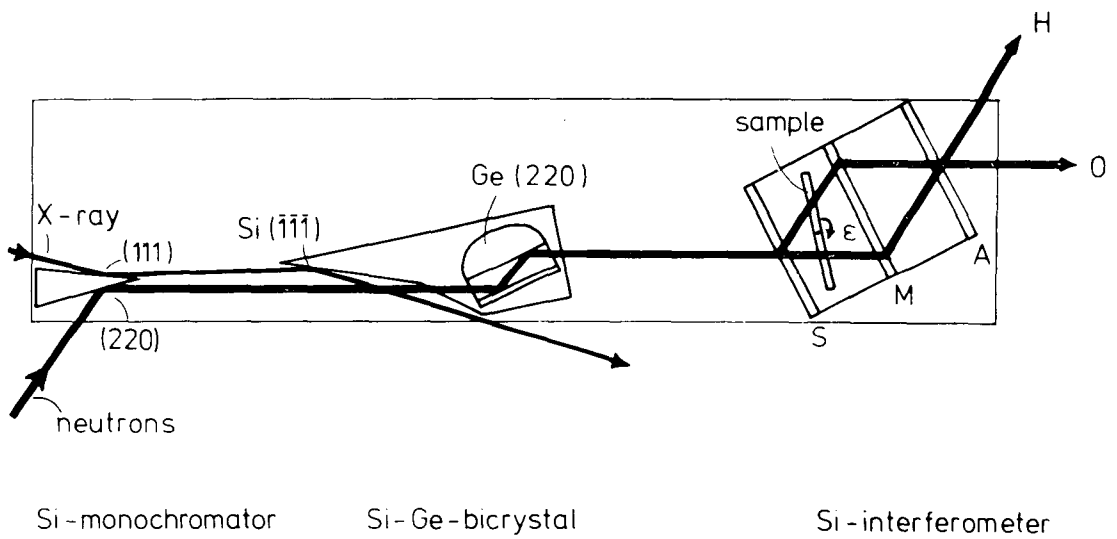


Fig. 3. Schematic Arrangement of Precision Neutron Interferometer.

The beam is deflected out of the guide by a perfect silicon monochromator crystal using the same Bragg planes 220 as are used within the interferometer. The width of the wavelength band[12] after the Ge 220 double reflexion groove is $\Delta\lambda/\lambda = 1.1 \times 10^{-3}$. Furthermore the center λ_o of this band is fixed to $10^{-4}\lambda_o$ by keeping the relative orientation of the silicon and germanium crystal stationary to better than 1 sec. of arc. The latter is achieved by monitoring the intensity of an auxiliary X-ray beam which undergoes double crystal $(111,\bar{1}\bar{1}\bar{1})$ reflexion by the monochromator and a second silicon crystal glued permanently to the germanium groove. λ_o is effectively determined beforehand in the glueing process which again is performed under the control of a simultaneous 220 reflexion of a suitable characteristic X-ray line (e.g. Co-Kα_1 with $\lambda_o = 1.7889$ Å) by the germanium groove crystal and by the silicon crystal to be attached to it. The merits and characteristics of such a Si-Ge-bicrystal arrangement will be described elsewhere[13].

In addition to the definition of the wavelength λ_o by the bicrystal it is directly measured by turning the interferometer through two Bragg reflexions (e.g. 220 and 331) and calculating the wavelength from the angular distance of the Bragg reflexions. The neutron wavelength in the present experiment is given in the table below. Measurements at other wavelengths are possible with other sets of bicrystals.

STABILITY REQUIREMENTS

Accurate measurements require high reliability in long time operation of the interferometer. We therefore discuss briefly the principal sources of disturbances.

Generally one cannot distinguish whether observed intensity variations result from a real phase shift between paths I and II or from a distortion of the interferometer itself. Consequently there are three chief enviromental parameters which have to be controlled closely: temperature gradients, mechanical strains and vibrations.

Because silicon is a very good heat conductor thermal gradients can

be kept small enough even with larger interferometer crystals by means of a crude but tight thermal shield.

If not performed with extreme care the mounting procedure is a typical source of mechanical strain. In our experiments the interferometer rests freely on three glas spheres. Residual strain in the crystal generates the well-known built-in pattern which we compensate away by loading the interferometer with small brass weights in a suitable manner. The compensation is preferably made under the control of an X-ray interference pattern.

When passing through the interferometer the thermal neutron has a sufficiently long flight time t_f (e.g. $t_f \approx 30\mu s$ for $\lambda = 1.8$ Å) to 'see' crystals S, M, A at different positions if the interferometer is moving. From the relativity argument it follows that only an accelerated motion is of importance. (An accelerated motion of the neutrons also yields a phase change as was demonstrated by Colella et al.[5]). Thus the acceleration a of the interferometer has to be controlled, vibrations - even at low frequencies - have to be eliminated. Rough calculations yield $a < 4\times10^{-3}$ g as upper limit for an arbitrary phase shift of 0.2π. Interference oscillations were not visible until the whole goniometer bench had been put onto springs isolating it from vibrations due to various machinery at the reactor site. The remaining amplitude was $a < 10^{-4}$ g. The deterioration and complete loss of fringe contrast could be induced by arbitrarily generated vibrations with varying amplitude from a medium size vacuum pump.

RESULTS OF SCATTERING LENGTH MEASUREMENTS

Measurements were made for Sn, Al, and Bi. The results are listed in Table 1. N is the number of atomes per cubic cm used in calculating b_c from equation (1). For Sn the most accurate value was obtained. Improvement of the other data and the measurment of b_c for a variety of other materials is in preparation. Literature data[14] are given in the last line of Table 1. Because of their limited accurary there is no serious disagreement to the new value presented here.

Table 1. RESULTS OF SCATTERING LENGTHS MEASUREMENTS

		Sn	Al	Bi
D	[cm]	0.7201±0.0004	1.0057±0.0013	0.803±0.005
λ_o	[Å]	1.7860±0.0002	1.8322±0.0009	1.8264±0.0005
N	$[10^{22}cm^{-3}]$	3.6990±0.0004	6.0204±0.001	2.821±0.003
purity	[%]	99.9995	99.996	99.9995
b_c	$[10^{-13}cm]$	6.220±0.002	3.447±0.005	8.58±0.05
b_c [14]	$[10^{-13}cm]$	6.1	3.5	8.6

REFERENCES

1. H. Rauch, W. Treimer and U. Bonse, Phys. Lett. 47A, 369 (1974).
2. W. Bauspiess, U. Bonse, H. Rauch and W. Treimer, Z. Physik 271, 177 (1974).
3. U. Bonse and M. Hart, Appl. Phys. Lett. 6, 154 (1965).
4. M. Hart and U. Bonse, Phys. Today 23, 26 (1970).
5. R. Colella, A.W. Overhauser and S.A. Werner, Phys. Rev. Lett. 34, 1472 (1975).
6. S. Kikuta, I. Ishikawa, K. Kohra and S. Hoshino, J. Phys. Soc. Japan 39, 471 (1975).
7. H. Rauch, W. Schindler, W. Bauspiess and U. Bonse, 39. Physikertagung München 1975, paper D 16-2.
8. H. Rauch, A. Zeilinger, G. Badurek, A. Wilfing, W. Bauspiess and U. Bonse, Phys. Lett. 54A, 425 (1975).
9. S.A. Werner, R. Colella, A.W. Overhauser, C.F. Eagen, Phys. Rev. Lett. 35, 1053 (1975).
10. G. Badurek, H. Rauch, A. Zeilinger, W. Bauspiess and U. Bonse, Phys. Rev. to be published.
11. W. Bauspiess, U. Bonse and W. Graeff, J. Appl. Cryst. 9, 68 (1976).
12. U. Bonse, G. Materlik and W. Schröder, J. Appl. Cryst. in press.
13. W. Bauspiess, U. Bonse, W. Graeff, Z. Physik to be published.
14. G.E. Bacon, Neutron Diffraction, p. 38, Clarendon, Oxford, (1975).

or numerically : $\vec{M}^* = 3.70\ B\ \vec{I}$, M^* being expressed in Bohr magnetons and B in 10^{-12}cm.

So, when a neutron crosses a polarized target, it undergoes the same effect as if it was "seeing" a magnetic induction :

$$\vec{\mathcal{B}}^* = 4\pi\ N\ M^*\ \vec{P}$$

N being the number, per unit volume, of nuclei with pseudomagnetic moment M^* and polarization $\vec{P}$. As a consequence, the spin of this neutron should precess around the nuclear polarization direction with a frequency :

$$\omega = \gamma_n\ \mathcal{B}^*$$

γ_n being the neutron gyromagnetic ratio. Such an effect had been previously predicted, using as a start neutron optics equations[9].

THE REALITY OF PSEUDOMAGNETISM

This precession, and accordingly the correctness of the pseudomagnetic concept, has been demonstrated in an experiment where polarized neutrons, crossing a lanthanum magnesium nitrate (LMN) crystal, underwent a resonant depolarization from the pseudomagnetic induction due to proton polarization of the LMN target[10].

A non negligible by-product of this experiment was the observation of a non uniform volume polarization of the protons inside the crystal, this polarization being obtained dynamically[11]. Polarization measurements by other methods give in fact the mean value of P but not its spatial distribution as could be obtained in this experiment.

THE PRECESSION METHOD

The above kind of experiment requires high nuclear polarization (~ 50%), such as those obtained by dynamical methods, and large pseudomagnetic moments. It is nevertheless possible to work with the more modest polarizations obtained for example in metals by brute force, and much

smaller magnetic moments, in the following way suggested by A. Abragam[12] using the two coil Ramsey method. Completely polarized neutrons processing in the gap of a magnet giving a uniform field $\vec{H}_o$

a) enter with their polarization parallel to $\vec{H}_o$
b) cross a flipping coil C which rotates their spins through 90°, so that, when they come out from C, their spins precess coherently in the plane perpendiculaire to $\vec{H}_o$
c) cross a second flipping coil C', identical to C, which again rotates the neutron spins through 90° in such a way that when the neutrons come out from C', their spins are antiparallel to the $\vec{H}_o$ direction.

Thus, neutron polarization along $\vec{H}_o$ is +1 at the entrance and -1 at the end of the magnetic field region. If now one inserts a polarized nuclear target between C and C', neutrons will feel inside the target, besides the $\vec{H}_o$ field, the pseudomagnetic induction $\vec{\mathcal{B}}^*$ due to the nuclear polarization, which will give to the neutron spins the additional precession :

$$\alpha = \omega t = \gamma_n \mathcal{B}^* t$$

t being the transit time of the neutron across the target. And it is easy to show that polarization of the neutrons outgoing from coil C' is now $-\cos\alpha$. This polarization, and thus α, can be easily measured with an analyzer on the path of the transmitted beam. This measurement gives $\mathcal{B}^*$, whence B provided P is known.

To test the efficiency of this method, measurements were performed on hydrogen and vanadium[13], then B values for a score of nuclei were measured in metals in this way[14,15]. In those experiments, to get reasonable nuclear polarizations in the moderate field (H_o = 25 kOe) of the magnet, temperature of the sample could be lowered down to 20 mK in a dilution refrigerator. For some metals (Cu and Ag) where the natural element contained two isotopes with non-zero spin, measurements were performed on the natural element and at least one isotope.

For non-metals, the length of the nuclear relaxation times at low temperatures may be a hindrance. The polarization can then be obtained by dynamical methods with the great advantage that it is possible to polarize selectively one particular nuclear species, and to give it polarizations of either sign[5,14].

The pseudomagnetic precession allows the study of relaxation processes when resonance methods fail. Such a study was undertaken recently on holmium ethylsulphate ($Ho(C_2H_5SO_4)_3.9H_2O$). The primary aim of the experiment was to measure by another way the B value of holmium, previously obtained by diffraction[6,7]. Nuclear polarization of holmium, which in HoES remains paramagnetic in high fields down to very low temperatures, was essentially due to strong hyperfine coupling. Unfortunately, protons, although much less polarized than holmium, give a non negligible contribution to the neutron spin precession, due to the high value of their pseudomagnetic moment, and their abundance in the compound (33 protons for one Ho). Thus, the possibility of separating the holmium contribution depended mainly on the nuclear relaxation times of Ho and H.

The experiment was performed with the field $\vec{H}_o$ parallel and perpendicular to the crystal axis[16]. For the parallel configuration, the two relaxation times were found sufficiently different to make possible separation of holmium and proton contributions. This time was very long for protons, ten to thousand hours in the range 1 - 0.1 K, and moderately short for holmium, of the order of 15 minutes and independent of T below 0.5 K. The proton relaxation time may be attributed to magnetic impurities, but for holmium, a careful examination of the possible processes showed that the observed relaxation time can only be explained by a direct process between the two lowest hyperfine levels. When the field is perpendicular to the crystal axis, the holmium signal is completely masked by the protons whose relaxation time is very short (from one to ten minutes when T goes from 0.1 to 0.03 K). This result can only be explained by thermal coupling between the proton Zeeman system and the spin-spin system of the holmium nuclei, a process that had not been described in the litterature previously.

CONCLUSION

Temperatures in the range of 0.01 K can now be obtained rather easily with dilution cryostats, and maintained for a long time. It then becomes easier that in the recent past to get targets with appreciable polarizations and to perform experiments with polarized neutrons and polarized nuclei. The above examples show that, in this way, it is possible to measure with acceptable accuracy the spin-dependent part of neutron scattering amplitudes, the knowledge of which may be of value :

a) in diffraction experiments (which offer a way to solve phase problems in crystallography[17])
b) in the measurement of nuclear polarization if no other method can be used
c) to analyze polarization distribution in polarized targets
d) to study nuclear relaxation processes.

REFERENCES

1. R.M. Moon, T. Riste, W.C. Koehler, Phys. Rev. 181, 920 (1969)
2. R.I. Schermer, M. Blume, Phys. Rev. 166, 554 (1968)
   See also : ibid 130, 1670 (1963) and 133, A1366 (1964)
3. C.G. Shull, R.P. Ferrier, Phys. Rev. Letters 10, 295 (1968)
4. Y. Ito, C.G. Shull, Phys. Rev. 185, 961 (1969)
5. A. Abragam, G.L. Bacchella, C. Long, P. Mériel, J. Piesvaux, M. Pinot, Phys. Rev. Letters 28, 805 (1972) and ibid. p. 1225.
6. A. Herpin, P. Mériel, J. de Physique 34, 423 (1973)
7. G.R. Little, R.A. Erickson, AIP Conf. Proc. 1974, 18, Pt 1, 411.
8. H.H. Akopian, V.P. Alfimenkov, L. Lason, O.N. Ovchinnikov, E.I. Sharapov, Prep. of the Joint Inst. for Nucl. Res., Dubna, P3-8458, Dubna.
9. V. Baritchevski, M. Podgoretzki, J.E.T.P. 47, 1050 (1964).
10. A. Abragam, G.L. Bacchella, H. Glättli, P. Mériel, J. Piesvaux, M. Pinot M. Pinot, C.R. Série B, 274, 423 (1972).
11. A. Abragam, G.L. Bacchella, H. Glättli, P. Mériel, J. Piesvaux, M. Pinot, P. Roubeau, XVII° Congrès Ampère, 1, (1973) (V. Hovi éd. North Holland).

12. A. Abragam, Trends in Physics, 177 (European Phys. Soc., Geneva, Switzerland, 1973).
13. A. Abragam, G.L. Bacchella, H. Glättli, P. Mériel, M. Pinot, J. Piesvaux, Phys. Rev. Letters 31, 776 (1973).
14. P. Roubeau, A. Abragam, G.L. Bacchella, H. Glättli, A. Malinovski, P. Mériel, J. Piesvaux, M. Pinot, Phys. Rev. Letters 33, 102 (1974).
15. A. Abragam, G.L. Bacchella, H. Glättli, P. Mériel, J. Piesvaux, M. Pinot, J. de Physique Lettres 36, L 263 (1975).
16. A. Abragam, G.L. Bacchella, H. Glättli, P. Mériel, J. Piesvaux, M. Pinot, Physica 81B, 245 (1976).
17. J.B. Hayter, G.T. Jenkin, J.W. White, Phys. Rev. Letters 33, 696 (1974).

GAMMA RAYS AND/OR NEUTRONS?

W. B. Yelon
University of Missouri Research Reactor Facility
Columbia, Missouri 65201

ABSTRACT

Since intense sources of gamma-rays can be produced at many of the reactors used for neutron scattering, it is natural to use these sources as a complement to neutron scattering. The simplest use of gamma-rays is as a probe for determing the quality of a neutron sample since the absorption lengths for neutrons and gamma-rays are comparable and the resolution for gamma-rays is superior to the neutron resolution. Due to the reduced extinction and absorption at short wavelength, gamma-ray diffraction may give more accurate crystallographic data than X-rays, which may be combined with neutron data, particularly at short wavelength, to give accurate electron density maps. As a further extension; the intrinsic energy resolution of the gamma-rays is sufficiently good to permit inelastic scattering measurement to be performed using a number of different techniques. As a complement to neutron scattering this is a very exciting prospect, since one is able to measure at very large $\vec{Q}$ and on specimens which are high neutron absorbers, e.g., He-3. We are proceeding with the installation of a gamma-ray facility at the MURR which we hope will exploit these and other uses of intense, monoenergetic beams of gamma-rays. We give details of the installation which will be unique in the United States and discuss the various experimental applications of gamma-rays.

Neutron scattering is now a fully mature field which has proved extremely valuable in the study of condensed matter physics. However, the neutron scattering technique has several limitations imposed by the nature of the source or of the sample. These include relatively poor resolution, limited momentum and energy transfers and high absorption in certain materials. In many cases it is believed that gamma-ray scattering can overcome these limitations and so prove a useful complement to neutron scattering.

In contrast to neutron scattering, gamma-ray scattering is in its infancy, the first diffractometer was installed about four years ago at the institute Laüe-Langevin (Grenoble)[1]. As was the case in the early days

of neutron scattering, this machine has been used only for elastic scattering experiments. There is good evidence that these uses may be extended to inelastic scattering and that whole new areas of research may arise from these applications.

Table 1. Characteristics of some of the sources considered for gamma-ray scattering. Activities are for irradiation at 4 x 10^{14} n/cm^{2}sec to peak for natural (unenriched) sources[2]. Significantly higher fluxes can be achieved for Lu-177, Yb-169, and Se-75 by irradiating enriched material. Underlined energies correspond to ground state (Mössbauer) transitions.

Isotope	Half Life (Days)	Specific Activity (Ci/gm)	γ-ray Energy (keV)	Flux (γ/gm sec) X 10^{-12}
Au-198	2.69	700	411.79	25.
Ir-192	74.2	1300	295.90	12.
			308.43	14.
			316.50	39.
			468.05	23.
Tb-160	72.3	600	86.78	3.1
			298.57	5.8
Tb-161[a]	7.	1000	48.9	6.0
			74.68	3.7
Lu-177	6.71	860	112.95	1.4
			208.36	2.3
Yb-169	32.	27	63.50	0.58
			110.00	0.18
			177.00	0.20
			197.80	0.35
			307.50	0.11
Sm-153	1.92	2200	103.23	20.
Re-186	3.75	1300	137.00	7.
Re-188	0.7	1500	155.03	50.
Se-75	120.	15	136.00	0.33
			264.65	0.35

[a]Produced by 2 neutron capture from Tb-159.

Intense monoenergetic beams of gamma-rays can be obtained by activating certain isotopes in a nuclear reactor. The neutron capture process yields neutron rich isotopes which decay with the emission of characteristic gamma-rays. The reactors best suited for neutron scattering, by virtue of their high neutron fluxes, are thus ideally suited to the

production of gamma-ray sources. In Table 1 we list several of these sources as well as their specific activities, characteristic gamma-ray energies and intensities for activation in the University of Missouri Research Reactor (MURR) flux trap which has a peak flux of 7 x 10^{14} n/cm^2 sec. The specific activities are a factor of 5 greater than possible at Grenoble and by virtue of the unique configuration of the MURR, (Fig. 1) larger sources, limited only by the self-shielding, can be handled than at ILL.

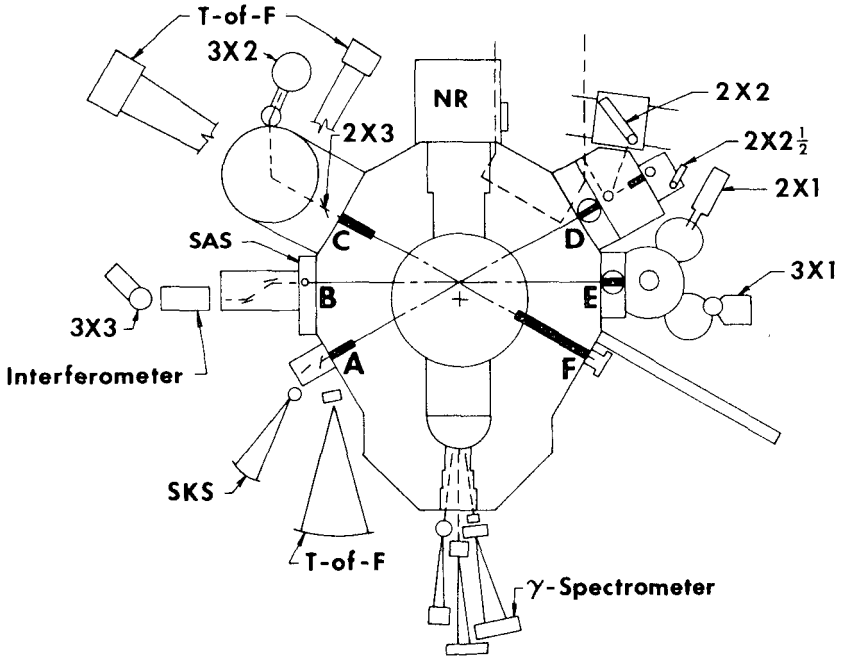


Fig. 1: Overall view of beam area of MURR. Gamma-ray facility will be located at the spent fuel area.

The intrinsic line width of the characteristic gamma-rays are on the order of 1 μeV for recoilless emission, and <0.1 eV for the Doppler broadened emission. For diffraction purposes these resolutions are extremely good and the resolution for a rocking curve is limited only by the angular divergence of the incident beam. The most intense sources will emit >10^{13}γ/sec and, hence, extremely tight collimation can be provided while maintaining high fluxes (>10^6/cm^2sec) on the sample. In fact the available fluxes are comparable to the best available monoenergetic neutron fluxes on the sample while the energy resolution is greatly superior.

In addition to the improved resolution, the absorption of gamma-rays is strongly reduced compared to X-rays, and is, in fact, comparable to neutron absorptions in most materials. Thus, the same samples can be investigated with both techniques. However, the absorption of gamma-rays is a systematic function of the atomic number and unlike neutrons there are no special cases of extremely high absorption such as ^{3}He, ^{10}B, Cd, etc. Thus, specimens black to neutrons may be studied by gamma-ray scattering.

The short wavelengths of the gamma-rays under consideration (0.2 - 0.03 Å) permit extinction free diffraction[3]. Furthermore, the extreme thinness of the Ewald sphere virtually eliminates multiple reflections[4], as does the relative inefficiency for scattering (compared to X-rays) at these wavelengths. Therefore, extremely accurate crystallographic studies should be possible, with data collection rates comparable to or greater than neutron crystallographic collection rates.

These applications have previously been discussed, and to some extent put into practice, but in addition the high resolution may yield a better probe of the Huang defect scattering[5] than either X-rays or neutrons. This scattering is generally several orders of magnitude less intense than the Bragg peaks about which it is centered, and with the ILL Gamma-diffractometer is probable not visible due to high backgrounds. These are the result of the detection of Compton scattering which can be greatly reduced by replacing the NaI(Tl) detector in use with a Ge or Ge(Li) detector with greatly improved resolution. Should this prove inadequate further reduction should be achievable by using a back-scattering analyzer (see below) just as analyzers are used with elastic neutron scattering to reduce background.

Inelastic scattering should be possible with gamma-rays despite the high incident energy, due to the extremely high resolution. Several methods may be envisioned for these applications. For energy transfers of the order of 0.1 - 100 eV back-scattering may be used (Fig. 2). This is entirely analogous to the neutron back-scattering apparati at ILL and Jülich which give resolutions of the order of $\Delta E/E \simeq 10^{-5}$. For such

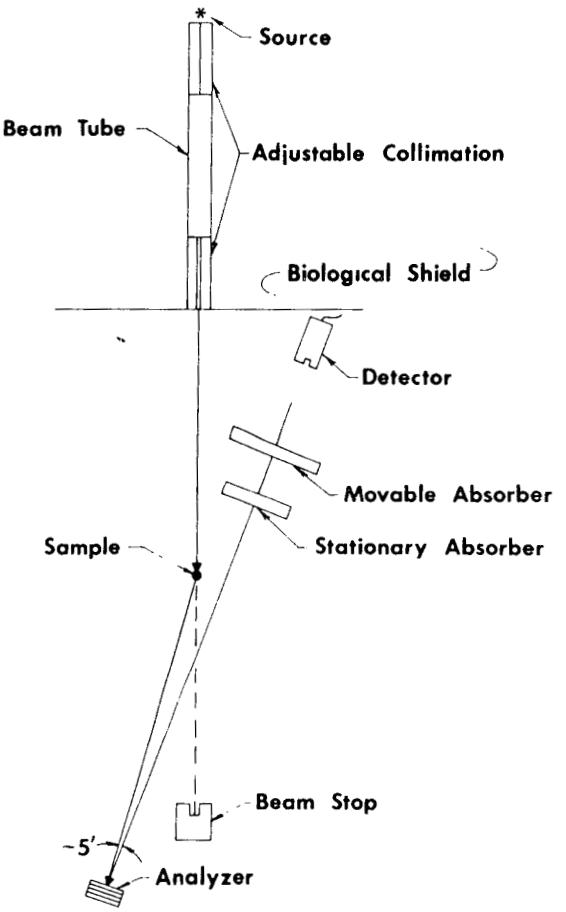


Fig. 2: Apparatus for inelastic gamma-ray scattering. Back-scattering will be used alone for 0.1 eV resolution and up to 100 eV transfers, resonant absorption will give μeV resolution and up to 0.1 eV transfers.

applications the energy will be scanned by varying the temperature (and the d spacing) of the analyzer crystal. Since backscattering is used only for analysis and not to monochromate, as with neutrons, the method is relatively conservative of flux. For these applications the lower energy sources ($E \simeq 100$ keV) will be employed. The most serious question is the efficiency for backscattering which will be studied as soon as a beam is available. There is reason to believe, however, that, with careful choice of crystal and 0.2 - 0.1Å gamma-rays reasonable efficiencies can be achieved.

A large number of interesting problems can be solved with this technique. Of particular interest is the direct measurement of the detailed band structure of metals (as a function of $\vec{q}$). The experimental arrangement would be entirely analogous to a triple axis neutron spectrometer in which the crystal and scattering angles are varied to satisfy the energy and momentum conservation laws.

For higher resolution, and energy transfer comparable to phonon energies, resonant absorption (Mössbauer) techniques can be employed. Since only the recoilless fraction of the gamma-rays can be resonantly absorbed, it is necessary to use low energy ($E \lesssim 100$ keV) gamma-rays to preserve a high recoilless fraction. In addition, the characteristic gamma-ray must be emitted in a transition to the ground state of the absorber material which is ideally an abundant, stable isotope. Fortunately the underlined sources in Table 1 fit this description and are usable. The arrangement for such an experiment is indicated in Fig. 2. A stationery absorber would be used to eliminate the elastically scattered gamma-rays and the movable absorbers would be on a centrifuge system at velocities up to about 500m/sec. corresponding to energy transfers up to about 0.1 eV. The backscattering analyzer (set for elastic scattering) is employed as a filter to reduce background, since only gamma-rays in a 0.2 eV band will be diffracted and the Compton scattering will not be detected in the Ge or Ge(Li) system due to the large energy shift. Source strengths are a factor of 10^3 to 10^4 greater than traditional Mössbauer sources, which suggests that this type of scattering experiment will be possible despite the inefficiencies of the various steps. A recent inelastic Mössbauer scattering experiment performed with a 100 mCi source gives us strong encouragement[6].

Among the experiments possible with these techniques are studies of phonons or other elementary excitations in materials which can be studied by neutrons only with great difficulty due to high absorption; such as ^{3}He, and studies at high $\vec{Q}$ which cannot be performed with neutrons due to the limited incident momentum; such as the free particle excitations in ^{3}He and ^{4}He in the range 30 - 60 $\mathring{A}^{-1}$.

The overall configuration of the MURR facility is shown in Fig. 1. Sources which will be irradiated in the flux trap can be transported to the spent fuel area where a beam port facility is located. Three beam tubes will be positioned to look at three separate sources. Since the sources will never leave the swimming pool of the reactor, large intense sources can be handled with no exposure risk. Variable collimation will be provided by positioning lead slits at the ends of the flight path.

Initially we expect to install one high precision diffractometer to study and develop the inelastic scattering techniques and to perform elastic scattering studies. Eventually, three or more instruments will be installed (Fig. 3) including a full-circle diffractometer dedicated to crystallography and one instrument dedicated to inelastic scattering applications. These instruments are expected to interface with and complement strongly the expanding neutron scattering program at MURR.

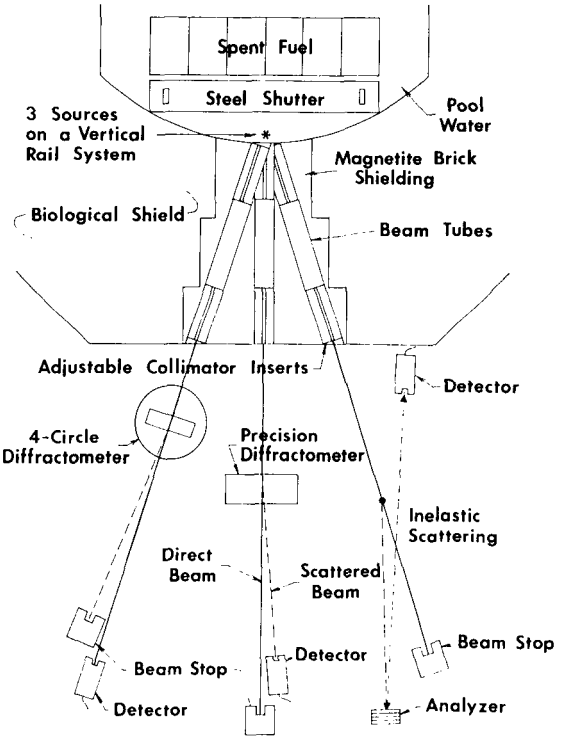


Fig. 3: Experimental arrangement of the gamma-ray scattering facility. Each beam will have a separate source which will be chosen for the experiment.

REFERENCES

1. J. R. Schneider, J. Appl. Cryst. 7, 541 (1974).
2. T. C. Whitson and C. W. Friend, Reactor Yield Calculations for 81 Radioisotopes, ORNL, Publication 11C-8 (1966).
3. See e.g., S. A. Werner, J. Appl. Phys. 45, 3246 (1975).
4. J. R. Schneider, J. Appl. Cryst. 8, 530 (1975).
5. H. Peisl, J. Appl. Cryst. 8, 143 (1975).
6. B. W. Batterman, Phys. Rev. To be published.

USE OF SINGLE CRYSTAL SILICON AS A THERMAL NEUTRON FILTER

Robert M. Brugger and William Yelon
Research Reactor Facility, University of Missouri
Columbia, Missouri 65201

ABSTRACT

Large single crystals of silicon are now being used at MURR as neutron band pass filters to pass thermal neutrons while excluding fast neutrons and gamma rays. Filters as long as 35 cm are now in service. These are held at liquid nitrogen temperature to increase the transmission of the thermal neutrons. The measured and estimated cross sections, effects of thermal cycling and radiation damage, and experience on double axis spectrometers is discussed.

Brugger[1] measured the cross section of single crystal silicon and showed that this material has the characteristics to be a very effective thermal neutron band pass filter. These measurements were made for a few energies in the thermal neutron range and for silicon at room temperature and liquid nitrogen temperature. A simple approximation equation was used to predict the cross section at other energies (see figure 1).

Additional data have now been collected or measured. Figure 2 shows the cross section for powdered silicon (solid circles) as presented in BNL-325 (1958)[2] and the initial measurements (X) of reference 1. Added to the graph are new data (open circles) obtained by Shull[3] for room temperature single crystal silicon as a function of energy. These data agree with MURR data at 0.025eV and 0.05-0.07eV and are not in disagreement with the extrapolating equation at higher energies.

Figure 2 shows also new measurements (solid triangles) of single crystal silicon at room, liquid nitrogen and liquid helium temperatures

obtained at the University of Missouri Research Reactor - MURR. To take this data, the tail piece of a helium cryostat was modified to hold a 3" diameter cylinder of silicon. The neutron beam passed along a radius of the cylinder perpendicular to the (111) axis of the crystal and cylinder. The energy of the transmitted neutrons was 72.8 meV. These measured cross sections shown in figure 2 are not of high accuracy because the sample and open could not be cycled and a correction had to be made for the cryostat walls. However, these data show that cooling single crystal silicon to liquid helium temperatures gives a significant further increase in the transmission of 100 meV neutrons.

The high flux reactor at the Institute Laue - Langevin, ILL, has become the standard against which to compare neutron beams. The ILL Users Manual[4] shows the fluxes of several beams at ILL without and with guide tubes. Figure 3 shows these flux spectra and also several flux spectra as they would be modified by filtering through single crystal silicon filters. The designation for the curves is:

1. beam tube (H3) on hot source,
2. beam tube (H12) from heavy water reflector,
3. neutron guide (H15) (radius = 2700m) on cold source,
4. neutron guide (H18) (radius = 25m) on cold source,
5. neutron guide (H22) (radius = 27000) from heavy water reflector,
6. H3 on hot source filtered through 100 cm silicon at 6.2°K,
7. H3 on hot source filtered through 50 cm silicon at 77°K,
8. H12 from heavy water reflector filtered through 50 cm silicon at 77°K.

It is seen that the filters are more effective at passing thermal and hot neutrons than are guide tubes while being quite effective in reducing the fast neutron background.

A 20 cm long silicon filter has been in use at D beamport of MURR for the last four months. The filter is quite effective in removing fast background. No effect is expected for irradiation damage and non has been observed to date. As stated in reference 1, quenching the

silicon rapidly in liquid nitrogen several times did appear to increase the cross section. The silicon in the filter at D is not in direct contact with the liquid nitrogen and no effect of thermal cycling has been detected on this filter.

The MURR is a light water moderated reactor with reentrant beam holes. Single crystal silicon filters will be a great help in suppressing fast neutron background and gamma background while passing most of the thermal flux. Figure 4 shows a cross section of the reactor with present or planned instruments and present or planned filters (broad lines.) Five of the six neutron beam tubes will be equipped with silicon filters. The only beam not so equipped will be used predominantly at long wavelengths (>2 Å); and Be filters will be used for certain applications. The use of the filters will permit a relaxation of the shielding requirements at the various spectrometers and will simplify the mechanical design of the instruments to be built. The fast neutron "gas" outside the shielding is expected to be nearly negligible.

At F beamport there is now a 210 cm long 2.5 cm diameter filter made from seven pieces of 1" diameter single crystal silicon held at room temperature. This passes 10^6 n/cm^{2}sec of 144 keV energy neutrons but also passes 10^7 n/cm^{2}sec of thermal neutrons. This flux is measured 2 meters outside the face of the reactor.

Filters are being made for D & E beamports that will fit into the saddle of the spectrometers. These will be 35 cm long and cooled to liquid N_2 temperature. A room temperature filter will be placed after the monochrometer at D to act as a beam stop and to pass a thermal beam through to a utility spectrometer, 2X2½.

A 50 cm long filter at liquid N_2 temperatures is planned for A beamport to be used with a small kappa spectrometer SκS. Here the filter will be slipped into the beam hole in the biological shielding. This filter reduces the stringencies placed on the chopper, monochrometer and flight path that can be used for small kappa experiments. The time-of-flight instruments at C beamport are to be replaced with a triple and double axis spectrometer. Then a silicon filter at liquid N_2

temperatures will replace the present polycrystalline beryllium filter.

Besides the silicon single crystal filters at MURR and the one observed at JRR-II, JAERI,[5] Mook at ORNL has tried one.[6] Mook improved his signal to noise ratio by a factor of 50 by inserting a silicon filter into his instrument.

All evidence to date indicate that silicon single crystal thermal band pass filters are effective and hold great promise.

The authors thank Professor Shull for permitting his data to be included in figure 2 and Monsanto Company for providing the silicon crystals.

REFERENCES

1. R. M. Brugger, Nucl Inst Meth (accepted for publication).

2. D. J. Hughes and R. B. Schwartz, BNL-325 2nd Ed. (1958).

3. C. Shull (private communication).

4. B. Maier "ILL Neutron Beam Facilities at the HFR" Instrument Description from ILL, (June 3, 1975).

5. Y. Hanaguchi (private communication).

6. H. Mook (private communication).

$$\sigma = \sigma_{ab} + \sigma_{TD} = \sigma_{ab} + \sigma_{FA}\left\{1 - e^{-2W}\right\}$$
$$= \frac{0.8}{\sqrt{E}} + 2.25\left\{1 - e^{-CET}\right\}$$

Where:

σ_{ab} = the absorption cross-section = 160 mb at 25 meV
σ_{TD} = the thermal diffuse cross-section
σ_{FA} = the free atom cross-section = 2.25 b
e^{-2W} = the Debye Waller factor
E = energy in meV
C = 1.439×10^{-5}, is constant normalizing the curve to $\sigma = 0.55$ b at E = 50 meV and T = 300° K.

Figure 1. APPROXIMATE EQUATION FOR ESTIMATING BAND PASS OF SILICON FILTERS.

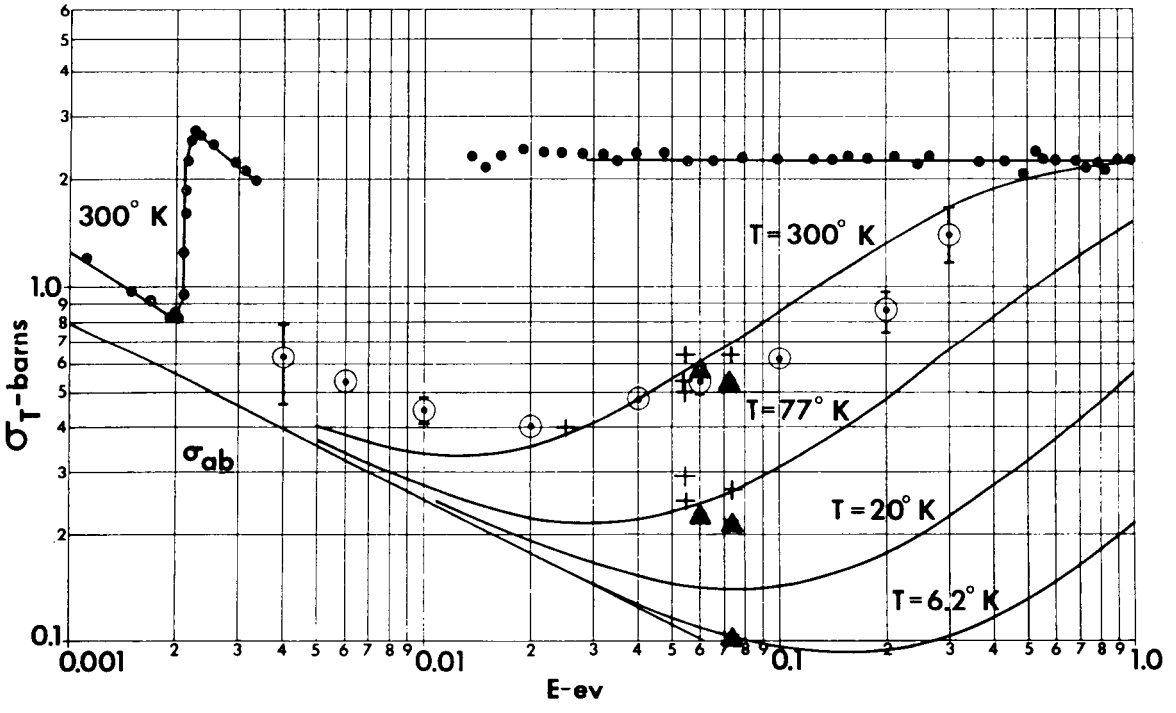


Figure 2. CROSS-SECTION OF SILICON

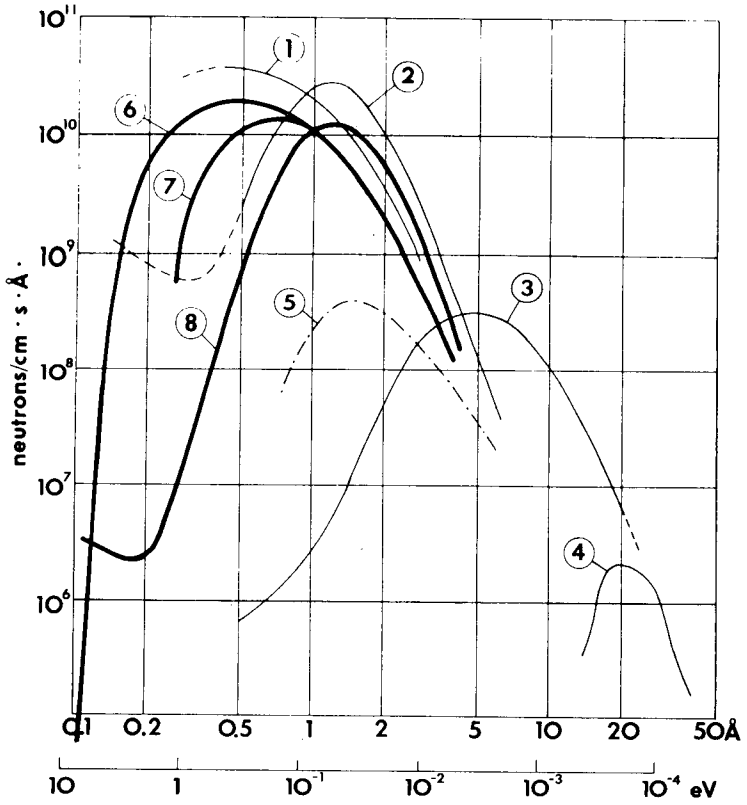


Figure 3. FLUX DISTRIBUTION FROM BEAMTUBES AT ILL.

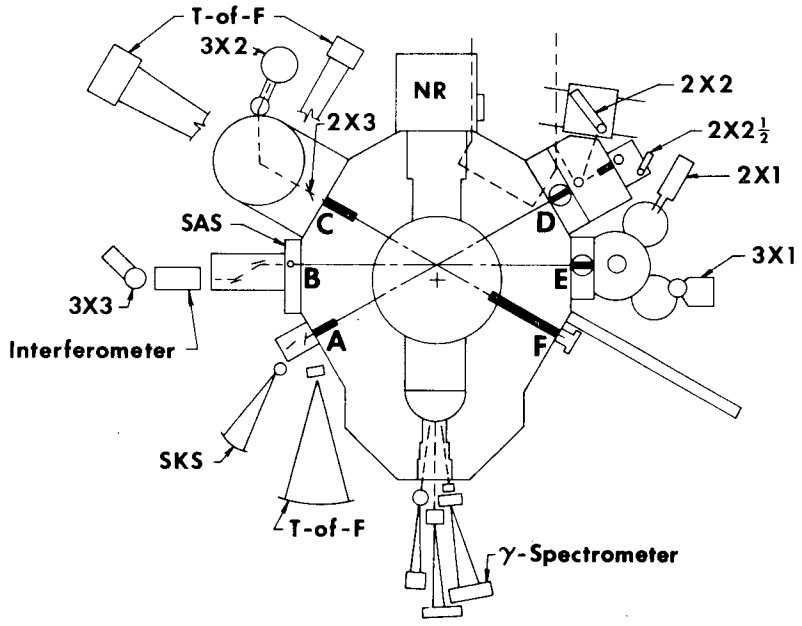


Figure 4. BEAM EXPERIMENTS AT MURR.

IRON-GERMANIUM MULTILAYER NEUTRON POLARIZING MONOCHROMATORS*

J. W. Lynn, J. K. Kjems†, L. Passell, and A. M. Saxena
Brookhaven National Laboratory
Upton, New York 11973

A new type of thermal neutron polarizing monochromator, consisting of alternate thin layers of iron and germanium, has been constructed and tested. Bragg reflection from such multilayer "crystals" in the fully magnetized state (which requires a field of only 100 Oe) yields an intense highly polarized beam, the reflecting efficiency being ∿0.84 for the reflected spin state. An important advantage of multilayer monochromators is that higher order harmonics in the reflected beam are almost completely suppressed. Since d-spacings achieved thus far are large (∿100 Å), the wavelength distribution produced is broader than that from conventional single crystal polarizing monochromators. Nevertheless, there are many applications where wavelength resolution is of secondary importance and the large gain in intensity (∿40 fold) of iron-germanium multilayers over conventional polarizing crystals can be valuable. Multilayers can also be used in combination with good monochromating crystals such as pyrolytic graphite or beryllium to produce polarized beams of high intensity and good wavelength resolution.

* Work performed under the auspices of the U. S. Energy Research and Development Administration.

† Guest scientist. Present address: Research Establishment Risø, Roskilde, Denmark.

APPLICATIONS OF THE FLY'S NEUTRON CAMERA: DIFFRACTION TOMOGRAPHY AND PHASE TRANSITION STUDIES*

J. B. Davidson and A. L. Case
Instrumentation and Controls Division, Oak Ridge National Laboratory
Oak Ridge, TN 37830

ABSTRACT

Application of the fly's eye intensifier-TV neutron counting camera to crystal examination by diffraction topography and tomography is described. Neutron diffraction topography is a volume effect in which the recorded image of a Bragg reflection is a superposition of the reflectivity of all the Bragg planes. In diffraction tomography virtual cuts are made through the crystal with a narrow neutron beam, and a series of images of a Bragg reflection is obtained which reveals the reflectivity of the crystal at isolatable regions through the crystal. Also described is the application of the camera to observation of phase transitions by monitoring a wide region in reciprocal space and recording the location and intensity of super lattice points as the temperature of the crystal is changed.

INTRODUCTION

The Fly's Eye Neutron Camera[1,2] consists of an image intensifier tube having a 150 mm diameter, fiber optic, input plate and a 25 mm diameter, fiber

*Research sponsored by the Energy Research and Development Administration under contract with the Union Carbide Corporation.

optic, output plate. The output plate is in optical contact with the input fiber optic of a secondary-electron-conducting (SEC) TV camera tube. A 150-mm-diameter, 0.5-mm-thick neutron phosphor layer (Li^6F + ZnS + plastic binders) contacts the input face plate of the image intensifier tube. Neutron-induced scintillations in the phosphor are intensified and then stored as positively charged spots on the target of the SEC camera tube until scanned by its electron beam. As the scanning beam detects and erases the spots, the coordinates of the neutron locations are derived from the beam deflection timing and are stored in a 200 x 100 channel magnetic core memory. As the counts accumulate in the memory, an image is built up and may be displayed in plan and isometric views, as well as in histograms of the intensity versus X or Y directions.

DIFFRACTION TOPOGRAPHY AND TOMOGRAPHY

The first of the two applications which this paper describes is that of neutron diffraction tomography (or "neutron diffraction section topography" as used by Schlenker et al.[3] in describing their photographic methods). Tomography is from the root word meaning "to cut" - as in "microtome" or "atom" (indivisible) - and has had long usage in medical radiography. Diffraction tomography may be considered a part of the more general technique or topography in which diffracted radiation intensity is observed versus position. When used with xrays, it is primarily a surface technique. Topography with highly penetrating neutrons gives a volume image, i.e., an image resulting from neutrons Bragg-scattered from the entire sample (Ref. 4).

Figure 1 shows a series of volume topographs versus rotation of a sucrose crystal measuring 4 x 4 x 4 mm. The dark, unreflecting regions in the top and middle row of pictures reveal a misoriented part of the crystal having dimensions of approximately 2 x 2 mm. The contour plot (bottom left) is a cut through the isometric display (bottom center) at the level of the "shelf" in the intensity and shows the weakly reflecting misoriented portion as a white spot on the contour ring.

Reference 2 describes some topographic applications of the fly's eye camera, including magnetic diffraction images of spin density wave domains in chromium. Crude tomographs were made of large crystals to determine crystal quality and to isolate grains in bulk specimens within minutes.

In the present application, following Schlenker et al., the specimen is illuminated with a thin sheet-beam of neutrons through collimating slits (Fig. 2) while the crystal is set to reflect at some Bragg angle. The resulting image is a diffraction tomograph of a narrow section of the crystal whose thickness is defined by the slit system. As the crystal is translated across the illuminating slits in steps and a picture is accumulated at each step, a series of tomographs is obtained which shows the reflectivity of the crystal in three dimensions. Such a series of pictures of a lead crystal, taken every 0.6 mm, is shown in Fig. 3. A selected 0.6 mm tomograph from the middle of a stainless steel crystal is shown in Fig. 4. Various display modes available in the fly's eye system are illustrated in this figure. The pseudo-color representation is obtained by turning on the display screen at three different levels of neutron diffracted intensity in the stored digital image and photographing the image successively through red, blue, and green filters using a single piece of film.

Figure 5 illustrates the speed with which unknown specimens - - as, perhaps, directly from a crystal-growing apparatus - - may be examined. The "unknown" was a rough, 2.5 cm cube of limonite-probably $Fe_2O_3.3H_2O$. A neutron transmission radiograph observed instantaneously on the TV monitor showed a transmitting region in the center of the cube. The water in the specimen provided good neutron contrast to outline the cube. On rotating the sample, a strong Bragg reflection was observed on the monitor a few seconds later. The size of of the reflection was comparable to the transmitting region. A series of tomographs (2-min exposure) was then taken to locate the crystal (probably Fe_2S) within the specimen. Two views of these tomographs is shown on the right of

Fig. 5, along with two views of the transmission radiograph.

Another method of displaying the tomographs which results in a three-dimensional diffraction image of the specimen is shown in Fig. 6. Negatives of the tomographs are separately mounted and placed together as overlays with good registration. Care is taken to keep the unexposed portions of the negatives clear. When held in front of a strong light, the tomographs are seen together in three dimensions, creating a hologram-like image in which variously diffracting features of the crystal appear at their appropriate depths.

PHASE TRANSITION STUDIES*

Unlike the tomographic application in which attention is centered on one reflection, the application to phase transitions utilizes the entire area of the detector to monitor a large region in reciprocal space and to record the appearance (or disappearance) of lattice points. In this way unknown reflections resulting from phase transitions may be located and measured. In the illustrative example shown in Figs. 7-9 a $RbCaF_3$ crystal was cooled through its known transition temperature of 195K, with the camera placed as shown in Fig. 7. The angles subtended by the camera were 30 deg horizontally and vertically. A broad monochromatic beam ($\lambda \sim 2.6$ Å) was used. Two 100 x 100 point images were obtained: the first at 205K, above the transition; the second at 190K (Fig. 8). The exposure time for accumulating in the memory was 15 min. As the temperature passed through the transition point, the R-point reflection [3/2, 1/2, 1/2] increased on the monitor and the counts were stored in memory. Four 10-min runs in Figure 9 show the increase of intensity of the R-point with decreasing temperature.

---

*This work was done in collaboration with C. A. Rotter, Dept. of Physics, Univ. of West Va. A similar experiment was performed with H. A. Mook on TTF-TCNQ (Ref. 5).

REFERENCES

1. J. B. Davidson, Acta Cryst. A25, S66 (1969).
2. J. B. Davidson, J. Appl. Cryst. 7, 356 (1974).
3. M. Schlenker et al., J. Appl. Phys. 46 (7), (1975).
4. K. Doi et al., J. Appl. Cryst 4, 528 (1971).
5. J. B. Davidson, Brookhaven Symp. Biology, No. 27, (1976) Beuno Schoenborn, Editor.

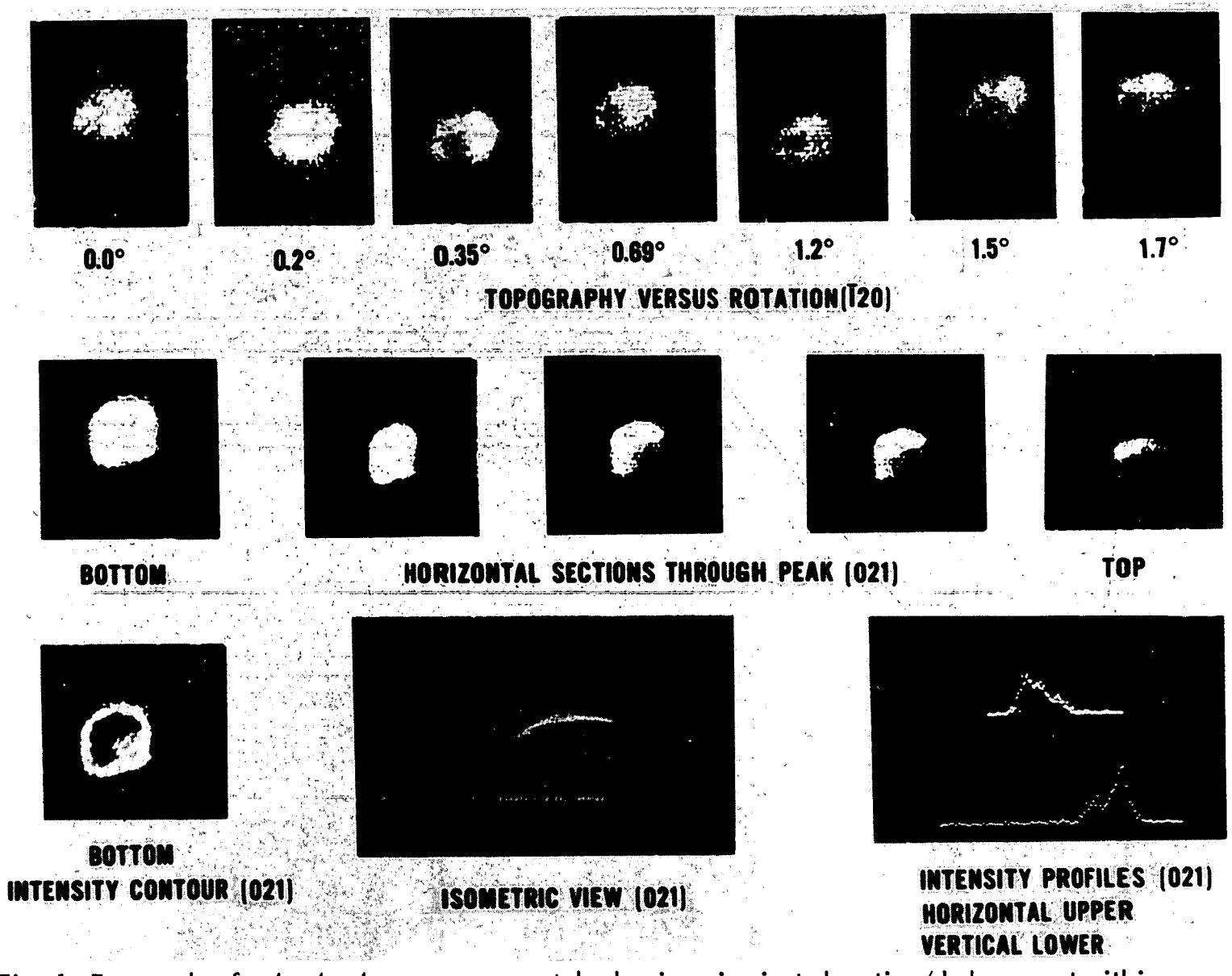


Fig. 1. Topographs of a 4 x 4 x 4 mm sucrose crystal, showing misoriented portion (dark segment within round image).

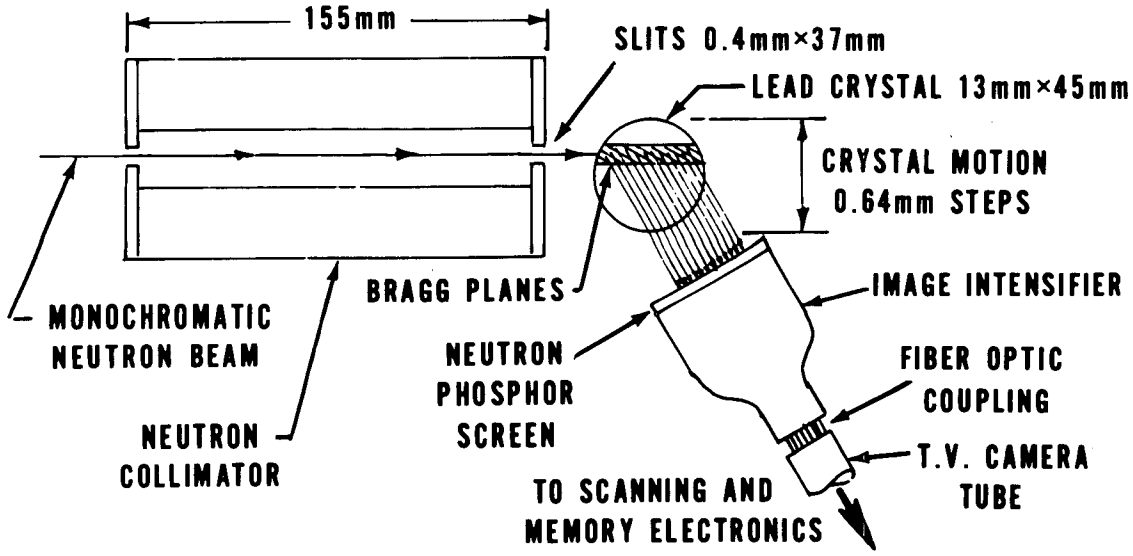


Fig. 2. Experimental set up for tomography.

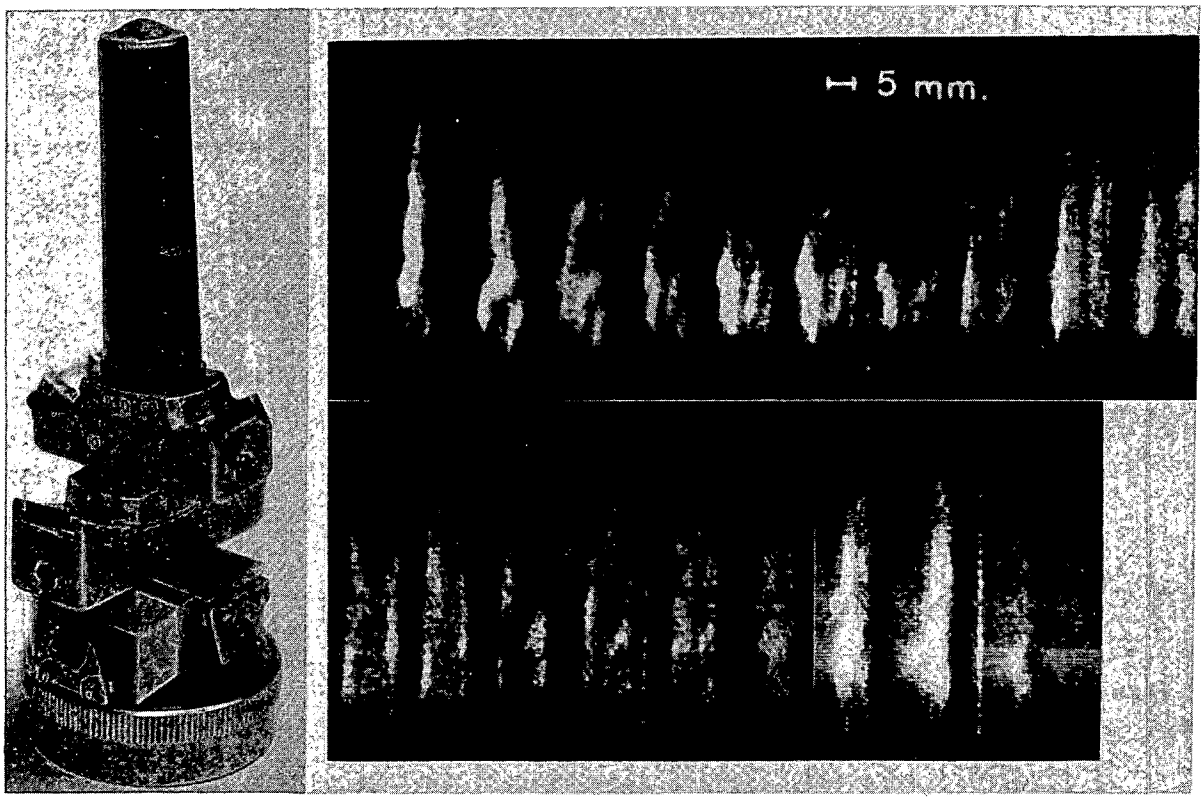


Fig. 3. Diffraction tomographs of lead crystal taken at 0.8 mm intervals with 2-min exposure and 0.4-mm slits.

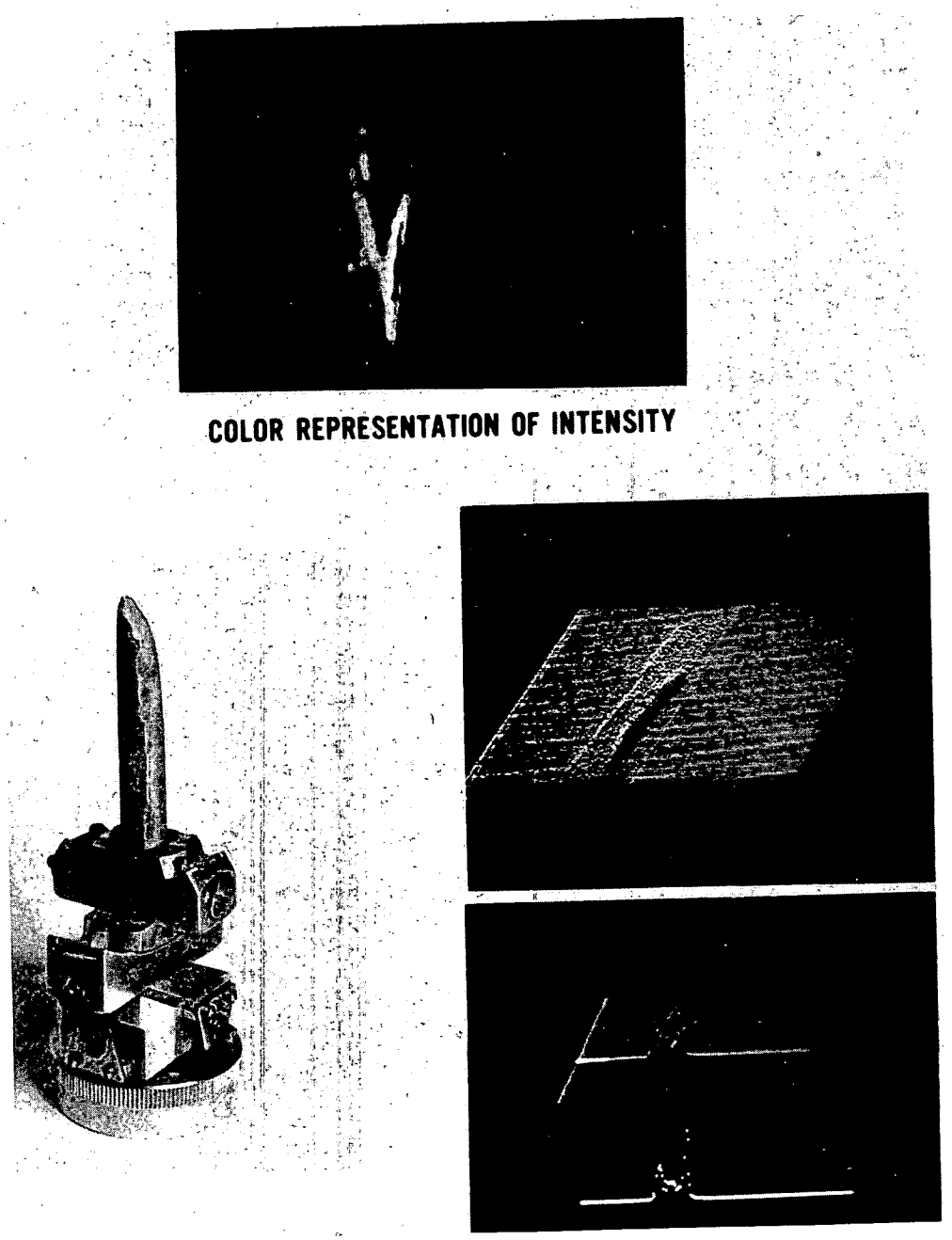


Fig. 4. Diffraction tomograph of stainless steel crystal illustrating various display modes.

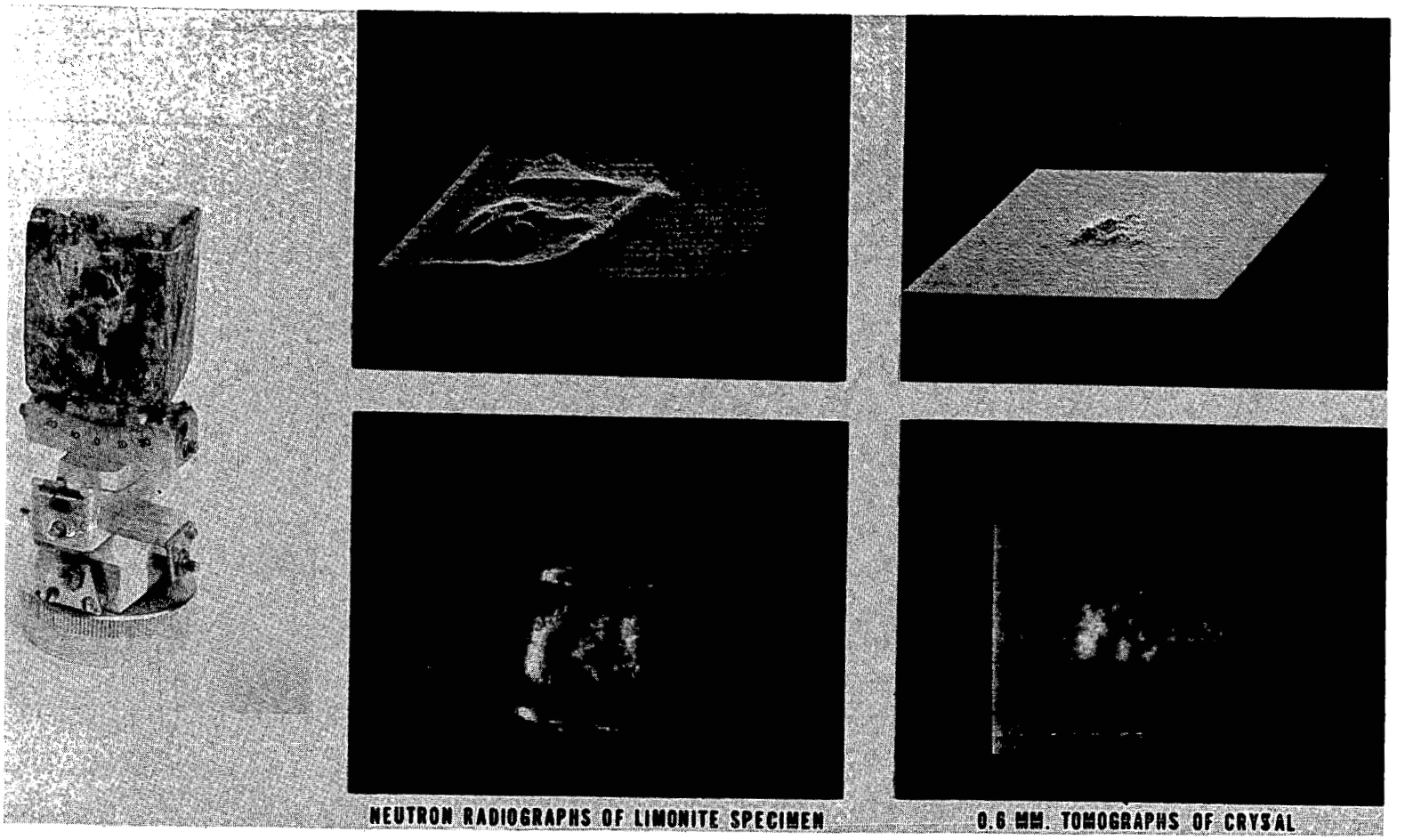


Fig. 5. Diffraction tomograph and radiograph of limonite specimen containing "unknown" crystal.

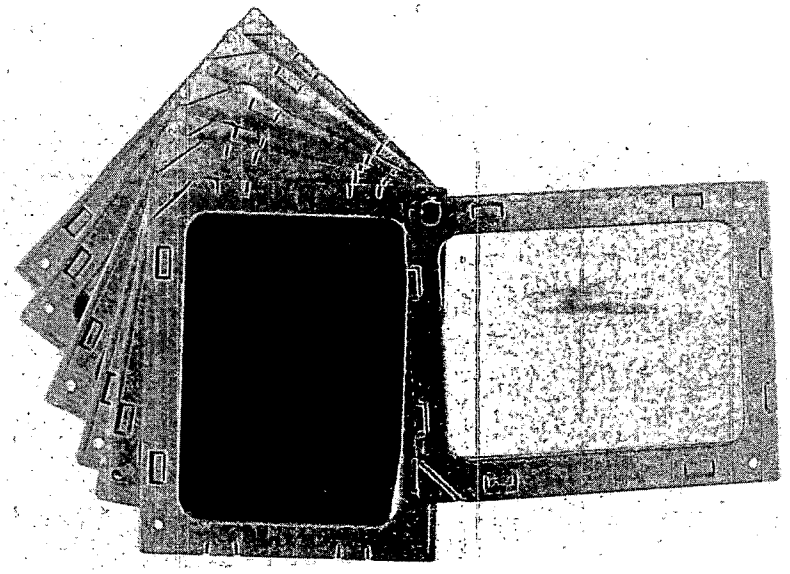


Fig. 6. Method of holding negatives of tomographs for three-dimensional viewing.

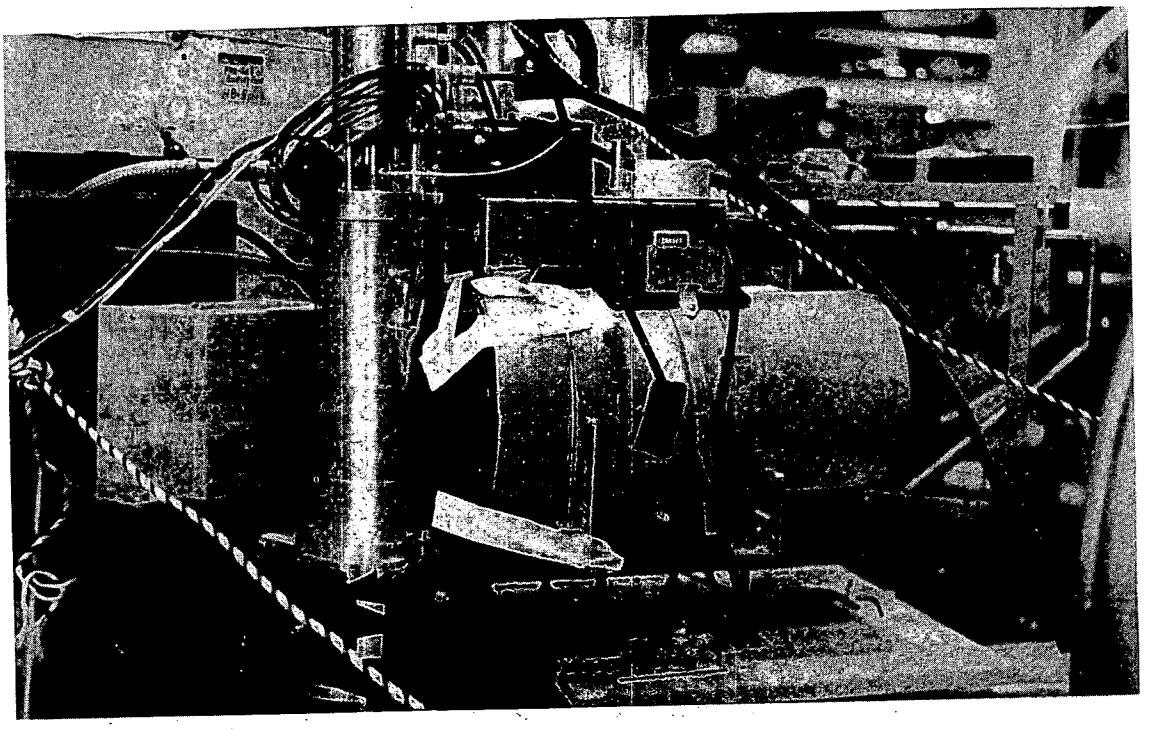


Fig. 7. Arrangement of camera and cryostat for phase transition studies.

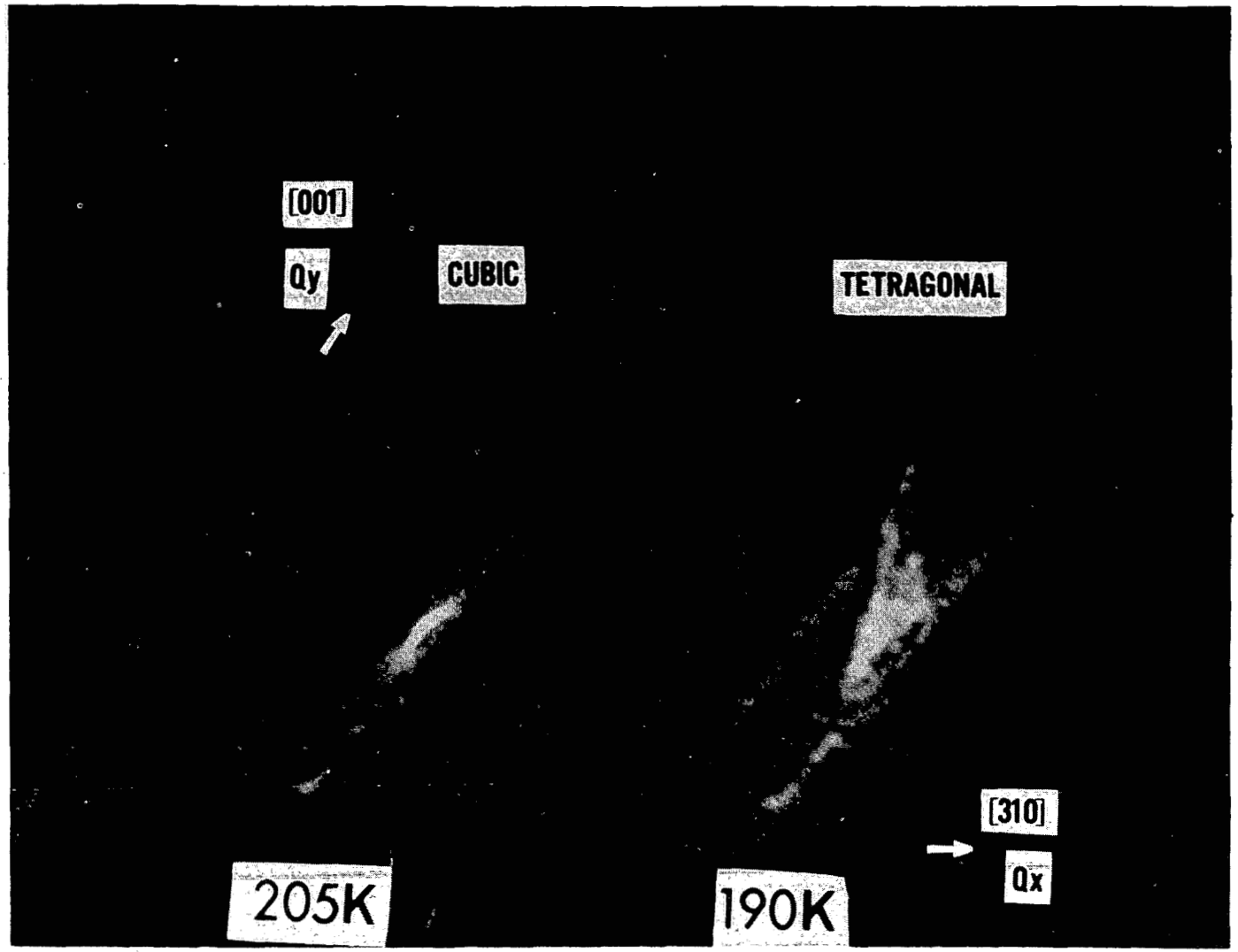


Fig. 8. Display of elastic scattering intensity of super lattice R-point at temperatures above and below transition point (195K) in $RbCaF_3$.

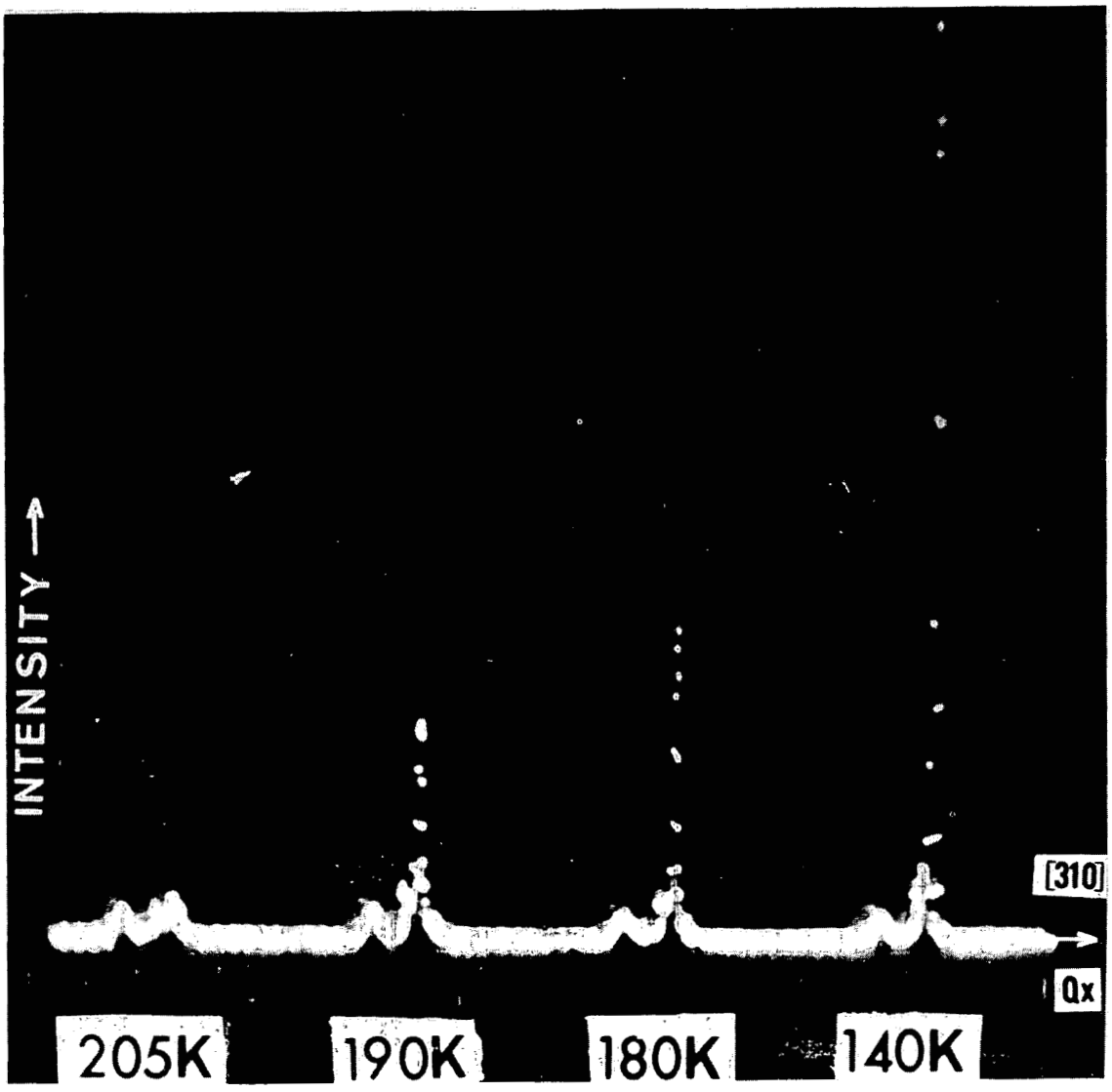


Fig. 9. One-dimensional cuts showing intensity at R-point in $RbCaF_3$ at four temperatures.

NEUTRON DIFFRACTION TOPOGRAPHY : RECENT RESULTS IN THE INVESTIGATION OF DOMAINS AND CRYSTAL DEFECTS*

M. Schlenker and J. Baruchel
Laboratoire de Magnétisme du CNRS
166X, 38042 Grenoble, France

ABSTRACT

The principle of neutron diffraction topography and two distinct types of applications - either, in a crude form, as a valuable aid to "normal" scattering experiments, or as an observation technique - are outlined. Recent results of investigations of defects both in rather perfect and very distorted crystals and of antiferromagnetic and ferromagnetic domains are shown and briefly discussed.

INTRODUCTION

Neutron diffraction topography (NDT) can be described as a complementary approach to diffraction measurements. In "normal" scattering work, the intensities of as many scattered beams as possible are measured to determine the crystal structure or excitation spectrum of a specimen, but they are averaged over the sample volume. Any information that could be derived from the local distribution, within the crystal, of Bragg reflectivity or peak position is then lost ; it is the purpose of topographic techniques to retrieve and use it.

The most natural way of retrieving information about a spatial distribution is to make a picture, and this is indeed the way it is done : a single crystal C is set for a given, strong Bragg reflection, and a photographic detector P is placed in the diffracted beam, as near as possible

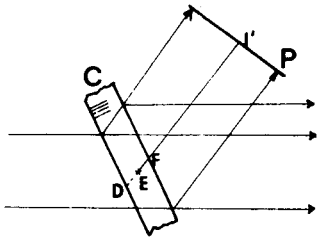


Fig. 1

* Work partly performed at Institut Laue-Langevin

to the specimen, so that local variations in diffracted intensity, hence in detector blackening - in other words, contrast - can be traced to a region in the sample.

Two different approaches can be made of the use of this information and the choice involves differences in the instrument and detector to be used : NDT can be used as an aid in "normal" diffraction work, or it can be developed into an observation technique for crystal defects and domains.

TOPOGRAPHY AS AN AID TO "NORMAL" SCATTERING WORK

Even a very crude form of NDT can be a great help in "normal" scattering work, and it is so simple, fast and cheap that we think it should be strongly advocated. Two of the plagues affecting scattering work are inhomogeneous extinction effects, making correction procedures futile and, even worse of course, allegedly single crystals which turn out not to be single ! Both effects can often be detected in minutes by setting the crystal for a strong reflection and putting a Polaroid camera equipped with a neutron-sensitive scintillator[1] across the diffracted beam ; this procedure can be complemented by tricks such as rocking the crystal during exposure or, in the case of very thick crystals, using a thin incident beam to obtain a "section topograph"[2] in which only a (virtual) slice of the specimen is seen. It immediately evidences macroscopic inhomogeneities, can distinguish extinction changes from local misorientations, and thus is a precious tool in determining both whether the data that can be collected from a crystal is likely to be usable, and how it should, if necessary, be cut.

As an indication of the exposure times involved, our neutron Polaroid camera requires an exposure of 3.10^5 $n.cm^{-2}$. This work nicely complements γ-ray diffractometry[3], and it can be carried out on any instrument. More sophisticated equipment such as the "fly's eye neutron camera"[4] of course have further possibilities.

TOPOGRAPHY AS AN OBSERVATION TECHNIQUE

Neutron diffraction topography can also be viewed as a technique for the direct observation of crystal defects and domains, in many respects comparable to electron or optical microscopy but of course closest to X-ray topography[5]. As such, it has original capabilities, which are no surprise to neutron diffractionists : the possibility of investigating large crystals, too absorbing both for light and for X-rays, and, because of the magnetic interaction of neutrons with matter, unique possibilities for the investigation of magnetic domains of all kinds. Both of these features were used in the pioneering work in neutron topography of Doi, Minakawa, Motohashi and Masaki[6] and of Ando and Hosoya[7].

To the best of our knowledge, three instruments especially designed for NDT are in or very near operation at Tokai-Mura (Japan), Saclay (France) and at ILL in Grenoble (France). We will briefly describe the Grenoble instrument and scan across some recent results.

Instrument

The Grenoble instrument for NDT went into operation in November 75 ; its design was based on the possibility to install it between an existing instrument and a beam-catcher, downstream of the end of a curved thermal guide-tube, on a very clean, well-collimated beam, obviating the need for shielding around the monochromator. It was thus possible to build a compact instrument, resting on a single stand, with a monochromator to specimen distance of only 40 cm. As a result, changes in monochromator - crystal, wavelength or specimen reflection are easy ; furthermore, the instrument can be converted to polarized neutron work very simply[8].

Whenever NDT is used as an observation technique, better resolution than provided by the very fast Polaroid camera is needed : the usual detector is X-ray film with a (n-β) Gd converter[9], but n-α converters in association with cellulose nitrate are also used[10, 11]. In accordance with X-ray topographic tradition, high intensity areas are printed as dark contrast.

Recent results

Observation of defects in heavy crystals

Although the heaviest drawback of NDT is its poor resolution, it was proved possible, in very good crystals, to reveal individual defects such as inclusions and dislocations [12, 11]. NDT becomes really useful when it comes to investigating heavy crystals.

It is a truism to say that a crystal can be heavy because it is made up of heavy elements or / and because it is just big. In either case absorption will make its investigation by X-ray topography impossible. In NDT, on the other hand, few elements give rise to heavy absorption, and, e.g., lead compounds are no problem at all [13]. NDT thus offers new possibilities for the investigation of bulk crystals. The choice of the topographic technique is a matter of geometry. In most cases the image can be considered as a projection of the defect structure along the diffracted beam direction. For plate-shaped specimens, it is adequate to make "ordinary" topographs, by illuminating, as in fig. 1, a large part of the specimen surface or all of it. When it comes to very thick crystals, this would result in an unresolvable muddle, and it is necessary to examine only a slice at a time. This can be done without cutting the sample by restricting the incident beam with a slit : this is section topography [14,2] a technique devised by Lang [15] in the X-ray case, but which acquires a new dimension in NDT ; its principle is illustrated on the inset to Fig. 3

Fig. 2 shows a section topograph of a natural crystal of smoky quartz, made using a 0003 reflection at a wavelength of 1.35 Å with a pyrolytic graphite monochromator ; the exposure time was 24 hours. Valuable insight on the growth history of the crystal can be derived from a set of such topographs. This is a good crystal. At the other extreme, Fig. 4 shows section topographs of a germanium

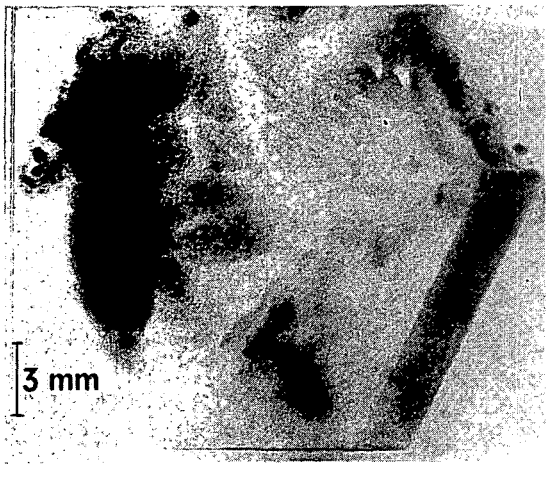
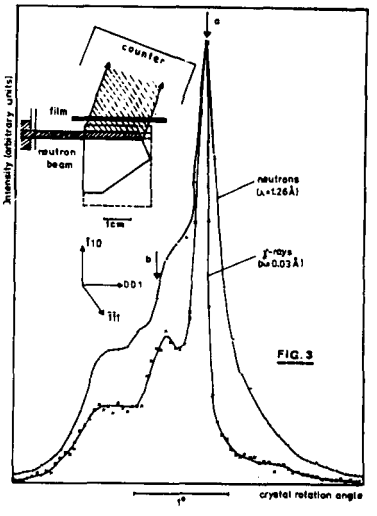
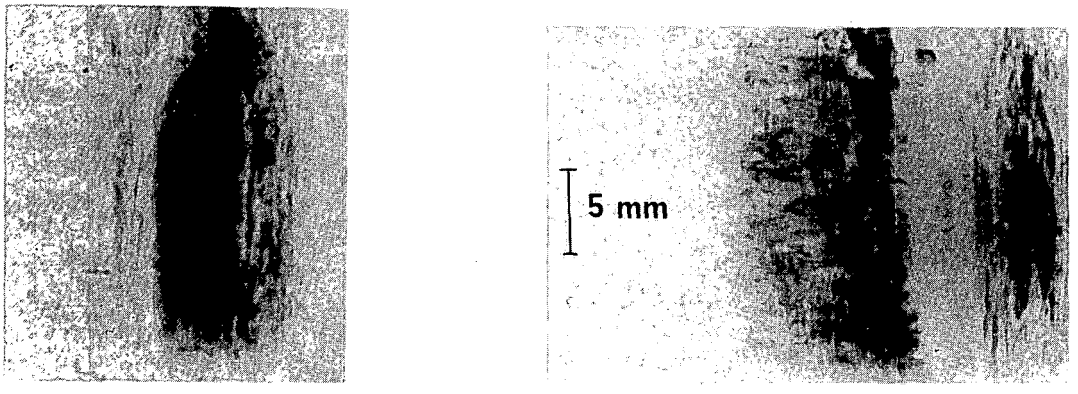


Fig. 2

crystal which was heavily distorted by A. Freund[16] towards use as a monochromator. Fig. 3 contains rocking curves, made respectively with γ-rays by A. Freund using a 220 reflection at a wavelength of 0.03 Å and with neutrons, on the topographic instrument using a $33\bar{3}$ reflection at a wavelength of 1.26 Å chosen so that the virtual section plane be along (110) and thus that identical locations in the specimen be probed in both cases. The section topographs on





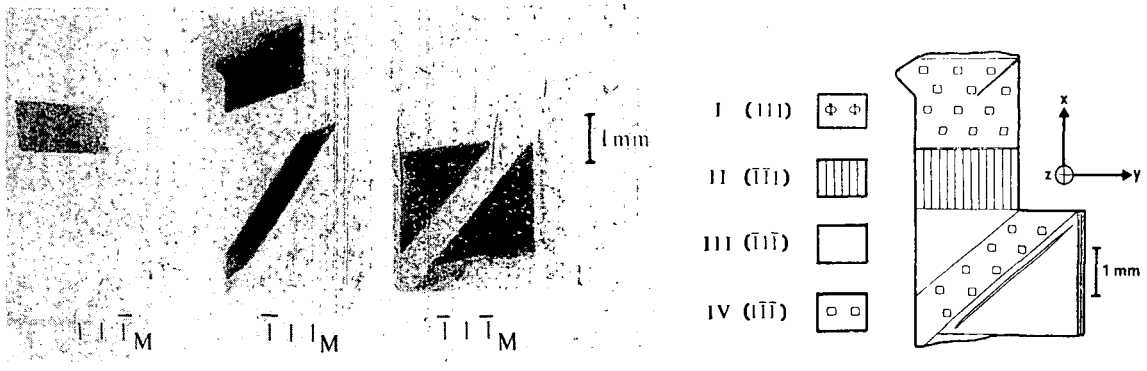
(a) Fig. 4 (b)

Fig. 4 a and 4 b correspond to exactly the same region, with just a slight difference in crystal angle ω : the corresponding angular positions are denoted by a and b on the rocking-curves of Fig. 3 . The area diffracting on a obviously is a part that did not slip. The geometry of this experiment is shown on the inset to Fig. 3 .

Observation of antiferromagnetic domains[17]

NDT is at present the only technique capable of revealing antiferromagnetic domains directly, i.e. through interaction either with the arrangement (T-domains) or direction (S-domains[18]) of the sublattice magnetization ; all other techniques for the observation of antiferromagnetic domains (optical or electron microscopy, X-ray topography) rely solely on the lattice distorsion associated with the domain structure via exchange

striction or magnetostriction ; of course this effect also exists in NDT, and topographs made using nuclear reflections show T-wall contrast. But, using 111-type magnetic reflections, only one type of T-domains is imaged at a time : Fig. 5a shows the topographs obtained with exposure times of 24 hours; they provide unambiguous identification of the ferro-



(a) Fig. 5 (b)

magnetically-coupled planes within each domain, leading to the map of Fig. 5b.

Observation of ferromagnetic domains[8]

Using polarized neutrons, NDT also is the only method for directly revealing ferromagnetic domains within non-transparent specimens. In the simplest case of domains with antiparallel magnetization, the ratio of the intensities diffracted by the domains is just the ratio of the intensities diffracted by a single-domain specimen for opposite incident-beam polarization, i.e. the flipping-ratio, R. The feasibility of this technique was demonstrated[19] using a standard polarized-neutron set up in a high R case (Co - 8% Fe) ; but attempts to observe domains in Fe-Si crystals, where R is rather small, had failed. Work is now in progress on the topographic instrument at ILL, using a simple polarizing attachment ; presumably due to the low background level, we succeeded in visualizing domains in Fe-Si with good contrast.

CONCLUSION

Neutron diffraction topography is a very young technique, and it can

be expected to improve as more effort is invested into it. Topography, in a crude form, can save time and we suggest that it should become a routine in "normal" scattering experiments. As an observation technique, it suffers from poor resolution, but has original capacities, both in the study of domains of all kinds and in the visualization of defects. What other technique could one think of to investigate the crystal defects of the diamonds in the Crown Jewels without dismounting them ?

REFERENCES

1. S.P.Wang, C.G.Shull and W.C.Phillips, Rev. Sci. Instrum. 33,126 (1962).
2. M. Schlenker, J. Baruchel, R. Perrier de la Bathie and S.A.Wilson, J. Appl. Phys. 46, 2845 (1975).
3. Jochen Schneider, J. Appl. Crystall. 8, 195 (1975).
4. J.B.Davidson, J. Appl. Crystall. 7, 356 (1974).
5. An excellent review was given by A.R.Lang in Modern Diffraction and Imaging Techniques in Material Science, ed. by S. Amelinckx et al. North Holland, Amsterdam 1970.
6. K. Doi, N.Minakawa, H.Motohashi and N.Masaki. J. Appl. Crystall. 4, 528 (1971).
7. M.Ando and S.Hosoya, Phys. Rev. Lett. 29, 281 (1972).
8. M.Schlenker, J.Linares Galvez and J.Baruchel, paper to be presented at International Conference on Magnetism. Amsterdam 1976, to be published in Physica B.
9. H.Berger, Ann. Rev. Nucl. Sci. 21, 335 (1971).
10. H.Berger, Nucl. Techn. 19, 188 (1973).
11. C. Malgrange, J. F. Pétroff, M. Sauvage, A. Zarka, M. Englander, Phil. Mag. 33;743 (1976)
12. M.Schlenker, J.Baruchel, J.F.Pétroff and W.B.Yelon, Appl. Phys. Lett. 25, 382 (1974).
13. M.Schlenker and J.Baruchel in New Methods and Techniques in Neutron Diffraction RCN-234, Petten (Holland) 1975, p.487.
14. H.Tomimitsu and K.Doi, J. Appl. Cryst. 7, 59 (1974).
15. A.R.Lang, J. Appl. Phys. 29, 597 (1958).
16. A.Freund : paper at this Conference.
17. J.Baruchel, M.Schlenker and W.L.Roth : to be published.
18. W.L.Roth, J. Appl. Phys. 31, 2000 (1960) ; G.A.Slack, J. Appl. Phys. 31, 1571 (1960).
19. M.Schlenker and C.G.Shull, J. Appl. Phys. 44, 4181 (1973).

PROGRESS IN NEUTRON MONOCHROMATOR DEVELOPMENT AT THE INSTITUT LAUE-LANGEVIN

A. Freund
Institut Laue-Langevin, 156X Centre de Tri, 38042 Grenoble

ABSTRACT

Results of progress in neutron monochromator development at the ILL are presented. A very short description of the four instruments for crystal testing is also given.

INTRODUCTION

"Getting good monochromating crystals for neutron scattering is still a matter of chance". This statement was made by Dorner and Kollmar[1] in a paper on pyrolytic graphite in 1973. Pyrolytic graphite was at that time the only monochromator material with highly reproducible excellent neutron reflexion properties as shown by these authors and by Riste[2] already before. However, the use of PG is limited due to its large unit cell and to the fact that the mosaic spread η cannot be made smaller than 0.4°. For small neutron wavelengths and high resolution other materials have to be used. The integrated intensity obtained from such materials as metals and semiconductors was always lower than the calculated one by a more or less large amount. Therefore a considerable effort was made at the Institut Laue-Langevin in the past several years in order to analyse the low reflectivity of these crystals and to improve their efficiency. Parallel to this work several studies were undertaken to produce monochromators and monochromator systems consisting of perfect or nearly perfect crystals for special focusing techniques. The cost of these investigations is still very small compared to the cost of constructing and running neutron sources. The present paper will give some results of recent developments concerning the production of mosaic crystals and systems with high reflectivity because they are of quite general use. For the more sophisticated systems using perfect crystals the literature should be consulted[3-13] the space being too

small for a description in the present paper. Also polarizing crystals will not be mentioned here.

MONOCHROMATOR TEST FACILITIES

Monochromator development is inconceivable without machines for crystal characterization in view of their defect structure and the reflecting properties related to it. At the ILL four instruments for crystal testing exist :

i) An X-ray double-crystal diffractometer[14] for studying local defect structures and the tilts and strains related to them, for lattice constant determinations and crystal orientation.

ii) A γ-ray diffractometer[14,15,16] working as a single crystal instrument and using highly monochromatic ($\frac{\Delta\lambda}{\lambda} = 10^{-6}$) and well-collimated (10") γ-radiation of 0.03 Å wavelength emitted by a radioactive gold platelet. The short wavelength reduces extinction effects considerably so that the real mosaic structure of monochromator crystals or any other monocrystalline samples can be studied. The small absorption of this radiation permits the investigation of quite thick samples which can be contained in furnaces, cryostats, pressure cells etc.

iii) A neutron double-crystal instrument[17] working in a large wavelength and angular range on which the neutron reflectivity and the shape and width of the neutron rocking curves of monochromator crystals are determined.

iv) An instrument for neutron diffraction topography[18] where crystal imperfections can be located in the sample thus permitting a "mapping" of crystal inhomogeneities as e.g. inclusions, large grains or other dislocation all structure related to the mosaic structure observed on an angular scale by rocking curve measurements.

The characteristic features of these four test methods have been summarized recently in more detail and in connection with monochromator development[19].

WHY A LOW CRYSTAL REFLECTIVITY ?

Before improving the ILL neutron monochromators we had to find out why their reflectivity was lower than theoretically expected. Besides extinction and absorption effects -where absorption does not include only neutron capture but also parasitic and inelastic scattering events- inhomogeneities of the crystal defect structure were found to be mainly responsible for low reflectivity. The γ-ray diffractometer was very useful for these studies as shown clearly in Fig. 1 where a γ-ray and a neutron rocking curve obtained from the same volume of a Be crystal are represented. The crystal inhomogeneity revealed by the multiple peak γ-ray curve are hidden in the neutron curve due to extinction effects.

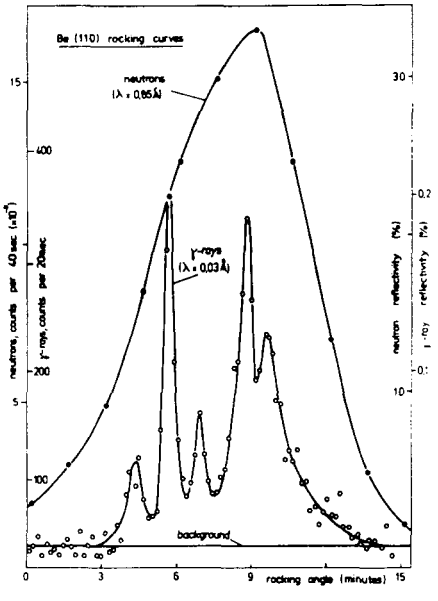


Fig. 1

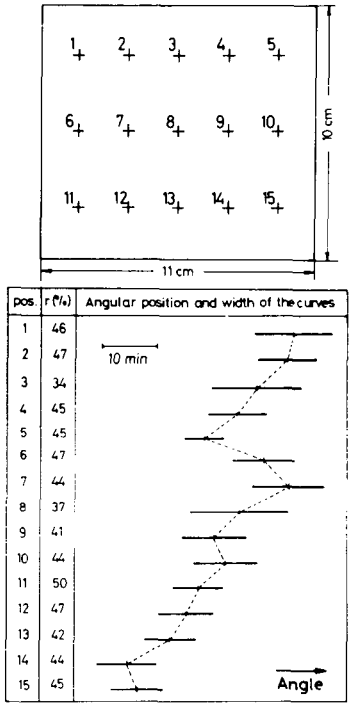


Fig. 2

A second type of inhomogeneity on a larger scale was observed in most cases by probing successively adjacent volume elements in a Cu monochromator as shown in Fig. 2. These results were obtained on the neutron diffractometer the beam cross-section being 6 x 6 mm^2. The rocking curves corresponding to the different parts of the crystal

exhibit a variation not only of their widths but also of their angular positions. Both types of inhomogeneities reduce considerably the integrated reflectivity of such a monochromator crystal as demonstrated also theoretically by model calculations[20].

HOW TO OBTAIN HIGH REFLECTIVITY ?

There have been essentially three methods which have been tried in the past to produce crystals with a controlled mosaic spread :

i) Variation of growth conditions and adding impurities[21]

ii) Machining the reflecting surface of the crystals[22]

iii) Plastic deformation of as-grown crystals[23].

Methods i) and ii) have been applied only to metals whereas method iii) was also used for Ge at high temperatures[11]. Our studies revealed that the technique iii) gave best results concerning the homogeneity and the mosaic block size necessary to avoid primary extinction to a large amount. Cu, Ge and Si crystals have been deformed plastically on the γ-ray diffractometer where it was possible to follow the evolution of the mosaic structure during the deformation process at room (Cu) and at high temperatures (Ge, Si) as a function of pressure and of temperature. Three points were found to be essential for the reproducibility and the quality of the results. Firstly, the as-grown crystals before deformation must have a low and homogeneous dislocation density (no subgrain boundaries). Secondly, the height of the samples to be deformed must be bigger than their diameter in order to get a homogeneously deformed region in the center of the samples. Thirdly, a special crystal orientation activating only one glide system when pressing should be chosen The last condition yields another additional advantage. The mosaic spread is highly anisotropic because of the special dislocation arrangement. Thus it is possible to vary the width of the rocking curve by about a factor 4 e.g. between 30' and 120' using the same set of reflecting planes and turning the crystal about an axis normal to these planes. Details of this technique have been recently given for Cu[24]. Figs. 3 and 4 give results recently obtained on Ge. Fig. 3 shows the variation of the neutron (111)-rocking curve width β and of the peak

reflectivity r as a function of the above mentioned rotation about the diffraction vector as axis (angle ϕ). Fig. 4 represents the rocking curves with the minimum and the maximum width using the same crystal of 30 x 30 x 10 mm^3 in dimension (reflection geometry).

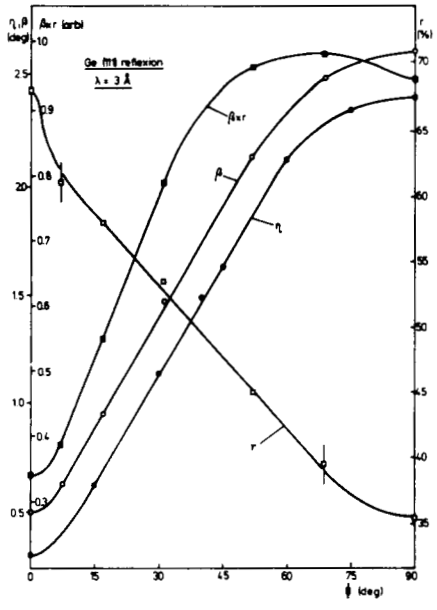


Fig. 3

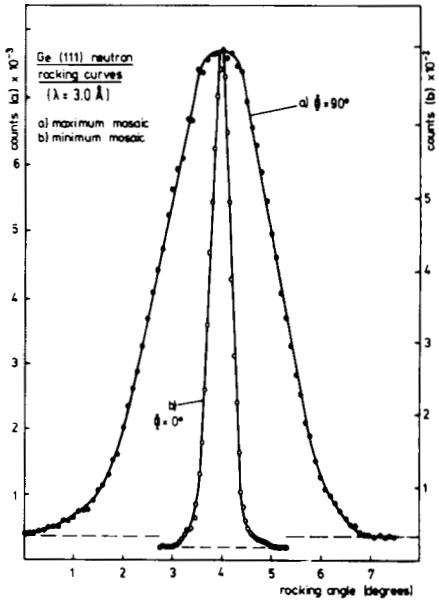


Fig. 4

Similar results have been obtained for Si. The deformation technique and results of neutron and γ-ray diffraction measurement will be published in more detail elsewhere[25]. Neutron monochromators produced in this way are now commercially available from the firm Cristal-Tec, B.P. 85 Centre de Tri, F-38041 Grenoble Cédex, France, which has contributed considerably to their development.

Another reproducible way to obtain a well-controlled and homogeneous mosaic spread has been discovered namely the diffusion of D in Nb single crystals. Nb has a somewhat smaller unit cell than Cu, low absorption and almost no incoherent scattering so that it is of great use for high energy neutron monochromators. Details about this technique have been published recently[26].

The NbD crystals as well as the deformed Cu, Ge and Si samples are smaller than the size required by the neutron beam cross-section. Monochromators have therefore to be assembled and a technique has been set

up to mount such composite monochromators. This technique permits at the same time the production of vertically and/or horizontally focusing monochromators which give a great gain in intensity when the samples to be studied are small.

CONCLUSION

It has become possible now to produce high quality neutron monochromators in a reproducible way at least as Cu, NbD and Si is concerned. Now as the mosaicity is controllable, studies of the wavelength dependence of the reflectivity at constant mosaic spread are sensible to be performed on different materials. Results of such investigations which are under way at present will permit to establish a comparative list of the efficiency of these materials and to choose the type of crystal which is suited best for given experimental conditions, i.e. wavelength, resolution, background, importance of second order contamination, etc. The corresponding monochromator system will then be "tailored" taking into account also focusing requirements.

Finally, some numbers are given: The mosaic spread η can be chosen between a few minutes and several degrees for Cu, Ge, Si and between 15 minutes and 90 minutes for NbD crystals. The absolute reflectivity in transmission geometry of 10 mm thick NbD crystals was 35% at $\lambda = 1.5$ Å and $\beta = 31'$ using the (110)-reflection. The peak reflectivity in reflection of Cu(200) crystals reached 73% at $\lambda = 1.5$ Å and $\beta = 11'$, thickness 5 mm. A "tailored" vertically focusing system made out of these crystals increased the flux on the sample by a factor 20 at the ILL instrument D10.

The Ge(111) peak reflectivity was 66% at $\lambda = 2.35$ Å and $\beta = 29'$ in reflection geometry. For comparison, under the same conditions (nearly the same d-spacing) Si(111) reflected slightly less (60%) and PG ZYA yielded 78% at $\beta = 29'$. However, using PG as monochromator one has to eliminate the second order beam contamination by a PG filter whereas Ge(111) does not reflect $\lambda/2$ neutrons. Taking 78% as transmission factor of the PG filter the PG monochromator + filter system gives a total

peak reflectivity of only 61% for a clean beam compared to 66% of Ge(111) showing a slight superiority of Ge. In addition, however, Ge has the advantage of offering several reflections with different d-spacings without second order, and the anisotropic mosaic spread - which is possible for all reflections - allowing e.g. the change of resolution without changing the monochromator or the production of a small vertical divergence of the monochromatic beam - an advantage especially for vertical focusing.

The high reproducibility of the plastic deformation technique as well as the numbers cited above show clearly that the statement given at the beginning of this paper is no more true - at least as far as thermal and slow neutrons are concerned. For fast neutrons a great effort has still to be made. Monochromator crystals of Be and of rare earth compounds (using magnetic reflections) are now being developed for this application.

REFERENCES

1. B. Dorner and A. Kollmar, J. Appl. Cryst. 7, 38 (1974).
2. T. Riste, Instrumentation for Neutron Inelastic Scattering Research, pp. 91-98. IAEA, Vienna (1970).
3. M. Antonini, M. Corchia, E. Nicotera and F. Rustichelli, Nucl. Instr. and Meth. 104, 147 (1972).
4. P. Thomas, J. Appl. Cryst. 5, 78 (1972).
5. J. Kalus, G. Gobert and E. Schedler, J. Phys. E: Sci. Instr. 6, 488 (1973).
6. H. Maier-Leibnitz, Ann. Acad. Sci. Fenn. Phys. Ser. A6, 267 (1967).
7. F. Rustichelli, Nucl. Instr. and Meth. 74, 219 (1969).
8. F. Rustichelli, Nucl. Instr. and Meth. 83, 124 (1970).
9. A. Freund, P. Guinet, J. Marechal, F. Rustichelli and F. Vanori, J. Cryst. Growth 13/14, 726 (1972).
10. A. Boeuf and F. Rustichelli, Nucl. Instr. and Meth. 107, 429 (1973).
11. Proceedings Discussion Meeting on Neutron Monochromators, ILL Internal Report 74F42S (1974).
12. D. Hohlwein, J. Appl. Cryst. 8, 465 (1975).

13. G. Albertini, A. Boeuf, S. Lagomarsino, S. Mazkedian, S. Melone, F. Rustichelli, this Conference.
14. A. Freund and J. Schneider, J. Cryst. Growth 13/14, 247 (1972).
15. J.R. Schneider, J. Appl. Cryst. 7, 541 (1974).
16. J.R. Schneider, J. Appl. Cryst. 7, 547 (1974).
17. A. Boeuf, G. Gobert and F. Rustichelli, Nucl. Instr. and Methods 124, 533 (1975).
18. M. Schlenker and J. Baruchel, this Conference.
19. A. Freund and J.R. Schneider, Proceedings of the "Dreiländer Jahrestagung über Kristallwachstum und Kristallzüchtung", Jülich, Germany, Sept. 1975.
20. J. Schneider, J. Appl. Cryst. 8, 195 (1975).
21. K.C. Turberfield, Harwell Report AERE-R 5647 (1968).
22. A. Modrzejewski and J. Kobla, Krist. und Tech. 4, 135 (1969).
23. R.R. Dymond and B.N. Brockhause, Instrumentation for Neutron Inelastic Scattering Research, p. 105, IAEA Vienna (1970).
24. A. Freund, Nucl. Instr. and Meth. 124, 93 (1975).
25. A. Freund, in preparation.
26. J.R. Schneider and N. Stump, Nucl. Instr. and Meth. 125, 605 (1975).

NEUTRON PROPERTIES OF CURVED MONOCHROMATORS

G. Albertini[x], A. Boeuf[+], S. Lagomarsino[+,xx], S. Mazkedian[xx], S. Melone[x], F. Rustichelli[+]
x Facoltà di Medicina, Universitá di Ancona (Italy)
+ J.R.C. Euratom Ispra (Italy) and
Institut Laue-Langevin, 156X Centre de Tri, 38042-Grenoble (France)
xx Facoltà di Ingegneria, Universitá di Ancona (Italy)

ABSTRACT

Several experimental data on the neutron reflectivity of curved monochromators obtained by different physicists are interpreted by using a simple model for deformed crystals based on the dynamical diffraction properties of perfect crystals.

INTRODUCTION

Curved monochromators have been developed in several laboratories in order to improve the performances of the several diffractometers and spectrometers utilized in neutron scattering experiments. Different techniques to induce a curvature in perfect or nearly perfect crystals have been used. In particular Egert and Dachs[1] have carried out neutron diffraction experiments on mechanically curved Ge monochromators to be used in Johansson or Cauchois geometries. Kalus, Gobert and Schedler[2] have bent thermally CaF_2 neutron monochromators, and they measured neutron diffraction patterns. Boeuf and Rustichelli[3] have measured integrated neutron reflectivities of Si crystals, whose curvature was obtained by microscopic techniques. In reference 4 other experiments are mentioned which will not be discussed in this paper. Moreover new data will be presented concerning the diffraction patterns of curved Si crystals. In order to interpret in a rigorous way the neutron diffraction data on ideally curved crystals one should use the dynamical theory of neutron diffraction by curved crystals, as was done by Klar and Rustichelli[5] on the basis of the wave-optical dynamical theories developed by Takagi[6] and Taupin[7] for X-ray diffraction. However simpler theoretical approaches have been used by the different authors to in-

terpret the data of references 1, 2 and 3. Recently Albertini et al[4-8] have developed a simple model to predict the neutron dynamical diffraction properties of deformed crystals. The validity of this model was checked by comparison with the theoretical diffraction patterns of ref. 5. The interpretation on the basis of this model of data published in the litterature and of some new data will be presented in this paper.

MODEL DESCRIPTION

A detailed description of the model is done in ref. 4. Only the essential physical aspects will be reported here. According to the model the curved crystal is supposed to be divided in several perfect crystals of the same thickness. Each one of these crystals has the same orientation as its median plane has in the real curved crystal. The assumption is made that each one of these crystals diffract neutrons according to its orientation, independently from the others. The thickness of each layer is determined by the condition that the misorientation between the two faces of the layer, in the real curved crystal, is equal to the width of the Darwin curve. The thickness of the layers will depend on the curvature, on the reflection and on the neutron wavelength. The reflectivity r of each layer is calculated according to the conventional dynamical theory[9]. By calling r_j the reflectivity of the generic layer, the total reflectivity r_c of the curved crystal (for a given orientation) is given by :

$$r_c = 1 - \prod_{j=1}^{n} (1-r_j) \qquad (1)$$

By calculating r_c for each orientation of the curved crystal a diffraction pattern can be obtained. In ref. 8 it is shown how neutron absorption, not considered here, could be included in the model. As the model is based on simplifying assumptions, its validity has been checked by comparison with the exact dynamical theory calculation. The agreement is very satisfactory[4-5].

EXPERIMENTAL DATA INTERPRETATION

Ge mechanically bent monochromators

Egert and Dachs[1] have measured the integrated neutron reflecting powers of mechanically bent Ge monochromators for the Bragg and Laue condition. Only the Bragg case will be discussed here. The crystal thickness was 1 mm. The integrated reflecting powers were measured as a function of the curvature at different neutron wavelengths. The 220 symmetrical reflection was measured for a radius of curvature which varied between 500 cm and 167 cm at neutron wavelength $\lambda = 1.71$ Å, $\lambda = 1.08$ Å and $\lambda = 0.85$ Å. The 351 and 531 reflections were measured in the asymmetrical case for a radius of curvature which varied between 1000 cm and 167 cm at $\lambda = 1.04$ Å. All this data have already been compared with that predicted by the model in ref. 8. Figure 1 reports a typical experimental curve for the integrated reflecting power (R^{θ}_{exp}) of the 220 reflection at $\lambda = 1.71$ Å as a function of the radius of curvature. R^{θ}_{theor} represents the curve predicted by the model. The two intersecting straight lines (R^{θ} and R^{θ}_{o}) depict the theoretical curve proposed by Egert and Dachs[1]. The experimental results as well as those discussed in ref. 8 for the same kind of monochromators appear to be in satisfactory agreement with the theoretical predictions of the model.

CaF_2 thermally bent monochromators

Kalus, Gobert and Schedler[2] have curved a 0.5 cm thick CaF_2 crystal by using a thermal gradient. They measured diffraction profiles of reflection 333 and 440 by using neutrons of wavelength $\lambda = 1.37$ Å. The measurements were carried out at three radii of curvature 27 m, 13.3 m and 8.8 m for the 333 reflection and at three radii of curvature 6.7 m, 5.4 m and 4.3 m for the 440 reflection. For each one of these experimental situations a theoretical rocking curve was calculated by using the simple model[8]. A typical diffraction pattern (r_{exp}) obtained for the 4.3 m curvature and the 440 reflection is presented in fig. 2 together with the theoretical estimation deduced from the model (r_{theor}). The dotted straight line represents the theoretical peak reflectivity evaluated by Kalus, Gobert and Schedler[2]. The experimental peak

reflectivity is roughly a factor two lower than that predicted by the model and the width is roughly a factor two higher, so that the integrated reflecting powers are nearly equals. The discrepancy could be due to the bad quality of the crystal or to a broadening effect arising from the finite width of the primary beam as discussed below for the Si. The same kind of discrepancy is found for the other data concerning CaF_2 discussed in ref. 8.

Integrated reflecting powers of curved Si monochromators

Boeuf and Rustichelli[3] have measured the ratio of integrated neutron reflectivities between plane and curved Si crystals. The crystals were 0.5 mm and 1 mm thick. The curvature was introduced in perfect crystals of 4 cm in diameter by chemical reaction at high temperature on one face. A Si_3N_4 film is produced which has a different thermal expansion coefficient from Si. As a consequence when the crystal is cooled, a spherical curvature is obtained. The measurements were carried out at different neutron wavelengths by using the (111), (115), (551) reflecting planes. The (111) planes were used in the symmetrical condition, the others in the asymmetrical condition. By a suitable change of variables, the wavelength dependence of the integrated reflecting power was converted to a curvature dependence. All the data have been interpreted in ref. 4. Fig. 3 shows the results of a typical experimental set of data obtained with the 551 reflection for two crystals of curvature radii 90 m (B_1) and 55 m (C_1) and 1 mm thick. The ratio between the integrated reflecting power (R_H^y) of the curved and perfect crystals normalized to their kinematical reflecting power (R^y (kine)) is represented as a function of c which depicts the curvature in dynamical theory units. The full line is predicted by the model. A very satisfactory agreement appears between the experimental results and the theory.

Diffraction patterns of curved Si monochromators

Some diffraction patterns of chemically curved Si crystals were recorded using the D13 double crystal diffractometer[10] at the HFR of Grenoble. Fig. 4a shows the experimental set up. The monochromatic beam was obtained using the 111 symmetrical Bragg reflection of a perfect

Si crystal. The diffraction patterns of two different Si curved crystals were recorded. Both crystals were 0.5 mm thick. The first crystal was cut with the surface parallel to the (111) plane and had a radius of curvature of 20 m. The other was cut with the surface at 10° of the (111) plane and had a radius of curvature of 12 m. The 111 reflection of both crystals was investigated. A slit of variable width was positionned in the monochromatic beam as shown in fig. 4a. Different diffraction patterns were recorded for different width of the beam ranging from a = 0.6 mm to a = 5 mm at a neutron wavelength λ = 1.8 Å. For an infinitely narrow monochromatic beam, the width of the diffraction pattern (called intrinsic width in this case) depends on the relative misorientation of the crystal planes between the points A and B (see fig. 4b). The fact that the impinging beam has a finite width introduces a broadening of the diffraction pattern which is equal to the relative misorientation of the crystal planes between the points A and D of fig. 4b. This broadening produces a reduction in the peak reflectivity. Thus the integrated reflecting power has the same value at any beam width. Fig. 5 and 6 show the rocking curves obtained with different beam widths together with the intrinsic diffraction pattern calculated from the model for the symmetrical (Fig. 5) and asymmetrical (Fig. 6) cases at a neutron wavelength λ = 1.8 Å.

Table 1. R^{θ} for different beam widths

Beam width (mm)	Symmetrical case					Asymmetrical case				
	5	3.5	1.5	1	0.6	5	3.5	1.5	1	0.6
R^{θ}_{exp} (min)	0.32	0.32	0.29	0.30	0.29	0.33	0.34	0.31	0.32	0.33
R^{θ}_{theor} (min)	0.31					0.31				

Table 1 reports the integrated reflecting powers (R^{θ}_{exp}) obtained with different beam widths at λ = 1.8 Å and the corresponding values

calculated from the model (R^{θ}_{theor}). Table 2 reports the experimental and theoretical values of R^{θ} at different wavelengths

Table 2. R^{θ} for different wavelengths

	Symmetrical case				Asymmetrical case			
λ Å	1.4	1.6	1.8	2.0	1.4	1.6	1.8	2.0
R^{θ}_{exp} (min)	0.36	0.35	0.33	0.28	0.29	0.32	0.33	0.33
R^{θ}_{theor} (min)	0.38	0.34	0.31	0.28	0.33	0.33	0.31	0.29

As it can be seen from table 1 and 2 the agreement between the model predictions and the experimental results is very satisfactory. Finally, the diffraction pattern for a beam width of 3.5 mm in the symmetrical Bragg case has been computed. The result (r_{theor}) is shown in fig. 7 together with the corresponding experimental curve (r_{exp}) (λ = 1.8 Å).

It is worthwhile to note that it is possible to obtain a foreshortening effect as proposed by Fankuchen[11] with an asymmetrical reflection in curved Si crystals without loosing in peak reflectivity. In fact from fig. 6 it can be seen that with an infinitely narrow beam, the experimental reflectivity would reach the theoretical dynamical value. More details on this effect could be found in ref. 12. In conclusion the agreement between experimental results and model predictions is very satisfactory particularly for chemically curved Si crystals.

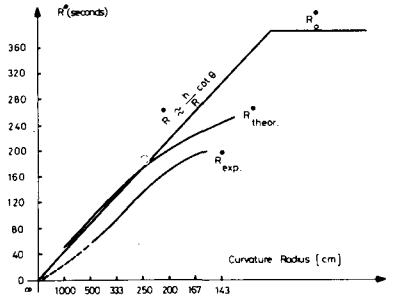


Fig. 1. Integrated reflection power of a Ge curved crystal as a function of the curvature

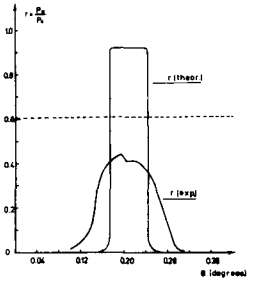


Fig. 2. Diffraction pattern of a CaF_2 curved crystal

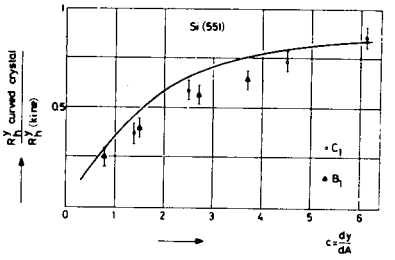


Fig. 3. The integrated reflecting power normalized by the kinematical reflecting power as a function of c for Si curved crystals

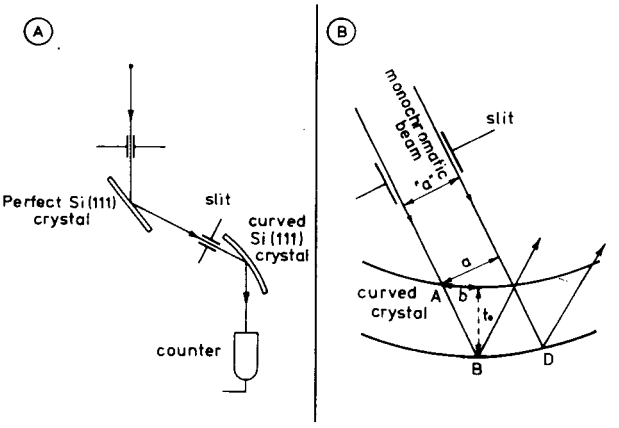


Fig. 4. a) Experimental set-up
b) the curved crystal with the impinging neutron beam

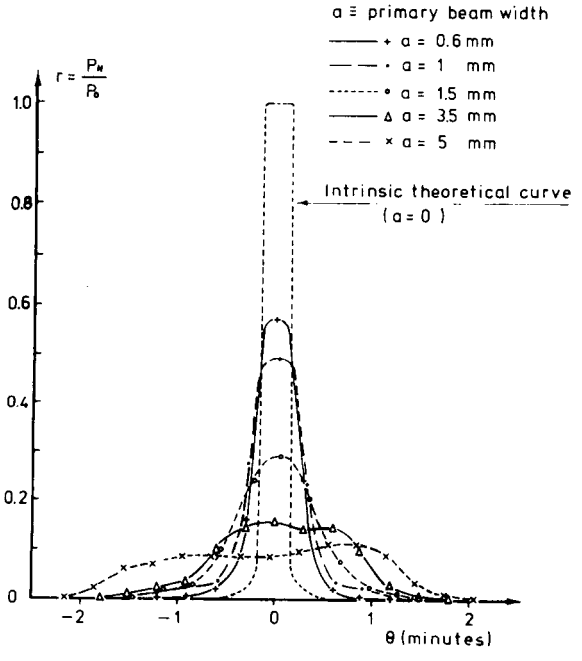


Fig. 5. Diffraction pattern of curved Si crystal for different beam widths. Symmetrical Bragg case

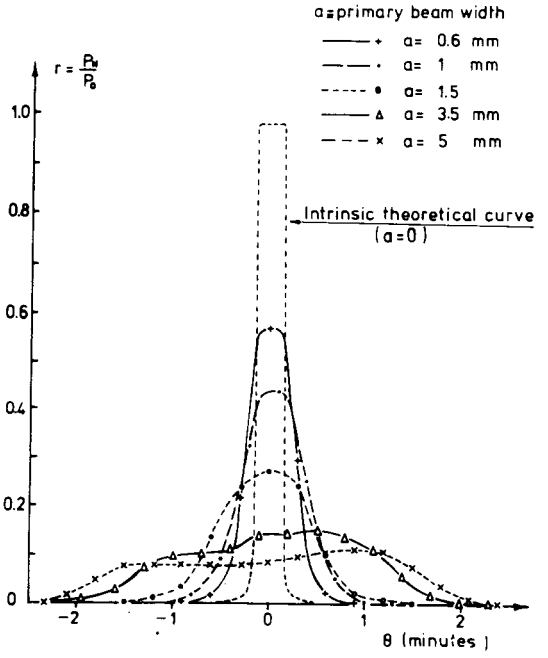


Fig. 6. Diffraction pattern of curved Si crystal for different beam widths. Asymmetrical Bragg case

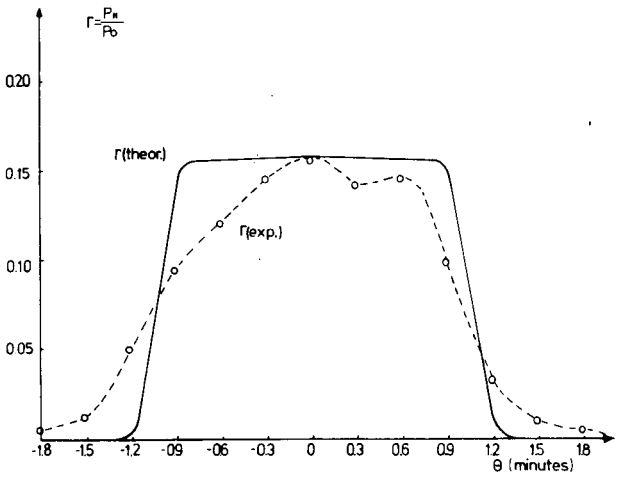


Fig. 7. Diffraction pattern of curved Si crystal
Symmetrical Bragg case. Theoretical and experimental curves

REFERENCES

1. G. Egert and H. Dachs, J. Appl. Cryst. 3, 214 (1970)
2. J. Kalus, G. Gobert, E. Schedler, J. of Phys. E, 6, 488 (1973)
3. A. Boeuf, F. Rustichelli, Acta Cryst. A30, 798 (1974)
4. G. Albertini, A. Boeuf, G. Cesini, S. Mazkedian, S. Melone, F. Rustichelli, Acta Cryst. A, in print.
5. B. Klar and F. Rustichelli, Nuovo Cimento 13B, 249 (1973)
6. S. Takagi, Acta Cryst. 15, 1311 (1962) and J. Phys. Soc., Japan 26, 1239 (1969)
7. D. Taupin, Bull. Soc., Fr. Miner. Cust. 87, 469 (1964)
8. A. Albertini, A. Boeuf, S. Mazkedian, S. Melone, V. Rozzi, F. Rustichelli, submitted to J. of Appl. Cryst.
9. W.H. Zachariasen, "Theory of X-ray diffraction", p. 24 Dover New-York (1967)
10. A. Boeuf, G. Gobert, F. Rustichelli, Nucl. Inst. and Meth., 124 533 (1975)
11. I. Fankuchen - Nature 139, 193 (1937)
    - Phys. Rev. 53, 910 (1938)
12. G. Albertini, A. Boeuf, S. Lagomarsino, S. Mazkedian, S. Melone, F. Rustichelli, submitted to Acta Cryst.

SURVEY OF DETECTION SYSTEMS AND ELECTRONICS FOR I.L.L EXPERIMENTS

J. Jacobé
Institut Laue - Langevin
Avenue des Martyrs, Cedex 156
38042 - Grenoble Centre de Tri
Cedex, France

ABSTRACT

Various systems of counting and sensing which have been developed are described. The first generation of these instruments consists of conventional detectors filled with ^3He at high pressure. Different types of BF_3 Position Sensitive Detectors (PSDs) have been developed. For powder studies we have a 400-cell curved detector (Banana) with 5 mm resolution in one dimension, angular aperture 80 and radius of curvature 1.5 m. For small angle scattering we use an area detector with 4000 and 16000 cells, position sensing in two dimensions with 5 mm of resolution and active detection diameter of 64 cm. The new high pressure ^3He PSDs are developed with 2 mm of resolution and the new electronic use the hybrid circuit technique for analogue channel.

I - INTRODUCTION

When the I.L.L was established in 1967, our first task was the selection of different types of detectors and the associated electronics. It soon became clear that the equipment available was often unsuitable for our problems. In addition the financial aspect was very important in view of the volume of our requirements.

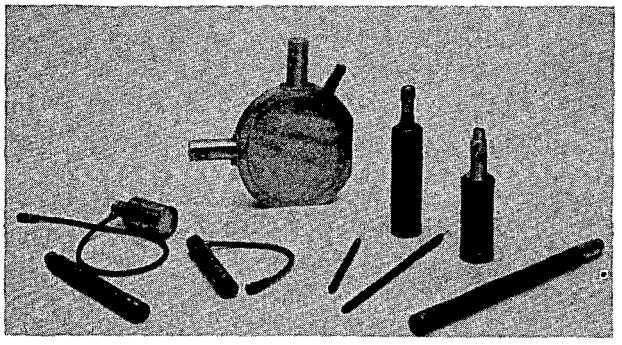
We therefore designed the equipment we required, which was then produced on a commercial basis. In this way various types of ^3He detectors* and boron-deposit monitors** suitable for our neutron beams were designed and produced commercially.

Similarly, for the electronics associated with the detectors, we have standardised*** a compact amplifier-discriminator, which can be used with all types of gas detectors.

---

*Manufactured for I.L.L by LMT **CENG-SAPTA ***MERLIN-GERIN

II - FIRST GENERATION DETECTORS AND ELECTRONICS



At I.L.L we have almost 1500 detectors (Fig. 1) which can be divided into 3 groups :

Axial Ceramic-Window Detectors (Type Ax) - For diffraction experiments ; they have diameters of 25 and 50 mm, usable lengths of 50 and 100 mm, and filling pressures of 3 and 5 bars ^3He.

Time-of-Flight Detectors TOF, with diameters of 10,25 and 50 mm, usable lengths between 10 and 30 cm and ^3He pressures of 4 to 10 bars. These detectors are characterized by a slight slope ($\Delta N/\Delta V < 1$ %/100V) which ensures a high degree of stability. In addition their technology permits very low levels of background noise (10 to 20 counts/h for the type Ax and 2 to 4 counts/h for the type TOF).

They are constructed of stainless steel, monel or aluminium ; in the last case an internal deposit of nickel ($\sim$ 50 μ) reduces the α activity and hence the background noise. The ceramic seals are vitrified, and the anode is a 50 μ tungsten wire.

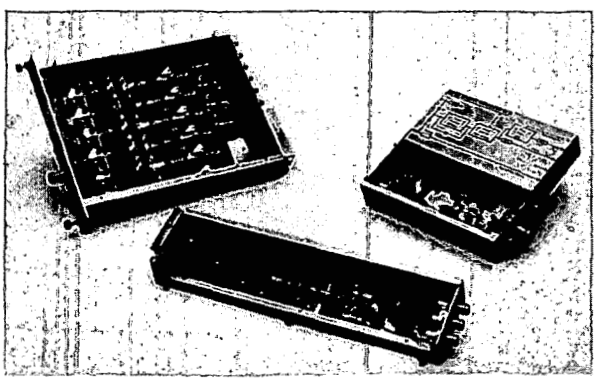
The Monitor Detectors (Fig. 2) are plane chambers operating by direct collection of charges. As a converter we use a boron deposit which is more advantageous than the uranium used in conventional fission chambers.



The cost is less and implementation is easier ; in addition the amplitude spectrum has two distinct peaks, which makes it possible to obtain two different sensitivities with good stability. They also use an unstabilized high voltage power supply. We have produced 4 types of monitors with usable diameters of 20, 50, 85 and 150 mm, the efficiency being between 10^{-6} and 10^{-2}.

In addition we are developing position sensitive monitors (X, Y coordinates) (Fig. 1) with a position sensing resolution of about 2.5 mm. These instruments permit quantitative of work on monochromatic beams to be done more quickly than by photographic systems.

The Associated Electronic is comprising in a single case (Fig. 3) the charge preamplifier (PAC), the pulse shaping amplifier and the trigger discriminator.



This analogue channel includes the high voltage supply to the detector, and the controls are limited to an adjustment of the gain and of the discrimination threshold ; this emits a TTL signal permitting transmission to the acquisition system. Various models are now produced on a commercial basis in cases with one or two channels, and also standard NIM and CAMAC cards.

The main characteristics are :

sensitivity $\sim$ 50 V/picocoulomb
input noise equivalent charge 5.10^{-16} Cb
stability $< 10^{-3}$/degree
dynamic input capacity : 1500 pF.

III - NEW GENERATION ELECTRONICS AND MULTIDETECTORS

A new generation of even more compact amplifiers has recently been developed using the hybrid circuit technique*. The unit consists of two Dual in Line (DIL) metal cases.

The First Case (16 pins) containes the PAC ; only the capacitor resistance integration loop is outside. The output is single-pole or two pole which makes it possible to attach a twisted line.

The Second (24 pins) consists of a fast linear amplifier with current and voltage input and a trigger discriminator. The only external elements are the 3 capacitors for the amplifier and the discriminator, and the two control potentiometers (gain and threshold). This may be associated with the PAC and consists of a very compact analogue channel with a very competitive price-performance ratio. It can also be used by itself as a fast current discriminator amplifier with the following main characteristics :

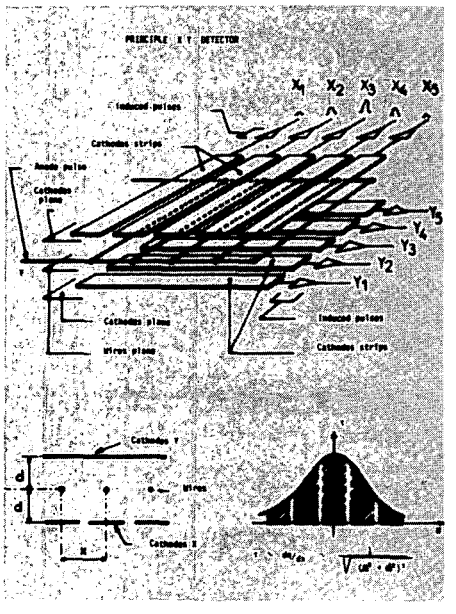
sensitivity	:	0.4 V/μA
input equivalent noise	:	0.2 μA
total voltage gain	:	5000
rise time	:	20 ηsec

*Manufactured by LMT for I.L.L

Neutron multidetectors 1, 2

Introduction - The first design studies on multidetectors for neutrons were carried out at Grenoble in 1967*. We then produced prototypes using the multi-electrode mode, which is now well-known, and a number of instruments of this type have been operational for several years at the I.L.L and in other research centres, where they increase the facilities provided for neutron diffraction and scattering.

Principle - Fig. 4 - These detectors consist of an entirely welded aluminium container. This permits the achievement of reliability equivalent to that of conventional detectors. In this container is the detection gas (BF_3) and the electrodes. These electrodes consist of two planes of cathodes situated one on each side of the plane containing the multiplication wires. As these two planes are orthogonal, they constitute the lines and columns of a matrix, the interaction of which defines an elementary detection cell.



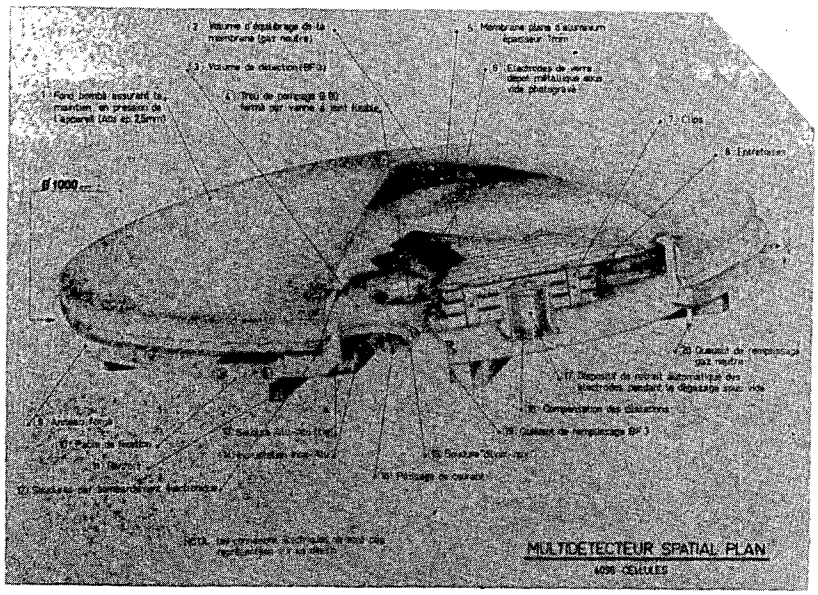
The charged particles produced by the interaction of neutrons with the ^{10}B are multiplied near the anode wires, which induces coincident electrical charges on the cathodes. The amplitude is proportional to the solid angle at which cathode band sees the multiplication point. A single neutron will produce several electrical signals on each of the planes. The processing of this information makes it possible to identify the point of the reaction with a resolution defined by the spacing of the wires for the cathodes parallel to the wires and by the path of the ionizing particles for the cathodes perpendicular to them.

*These BF_3 PSD are now built by LMT for linear detectors and by LETI-CENG for area detectors.

These cathodes consist of parallel conductive bands deposited on an insulating support ; they have a zero potential. All the anode wires are combined and are of high voltage (∿ 4 KV). An amplifier is associated with each line and column so that there are only 2n amplifiers for n^2 cells.

It is also possible to combine a "linear matrix" to make a linear detector. In this case it is necessary to pick-up the signal on the anode wire and cathode plane.

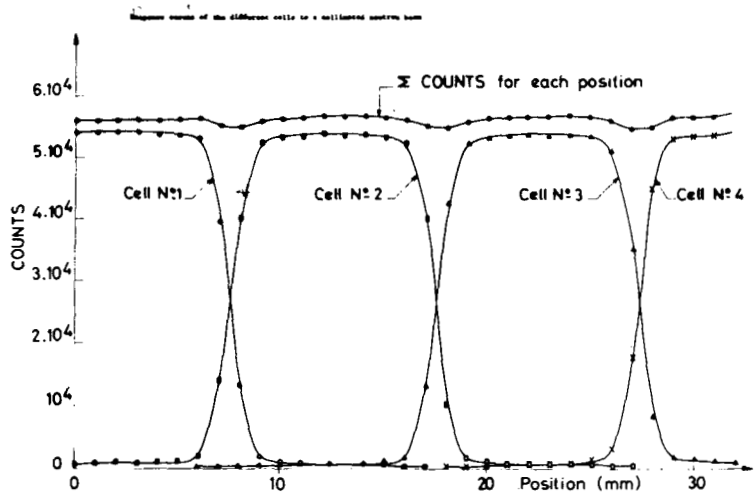
Two Dimensional (XY) Multidetector with 4000[1] or 16000[2] cells - Fig. 5



This instrument (1) has been operating since 1973 at I.L.L on the experiment D11 for the study of small angle scattering. It consists of a matrix of 64 x 64 elementary cells. This detector uses an advanced technology which guarantees very good performance and stability. A new detector with 16000 cells is at present operating on the experiment D17. The resolution is half that of the first one.

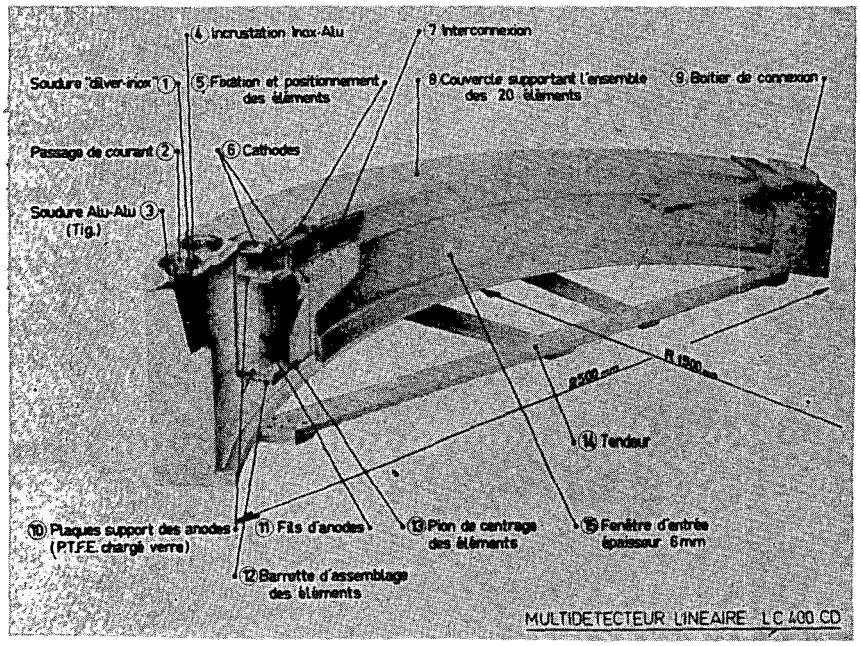
The general characteristics for (1) and (2) are :

- Spacing between cells : 10 mm, 5 mm
- Detection gap : 20 mm, 10 mm
- BF_3 filling pressure : 900 Torr, 1500 Torr
- Detection efficiency (6 Å) : 55 %, 50 %
- Background noise : 1 C/H/cells
- Stability : $\sim 2.10^{-3}$ for several days.



The response curve of the different cells to a collimated neutron beam is illustrated in Fig. 6. The linearity is good as regards sensitivity and position because these characteristics are defined by the mechanical position of the cell. The dispersion is less than 5 %. The count rate level corresponding to the base of each response curve due to the scattering of the neutron in the entry window is low ($\sim$ 0,3 %).

Linear Detector with 400 cells - Fig. 7 - This apparatus has been used at I.L.L on the experiment D1B since 1974 for power studies. It consists of a row of 20 x 20 elementary cells.



The major characteristics are :

- Angular aperture in 2θ : 80°
- Spacing between cells : 5,2 mm
- Radius of curvature : 1,50 m
- Useful height of cells : 10 cm
- Detection gap : 4,5 cm
- Detection efficiency (λ : 1.8 Å) 55 %
- Background noise : 6 C/H/cells
- Stability of several days : 2.10^{-3}

In this case the pulses are taken on the anode wire and in the cathodes, which consist of a block of 20 cells. 20 blocks are interconnected to obtain a "linear matrix". The response curve obtained is similar to that in Fig. 6 with 5 mm of resolution.

Finally it can be said that the comparative tests between these instruments and conventional diffractometers have shown that for the same measuring accuracy of the intensity of Bragg reflections, the duration of these experiments with PSD are considerably reduced (20 to 40 time).

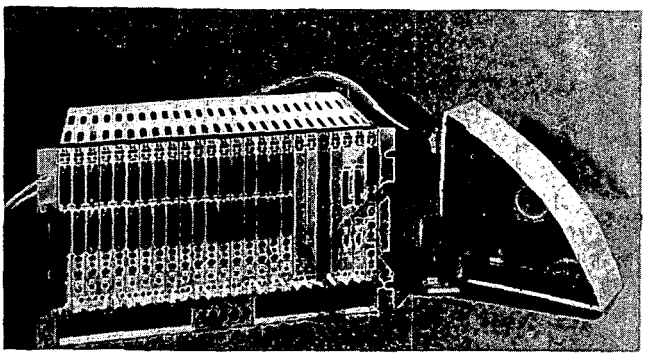
Associated Electronics - For a 400 cell multidetector, the first generation of electronics is contained in single NIM crate with :

- 40 analogue channels (8 cards of 5 channels)
- 1 logic system which will provide the computer with a word of 9 bits.

This system uses multiple electrical pulses induced by each neutron. For this purpose we use two priority encoders operating in opposite directions, i.e. one coder looks for the address above (X sup) while the second looks for the address below (X inf) and the exact address is obtained easily by $Xo = Xinf + \frac{\Delta X}{2}$

- the dead time for each event is 0,5 to 1 µsec
- the probability of address error is very low.

For the new 16000 cell multidetector we have used the new hybrid circuits technique, the whole of the electronics (Analogue and Logic) are illustrated in Fig. 8.



The PAC are near the detector and the connection to the main amplifier and discriminator are made by twisted pairs.

In the Camac crate we have 17 cards of 16 channels each and 7 cards for logic.

These techniques are now standardised for all experiments at I.L.L.

DEVELOPMENTS IN PROGRESS

To increase the efficiency of these instruments and also to permit their use with hot neutrons, we are now developing PSDs operating at high ^3He pressures. For this purpose we have filling facilities at I.L.L which enable us to carry out the various operations.

A first prototype filled under 10 bars of ^3He was successfully tested recently ; a second with lower resolution is currently being tested. This represent the new generation of linear multidetectors which will soon be operational. The general characteristics will be close to those of the current types, although the X resolution will be reduced to 2 mm with the possibility of position sensing over the detection height (Y) in steps of 5 to 10 mm ; the efficiency being 80 % for 1 Å neutrons.

We are also considering a model in the form of a hemisphere with drift space, which could be considered as the ideal detector of the future.

REFERENCES

1. R. Allemand et al., Nuclear Instrument and Methods 126, 29 (1975)

2. J. Jacobé, I.L.L Internal Report 75M42, 20 (1975)

3. B. Chardonnet and J. Jacobé, Procedings 2nd Ispra Nuclear Symposium EUR 5370, 135 (1975)

AUTHOR INDEX

Abragam, A. 1103
Albertini, G. 1151
Alefeld, B. 330
Allen, D. 102
Alperin, H. A. 517, 783
Andresen, A. F. 630
Arnau, J. L. 152
Axe, J. D. 187, 353, 406

Bacchella, G. L. 1103
Bader, S. D. 136
Barbara, B. 452
Baruchel, J. 1136
Bau, R. 507
Bauspiess, W. 1094
Begum, R. J. 643
Berney, C. V. 337
Bevaart, L. 697
Bilz, H. 195
Blume, M. 807
Bobrovsky, V. I. 230
Boeuf, A. 1151
Bonse, U. 1094
Boucherle, J. X. 452
Brown, G. M. 41, 43
Brown, P. J. 616, 650
Brugger, R. M. 1117
Brun, T. O. 529, 535, 873
Bührer, W. 77
Büldt, G. 109
Busing, W. R. 41
Buyers, W. J. L. 771

Cable, J. W. 577
Cain, J. 35
Capiomont, A. 650
Cartz, L. 55
Case, A. L. 1124
Chakravarthy, R. 638, 690
Chandra, P. P. 288
Chenavas, P. 650
Chen, S. H. 337, 962
Chesser, N. J. 295
Child, H. R. 425, 873
Christen, D. K. 481
Clarke, J. H. 955, 975, 1022
Colella, R. 1060
Collins, M. F. 418
Còmes, R. 432
Conrad, H. M. 303
Cooke, J. F. 723, 793
Coulomb, J. P. 85
Cowley, R. A. 399, 412, 935
Cox. D. E. 45, 399
Coy, R. A. 210
Croset, B. 85

Daniels, W. B. 187
Danner, H. R. 982
Darling, G. 35
Dasannacharya, B. A. 288
Daughton, W. J. 145
Daoud, M. 466
Davidson, J. B. 1124
Davis, H. L. 793
Davis, J. R. 684
de Jongh, L. J. 697
de Raedt, H. 317
Dolling, G. 243, 263
Dore, J. C. 955, 975, 1022
Dorner, B. 194, 216
Drexel, W. 558
Dufty, J. W. 968

Eagen, C. F. 1060
Eckert, J. 187
Edelstein, A. S. 873
Eder, O. J. 1028
Egelstaff, P. A. 909, 968
Eibschütz, M. 399
Ellenson, W. D. 394
Epperson, J. E. 102

Farnoux, B. 459
Farr, M. K. 152, 237
Faulkner, J. S. 800
Flaig, B. D. 40
Flotow, H. E. 517, 535
536, 543
Freeman, A. J. 250, 592
Freund, A. 1143
Frey, A. 216
Frikkee, E. 697, 832

Gerold, V. 102
Ghosh, R. E. 323
Gigüere, P. A. 152
Glättli, H. 1103

Glinka, C. J. 536, 543
Glyde, H. R. 989
Gompf, F. 129
Goshchitskii, B. N. 230
Goyal, P. S. 288
Groome, L. J. 968
Gubbins, K. E. 968
Guggenheim, H. J. 399
Gupta, M. 250
Gürmen, E. 145, 210

Hall, D. G. 800
Hastings, J. M. 393
Hautecler, S. 281
Hayter, J. B. 1074
Heger, G. 71, 439
Hellner, E. 71
Hennig, K. 878
Hennion, B. 825
Hicks, T. J. 684
Higgins, J. S. 323, 344
Hilton, P. A. 1003
Holden, T. M. 771
Houmann, J. G. 743, 840
Hutchings, M. T. 825

Iizumi, M. 406
Iyengar, P. K. 288

Jacobé, J. 1159
James, V. J. 62
Jankowska, J. 818
Jannink, G. 465
Johnson, D. H. 337
Jorgensen, J. D. 55, 529, 535

Kaiser, W. 216
Kalus, J. 243
Kaplan, T. 202
Kaun, L. 878
Kehr, K. W. 568
Khanna, F. C. 989
Kim, H. 982
Kjems, J. K. 394, 1123
Kley, W. 558
Kjekshus, A. 630
Kleb, R. 996
Koehler, W. C. 577
Kollmar, A. 330
Knapp, G. S. 136
Koetzle, T. F. 507
Koon, N. C. 783
Kostorz, G. 102
Kraan, W. H. 720
Kress, W. 175, 216
Kroeger, D. M. 473
Kunc, K. 195
Kunsch, B. 1028

Lagomarsino, S. 1151
Lander, G. H. 623
Lechner R. E. 310
Legrand, E. 281
Levy, H. A. 40, 41
Lewis, J. W. E. 954
Lippold, B. 878
Loewenhaupt, M. 856
Loveluck, J. M. 847
Lovesey, S. W. 343, 847, 954
Lowde, R. D. 825
Lynn, J. W. 1123

Majewski, R. 873
Malinovski, A. 1103
Martel, P. 1010, 1017
Marti, C. 85
Matsumoto, T. 522
Matz, W. 878
Mazkedian, S. 1151
Meister, H. 445
Melamud, M. 864
Melone, S. 1151
Men'shikov, A. Z. 663
Menzinger, F. 677
Mériel, P. 1103
Messoloras, S. 102
Meyer, J. 243
Mezei, F. 670
Michel, K. H. 317
Mikhailov, Yu. N. 230
Mikke, K. 818, 832
Miller, J. F. 529
Miller, R. J. 535
Milstein, J. B. 783
Mirmelstein, A. V. 230
Møller, H. B. 743
Mook, H. A. 481
Moon, R. M. 577
Moore, F. H. 62
Mostoller, M. 160, 167, 202
Mullen, D. 71, 439
Murani, A. 558, 657

Narten, A. H. 889

Nicklow, R. M. 117, 789
Noe-Spirlet, M. -R. 41

Ollis, J. 62
Ostrowski, G. E. 136, 996
Overhauser, A. W. 1060
Oyedele, J. A. 418

Paranjpe, S. K. 643
Passell, L. 1123
Paureau, J. 243
Pelizzari, C. A. 535, 873, 996
Peterson, S. W. 17
Piesvaux, J. 1103
Pinot, M. 1103
Pintschovius, L. 129, 432
Postol, T. A. 962
Prask, H. J. 295

Radelaar, S. 92
Radhakrishna, P. 650
Rahman, A. 535, 536
Rakhecha, V. C. 638, 690, 778
Rao, K. R. 288, 778
Rauch, H. 1094
Reddy, J. F. 623
Reichardt, W. 129, 175
181, 223
Reis, A. H. (Jr.) 17
Rekveldt, M. Th. 720
Renker, B. 432
Rhyne, J. J. 517, 783
Richter, D. 568
Rieder, K. H. 181
Riste, T. 379
Ross, D. K. 558
Rossignol, M. F. 452
Roubeau, P. 1103
Rowe, J. M. 491, 536, 543
Rush, J. J. 517, 536, 543
Rustichelli, F. 1151

Sacchetti, F. 677
Satterthwaite, C. B. 529
Satya Murthy, N. S. 638, 690
778
Saxena, A. M. 1123
Schärpf, O. 706, 713
Scheerer, B. 129
Schelten, J. 473
Scherm, R. 1003
Scheuer, H. 856
Schlenker, M. 1136
Schmatz, W. 856, 1037
Schneider, E. 223
Schofield, P. 343
Schoenborn, B. P. 35
Schweiss, P. 223
Schweizer, J. 452, 650
Sears, V. F. 36
Seelig, A. 109
Seelig, J. 109
Selte, K. 630
Shaked, H. 864
Shamir, N. 864
Shapiro, S. M. 399
Sharma, Y. P. 982
Shelton, R. N. 136
Shestakov, V. A. 663
Shimaoka, K. 406
Shirane, G. 406
Shull, C. G. 1
Sidorov, S. K. 663
Sinha, S. K. 136, 536, 873
Sköld, K. 529, 535
962, 996
Sleight, A. W. 45
Sosnowska, I. 558
Spooner, S. 481
Springer, T. 568
Srinivasa, S. R. 55
Standley, R. 535
Stanton, G. W. 955
Steiner, M. 811
Stevens, J. D. 62
Stewart, R. J. 102
Stirling, W. G. 1003, 1017
Stockmeyer, R. 303
Stortnik, H. J. 303
Stringfellow, M. W. 825
Strothmann, H. 713
Strydom, O. A. W. 43
Svensson, E. C. 771, 1010
1017

Tasset, F. 481
Thaper, C. L. 288
Thiessen, W. E. 40
Thorel, P. 85
Tocchetti, D. 558, 825
Tompson, C. W. 145, 210
Treutmann, W. 71
Trevino, S. F. 152, 237

Vagelatos, N. 543
Vanderhaeghen, J. 281
van Dijk, C. 92
Van Gerven, L. 281
Van Loef, J. J. 720
Venkatesh, A. H. 288
Vettier, C. 243
Vrijen, J. 92

Wagner, V. 175
Wakabayashi, N. 789
Walford, G. 975, 1022
Wegener, W. 281
Werner, S. A. 1060
White, J. W. 261
Wood, R. F. 160, 167
Woods, A. D. B. 1010, 1017
Worlton, T. G. 55

Yelon, W. B. 1110, 1117
Yip, S. 337

Zaccai, G. 109
Zeyen, C. M. E. 445
Zeyher, R. 550
Ziebeck, K. R. A. 616, 840

*U.S. GOVERNMENT PRINTING OFFICE: 1976-641-358/28